Department of Chemical and Environmental Engineering

LIQUID-LIQUID FLOW IN BAFFLED VESSELS AND PIPES

Ebiundu Komonibo

B Tech, MRes

November 2017

DECLARATION

I hereby declare that except where specific reference is made to the work of others, the contents of this dissertation are original and have not been submitted in whole or in part for consideration for any other degree or qualification in this, or any other University. This dissertation is the result of my own work and includes nothing which is the outcome of work done in collaboration, except where specifically indicated in the text. This dissertation contains 76,000 words including appendices, bibliography, footnotes, tables and equations.

Ebiundu Komonibo

ABSTRACT

Oil and water separation processes in primary separators and transportation of these fluids through pipelines for further processing, is very vital but has often proved problematic due to changes in composition of the fluids together with build-up of sand or asphaltenes, in many petroleum industries. These separator vessels are large and cost effective to install together with safety implications due to equipment failure. Hence an understanding of the two-phase flow dynamics and motivation to improve upon their design and performance is necessary. Therefore, the main aim of this research programme is to investigate the coalescence efficiencies of droplet size in both stirred tank and horizontal pipe line under turbulence in oil-water two phase systems and also to determine the possibility of using a compact sudden pipe expansion as a phase separator for converting dispersed flow to segregated flow.

For the purpose of experimental investigations, a sudden pipe expansion rig was designed, constructed and commissioned in L3 main laboratory of the department of Chemical and Environmental Engineering, University of Nottingham, UK. The fluids used are tap water ($\rho_w = 998 Kgm^{-3}; \mu_w = 0.0010 Kgm^{-1}s^{-1}$) and silicone oil 5cp, ($\rho_w = 916 Kgm^{-3}; \mu_w = 0.0052 Kgm^{-1}s^{-1}$) at operating conditions for mixture velocities between 0.20 ms^{-1} – 3.50 ms^{-1} and input oil volume fraction from 20% OVF to 80% OVF at different pipe inclinations ($+4^0$, $+2^0$, 0^0, -2^0,-4^0). Ring conductance probes were used to obtain phase layer distribution information of the oil-water flow together with the backscatter Lasentec FBRM M500P laser for drop size measurements and Phantom PCC 2.7 high speed camera for imaging.

In both horizontal and upward inclined flows, the input oil volume fraction and mixture velocity strongly influenced the formation of drop sizes downstream of the expansion, due to coalescence mechanism. Coalescence of both oil and water dispersed phase droplets and segregation was found to start at short distance from the inlet section and progresses gradually downstream of the pipe expansion. The water droplets coalesce and settles faster than dispersed oil droplets in water continuous phase flow system and also the bulk oil layer was observed to flow faster at the top than the bottom water layer for the horizontal and upward flow conditions. Therefore

the results reveals a strong influence of mixture velocity, input oil volume fraction and pipe angle inclination on drop break up and coalesce mechanisms in oil-water flow systems.

The results obtained satisfactorily agree well with the existing conventional flow patterns and flow pattern maps. The flow patterns identified includes, stratified flow (ST), stratified with mixed interface (ST& MI), oil-water intermittent flow, stratified wavy flow and dispersed flow in all pipe orientations. Additional flow patterns were also observed such as Raleigh Taylor 'plume shaped' flow in the horizontal flow and plug wavy flow (Caterpillar like waves) in both upward and downward inclination, which have not been reported in large diameter pipes. There was evidence of stratification for fully developed ST regime at short distance from inlet (10D) at mixture velocities below $0.30ms^{-1}$ in both horizontal and upward inclinations.

Therefore, in order to achieve stratified flow in oil-water two-phase flow system, a sudden pipe expansion was used successfully to convert a dispersed flow to segregated flow within a 6m long test pipe distance. The best orientation was that of the horizontal flow position for dispersed flows to separate quickly as both the upward and downward inclined pipe flow conditions tend to hamper the evolution process by increasing the mixed layer region.

ACKNOWLEDGEMENT

First and foremost I want to thank the Almighty God for the successful completion of my PhD research work. May His name be praised and let all Glory be ascribed to Him in Jesus name Amen.

I would like to express my sincere thanks and appreciation to my principal supervisor, Dr Buddhika Hewakandamby for an excellent supervision and guidance. He was patient with me and devoted time to my queries and was forthcoming with support, advice and suggestions. I would also like to extend my gratitude to my second supervisor, Prof Barry J. Azzopardi, my academic mentor and granddad for his assistance and his great support throughout this work.

I want to express my thanks to all the entire technician crew led by Phil Bennet, and others especially Fred Anderton, Karl Gregg, Alex, Mel Hemslay, Mick, Rech for their help during my experimental work in the lab. I will also not forget to express my sincere appreciation and respect to Mrs Marion Bryce and Mrs Katy A, for their invaluable laboratory assistance and administrative support.

My thanks and appreciation to all the members of my research group, Fluid and Thermal Engineering (FLUTE) including; Dr David Hann, AlAuufi, Yusuf, Al-Behadili Mustafapha, Escreg Joseph, Loizou Katerina, Mohammed Shara, Omar Rajab, Vasques Joao, Yates Mathew, and Ibrahim Abubakr and other students in the Department of Chemical and Environmental Engineering at the University for their input in various capacities.

This research project was financially supported by a postgraduate scholarship from the Nigerian government through the PTDF. I gratefully acknowledge this support.

I wish to express my sincere thanks to my parents, Late HRH Jesse Bosson Komonibo and Late Mrs Lady Komonibo and family members for their moral support and prayers. Special love and thanks to my beloved, lovely wife Mrs. Esther Komonibo and my lovely children, Ebiowei Emmanuel Komonibo, Ebiere Emmanuella Komonibo, Ebiokpo David Komonibo and step children, Tonye Breana and Grace Ebitare Johnson for their moral and spiritual support, encouragement and prayers.

TABLE OF CONTENT

DECLARATION ..... **i**

ABSTRACT ..... **ii**

ACKNOWLEDGEMENT ..... **iv**

TABLE OF CONTENT ..... **v**

LIST OF FIGURES ..... **xii**

LIST OF TABLES ..... **xxxi**

NOMENCLATURE ..... **xxxii**

Chapter 1 INTRODUCTION **1**

1.1 Background 2

1.2 Challenges identified in crude oil production 3

1.3 Motivation 5

1.4 Research aims and objectives 6

1.5 Thesis Overview 7

Chapter 2 LITERATURE REVIEW **10**

2.1 Introduction 10

2.2 Liquid – Liquid Flow patterns and Flow pattern maps in pipes 15

2.2.1 Flow pattern in horizontal pipes 16

2.2.2 Flow pattern maps and identification in vertical and inclined pipes 28

2.2.2.1 Flow Pattern in Vertical Pipe Systems 28

2.2.2.2 Flow Pattern in inclined Pipe Systems 29

2.2.3 Stratifying Oil – Water Flows 34

2.2.4 Phase inversion and flow pattern transitions 36

2.2.4.1 Phase inversion 36
2.2.4.2 Flow pattern transitions and boundaries 38
2.2.5 Parameters with impact on the flow patterns 44
2.3 Fundamentals of Liquid-Liquid Coalescence and Dispersion 45
2.3.1 Drop breakage and coalescence mechanism 49
2.3.2 Models and correlations for mixing vessels and stirred tanks 57
2.3.3 Drop size distribution measurement techniques 60
2.3.3.1 Laser Diffraction 60
2.3.3.2 Photographic and video technique 61
2.3.3.3 Droplet encapsulation 61
2.3.3.4 Dual optical probe technique 61
2.3.3.5 Electrical Conductivity or Capacitance 62
2.3.3.6 Laser backscatter technique - Lasentec Focused Beam Reflectance Measurement (FBRM M500P) 63
2.3.3.7 Endoscope (Bores scope) measurement techniques 64
2.3.4 Drop size estimation 66
2.4 Liquid holdup and phase fraction measurement technique 69
2.4.1 Measurement of oil volume fraction 69
2.4.1.1 Electrical process technology 70
2.4.1.2 Gamma radiation attenuation 71
2.4.1.3 Wire Mesh Sensor (WMS) 72
2.4.1.4 Conductance probe 74
2.4.2 Physical models and correlations for oil volume fraction estimation 77
2.4.2.1 Two fluid model 77
2.4.2.2 Homogeneous model 78
2.4.2.3 Models for pressure gradient 78
2.5 Summary 80

Chapter 3 LIQUID-LIQUID FLOW IN STIRRED BAFFLED VESSEL 82
3.1 Introduction 82
3.2 Theory of drop breakup and coalescence 82

3.3 Description of experimental facility and properties of fluids used.....84
3.4 Experimental procedure and test conditions.....88
3.4.1 Experimental procedure.....88
3.4.2 Test conditions.....90
3.5 Instrumentation.....91
3.5.1 Laser backscatter equipment and drop size measurement.....91
3.5.1.1 Verification of Lasentec FBRM M500P.....92
3.5.1.2 Drop size measurements.....95
3.5.2 HotShot High speed camera video recording.....95
3.6 Experimental results and discussions.....96
3.6.1 Droplet size estimation and calculations.....101
3.6.2 Characteristics of drops distribution.....101
3.6.3 Drop breakup and coalescence in turbulence dispersions.....116
3.6.4 Video analysis.....120
3.7 Summary.....123

Chapter 4 EXPERIMENTAL RIG AND INSTRUMENTATION.....124
4.1 Description of liquid-liquid horizontal flow sudden expansion rig facility.....124
4.1.1 Separator and fluids storage tanks.....126
4.1.2 Control systems.....128
4.1.3 Fluids requirements.....130
4.1.4 Test section.....130
4.1.5 Fluids properties.....133
4.2 Experimental design.....133
4.2.1 Determination of inlet parameters.....133
4.2.2 Test matrix.....135
4.3 Instrumentation.....139
4.3.1 Lasentec FBRM M500P Laser and drop size measurement.....139

4.3.2 Differential pressure transducers 141
4.3.3 Flowrate meters 142
4.3.4 Conductance probe 144
4.3.4.1 Design and principles of conductance ring probes 145
4.3.4.2 Calibration and validation of conductance probes 148
4.3.4.3 Measurement protocol 151
4.3.4.4 Data acquisition system and normalization with conductance ring probe 152
4.3.4.5 Determination of oil volume fraction (OVF) 153
4.3.5 Thermocouple 153
4.3.6 Phantom PCC 2.7 High Speed Camera 153
4.3.6.1 Investigation of oil-water interface 154
4.4 Uncertainty of experimental measurements 155

Chapter 5 DROP SIZE RESULTS AND DISCUSSIONS ON LIQUID-LIQUID FLOW IN PIPES 157
5.1 Theory and characteristics of drop distribution 157
5.1.1 Rosin-Rammler distribution 158
5.1.2 Log normal distribution 158
5.1.3 Sauter mean diameter 158
5.2 Inlet parameters, rig configuration and experimental design 159
5.2.1 Drop size in horizontal flow 160
5.2.1.1 Effect of input oil volume fraction 161
5.2.1.2 Effect of mixture velocity 164
5.2.1.3 Effect of probe position 171
5.2.1.4 SMD in mixed layer and vertical distance from interface 173
5.2.2 Drop size in upwardly inclined flow 177
5.2.2.1 Effect of input oil volume fraction on SMD 178
5.2.2.2 Effect of mixture velocity 181
5.2.2.3 SMD in mixed layer and vertical distance from interface 186
5.2.2.4 Effect of probe position 191

5.2.3 Drop size in downwardly inclined flow 194
5.2.3.1 Effect of input oil volume fraction 194
5.2.3.2 Effect of mixture velocity 197
5.2.3.3 SMD in mixed layer and vertical distance from interface 204
5.2.3.4 Effect of probe position 208
5.3 Comparison between different angles of inclination 212
5.4 Comparison with existing models 220
5.5 Summary 234

Chapter 6 ESTIMATION OF OIL VOLUME FRACTION DOWSTREAM OF PIPE EXPANSION 237
6.1 Experimental data analysis 237
6.1.1 Probability density function (PDF) 237
6.1.2 Cross correlation and structure velocity 238
6.1.3 Power Spectrum Density (PSD) 239
6.2 Conductance probe results and discussions 240
6.2.1 Flow pattern development downstream of pipe expansion 240
6.2.1.1 Horizontal pipe expansion 241
6.2.1.2 Upwardly inclined pipe expansion 253
6.2.1.3 Downwardly inclined pipe expansion 256
6.3 Evolution of interface and the Effect of Inlet parameters and rig configuration on oil volume fraction (OVF) in horizontal flow. 258
6.3.1 Effect of input oil fraction 259
6.3.2 Effect of mixture velocity 262
6.3.3 Mixed interface height and mixture velocity 264
6.3.4 Evolution of mixed interface height 267
6.4 Evolution of interface and Effect of Inlet parameters and rig configuration on oil volume fraction (OVF) in upwardly inclined flow 267
6.4.1 Effect of input oil fraction 268
6.4.2 Effect of mixture velocity 270

6.4.3 Mixed interface height and mixture velocity 272
6.4.4 Evolution of mixed interface height 272
6.5 Evolution of interface and Effect of Inlet parameters and rig configuration on oil volume fraction (OVF) in downwardly inclined flow 276
6.5.1 Effect of input oil fraction 276
6.5.2 Effect of mixture velocity 278
6.5.3 Mixed interface height and mixture velocity 280
6.5.4 Evolution of mixed interface height 280
6.5.5 Comparison between different angles of inclination 283
6.5.6 Characteristics of oil-water two-phase structure in 127mm pipe 286
6.5.6.1 Time series and Probability Density Function (PDF) 286
6.6 Summary 290

Chapter 7 CONCLUSION AND RECOMMENDATIONS 292
7.1 Findings and Contributions to knowledge 292
7.2 Comments on experimental programme 292
7.3 Drop size distribution 293
7.4 Flow patterns and flow pattern maps 295
7.5 Stratification of dispersion in large diameter pipe 296
7.6 Oil volume fraction 296
7.7 Recommendations for future work 297

REFERENCE 299

APPENDIX A 313

APPENDIX B 318

APPENDIX C 321

APPENDIX D 325

APPENDIX E **329**

APPENDIX F **335**

APPENDIX G **344**

APPENDIX H **346**

LIST OF FIGURES

Figure 2-1: Sudden pipe expansion configurations 11
Figure 2-2 (a)-(b) Single and Two phase sudden pipe expansion, Azzopardi and Hills (2001).....12
Figure 2-3 Flow patterns classification for oil-water flow (Oglesby, 1979) 18
Figure 2-4 Flow patterns defined by (Arirachakaran et al., 1989). 19
Figure 2-5 Horizontal oil-water flow pattern sketches (Trallero, 1995). 21
Figure 2-6 Horizontal oil-water flow pattern map (Trallero, 1995). 21
Figure 2-7 Horizontal oil-water flow patterns (Nädler and Mewes, 1997) 22
Figure 2-8 Experimental horizontal flow pattern map – superficial velocities of oil and water (Nädler and Mewes, 1997).....23
Figure 2-9 Schematic of multi-point sampling probe (Fairuzov et al., 2000) 24
Figure 2-10 Comparison of experimental data with theoretical transition boundaries (Fairuzov et al., 2000).....24
Figure 2-11 Flow conditions for measurements of the thickness of the three phase layers in the ST & MT regime (Yang et al., 2003).....25
Figure 2-12 Experimental flow pattern map D = 38.1 mm, $\mu_o/\mu_w = 5.5$ $\rho_o/\rho_w = 0.83$, $\sigma = 0.039 Nm$ (Lovick and Angeli, 2004b).....26
Figure 2-13 Experimental flow pattern map D = 14 mm, $\mu_o/\mu_w = 5.5$ $\rho_o/\rho_w = 0.83$, $\sigma = 0.039 Nm$, Flow patterns: ST (stratified smooth or wavy), DC (dual continuous), SG (slug), Bb (bubble) and AN (annular), (Al-Wahaibi and Angeli, 2011). 26
Figure 2-14 Experimental flow pattern map of (Yusoff, 2012) showing mixture velocities after orifice (Usmo) and mixture velocities downstream (Usme) of flow pattern encountered within the rig and possible operational limits plotted on flow pattern map of (Trallero et al., 1997)Trallero et al. (1997). 27
Figure 2-15 Experimental flow pattern map (Barral and Angeli, 2014). 27
Figure 2-16 Schematic representations of vertical oil-water flow patterns by (Flores et al., 1997) 28
Figure 2-17 Experimental Measurent Set – Up for (Vigneaux et al., 1988) 30

Figure 2-18 Schematic representation of upward inclined oil-water flow patterns by (Flores et al., 1997) 31
Figure 2-19 (a) Sketch of some observed water–gas flow patterns with typical corresponding inclinations; (b) sketch of some observed oil–water–gas flow patterns with typical corresponding inclinations, (Oddie et al., 2003) 32
Figure 2-20 Comparison of Phenomenological model predictions for water holdup, ε_w with experimental dataset, (Rodriguez and Baldani, 2012). 35
Figure 2-21 Comparison of Phenomenological model predictions for pressure gradients with experimental dataset, (Rodriguez and Baldani, 2012). 36
Figure 2-22 Phase inversion process for an O/W flow (Arirachakaran et al., 1989). 37
Figure 2-23 Flow Pattern Map of (Brauner and Moalem Maron, 1992) compared with experimental data of (Guzhov, 1973) 40
Figure 2-24 Drop Breakup Mechanism 52
Figure 2-25 Drop Coalescence Mechanism 54
Figure 2-26 Conceptual framework for coalescence modelling, (Thomas, 1981, Chesters, 1991) 54
Figure 2-27 Operation of Malvern 2600 instrument 60
Figure 2-28 The Focused Beam Reflectance Measurement Technique (FBRM) probe using light back scattering effects for drop sizing (Ruf et al., 2000). 63
Figure 2-29 Principle of operation of the Par-Tec instrument. 64
Figure 2-30 Detail 3D drawing of the endoscope probe and general set-up (Maaß et al., 2011) 65
Figure 2-31 Example images, representing samples taken with the endoscope technique using different lenses according to the expected particle size for two different liquid-liquid systems as presented by (Maaß et al., 2011) 65
Figure 2-32 Principle of wire-mesh sensor having 2 x 8 electrodes (a). Wire-mesh sensor for the investigation of pipe flows and associated electronics (b), (Helmholtz - Zentrum and Dresden-Rossndorf., 2012) 72
Figure 2-33 Electrical schematic of capacitance WMS (Da Silva et al., 2007) 73
Figure 2-34 Two-phase multiplier versus Lockhart - Martinelli parameter 79
Figure 3-1 Experimental set-up for droplet size measurements in liquid-liquid agitated vessel. 85
Figure 3-2 Measurements performed on pendant drop of silicone oil and water 87

Figure 3-3 The effect of mixing time for silicone oil volume fraction, 40% OVF at impeller speed, N = 1200 rpm. Note: Channels (Ch), represents number of drop diameter bins (1-100%) 89
Figure 3-4 Experimental set up of a Cylindrical Baffled Stirred Tank 90
Figure 3-5 Typical diagram of Lasentec FBRM system connected to a computer (Mettler Toledo).....92
Figure 3-6 PVC Reference procedure set up Lasentec (2007) 93
Figure 3-7 PVC reference calibration sample cumulative frequency curves (%) Lasentec (2007.....94
Figure 3-8 Chord length distribution for dispersed phase oil volume fraction, ε_d = 20% at impeller speed of 800 rpm and 1200 rpm at 105 mm probe position.....96
Figure 3-9 Drop diameter distribution for dispersed phase oil volume fraction, ε_d = 20% at impeller speed of 800 rpm and 1200 rpm at 105 mm probe position.....97
Figure 3-10 Chord length distribution for dispersed phase oil volume fraction, 30% at impeller speed of 800 rpm and 1200 rpm at 105 mm probe position.....97
Figure 3-11 Drop diameter distribution for dispersed phase oil volume fraction, ε_d = 30% at impeller speed of 800 rpm and 1200 rpm at 105 mm probe position.....98
Figure 3-12 Chord length distribution for dispersed phase oil volume fraction, ε_d = 80% at impeller speed of 800 rpm and 1200 rpm at 105 mm probe position.....98
Figure 3-13 Drop diameter distribution for dispersed phase oil volume fraction, ε_d = 80% at impeller speed of 800 rpm and 1200 rpm at 105 mm probe position.....99
Figure 3-14 High speed camera images of dispersed phase oil volume fraction (OVF), ε_d = 20%, 30% and 80% at impeller speed of 800 rpm and 1200 rpm respectively. 99
Figure 3-15 Effect of low impeller speed, 800rpm, (Re 7434) on drop size distribution for dispersed phase oil volume fraction, ε_d = 0.2, 0.4, 0.6 and 0.8 100
Figure 3-16 Effect of high impeller speed, 1200 rpm, (Re 11218) on drop size distribution for oil volume fraction, ε_d = 0.2, 0.4, 0.6 and 0.8.....101
Figure 3-17 Rosin-Rammler distribution fit to 800 rpm, (Re 7434) for oil volume fraction, ε_d = 20% OVF.....103

Figure 3-18 Rosin-Rammler distribution fit to 800 rpm, (Re 7434) for oil volume fraction, ε_d = 30% OVF.....103
Figure 3-19 Rosin-Rammler distribution fit to 800 rpm, (Re 7434) for oil volume fraction, ε_d = 50% OVF.....104
Figure 3-20 Rosin-Rammler distribution fit to 800 rpm, (Re 7434) for oil volume fraction, ε_d = 80% OVF.....104
Figure 3-21 Comparison of Rosin-Rammler distribution fits to 800 rpm, (Re 7434) for oil volume fractions, ε_d = 20%, 30% and 50% OVF 105
Figure 3-22 Rosin-Rammler distribution parameter, (ζ) vs dispersed phase oil volume fraction.....105
Figure 3-23 Log-normal distribution parameter, (δ) vs dispersed phase oil volume fraction.....108
Figure 3-24 Comparison of Log-normal and R-R distribution fits to 800rpm, (Re 7434) for oil volume fraction, ε_d = 30% 108
Figure 3-25 Comparison of Log-normal and R-R distribution fits to 800rpm, (Re 7434) for oil volume fraction, ε_d = 70% 109
Figure 3-26 Comparison of Log-normal and R-R distribution fits to 800rpm, (Re 7434) for oil volume fraction, ε_d = 80% 109
Figure 3-27 Sauter mean diameter vs impeller speed for different dispersed phase oil volume fractions. 112
Figure 3-28 Sauter mean diameter vs dispersed phase oil volume fraction for various impeller speeds. 112
Figure 3-29 Chord length vs time for 30% dispersed phase oil volume fraction at 105 mm probe position and impeller speed 1000 rpm. 113
Figure 3-30 Chord length vs time for 40% dispersed phase oil volume fraction at 105 mm probe position and impeller speed 900 rpm. 114
Figure 3-31 Volume of oil layer vs time of coalescence for 30% dispersed phase oil volume fraction.....115
Figure 3-32 Volume of oil layer vs time of coalescence for 40% dispersed phase oil volume fraction.....115

Figure 3-33 Sauter mean diameter vs impeller speed for 30% dispersed phase oil volume fractions in drop breakup experiment 116
Figure 3-34 Sauter mean diameter vs impeller speed for 30% dispersed phase oil volume fractions in drop coalescence experiment 118
Figure 3-35 High speed camera images of 30% oil fraction (a) 800 rpm (b) 900 rpm (c) 1200 rpm. 120
Figure 3-36 High speed camera images of 40% oil fraction (a) 350 rpm (b) 400 rpm (c) 1200 rpm. 121
Figure 3-37 High speed camera images of 50% oil fraction (a) 800 rpm (b) 900 rpm (c) 1200 rpm. 121
Figure 3-38 High speed camera images of 70% oil fraction (a) 800 rpm (b) 900 rpm (c) 1200 rpm. 121
Figure 3-39 Photographs of drop break up from (a) to (b). 122
Figure 3-40 Photographs images of (a) drop coalescence (b) drop coalescence at the liquid –liquid silicone oil/water interface. 122
Figure 4-1 Schematic diagram of liquid-liquid flow sudden pipe expansion rig facility 125
Figure 4-2 Liquid Storage Tanks and Separator vessel 126
Figure 4-3 Internal arrangement of Separator tank 127
Figure 4-4 Two Centrifugal pumps for water and silicone oil 128
Figure 4-5 Pressure transducers installed at bottom of water storage tank for level sensing 128
Figure 4-6 Control valves for fluids inlet 129
Figure 4-7 Large scale liquid-liquid rig facility model (Pipe diameter ϕ 127 mm) 130
Figure 4-8 Liquid – liquid horizontal flow pipeline sudden expansion rig in L3 Main Laboratory, ... 131
Figure 4-9 Cross- section of sudden pipe expansion 131
Figure 4-10 Photograph of both flow meters in place for flowrate measurements . 132
Figure 4-11 Specially fabricated homogenizer made of Perspex block with inner mixing chamber, connected with two pipes for oil and water dispersions. 132
Figure 4-12 Experimental flow pattern map of current work. $D = 127mm$, $\mu_o/\mu_w = 5.2$, $\rho_o/\rho_w = 0.918$ 138

Figure 4-13 Possible operational limits and flow patterns to be encountered within the rig in current study, plotted in the flow pattern map of Trallero et al. (1997).....138
Figure 4-14 Photograph of the removable measurement section with position for FBRM M500P laser instrumentation.....139
Figure 4-15 FBRM M500P laser measurements at top, interface and bottom of pipe 140
Figure 4-16 FBRM M500P laser measurements (i) Chord length distribution, (CLD) (ii) Drop diameter distribution (DDD) 141
Figure 4-17 Photograph of Differential pressure transducers installed on the rig...141
Figure 4-18 Calibration results of the differential pressure cells. 142
Figure 4-19 Electromagnetic flowmeter (M920).....143
Figure 4-20 Paddle wheel truflo meter (TKM-50-RS-PVC).....144
Figure 4-21 Original conductance probe electronics diagram (Fossa, 1998).....147
Figure 4-22 Schematic diagram of modified electrical circuit of conductance probes. 147
Figure 4-23 Electrode arrangement in the cylindrical test section pipe (ϕ127mm) 148
Figure 4-24 Relationship between voltage constant E, and variable resistance R_x and reference resistance R_{ref}.....149
Figure 4-25 Calibration curve of oil volume fraction (OVF), vs dimensionless conductance Ge* for individual probes (CP 1, CP2, CP3, CP4 – conductance probe positions).....150
Figure 4-27 Data acquisition system 151
Figure 4-28 An example of conductance probe measurements (oil volume fraction time series plot for water cut 20%, 50% and 80%, mixture velocity 0.35m/s and horizontal flow at the different probe positions) 152
Figure 4-29 Type K thermocouple 1.5mm 153
Figure 4-30 Phantom PCC 2.7 Camera setup on the Liquid-liquid rig facility.....154
Figure 4-31 Interface height image processing, showing dimensionless oil and water heights.....155
Table 4-3 Total instrumental deviations.....156
Figure 5-1 Lasentec FBRM M500P laser probe positions, downstream of expansion and vertical height in a pipe cross-section from bottom to top of the pipe 160

Figure 5-2 Mixture velocities upstream and downstream of flow pattern transition through the sudden expansion plotted on the flow pattern map of Trallero et al. (1997) 161
Figure 5-3 Sauter Mean Diameter (d_{32}), for downstream mixture velocity, U_{sme} = 0.20 ms^{-1}, within axial distances of test section in horizontal pipe orientation, probe position 15.9 mm from bottom of pipe at different oil volume fraction, OVF.....162
Figure 5-4 Sauter Mean Diameter (d_{32}), for downstream mixture velocity, U_{sme} = 0.20 ms^{-1}, within axial distances of test section in horizontal pipe orientation, probe position interface (63.5 mm) from bottom of pipe at different oil volume fraction, OVF. 163
Figure 5-5 Sauter Mean Diameter (d_{32}), for downstream mixture velocity, U_{sme} = 0.20 ms^{-1}, within axial distances of test section in horizontal pipe orientation, probe position Top (111.3 mm) from bottom of pipe at different oil volume fraction, OVF. 164
Figure 5-6 Effect of downstream mixture velocity on Sauter Mean Diameter (d_{32}) for flow condition, at 10D axial distance of test section in horizontal pipe orientation, probe position (15.9 mm) from bottom at different input oil volume fraction.....165
Figure 5-7 Effect of downstream mixture velocity on Sauter Mean Diameter (d_{32}) for flow condition, at 10D axial distance of test section in horizontal pipe orientation, probe position Top (111.3 mm) from bottom at different input oil volume fraction 166
Figure 5-8 Influence of downstream mixture velocity on Sauter Mean Diameter (d_{32}) for flow condition, 80% OVF at 10D axial distance of test section in horizontal pipe orientation, at different probe position 167
Figure 5-9 Effect of downstream mixture velocity on Sauter Mean Diameter (d_{32}) for flow condition, at 30D axial distance of test section in horizontal pipe orientation, probe position Top (111.3 mm) from bottom at different input oil volume fraction 167
Figure 5-10 Sauter Mean Diameter (d_{32}) for flow condition, 20% OVF, within axial distance of test section in horizontal pipe orientation, probe position Top (111.3 mm) from bottom of pipe at different downstream mixture velocity, U_{sme}. 168
Figure 5-11 Sauter Mean Diameter (d_{32}) for flow condition, 40% OVF, within axial distance of test section in horizontal pipe orientation, probe position Centre (63.5 mm) from bottom of pipe at different downstream mixture velocity, U_{sme}. 169

Figure 5-12 Sauter Mean Diameter (d_{32}) for flow condition, 60% OVF, within axial distance of test section in horizontal pipe orientation, probe position Centre (63.5 mm) from bottom of pipe at different downstream mixture velocity, U_{sme}. 170
Figure 5-13 Sauter Mean Diameter (d_{32}) for flow condition, 80% OVF, within axial distance of test section in horizontal pipe orientation, probe position Bottom (15.9 mm) from bottom of pipe at different downstream mixture velocity, U_{sme}.....170
Figure 5-14 Sauter Mean Diameter (d_{32}), of oil droplets for mixture velocity, U_{sme} = 0.20 ms^{-1}, oil volume fraction 20% OVF in horizontal pipe orientation, at different probe positions.....171
Figure 5-15 Sauter Mean Diameter (d_{32}), of oil and water droplets for mixture velocity, U_{sme} = 0.20 ms^{-1}, oil volume fraction 50% OVF in horizontal pipe orientation, at different probe positions.....172
Figure 5-16 Sauter Mean Diameter (d_{32}), of water droplets for mixture velocity, U_{sme} = 0.20 ms^{-1}, oil volume fraction 80% OVF in horizontal pipe orientation, at different probe positions.....173
Figure 5-17 Sauter Mean Diameter (d_{32}), as a function of interface height from pipe bottom for mixture velocity, U_{sme} = 0.20 ms^{-1}, and distance from expansion 40D in horizontal pipe orientation, for 80% OVF input oil volume fraction. 174
Figure 5-18 Sauter Mean Diameter (d_{32}), as a function of interface height from pipe bottom for mixture velocity, U_{sme} = 0.20 ms^{-1}, and distance from expansion 40D in horizontal pipe orientation for 50% OVF input oil volume fraction 174
Figure 5-19 Sauter Mean Diameter (d_{32}), as a function of interface height from pipe bottom for mixture velocity, U_{sme} = 0.20 ms^{-1}, and distance from expansion 40D in horizontal pipe orientation for 20% OVF input oil volume fraction 175
Figure 5-20 Sauter Mean Diameter (d_{32}), as a function of the distance from the interface for input oil volume fraction 80% OVF and distance from expansion 40D in horizontal pipe orientation, at different downstream mixture velocities, U_{sme}.....176
Figure 5-21 Sauter Mean Diameter (d_{32}), as a function of the distance from the interface for input oil volume fraction 50% OVF and distance from expansion 40D in horizontal pipe orientation, at different downstream mixture velocities, $U_{sme.}$.....176
Figure 5-22 Sauter Mean Diameter (d_{32}), for downstream mixture velocity, U_{sme} = 0.20 ms^{-1}, within axial distances of test section in + 2^0 degrees upward pipe inclination orientation, probe position 15.9 mm from bottom of pipe at different oil volume fraction, OVF. 179

Figure 5-23 Sauter Mean Diameter (d_{32}), for downstream mixture velocity, U_{sme} = 0.20 ms^{-1}, within axial distances of test section in + 2^0 degrees upward pipe inclination orientation, probe position 63.5mm from bottom of pipe at different oil volume fraction, OVF. 179
Figure 5-24 Sauter Mean Diameter (d_{32}), for downstream mixture velocity, U_{sme} = 0.20 ms^{-1}, within axial distances of test section in + 2^0 degrees upward pipe inclination orientation, probe position 111.3 mm from bottom of pipe at different oil volume fraction, OVF. 180
Figure 5-25 Sauter Mean Diameter (d_{32}) for flow condition, 80% OVF, within axial distance of test section in + 2^0 degrees upward pipe inclination orientation, probe position (15.9 mm) from bottom of pipe at different downstream mixture velocity, U_{sme}. 181
Figure 5-26 Sauter Mean Diameter (d_{32}) for flow condition, 60% OVF, within axial distance of test section in + 2^0 degrees upward pipe inclination orientation, probe position Centre (63.5 mm) from bottom of pipe at different downstream mixture velocity, U_{sme}. 182
Figure 5-27 Sauter Mean Diameter (d_{32}) for flow condition, 40% OVF, within axial distance of test section in + 2^0 degrees upward pipe inclination orientation, probe position Centre (63.5 mm) from bottom of pipe at different downstream mixture velocity, U_{sme}. 183
Figure 5-28 Sauter Mean Diameter (d_{32}) for flow condition, 20% OVF, within axial distance of test section in + 2^0 degrees upward pipe inclination orientation, probe position Top (111.3 mm) from bottom of pipe at different downstream mixture velocity, U_{sme}. 184
Figure 5-29 Effect of downstream mixture velocity on Sauter Mean Diameter (d_{32}) for flow condition, at 10D axial distance of test section in + 2^0 degrees upward pipe inclination orientation, probe position (15.9 mm) from bottom at different input oil volume fraction. 185
Figure 5-30 Effect of downstream mixture velocity on Sauter Mean Diameter (d_{32}) for flow condition, at 20D axial distance of test section in + 2^0 degrees upward pipe inclination orientation, probe position (15.9 mm) from bottom at different input oil volume fraction. 185
Figure 5-31 Effect of downstream mixture velocity on Sauter Mean Diameter (d_{32}) for flow condition, at 40D axial distance of test section in + 2^0 degrees upward pipe

inclination orientation, probe position (15.9 mm) from bottom at different input oil volume fraction. 186
Figure 5-32 Sauter Mean Diameter (d_{32}), as a function of interface height from pipe bottom for mixture velocity, U_{sme} = 0.20 ms^{-1}, and distance from expansion 40D in + 2^0 degrees upward pipe inclination, for 80% OVF input oil volume fraction. 187
Figure 5-33 Sauter Mean Diameter (d_{32}), as a function of interface height from pipe bottom for mixture velocity, U_{sme} = 0.20 ms^{-1}, and distance from expansion 40D in + 2^0 degrees upward pipe inclination, for 50% OVF input oil volume fraction. 188
Figure 5-34 Sauter Mean Diameter (d_{32}), as a function of the distance from the interface for input oil volume fraction 80% OVF and distance from expansion 40D in + 2^0 degrees upward pipe inclination orientation, at different downstream mixture velocities, U_{sme}. 189
Figure 5-35 Sauter Mean Diameter (d_{32}), as a function of the distance from the interface for input oil volume fraction 50% OVF and distance from expansion 40D in + 2^0 degrees upward pipe inclination orientation, at different downstream mixture velocities, U_{sme}. 189
Figure 5-36 Sauter Mean Diameter (d_{32}), as a function of the distance from the interface for input oil volume fraction 20% OVF and distance from expansion 40D in + 2^0 degrees upward pipe inclination orientation, at different downstream mixture velocities, U_{sme}. 190
Figure 5-37 Sauter Mean Diameter (d_{32}), of oil droplets for mixture velocity, U_{sme} = 0.20 ms^{-1}, oil volume fraction 20% OVF in + 2^0 degrees upward pipe inclination, at different probe positions 191
Figure 5-38 Sauter Mean Diameter (d_{32}), of oil and water droplets for mixture velocity, U_{sme} = 0.20 ms^{-1}, oil volume fraction 50% OVF in in + 2^0 degrees upward pipe inclination, at different probe positions 192
Figure 5-39 Sauter Mean Diameter (d_{32}), of water droplets for mixture velocity, U_{sme} = 0.20 ms^{-1}, oil volume fraction 80% OVF in in + 2^0 degrees upward pipe inclination, at different probe positions 193
Figure 5-40 Sauter Mean Diameter (d_{32}), for downstream mixture velocity, U_{sme} = 0.20 ms^{-1}, within axial distances of test section in - 2^0 degrees downward pipe inclination orientation, probe position 15.9 mm from bottom of pipe at different oil volume fraction, OVF. 195

Figure 5-41 Sauter Mean Diameter (d_{32}), for downstream mixture velocity, U_{sme} = 0.20 ms^{-1}, within axial distances of test section in - 2^0 degrees downward pipe inclination orientation, probe position 63.5mm from bottom of pipe at different oil volume fraction, OVF. 196
Figure 5-42 Sauter Mean Diameter (d_{32}), for downstream mixture velocity, U_{sme} = 0.20 ms^{-1}, within axial distances of test section in - 2^0 degrees downward pipe inclination orientation, probe position 111.3 mm from bottom of pipe at different oil volume fraction, OVF. 197
Figure 5-43 Sauter Mean Diameter (d_{32}) for flow condition, 80% OVF, within axial distance of test section in - 2^0 degrees downward pipe inclination orientation, probe position (15.9 mm) from bottom of pipe at different downstream mixture velocity, U_{sme}. 198
Figure 5-44 Sauter Mean Diameter (d_{32}) for flow condition, 60% OVF, within axial distance of test section in - 2^0 degrees downward pipe inclination orientation, probe position Centre (63.5 mm) from bottom of pipe at different downstream mixture velocity, U_{sme}. 199
Figure 5-45 Sauter Mean Diameter (d_{32}) for flow condition, 40% OVF, within axial distance of test section in - 2^0 degrees downward pipe inclination orientation, probe position Centre (63.5mm) from bottom of pipe at different downstream mixture velocity, U_{sme}. 200
Figure 5-46 Sauter Mean Diameter (d_{32}) for flow condition, 20% OVF, within axial distance of test section in - 2^0 degrees downward pipe inclination orientation, probe position Top (111.3 mm) from bottom of pipe at different downstream mixture velocity, U_{sme}. 201
Figure 5-47 Effect of downstream mixture velocity on Sauter Mean Diameter (d_{32}) for flow condition, at 10D axial distance of test section in - 2^0 degrees downward pipe inclination orientation, probe position (15.9 mm) from bottom at different input oil volume fraction. 202
Figure 5-48 Effect of downstream mixture velocity on Sauter Mean Diameter (d_{32}) for flow condition, at 20D axial distance of test section in - 2^0 degrees downward pipe inclination orientation, probe position (15.9 mm) from bottom at different input oil volume fraction. 203
Figure 5-49 Effect of downstream mixture velocity on Sauter Mean Diameter (d_{32}) for flow condition, at 40D axial distance of test section in - 2^0 degrees downward pipe

inclination orientation, probe position (15.9 mm) from bottom at different input oil volume fraction. 203
Figure 5-50 Sauter Mean Diameter (d_{32}), as a function of interface height from pipe bottom for mixture velocity, U_{sme} = 0.20 ms^{-1}, and distance from expansion 40D in - 2^0 degrees downward pipe inclination, for 80% OVF input oil volume fraction.. ..204
Figure 5-51 Sauter Mean Diameter (d_{32}), as a function of interface height from pipe bottom for mixture velocity, U_{sme} = 0.20 ms^{-1}, and distance from expansion 40D in - 2^0 degrees downward pipe inclination, for 50% OVF input oil volume fraction.. ..205
Figure 5-52 Sauter Mean Diameter (d_{32}), as a function of the distance from the interface for input oil volume fraction 80% OVF and distance from expansion 40D in - 2^0 degrees downward pipe inclination orientation, at different downstream mixture velocities, U_{sme}. 206
Figure 5-53 Sauter Mean Diameter (d_{32}), as a function of the distance from the interface for input oil volume fraction 50% OVF and distance from expansion 40D in - 2^0 degrees downward pipe inclination orientation, at different downstream mixture velocities, U_{sme}. 207
Figure 5-54 Sauter Mean Diameter (d_{32}), as a function of the distance from the interface for input oil volume fraction 20% OVF and distance from expansion 40D in - 2^0 degrees downward pipe inclination orientation, at different downstream mixture velocities, U_{sme}. 208
Figure 5-55 Sauter Mean Diameter (d_{32}), of oil droplets for mixture velocity, U_{sme} = 0.20m/s, oil volume fraction 20% OVF in - 2^0 degrees downward pipe inclination, at different probe positions. 209
Figure 5-56 Sauter Mean Diameter (d_{32}), of oil and water droplets for mixture velocity, U_{sme} = 0.20m/s, oil volume fraction 50% OVF in - 2^0 degrees downward pipe inclination, at different probe positions 210
Figure 5-57 Sauter Mean Diameter (d_{32}), of water droplets for mixture velocity, U_{sme} = 0.20 ms^{-1}, oil volume fraction 80% OVF in - 2^0 degrees downward pipe inclination, at different probe positions 211
Figure 5-58 Sauter Mean Diameter (d_{32}), as a function of the distance from interface for downstream mixture velocity, U_{sme} = 0.20 ms^{-1}, input oil volume fraction 80% OVF at axial test distance 10D, at different pipe inclination angles. 213

Figure 5-59 Sauter Mean Diameter (d_{32}), as a function of the distance from interface for downstream mixture velocity, U_{sme} = 0.20 ms^{-1}, input oil volume fraction 20% OVF at axial test distance 10D, at different pipe inclination angles. 213
Figure 5-60 Sauter Mean Diameter (d_{32}), as a function of the distance from interface for downstream mixture velocity, U_{sme} = 0.35 ms^{-1}, input oil volume fraction 80% OVF at axial test distance 20D, at different pipe inclination angles. 214
Figure 5-61 Sauter Mean Diameter (d_{32}), as a function of the distance from interface for downstream mixture velocity, U_{sme} = 0.35 ms^{-1}, input oil volume fraction 20% OVF at axial test distance 20D, at different pipe inclination angles. 215
Figure 5-62 Sauter Mean Diameter (d_{32}), of oil droplets for downstream mixture velocity, U_{sme} = 0.20 ms^{-1}, oil volume fraction 20% OVF at bottom (15.9 mm), probe position, within axial test distance at different pipe inclination angles. 216
Figure 5-63 Sauter Mean Diameter (d_{32}), of oil droplets for downstream mixture velocity, U_{sme} = 0.20 ms^{-1}, oil volume fraction 20% OVF at Top (111.3 mm), probe position, within axial test distance at different pipe inclination angles. 216
Figure 5-64 Sauter Mean Diameter (d_{32}), of oil droplets for downstream mixture velocity, U_{sme} = 0.35 ms^{-1}, oil volume fraction 20% OVF at bottom (111.3 mm), probe position, within axial test distance at different pipe inclination angles. 217
Figure 5-65 Sauter Mean Diameter (d_{32}), of water droplets for downstream mixture velocity, U_{sme} = 0.20 ms^{-1}, oil volume fraction 80% OVF at bottom (15.9 mm), probe position, within axial test distance at different pipe inclination angles. 218
Figure 5-66 Sauter Mean Diameter (d_{32}), of water droplets for downstream mixture velocity, U_{sme} = 0.35m/s, oil volume fraction 80% OVF at bottom (15.9mm), probe position, within axial test distance at different pipe inclination angles. 219
Figure 5-67 Experimental data fitted to the Rosin-Ramler function for downstream mixture velocity, U_{sme} = 0.20 ms^{-1}, oil volume fraction 20% OVF at Centre (63.5 mm) probe position, 40D axial test distance at horizontal pipe orientation. 222
Figure 5-68 Experimental data fitted to the Rosin-Ramler function for downstream mixture velocity, U_{sme} = 0.20 ms^{-1}, oil volume fraction 50% OVF at Centre (63.5 mm) probe position, 40D axial test distance at horizontal pipe orientation. 222
Figure 5-69 Experimental data fitted to the Rosin-Ramler function for downstream mixture velocity, U_{sme} = 0.20 ms^{-1}, oil volume fraction 80% OVF at Centre (63.5 mm) probe position, 40D axial test distance at horizontal pipe orientation. 223

Figure 5-70 Comparison of experimental data fitted to the Rosin-Ramler function for downstream mixture velocity, U_{sme} = 0.20 ms^{-1}, oil volume fractions 20%, 50% and 80% OVF at Centre (63.5 mm) probe position, 40D axial test distance at horizontal pipe orientation. 223
Figure 5-71 Experimental data fitted to the Rosin-Ramler function for downstream mixture velocity, U_{sme} = 0.35 ms^{-1}, oil volume fraction 20% OVF at Centre (63.5 mm) probe position, 10D axial test distance at horizontal pipe orientation. 224
Figure 5-72 Experimental data fitted to the Rosin-Ramler function for downstream mixture velocity, U_{sme} = 0.35 ms^{-1}, oil volume fraction 50% OVF at Centre (63.5 mm) probe position, 10D axial test distance at horizontal pipe orientation. 224
Figure 5-73 Experimental data fitted to the Rosin-Ramler function for downstream mixture velocity, U_{sme} = 0.35 ms^{-1}, oil volume fraction 80% OVF at Centre (63.5 mm) probe position, 10D axial test distance at horizontal pipe orientation. 225
Figure 5-74 Comparison of experimental data fitted to the Rosin-Ramler function for downstream mixture velocity, U_{sme} = 0.35 ms^{-1}, oil volume fractions 20%, 50% and 80% OVF at Centre (63.5 mm) probe position, 10D axial test distance at horizontal pipe orientation 225
Figure 5-75 Evolution of the Rosin-Ramler parameter for downstream mixture velocity, U_{sme} = 0.20 ms^{-1}, probe position Centre (63.5 mm), within axial test distance and horizontal pipe orientation at different input oil volume fractions. 226
Figure 5-76 Evolution of the Rosin-Ramler parameter for downstream mixture velocity, U_{sme} = 0.35 ms^{-1}, probe position Centre (63.5 mm), within axial test distance and horizontal pipe orientation at different input oil volume fractions 227
Figure 5-77 Evolution of the Rosin-Ramler parameter for input oil volume fraction 20% OVF at Centre (63.5 mm) probe position, within axial test distance and horizontal pipe orientation at different downstream mixture velocity, U_{sme} 227
Figure 5-78 Evolution of the Rosin-Ramler parameter for input oil volume fraction 80% OVF at Centre (63.5 mm) probe position, within axial test distance and horizontal pipe orientation at different downstream mixture velocity, U_{sme} 228
Figure 5-79 Comparison of Log – normal and R-R distribution fits to 0.20 ms^{-1} downstream mixture velocity, 20% OVF input oil volume fraction at Centre (63.5 mm) probe position, 10D axial test distance and horizontal pipe orientation. 230

Figure 5-80 Comparison of Log – normal and R-R distribution fits to 0.20 ms^{-1} downstream mixture velocity, 50% OVF input oil volume fraction at Centre (63.5 mm) probe position, 40D axial test distance and horizontal pipe orientation. 230
Figure 5-81 Comparison of Log – normal and R-R distribution fits to 0.20 ms^{-1} downstream mixture velocity, 80% OVF input oil volume fraction at Centre (63.5 mm) probe position, 10D axial test distance and horizontal pipe orientation. 231
Figure 5-82 Comparison of the experimental Sauter Mean Diameter (d_{32}) for flow condition, 20% OVF at 10D axial distance of test section in horizontal pipe orientation, probe position (111.3 mm) from bottom at downstream velocities of 0.20 m/s, 0.25 ms^{-1} and 0.35 ms^{-1}. 232
Figure 5-83 Comparison of the experimental Sauter Mean Diameter (d_{32}) for flow condition, 80% OVF at 10D axial distance of test section in horizontal pipe orientation, probe position (15.9 mm) from bottom at downstream velocities of 0.20m/s, 0.25 ms^{-1} and 0.35 ms^{-1}. 233
Figure 6-1 Horizontal oil-water flow pattern images observed downstream of the sudden pipe expansion. 242
Figure 6-2 Flow patterns encountered within the rig in current study, plotted on the flow pattern map of (Trallero et al., 1997). 243
Figure 6-3 Experimental flow pattern map, horizontal for current study. 243
Figure 6-4 Images on the effect of increasing mixture velocity at all input oil volume fraction (20% to 80%), close to inlet axial test distance position 20D. 244
Figure 6-5 In-situ oil volume fractions in a pipe cross section at the various axial distance, input oil volume fraction (80% OVF), and horizontal flow at low downstream mixture velocities. 246
Figure 6-6 In-situ oil volume fractions in a pipe cross section at the various axial distance, input oil volume fraction (50% OVF), and horizontal flow at low downstream mixture velocities. 246
Figure 6-7 In-situ oil volume fractions in a pipe cross section at the various axial distance, input oil volume fraction (20% OVF), and horizontal flow at low downstream mixture velocities. 247
Figure 6-8 In-situ oil volume fractions in a pipe cross section at the various axial distance, input oil volume fraction (80% OVF), and horizontal flow at higher downstream mixture velocities. 248

Figure 6-9 In-situ oil volume fractions in a pipe cross section at the various axial distance, input oil volume fraction (50% OVF), and horizontal flow at higher downstream mixture velocities. 248
Figure 6-10 In-situ oil volume fractions in a pipe cross section at the various axial distance, input oil volume fraction (20% OVF), and horizontal flow at higher downstream mixture velocities. 249
Figure 6-11 Average in-situ oil volume fraction vs superficial oil and water velocities. 250
Figure 6-12 Velocity ratio at low mixture velocities and horizontal flow. S > 1 indicates oil flowing faster than water; S < 1 indicates oil flowing slower than water. 252
Figure 6-13 Velocity ratio at higher mixture velocities and horizontal flow. S > 1 indicates oil flowing faster than water; S < 1 indicates oil flowing slower than water. 252
Figure 6-14 Upward inclined oil-water flow pattern images observed at lower mixture velocities (0.20 ms^{-1} – 0.35 ms^{-1}), downstream of the sudden pipe expansion. 254
Figure 6-15 Upward inclined oil-water flow pattern images observed at higher mixture velocities (0.50 ms^{-1} – 1.50 ms^{-1}), downstream of the sudden pipe expansion. 255
Figure 6-16 (a) Caterpillar waves observed at mixture velocities (0.50 ms^{-1} – 1.00 ms^{-1}), downstream of the sudden pipe expansion in current work. (b) Similar caterpillar waves observed in the work of (Rodriguez and Oliemans, 2006). 256
Figure 6-17 Downward inclined oil-water flow pattern images observed at lower mixture velocities (0.20 ms^{-1} – 0.35 ms^{-1}), downstream of the sudden pipe expansion. 257
Figure 6-18 Downward inclined oil-water flow pattern images observed at higher mixture velocities (0.50 ms^{-1} – 1,50 ms^{-1}), downstream of the sudden pipe expansion. 258
Figure 6-19 Phase layer evolution of interface height downstream of the pipe expansion for flow conditions: 50% OVF, downstream mixture velocity 1.00 ms^{-1} horizontal at different axial test distances. 259
Figure 6-20 Effect of different oil volume fraction (OVF) on phase layer evolution of interface height downstream of the pipe expansion for flow conditions: downstream mixture velocity 0.30 ms^{-1}, horizontal flow at different axial test distances. 260

Figure 6-21 Effect of different oil volume fraction (OVF) on phase layer evolution of interface height downstream of the pipe expansion for flow conditions: downstream mixture velocity 0.50 ms^{-1}, horizontal flow at different axial test distances. 261
Figure 6-22 Effect of different oil volume fraction (OVF) on phase layer evolution of interface height downstream of the pipe expansion for flow conditions: downstream mixture velocity 1.00 ms^{-1}, horizontal flow at different axial test distances. 262
Figure 6-23 Effect of mixture velocity on the phase layer evolution downstream of the singularity with flow conditions, 80% OVF and horizontal flow at different axial test distances. 262
Figure 6-24 Effect of mixture velocity on the phase layer evolution downstream of the singularity with flow conditions, 50% OVF and horizontal flow at different axial test distances. 263
Figure 6-25 Effect of mixture velocity on the phase layer evolution downstream of the singularity with flow conditions, 20% OVF and horizontal flow at different axial test distances. 263
Figure 6-26 Oil/water mixed interface region vs mixture velocity on the phase layer evolution downstream of the singularity with flow conditions, 20% OVF, 50% OVF, 80% OVF and horizontal flow at different axial test distances. 265
Figure 6-27 Oil/water mixed interface region vs axial distance along pipe expansion at various mixture velocities (a) 0.30m/s (b) 0.50m/s (c) 1.00m/s (d) 1.50m/s; horizontal pipe flow orientation. 266
Figure 6-28 Effect of oil volume fraction (OVF) on phase layer evolution of interface height downstream of the pipe expansion for flow conditions: downstream mixture velocity 0.30 ms^{-1}, upward inclination angle pipe ($+2^0$) flow at different axial test distances 268
Figure 6-29 Effect of oil volume fraction (OVF) on phase layer evolution of interface height downstream of the pipe expansion for flow conditions: downstream mixture velocity 0.50 ms^{-1}, upward inclination angle pipe ($+2^0$) flow at different axial test distances 269
Figure 6-30 Effect of oil volume fraction (OVF) on phase layer evolution of interface height downstream of the pipe expansion for flow conditions: downstream mixture velocity 1.00 ms^{-1}, upward inclination angle pipe ($+2^0$) flow at different axial test distances 269

Figure 6-31 Effect of mixture velocity on the phase layer evolution downstream of the singularity with flow conditions, 80% OVF and upward inclined pipe ($+2^0$) flow at different axial test distances.....271
Figure 6-32 Effect of mixture velocity on the phase layer evolution downstream of the singularity with flow conditions, 50% OVF and upward inclined pipe ($+2^0$) flow at different axial test distances.....271
Figure 6-33 Effect of mixture velocity on the phase layer evolution downstream of the singularity with flow conditions, 20% OVF and upward inclined pipe ($+2^0$) flow at different axial test distances.....272
Figure 6-34 Oil/water mixed interface region vs mixture velocity on the phase layer evolution downstream of the singularity with flow conditions, 20% OVF, 50% OVF, 80% OVF and Upward flow at different axial test distances 274
Figure 6-35. Oil/water mixed interface region vs axial distance along pipe expansion at various mixture velocities (a) 0.30 ms^{-1} (b) 0.50 ms^{-1} (c) 1.00 ms^{-1} (d) 1.50 ms^{-1}; Upward pipe flow orientation. 275
Figure 6-36 Effect of oil volume fraction (OVF) on phase layer evolution of interface height downstream of the pipe expansion for flow conditions: downstream mixture velocity 0.30m/s, downward inclination angle pipe (-2^0) flow at different axial test distances.....276
Figure 6-37 Effect of oil volume fraction (OVF) on phase layer evolution of interface height downstream of the pipe expansion for flow conditions: downstream mixture velocity 0.50m/s, downward inclination angle pipe (-2^0) flow at different axial test distance 277
Figure 6-38 Effect of oil volume fraction (OVF) on phase layer evolution of interface height downstream of the pipe expansion for flow conditions: downstream mixture velocity 1.00m/s, downward inclination angle pipe (-2^0) flow at different axial test distance 277
Figure 6-39 Effect of mixture velocity on the phase layer evolution downstream of the singularity with flow conditions, 80% OVF and downward inclined pipe (-2^0) flow at different axial test distances.....278
Figure 6-40 Effect of mixture velocity on the phase layer evolution downstream of the singularity with flow conditions, 50% OVF and downward inclined pipe (-2^0) flow at different axial test distances.....279

Figure 6-41 Effect of mixture velocity on the phase layer evolution downstream of the singularity with flow conditions, 20% OVF and downward inclined pipe (-2^0) flow at different axial test distances.....279
Figure 6-42 Oil/water mixed interface region vs mixture velocity on the phase layer evolution downstream of the singularity with flow conditions, 20% OVF, 50% OVF, 80% OVF and Downward flow at different axial test distances 281
Figure 6-43 Oil/water mixed interface region vs axial distance along pipe expansion at various mixture velocities (a) 0.30m/s (b) 0.50m/s (c) 1.00m/s (d) 1.50m/s; Downward pipe flow orientation. 282
Figure 6-44 Effect of the angles of pipe inclination on the phase layer evolution downstream of the singularity with flow conditions, 20% OVF and downstream mixture velocity 0.30m/s within axial test distance.....283
Figure 6-45 Effect of the angles of pipe inclination on the phase layer evolution downstream of the singularity with flow conditions, 20% OVF and downstream mixture velocity 0.50m/s within axial test distance.....284
Figure 6-46 Effect of the angles of pipe inclination on the phase layer evolution downstream of the singularity with flow conditions, 50% OVF and downstream mixture velocity 0.30m/s within axial test distance.....285
Figure 6-47 Effect of the angles of pipe inclination on the phase layer evolution downstream of the singularity with flow conditions, 80% OVF and downstream mixture velocity 0.30m/s within axial test distance.....285
Figure 6-48 Time series of in-situ oil volume fraction 80% OVF in the 127 mm pipe, (a) stratified (ST), (U_{sme} 0.20 ms^{-1}), (b) stratified with mixed interface (ST & MI), (U_{sme} 0.50 ms^{-1}), (c) dispersed flow ($D_{o/w}$ & $D_{w/o}$), (U_{sme} 2.00 ms^{-1}), transition and typical PDFs at fully developed flow downstream of expansion (40D).....287
Figure 6-49 Time series of in-situ oil volume fraction 50% OVF in the 127 mm pipe, (a) stratified (ST), (U_{sme} 0.20 ms^{-1}), (b) stratified with mixed interface (ST & MI), (U_{sme} 0.50 ms^{-1}), (c) dispersed flow ($D_{o/w}$ & $D_{w/o}$), (U_{sme} 2.00 ms^{-1}), transition and typical PDFs at fully developed flow downstream of expansion (40D).....288
Figure 6-50 Time series of in-situ oil volume fraction 20% OVF in the 127 mm pipe, (a) stratified (ST), (U_{sme} 0.20 ms^{-1}), (b) stratified with mixed interface (ST & MI), (U_{sme} 0.50 ms^{-1}), (c) dispersed flow ($D_{o/w}$ & $D_{w/o}$), (U_{sme} 2.00 ms^{-1}), transition and typical PDFs at fully developed flow downstream of expansion (40D).....289

LIST OF TABLES

Table 2-1 Summary of previous work on drop size measurement technique.....47
Table 2-1 Summary of previous work on drop size measurement technique continued 48
Table 2-2 Brief summary of previous work on liquid – liquid dispersions in stirred vessels.....58
Table 3-1 Physical properties of fluids (Silicone oil and Water) at 21^0C 86
Table 3 2 Rosin - Rammler distribution parameter and standard deviation estimate 106
Table 3-3 Log-normal distribution parameters and standard deviation estimate 107
Table 3-4 Sauter mean diameter values from FBRM M500P Laser 111
Table 4-1 Physical properties of fluids (Silicone oil and Water) @ 21^0C.....133
Table 4-2 Experimental conditions.....136
Table 4-3 Total instrumental deviations.....156
Table 5-1 Rosin-Rammler parameter values of probe position at Centre (63.5mm) for horizontal pipe orientation.....221
Table 5-2 Comparison of Rosin-Rammler parameters in liquid-liquid flow experiments with published work.....221
Table 5-3 Log – normal distribution parameters values of probe position at Centre (63.5mm) for horizontal pipe orientation 229

NOMENCLATURE

Symbol	Description	Dimension
Roman letters		
$A(h_o)$	Function of energy in Equation 3.4	(-)
A	Cross sectional area of pipe	(m^2)
a	Interfacial area per unit volume	(-)
C	Constant	(-)
D	Impeller diameter	(m)
D_t	Diameter of baffled stirred tank	(m)
d	droplet diameter	(m)
d_{max}	Maximum drop size diameter	(mm)
d_{min}	Minimum drop size diameter	(mm)
D_{32}	Sauter mean drop diameter	(mm)
E_{oD}	Eotvos Number	(-)
f	Friction factor	(-)
F	Force of attraction of bubbles or droplets	(Nm^{-2})
g	gravitational acceleration	(ms^{-2})
K	Constant	(-)
l	Kolmogorov length scale	(m)
h	*Film thickness*	(mm)
N_{vi}	Viscosity Number	(-)
N_{we}	Weber Number	(-)
$N_{we(crt)}$	Critical Weber Number	(-)
N	Impeller speed	(m/s)
Q	Volumetric flow rate	(m^3s^{-1})
P*i*	probability of obtaining i^{th} chord size	(-)
Re	Reynolds number	(-)
S	perimeter	(m^2)
u	Velocity	(ms^{-1})
U	Velocity	(ms^{-1})
V_t	Volume of stirred tank	(m^3)

Greek symbols

ε_o	*In-situ* Oil phase volume fraction or hold up	(m^3)
ε_w	*In-situ* Water phase volume fraction or hold up	(m^3)
ε_d	Dispersed phase volume fraction or hold up	(m^3)
ε_c	Continuous phase volume fraction or hold up	(m^3)
W_c	Water cut	(-)
O_c	Input oil volume fraction	(-)
ε	Energy of dissipation	(Joules or m^2s^{-2})
$\bar{\varepsilon}$	Average energy of dissipation	(Joules)
σ	Interfacial tension	($dynecm^{-1}$ or Nm^{-1})
ρ	Fluid density	(Kgm^{-3})
ϕ	Diameter	(m)
μ	Viscosity	($Kgm^{-1}s^{-1}$ or Pa.s)
ν	Kinematic viscosity	($Kgm^{-1}s^{-1}$ or Pa.s)
λ	Linear attenuation coefficient	(-)
ς	Rosin-Rammler parameter (slope of curve)	(-)
ξ	Log-normal distribution parameter	(-)

Subscripts

c	continuous
d	dispersed
l	lower part of horizontal pipe
u	upper part of horizontal pipe
i	interface between oil and water
m	mixture
o	oil
water	mean
max	maximum
min	minimum
os	oil superficial velocity

ws	water superficial velocity

Chapter 1 INTRODUCTION

Liquid – Liquid systems are common occurrences in the Petroleum and Process Industries. These areas include: crude oil exploration, production, downstream oil/water primary separation process and transportation through pipelines. Other areas are metal extraction, food processing and emulsification processes. Ineffective design of some of this conventional equipment such as separators, reactors, heat exchangers and pipeline configurations, in handling liquid-liquid systems result in numerous operational problems, which include:

- Fluid transportation difficulties in pipelines
- Space limitations in offshore oil platforms operations
- Cost implications as a result of safety and environmental hazards due to equipment failure
- Difficulties in metal extraction processes.
- Difficulties in obtaining stable dispersions or emulsions (food processing)

In the case of multiphase flows in oil production fields, it is pertinent to minimize these operational problems by separating the multiphase mixtures of gas, oil, water and solids for further downstream processing. There is recently an increasing interest in the study of liquid-liquid systems in the petroleum industry, where crude oil and water are been produced from reservoir wells and often transported together for a long distance for downstream central processing units to obtain petroleum products (Jayawardena et al., 2000). In the petrochemical industries, oil-water flow systems are inevitable. This requires an efficient separation process of reservoir fluids of the immiscible oil-water before transportation through pipelines.

Several conventional separators and pipeline configurations have been designed to solve the common problems encountered in liquid – liquid systems. However, such separators are capital intensive and expensive to install with extremely restricted safety measures. Thus an alternatively cheaper and efficient separation

method is proposed using a sudden pipe expansion geometry. Therefore, this sudden pipe expansion phase separator design, will be used in the present work to obtain liquid-liquid stratification and hydrodynamic information.

Also in the chemical and process industries, liquid-liquid dispersion systems are encountered mostly in two – phase reactions, liquid-liquid extraction and emulsification processes. The resultant dispersed phase has great impact on the pressure drop, the heat and/or mass transfer and the design of the downstream separation equipment.

In all these processes, it is important also to determine the droplet size and droplet size distribution of the liquid – liquid dispersions, for a clearer understanding of the hydrodynamics of the system. If two immiscible liquids are agitated, dispersion is formed, in which continuous break-up and coalescence of droplets of phases occurs simultaneously. It has been established from research that these two phenomena mostly govern the process (Shinnar, 1961).

Experimental investigations on pipeline dispersions mostly concentrate on the breakup mechanism other than the coalescence process. Together with breakup and mass transfer, coalescence controls the evolution of drop sizes in the liquid-liquid dispersion. Hence, it is pertinent to experimentally investigate also the coalescence efficiencies of liquid – liquid dispersions and develop empirical or semi-empirical models to validate these phenomena in both mechanically agitated vessels and pipelines.

This chapter is an introduction of the scope of my thesis; that is, investigating the coalescence efficiencies of droplet size in both baffled stirred tanks and in a sudden pipe expansion under turbulence in oil/water systems. Challenges and motivations, together with research aims and objectives are highlighted in this chapter and detailed thesis overview is given.

1.1 Background

In chemical and petroleum industries, multiphase flow is a common phenomenon, which is frequently encountered during its operations. Multiphase system is a complex mixture of gas, liquid and solid.

Oil reservoir are examples of very complex multiphase flow system, made up of porous rocks (i.e. limestone or sandstone) with pores and fractures filled with pressurized natural gas, crude oil, water, solids, impurities, mud or sand. The gas tends to occupy mostly the upper cavities of the reservoir, allowing the crude oil to accumulate in between while the water settles at the bottom. As a result the reservoir is under pressure and its multiphase flow composition varies at different wells across the reservoir field. This complex scenario makes it difficult for effective separation of the different phases of reservoir fluid in the downstream sector of petroleum industries, even with conventional primary separators and cyclones.

A similar situation is encountered in the transportation of these phases to the downstream petroleum sector and processing plant through pipelines and equipment. This multiphase flow phenomena also exist in metal extraction processes as well as in food processing industries.

Multiphase flow is also applied in many industrial fields, such as heat exchangers, steam generators; nuclear plants chemical reactors, boilers and re-boilers. The number of phases in such complex system is a dominant parameter to be considered, coupled with flow geometries, physical properties of fluids and inlet conditions. Among these phases, quite extensive research efforts have been done in the areas of gas-liquid systems, liquid-solid, leaving liquid-liquid systems with inadequate attention.

1.2 Challenges identified in crude oil production

The complexity of oil production in both the upstream and downstream sectors of the oil and gas industries, poses huge challenges to engineering designs and operations in onshore and offshore platforms. This unavoidable condition in reality causes ineffective separation of the phases, especially crude oil and water mixtures. For example, the motion effect of offshore production platforms as a result of sea waves sloshes oil and water in the separator, promoting the occurrence of droplets and impedes its separation. The presence of pressurized

gas and internal design configuration with baffled plates, contributes to droplet entrainment within the primary separator vessel. The introduction of artificial crude oil recovery mechanisms such as water flooding, also changes the composition of crude oil stream leaving the reservoir.

Another challenge is the large size of gravity separator vessels, which occupy more than half of the operational platforms. These require massive construction of steel pipe frame support, which is cost effective and expensive. Research is now focused on the design of alternatively cheap, safe, simple and more compact separation systems with different pipe configurations. One of such configuration is a sudden pipe expansion, which has been investigated by (Yang et al., 2003, Hasan, 2006, Yusoff, 2012) and achieved some successful results on liquid-liquid stratification.

Researchers have also recently indicated interest in investigating the behavior of oil-water mixtures during transportation through pipelines. A number of issues results from such operations, which affects the flow patterns, the oil-water phase change, liquid entrainments (i.e. formation of oil-in-water or water-in-oil droplets), the pressure drop along the pipe and other transport properties as the mass and heat transfer coefficients.

Extensive research efforts have been made in the area of gas-liquid flows over the past years to obtain design methods for gas-oil-water multiphase flow systems. However, no corresponding attention was made towards the understanding of the simultaneous flow of oil-water liquid-liquid mixtures. The limited availability of data on average drop coalescence dynamics in oil-water flow systems under turbulence is partly due to the difficulty in performing such measurements experimentally. The flow patterns of oil-water are quite different from that of the gas-liquid mixtures as presented by some researchers in the area. This according to (Trallero et al., 1997), is partly caused by a number of factors, which includes the liquid-liquid momentum transfer capacity, buoyancy forces and free energy at the interface. Despite the importance of two immiscible liquid-liquid flow systems, not much information has been reported in the literature regarding such topics as flow patterns, pressure drop and holdup profile.

1.3 Motivation

The motivation of this present work is based on some of the challenges identified in oil and gas production as indicated in section 1.2. Research into multiphase flow has been prompted by these critical industrial problems. The general problem of oil-water mixing that poses complications during separation steps and transportation of crude through pipelines at different stages constitute a motivation for this investigation.

Modern technology of enhanced oil recovery from ultra-deep wells, such as those in the oil fields of the Santos Basin, Brazil and the Gulf of Mexico, has benefited from the development of multiphase pumping (Bell et al., 2005). However, in these applications, it is often necessary to pass the multiphase mixtures through pipelines to a central processing facility. The configuration in which the two phases flow can be quite complex (separated flow, dispersed flow, intermittent flow) and depends on the flow rates, pipe diameter and inclination, which makes the prediction of the pressure drop and liquid hold – up in the pipe complicated. The design of the subsea infrastructure, such as flowline sizing, hinges on being able to predict the hydrodynamic behaviour of the flows they contain. An improved understanding of the rheological behaviour and flow dynamics of such multiphase flows can lead to significant advancements in empirical and phenomenological models capable of the accurate prediction of these flows, and in turn to better designs and operation of related industrial facilities. Belt et al. (2011), stated that most commercial softwares are currently not being able to predict flow parameters with good accuracy in stratified flow, which support the need for further experimental work.

Due to the difficulties in measurement of drop size distribution in liquid – liquid oil – water flow systems, there is limited work done and data available in the area. Most experiments are based on dilute dispersions, which are compared with models for drop breakup mechanism other than the drop formation process. Angeli (2001), however did a review by comparing available experimental data with existing models, which shows under prediction of the experimentally found

maximum drop size. As a result, (Angeli, 2001) stated that most theoretical models and correlations cannot accurately predict droplet sizes i.e. maximum and minimum droplets sizes. Therefore a more comprehensive dataset is needed for the further development and refinement of theoretical models.

Current separators used on offshore platforms are large and are costly, both to manufacture and to install. They contain large inflammable inventory, which require extreme safety measures to keep them secured in offshore platforms. The high construction costs have led to a considerable amount of motivation to develop methods which will enable reduction in size of these vessels. This led to the introduction of T-junctions as phase separators, which worked well for gas-liquid flow but was not suitable for liquid-liquid flow. Therefore, efforts were geared towards developing a new approach using a sudden pipe expansion. Results from researchers, such as (Yang et al., 2003, Hasan, 2006, Yusoff, 2012) showed that an expansion pipe can be used as a phase separator for converting dispersed flow to stratified flow patterns. However, not much information is obtained regarding drop formation and entrainment as it affects phase separation in oil-water flow through pipe expansion. Thus the motivation of this present work is to establish a closure relationship between the coalescence mechanism of droplets, fluids properties and a sudden pipe expansion for efficient phase separator design and performance.

1.4 Research aims and objectives

The current study attempts to provide a comprehensive dataset for oil-water liquid-liquid flow systems in both agitated baffled vessels and horizontal pipe expansion. The following aims and objectives are to be achieved:

- To obtain minimum d_{min}, and maximum d_{max} droplet size measurements and droplet size distribution in a bench top experiment. Investigating the effects of volume fraction of dispersed phase ε_d and Impeller speed N, on droplet size in dispersed phase flow in agitated vessel. In addition, to characterise the drop size distribution of dispersions fitted with Log-

normal distribution, Rosin-Rammler distribution (RR) and Sauter mean diameter (SMD)

- Comparison of experimentally measured minimum droplet size, d_{min} with published correlations will be made to have an in-depth knowledge and explanation of the coalescence process in dispersed homogeneous two phase liquid – liquid flow.
- Design and construct a new versatile oil-water liquid-liquid flow horizontal sudden expansion rig facility capable of handling 5,000 litres of silicone oil with viscosity of 5 cs.
- To acquire high quality experimental steady state data on oil-water flow patterns and their transitions, two-phase pressure gradient, liquids flow rate and holdups (oil and water volume fractions) on the horizontal test facility over a wide range under varying operating conditions, with the use of Conductance probe.
- Characterisation of drop size distribution of dispersed flows and identification of flow pattern development downstream the sudden pipe expansion for different experimental conditions

The findings from this study will serve as additional information to give a better understanding of the hydrodynamics of oil-water flows in pipelines and to consolidate on the previous work done on this area. It will also be useful in the design and performance of a phase separator if sudden pipe expansion is to be employed.

1.5 Thesis Overview

The following layout gives a summary of the current project which is majorly an experimental study.

Chapter 1: The introduction will contain brief background information of multiphase flow, the challenges encountered and motivations and research objectives on the subject area, (liquid – liquid) systems.

Chapter 2: Comprehensive literature surveys on previous work done in liquid – liquid systems are recorded in this section. Recent research developments, publications and findings in the subject area is made as an update. This chapter will focus on discussing briefly the flow patterns and flow pattern identification maps for the various different geometries and configurations. A review of oil-water stratification is also highlighted. The fundamentals of liquid-liquid coalescence and dispersion is reviewed. Various drop size measurement techniques, and drop size estimation with published models and correlations are also considered. There are several techniques applied in the measurement of phase fractions and liquid holdups (oil volume fraction) by different researchers, a few of which are enumerated in this chapter.

Chapter 3: This chapter basically contains a small scale preliminary experimental work that was carried out on liquid-liquid flow in baffled vessel. A description of all instrumentation and the experimental methodology that was used is provided in this chapter. These instruments include: Focused Beam Reflectance Measurements (FBRM) Laser for the measurement of drop size and HotShot High Speed camera with an endoscope attached for imaging purpose. The principles of operation and parameters to be determined are ascertained. Experimental results, discussions and findings are made, which helps in understanding the hydrodynamics of drop coalescence and drop breakup mechanism in turbulence dispersions.

Chapter 4: This chapter describes the design of the large scale liquid-liquid horizontal rig facility and the experimental programme that was employed. The properties of the liquids used and the technique for measurements of drop size, pressure gradient and phase fractions are discussed in Chapter 4. Experiments conducted with Focused Beam Reflectance Measurement (FBRM) Laser, conductance probe, and Phanton PCC 2.7 High speed camera are recorded in this chapter. A comprehensive experimental design for data acquisition system from the various instruments is drawn for the campaign and uncertainty of experimental measurements provided in this Chapter 4.

Chapter 5: The results obtained from the Focused Beam Reflectance Measurement (FBRM) Laser on drop sizes and drop size distributions are analyzed in this Chapter 5, which also covers the critical evaluation of pipe geometry and their effect on drop size distribution. Findings on drop size characterization and drop size distribution over the cross section of the pipe downstream of an expansion are presented.

Chapter 6: A detailed analysis of results obtained with conductance probe and video recordings from the Phantom High speed camera are presented and discussed in *Chapter 6.* Estimation of oil volume fraction and effect of flow parameters together with rig geometry on interface evolution is discussed. Subsequently, spectral density analysis, estimation of time average flow parameters, flow development and stratification through a sudden expansion in the various geometries is illustrated.

Chapter 7: Possible findings drawn from this research project and conclusions are recorded in this chapter. Some suggestions and recommendations for further work are presented. This final chapter also includes areas to improve upon and additional investigations to be done

Chapter 2 LITERATURE REVIEW

2.1 Introduction

The widespread occurrence of multiphase flow in pipes and in crude oil reservoirs is an important phenomenon in the petroleum industry, which has prompted extensive research in this area. Accurate modelling of fluid flow in subsurface formations is essential for the proper management of petroleum reservoirs. Reservoir simulators are commonly applied for the purpose of modelling the flow and transport of reservoir fluids (Jayawardena et al., 2000). Within the reservoir simulator, it is important to accurately represent the interaction of the reservoir with the wellbore. This modelling is complicated because of wellbore hydraulics, which can impact the flow from the reservoir into the wellbore.

In the case of long horizontal or deviated wells, the effect of pressure losses within the wellbore can be very significant and can lead to a number of deleterious effects (Dikken, 1990), such as the premature coning (unwanted water or gas zone moves up towards the wellbore like a cone), or the loss of production at the far end of the well. In order to predict and thereby mitigate these effects, it is essential that accurate models for multiphase wellbore flow be included in reservoir flow simulators.

There is the need for proper and reliable design methods for multiphase flow systems, which has been the driving force behind rigorous research efforts in this area, especially for gas/liquid flow, over the past years. As the name denotes, multiphase systems includes the gas/liquid/solid phase's systems in the chemical and petroleum industries. Recently, research has turned its attention towards the understanding of the simultaneous flow of liquid/liquid flow, i.e. oil/water mixtures.

Studies of liquid-liquid flow in a pipe often include observation of flow patterns, either, the shape and spatial distribution of the two-phase flow within the pipe. Important information can be derived and extracted from the investigation of phase

hold up and pressure drop in the oil, gas and water production rates in oil reservoirs. Today, measurements of liquid holdup and pressure gradient in the different flow patterns, as well as the development of models are subjected to a lot of research.

An extensive literature search has been carried out for the gas-liquid flows with considerable understanding of the important parameters influencing the phase separation of some geometries and flow patterns. Some reviews on this subject has been published by (Yang et al., 2001), with the use of T-Junctions, with such a separator designed and installed in the University of Nottingham. This T-Junction Rig was also used by several other researchers to investigate the behaviour of liquid-liquid flow, especially oil/water systems. Some work has also been done and published on liquid-liquid two phase flow phenomena in horizontal, moderately inclined and vertical pipes. Researchers such as (Lovick and Angeli, 2004b, Brauner and Moalem Maron, 1992, Nädler and Mewes, 1997, Trallero et al., 1997, Angeli and Hewitt, 2000a, Rodriguez and Oliemans, 2006) studied the flow structure and flow patterns in horizontal pipes, whilst (Karabelas, 1978, Simmons and Hanratty, 2001) measured the drop sizes and drop distributions in two liquid flows.

Even though some extensive research work has been done on two-phase, liquid-liquid flow in straight, vertical and inclined pipes, the flow through pipe fittings shown in Figure 2.1, and use of sudden expansion has not been addressed properly.

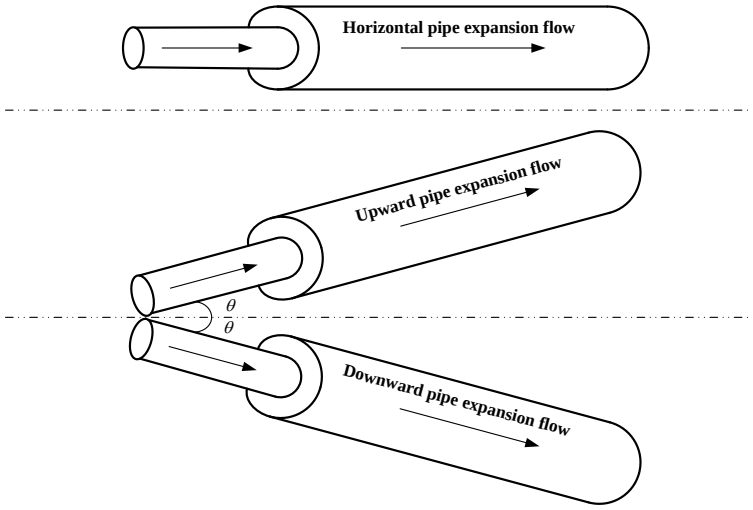

Figure 2-1: Sudden pipe expansion configurations

While considering the importance of the equipment and pipe geometries for liquid-liquid systems in the chemical and petroleum industry, there is need to understand the dynamic changes that takes place within the internal configuration and pipe fittings of either the pipelines and/or the processing equipment. These changes in parameters normally results in economic loss during transportation, upstream and downstream processing of crude oil through pipelines and process equipment. Only recently, research has been focused on studying the behaviour of liquid-liquid systems in sudden pipe expansion, (Yang et al., 2003, Hasan, 2006, Yusoff, 2012).

Frictional losses becomes evident when there is liquid-liquid flowing through a sudden expansion, as a result of change in diameter of the pipe according to Bernoulli's energy equation. For instance in a conical diffuser, any reduction in velocity causes the kinetic energy to be transformed to pressure energy. Figure 2.2 (a)-(b), shows a single and two phase flow through sudden expansion with the assumption of a mass flow rate, velocity and pressure which are acting over the small diameter. As a balance to these parameters over the large diameter section of the sudden enlargement, it is found that the pressure acting over plane one before the expansion, P_1 is equal to the pressure at the infinite small distance after the expansion.

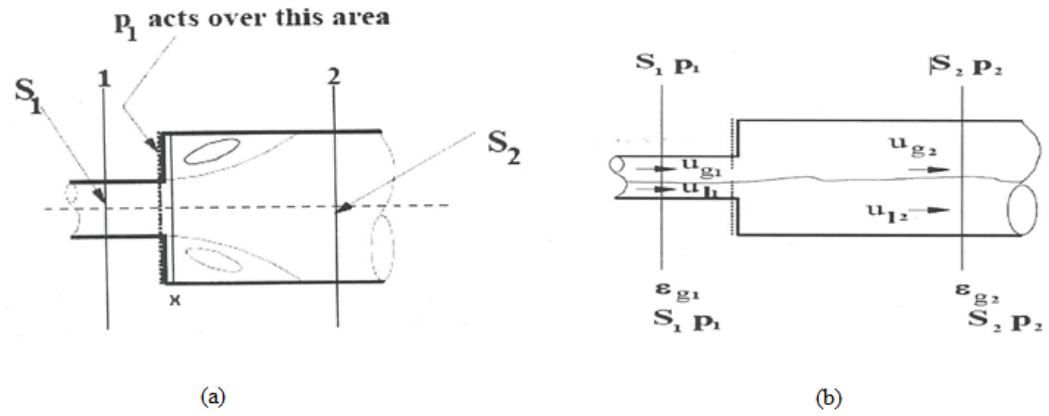

Figure 2-2 (a)-(b) Single and Two phase sudden pipe expansion, Azzopardi and Hills (2001)

(Delhaye, 1981) used this approach to derive momentum equations for single phase flow for the reversible and irreversible pressure drop expressions as follows:

$$-\left(\frac{dp}{dz}\right)_R = \frac{m_1^2}{2\rho}\left(1-S^2\right) \qquad 2.1$$

$$-\left(\frac{dp}{dz}\right)_I = \frac{m_1^2}{2\rho}\left(1-S\right)^2 \qquad 2.2$$

Where m_1^2 is the liquid mass flux defined by the total volumetric flow divided by the cross sectional area S, which is a ratio between the small diameter section and the large diameter section;

$$S = \frac{S_1}{S_2} \qquad 2.3$$

Azzopardi and Hills (2001), also used a similar approach in the characterization of one dimensional flow through a sudden enlargement and contraction for two phase gas-liquid flow. Currently, the Two-fluid and Homogeneous modelling approach is used in solving the resultant momentum equations, which will be reviewed in later sections of this chapter 2.

Regardless of other forms of crude oil transportation from production platforms to market places and central processing units (Refineries, Chemical plants etc.), pipelines remains the safest, efficient and most economical way of moving this hydrocarbon product from one location to another. In many of these applications, pumping of dispersions or emulsions through pipelines and pipe fittings is inevitable and consequently changes the physical condition and parameters of the crude, resulting in the formation of water in oil droplets that can harper process plant operation.

Therefore, pipeline geometrical configuration and fittings is very important in determining the flow pattern of liquid-liquid and has some role in the operational conditions of the hydrodynamics of the system. These have been reported by some researchers such as (Nädler and Mewes, 1997, Yang et al., 2003).

In order to understand and effectively describe the hydrodynamic behaviour of liquid – liquid dispersions in the various multiphase fluid handling facilities in Petroleum, Petrochemical and Process industries, it is pertinent to carryout investigations on both

bench top mixing vessels and online pipe loop facilities. To mention but a few of some of the liquid-liquid dispersion processes, include:

- Petrochemical Industry

    i. Efficient separation of reservoir fluid of oil/water before transportation through pipe lines
    ii. Water breakthrough in aged oil wells.

- Chemical and Process Industry

    i. Emulsification
    ii. Two – phase reactions resulting in pressure drop, heat and/or mass transfer rates and separation at downstream.

All of these processes are governed principally by the phenomena of drop breakup and coalescence.

In light of the above information, this literature review focuses on three distinct but linked areas. Thorough investigation and re-examination of the characteristics flow patterns and flow pattern maps of liquid-liquid pipeline flow will be made. Drop size measurement techniques and a review of instrumentation in liquid-liquid dispersions shall be presented. The fundamentals of the hydrodynamics and physics of phase separation, resulting from the two basic phenomena of drop breakage and coalescence, will be discussed. Some existing models and correlations, together with possible new modelling techniques will be critically reviewed. Finally, experiments made and published work done on bench top stirred tanks and online liquid-liquid research facilities or in the industry on such vessels will be presented.

A programme of work will be proposed from this information which will be able to expand upon the database of existing information and will lead to an increased understanding of the preferred coalescence process modelling and the nature of liquid – liquid turbulent dispersions in horizontal pipeline systems.

2.2 Liquid – Liquid Flow patterns and Flow pattern maps in pipes

The understanding of multiphase flow pattern behaviour is important in arriving at the correct interpretation of the response of several oil and gas facilities in the chemical and petroleum industries. Interestingly, the limiting case where gas phase is not present i.e. oil/water mixtures, especially in the natural crude oil production in the petroleum industry, has received great attention. The flow structure of oil/water mixtures in pipes is quite different from that of gas/liquid mixtures due to the formation of droplets.

When a mixture of two liquid phases flow through a pipe, the interfaces between the phases can present different shapes, sizes and dispersions, depending on the prevailing flow conditions of either laminar or turbulence in the system. Such circumstance results from a number of factors, e.g., mixture velocity, phase ratio, pipe material, pipe geometry and pipe orientation. Trallero et al. (1997), stated that the different flow structure is also caused by the large liquid/liquid momentum transfer capacity and small buoyancy effects. In addition, the lower free energy at the interface allows the formation of shorter interfacial waves and smaller dispersed phase droplet size. If the dominating flows have similar interfacial shapes and spatial distributions, then they can be classified and considered as a flow pattern or regime.

Several studies of drop sizes and flow patterns have been made for two fluid systems, in particular for oil/water systems to both obtain experimental data and develop means for predicting flow patterns, pressure drop and hold up. According to (Trallero et al., 1997) most of the previous studies centred on identifying the flow patterns visually and/or based on average pressure drop measurements and the physics of the transition mechanisms has not been investigated thoroughly. Therefore, for the sake of developing a very good coalescence model in liquid-liquid dispersed systems, standard flow pattern maps need to be identified and used for proper optimization.

Some attempts have been made to obtain experimental data and to develop means of predicting flow patterns, pressure drop and in-situ volume fraction. Oil/water flow systems is very wide and therefore a single clear cut way cannot be used to describe it effectively. The densities of oil and water can vary and the rheological behaviour can be Newtonian or non-Newtonian, depending on existing and prevailing conditions.

In most of the reported studies as summarised by (Brauner, 2001), the identification of the flow pattern is based on visual observations, photographic/video techniques, or on abrupt changes in the average system pressure drop. In some recent studies, the visual observation and pressure drop measurements are backed-up by conductivity measurements, high frequency impedance probes or Gamma densitometers for local holdup sampling, or local pressure fluctuations and average holdup measurements (see Table 2.1). Other modern techniques now include the use of Lasentec Focused Beam Reflectance Measurements (FBRM) and Wire Mesh Sensor CapWMS (Beyer et al., 2012). The flow patterns can be classified into four basic prototypes: Stratified layers with either smooth or wavy interface; Large slugs, elongated or spherical, of one liquid in the other; A dispersion of relatively fine drops of one liquid in the other; Annular flow, where one of the liquids forms the core and the other liquid flows in the annulus. In many cases, however, the flow pattern consists of a combination of these basic prototypes. As a result of the complex nature of the liquid – liquid two – phase system, an empirical or semi-empirical approach is adopted.

2.2.1 Flow pattern in horizontal pipes

Different flow patterns will appear when two immiscible liquids, oil – water, flow together in a horizontal pipe. Mixture flow rate, density ratio, viscosity ratio, wetting properties, input volumetric flow phase ratio, surface tension and pipe geometry are crucial and important parameters for the formation of each flow pattern. Pressure drop, fluids holdup, heat transfer, corrosion and structural vibration are also topics that depend on the geometrical configuration or flow patterns of the immiscible phases. Identification of the different flow patterns in horizontal flow pipes can be done in several ways:

- High speed Cameras and video camera recorders are helpful tools used for visualizing flow patterns through transparent pipes. Early studies by (Russell et al., 1959, Charles et al., 1961) together with the more recent work of (Arirachakaran et al., 1989) make use of this technique. The main disadvantages of visual observations is that they are subjective and even being exposed to light refractions.

- The use of conductivity probes as in (Trallero, 1995, Nädler and Mewes, 1997) as well as the use of high frequency impedance probes as in (Vigneaux et al., 1988, Angeli and Hewitt, 2000) gives perhaps a more precise and objective discrimination of flow regimes.
- Gamma ray densitometry used for instance by (Soleimani et al., 1997, Elseth et al., 2001) represents another useful method.
- Lasentec Focused Beam Reflectance Measurement (FBRM) Laser, (Simmons and Azzopardi, 2001)
- Wire Mesh Sensor, CapWMS, (Yusoff, 2012).

Over the years from the late 1950's and of recent times the investigation of flow patterns has developed both in observation techniques, presentations and instrumentation. (Russell et al., 1959, Charles et al., 1961), (Arirachakaran et al., 1989) and the studies of (Trallero et al., 1997) and (Nädler and Mewes, 1997), were among the pioneer researchers who made valuable contributions in determining flow patterns in horizontal pipe systems.

Initially, (Russell et al., 1959, Charles et al., 1961) describe three flow patterns in oil-water flow in a horizontal circular pipe, which include mixed flow (M), stratified flow (S) and bubble flow (B). They varied the oil-water volume ratio, from 0.1 to 10.0, and the superficial water velocity from 0.0354 to 1.082 ms^{-1}. The three flow regimes were found to appear in both laminar and turbulent flows. At the lowest input ratio the oil phase appears as large stretched out bubbles. With increasing input ratio the flow approaches the stratified pattern. By further increase of input ratio the flow becomes mixed or dispersed.

Charles et al. (1961), observed a series of flow patterns for a decrease of the oil flow rate at constant water flow rate. The flow patterns are similar to the two-phase systems with the less viscous oils except at low water velocities. At such low water velocities a series of oil continuous flow patterns were identified and an inversion line (P-Q) was drawn. For given oil velocities, mixtures with lower water velocity than indicated at the inversion line gave oil continuous flow. Figure 2.3 shows several classical oil-water flow patterns observed by (Oglesby, 1979).

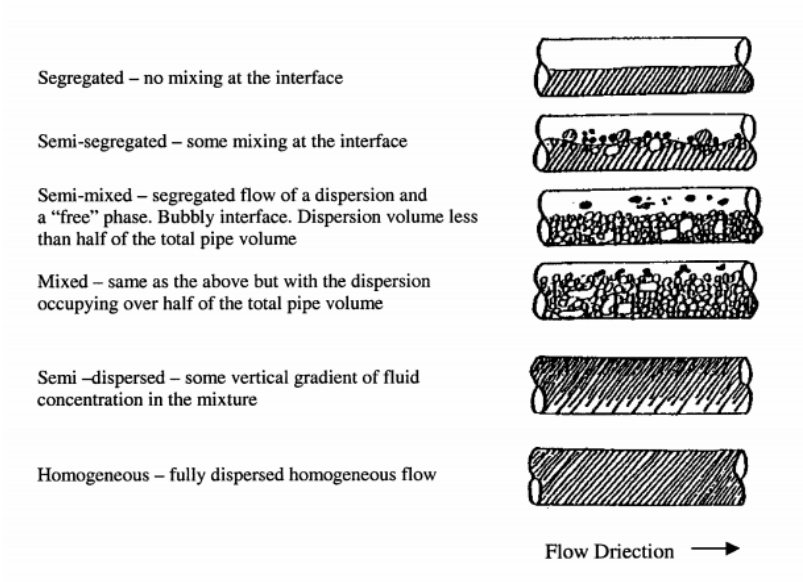

Figure 2-3 Flow patterns classification for oil-water flow (Oglesby, 1979)

Subsequently, several researchers have classified oil-water flow patterns based on their own investigations on horizontal pipe systems flows. A few of them includes: (Scott, 1985, Arirachakaran et al., 1989, Trallero et al., 1997, Nädler and Mewes, 1997, Simmons, 1998, Angeli and Hewitt, 1998, Angeli and Hewitt, 2000a) etc. A brief summary of some experimental work done by researchers over the past years and of recent, on Liquid- Liquid horizontal flow systems is presented by (Yusoff, 2012) and in more detail by (Brauner, 2001) as shown in (APPENDIX A , Table 2.1). The various observed flow patterns includes: Stratified flow of two separated layers (S, possibly with mixing at the interface, SM); Stratified layers of a free-liquid and a dispersion of the other liquid (e.g. oil – in – water dispersion above a water layer, $D_{o/w\ \&\ w}$); Stratified layers of a free liquid and a dispersion in the other liquid (e.g. oil and oil – in – water dispersion. $D_{w/o\ \&\ w}$); Layers of dispersions (e.g. water – in – oil dispersion above oil in water dispersion $D_{w/o\ \&\ o/w}$, possibly with pure oil at the top and/or water at the other liquid (e.g. water – in – oil or oil – in – water dispersion or emulsion. $D_{w/o}$ or $D_{o/w}$); Core annular flow: a core of one liquid within the other liquid (e.g. a core of viscous oil and water in the annulus, AN_w. Oil in the annulus, AN_o); Annular flow of a liquid with a dispersion in the core (water in the annulus DAN_w, oil in the annulus DAN_o; Core annular flow of two dispersions (CAD_w or CAD_o); Intermittent flow (one liquid alternately occupying the pipe as a free liquid or as a

dispersion, I_o or I_w; Large elongated or spherical bubbles of one liquid in the other (SL_o, B_o, or SL_w, B_w).

Arirachakaran et al. (1989), did some experimental work on oil/water flow in horizontal pipes for a selection of viscosities in order to determine any viscosity effect on the flow patterns. The flow pattern for a range of velocities between 0.45 - 3.65 ms^{-1} with an input oil fraction from 10 to 95% was investigated (Figure 2.4). His experimental data includes; Flow temperature (28^oC – 54^0C), Oil viscosity 4.7 mPas, Pipe diameter of 26.6mm and 41mm, Interfacial tension 29 $2x10^{-3}$ – $32.2x10^{-3}$ Ncm^{-1}, Oil density 868 – 898 kgm^{-3} and test section length 6.1 m and 12.8 m.

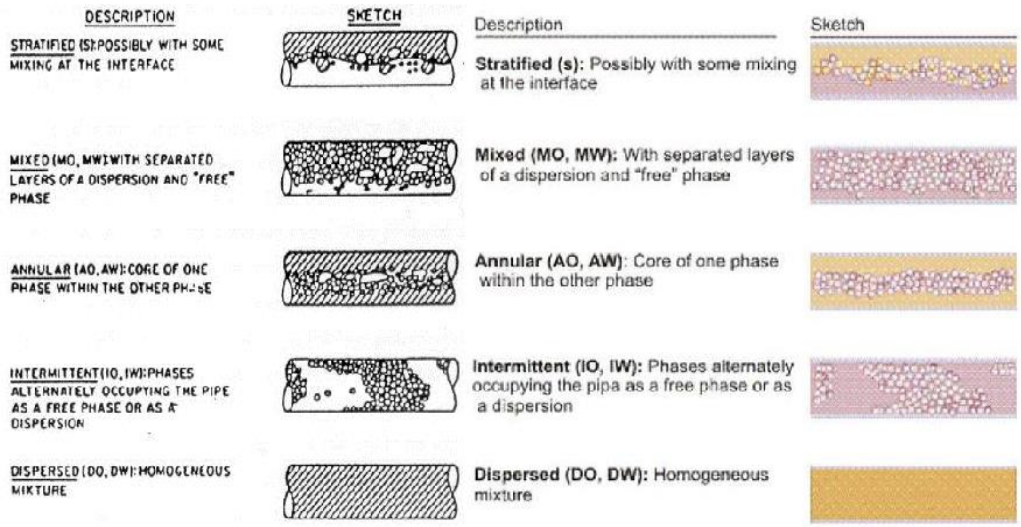

Figure 2-4 Flow patterns defined by (Arirachakaran et al., 1989).

Stratified flow (S) with or without mixing at the interface and fully dispersed flow, either an oil-in-water dispersion or a water-in-oil dispersion (DO, DW) were the extremes. The mixed flow (MO, MW), and mixed in the sense that the flow consists of both a dispersed and a “free” phase, could appear with either water or oil as the “free” phase. Annular flow (AO, AW) had a core of one phase within the other. The core could be both oil and water. Finally, intermittent flow (IO, IW) was described as a flow pattern that was alternating between a “free” phase flow and a fully dispersed flow. The results showed that the flow pattern disappeared for lower oil viscosity and the oil-annulus annular flow pattern diminished in size as the oil viscosity decreased.

It can be concluded from the attained data that, in general, the oil viscosity has little effect on the flow behaviour when water is the continuous phase.

Trallero (1995), identified and reclassified the flow pattern nomenclature and defined six flow patterns based on his experiments and the results of previous investigators for horizontal flow. They categorized the various oil-water flow patterns into two major groups namely, Segregated Flow and Dispersed Flow.

Segregated flows:

Stratified flow (ST)

Stratified flow with mixed layer at the interface (ST&MI)

Dispersed flows:

Water dominated

- Dispersion of oil in water and water (Do/w & w)
- Oil in water emulsion (o/w)

Oil dominated

- Dispersion of water in oil and oil in water (Dw/o & Do/w)
- Water in oil emulsion (w/o)

A sketch of the flow patterns and flow pattern maps are shown in Figure 2.5 and Figure 2.6 respectively. Trallero (1995), used mineral oil and water as working fluids ($\mu_o / \mu_w = 29.6cP$, $\rho_o / \rho_w = 0.85kg/m^3$, and $\sigma = 0.036N/m$ at 25.6^0C) and employed an acrylic pipe as the test section.

Segregated flow: The two fluids flow in separate layers according to their different densities. Segregated flows are made of Stratified flow (ST) and Stratified flow with mixed at the interface (ST&MI). The stratified flow (ST) is identified when the smooth interface exists. As the velocities of the phases increase, the interface becomes more disturbed or wavy and drops of the two liquids may also appear. At that time the flow pattern shifts to the stratified flow with a mixed layer at the interface (ST&MI). There exist water droplets in the oil and oil droplets in the water layer. Both kinds of

droplets remain close to the interface. In this case, dynamic and buoyant forces are acting simultaneously on the droplets. The former, which tends to spread the droplets throughout the pipe cross-section, is not large enough to overcome the settling tendency of the counteracting gravity force (Arirachakaran et al., 1989, Brauner et al., 1998, Kurban et al., 1995, Vedapuri et al., 1997)).

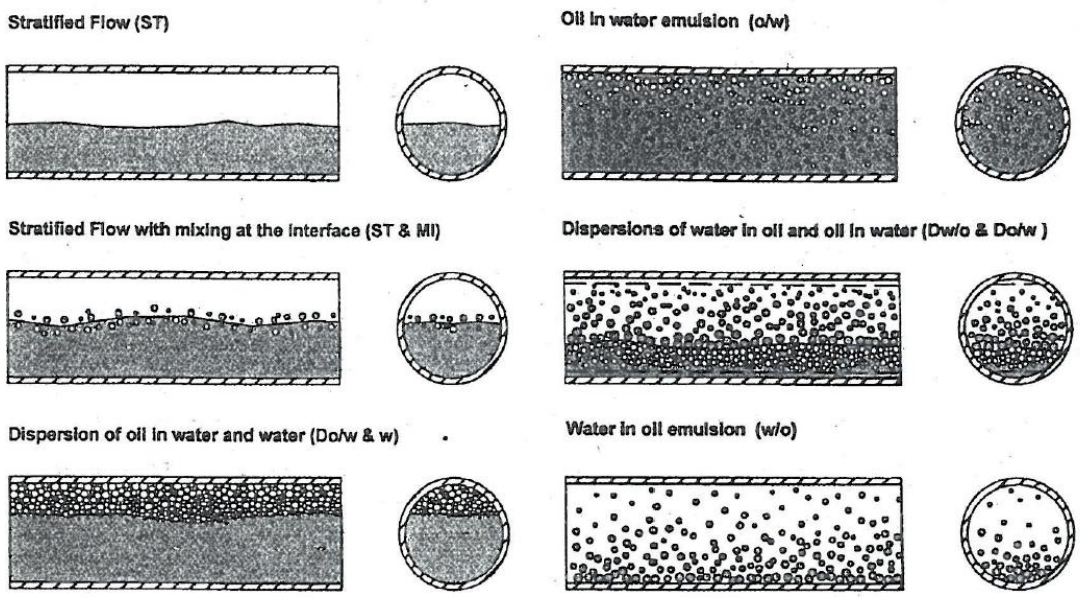

Figure 2-5 Horizontal oil-water flow pattern sketches (Trallero, 1995).

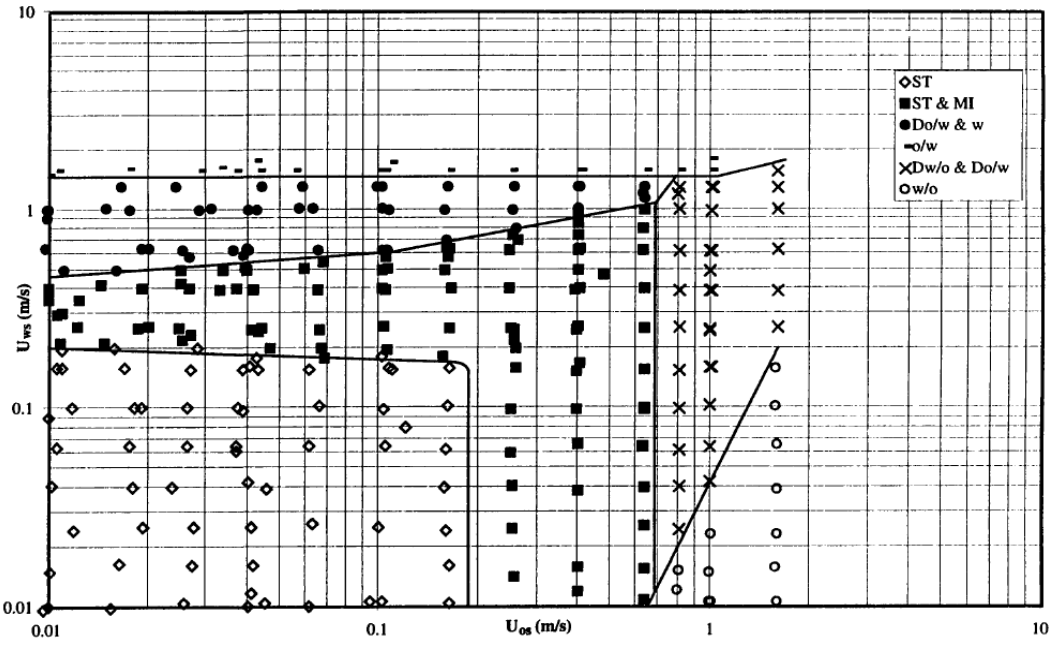

Figure 2-6 Horizontal oil-water flow pattern map (Trallero, 1995).

Dispersed flow: In dispersed flow one phase is dispersed in the other continuous phase. The dispersed phase often present in the form of small droplets that are non-uniformly scattered within the continuous phase in two immiscible liquids. According to the size of the drops and their distribution in the continuous medium, several subdivisions of this flow pattern can be observed. The dispersed flow can either be water dominated or oil dominated. As for water-dominated flows, the water is always the continuous (dominant) phase and vice versa. A dispersion of oil in water over a water layer (Do/w & w) and emulsion of oil in water (o/w) are dispersed flow patterns where water is the dominant phase. On the other hand, an emulsion of water in oil (w/o) and the coexistence of both type of dispersions (Dw/o & Do/w) are oil dominated flow patterns (Karabelas, 1978, Trallero et al., 1997, Angeli and Hewitt, 2000, Jayawardena et al., 2000). Dual continuous dispersed flow namely oil continuous and water continuous, have been experimentally identified by (Jayawardena et al., 2000, Lovick and Angeli, 2004b). Nädler and Mewes (1997), measured flow regimes and pressure drops in oil-water flows depending on the oil viscosity ratio from approximately 18cP to 35cP. The observed flow regimes are schematically presented in Figure 2.7 and compared in the flow pattern map in Figure 2.8. A summary of their work is presented by (Brauner, 2001) in (APPENDIX A, Table 2.1). About seven flow patterns were generated, which are similar to that of (Trallero et al., 1997), and classified as stratified flow or dispersed flow. They precisely distinguished them into sub-patterns as a combination from those flow patterns.

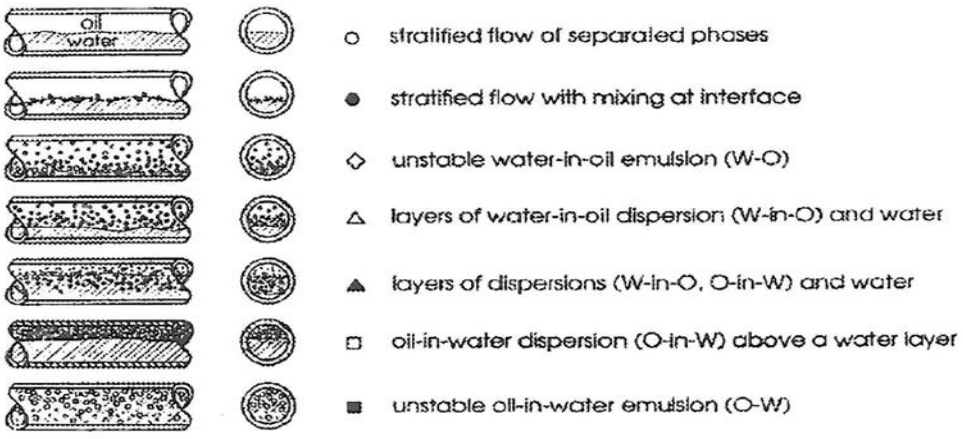

Figure 2-7 Horizontal oil-water flow patterns (Nädler and Mewes, 1997)

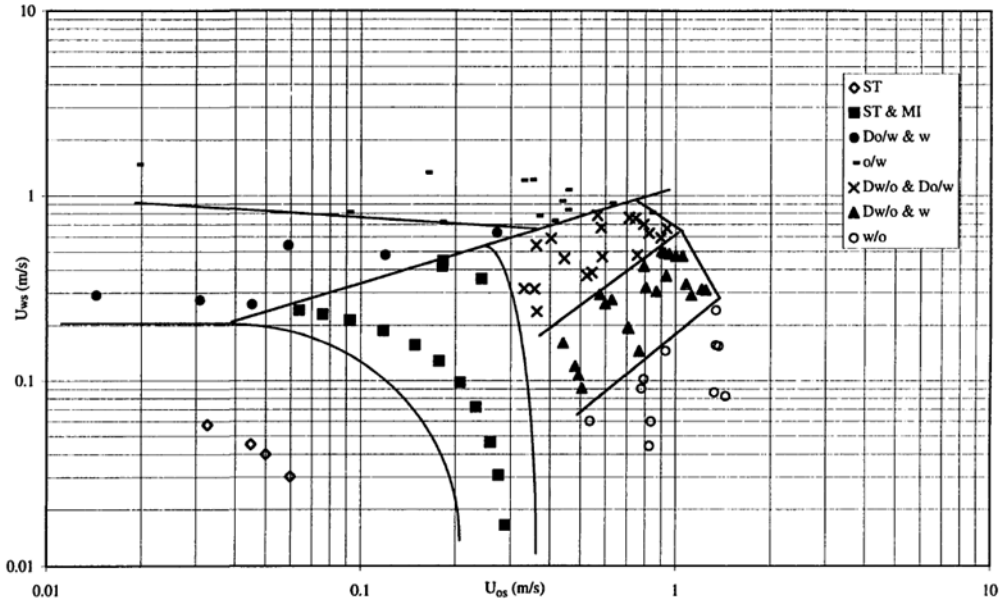

Figure 2-8 Experimental horizontal flow pattern map – superficial velocities of oil and water (Nädler and Mewes, 1997)

Angeli and Hewitt (2000a), implemented two methods for the flow pattern identification, namely high speed video recording and determination of the local phase fractions with a high frequency impedance probe, while the continuous phase in dispersed flows was recognised with a conductivity needle probe. The flow patterns observed had substantial differences in that the propensity for dispersion was greatly increased in the steel pipe, whereas the oil tends to be the continuous phase for a wider range of flow in the acrylic pipe than in the steel pipe. In certain ranges of conditions the distribution of the phases differed dramatically between the stainless steel and liquid – liquid two phase flows.

Full-scale experiments were conducted by (Fairuzov et al., 2000) in order to investigate flow pattern transitions in horizontal pipelines carrying oil-water mixtures. In the experiments, a 16-in. pipeline conveying light crude oil was used. The identification of flow patterns was carried out based on measurements of the transversal water fraction profile using a Multi-Point Sampling Probe MPSP, which has several take-off points, as shown in Figure. 2.9.

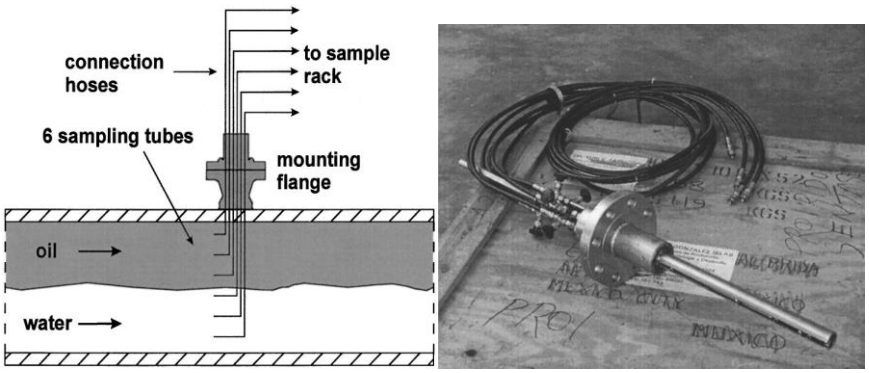

Figure 2-9 Schematic of multi-point sampling probe (Fairuzov et al., 2000)

Both stratified and dispersed flow patterns have been obtained and identified by analysing measured water volume fraction profiles based on the experimental data obtained. A simplified flow pattern map was constructed from the data obtained, which shows the transition from stratified to non-stratified flow configurations Figure 2.10.

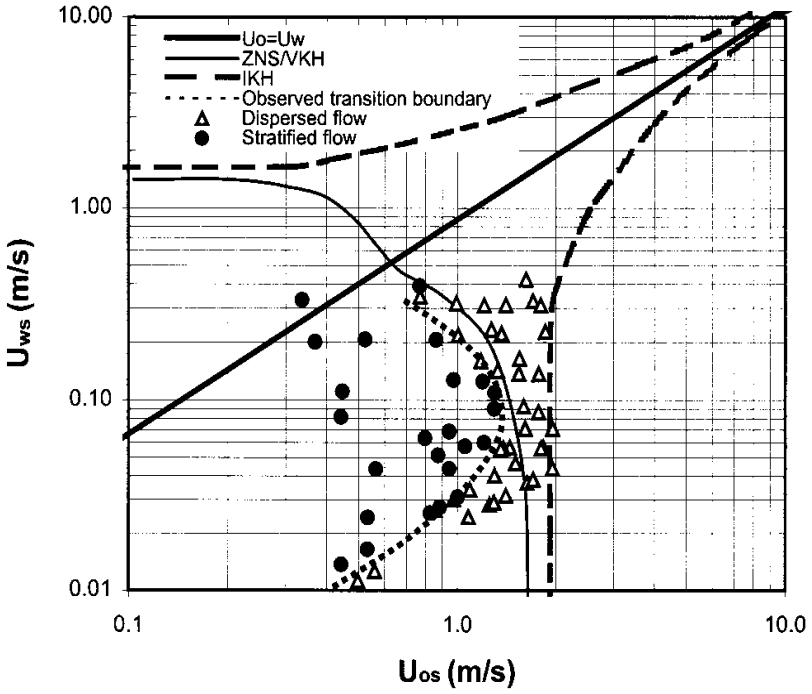

Figure 2-10 Comparison of experimental data with theoretical transition boundaries (Fairuzov et al., 2000).

Yang (2003), observed and recorded flow patterns using the naked eyes and a high speed video camera of oil-water flow which was confined to stratified wavy flows

approaching a T-junction. Their investigation shows that the different flow patterns depend on variation of the superficial velocity used in a range of studies. At low superficial velocities for both phases, the stratified (ST) flow pattern was observed. Any increase in either phase velocity, results in a flow pattern transition to stratified flow with mixed layer at the interface (ST&MI). The thickness of the mixed layer increases as the velocity increased and the flow pattern transit to a dispersed flow. The flow patterns observed by (Yang et al., 2003) are very similar to that given by (Trallero et al., 1997).

Currently, different flow pattern maps have been used by researchers to describe their experimental results found in oil-water mixtures. The experimental patterns are usually represented by either plotting the mixture velocity against water cuts and input oil fractions or superficial velocity of oil in the x axes and that of water in the y axes. For example, Figures 2.11 – 2.15, shows some flow pattern maps used by different authors in there works on oil-water mixtures on horizontal pipe line.

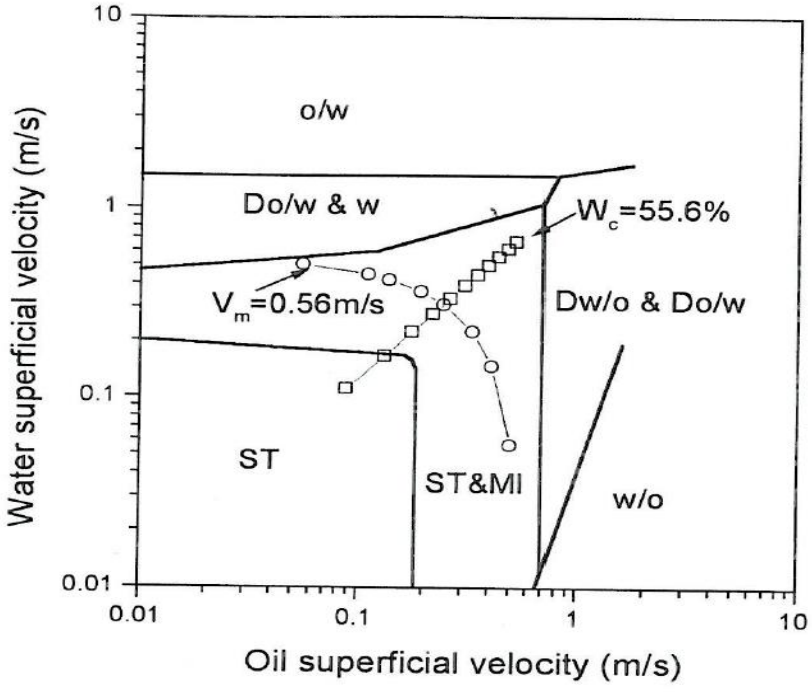

Figure 2-11 Flow conditions for measurements of the thickness of the three phase layers in the ST & MT regime (Yang et al., 2003).

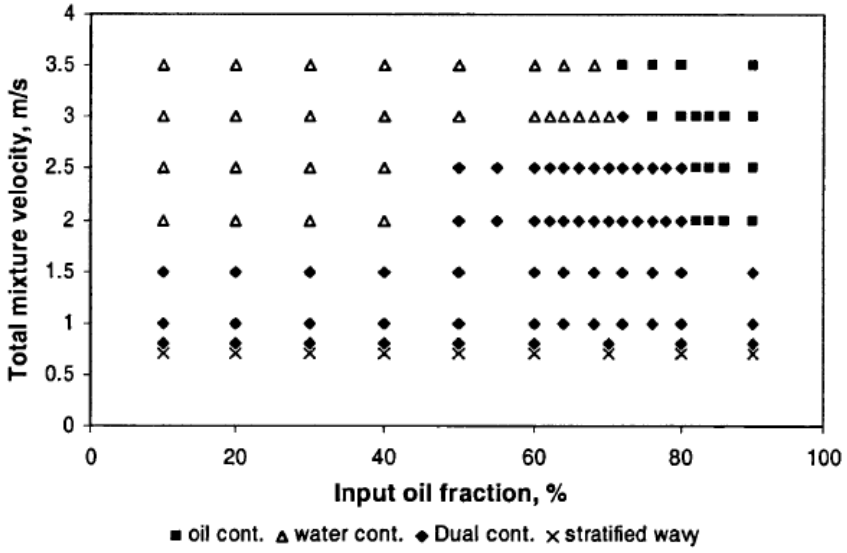

Figure 2-12 Experimental flow pattern map D = 38.1 mm, $\mu_o/\mu_w = 5.5$ $\rho_o/\rho_w = 0.83$, $\sigma = 0.039 Nm$ (Lovick and Angeli, 2004b).

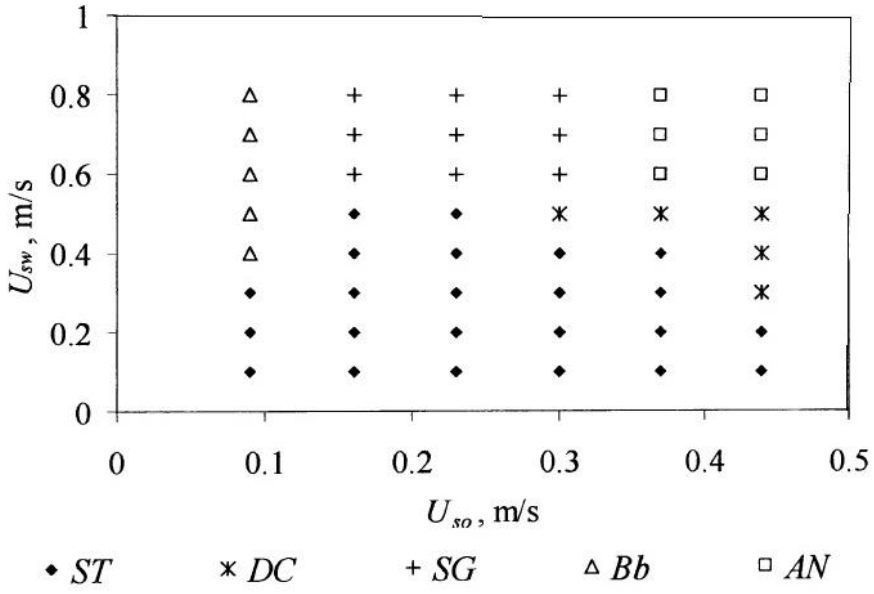

Figure 2-13 Experimental flow pattern map D = 14 mm, $\mu_o/\mu_w = 5.5$ $\rho_o/\rho_w = 0.83$, $\sigma = 0.039 Nm$, Flow patterns: ST (stratified smooth or wavy), DC (dual continuous), SG (slug), Bb (bubble) and AN (annular), (Al-Wahaibi and Angeli, 2011).

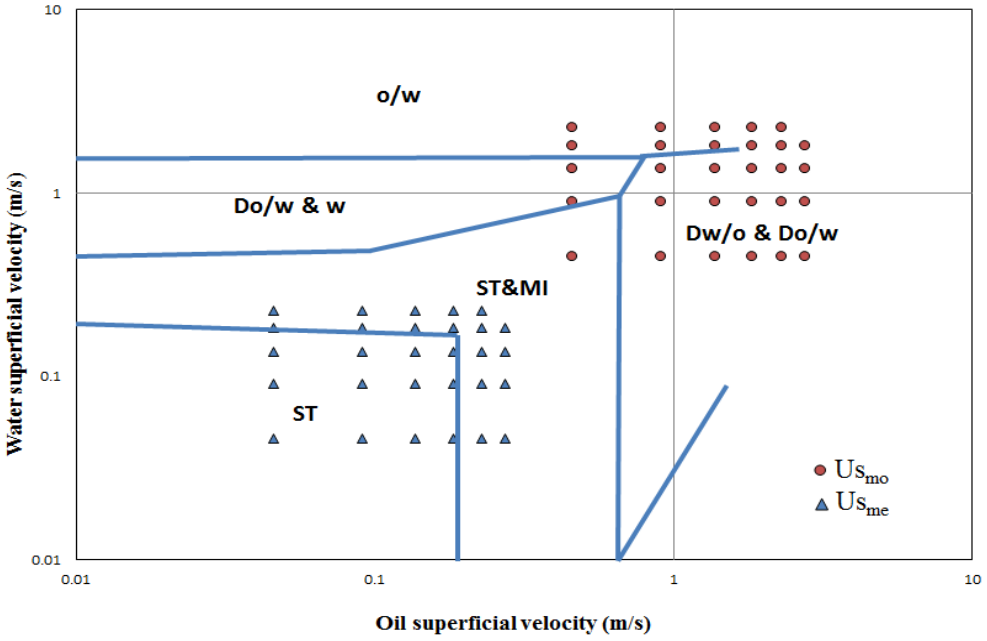

Figure 2-14 Experimental flow pattern map of (Yusoff, 2012) showing mixture velocities after orifice (Usmo) and mixture velocities downstream (Usme) of flow pattern encountered within the rig and possible operational limits plotted on flow pattern map of (Trallero et al., 1997)Trallero et al. (1997).

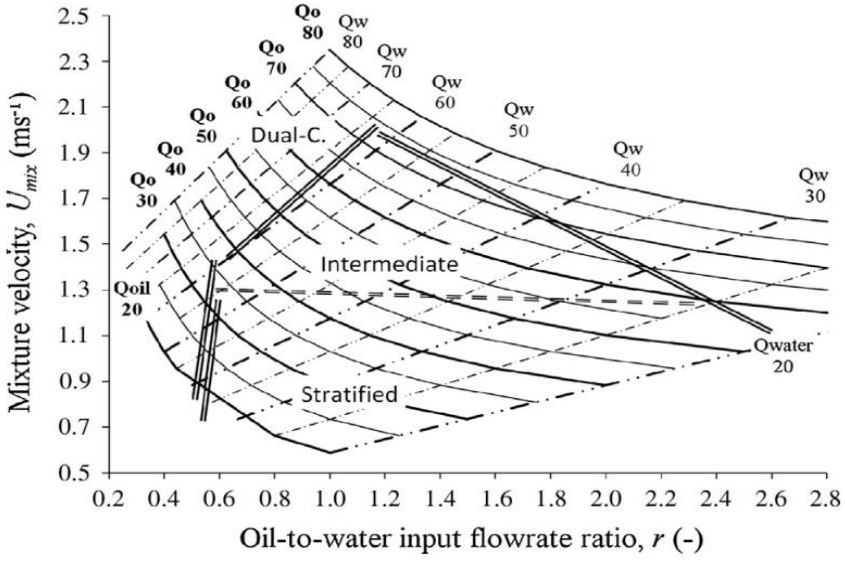

Figure 2-15 Experimental flow pattern map (Barral and Angeli, 2014).

The experimental study carried out by (Rodriguez and Oliemans, 2006) on oil-water flow in horizontal and slightly inclined pipes showed that a stratified smooth flow pattern and stratified wavy (SW) flow patterns exist at the interface. Therefore, two

immiscible liquids of different densities tend to stratify when flowing together in a pipe. The difference in density determines the extent of the stratification.

2.2.2 Flow pattern maps and identification in vertical and inclined pipes

2.2.2.1 Flow Pattern in Vertical Pipe Systems

Two-phase flows in vertical pipelines are common occurrences in the industries. However, very few experiments have been conducted with vertical pipeline for oil-water systems.

Flores et al. (1997), in their work investigated oil-water flow behaviour in vertical and large deviated inclined pipe to characterize flow pattern in a transparent pipe of 50mm internal diameter. Conductance probes were used and positioned at different pipe test sections in both vertical and inclined geometries and the oil-water flow patterns were studied. Figure 2.16; bellow illustrates a schematic representation of the flow patterns obtained in the vertical position.

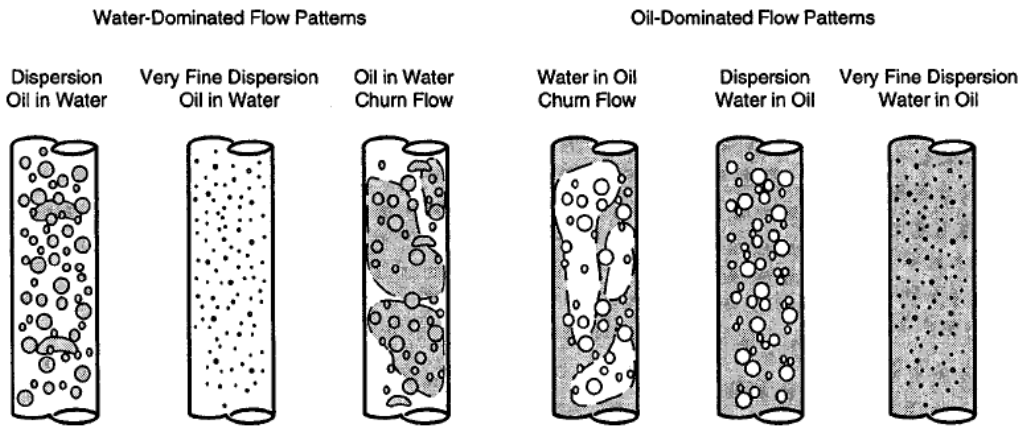

Figure 2-16 Schematic representations of vertical oil-water flow patterns by (Flores et al., 1997)

Basically, they were able to establish that the flow pattern transition observed seems to be governed by the mechanisms of droplet breakage and coalescence. Two distinct dispersed flow regimes were identified mainly water dominated flow patterns and oil

dominated flow patterns. For the water-dominated flows, a very fine dispersion of oil in water, dispersion of oil in water, and oil in water churn flow were observed. While in the oil-dominated flows, very fine dispersion of water in oil, dispersion of water in oil and water in oil churn flow, were seen.

(Brauner, 2001) stated that in vertical upward flow and low oil viscosities, the observed flow patterns typically include oil drops, bubbles or slugs in water, transitional flow (TF, churn), water drops in oil and oil-in-water or water-in-oil emulsions. A summary of some research work done on vertical pipe systems is compiled and presented by (Brauner, 2001).

The physical interpretation of flow patterns transitions is similar to that described for vertical gas-liquid systems. However, the clearly defined bullet-shaped bubbles that characterize slug flow in gas-liquid slug flow are normally not observed in oil-water systems. The churn flow is characterized as intermittent flow of complex and irregular structures of continuous oil phase (oil-dominated) and continuous water phase (water-dominated). The drops size decreases with increasing the mixture velocity, and for high velocity the liquids, either homogeneous Dw/o or Do/w of fine droplets are formed.

It was noticed that segregated flow did not appear for vertical flows. This absence of segregated flow will be investigated further when examining horizontal and moderately inclined pipe flows.

2.2.2.2 Flow Pattern in inclined Pipe Systems

This is also a common occurrence in the industry, together with the usual vertical and horizontal pipeline flows experienced in the industry. A summary of some recently published research experimental work done, on systems of Liquid-Liquid Inclined flow is presented, as investigated by (Brauner, 2001). It was stated that in large Eotvos number, Eo_D systems, a considerable drift between the lighter oil phase and water phase exists at low mixture velocities. A deviation of an oil-water pipeline from the horizontal modifies the force equilibrium conditions between the two liquids. This new dynamic equilibrium causes a perturbation of the initial state that affects the flow pattern.

The flow patterns observed generally are similar to those obtained in the horizontal pipeline flows. The main difference from the horizontal flows seems to be the presence of gravity – driven buoyancy effects. In the downward inclination flow, the heavier phase at the bottom part of the pipe moves much faster than the lighter phase and has a lower slip ratio. When the pipe is inclined upwards, then the lighter phase (usually oil) gathers at the upper part of the flow tube section and has a higher slip ratio.

Some experiments were conducted on inclined pipes by (Vigneaux et al., 1988, Scott, 1985, Flores et al., 1997), on inclined pipes with oil – water two – phase systems. They were able to investigate the effect of a range of pipe angle deviations between 0^0 and 65^0 from the vertical in 100mm and 200mm internal diameter pipes for a mixture velocity ranges from 0.1m/s to 0.5 ms^{-1}, on the flow behaviour and volume fraction profiles. They observed water holdup to be strongly affected by flow pattern and inclination and proposed a mechanistic model to predict holdup in vertical wells. They found that a homogeneous model was adequate for flow patterns showing negligible slippage and a drift-flux approach gave reasonable results for the high slippage flow patterns.

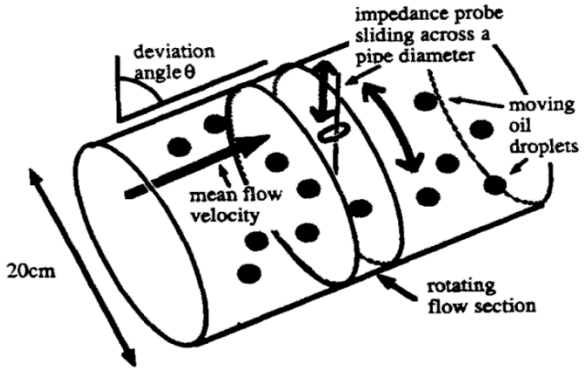

Figure 2-17 Experimental Measurent Set – Up for (Vigneaux et al., 1988)

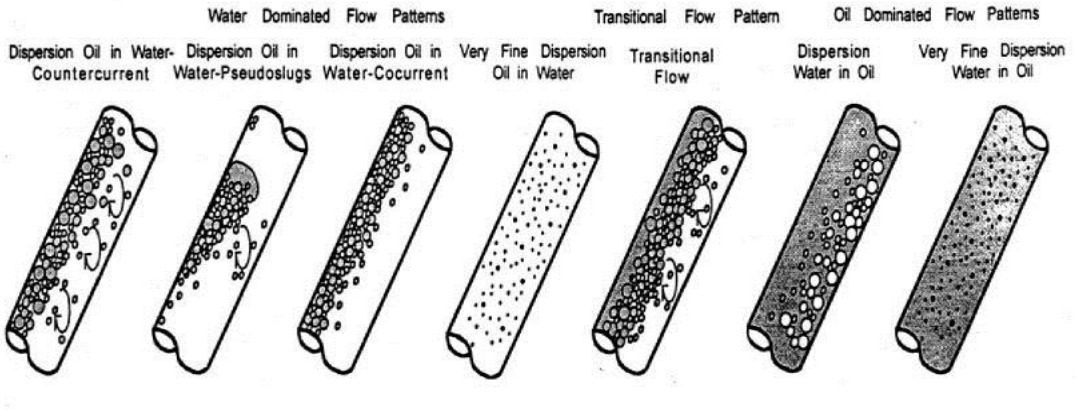

Figure 2-18 Schematic representation of upward inclined oil-water flow patterns by (Flores et al., 1997)

Holdup and velocity profiles of oil–water flows in 10 cm diameter inclined pipes were investigated by (Vedapuri et al., 1997). The experiments were performed at six different inclinations (±2°, ±5°, ±15°). Inclination was found to affect both holdup and velocity profiles. In the case of large diameter pipes, (Wilkens, 1997) investigated the flow regime transitions and the effects of inclination, pressure, and water cut for a light oil–saltwater–carbon dioxide system. The experiments were carried out on an 18 m long, 10 cm diameter, high-pressure (13 MPa), high temperature (90 °C), inclinable stainless steel flow-loop at inclinations of 0°, ±2° and ±5° from horizontal. A mechanistic model was developed to predict the flow regime transitions. The mechanistic model developed by (Petalas and Aziz, 2000) was able to predict the experimentally observed flow pattern with high accuracy and holdup with reasonable accuracy.

In oil– water flow, the formation of emulsions, which requires a proper calculation of emulsion viscosity, and phase inversion, which causes a sudden increase or decrease in pressure drop and mixture viscosity, make the problem even more complicated, (Shi et al., 2001). Furthermore, drag reduction, in which the more viscous phase is dispersed in the less viscous phase, thus causing a reduction in pressure gradient, was observed by (Pal, 1993, Angeli and Hewitt, 1998) for turbulent flows. The later also found that oil–water flow behaves differently depending on the tube wall material

Oddie et al. (2003), in their experimental study of two and three phase flow in large diameter inclined pipe, observed Bubble, churn, elongated-bubble, slug, and stratified/stratified-wavy flows for water–gas and oil–water–gas flows, while dispersed/homogeneous, mixed/semi¬mixed and segregated/semi-segregated flows were observed for oil–water flows. Figure 2.19 bellow gives a sketch of their work.

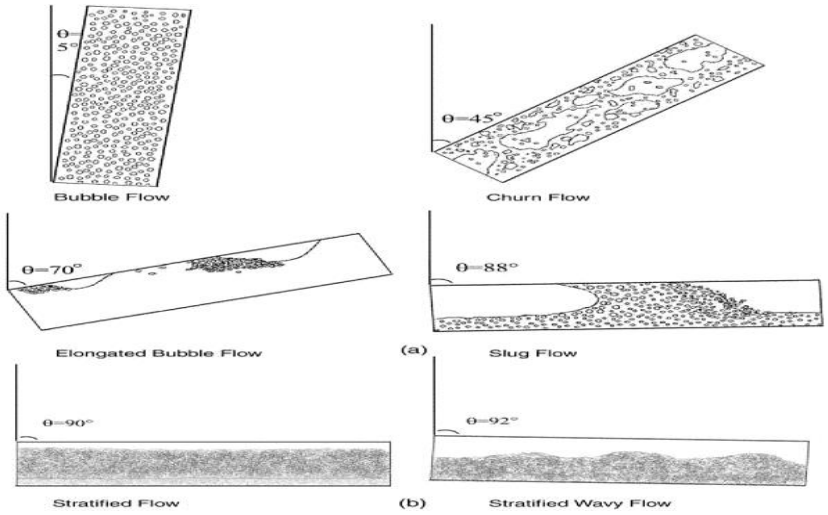

Figure 2-19 (a) Sketch of some observed water–gas flow patterns with typical corresponding inclinations; (b) sketch of some observed oil–water–gas flow patterns with typical corresponding inclinations, (Oddie et al., 2003)

Extensive results for holdup as a function of flow rates, flow pattern and pipe inclination were reported. The flow pattern and shut-in holdup are also compared with the predictions of a mechanistic model. Results show close agreement between observed and predicted flow pattern, and a reasonable level of agreement in holdup.

In a view to do more investigations on liquid – liquid flow in inclined pipes, (Yang, 2003), did some experiment on small inclination angle between -7^0 and $+6^0$ from the horizontal downstream of a pipe expantion. He discovered interfacial waves between the water and mixed layers for both upward and downward inclinations, whose wave amplitude increases and decreases respectively for larger angles. Also in their experimental work on oil-water flow in horizontal and slightly inclined pipes identified seven flow patterns. They observed both stratified smooth and wavy flow patterns, as they moved from horizontal to inclination.

Rodriguez and Oliemans (2006) conducted an experimental study on oil-water flow in horizontal and slightly inclined pipes in a 82.8 mm internal diameter steel pipe at the inclination angles of -5^o, -2^o, -1.5^o, +1^o, +2^o, +5^o and horizontal flow. Basically, seven flow patterns were observed for horizontal, upward and downward inclined flow, and are reasonably well described by the (Trallero et al., 1997) flow pattern map. They observed a stratified smooth flow pattern and stratified wavy (SW) flow patterns.

Researchers such as (Hasan, 2006, Yusoff, 2012), also used the expansion rig facility that was used by (Yang, 2003) in their recent experiment on stratifying liquid-liquid flow of oil-water flow and identifird three (3) different interface shapes for stratified flow, which includes; plane horizontal, concave and convex interfaces. Yusoff (2012) in his study on stratifying of Liquid – Liquid two phase flow through sudden expansion also showed results on the various flow patterns as stated by (Trallero et al., 1997) and other researchers in the segregated and dispersed flow regimes. The Wire Mesh Sensor, CapWMS was used and the pipe orientation of the expansion test section were adjusted depending on the inclination desired. Experiments were conducted for input oil fractions ranging from 0.2 to 0.8 OVF, orifice open area 32%, downstream expansion mixture velocities $_{(Usme)}$ of 0.20, 0.30, & 0.35 m/s with a horizontal pipe or inclined at angles of +6, +3, -3 & -6 degrees. His results also confirmed the plane horizontal , convex interface and concave interface of the stratified smooth and wavy interface, observed by (Brauner et al., 1998, Yang et al., 2001, Hasan, 2006, Rodriguez and Bannwart, 2006, Rodriguez and Oliemans, 2006).

In all the inevestigations, their has not been any concrete conclusion made on the effect of the coalescence mechanism in relation to the separation of the phases, which constitute part of the current reaserach work. Different types of inlet design have been used in the investigation of stratified and dispersed flow patterns, but a thorough description in relation to inclined pipe configuration is not usually available in the literature Further experimental work is therefore needed to investigate external elements such as sudden pipe expansion and orientation, inlet design, flanges etc as it affects the formation of drops or foams that are quite stable due to dificulties in coalescnece.

2.2.3 Stratifying Oil – Water Flows

The onset of droplet entrainment and formation of dispersions in oil-water mixtures is best understood by investigating stratified flow as a starting point. The mechanism of drop entrainment in oil-water is a complex process, which is not well understood and straightforward. Quite a number of researchers over the past years focus their investigations on developing stratified flow models that can predict drop formation via stability analysis. This stratified flow pattern of oil-water entrainment is quite common in the oil and gas industries, and requires experimental investigation in addition to the existing predictive models to fully understand its mechanism.

(Hadziabdic and Oliemans, 2007) in their modelling work stated that entrainment of one phase into the other occurs when the interfacial-shear stress becomes sufficiently high to drag part of the fluid into the continuous layer of the opposite phase. The high-amplitude interfacial waves can create a condition for entrainment occurrence since the drag between phases increases rapidly at the crest of the waves. (Brauner and Maron, 1989) had earlier presented an initial model on liquid-liquid flow based the assumption that the oil and water phases maintain their individual continuity and momentum equations. It was established in their predictive model that oil and water flow separately with a clear interface. This assumption was used together with some closure relations on frictional losses and shear stress to predict interface heights, pressure gradients and liquid hold up.

Subsequently, further investigations on oil-water flows by researchers such as (Trallero, 1995, Jayawardena et al., 2000, Bannwart et al., 2004) etc., has shown the existence of interfacial waves, which was not considered earlier. Other factors such as interfacial tension, fluid properties and pipe orientation were also put into consideration in the work of (Ng et al., 2001). Some modifications were also made by (Brauner et al., 1998) on the existing stratified flow model to include interface curvature.

A modified two fluid model together with new set of closure relations was presented by, (Ullmann and Brauner, 2006), which incorporated the effect of drop entrainment and interfacial waves. They made some successful attempts to validate the two fluid and homogenous models to experimental data on water hold up and pressure gradients, which gave better fits. (Al-Wahaibi and Angeli, 2011) in their work presented that a

drag force exist due to the differences in oil and water velocities, which results in drop entrainment. This approach was used to explain drop break up and formation mechanism.

Also, (Rodriguez and Baldani, 2012) in their work have used the phenomenological two fluid and homogenous models to validate experimental data of (Elseth, 2001, Raj et al., 2005, Rodriguez and Oliemans, 2006) and obtained quite good agreements as shown in Figure 2.20 and 2.21. In other to consolidate on these theoretical models, it is however very important to validate these predictive models with large amount of oil-water experimental data set, which are not available.

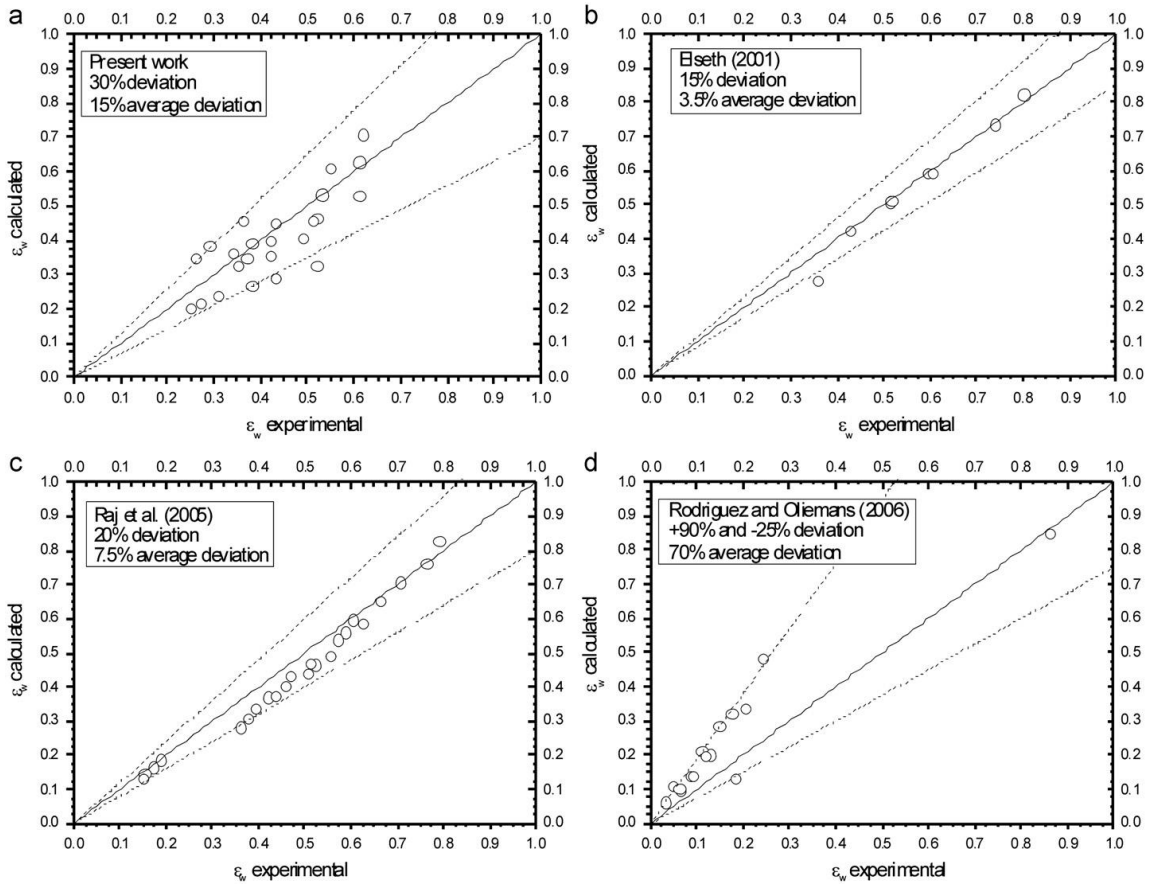

Figure 2-20 Comparison of Phenomenological model predictions for water holdup, ε_w with experimental dataset, (Rodriguez and Baldani, 2012).

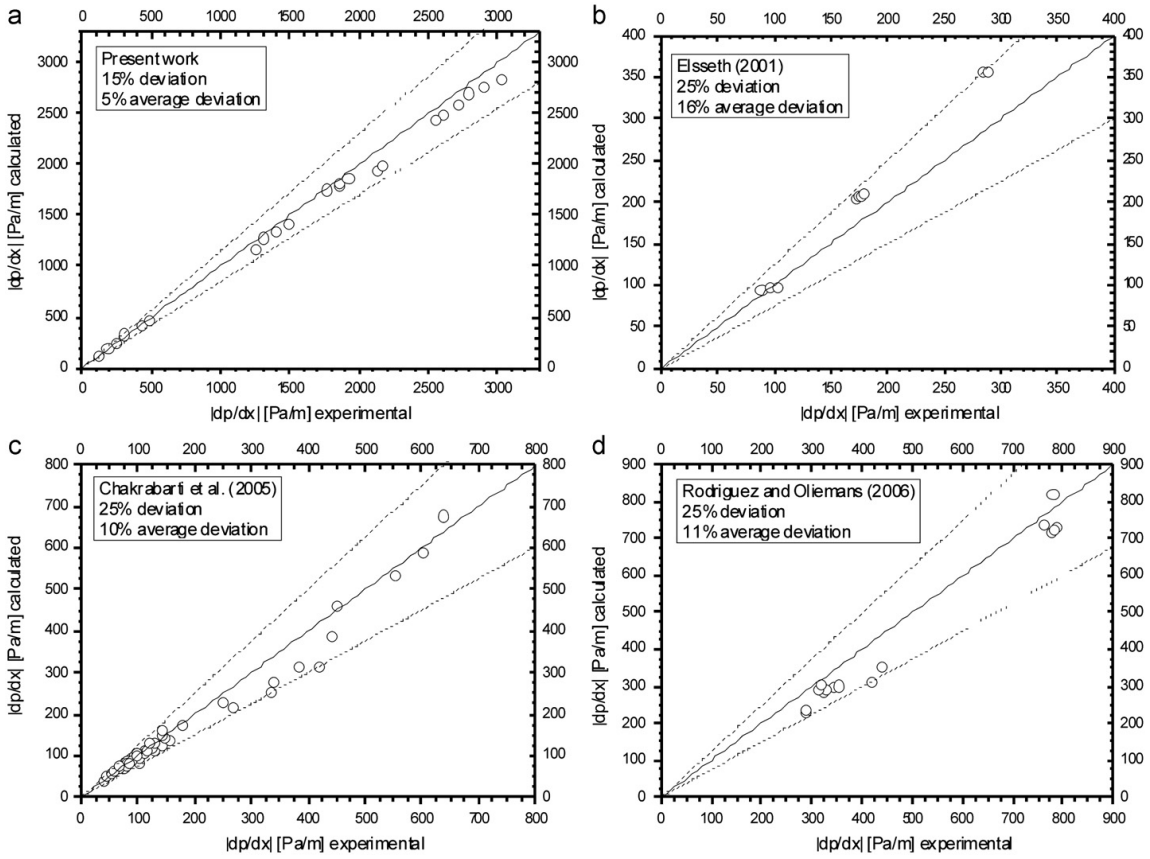

Figure 2-21 Comparison of Phenomenological model predictions for pressure gradients with experimental dataset, (Rodriguez and Baldani, 2012).

Barral (2014) in his work on stratified wavy oil-water flows used a statistical methodology to investigate fluctuating oil-water interface via double wire parallel conductance probes and obtained quite good results, which require further work and consolidation. The present work however will focus more on the investigation of the coalescence mechanism by measurement of drop sizes and drop size distribution

2.2.4 Phase inversion and flow pattern transitions

2.2.4.1 Phase inversion

Phase inversion is a phenomenon which occurs when there is a little change in the operational conditions that leads to the continuous and dispersed phase spontaneous inversion. For instance, in oil-water systems, dispersion (emulsion) of oil drops in

water becomes dispersion (emulsion) of water drops in oil, or vice versa. This is an important parameter to be considered in designing pipelines for oil-water systems.

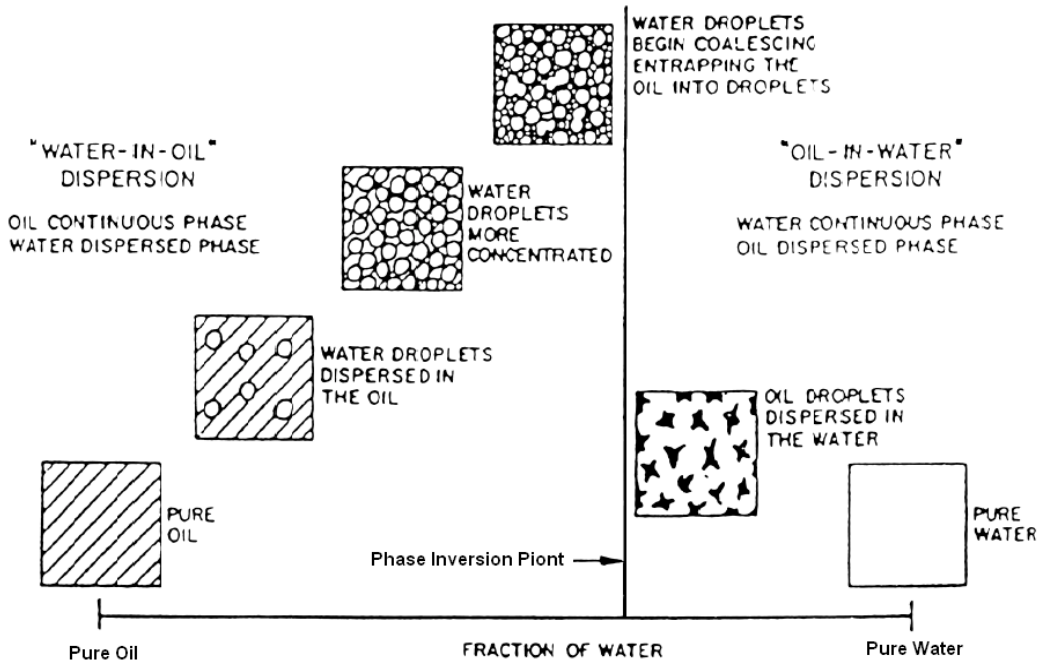

Figure 2-22 Phase inversion process for an O/W flow (Arirachakaran et al., 1989)

The rheological characteristics of the dispersion and the associated pressure drop, holdup and corrosion of the conduit pipeline are determined especially by the respective phase that wets it (Arirachakaran et al., 1989), (Angeli and Hewitt, 1998) and (Brauner and Ullmann, 2002). The critical volume fraction of the dispersed phase refers to the point of inversion. (Arirachakaran et al., 1989) proposed the following correlation for the critical water cut, ε_w^I as follows:

$$\varepsilon_w^I = \left(\frac{U_{ws}}{U_m}\right) 0.5 - 0.1108 \log_{10}\left(\frac{\mu_o}{\mu_r}\right); \mu_r = 1 mPa.s \qquad 2.4$$

Where, μ_r is the relative or mixture viscosity. (Brauner and Ullmann, 2002) also obtained a similar correlation for the critical oil hold-up, ε_o^I, in terms of liquid – solid wettability angle, α.

$$\varepsilon_o^I = \frac{(\sigma/d_{32})_{w/o} + \frac{s}{6}\sigma\cos\alpha}{(\sigma/d_{32})_{w/o} + (\sigma/d_{32})_{o/w}} \qquad 2.5$$

Where, s represents the surface wetted area per unit volume (s = 4/D for pipe flow), $0 < \alpha < 90^0$ corresponds to a surface which is preferentially wetted by water (hydrophilic surface), whereas for $90^0 < \alpha < 180^0$ the oil is the wetting fluid (hydrophobic surface). However, it was proposed by some researchers such as (Brauner and Ullmann, 2002) that phase inversion is a spontaneous phenomenon and that its prediction can be made on the minimization of the total system free energy. Therefore, under constant temperature and composition systems, only the free energies of the interfaces have to be considered.

Phase inversion points are made clearer by presenting flow patterns on maps of mixture velocity against water cut. (Nädler and Mewes, 1997) employed a conductivity probe to detect the flow patterns. This is shown in (Figure 2.7 & 2.8). Trallero et al. (1997) in Figure 2.6 clearly show that the two regions of unstable water-in-oil emulsion and region of layers of water-in-oil dispersions and water merge to one region of water – in - oil emulsion when there is an increase in velocity more than 2 m/s. It also indicates that the phase inversion point occurs at the water cut of 38%.

2.2.4.2 Flow pattern transitions and boundaries

For liquid-liquid systems, a wide range of physical parameters affect the flow pattern characterisations and transitions. The dominant flow patterns and shape of the interface are classified according to the Eotvos number in Equation 2.6 below:

$$Eo_D = \frac{\Delta\rho g D^2}{8\sigma} \qquad 2.6$$

Where D is the tube diameter, $\Delta\rho$ is the difference in density between phases; g is the acceleration due to gravity and σ is the interfacial tension. . It was investigated and has been shown that preliminary classification and characterisation of flow pattern transitions and boundaries of liquid – liquid systems can be made according to whether $Eo_D >> 1$ or $Eo_D < 1$ (Brauner et al., 1998). In gravity dominated systems, with large Eotvös numbers, the density difference and inclination, controls flow pattern boundaries. On the other hand, in small Eo_D (surface tension dominated) systems,

inclination does not play a role, whereas liquids wettability with the pipe material, entry conditions and start-up procedure are important.

Segregated or Stratified Flow:

Prediction of the properties of stratified or separated flow was first developed as a plane interface two-fluid model by (Taitel and Dukler, 1976). The analysis was further extended to include transients and curved interfaces by (Brauner and Moalem Maron, 1992). For systems where the value of Eo_D >>1, annular flow is unlikely as surface tension and wall adhesion forces are insufficient to hold the liquid onto the tube walls. The interface can be assumed to be planar in stratified flow. This boundary defines transition from smooth stratified flow (S) to stratified flow with waves/mixing at the interface, (SW or SM). The transitional criterion evolves from a linear stability analysis carried out on the transient formulation of the two-fluid model, and corresponds to the long-wave neutral stability boundary as stipulated by, (Brauner and Moalem Maron, 1992).

Currently, the criterion for the onset of stratified wavy flow patterns cannot be determined for liquid - liquid systems, since the wave propagation velocity, shape function and the interfacial shear coefficients are not known.

In the two-fluid approach, the momentum equations are solved for each phase with an assumption that no mixing occurs at the interface. The interface is assumed to be flat. The momentum equations for the two fluids can be written as:

$$-\frac{dP}{dx}+\tau_u\frac{S_u}{A_u}\pm\tau_i\frac{S_i}{A_u}+\rho_u g\sin\alpha=0 \qquad 2.7$$

$$-\frac{dP}{dx}+\tau_l\frac{S_l}{A_l}\pm\tau_i\frac{S_i}{A_l}+\rho_l g\sin\alpha=0 \qquad 2.8$$

where P is the pressure, τ stands for the wall-shear stress, S_u and S_l are the wall perimeters of the upper and lower fluids respectively, S_i is the interfacial perimeter, A is the cross-sectional area, ρ is the density, g is the gravitational acceleration and α, is the inclination angle from the horizontal. The subscripts1 *u, l* and *i* refer to the upper phase, the lower phase and the interface, respectively.

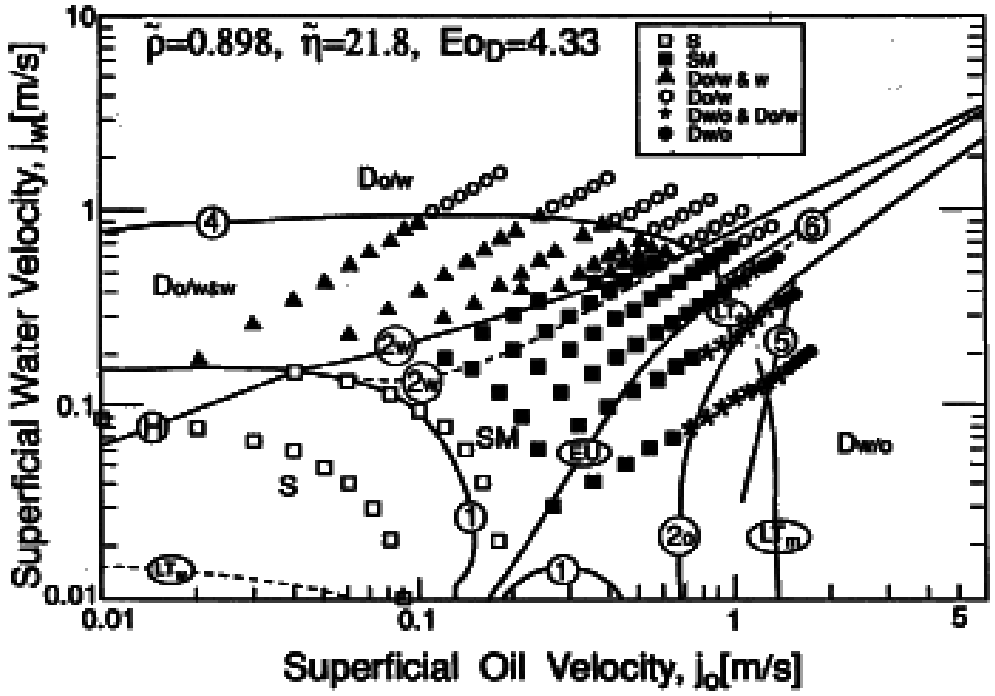

(S – stratified flow with smooth or wavy interface; SM – stratified flow with interface mixing; $D_{o/w+w}$ – dispersion of oil in water plus a water layer; $D_{o/w}$ – dispersion of oil in water; $D_{w/o+}$ $D_{o/w}$ – two inter-dispersed layers of oil in water and water in oil; $D_{w/o}$ – dispersion of water in oil).

Figure 2-23 Flow Pattern Map of (Brauner and Moalem Maron, 1992) compared with experimental data of (Guzhov, 1973)

Upper Bound on Stratified Flow Patterns

Stratified flow patterns exist outside the boundary predicted, albeit with some degree of dispersion or other forms of mixing at the interface. This stratified flow pattern exists until the two fluid model becomes ineffective and not proper to be applied (Brauner and Moalem Maron, 1992). This condition is given by:

$$\tilde{\rho}_2 u_2^2 \gamma_2(\gamma_2 - 1) + \tilde{\rho}_1 u_1^2 \gamma_1(\gamma_1 - 1) - (\gamma_2 u_2 - \gamma_1 u_1)^2 + \frac{D}{\rho_{12}}\left[(\rho_2 - \rho_1) g \cos\beta - C_h \rho (u_1 - u_2)^2 P_I (S_1^{-1} + S_2^{-1})\right] \geq 0 \qquad 2.9$$

Where, $\tilde{\rho}_2 = 1 + \frac{\rho_2 S_1}{\rho_1 S_2}$; $\tilde{\rho}_1 = 1 + \frac{\rho_1 S_2}{\rho_2 S_1}$; $\rho_{12} = \frac{D\left(\frac{dS_2}{dh}\right)\rho_1 \rho_2}{S_2\left[\rho_1 + \rho_2 \frac{S_1}{S_2}\right]}$ 2.10

This boundary can be constructed in two parts, depending on which phase travels at a higher velocity. In Figure 2.23, for a faster water layer, the boundary 2w marks the transition from SM to Do/w +w transition. The boundary 2o, for a faster oil layer, gives the transition between SM and Do/w and Dw/o. Additionally, constructing the line EU, where the actual phase velocities are equal ($u_1=u_2$), it is shown on Figure 2.23 that flow patterns which involve a layer of w/o dispersion lie to the right of this line.

Dispersed Flow Transition to $D_{w/o\ \&\ w}$:

This is a condition in which the water velocity U_w is greater than the oil velocity U_o i.e. $U_w >> U_o$. Due to the forces of inertia, fragmentation of oil drops occurs at the wavy oil – water interface. This mechanism can be relevant to the formation of liquid dispersions in the entry region of the pipe, in particular, when nozzles are used for injection of the liquid, or for drop entrainment from the interface between slow and fast moving layers. This phenomenon has been investigated by some researchers (Hinze, 1955, Kubie, 1977, Karabelas, 1978, Chesters, 1991, Cohen, 1991) (Azzopardi, 1997), . The following power-law empirical correlation for $N_{We(crt)}$ is often used to evaluate d_{max}:

$$N_{We(crt)} = \frac{\rho_c \overline{U^2} d_{\max}}{\sigma} \qquad 2.11$$

Where, $\overline{U^2}$ - Average value of square of difference in turbulence velocity, (sq. cm/(s)^2, over the distance equal to d_{max} – Largest drop size (cm). Considering the energy distribution law of Kolmogorov in an isotropic homogeneous turbulence in which the kinetic energy is the major contributor to fluctuation, then for the inertial sub-region:

$$\overline{U^2} = C_1(\varepsilon d)^{2/3} \qquad 2.12$$

For the Kolmogorov length scale of viscous flow given by, $\eta = \left(U_c^3/\varepsilon\right)^{1/4}$, and if we assume that $N_{Vi} \ll 1$, then we have:

$$\frac{\rho_c d_{\max}}{\sigma} C_1 (\varepsilon d_{\max})^{2/3} = const \qquad 2.13$$

$$d_{\max} (\frac{\rho_c}{\sigma})^{3/5} \varepsilon^{2/5} = C \qquad 2.14$$

Where, C is a constant that is determined experimentally. The following transitional criterion was suggested by (Brauner, 2000), in the case of turbulent flow in the faster (Hobbel et al.) layer, $U_c \equiv U_w$:

$$\Delta U_c \equiv U_w - U_o \geq 4.36 \left[\frac{\sigma \Delta \rho g \cos \beta}{\rho_c^{\,2}} \right]^{1/4} \left\{ 1 + 1.443 (N_{vd} \cos \beta)^{0.4} \right\}^{1/2}$$

2.15

$$\{\beta < 45^0$$

Where, $Eo_D = \frac{\Delta \rho g D^2}{8\sigma}$; $$\{90^0 - \beta > 45^0$$

Dispersed Flow Transition to $D_{o/w\ \&\ w}$:

In this condition the oil velocity U_o is greater than the water velocity U_w i.e. $U_o >> U_w$. Equation 2.11 is applied with $\Delta U_c = U_o - U_w$, $\mu_d \equiv \mu_w$, $\rho_c \equiv \rho_o$ and $\rho_d \equiv \rho_w$. Capillarity effects can cause systems with $E_{oD} = 0$, to transit into $D_{w/o\ \&\ o.}$

Dispersed Flow Transition to $D_{o/w}$:

This is a homogeneous oil – water dispersion (emulsion) resulting from the maintenance of turbulence level in the continuous water phase, which is sufficiently high to disperse the oil phase into small stable droplets of $d_{max} < d_{crt}$. (Brauner, 2001) established a transitional criterion as follows:

$$C_{(\varepsilon d)} E_{oD}^{\,1/2} N_{We(crt)}^{\,0.6} \mathrm{Re}^{0.08} \geq 1 \qquad 2.16$$

Where, $C_{(\varepsilon d)}$ is a variation of the dispersed phase hold-up.

Dispersed Flow Transition to $D_{w/o}$:

A resultant maintenance of turbulence level in the continuous oil phase gives rise to a dispersion of water phase into small stable droplets forming homogeneous water – oil dispersion (emulsion). In this condition, equation 2.11 is applied with $U_c = U_m$, $U_{cs} = U_{os}$, $U_{ds} = U_{ws}$, $\mu_c = \mu_o$, $\rho_c = \rho_o$ and $\rho_d = \rho_w$. Hence, $\varepsilon_d = U_{ws}/U_m$ and $N_{We(crt)} = \frac{\rho_o d U_m^{\,2}}{\sigma}$; $\mathrm{Re}_c = \frac{\rho_o d U_m}{\mu_o}$.

Capillarity effects can cause systems with $E_{oD} = 0$ to transit into $D_{w/o\ \&\ o.}$

Dispersed Flow Transition to $D_{o/w}$ and to $D_{w/o}$:

The phase inversion model is applicable for predicting this transition when the oil and water flow rates are sufficiently high to sustain both a homogeneous Do/w and Dw/o. As shown in Figure 2.30, boundaries 4 and 5 indeed define an ambivalent range where either of the oil or water phase can be homogeneously dispersed. It is the phase inversion phenomenon which eventually defines the boundaries of Do/w and Dw/o.

Dispersed Flow Transition to w/o

If turbulence in the oil layer is sufficiently high, the water phase can be dispersed into stable small droplets. Applying Hinze's theory, the following criterion can be derived.

$$\left[\frac{0.4\sigma}{\Delta\rho g D^2}\right]^{1/2}\left(\frac{\rho_o D j^2}{\sigma}\right)^{0.6}\left(\frac{\upsilon_o}{Dj}\right)^{0.08} = 1.88\left[1 + a\left(\frac{j_w}{j}\right)^{1/2}\right] \qquad 2.17$$

This condition applies as long as the oil phase is turbulent. The constant, *a*, is determined experimentally. This transition is indicated by the boundary to the right-hand side of $D_{w/o}$.

When $Eo_D << 1$ the interface is curved and **annular flow** becomes the dominating flow pattern. This is not a priority in the current study as the investigation is tailored towards stratified and dispersed flow regimes in a homogeneous mixture of oil and water in an horizontal pipe system.

2.2.5 Parameters with impact on the flow patterns

Mixture velocity and input water cut: The effect of mixture velocity and water cut was investigated early by (Russell et al., 1959). In general low mixture velocities allow the flow to be separated or stratified, while high mixture velocity disperses the flow. However, dispersed flows may appear at low velocities provided the water cut is very low or very high. A summary of some experimental work done by several researchers on the effect of input water cut or water hold-up has been made by (Brauner, 2001) in (APPENDIX A Table 2.1).

Viscosity, density and surface tension: The viscosity effect, studied by (Russell et al., 1959), (Charles et al., 1961) and (Arirachakaran et al., 1989), seems to have little or no effect on the observed flow patterns for oil/water flows. The observed flow patterns are the same, but transitions from one flow regime to another may appear at different superficial velocities when oils of different viscosities are used. In two-phase flows with high density difference between the phases, stratified flow will generally appear for a larger range of mixture velocities and water fractions than for the case of low density difference two-phase flows. The surface tension also affects the flow pattern and the nature of the drop sizes formed (Hwang et al., 1997). (Yusoff, 2012) in his experiment relates the dominance of coalescence process and formation of large droplets to one due to the impurities (surfactant) in the water phase, which caused reduction of systems interfacial tension, i.e. energy per unit surface area. The resulting droplets move more freely, hence less restriction for the water droplets to have a collision.

Pipe Orientation and Geometry: The flow geometry such as pipe diameter, pipe inclinations, vertical pipes, horizontal pipes, T-Junctions, pipe sudden contraction and pipe sudden expansion, etc., are studied by most researchers and is found to affect the resultant flow pattern. Some experimental work done recently by (Yang et al., 2001, Simmons et al., 1997, Yusoff, 2012) on liquid – liquid flow through T – Junctions and Expansions confirms the commonly observed flow patterns in segregated and dispersed flow regimes as classified according to (Trallero et al., 1997).

Liquid – liquid Wetting properties: The wetting properties can also influence the flow patterns as investigated by (Angeli and Hewitt, 2000a). In general hydrophilic

materials that prefer wetting by oil favour oil continuous dispersions and hydrophobic materials that prefer wetting by water favour water continuous dispersions.

Temperature and pressure: Temperature and pressure have influence on the flow patterns. Some experimental work has been done on pressure drop measurements as summarized in APPENDIX A Table 2.1)..

Oil Volume fraction (OVF) or in - situ Oil hold-up: Oil volume fraction is a dimensionless quantity, which varies from 0 to 1 sometimes expressed as a percentage between 0 - 100%. This indicates a temporal domain occupied by the oil in a two-phase oil-water flow. There are many typical methods of measurement for oil volume fraction, which are either intrusive or non-intrusive measurement techniques. Examples of some non-intrusive techniques are x-ray tomography, gamma-densitometry tomography, ultrasonic system, electrical capacitance tomography, electrical resistance tomography and impedance tomography, High speed camera Endoscope (Borescope) etc. While, the intrusive techniques include: needle-contact probe, parallel wire probe, Laser Focused Beam Reflectance Measurement (FBRM). However, in the recent years, much attention has been focused to a newly developed intrusive method namely the wire-mesh sensor (WMS) method, which has been used by (Yusoff, 2012).

Therefore, optimization of pipeline operations for transport of these fluids requires the knowledge of the several parameters. One of the major parameters is the knowledge of the volume ratio of each phase over the total volume also known as volume fraction.

2.3 Fundamentals of Liquid-Liquid Coalescence and Dispersion

Liquid – Liquid dispersion is a common phenomenon in several flow patterns, especially, stratified wavy dispersed at the interface, dispersed and annular flows. Measurement of drop size is an important tool, which describes the hydrodynamics of liquid – liquid dispersions in Petroleum and Process Industries. A variety of measurement and analysis techniques have been performed and a summary of this research can be found in Table 2.1. The measurements of drop size in pipelines are very difficult, especially for high dispersed phase liquid – liquid flow. Measurement

techniques used are generally either optically, electrically or laser based. There is a potential problem with physical measurement of drop size as any intrusion may alter the size distribution, possibly by causing local changes in the condition of the continuous phase, which may cause break-up or coalescence. A selection of the measurement techniques used is reported in the following sections, together with some reported correlations for drop size.

Description of the various non-intrusive and intrusive measurement techniques for droplet sizes in liquid-liquid dispersed flow systems will be discussed

Table 2-1 Summary of previous work on drop size measurement technique

Author	d_t ***(cm)***	σ ***(N/m)***	μ_o ***(kg/ms)***	ρ_o **(kg/m^3)**	***Dispersion***	***Measurement Technique***
(El-Hamouz and Stewart, 1996)	0.025	0.038	0.00096	800	o/w	Malvern 2600 & Par-Tec M300
(Karabelas, 1978)	0.05; 0.05	0.033; 0.03	0.018; 0.00186	890; 808	w/o	Photography of encapsulated sampled drops
(Kubie, 1977) (water/alcohol)	0.017; 0.017	0.0049; 0.0045	0.0048; 0.0048	828 884	w/o and o/w	Photography of drops inside pipe
(Kurban et al., 1995)	0.025	0.017	0.0016	800	w/o	Photography using borescope plus conductivity probe
(Angeli et al 2004)	0.04; 0.09	0.005	0.006	828	Oil and water	Dual impedance probe

Table 2-1 Summary of previous work on drop size measurement technique continued

Author	d_t ***(cm)***	σ ***(N/m)***	μ_o ***(kg/ms)***	ρ_o **(kg/m^3)**	***Dispersion***	***Measurement Technique***
(AI-Wahaibi and Angeli, 2008)	2.00	0.038	0.0055	828	oil /water	Dual Impedance probe
(Morgan et al., 2013)	0.41	0.038	0.0023	797	Exxsol D8O oil /water	Planar Laser Induced Florence (PLIF)
(Victor et al., 2016)	0.015	0.0329	0.0055	828	Exxsol D14O oil /water	Conductivity probe

2.3.1 Drop breakage and coalescence mechanism

Determination of maximum drop diameter (d_{max}) that can resist breakup in a turbulent flow field is the major issue in contention. Some researchers refer this to be the **Sauter Mean diameter**, which is a measure of the interfacial area in dispersion. This actually depends on the interaction of forces within the system that tends to destabilize and stabilize liquid – liquid droplets. The following forces are predominating in the deformation process:

- **Breakup forces**: External forces due to turbulence, τ **- (Nm^{-2}).** Viscous stress or dynamic pressure set up in the surrounding continuous phase
- Magnitude of the interfacial surface tensional forces, σ/d (dyne/cm), where *d* - diameter of droplet. This force counteracts the external force producing turbulence. ***Stabilizing or counteracting forces***
- Magnitude of the viscous force causing flow velocities, $\mu_d/d\sqrt{\tau/\rho_d}$. ***Stabilizing or counteracting forces***. Where μ_d - absolute viscosity of droplet, (kgm^{-1}s^{-1}) and ρ_d - density of droplet (kgm^{-3})

Therefore, a combination of these forces results in dimensionless groups in which two are independent; Weber number (Ratio of external forces to Interfacial forces),

Weber number $$N_{We} = \frac{\rho U^2 d}{\sigma} = \frac{\tau d}{\sigma} \qquad 2.18$$

Where, ρU^2 - dynamic pressure and U^2 – relative velocity with respect to droplet.

Reynolds number, $$N_{\mathrm{Re}} = \frac{\tau d}{\mu_d}\sqrt{\frac{\rho_d}{\tau}} = \frac{\rho_d d}{\mu_d}\sqrt{\frac{\tau}{\rho_d}} \qquad 2.19$$

Viscosity number, $$N_{vi} = \frac{\mu_d}{\sqrt{\rho_d \sigma d}} \qquad 2.20$$

A combination of the ratios of the Reynolds number gives an independent number, Viscosity number N_{Vi}, which contains the external force τ.

During the interaction of forces, breakup of droplets occurs when the external forces, becomes greater than the interfacial forces, until a critical point is reached. This critical point is **$N_{We(crt)}$.** The disintegration process becomes more chaotic when this critical point is exceeded and can result to bursting of the droplet or globules.

Therefore, the deformation process can be described in relation to the two dimensionless groups, in that the $N_{We(crt),}$ is a function of $N_{Vi.}$ A correlation was drawn from the above as follows:

$$N_{We(crt)} = C(1+\varphi(N_{vi}) \qquad 2.21$$

Where, φ decreases to zero when N_{vi} tends to zero. C – Corresponds to $N_{We(crt),}$ for vanishing viscosity effects of the droplets. Equation 2.21 can be used as the basic Hinze (1955) model. This equation depends on the external conditions of the interacting forces and types of flow patterns. For turbulent or chaotic systems, where there is varying local flow patterns and velocities, the value of $N_{We(crt)}$, will not be the same. Therefore, a mean statistical value of $N_{We(crt)}$, can be determined from which an average size of the maximum droplet diameter, d_{max},, is deduced.

Droplet size distributions mainly depend on the equilibrium balance between the turbulence forces and the coagulating forces. Size distribution of the disperse phase affects the overall performance efficiency. Smaller droplets provide larger interfacial area per unit volume and converse is the case for larger droplets. The sizes distribution of the drops depend on several factors as mentioned earlier. In order to understand the dispersive process better, it is important that drop break-up and coalescence be investigated.

Drop breakup

Drops breakup at interfacial sub-range of turbulent eddies or pressure fluctuations (Kolmogoroff, 1949). Therefore the mean dissipation energy per unit mass for pipe flow, ε is equal to:

$$\varepsilon = \frac{fU_c^3}{2d} \qquad 2.22$$

Where, f – Friction factor, U_c – Velocity, *d* – Pipe diameter. At low viscosity, drops will break above a critical Weber number, $N_{We(crt)}$. (Karabelas, 1978), found the maximum diameter (d_{max}), using the differences in velocity across the pipe.

$$(\frac{d_{\max}\rho_c U_c^2}{\sigma})(\frac{fd_{\max}}{4d})^{2/3} = 0.369 \qquad 2.23$$

Kubie (1977), used fluctuating turbulent velocity $u_{\cdot f} \approx 1.3u_*$ to get the (d_{max}), where frictional velocity, $u_* = (f/8)^{0.5}U_c$.

$$\frac{fd_{\max}\rho_c U_c^2}{\sigma} = 5.53 \qquad 2.24$$

These correlations are however, based on interaction of single drops with the continuous phase, assuming dilute dispersions. For denser dispersions, other correlation works were done and modifications made accounting for the energy dissipation, ε^*, damping effects of turbulence in equation 2.25. (Tsouris and Tavlarides, 1994), based it on mixture viscosity, ν^*

$$\varepsilon^* = \varepsilon_c(\frac{\nu_c}{\nu^*})^3 \qquad 2.25$$

Where, ε_c energy dissipation of the continuous phase

Turbulence mechanism of drop breakup

The turbulence eddies are considered to fall broadly into three categories, referred to as the energy-containing range, the inertial sub-range and the viscous range. Energy is cascading from small to large wave number components or spectrum of the flow, i.e. from the energy-containing range to the dissipative structures of the viscous range via the eddies of the inertia sub-range. The velocity, U, and length scale, *l*, (the integral of the two-point velocity correlation function), defines the turbulence intensity of the system.

For a stirred tank, U, is referred to the speed of impeller tip, while *l*, is the impeller radius. This gives an energy dissipation per unit mass, ε, by plotting the torque-speed

curves for the impeller in the stirred tank arrangement or pressure drop measurements in flowing systems.

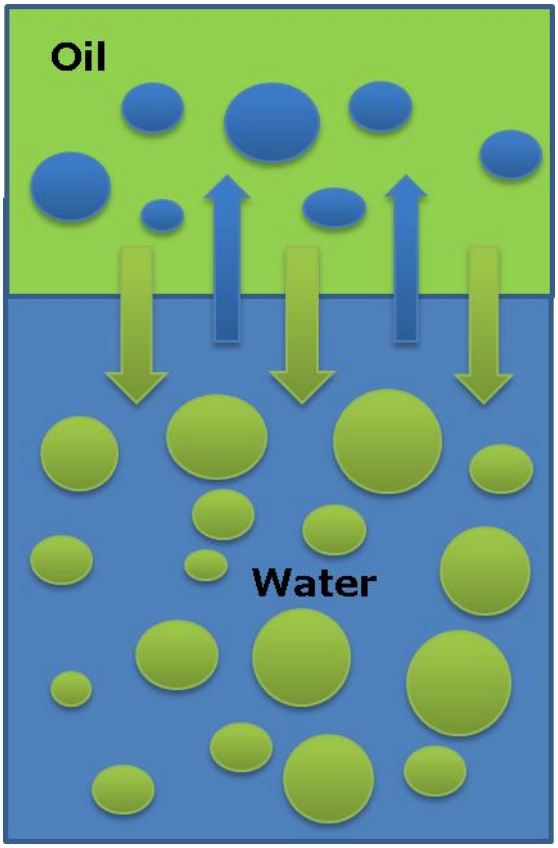

Figure 2-24 Drop Breakup Mechanism

The viscous range is responsible for the final degradation of mechanical energy into heat and is hypothesized to have a universal isotropic structure which depends only on the quantity of energy which it is required to dispose of, ε, and the kinematic viscosity, ν, the property which is the ultimate agency of dissipation. From dimensional analysis a natural length scale for the smallest eddies is obtained as $\left(\nu^3/\varepsilon\right)^{\frac{1}{4}}$. From (Kolmogoroff, 1949, Hinze, 1955) prediction, it is inferred that a bubble of maximum diameter, *d*, breaks up if a critical weber number of unity is exceeded:

$$\frac{\rho\Delta^2}{\sigma/d} > \text{Constant} \qquad 2.26$$

Where, ρ is the density of the continuous phase, σ is the surface tension and Δ is the velocity difference across the bubble. Therefore, the inertial sub-range is defined thus; $\left(\nu^3/\varepsilon\right)^{\frac{1}{4}} \ll$ d $\ll$ l. The largest bubble stable against breakup is therefore given as:

$$d_1 \approx \left(\sigma/\rho\right)^{3/5} \varepsilon^{-2/5} \qquad 2.27$$

Where, d_1 is the diameter of the largest bubble stable against breakup. The Sauter mean diameter is proportional to d_1.

Drop Coalescence

Coalescence of drops occurs when droplets are attracted or colliding with each other in the liquid – liquid flow fields, there by entrapping liquid film in the continuous phase. This is achieved by the interaction of the forces of attraction. Sufficient time is allowed for the film to drain to a critical thickness and then rupture occurs. Drop coalescence is therefore characterised by determining the minimum drop diameter (d_{min}) that can resist these forces of attraction. Some works have been done by the following researchers: (Chesters, 1991, Thomas, 1981, Liu and Li, 1999), etc.

Turbulence mechanism of drop coalescence

Thomas (1981), records that the coalescence of a pair of bubbles occurs in two stages: (i) the draining of the intervening film of continuous-phase liquid to a critical thickness, h (ii) the rupture of the remaining film by a mechanism which is not understood yet.

A steady force, F pressing the bubbles together attains a quasi-steady state, which is valid if coalescence is very rapid. The assumption of drainage between rigid planes (rather than free surfaces) restricts the analysis to bubbles whose surfaces have been immobilized by surfactants, to droplets of a dispersed phase whose viscosity is much higher than that of the continuous phase.

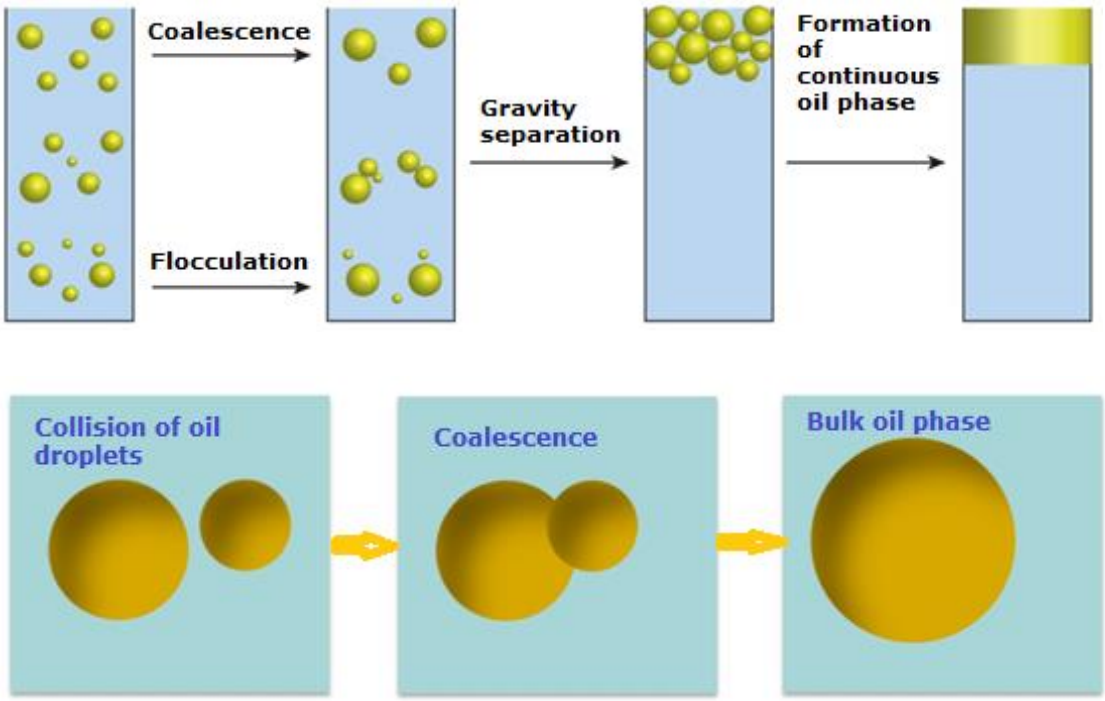

Figure 2-25 Drop Coalescence Mechanism

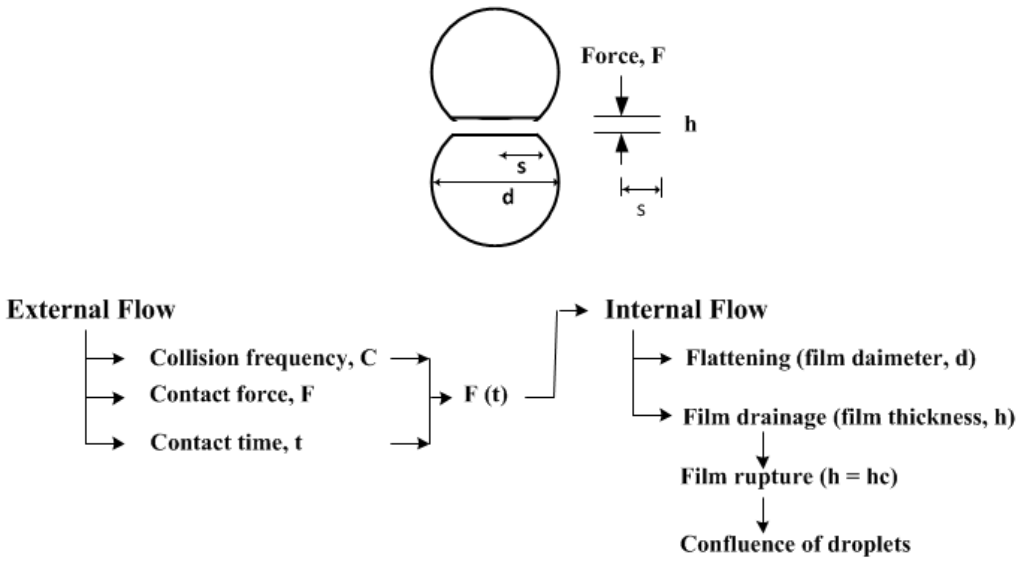

Figure 2-26 Conceptual framework for coalescence modelling, (Thomas, 1981, Chesters, 1991)

Calculation of the time, τ required for the films shown in Figure 2.26 to drain to the rupture thickness *h* is given by

$$\tau = \frac{3\pi\mu s^4}{2Fh^2} \qquad 2.28$$

Where, μ dynamic viscosity of the continuous phase, s is the radius of the film and F is the force pressing the bubbles together. If pressure is considered then we have the force, $F = 4\pi s^2 \sigma / d$ and the film drainage time, τ, expressed as:

$$\tau = \frac{3}{32\pi}\mu F\left(d/\sigma h\right)^2 \qquad 2.29$$

For minimum bubbles in turbulent flow, by assuming the (Kolmogoroff, 1949, Hinze, 1955) theory, that the eddy current responsible for coalescence belong to the inertial sub-range, then dimensional analysis indicates that $F = \rho\varepsilon^{2/3}d^{8/3}$. Therefore, substituting for the force F in equation 2.29 gives the film drainage time as:

$$\tau = \frac{3}{32\pi}\mu\rho\varepsilon^{2/3}d^{8/3}\left(d/\sigma h\right)^2 \qquad 2.30$$

Turbulent fluctuations move apart bubbles that are brought together continually through agitation. The characteristic time scale, i.e. the length of time T during which the situation shown in Figure 2.33 persists before the two bubbles are moved apart is given as:

$$T = \left(d^2/\varepsilon\right)^{1/3} \qquad 2.31$$

A simple criterion for coalescence is $\tau < T$. In other words, unless the intervening film thins down to the critical rupture thickness, h_c, in the time available before bubbles are separated again, coalescence does not occur. Therefore, combining equation 2.30 and 2.31, we obtain the result that coalescence is impossible unless $d<d_2$, where

$$d_2 = 2.4\left(\frac{\sigma^2 h^2}{\mu\rho\varepsilon}\right)^{1/4} \qquad 2.32$$

Equation 2.32 implies that bubbles whose diameter exceeds d_2 are much less likely to coalesce than smaller bubbles in the dispersion.

Prevention regime of coalescence

In the turbulent regime it is necessary to estimate ε by plotting the torque-speed curves for the impeller in the stirred-tank arrangement or by pressure measurements in flowing systems or alternatively estimated from the relation

$$\varepsilon = u^3/l \qquad 2.33$$

Substituting equation 2.33 into 2.32 for ε gives the value of d_2. For instance if D is the impeller diameter and N the number of revolutions per unit time, we take $u = \pi DN$, $l = D/2$ and $\varepsilon = u^3/l =$ $62D^2N^3$. Therefore, for a 5-inch paddle at 156rpm this method yields $\varepsilon = 17.6 m^2/s^3$. The appropriate physical properties such as ρ (kgm^{-3}), σ (Nm^{-1}) and μ (Nsm^{-2}), are to be determined from the fluids used.

If ε exceeded a critical value, ε_{crt}, it was no longer possible to prevent intermixing and the more usual variation of droplet size as, $\varepsilon^{-2/5}$, then appears. The region exhibiting this behaviour $\varepsilon < \varepsilon_{crt}$ was referred to as the coalescence prevention regime.

The dependence of d_2 on σ, ρ and μ cannot be deduced directly from equation 2.32 since the variation of *h* with physical properties is unknown. If however, h is independent of, μ, then the diameter of the largest coalescing bubble varies as $\mu^{-1/4}$ and therefore the average bubble size in an agitated dispersion decreases slowly as μ increases.

The (Kolmogoroff, 1949, Hinze, 1955), theory was extended to give a useful explanation of the coalescence process aside the usual droplet breakup process. Through dimensional analysis, the form of equation 2.32 was derived. Also an explanation of the coalescence prevention regime was established from the results of (Shinnar, 1961), experiments.

2.3.2 Models and correlations for mixing vessels and stirred tanks

Several models and correlations have been presented by researchers on how to predict fluid particle sizes (droplet sizes) and droplet size distributions, which influences the interaction of forces and very important for determining interfacial areas, heat and mass transfer rates in chemical reactor, separators and other chemical equipment design.

The majority of models are developed based on the (Kolmogoroff, 1949, Hinze, 1955) theory. Subsequent researchers built on this foundation especially a modified theory and experimental work done by (Shinnar, 1961) on liquid-liquid dispersions in agitated vessels. Dilute dispersions is used in most experimental investigations and compared with models for drop size breakup mechanism other than the simultaneous coalescence process. A review made by (Angeli, 2001), however showed under-predictions of the commonly used (Hinze, 1955) model for maximum drop size with experimental data. A major challenge in modelling coalescence process is the intrinsically complex nature of the phenomenon (Chesters, 1991). It involves the external flow (the continuous-phase flow, in which the particles are embedded) governs the frequency, force and duration of collisions. While the internal flow is characterised by deformation of the approaching interfaces and, if sufficient time is available, by rupture and confluence. Chesters (1991), suggested that modelling of such effects requires primarily a modification of the film drainage models, the basic equations describing the film drainage, diffusion equations relating bulk to interfacial concentration and interfacial tension of the species.

Different statistical correlations and models have been proposed using population balance in describing the range of droplet sizes in stirred vessels. Table 2.2 below highlights a summary of some experimental research work done.

Table 2-2 Brief summary of previous work on liquid – liquid dispersions in stirred vessels

Researcher	**Experimental work**	**Statistical Correlations/Average Droplet Sizes obtained**
Pacek et al. (1994)	Video Technique, Unstable dispersions at high concentrations	Uni-modal & bi-modal distributions (normal or Log-normal distribution), 4.0 μm, $d_{32} \propto \varepsilon^{b}$
Brown and Pitt (1972)	Photo electric probe, unstable dispersions of eight different systems of kerosene and water.	$(d_{32}^{5/3}\frac{\rho}{\sigma}\varepsilon^{2/3})\left(\frac{\varepsilon^{1/3}t_c}{T^{2/3}}\right)=C$ $Nt_c\left(\frac{W}{T}\right)\left(\frac{D}{T}\right)^{8/5}=0.0122$
Calabrese et al. (1986)	Direct photography; Experimental work on five different grades of silicone oil in water dispersions	$\frac{d_{32}}{d}=\left[1+11.5\left(\frac{\rho_c}{\rho_d}\right)\frac{\mu_d\varepsilon^{1/3}d_{32}^{1/3}}{\rho}\right]^{5/3}$ $\frac{d_{32}}{D}=2.1\left(\frac{\mu_d}{\mu_c}\right)^{3/8}\left(\frac{\rho_c ND^2}{\mu_c}\right)^{-3/4}$ $d_{32}=0.6d_{\max}\ ;\ d_{32}=0.5d_{\max}$
Shinnar (1961)	Dispersion of molten microcrystalline wax in hot water with poly vinyl alcohol as a colloid. Microscopic inspection	$C\rho K\varepsilon^{2/3}N^2D^{4/3}d^{8/3}/A(h_0)=cons\tan t$

Table 2.2 Continued

Sprow (1967)	Concentrated dispersion of (25%methyl isobutyl ketone (MIBK) and 75% salt water emulsion. Coutler counter Model B (Coutler Electronics Chicago) for droplet size measurements.	$d_{\min} = kF^{1/2}\nu_c^{1/4}\mu_c^{-1/2}N^{-3/4}D^{-1/2}$
Lovick et al. (2005)	3-dimensional optical reflectance measurement (3D ORM), Endoscope & High speed video recorder. Dense dispersed phase of Kerosene and water	Log-normal distribution. $d_{\min} = 3.5\mu m$
Chatzi et al. (1991)	Liquid-liquid dispersion of n-butyl chloride in water containing, Poly vinyl alcohol (PVA).	Steady State Population Balance Model
Zhou and Kresta (1998)	Phase Doppler particle analyser (PDPA); Dense dispersions or high concentrations	Erlang, Weibull and gamma distributions

2.3.3 Drop size distribution measurement techniques

The various techniques used in the measurement of drop sizes and drop size distribution are given in the subsections that follows.

2.3.3.1 Laser Diffraction

This method applies a mathematical principle, based on the theory of Fraunhofer diffraction. A low power He-Ne laser illuminates the flow, and the interception of the laser beam by a spherical particle creates a far-field diffraction pattern. This scattered light passes through a Fourier transform lens, and then falls onto a series of concentric photoelectric detectors. The size of the particles dictates the angle of scatter, Figure 2.27, and a least-squares analysis is used to fit a diffraction pattern from a generated size distribution to the experimentally obtained data.

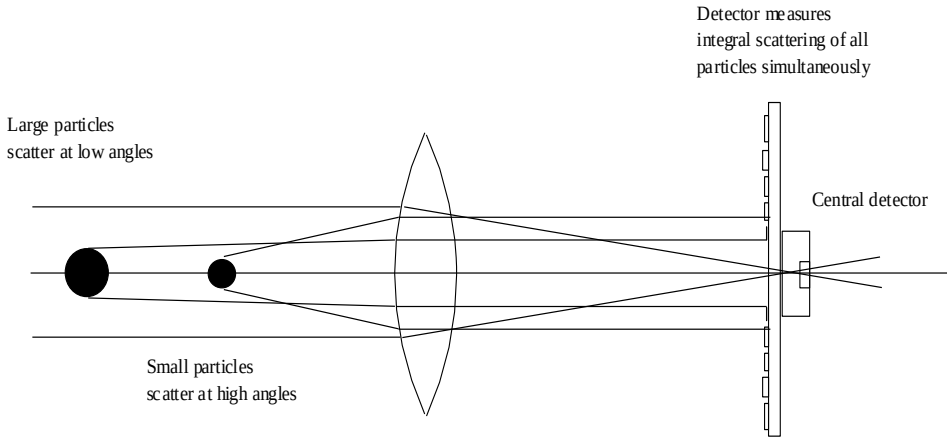

Figure 2-27 Operation of Malvern 2600 instrument

The technique is limited to low dispersed phase concentrations because the Fraunhofer theory is dependent upon the detected light being only scattered by individual particles and is invalid for high concentration of droplets.

The technique was adopted by Malvern Instruments Ltd and has been used extensively for drop size measurements in gas-liquid and oil-water mixtures through pipelines (Azzopardi, 1997, El-Hamouz and Stewart, 1996).

2.3.3.2 Photographic and video technique

Photographic techniques in general are slow because of the time required to process and size a representative sample of drops. (Karabelas, 1978) sized more than 300 drops to obtain a representative size distribution. In his experiment water droplets dispersed in two different hydrocarbons flowing in a 0.05m pipe were photographed. This technique was used in conjunction with droplet encapsulation to maintain the drop size distribution and prevent coalescence. The droplets were collected in a sampling vessel with an optical quality glass bottom. This allowed photographs to be taken of the settled drops, which could be magnified to allow the droplets to be sized by ruler or travelling microscope. The technique is also limited to low concentrations of the dispersed phase so that each droplet can be detected individually during measurement.

2.3.3.3 Droplet encapsulation

This technique was applied by (Karabelas, 1978) in conjunction with photography using high speed camera as described in section 2.3.3.2 above. The monomers used were piperazine in the aqueous phase and terephthalic acid chloride in the organic phase.

Coalescence of droplets is prevented in this technique and hence the droplet size distribution remains constant for sampling and measurement. A small quantity of monomer is introduced into the dispersed phase, and this reacts on the surface of the droplet to form a polymer when it comes into contact with another reacting monomer introduced into the continuous phase. This polymer layer then stops the droplets from sticking together or coalescing during analysis procedures.

2.3.3.4 Dual optical probe technique

The probe is made up of two separate fibres, both with a normal cut end, inserted into separate stainless steel tubes which are adhered together and enclosed in a 6mm inner diameter stainless steel holder. The axial and lateral separations of the two fibres were optimised to detect the same droplet and to produce sufficient resolution to calculate

the drop velocity accurately and at the same time minimise the meniscus effects from the leading probe tip affecting the readings from the trailing fibre. The principle of the dual optical probe is based on signals received with residence time ΔT. Approximately equal residence times, such as $\Delta T_1 \approx \Delta T_2$, were used to calculate the drop size because the cut chord of a drop intersected by the dual optical probe is almost equal to the diameter of the drop. From the drop velocity U_d detected by leading sensor and the residence time during which the sensor tip is contained within the drop, the diameter of the drop can be calculated from:

$$d = U_d \Delta T_1 \qquad 2.34$$

This dual optical probe was tested to measure kerosene drops in kerosene – water flows for water superficial velocity range 0.1 to 1m/s and the kerosene volume fraction range 0 to 50%.

2.3.3.5 Electrical Conductivity or Capacitance

It is possible to detect water droplets dispersed in an organic phase by placing 2 needles in line separated by a known distance. An electrical potential difference is imposed across the two needles and current flows when a conducting drop touches both. This can be counted electronically for a number of different needle spacing and converted to a diameter distribution. Alternatively, the capacitance of the two electrodes can be used to determine the droplet sizes in a similar way. Obviously the separation of the probes is critical for determining the size range of droplets which can be detected.

The technique is only useful for oil continuous systems and has been applied by (Kurban et al., 1995). For water continuous systems, an oil droplet touching one probe only can interrupt the flow of current and thus the technique becomes size independent and no longer useful. Another limitation is that drops can become stuck to the needles if the flow is slow or the interfacial tension is high.

2.3.3.6 Laser backscatter technique - Lasentec Focused Beam Reflectance Measurement (FBRM M500P)

The Focused Beam Reflectance Measurement (FBRM) Technique which uses light back scattering effects for in situ laser based measurement was employed. This drop size measurement technique has been used by several researchers in previous years to determine chord lengths in dispersions of liquid-liquid flow systems. The principle of the cylindrical FBRM probe is as shown in Figure 2.28 by (Ruf et al., 2000).

The optic rotates at a high velocity and focuses the laser beam near to the sapphire window. Passing particles backscatter the laser beam so that the chord length of the particle is computed by multiplying the scanning time with the beam speed. Usually, thousands of chord lengths are measured each second. This allows the determination of a robust chord length distribution, which can be used to illustrate changes in particle dimension, particle population and particle shape in time.

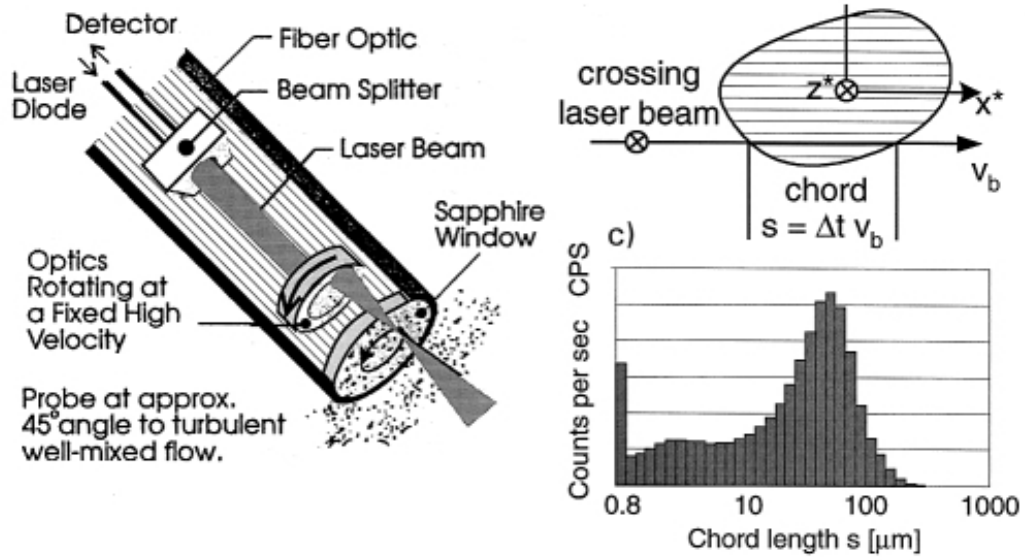

Figure 2-28 The Focused Beam Reflectance Measurement Technique (FBRM) probe using light back scattering effects for drop sizing (Ruf et al., 2000).

Characteristic chord length distributions (CLD) are measured. The backscattered pulse from the laser probe is measured in the focus plane from one edge of the particle to an opposing edge. In the first approximation, the chord length of a scanned particle

l_c can be accounted for by $l_c = U_s \Delta t_s$. Here, Δt_s is the time of flight for a pulse. The proportionality constant in this equation is U_s, the velocity of the scanning focal point. If the drop size distributions are assumed to be spherical, then suitable correlations can then be used to convert chord length distributions to drop size distributions.

The chord data obtained is not directly useful for comparison as most techniques measure droplet diameter. It is therefore necessary to convert this chord distribution to compare results with data obtained from other sources. The operation of the Focused Beam Reflectance Measurement (FBRM) technique as described above requires a method of converting the chords to actual drop diameters.

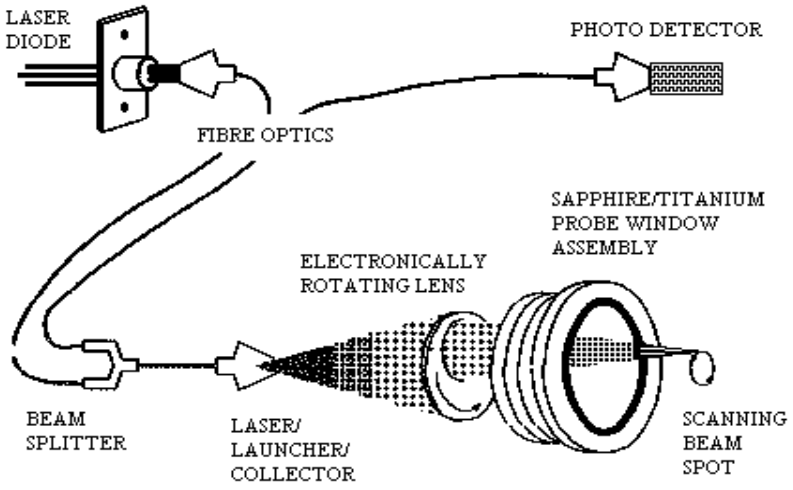

Figure 2-29 Principle of operation of the Par-Tec instrument.

There are several frequently used size distribution functions, which correlate particle or droplet size measurements. These distributions include Log-normal distribution, Rosin-Rammler distribution and Log-hyperbolic distribution (Clayton et al., 1998). Several correlations were published in an attempt to predict either the entire droplet size distribution or a characteristic of the distribution for liquid-liquid dispersions.

2.3.3.7 Endoscope (Bores scope) measurement techniques

Another major type of measurement techniques for sizing drops in-situ are photo based methods working with image recognition. This method gives accurate values

for the drop sizes in the analysed system, which is reliable and accurate (Pacek et al., 1994). The results obtained with the endoscope are used as a "standard" with which the other probes are compared.

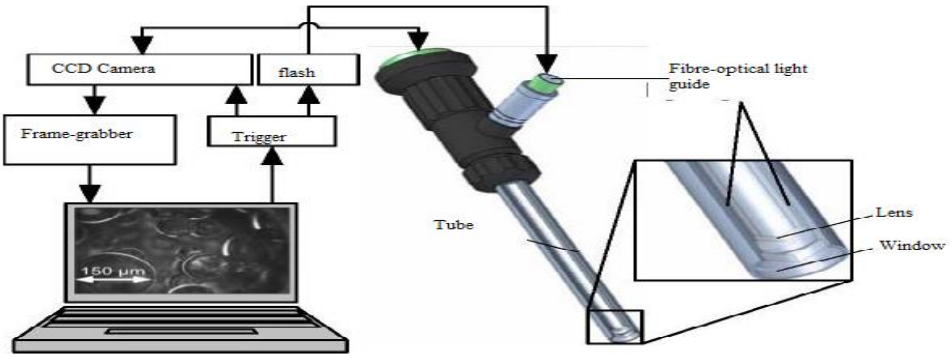

Figure 2-30 Detail 3D drawing of the endoscope probe and general set-up (Maaß et al., 2011)

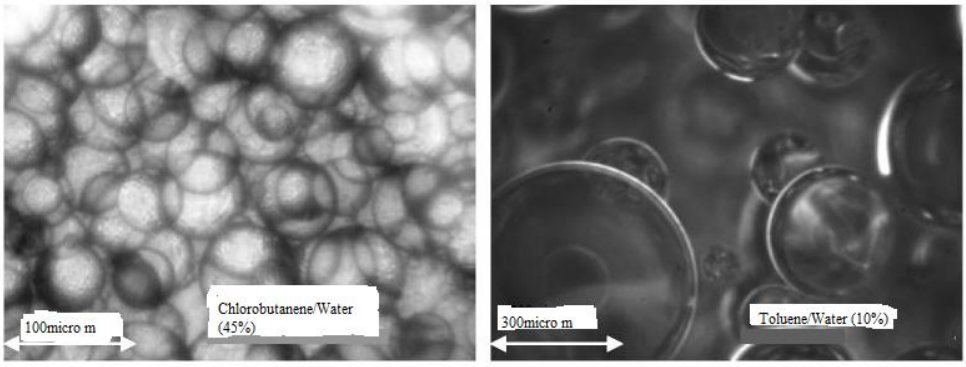

Figure 2-31 Example images, representing samples taken with the endoscope technique using different lenses according to the expected particle size for two different liquid-liquid systems as presented by (Maaß et al., 2011)

The images are taken intrusively from inside the vessel by placing a 7 mm thick endoscope in front of a CCD camera as a microscope lens (see Figure 2.30). To avoid disturbances by drops in front of the focal plane a covering tube with a window is placed at the tip of the endoscope lens. The drops are semi-automatically measured and counted at a pace around 500 drops an hour. The technique is capable of measuring drops from 5 to 5000 µm even at high dispersed phase fraction (see Figure 2.31).

Kurban et al. (1995) used a bores cope in conjunction with a video camera to examine droplets within oil-water dispersions in 0.0254m horizontal pipe. This had the added advantage of visualisation of the processes of droplet break-up and coalescence.

(Angeli and Hewitt, 2000) also used a video recorder coupled with an endoscope attached to a camera to study dispersed phase sizes at different locations inside a pipe. They successfully measured droplet size distributions and velocity profiles in liquid-liquid horizontal flows, which were used to analyse their results. Detailed working of the principles and application of the endoscope will be done in subsequent chapters as this measurement technique will also be used in conjunction with the Lasentec (FBRM) and Wire Mesh Sensor (WMS) for the present work.

2.3.4 Drop size estimation

Several different methods have been employed to estimate droplet sizes after using the different measurement techniques described. An important consideration is the dilute nature of the system from which most of these data are collected. For concentrated systems of dense dispersions obtained in the oil industries, accurate data is required, which entails accurate measurements of actual droplets sizes. Therefore, FBRM M500P instrument, developed by Lasentec, is one of very few techniques suitable for this task. However, the FBRM produces distributions of droplet chord lengths (CLD) whereas most other techniques produce diameter distributions directly. It is therefore necessary to process the CLD to give diameter distributions so that the present data could be compared with data obtained from other sources. The process of transformation from CLD to diameter distribution is known as estimating particle size.

Karabelas (1978) measured the size of water droplets in oil by an encapsulation technique discussed above and suggested that a Rosin-Rammler type equation was appropriate to predict the drop size distribution.

$$f(d) = 1 - exp\left[-2.996 \frac{d}{d_{95}} \right]^n \qquad 2.35$$

Where d is the drop diameter. The diameter at which 95% of the sample population are less than this size is represented by d_{95}.

Consequent upon this, a number of proposals were made, one of which was a more general approach where by normalising the distributions by dividing by the Sauter mean diameter, all distributions should fall onto one line, which can be described by a cumulative normal distribution.

$$f(d) = 0.5\left[1 + erf\left(\frac{X-\mu}{\sigma_v\sqrt{2}}\right)\right] \qquad 2.36$$

where X=d/d_{32}, $\mu$is the population mean and σ_v is the standard deviation. Values of =1.03 and σ_v = 0.37 were obtained for a Kenics type mixer used in these studies. Sauter Mean Diameter is a commonly referenced parameter defined as:

$$d_{32} = \frac{\sum_{i=1}^{N} n_i d_i^3}{\sum_{i=1}^{N} n_i d_i^2} \qquad 2.37$$

Where n_i is the number of droplets of diameter d_i. Many researchers have developed models to transform chord length distribution CLD, measurements into drop size distribution by applying the common distribution principles of Log-normal distribution, Rosin-Rammler distribution and Log-hyperbolic distribution (Clark and Turton, 1988, Liu and Clark, 1995). Some modifications and revisions were made on previous works by introducing the peeling method and Monte-Carlo simulation (Hobbel et al., 1991) and (Liu et al., 1998).

A major shortfall of the use of a normal distribution is that it assumes a finite number of drops of size zero and infinity, which is obviously not physically reasonable. Application of the normalising technique to an upper-limit log-normal distribution may prove to be more realistic.

Determination of the PSD from a CLD measurement is a typical inversion problem. The most widely used methods include the least squares (LS) and constrained least squares (CLS) algorithms, (Simmons et al., 1999, Langston, 2002, Wynn, 2003, Worlitschek et al., 2005), however, the implemented LS and CLS algorithms may give negative numbers of particles when the CLD measurement is disturbed with

measurement noise. Iterative probability apportioning using Bayes' theorem has then been developed to overcome the effect of noise (Langston and Jones, 2001, Langston, 2002).

(Li and Wilkinson, 2005) in their experiment did extensive theoretical studies on two important issues in translating a chord length distribution (CLD) measured by FBRM instrument into its particle size distribution (PSD) including PSD–CLD and CLD–PSD translation models for general non-spherical particles.

Simmons et al. (1999), proposed a Finite Element Method (FEM) and a Probability Apportioning Method (PAM). PAM is accurate only when the range of diameters is known, while FEM can be used with unknown diameter ranges but is inaccurate with discontinuous chord distributions. As a result, negative drop diameter number frequencies were predicted when the model was applied to experimental chord distribution data. An improved version of PAM (PAM2), based on Bayes' theorem, was later suggested by (Langston et al., 2001) It was found that when PAM2 was applied to mono- and bi-modal as well as real chord length distributions it predicted a large drop diameter frequency at the size of the most common chord length in the original chord size distribution, rather than a diameter distribution.

Equations 2.38 represent the Probability Apportioning Method (PAM) as presented by Simmons et al. (1999).

$$P(x_1, x_2) = \frac{\sqrt{D^2 - x_1^2} - \sqrt{D^2 - x_2^2}}{D} \qquad 2.38$$

Where $P(x_1,x_2)$ is the probability of obtaining a chord size between x_1 and x_2 of a sphere of diameter D with chord lengths, x.

The revised equation 2.38 as proposed by (Langston et al., 2001) incorporating the Bayes' theorem is as follows:

$$P(A_i / B) = \frac{P(B / A_i)P(A_i)}{\sum_{k=i}^{N} P(B / A_k)P(A_k)}; i = 1,2,.....N \qquad 2.39$$

The computational coding for the PAM2 has been updated and upgraded, allowing the chord length distribution measurements to be transformed into drop size distribution. This newer version 2.1 has been used successfully by (Hasan, 2006, Yusoff, 2012). Therefore, this modified and improved version of PAM, which is (PAM2), will be used for the analysis of results and discussions of the present work.

2.4 Liquid holdup and phase fraction measurement technique

Several techniques have been developed for measuring gas and liquid fractions and distributions as well as identifying various flow regimes in multiphase flow in pipes. Some of these common measurement techniques are briefly described in the subsections that follow.

2.4.1 Measurement of oil volume fraction

The fractional volume occupied by the oil in two-phase flow oil-water flows is known as oil volume fraction or liquid holdup. There is several process imaging techniques used by researchers to get detailed information on the behaviour of multiphase flow systems, which helps in the understanding of the hydrodynamics governing the process. These imaging techniques are however categorized into two major groups namely, intrusive (in-situ) and non-intrusive methods of measurements. The non-intrusive measurement sensors include, x-ray tomography, gamma-densitometry tomography, magnetic resonance imaging, ultrasonic system, infrared tomography, electrical process technology, etc. Some intrusive techniques employed by researchers include the Wire Mesh Sensor and Double wire conductance probes, which have been used over the years for the measurement of liquid film thickness in gas—liquid flows (Jurman et al., 1989, Andritsos, 1992, Azzopardi, 1997, Wang et al., 2004, Kadri et al., 2009). The various measurement techniques, whether intrusive or non-intrusive, as the case may be has their own unique advantages and disadvantages. A brief description of some of these techniques is highlighted in the sections that follow.

2.4.1.1 Electrical process technology

The electrical process measurement technique for obtaining information about the phase fraction in pipelines is based on the difference in electrical properties between the measured liquid and gas phases. There are several methods of electrical process tomography depending on the property variation being considered; however, the most commonly used methods are Electrical Capacitance Tomography (ECT) and Electrical Resistance Tomography (Greaves et al.). Generally, in these techniques electrodes are arranged around the circumference of the pipe to detect signals from the phases inside the pipe (Beck et al., 1987, Dyakowski, 1996, Reinecke et al., 1998, Dong et al., 2001).

In Electrical Capacitance Tomography, measurements are made based on the variations in the dielectric properties (capacitances) of the phases inside the pipe between inter-electrodes placed around the pipe. For example a basic ECT system consists of twelve capacitance sensors (made up of source and detector electrodes arranged around a pipe. The technique is a non-intrusive measurement method since the electrodes are not obstructing the flow inside the pipe. It is used where the phases have no electrical conductivity such as in gas/oil flows. (Dong et al., 2001) stated that images can also be reconstructed based on the permittivity distribution acquired from the ECT measurements through the electrodes. (Bolton et al., 1999) were among the pioneers to image liquid-liquid oil-water system in a 150 mm diameter stirred tank with 100 and 600 diameter of flow column using the ECT system.

The Electrical Resistance Tomography is a non-intrusive measurement technique used for phase fraction, phases distribution and imaging of multiphase flows in vessels and pipes. It is suitably applied for conductive phases (i.e. conductive phase with another phase with a different conductivity value such as air/water system or oil/water system) flowing through the cross section of a pipe. In the ERT system, several electrodes are usually placed at fixed positions around the circumference of the pipe in such a way that the electrodes do not interfere with the flow but make electrical contact with the fluids within the pipeline, thereby monitoring multiphase flows in process units on a real time basis. ERT measurements are given as resistance or conductance.

2.4.1.2 Gamma radiation attenuation

The gamma radiation attenuation technique is based on the fact that gamma rays are attenuated as they pass through two-phase media due to the interaction of their photons with the matter. The extent of this attenuation experienced by the gamma rays depends on the energy of the gamma rays and density of the absorbing media (Blaney and Yeung, 2008). There are two commonly used gamma ray measurement methods namely, single-beam gamma attenuation and dual-energy gamma attenuation.

The single-beam gamma densitometer consists of a gamma source and a detector unit. A collimated gamma ray is directed at the pipe with a sensor placed directly opposite the source on the other side of the pipe. The technique can be applied for gas-liquid and liquid-liquid systems. The capability of a media phase to absorb gamma radiation is dependent on the linear attenuation coefficient λ of the absorbing material. This can be used to measure the component fraction in the volume covered by the gamma beam. According to Beer-Lambert's law the intensity of the gamma beam decays exponentially as it passes through matter, which can be expressed thus: (Kumara et al., 2010).

$$I = I_o e^{\lambda d} \tag{2.40}$$

where I_o is the initial intensity and I the intensity of the gamma radiation detected after the gamma beam has travelled through the absorbing media on length d. A gamma ray will be attenuated differently by materials according to their density. Thus, the linear attenuation coefficient of water is higher than oil and gas and it is possible to employ this variance in the attenuation of gamma rays as an indication to distinguish these phases in the pipe.

The dual energy type gamma attenuation technique works on similar principle as the single-beam system, but with two gamma energy levels to measure the three components of a three-phase mixture in a pipe. The resultant attenuation intensity is expressed as follows; (Blaney, 2008).

$$I(e) = I_o(e).\exp^{-\left[\sum_{i=1}^{3}\lambda_i(e)D\right]} \tag{2.41}$$

where I is the measured gamma intensity, I_0 is the gamma intensity when the pipe is empty, D is the inside diameter of the pipe and λ is the attenuation coefficient of the component.

2.4.1.3 Wire Mesh Sensor (WMS)

Wire-mesh sensors belong to flow imaging techniques and allow the investigation of multiphase flows with high spatial and temporal resolution. The wire-mesh sensor principle is based on a matrix-like arrangement of the measuring points. Two set of wire electrodes are stretched along a vessel or pipe having a small axial separation between them and being perpendicular to each other. This way, a mesh or a grid of electrodes is formed in the cross-section (see Figure 2.32), (Helmholtz - Zentrum and Dresden-Rossndorf., 2012).

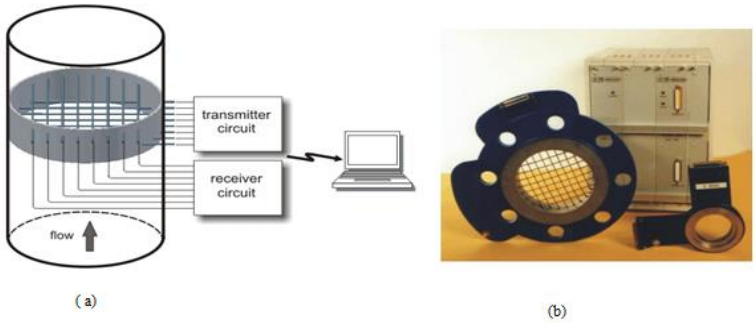

Figure 2-32 Principle of wire-mesh sensor having 2 x 8 electrodes (a). Wire-mesh sensor for the investigation of pipe flows and associated electronics (b), (Helmholtz - Zentrum and Dresden-Rossndorf., 2012)

The transmitter electrodes are sequentially activated while all receiver electrodes are parallel sampled, in such a way, that an electrical property (conductivity or permittivity) of the fluid in each crossing point is evaluated. Based on those measurements the sensor is thus able to determine instantaneous fluid distribution across the cross-section, of a pipe.

i. Types of Wire Mesh Sensors

a. Capacitance Wire Mesh Sensor: Capacitance Wire Mesh Sensor is a sensor based on measurements of the electrical permittivity (capacitance), which is suitable for the investigation of non-conducting fluids. Non-conducting fluids such as oil or

organic liquids often occur in industrial applications, for instance, in chemical and petrochemical industry. The experimental investigation of multiphase flows involving non-conducting fluids is therefore of large interest. The capacitance sensor uses an AC excitation and measuring scheme. Figure 2.33 shows a capacitance wire mesh sensor developed by (Da Silva et al., 2007). A sinusoidal alternating voltage is employed for excitation and the receiver circuit must encompass a demodulator.

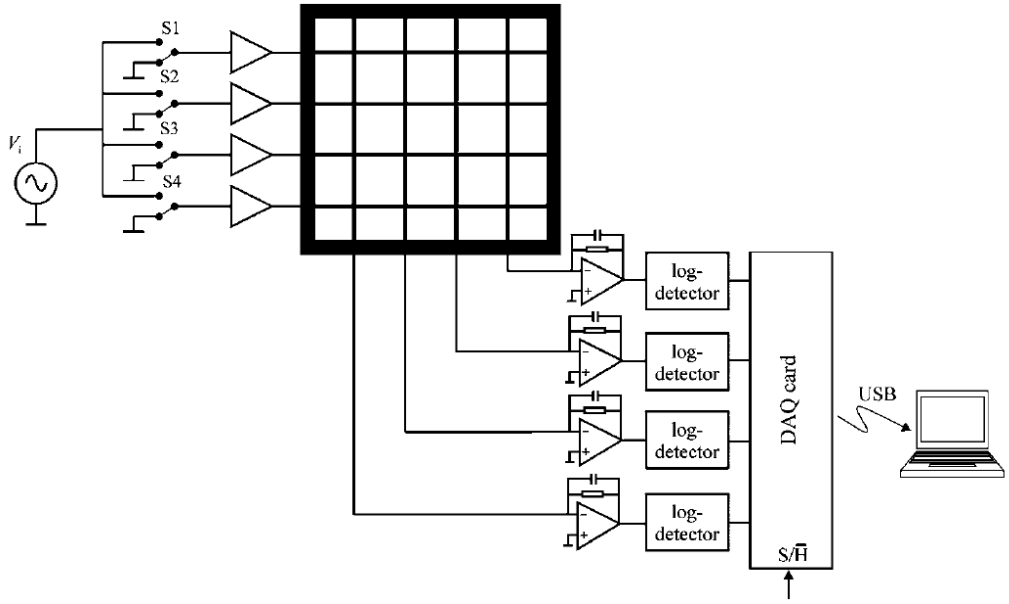

Figure 2-33 Electrical schematic of capacitance WMS (Da Silva et al., 2007)

b. Conductivity Wire Mesh Sensor: Conductivity wire-mesh sensors have been developed for the investigation of fluid flows with and without gas fractions. The measurement principle is based on a local measurement of electrical conductivity of the fluid within the cross-section of a vessel or pipe by means of a mesh of crossing electrodes. The wire-mesh sensor can measure the conductivity distribution at high sampling rates and with a spatial resolution down to 2 mm.

The measuring principle requires at least one continuous conductive phase. One plane of wires is used as transmitter and the other one is used as receiver. During the measuring cycle, the transmitter wires are activated in a successive order while all other wires are kept at ground potential. For each time slice a transmitter wire is

activated, the receiver wires are sampled in parallel. Therefore, in the conductivity wire-mesh sensor a bipolar excitation voltage and a DC measuring scheme is employed.

ii. Uses of Wire Mesh Sensors:

Wire Mesh Sensor is used to obtain flow maps, for vertical and horizontal pipeline flows. Through evaluation of velocity and gas fraction profiles generalized models for the behavior of two-phase flows under given geometric and thermodynamic boundary conditions are derived. Further areas of application for wire-mesh sensors are the investigation of substance mixing problems in chemical process plants and models of nuclear reactors, the investigation of cavitation and pressure shock phenomena in fluid pipelines, and water transport processes in soil.

iii Wire Mesh Sensor Measurements

The wire mesh sensor system allows you to make measurements of the instantaneous electrical conductivity and/or capacitance of the fluid in the cross section of the sensor with a high time and spatial resolution. From the measurements, the following parameters can be derived.

- Distribution of void fraction in a liquid face.
- Distribution of two not mixable liquids.
- Concentration distributions of salt or other tracers' materials, which affect the electrical conductivity.
- Determination of the phase portions, averaged over the measurement cross-section.
- Evaluation of the dispersion degree of the discontinuous phase.
- Velocity measurements (when using several planes of measurement).

2.4.1.4 Conductance probe

Conductance probe technique is commonly used for air/water systems as water is an electrical conductor, while air is essentially resistive. In this technique, the cross-sectional averaged void fraction can be estimated once the relationship between the electrical impedance and phase distribution has been established. Over the years most researchers

in the area of gas-liquid such as (Andreussi et al., 1988, Azzopardi, 1986, Tsochatzidis et al., 1992, Fossa, 1998, Alamu and Azzopardi, 2011) etc., have employed this impedance measurement to estimate average void fraction and liquid holdup. The work by (Andreussi et al., 1988) showed that a very simple, non-intrusive probe consisting of two ring electrodes mounted flush to the tube wall can be very effective for measurements under different flow conditions.

Recently, research in liquid-liquid flow systems is focused on the estimation of water fraction in oil-water pipe and horizontal wells with the use of multiple needle-conductance probes, (Zhai et al., 2012, Xu et al., 2012). Further attempts have also been made on the identification of flow patterns in oil-water flows by analysing conductance probe signals.

Conductance flush ring probes were firstly employed by (Asali et al., 1985) and with the understandings of this arrangement, a theoretical treatment was provided by (Andreussi et al., 1988, Tsochatzidis et al., 1992). Their numerical predictions were compared with experimental results by (Fossa, 1998, Devia and Fossa, 2003). They developed an expression for the optimum probe geometry behaviour by a Laplace equation for the electrodes with proper boundary conditions given by:

$$\nabla^2 V = 0 \tag{2.42}$$

where V represents electric potential. To compare the theoretical results with experimental data, dimensionless conductance is introduced defined by

$$Ge^* = \frac{Ge}{\gamma L} \tag{2.43}$$

where Ge is actual conductance in 1/Ω, γ is electrical conductivity in 1/Ωm, and L is the length of electrode in m. (Andreussi et al., 1988) ascertained the applicability of the correlation for the plate electrodes, which was provided by (Coney, 1973), to ring pair probes:

$$Ge^* = \frac{k(m)}{k(1-m)} \tag{2.44}$$

Where m,

$$m = \frac{Sinh^2\left(\frac{\pi s}{2h}\right)}{Sinh^2\left(\frac{\pi(s+De)}{2h}\right)} \quad 2.45$$

De represents the spacing of the electrodes, s is the width and *k* is the complete elliptic integral of the first kind given by

$$k(m) = \int_0^{\pi/2} \left(1 - mSin^2\theta\right)^{-1/2} d\theta \quad 2.46$$

For ring electrodes covered by a liquid layer (annular and stratified configurations), Equation 2.43 is still valid if the length L is replaced by the wetted length of the electrodes. Equation 2.42 was solved analytically by (Tsochatzidis et al., 1992) for ring probe response to a conducting annulus as follows:

$$Ge^* = \frac{\pi^3}{2}\left(\frac{(\lambda-1)}{(c_1+c_2)}\right)^2\left(\sum_{i=1}^{\alpha}\frac{1}{i^3}a_i^2 f_i\right)^{-1} \quad 2.47$$

$$a_i = Sin\left[k_i(c_1+\lambda)\right] - Sin\left[k_i(c_1+1)\right] - Sin\left[k_i(c_1-1)\right] + Sin\left[k_i(c_1-\lambda)\right] \quad 2.48$$

$$f_i = \frac{I_0(k_i R)}{I_1(k_i R)}\left[\frac{1+\frac{I_1(k_i r)K_0(k_i R)}{K_1(k_i r)I_0(k_i R)}}{1-\frac{I_1(k_i r)K_1(k_i R)}{K_1(k_i r)I_1(k_i R)}}\right] \quad 2.49$$

$$k_i = \frac{i\pi}{c_1+c_2} \quad 2.50$$

Where, I_0, I_1, K_0, K_1 is the first and second kind modified Bessel function, respectively.

Conductance probes technique will be employed for the measurement of phase fractions in the current experimental work as it is easier to fabricate, straightforward in application and cheaper.

2.4.2 Physical models and correlations for oil volume fraction estimation

A brief summary of some models and correlations of previous research work done on the subject of segregated and dispersed flows in horizontal pipes is given in the sections below.

A flow pattern – dependent model is used traditionally for the prediction of flow patterns along with the pressure loss and the phase hold-ups in horizontal pipe systems. An accurate prediction of these flow parameters is very vital in recent technologies in oil water production rates from limited down-hole information in oil wells. Therefore some models have been proposed for computing oil and water superficial velocities based on pressure gradient and hold-up information in horizontal oil-water flows.

Models are developed based on the flow-pattern dependent sub-models, the homogeneous model for dispersion flows and the two-fluid model for stratified flows (Brauner, 2001, Bannwart et al., 2004).

2.4.2.1 Two fluid model

In the two-fluid approach, the momentum equations are solved for each phase with an assumption that no mixing occurs at the interface. The interface is assumed to be flat. The momentum equations for the two fluids can be written as:

$$-\frac{dP}{dx}+\tau_u\frac{S_u}{A_u}\pm\tau_i\frac{S_i}{A_u}+\rho_u g\sin\alpha=0 \qquad 2.51$$

$$-\frac{dP}{dx}+\tau_l\frac{S_l}{A_l}\pm\tau_i\frac{S_i}{A_l}+\rho_l g\sin\alpha=0 \qquad 2.52$$

where P is the pressure, τ is the wall-shear stress, S_u and S_l are the wall perimeters of the upper (oil) and lower (Hobbel et al.) fluids respectively, S_i is the interfacial perimeter, A is the cross-sectional area, ρ is the density, g is the gravitational acceleration and α is the inclination angle from the horizontal. The subscripts u, l and

i refer to the upper phase, the lower phase and the interface, respectively. The flow parameters can be determined from the above equations 2.51 and 2.52.

2.4.2.2 Homogeneous model

The homogeneous model treats a mixture of the phases as a single fluid with the average properties defined as:

$$\rho_m = \varepsilon_o \rho_o + \varepsilon_w \rho_w \qquad 2.53$$

$$U_m = U_{os} + U_{ws} \qquad 2.54$$

Where, $\varepsilon_w = \frac{A_w}{A}$ and $\varepsilon_o = \frac{A_o}{A}$ are water and oil hold-ups, $U_{os} = \frac{A_o U_o}{A}$ and $U_{ws} = \frac{A_w U_w}{A}$ are water and oil superficial velocities respectively. The pressure drop is calculated as:

$$\frac{dP}{dx} = -\frac{2 f_m \rho_m U_m^{\,2}}{D} - \rho_l g \sin\alpha \qquad 2.55$$

Where, f_m and ρ_m are mixture friction factor and mixture density respectively, which is calculated based on the mixture Reynolds number, $\mathrm{Re}_m = \frac{\rho_m D U_m}{\mu_m}$. Correlations proposed by (Arirachakaran et al., 1989, Brauner, 2001, Guet et al., 2006) can be used to determine critical water and mixture viscosity.

2.4.2.3 Models for pressure gradient

Lockhart and Martinelli (1949), predicted the two-phase frictional pressure gradient using two-phase multiplier defined as,

$$\phi_l^2 = \frac{(\Delta P/\Delta z)_{TP}}{(\Delta P/\Delta z)_l}, \quad \phi_g^2 = \frac{(\Delta P/\Delta z)_{TP}}{(\Delta P/\Delta z)_g} \qquad 2.56$$

They correlated these parameters with a parameter χ (Figure 2.41),

$$\chi = \sqrt{\left(\frac{\Delta P}{\Delta z}\right)_l \Big/ \left(\frac{\Delta P}{\Delta z}\right)_g} \qquad 2.57$$

In the figure, the subscripts tt, vt, tv and vv represents viscous and turbulent for liquid and gas phase in order. (Chisholm and Laird, 1958) suggested the equations for this relationship given by

$$\phi_l^2 = 1 + \frac{C}{\chi} + \frac{1}{\chi^2} \qquad 2.58$$

For the turbulent-turbulent case, which can be applied for most cases, they suggested C = 21.

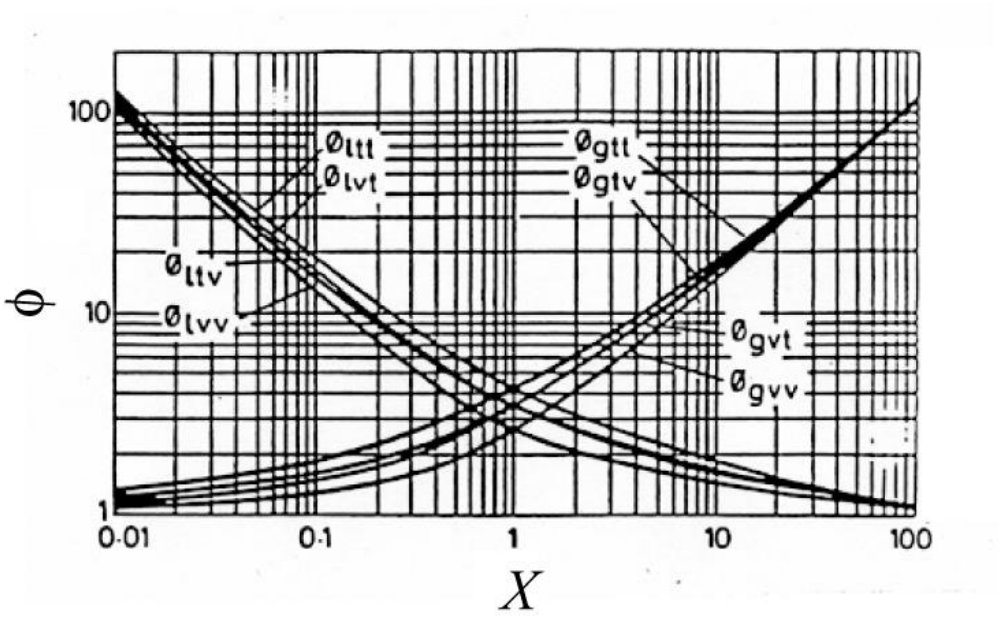

Figure 2-34 Two-phase multiplier versus Lockhart - Martinelli parameter

Overall models give good prediction for the first step; however there still exists significant error. Therefore understanding detailed flow structure is necessary to develop the physically-based model for specific flow pattern.

2.5 Summary

A comprehensive literature research is done on the subject area of liquid – liquid segregation (stratification) and dispersion systems in horizontal pipelines and mechanically agitated vessels. The review of published research work describes the theory, application and measurement techniques of drop size distribution in liquid-liquid oil – water systems. Some experimental investigations and theoretical models developed for the analysis and validation of flow parameters are ascertained in the literature. These can be summarised as the principle and phenomena of two – phase oil – water flow in horizontal, vertical and inclined pipeline. The complexities that exist in oil-water mixing, poses numerous operational problems involving oil from its initial separation and transportation through pipelines to a central processing unit such as the refinery. The literature review reveals that there is need for more investigation to be done in the case of transition from dispersed flow to stratified flow. This information can be used in the design and performance of phase separators.

Several efforts have been made to develop theoretical models for predicting flow parameters (i.e. pressure drop, liquids hold up or phase volume fractions, mixture velocities etc.), with limited datasets to validate the accuracy of these models and correlations. Also, comparison of different experimental investigations of the subject matter of liquid-liquid oil-water flow is needed to establish a generalised principle of flow behaviour. Even though from literature, a foundation is made in understanding the hydrodynamics and the mechanisms of drop breakup and coalescence, the later process is not fully understood and should be investigated further. This information together with an idea of the physical properties of the fluids and flow conditions will necessitate different approaches in modelling liquid-liquid flow in pipes.

Based on the above literature survey it is clear that the current information on liquid-liquid oil – water flow is limited, and that the data on the coalescence efficiencies of drop size in relation to separation of both phases is scares. In this work, an experimental investigation will be carried out on the coalescence efficiencies of droplet sizes in horizontal and inclined pipeline under turbulence in oil-water two phase systems. Apart from the overall parameters such as pressure gradient and

average in-situ hold-up, other parameters such as phase and drop size distribution will also be investigated.

Conductance ring probes are a straightforward, inexpensive and conventional technique employed for investigating two-phase flows that has widely been used in the past. The technique is quite efficient and has the ability to collect signal from the oil-water interface and phase volume fractions at high sampling frequency, which is promising. The conductance probes technique in combination with the use of the backscatter Lasentec FBRM M500P laser for drop size measurements and Phantom PCC 2.7 high speed camera for imaging, will provide the necessary dataset, useful for solving complex liquid-liquid system problems and also help improve models and better understand the phenomena that lead to the transition from dispersed flow to stratified flow patterns.

Chapter 3 LIQUID-LIQUID FLOW IN STIRRED BAFFLED VESSEL

3.1 Introduction

Mixing of fluids in tanks is a common operation in chemical industry. The resultant behavior of these liquid-liquid dispersions is unknown and of special interest, to investigate experimentally. It is however, established from previous research studies that when two immiscible liquids are agitated, a governing phenomenon of continuous break-up and coalescence of droplets occur simultaneously (Shinnar, 1961). The coalescence process is of more importance, as it is related to the evolution of drop sizes in the liquid-liquid dispersion, which affect phase separation process.

Hence, in this Chapter 3, a preliminary experimental investigation is carried out on the coalescence efficiencies of droplet sizes in oil-water dispersions. The findings of this preliminary bench top study will lay a foundation for better understanding of the hydrodynamics of oil-water flows in pipelines.

3.2 Theory of drop breakup and coalescence

Drop size distribution diameter depends on the rate of drop break-up and coalescence. Drops breakup when mixing of the volume fractions commences due to turbulence in the system, while drops coalescence once the mixing is stopped. In turbulent systems the theory developed by (Kolmogoroff, 1949, Hinze, 1955) is being used to predict the maximum drop sizes. Using dimensional arguments, they showed that the splitting of a drop depends upon a critical Weber number, which yields the maximal drop size, d_{max}, that can resist the stress due to dynamic pressure of turbulent eddies (τ). This theory is extensively discussed in the literature review. According to (Hinze, 1955):

$$N_{We(crt)} = \frac{\tau d_{\max}}{\sigma} = \frac{\rho U^2 d_{\max}}{\sigma} = C\left[1 + \varphi\left(N_{vis}\right)\right] \qquad 3.1$$

Where, $N_{vis} = \mu_d / \sqrt{\rho_d \sigma d}$, is the viscosity number. ϕ is a function, which decreases to zero when N_{vis} tends to zero. C is a constant, which corresponds to $N_{We(crt),}$ for vanishing viscosity effects of the droplets.

The conditions of turbulence in such a mixing vessel can be predicted from a modified Reynolds number, ND^2/ν, where D is the diameter of the agitator, ν is kinematic viscosity and N is its speed in revolutions per second. For fully developed turbulence (in the region of the agitator), the average energy of dissipation. $\bar{\varepsilon}$ in the liquid must therefore be a function of *N* and *D* only, and by dimensional analysis is given by:

$$\bar{\varepsilon} = kN^3D^2 \qquad 3.2$$

Here *k* is a dimensionless constant dependent on the geometry of the vessel and the agitator only. For dispersed phase with low viscosity equation 3.1 becomes

$$d_{\max} = K(\sigma/\rho_C)^{0.6}(N^3D^2)^{-0.4} \qquad 3.3$$

Where, *K* is a constant. (Coulaloglou and Tavlarides, 1977, Kumar et al., 1993, Tsouris and Tavlarides, 1994, Liu and Li, 1999, Pacek et al., 1994, Brauner, 2001, Lovick et al., 2005) have done some reasonable work on coalescence process in the literature. It is convenient to view the process as the drainage of the continuous-phase film entrapped between any two drops. The coalescence time, or the time required for film drainage and rupture, is an important parameter characterizing the process. However, these models usually deal with un-deformable interfaces (e.g., a film between two rigid spheres or a plane parallel film) so that the initial and/or critical film thicknesses are needed for calculating the coalescence time. (Shinnar, 1961) have investigated the influence of turbulence on coalescence of droplets and obtained;

$$d_{\min} = C\varepsilon^{-1/4}\rho_c^{-3/8}A(h_0) \qquad 3.4$$

where, C is a constant, $A(h_o)$ is the energy necessary to separate completely two drops with unit diameter, which are initially separated by a distance h_o and is determined by the properties of the liquids. (Thomas, 1981) derived a similar expression for the drops with tangentially immobile interface as presented in the literature review, equation 2.32.

$$d_{\min} = 2.4\left(\frac{\sigma^2 h^2}{\mu_c \rho_c \varepsilon}\right)^{1/4} \qquad 3.5$$

where, *h* is the film thickness at rupture between the two drops. Both models involve an empirical parameter, $A(h_0)$ or h, that has to be assumed or determined experimentally. This implies that the dependence of d_{min} on the physical properties is unknown (Thomas, 1981, Chesters, 1991). Several other models and correlations have been proposed and published, but not enough to satisfactorily establish the dependence of d_{min} on the physical properties and parameters involved in the coalescence process.

Therefore, this bench top experiment is primarily carried out to have an explicit understanding of the coalescence process of liquid dispersions in turbulent flow, (Homogeneous flow regime), by measurement of d_{min} in liquid – liquid dispersions in agitated vessels. A parametric study of a model to predict the minimum stable drop size d_{min}, drop size distribution and coalescence efficiency will be discussed.

3.3 Description of experimental facility and properties of fluids used

The experimental set up for measuring drop sizes consist of a cylindrical baffled stirred tank, (internal diameter = 125 mm; H = 250 mm), embedded in a Perspex block of dimensions 175 mm x 175 mm x 28 mm height. This is equipped with a four (4) bladed Ruston turbine impeller: 20mm x 10mm x 0.2mm thickness, made of steel. The impeller is connected to a variable D.C Motor through a transducer.

An in-situ Lasentec Focused Beam Reflectance Measurement (FBRM M500P) probe from Mettler Toledo, is mounted horizontally to the vessel at three different test positions (from the bottom: H1 = 25mm, H2 = 45mm, H3 = 105 mm). This was used to measure the chord lengths of droplets.

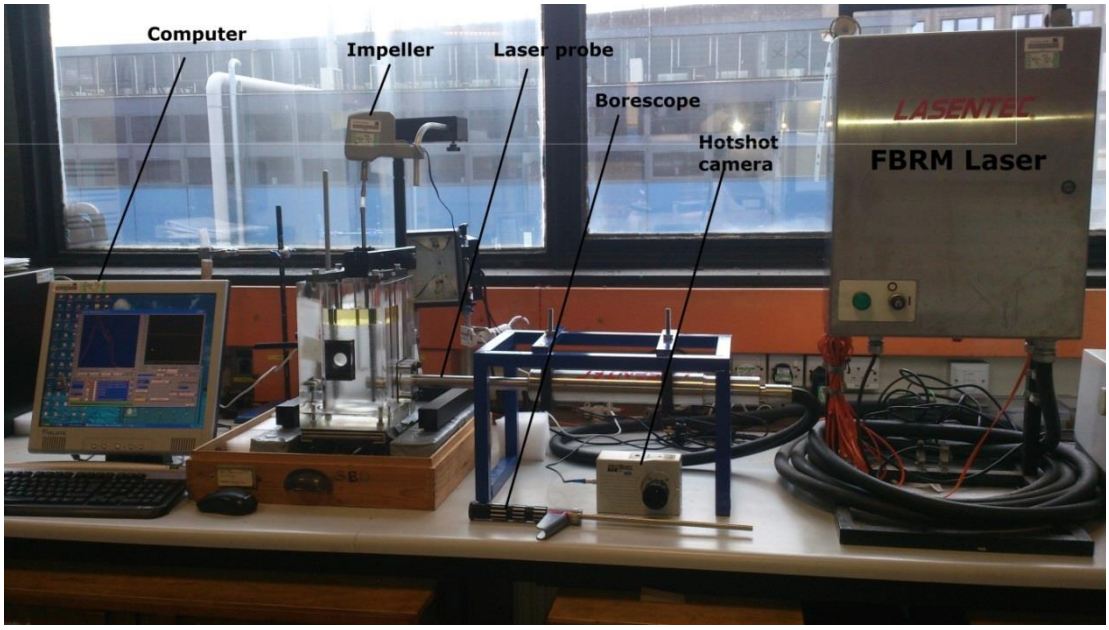

Figure 3-1 Experimental set-up for droplet size measurements in liquid-liquid agitated vessel.

HotShot high speed camera attached to a borescope was used to obtain droplet size images. The endoscope was inserted into the dispersion from the top of the vessel. The imaging system used is capable of recording up to 500 frames per second together with a proper lighting system.

The test fluids used are tap water and silicone oil, with the oil forming the dispersed phase. The silicone oil and water, volume fractions, are varied within 20%, 30%, 40%, 50%, 60%, 70% and 80%, depending on which phase is dispersed or continuous, at all impeller speeds. The speeds for the impeller are 800 rpm, 900 rpm, 1000 rpm, 1100 rpm, and 1200 rpm. This range allows for complete mixing and no air entrainment for all volume fractions used. Data is collected from the Lasentec FBRM M500P probe located at the different height positions from the bottom of the vessel and HotShot high speed video images and recordings were made.

Silicone oil and water were chosen for the present experimental work based on the physical properties required. Table 3.1, bellow presents a summary of the physical properties of the two fluids used.

Table 3-1 Physical properties of fluids (Silicone oil and Water) at 21^0C

Fluid	***Tap Water***	***Silicone oil, 5cSt***
Density (kgm^{-3})	ρ_w = 998	ρ_o = 916
Viscosity μ (kgm^{-1}s^{-1} or Pa s)	μ_w = 0.0010	μ_o = 0.0052
Refractive index	-	1.52045
Permittivity (α) (C^{2}N^{-1}m^{-2})	710 x 10^{-12}	23 x 10^{-12}
Relative permittivity	79	2.7

a. Density (ρ)

The density of the silicone oil and water can be obtained by use of a 25 cm^3 density bottle and a mass balance, which is a volumetric technique. Averages of 3 measurements were made for each liquid at 21^0C. The average density for silicone oil is 916 kgm^{-3} and that of water is 998 kgm^{-3}.

b. Dynamic Viscosity Measurements (μ)

Viscosity of the liquids is measured using an Ostwald viscometer, calibrated using water at 21^0C. The viscosity of water is 9.572x10^{-4} kgm^{-1}s^{-1} at 21^0C. The time t, for the liquid to fall through the viscometer was recorded. An average of 3 readings was made and the viscosity of silicone oil was calculated from equation 3.6., which is 5.2x10^{-3} kgm^{-1}s^{-1} at 21^0C.

$$\frac{\mu_i}{\mu_w} = \frac{\rho_i t_i}{\rho_w t_w} \qquad 3.6$$

c. Surface Tension (τ) and Interfacial Tension (σ)

The surface tension of silicone oil and water are 19.7 mNm^{-1} and 72.8 mNm^{-1}.at 20^0C respectively. The interfacial tension of silicone oil and water was determined using the pendant drop method as proposed by (Andrea et al., 1938), which is the most common method.

Theory of the pendant drop method

A HotShot high speed camera was used to snap and record droplet images of silicone oil injected into water with a string. These pendant drop images were then processed using a MATLAB programmer to obtain the interfacial tension.

The method calculates the surface tensions of the pendant drop profiles. The equatorial diameter d_e and the diameter d_s, in a selected plane, which is located by measuring vertically from the vortex a distance equal to d_e, are measured (see Figure 3.2). The ratio of the two diameters, d_s/d_e, is designated as S, the drop shape; the quantity 1/H is a function of S. The interfacial tension σ is calculated by the equation:

$$\sigma = \Delta\rho g d_e^2 / H \qquad 3.7$$

Where, g is the acceleration due to gravity, 1/H is a correction factor determined from d_s/d_e and ρ is the difference in density of the two phases. Three (3) measurements were made to obtain an average interfacial tension value of 44.7mNm^{-1}.

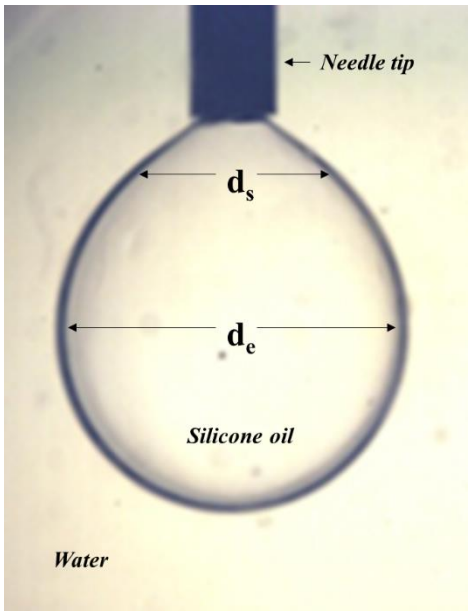

Figure 3-2 Measurements performed on pendant drop of silicone oil and water

3.4 Experimental procedure and test conditions

3.4.1 Experimental procedure

The experimental procedure followed for all droplet-size distribution measurements is carried out in two ways. These include drop breakup measurements and drop coalescence measurements. These measurements were done using a Focus Beam Reflectance Measurement (FBRM M50P) probe and HotShot camera together with a borescope (Endoscope).

a. Drop breakup measurements

Initially the system is thoroughly cleaned with tap water. A calibration and validation experiment of the FBRM probe is done first using the PVC reference particles. Reference procedure using PVC particles, is a means of verifying proper calibration of Lasentec FBRM instrumentation, which is explained in details in Appendix C.

The various oil/water fractions as given below in section 3.4.2 of the test conditions, ranging from 20% to 80% are mixed at the required impeller speed settings ranging from 800 rpm to 1200 rpm. With the FBRM probe positioned at the different heights of 25 mm, 45 mm and 105 mm of the baffled tank, measurements are recorded after about 5 mins of stirring the mixture. A continuous measurement was logged by a dedicated PC. The proprietary software was used to produce droplet chord length distributions. Subsequently, as reviewed in the literature, there are a number of methods available to transform measured chord length distributions into drop diameter distributions. The modified PAM programme in MATLAB by (Langston et al., 2001) was used to convert a measured chord length distribution (CLD) to a drop diameter distribution (DDD). In all the experiments, the two liquids are mixed for 5 mins to obtain stable droplets before any measurements are made. This procedure is performed to allow for an equilibrium balance to be maintained in the system. In Figure 3.3, it shows that stable droplets are formed after a period of 5mins from the initial start of mixing the liquids.

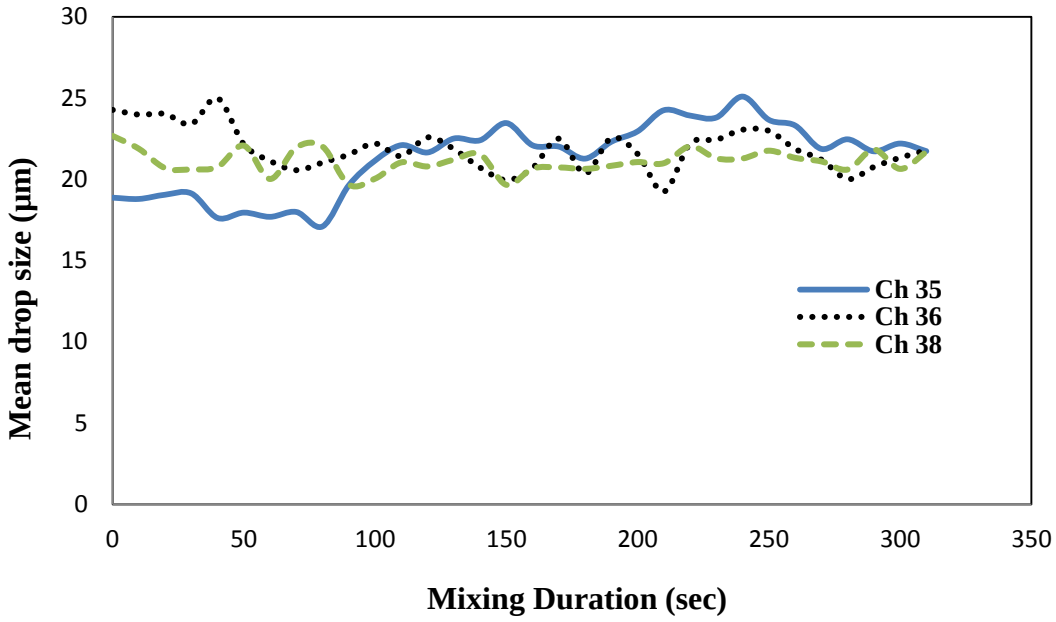

Figure 3-3 The effect of mixing time for silicone oil volume fraction, 40% OVF at impeller speed, N = 1200 rpm. Note: Channels (Ch), represents number of drop diameter bins (1-100%)

The volume of the baffled stirred tank V is 2.45 x 10^{-3} m^{-3} or 2.45 litres. The vessel is subsequently filled with the required volume fractions of Silicone Oil and tap water i.e. . The vessel temperature is measured with a thermocouple. The impeller speed is adjusted to the desired setting of between 800 rpm to 1200 rpm.

HotShot high speed attached to a bores cope imaging technique was used to obtain in-situ video recordings of droplet sizes in the dispersion. Photographic images and video recordings were taken at various silicone oil/water hold up fraction values between 0.2, 0.3, 0.4, 0.5, 0.6, 0.7, and 0.8 at impeller speeds of 800 rpm, 900 rpm, 1000 rpm, 1100 rpm and 1200 rpm. The unit was operated for 5mins before any recordings were obtained to allow the system reach equilibrium.

b. Drop coalescence measurements

In the case of drop coalescence measurements, the following procedure was adopted. The various oil/water fractions ranging from 20% to 80% are mixed at the required

impeller speed settings ranging from 800 rpm to 1200 rpm as mentioned above. When equilibrium is attained after about 10 mins of operation of the unit, the impeller is turned off and measurements are made of coalescing droplet sizes with the Focused Beam Reflectance Measurement (FBRM) laser and video recordings of coalescing droplets taken. This procedure is repeated for all experimental conditions.

3.4.2 Test conditions

The following test conditions were used for obtaining minimum and maximum droplet size measurements and drop size distributions in the baffled agitated tank.

- Volume fraction of dispersed phase (Silicone oil), (Dispersed phase holdup) = 20%, 30%, 40%, 50%, 60%, 70% and 80%. Impeller speed N = 800 rpm, 900 rpm, 1000 rpm, 1100 rpm and 1200 rpm
- Temperature at 14^{o}C; Mixing time = 15min; Measurement duration of instrument = 10 sec
- Focused Beam Reflectance Measurement (FBRM M500P) Probe test height of stirred tank = 25 mm, 45 mm, 105 mm.

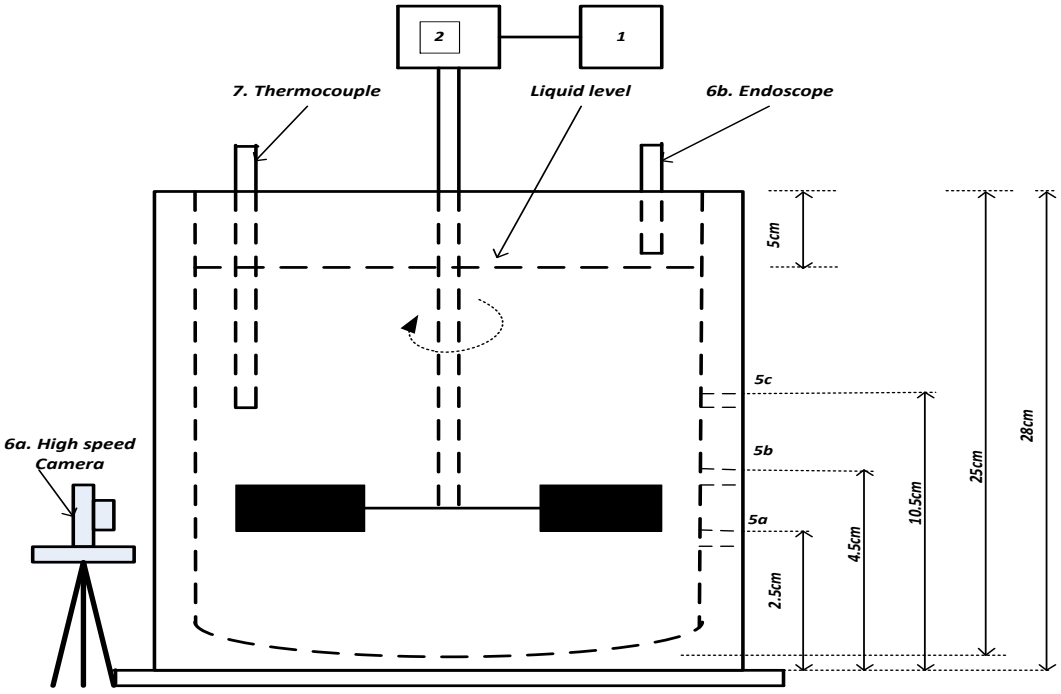

Figure 3-4 Experimental set up of a Cylindrical Baffled Stirred Tank

a. Impeller shaft connected with a transducer to produce torque
b. Paddle impeller type, made of four (4) steel square blades (20 mm x 10 mm) and 0.2 mm thick with impeller diameter of 30.5mm. Length of impeller from top is 800mm
c. Cylindrical Baffled Stirred Tank, (Dt = 12.5 cm; H = 20 cm) embedded in a Perspex box (17.5cm x 17.5 cm x 28 cm).
d. Four (4) longitudinal Baffle strips of equal lengths = 25 cm and width = 0.15Dt.
e. Lasentec FBRM M500P is fixed at 90^0 about 160mm length protrusion x 40 mm. Positions from bottom is: (a) H = 2.5 cm, (b) H = 4.5 cm, (c) H = 10.5cm and angular orientation of the three positions strategically located round the stirred tank at angle, 120^0 apart from each other.
f. (a). HotShot High speed Camera (b). Endoscope inlet with a rubber lid, (d= 8mm)
g. Thermocouple inlet with a rubber lid, for temperature measurements (d = 8 mm)

Details of all experimental conditions used are given in Table 3.1 in appendix A.

3.5 Instrumentation

The main instruments used for conducting experiments on the baffled stirred tank are laser backscatter equipment and HotShot high speed camera. An overview of the operational principle and procedures of how this equipment's work, are described in the following sections.

3.5.1 Laser backscatter equipment and drop size measurement

The Lasentec FBRM M500P instrument, which is a commercial instrument manufactured by Mettler Toledo Inc has been used by previous researchers namely, (Yang et al., 2003, Hasan, 2006, Yusoff, 2012) for their experimental study on liquid -liquid flow at the, University of Nottingham.

Focused Beam Reflectance Measurement (FBRM) technology is a probe based particle tracking instrument composed of three parts; a probe, which is inserted

directly into the agitated tank, the electronic field unit (EFU) and a dedicated computer for data acquisition as shown in Figure 3.8.

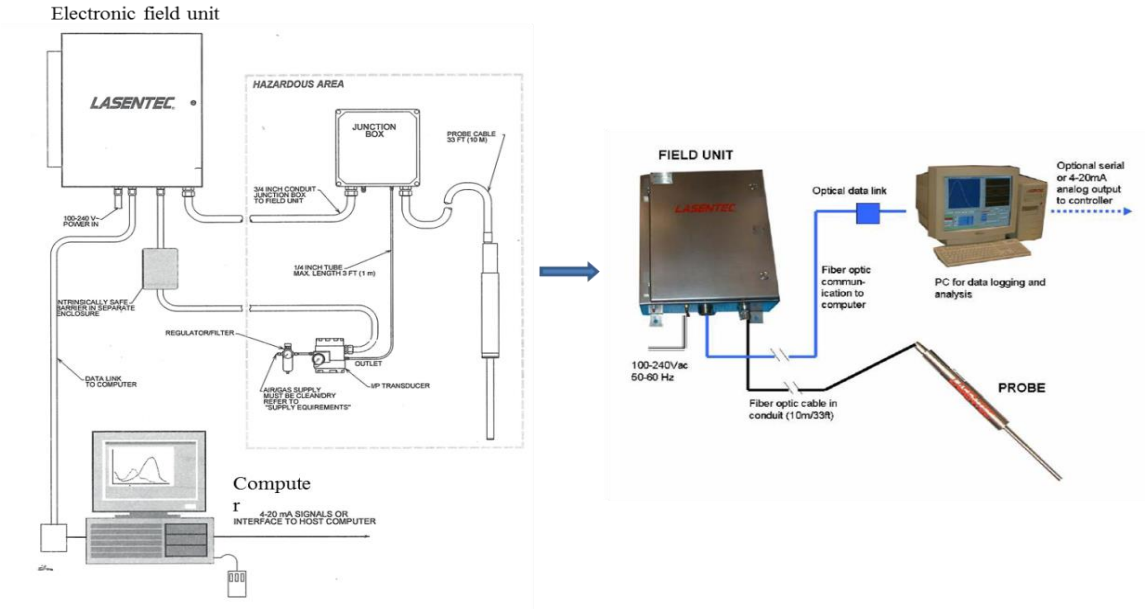

Figure 3-5 Typical diagram of Lasentec FBRM system connected to a computer (Mettler Toledo)

The optic rotates at a high velocity and focuses the laser beam near to the sapphire window. Passing particles backscatter the laser beam so that the chord length of the particle is computed by multiplying the scanning time with the beam speed. Usually, thousands of chord lengths are measured each second. This allows the determination of a robust chord length distribution, which can be used to illustrate changes in particle dimension, particle population and particle shape in time.

3.5.1.1 Verification of Lasentec FBRM M500P

It is recommended to carry out a PVC reference measurements to verify proper calibration of the Lasentec FBRM instrumentation regularly before use, in order to avoid spurious and inaccurate results. Therefore, since the FBRM instrument was last used in 2012, there was need for re-calibration to be done.

The procedure involves re-adjustment of the focal point position of the FBRM device to re-calibrate it according to the Windows Reference Procedure and validating the

signal with a PVC standard reference procedure provided by the Lasentec FBRM Company.

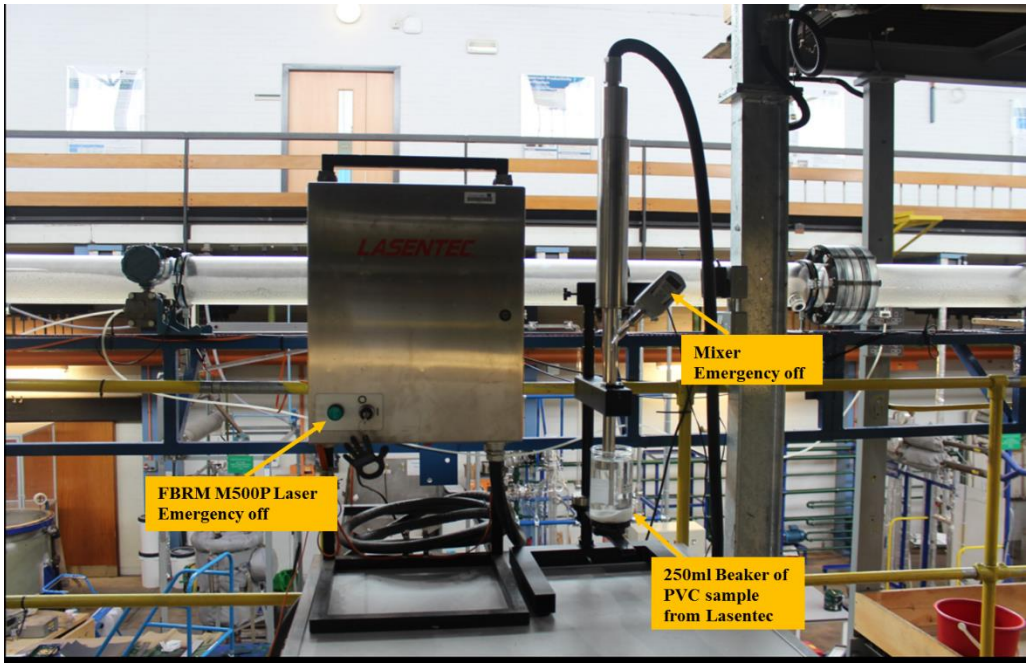

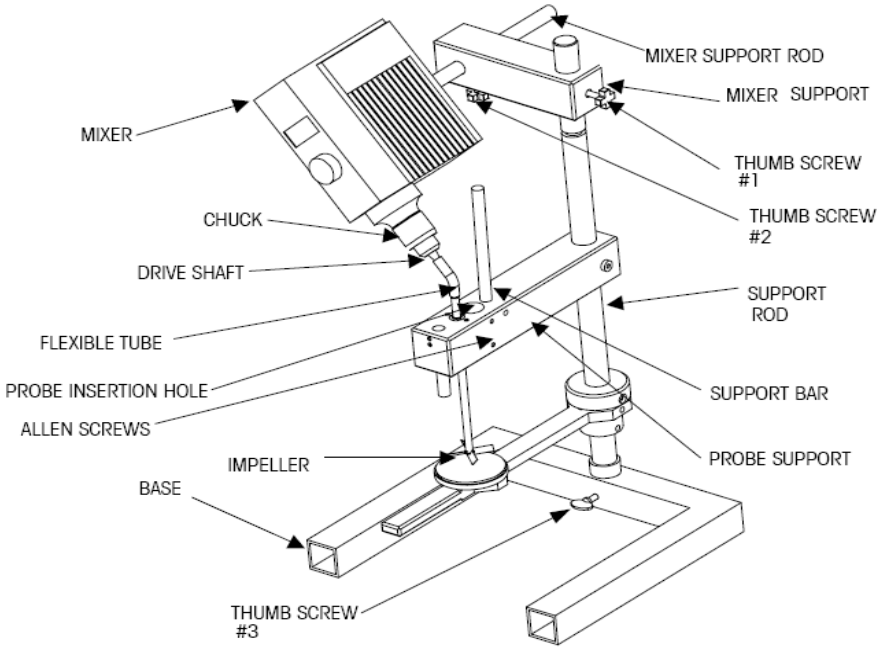

Figure 3-6 PVC Reference procedure set up Lasentec (2007)

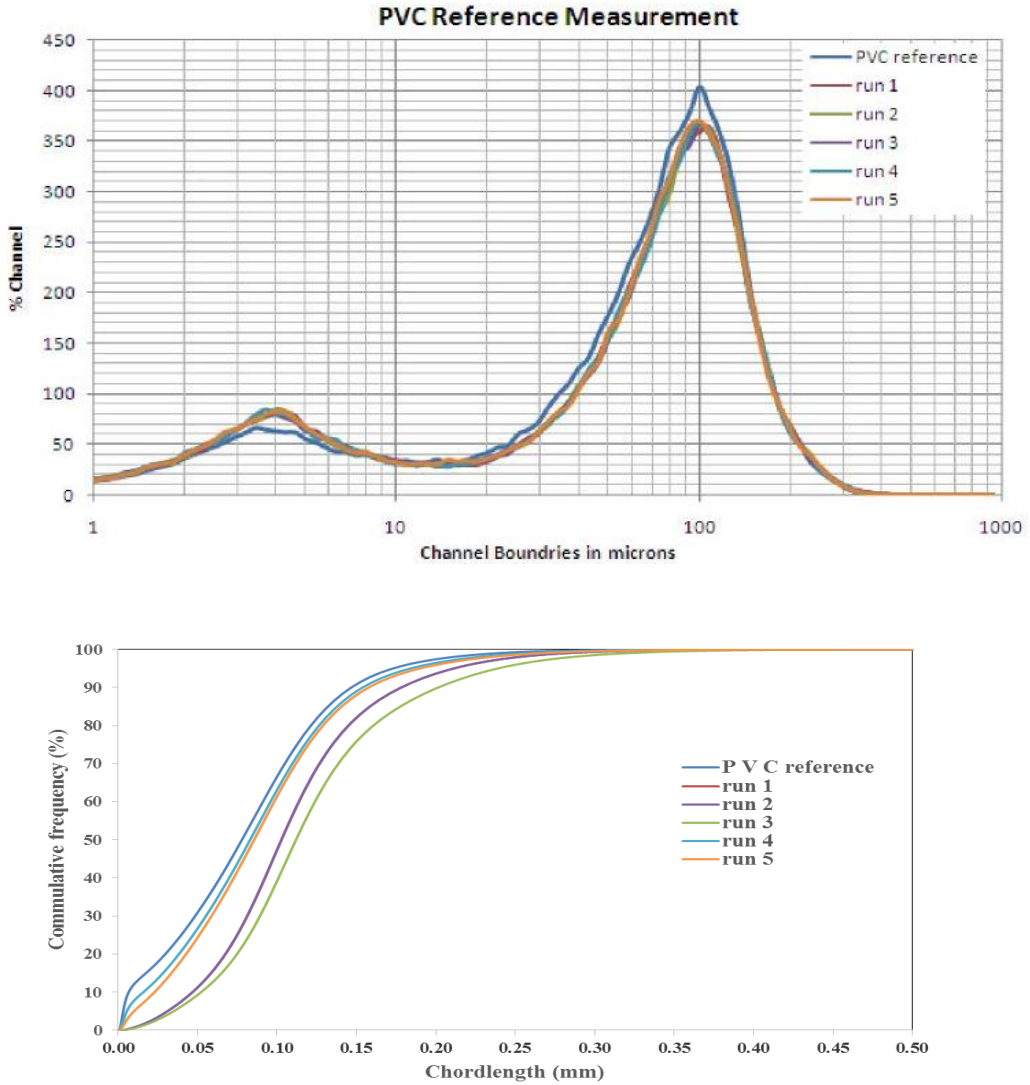

Figure 3-7 PVC reference calibration sample cumulative frequency curves (%) Lasentec (2007

FBRM probe was calibrated with Bimodal PVC reference material. A suspension of known diameter distribution (PVC reference samples) is supplied by the company. The bench top set up with the suspension as shown in Figure 3.6, are stirred with special impeller at 400 rpm and presented to the FBRM probe. Generally, the Particle Chord Length Distribution of the PVC has a peak at around 100 micron and another close to 10 micron. The tip of the probe was positioned at 25 mm above the impeller to ensure optimal sample presentation. A recommended duration of 30 seconds of stirring was made sufficient enough to disperse the beads.

Results from the PVC reference experiments are compared to the initial reference sample data file as provided by the FBRM instrument for this particular FBRM M500P to confirm the instrument repeatability (see Figure 3.7). This PVC reference procedure was carried out at different dates for the same parameters setting to ensure instrument repeatability. The percentage difference of the median and mean statistic was within the specified limits of ± 2% and ± 3% respectively.

3.5.1.2 Drop size measurements

As mentioned in the experimental procedure, section 3.4, measurement of drop size were made with FBRM M500P probe positioned on the baffled stirred tank at test height of 25 mm, 45 mm, 105 mm. The acquired data was logged continuously into a dedicated computer for further analysis. As explained briefly in section 2.3.4 of Chapter 2 in the literature review, characteristic chord length distribution (CLD) measurements are converted to drop size distribution by using the modified and improved version of the Probability Apportioning Method (PAM 2), MATLAB code.

3.5.2 HotShot High speed camera video recording

The HotShot 1280 cc high speed camera attached to a borescope (endoscope) was used to obtain droplet size images. The endoscope was inserted into the dispersion from the top of vessel. The imaging system used is capable of recording up to 500 frames per second together with a proper lighting system. The HotShot 1280 cc records brilliant color images with resolutions up to 1280 x 1024 pixels. In the current study, a resolution of 1024 x 612 pixels and a recording up to 1,000 fps was employed.

The HotShot cc 1280 high speed camera systems also has features such as remote control via a PC, Internet and external sync recording, memory segmentation and fast Gig-E Interface. The frame rates can be adjusted from the camera software and additional magnifying lens can also be fitted to obtain the right focal length of the images.

3.6 Experimental results and discussions

Figure 3.8 to 3.13 shows actual chord length distribution (CLD) measurements and the converted drop diameter distributions (DDD) from the Focused Beam Reflectance Measurement (FBRM) laser. Dispersed phase, silicone oil volume fraction (hold-up), of 20%, 30% and 80%, with water as the continuous phase were selected for illustration out of the total range from 20%, 30%, 40%, 50%, 60%, 70% and 80% volume fractions experimented. Drop size distributions were investigated for two impeller speeds, 800 rpm (Re = 7434) to 1200 rpm (Re = 11218) for the various oil fractions. Measured chord lengths were converted using the modified Probability Apportioning Method (PAM) as described in Chapter 2 and section 2.3.4. The standard deviation was approximately 0.3.

The effect of Reynolds number on drop size distribution

The trend in the graphs from Figure 3.8 to 3.16, shows that an increase in impeller speed results in the evolution of smaller droplet sizes. Mechanical energy is transferred from the impeller speed into the system thereby creating droplets to be formed, which is explained in section 3.2. This implies that there is an inverse proportionality relationship between the impeller speed and the drop sizes formed.

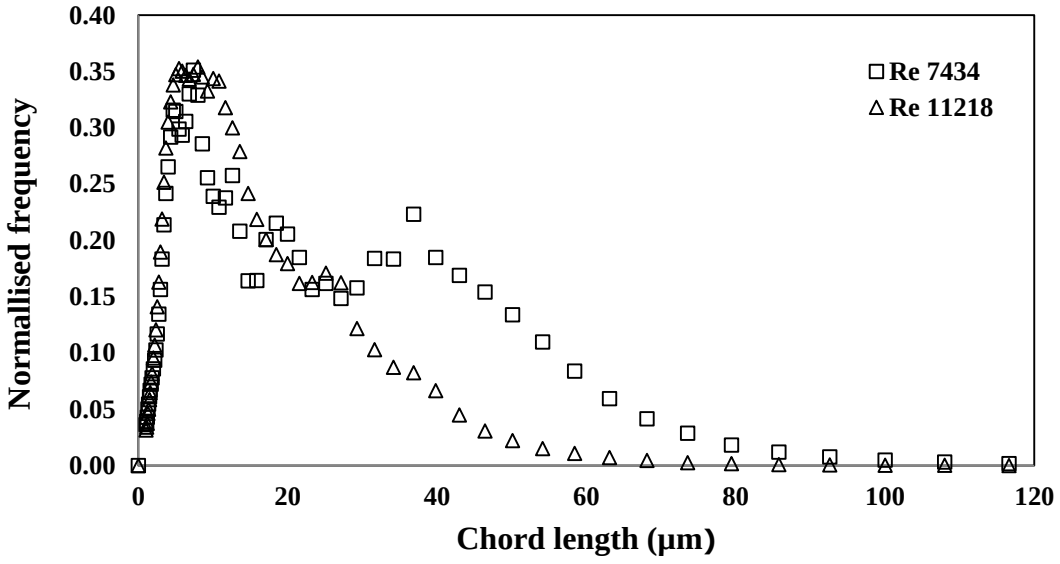

Figure 3-8 Chord length distribution for dispersed phase oil volume fraction, ε_d = 20% at impeller speed of 800 rpm and 1200 rpm at 105 mm probe position

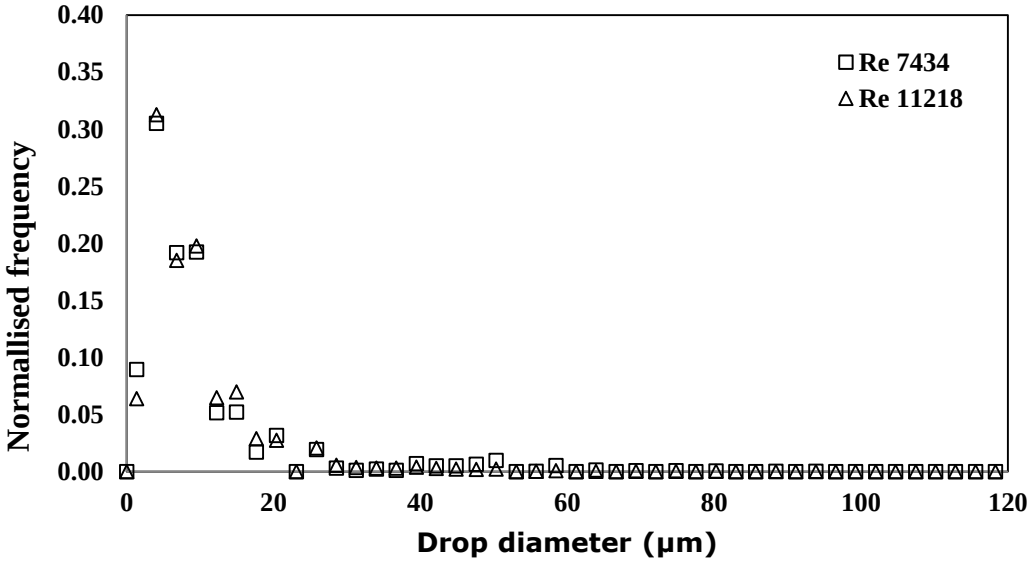

Figure 3-9 Drop diameter distribution for dispersed phase oil volume fraction, ε_d = 20% at impeller speed of 800 rpm and 1200 rpm at 105 mm probe position

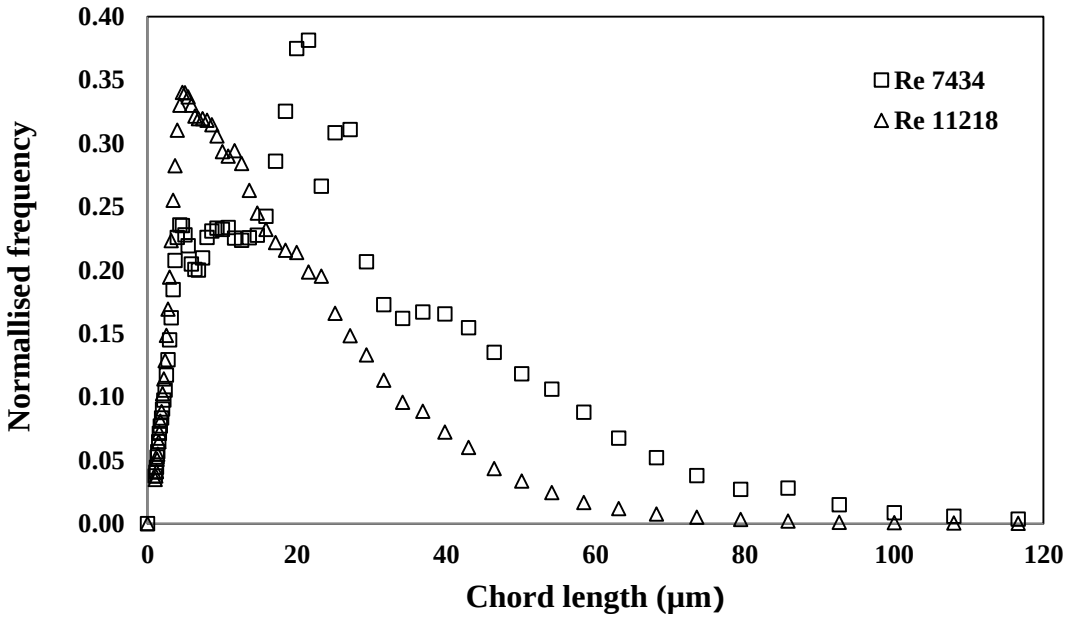

Figure 3-10 Chord length distribution for dispersed phase oil volume fraction, 30% at impeller speed of 800 rpm and 1200 rpm at 105 mm probe position

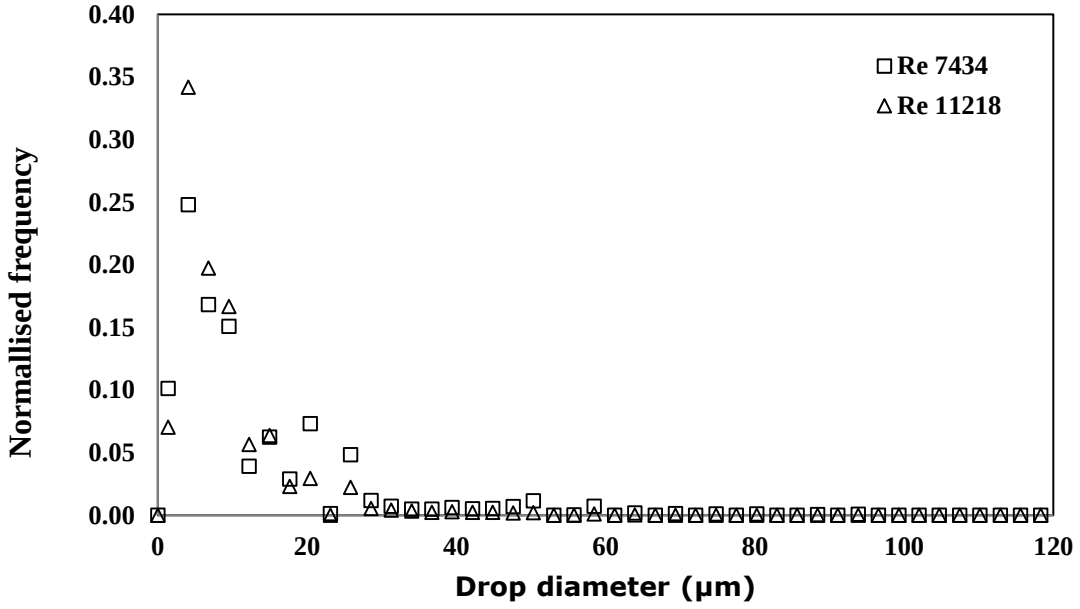

Figure 3-11 Drop diameter distribution for dispersed phase oil volume fraction, ε_d = 30% at impeller speed of 800 rpm and 1200 rpm at 105 mm probe position

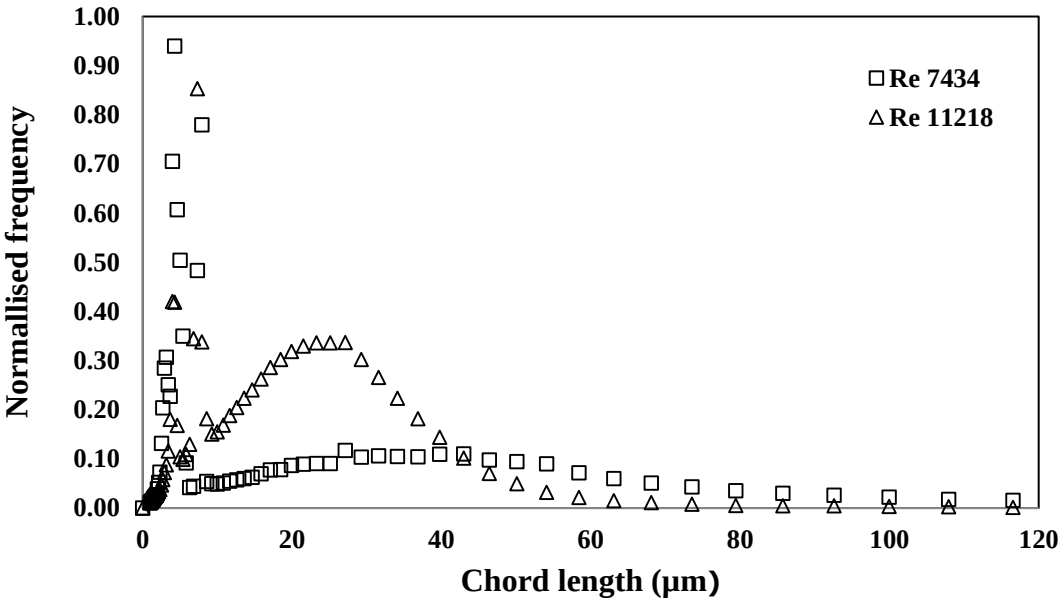

Figure 3-12 Chord length distribution for dispersed phase oil volume fraction, ε_d = 80% at impeller speed of 800 rpm and 1200 rpm at 105 mm probe position

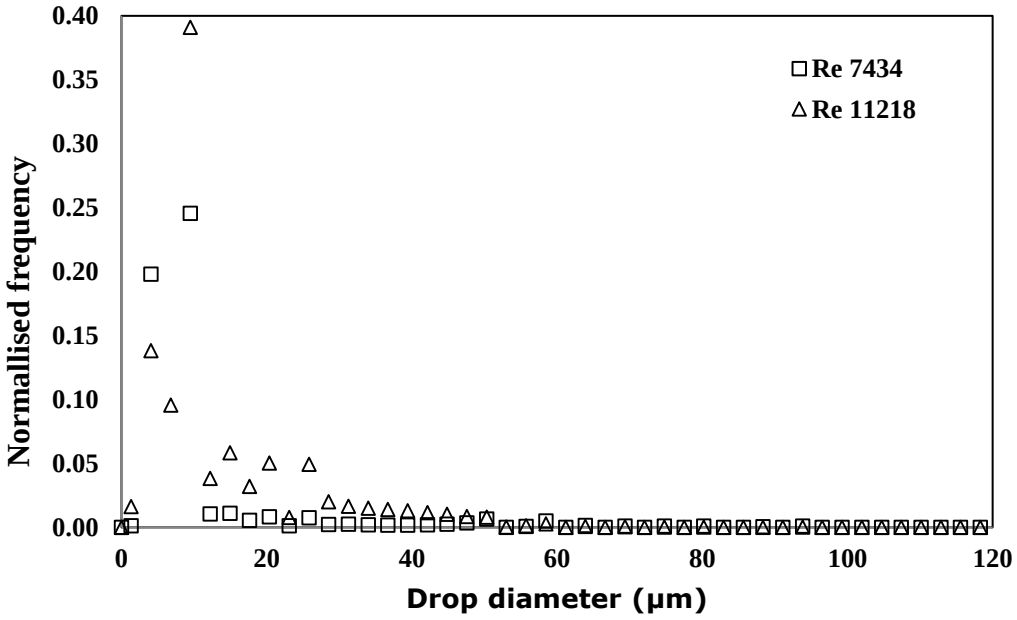

Figure 3-13 Drop diameter distribution for dispersed phase oil volume fraction, ε_d = 80% at impeller speed of 800 rpm and 1200 rpm at 105 mm probe position

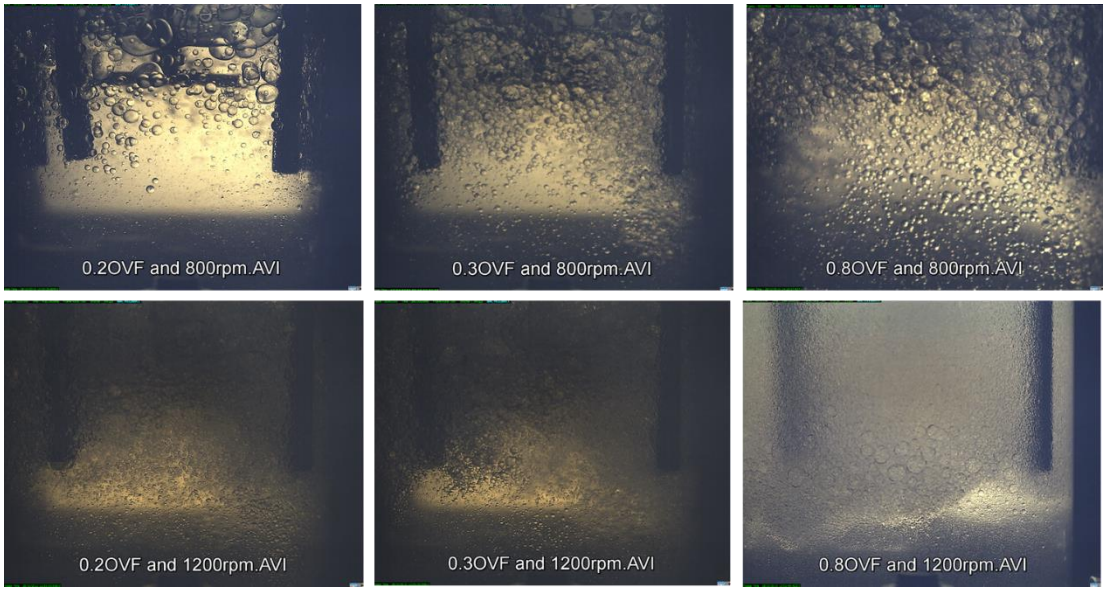

Figure 3-14 High speed camera images of dispersed phase oil volume fraction (OVF), ε_d = 20%, 30% and 80% at impeller speed of 800 rpm and 1200 rpm respectively.

In Figures 3.9, 3.11 and 3.13, where actual drop size are used, in all cases, it was noticed that increasing the impeller speed resulted in a shift in the distribution to smaller drop sizes. This observation was also seen and reported in the work of Lovick et al. (2005).

It can be seen from Figure 3.15 and 3.16 that large drop sizes are formed with low impeller speed and smaller drop sizes are observed when the Reynolds number is increased at increasing oil volume fractions. The frequency of chord length tends to slightly decrease as the Reynolds number increases from Re 7434 to Re 11218. At low impeller speed the minimum and maximum chord lengths where found to be 4 μ m and 38.9 μ m at the dominant frequencies (see Figure 3.15). Whereas at high impeller speed the minimum and maximum chord lengths were 7 μ m and 24 μ m at the dominant frequencies respectively (see Figure 3.16). The maximum diameters were also found to decrease with impeller speed, which is shown more clearly in Figures 3.27 and 3.28 using sauter mean diameter (SMD) analysis. A further investigation and analysis of the effect of impeller speed on the drop size distribution of silicone oil and water with various oil volume fractions using Sauter mean diameter (SMD) is carried out in section 3.6.2.

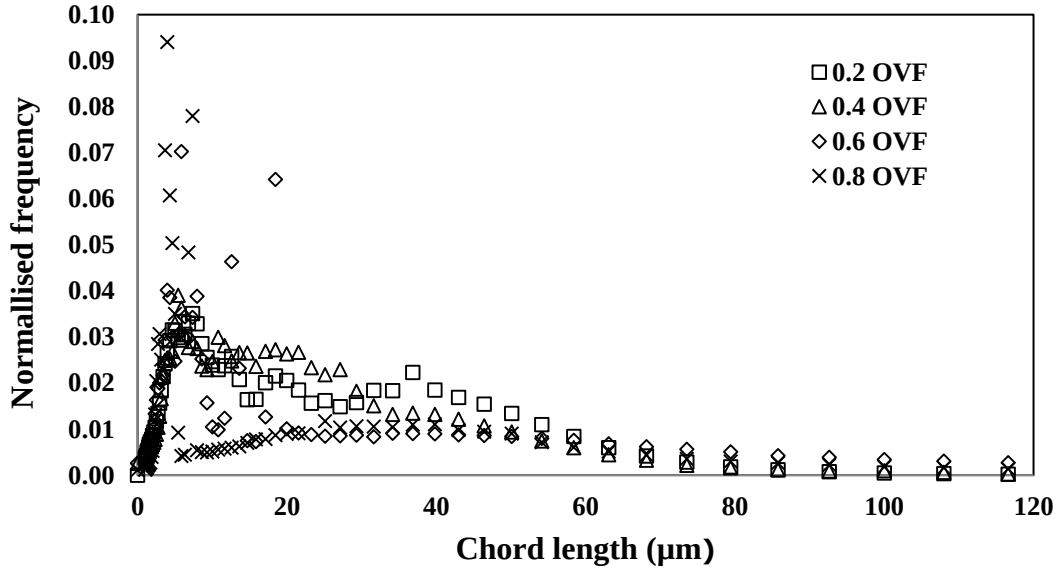

Figure 3-15 Effect of low impeller speed, 800rpm, (Re 7434) on drop size distribution for dispersed phase oil volume fraction, ε_d = 0.2, 0.4, 0.6 and 0.8

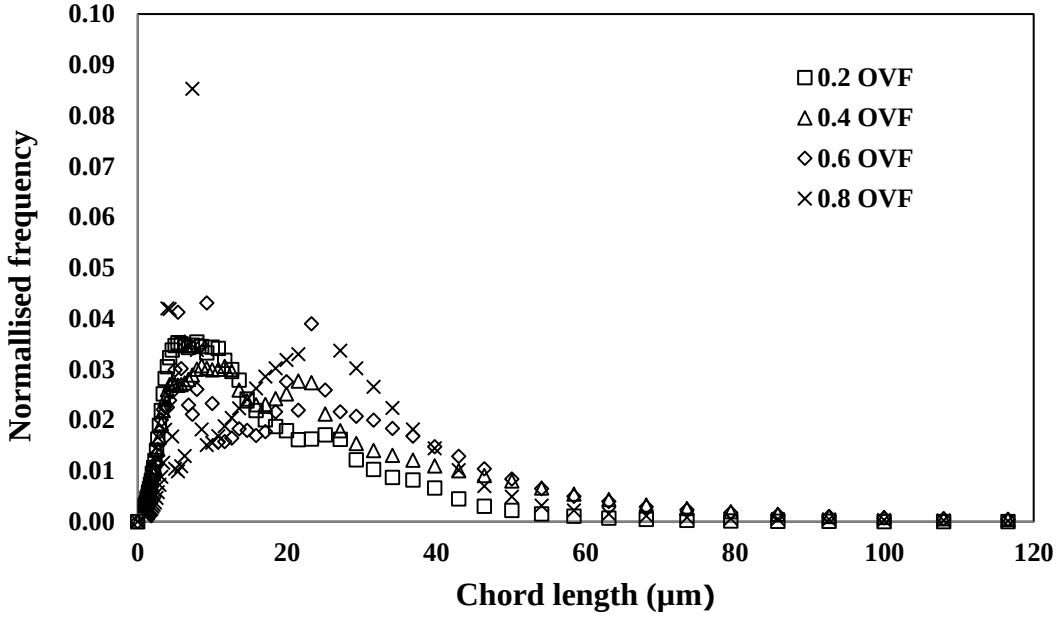

Figure 3-16 Effect of high impeller speed, 1200 rpm, (Re 11218) on drop size distribution for oil volume fraction, ε_d = 0.2, 0.4, 0.6 and 0.8

3.6.1 Droplet size estimation and calculations

Characteristic chord length distribution (CLD) measurements are converted to drop size distribution by using the modified and improved version of the Probability Apportioning Method (PAM 2), MATLAB code (Appendix B). This allowed estimation of the Sauter mean diameter (SMD) of each experimental measurement and are used for further analysis in the present work.

3.6.2 Characteristics of drops distribution

Drops measured using a laser backscatter technique can be characterized by a single number Sauter mean diameter (SMD) or a distribution. There are two frequently used drop size distributions, namely Rosin-Rammler and Log-normal distributions, which usually takes the form of an equation with two or more adjustable parameters. The upper limit log-normal distribution was also used by (Simmons et al., 1999, Simmons and Hanratty, 2001) and found good agreement with experimental data from pipe flow at dispersions below 43% volume fraction. Majority of the published work use Rosin-

Rammler and Log-normal distribution to correlate particle or droplet size measurements (Karabelas, 1978, Angeli and Hewitt, 2000a, Angeli and Hewitt, 2000, Lovick and Angeli, 2004a).

Rosin-Rammler Distribution

The Rosin-Rammler distribution is frequently used for representing droplet size distributions in sprays. It is expressed in terms of the cumulative mass distribution in the form

$$1 - V_{cum} = \exp\left[-\left(\frac{d}{\alpha} \right)^{\varsigma} \right] \qquad 3.8$$

where V_{cum} is the cumulative volume fraction of the drops with diameters less than *d*. The constants ς and α represents the slope of the curve and the diameter corresponding to $(1\text{-}V_{cum}) = 0.3679$ respectively. The volume distribution can be described in terms of d_{95}, defined as the diameter corresponding to the 95% per volume of drops with diameter less than d_{95} as follows:

$$V_{cum} = \exp\left[-2.996\left(\frac{d}{d_{95}} \right)^{\varsigma} \right] \qquad 3.9$$

The Rosin-Rammler distribution was found to fit the experimental data well for some cases (see Figure 3.17 to 3.20). The values of the slope, ζ was found to be 2.06, 1.87, 2.22, 1.90, 2.17, 2.27 and 2.17, with 95% confidence bounds uncertainty values as given in Table 3.2, for dispersed phase oil volume fractions of 20%, 30%, 40%, 50%, 60%, 70% and 80% respectively with constant impeller speed of 800rpm (Re = 7434), (see Figure 3.22). The slope is fairly constant and apparently independent of flow rate and dispersed phase oil volume fraction in each case. While the, drop diameter, α values ranged from 7µm to 108 µm. The uncertainties of measurements were determined from the slope of the Rosin – Rammler plots at the 95% confidence interval.

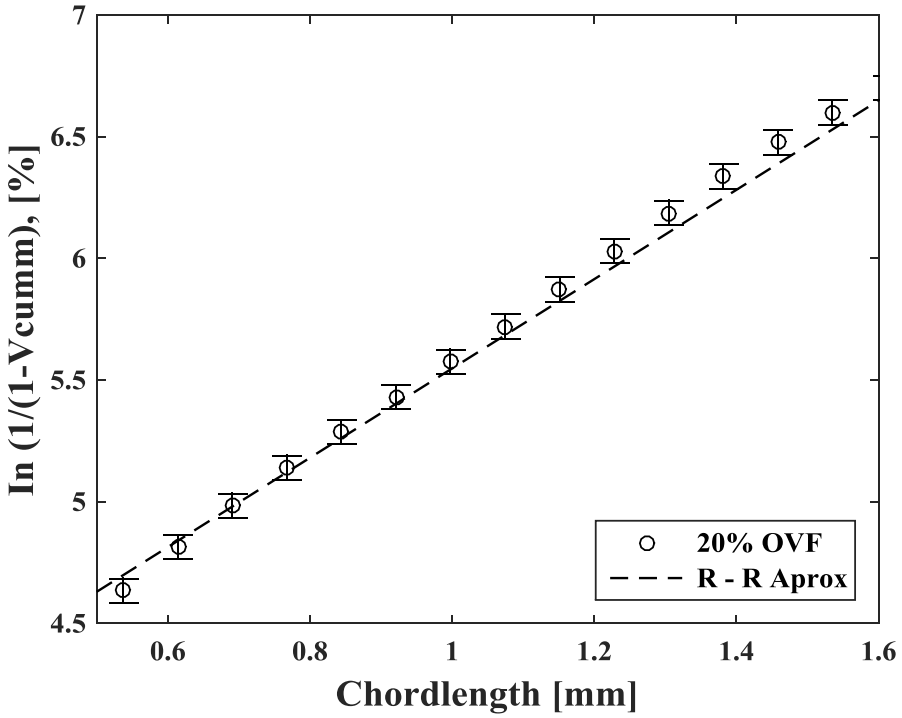

Figure 3-17 Rosin-Rammler distribution fit to 800 rpm, (Re 7434) for oil volume fraction, ε_d = 20% OVF

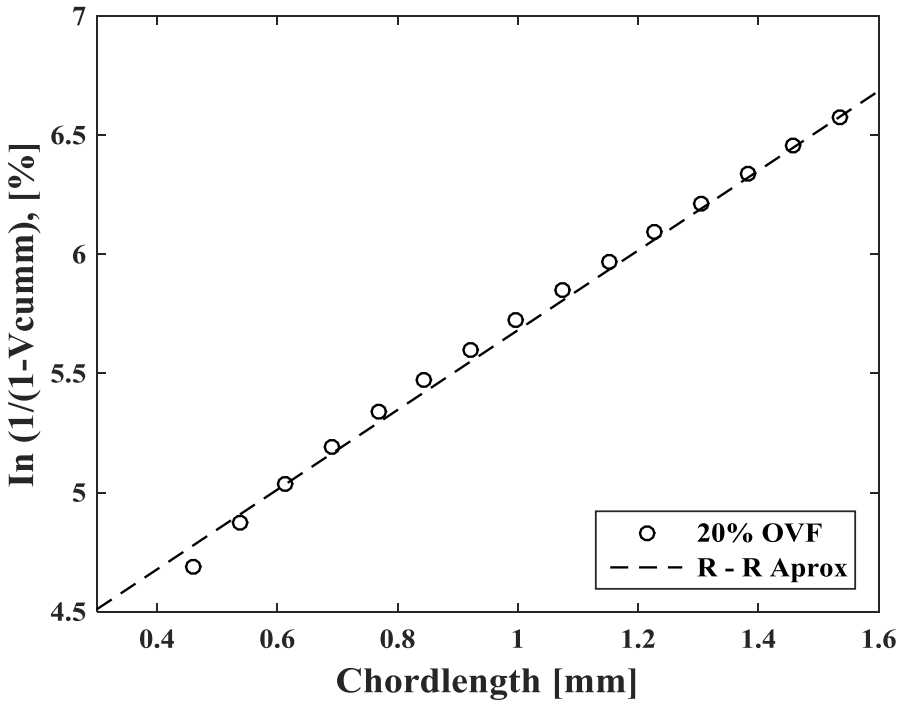

Figure 3-18 Rosin-Rammler distribution fit to 800 rpm, (Re 7434) for oil volume fraction, ε_d = 30% OVF

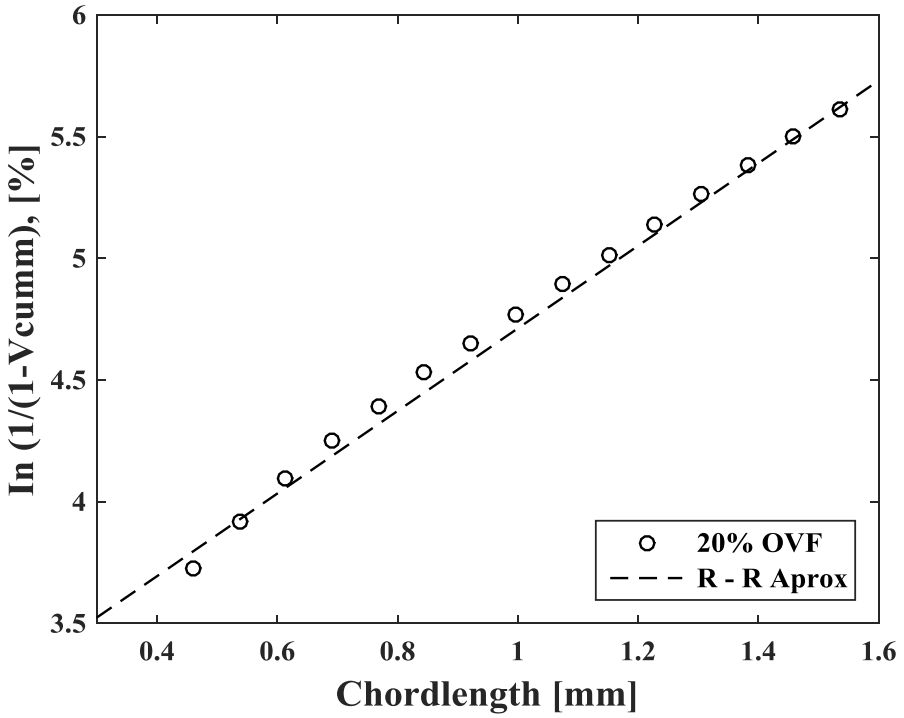

Figure 3-19 Rosin-Rammler distribution fit to 800 rpm, (Re 7434) for oil volume fraction, ε_d = 50% OVF

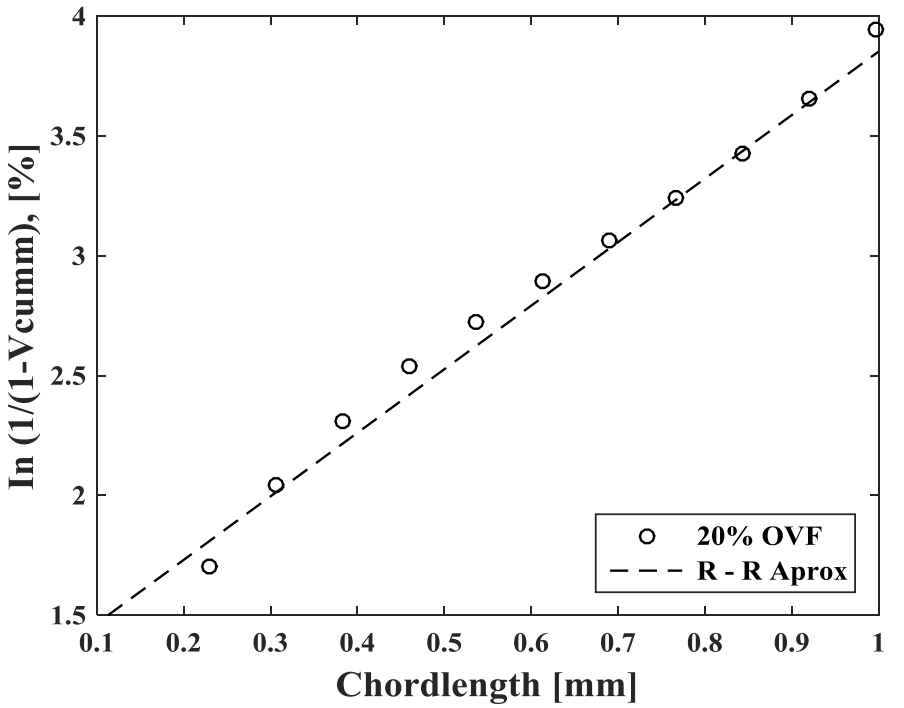

Figure 3-20 Rosin-Rammler distribution fit to 800 rpm, (Re 7434) for oil volume fraction, ε_d = 80% OVF

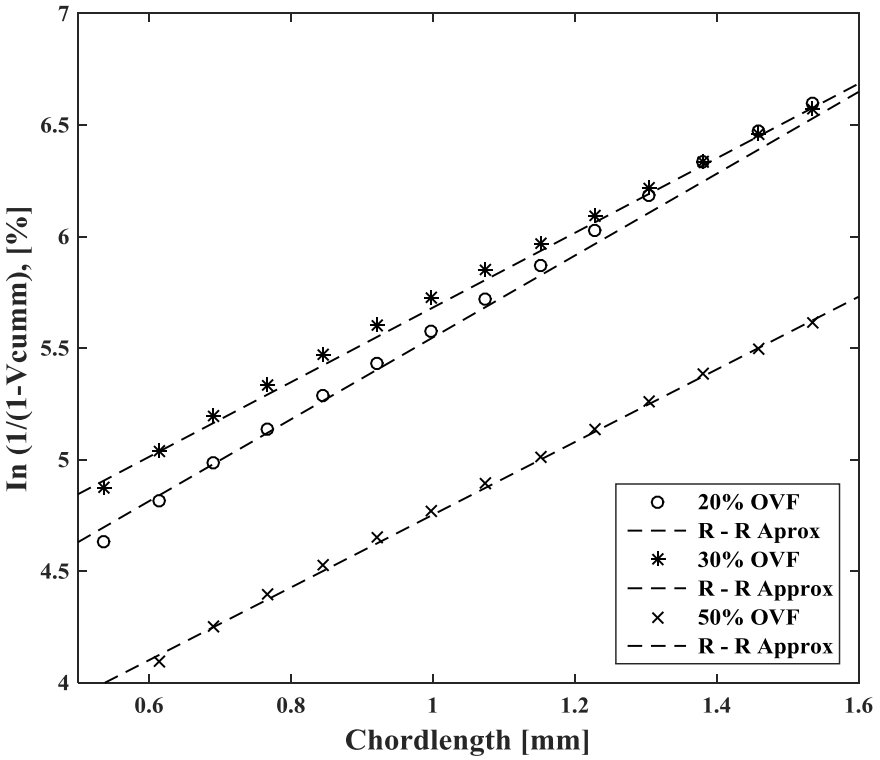

Figure 3-21 Comparison of Rosin-Rammler distribution fits to 800 rpm, (Re 7434) for oil volume fractions, ε_d = 20%, 30% and 50% OVF

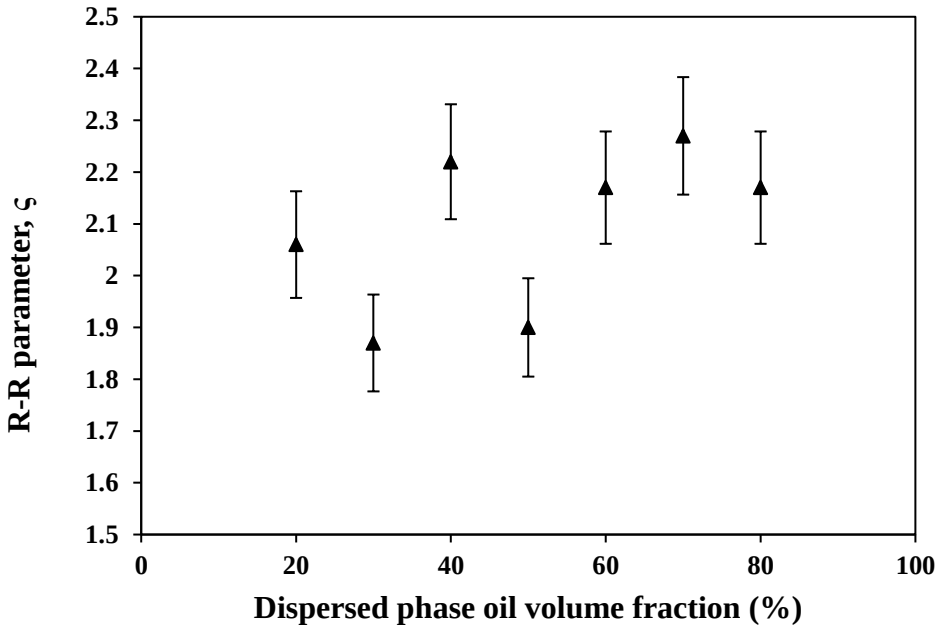

Figure 3-22 Rosin-Rammler distribution parameter, (ζ) vs dispersed phase oil volume fraction

Table 3 2 Rosin - Rammler distribution parameter and standard deviation estimate

Dispersed phase oil volume fraction (%)	R - R distribution parameters (ζ)	95% Confidence level Uncertainty
20	2.06	± 0.09
30	1.87	± 0.08
40	2.22	± 0.07
50	1.9	± 0.09
60	2.17	± 0.07
70	2.27	± 0.09
80	2.17	± 0.10

Log-normal Distribution

The log-normal distribution is also used to represent the size of droplets or particles in a dispersion system. The log-normal distribution derives from the normal or Gaussian distribution which is defined as

$$f(x) = \frac{1}{\sqrt{2\pi\sigma}} \exp\left[-\frac{1}{2}\left(\frac{x-\mu}{\sigma} \right)^2 \right] \qquad 3.12$$

where σ is the standard deviation and μ is the mean. This distribution is the well-known “bell-shaped” curve. The distribution has been normalized so the area under the curve is unity; that is:

$$\int_0^\infty f(x)dx = 1 \qquad 3.13$$

The log-normal distribution is obtained from the normal distribution by replacing the independent variable with the logarithm of the particle diameter. The number of particles with diameters between D and D + *d*D is:

$$f(D)dD = \frac{1}{\sqrt{2\pi\sigma_0}} \exp\left[-\frac{1}{2}\left(\frac{\ln D - \mu_0}{\sigma_0} \right)^2 \right] \frac{dD}{D} \qquad 3.14$$

where σ_0 and μ_0 are the standard deviation and the mean of the log normal distribution. The limits of the log-normal distribution range from zero to infinity. (Lovick et al., 2005) in their work described the log-normal distribution as follows:

$$y(d) = \frac{1}{\delta\sqrt{2\pi}} \exp\left[-\frac{1}{2}\left(\frac{\ln d - \xi}{\delta} \right)^2 \right] \qquad 3.15$$

where d is the drop size and δ and ξ are parameters of the log-normal distribution with δ affecting the distribution height and ξ affecting the distribution width.

Figure 3.23 shows plot of log-normal distribution parameter, δ, for various dispersed phase oil volume fractions. The parameter decreases with increasing dispersed phase oil volume fractions.

The Log-normal distribution fits were also found to be in good agreement with the experimental data, (see Figure 3.24 to 3.26). The values of the distribution parameters for impeller speed 800rpm (Re = 7434) are summarized in Table 3.3, at $\pm 2S_m$ confidence levels (95%), for δ and ξ respectively.

Table 3-3 Log-normal distribution parameters and standard deviation estimate

Dispersed phase oil volume fraction (%)	**Log-normal distribution parameters**					
	δ	**Stdev (S)**	**Uncertainty of measurement Standard error of mean, (Sm)**	**ξ**	**Stdev (S)**	**Uncertainty of measurement Standard error of mean, (Sm)**
20	0.89	0.01	± 0.01	0.83	0.02	± 0.02
30	0.84	0.01	± 0.01	1.89	0.03	± 0.02
40	0.68	0.07	± 0.04	1.84	0.02	± 0.01
50	0.76	0.01	± 0.01	2.06	0.03	± 0.02
60	0.77	0.06	± 0.03	1.87	0.02	± 0.01
70	0.59	0.06	± 0.03	1.77	0.03	± 0.02
80	0.65	0.02	± 0.01	0.67	0.02	± 0.01

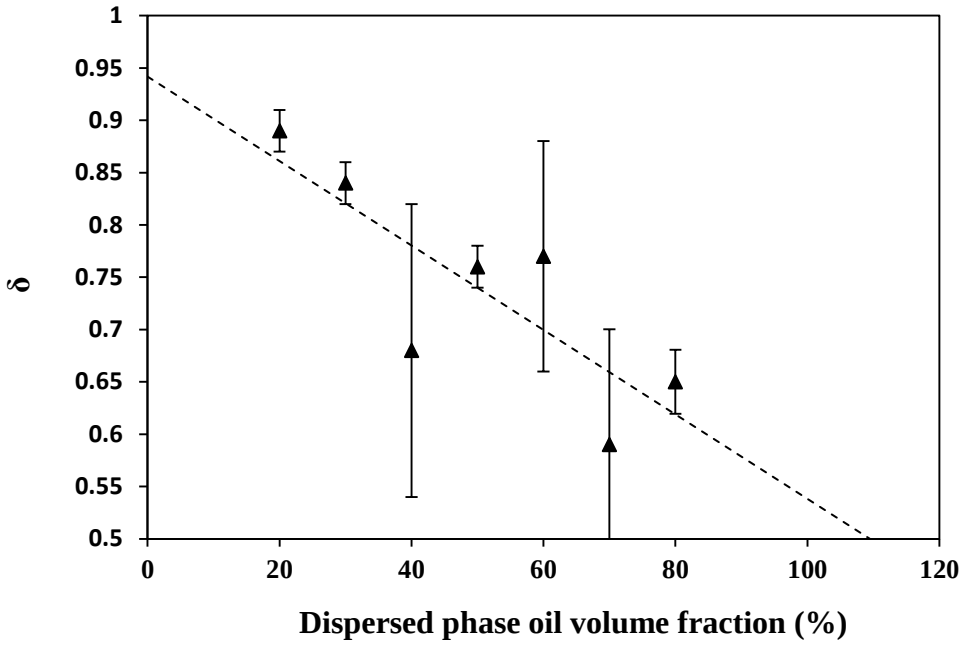

Figure 3-23 Log-normal distribution parameter, (δ) vs dispersed phase oil volume fraction

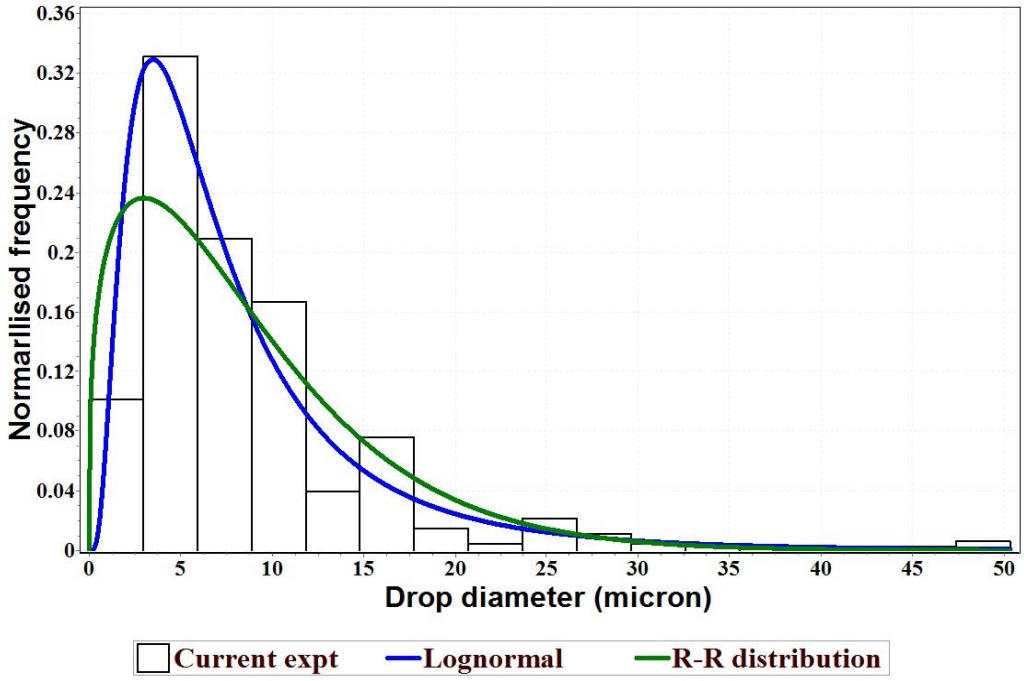

Figure 3-24 Comparison of Log-normal and R-R distribution fits to 800rpm, (Re 7434) for oil volume fraction, ε_d = 30%

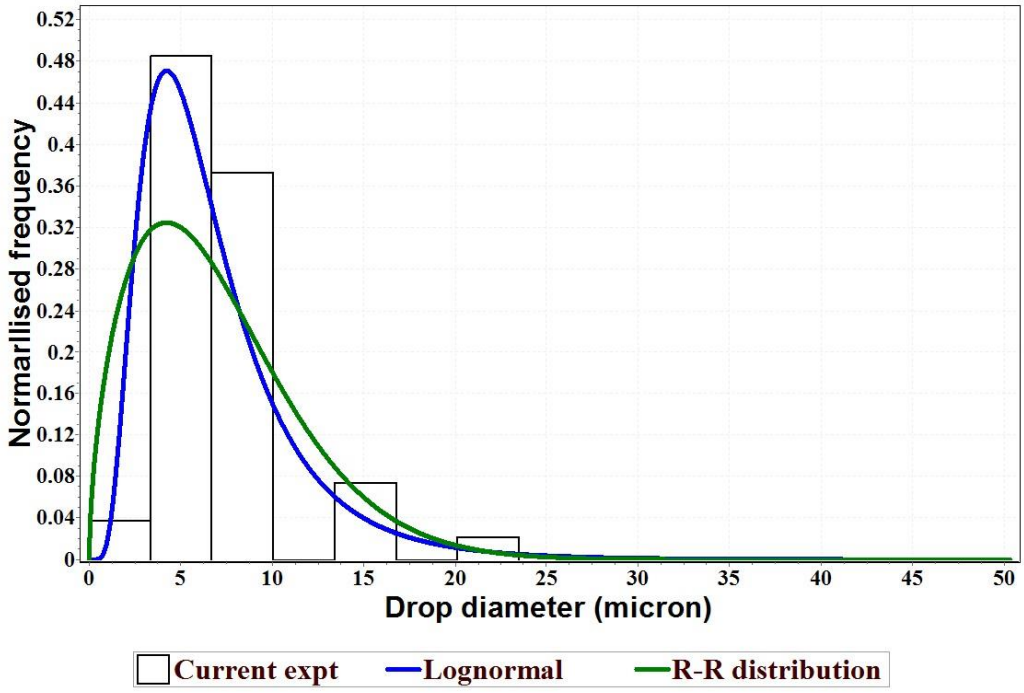

Figure 3-25 Comparison of Log-normal and R-R distribution fits to 800rpm, (Re 7434) for oil volume fraction, ε_d = 70%

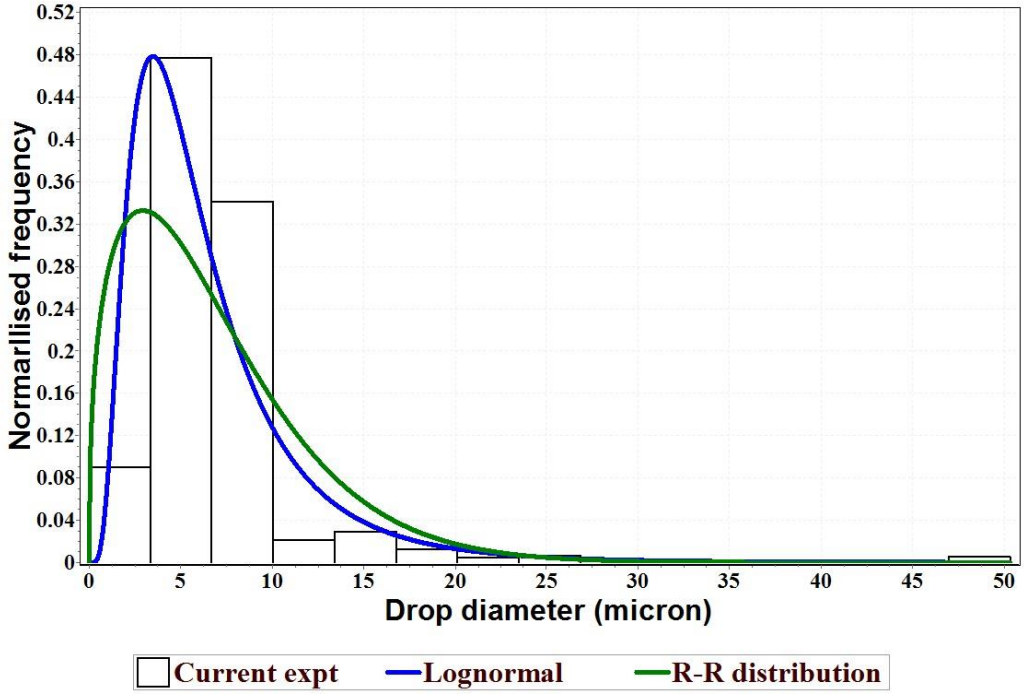

Figure 3-26 Comparison of Log-normal and R-R distribution fits to 800rpm, (Re 7434) for oil volume fraction, ε_d = 80%

The same data have been replotted in comparison of log-normal and Roson-Rammler distribution. The log-normal distribution fits better than Roson-Rammler as can be seen. The mean values of these parameters are nearly constant (i.e. $\delta = 0.74$, $\xi = 1.56$ and $\zeta = 2.10$), over a range of conditions. This implies that a reliable estimate of Sauter mean diameter (d_{32}), can be used to predict the entire distribution.

Sauter mean diameter (SMD)

The Sauter mean diameter, d_{32}, is commonly used in processes, which depends on the interfacial area and is defined as the ratio of the third moment to the second moment of the drop size distribution.

$$d_{32} = \frac{\sum_{i=1}^{k} n_i d_i^3}{\sum_{i=1}^{k} n_i d_i^2} \qquad 3.16$$

where d_i is the drop diameter in bin i and n_i is the number of drops with diameter in bin i. The maximum diameter, d_{max} and minimum diameter, d_{min} are generally considered proportional to the Sauter mean diameter, d_{32}. The Sauter mean diameter is a measure of the interfacial area per unit volume, which determines transfer rates of energy, mass and/or chemical reactions in dispersions (Zhou and Kresta, 1998b). Several correlations have been proposed to equate the Sauter mean diameter with the maximum and minimum drop diameter. A summary of some of these correlations and models can be seen in Table 2.4 in the literature review. Most significantly, the study by (Shinnar, 1961) gave relationships between the Sauter mean diameter with maximum and minimum drop diameter, which is a balance determined by the dynamics of drop breakup or coalescence mechanism of the system. In general the relation between the Sauter mean diameter and the physical properties of fluid in dispersion has been proven.

Effect of impeller speed on Sauter mean diameter (SMD), d_{32}

Table 3.4, shows a summary of Sauter mean diameter (SMD) values obtained from the FBRM M500P for some typical experimental conditions and the results plotted in Figures 3.26 and 3.27, with uncertainties to 95% of gradient confidence levels in all measurements. The best fit straight line and definition of the gradient and output of the fit function when 1st polynomial is fitted to the data is shown in Figure 3.29, with extremes of possible fits within the 95% confidence levels.

It can be seen from Figure 3.27 that there is an overall trend for the Sauter mean diameter, d_{32} to decrease with increasing impeller speed. This phenomenon has been observed by several other researchers that have worked on agitated tank such as (Shinnar, 1961, Sprow, 1967, Lovick et al., 2005). An increase in impeller speed will lead to drop breakup, thereby generating smaller droplets or drop sizes. The drop collision frequency will increase with less contact time for colliding drops thereby affecting the coalescence efficiency of droplets. There is also an overall trend in the values of Sauter mean diameter, d_{32} with increasing dispersed phase oil volume fractions at each impeller speeds. It was however, noticed that some local phenomena did occur as there was an initial decrease in Sauter mean diameter up to 40% (see Figure 3.28). A slight peak is observed at 50% oil volume fraction and then decreases as the dispersed phase volume fraction increases. This suggest a phase inversion point from dispersed phase oil volume fraction to dispersed phase water volume fraction. Similar observation was reported in the work of (Lovick et al., 2005) however, in their case there was no overall trend after the peak value compared to the decreasing trend in the current work. Some investigations have been done previously by (Kumar et al., 1998) to determine the peak value at high dispersed phase volume fraction.

Table 3-4 Sauter mean diameter values from FBRM M500P Laser

Impeller Speed (rpm)	Dispersed phase oil volume fraction (%)							Uncertainty to 95% of gradient confidence level (µm)
	20	30	40	50	60	70	80	
	SMD (µm)	SMD (µm)	SMD (µm)	SMD (µm)	SMD (µm)	SMD (µm)	SMD (µm)	
800	50	43	38	39	38	26	24	± 0.40
900	48	43	37	39	37	25	23	± 0.39
1000	45	38	36	38	34	22	22	± 0.37
1100	43	37	35	37	32	22	21	± 0.35
1200	38	33	33	36	31	21	20	± 0.29

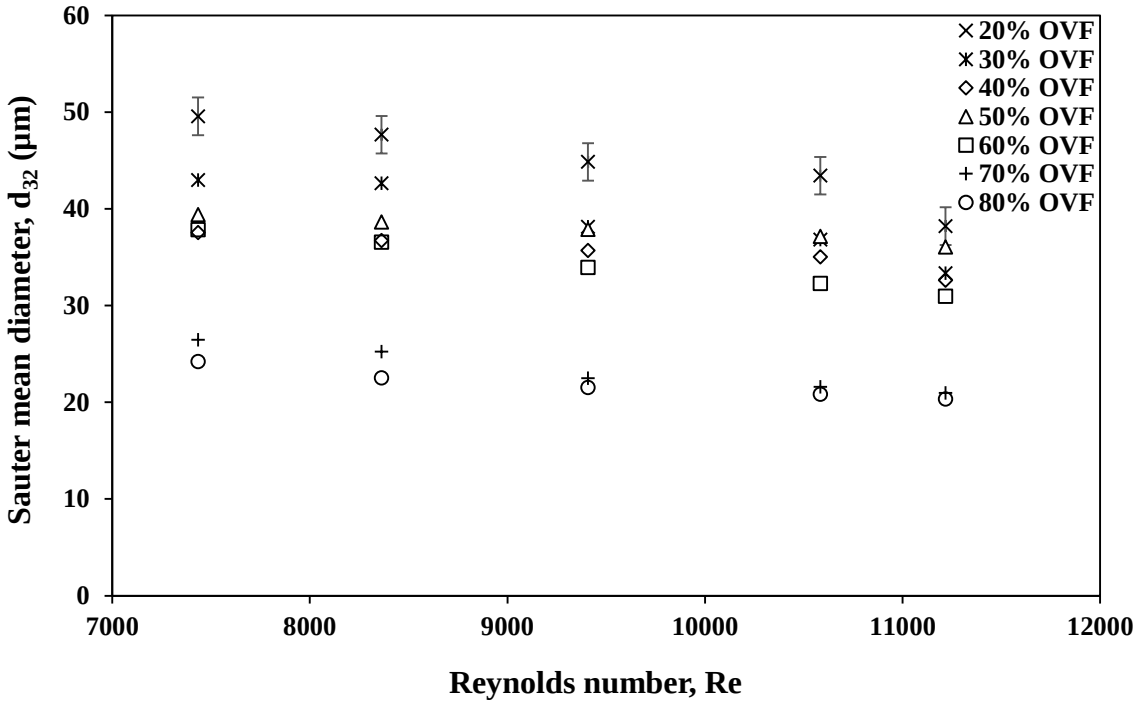

Figure 3-27 Sauter mean diameter vs impeller speed for different dispersed phase oil volume fractions.

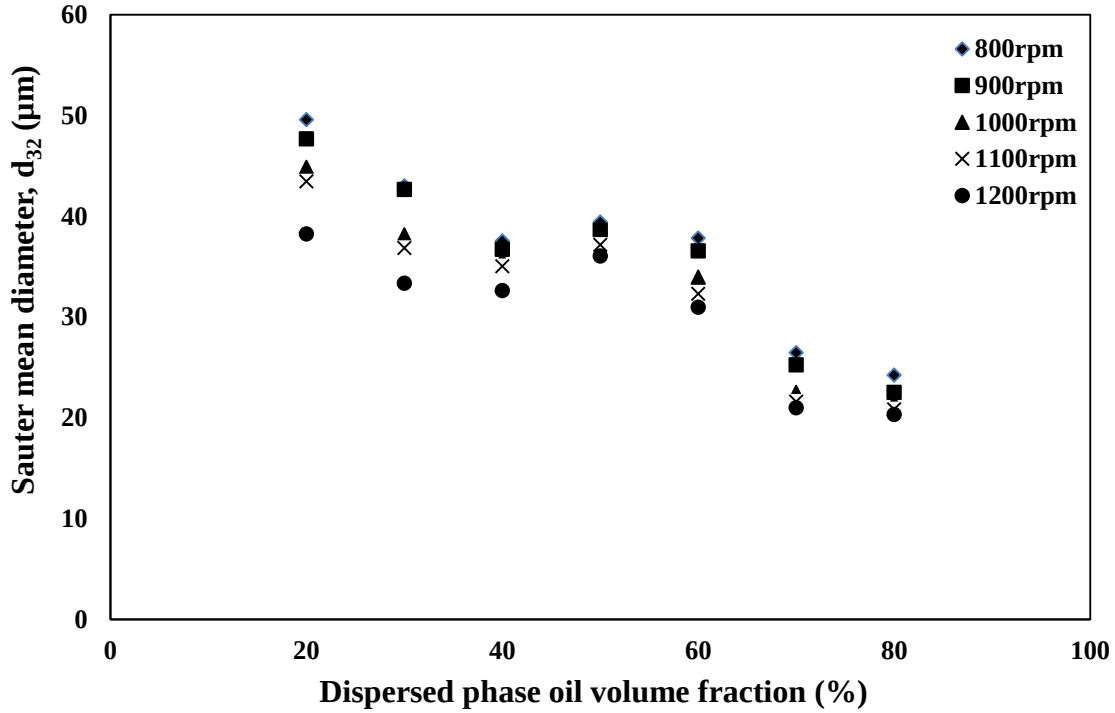

Figure 3-28 Sauter mean diameter vs dispersed phase oil volume fraction for various impeller speeds.

Coalescence of droplets

Drop coalescence is a complex occurrence in a turbulent dispersion as a result of droplets colliding with each other and combing to form larger ones. The coalescence process involves the approach of two droplets, drainage and eventual rupture of the entrapped liquid film with influence of the physical properties of the fluids and interface between the two liquids. A major indication however is the formation of large droplets, which can be seen from the experimental evidence, illustrated below.

The trend observed in Figure 3.29 and 3.30 shows that there is a significant increase in chord lengths, which indicates an increase in drop size as coalescence process progresses with time when the impeller is turned off as described in the experimental procedure. Higher volume fraction leads to more drop population, leading to more interaction, which is perhaps the reason for higher frequency of droplet collision rate. As a result there is an increased probability of drop - drop coalescence of the two liquid phases, i.e. silicone oil and water, forming larger droplets with time.

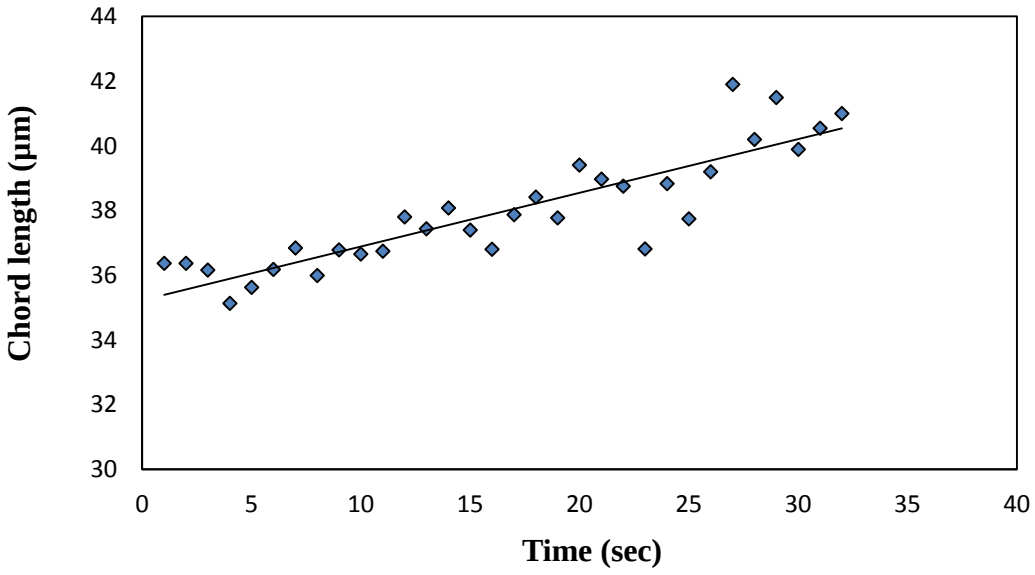

Figure 3-29 Chord length vs time for 30% dispersed phase oil volume fraction at 105 mm probe position and impeller speed 1000 rpm.

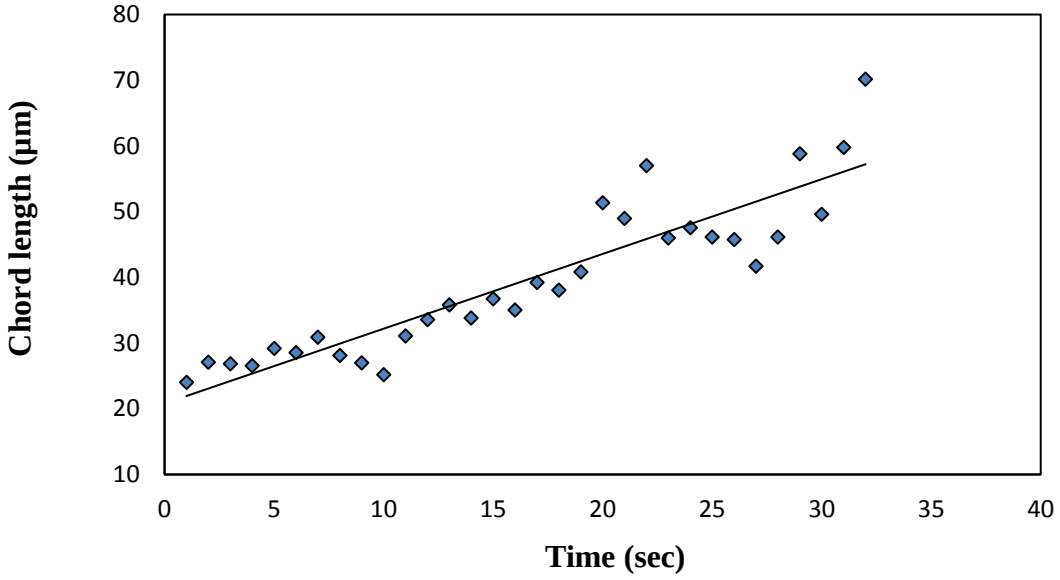

Figure 3-30 Chord length vs time for 40% dispersed phase oil volume fraction at 105 mm probe position and impeller speed 900 rpm.

A plot of the volume of oil layer against time in Figure 3.31 and 3.32 of oil dispersed phase fractions of 30% and 40% shows an increase in oil layer as coalescence progresses up to a maximum point, within which all the droplets have coalesced to form the bulk of the liquid, depending on the position of the oil/water interface from the top liquid level of the vessel. It was also noticed that droplets coalesce much faster within 5mins at high dispersed phase oil volume fraction (40%), than lower fraction 30% at 7.5 mins.

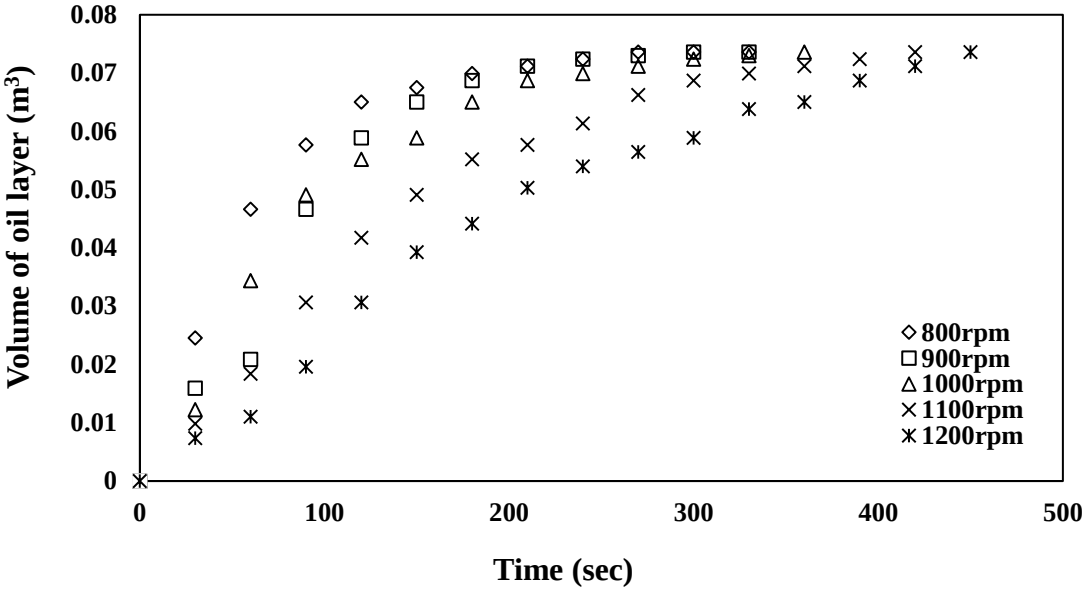

Figure 3-31 Volume of oil layer vs time of coalescence for 30% dispersed phase oil volume fraction

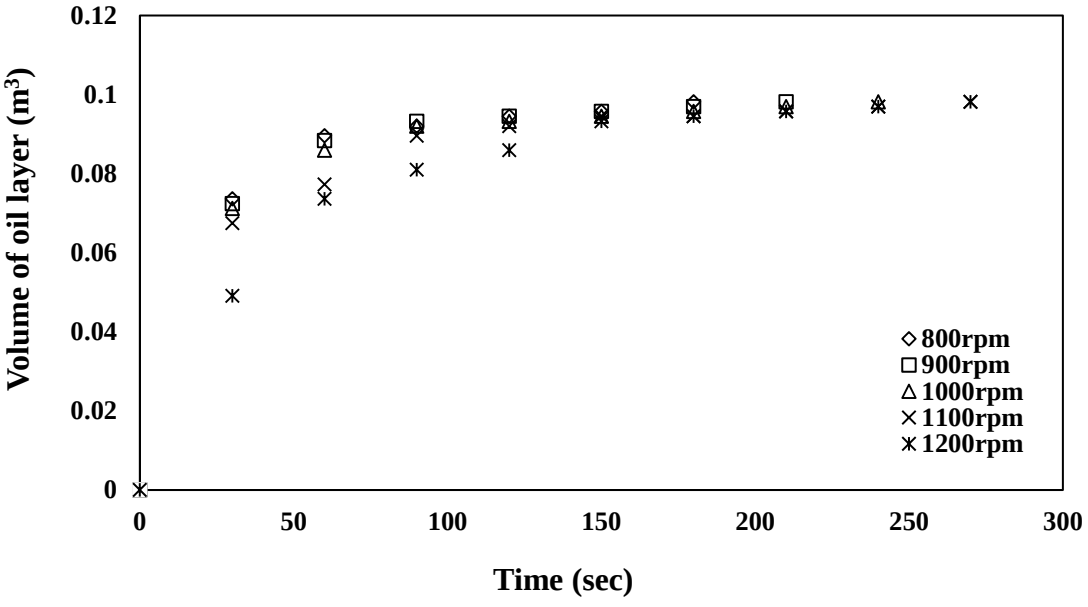

Figure 3-32 Volume of oil layer vs time of coalescence for 40% dispersed phase oil volume fraction

3.6.3 Drop breakup and coalescence in turbulence dispersions

a. Drop breakup analysis and estimation of average energy of dissipation ($\bar{\varepsilon}$)

Based on the experimental conditions in the current work the average energy of dissipation, $\bar{\varepsilon}$, can be estimated as follows: Considering equation 3.3, the value of the constant K can be evaluated. If we have the impeller speed, N = 800 rpm, impeller diameter, D = 0.0305m and the physical properties, density of continuous phase (ρ_c) = 998kgm^{-3}, viscosity μ_o = 0.0052 kgm^{-1}s^{-1}, interfacial tension (σ) = 44.7 mNm^{-1}), then equation 3.3 becomes

$$d_{\max} = 0.025(\sigma/\rho_C)^{0.6}(N^3D^2)^{-0.4} \qquad 3.17$$

Where, the constant K = 0.025, from the slope of the graph in Figure 3.33.

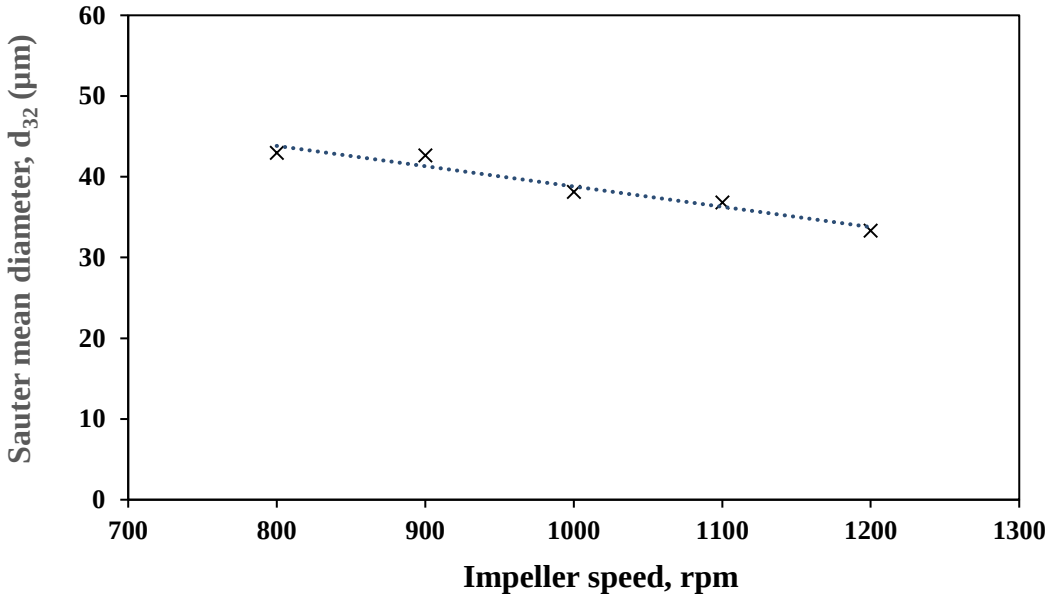

Figure 3-33 Sauter mean diameter vs impeller speed for 30% dispersed phase oil volume fractions in drop breakup experiment

For fully developed turbulence (in the region of the agitator), the average energy of dissipation $\bar{\varepsilon}$ in the liquid must therefore be a function of N and D only, and by dimensional analysis is given by:

$$\bar{\varepsilon} = kN^3D^2 \qquad 3.18$$

Here *k* is a dimensionless constant equal to 1, since the distribution of the main flow velocity in the vessel is universal. Therefore, from equation 3.18 the average value of the energy is approximately $1.95 \times 10^{-3} m^2 s^{-3}$. From (Kolmogoroff, 1949, Hinze, 1955) theory, the energy of dissipation is expressed as

$$\varepsilon = u^3 / l \qquad 3.19$$

where, l = D/2 and u is the velocity of droplets, is estimated to be approximately $2.95 \times 10^{-5} ms^{-1}$.

Therefore, considering equation 3.1, which is

$$N_{We(crt)} = \frac{\pi d_{\max}}{\sigma} = \frac{\rho U^2 d_{\max}}{\sigma} = C\left[1 + \varphi\left(N_{vis}\right)\right] \qquad 3.20$$

and equation 3.15 the critical weber number , $N_{We(crt)}$ was estimated to be 0.043. This shows that the splitting of a drop depends upon a critical Weber number, $N_{We(crt)}$ = 0.043, which yields the maximal drop size, $d_{max} = 43\,\mu m$ that can resist the stress due to dynamic pressure of turbulent eddies.

b. Coalescence of droplets

In section 3.2 above, some correlations are derived by (Shinnar, 1961, Thomas, 1981), specifically Equations 3.4 and 3.5 respectively, for determining the minimum drop size in an agitated tank.

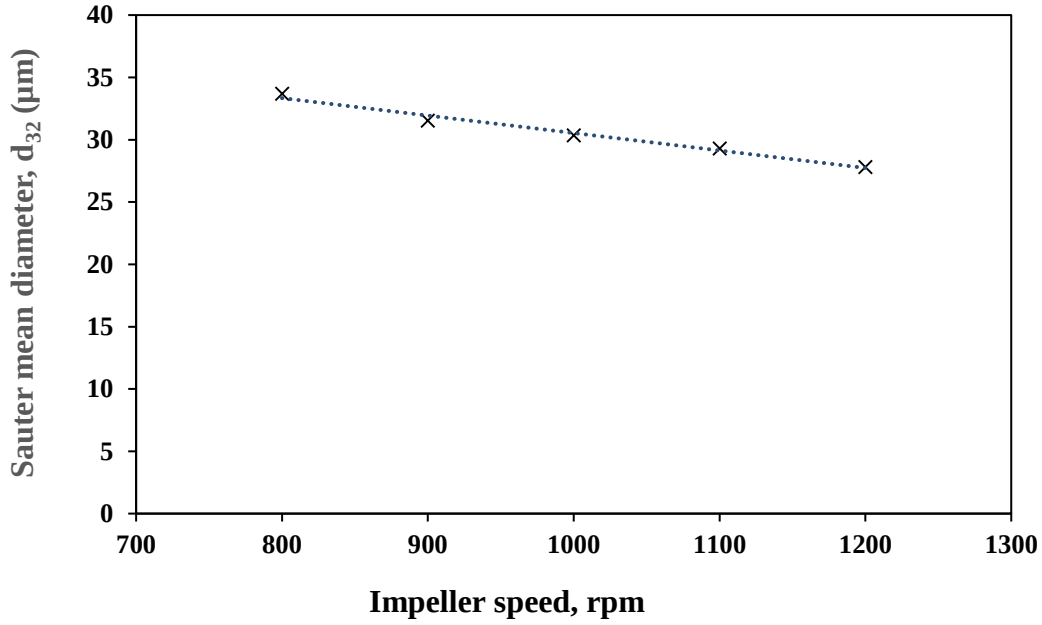

Figure 3-34 Sauter mean diameter vs impeller speed for 30% dispersed phase oil volume fractions in drop coalescence experiment

Considering equation 3.4 for the case of coalescence, which is

$$d_{\min} = C\varepsilon^{-1/4}\rho_c^{-3/8}A(h_0) \qquad 3.21$$

The constant C, can be evaluated. For a given pair of fluids $A(h_0)$ is constant (Shinnar, 1961). Assuming the critical drainage film thickness of droplets, h_o = 0.1µm, since it is unlikely that the thinner films sometimes observed in quasi-static coalescence experiments could survive in the highly agitated environment of a stirred tank. From Figure 3.35, the constant *C* is determined from the slope of the graph. If the estimated average energy input is 1.95 x $10^{-3}m^2s^{-3}$ and the minimum drop diameter, d_{min} = 33.7 μm, then from the (Kolmogoroff, 1949), length scale $\left(\nu^3/\varepsilon\right)^{\frac{1}{4}} \ll d \ll l$, the value of d_{min} obtained is within the specified inertial subrange of less than 0.09214 for droplets of that size to coalesce.

Coalescence efficiency

Once drops collide with each other the contact last for a period of time called the contact time, and then they either coalesce or bounce away from each other. Coalescence occurs when the random contact time exceeds the coalescence time or drain time.

In order to determine what fraction of drop collisions lead to coalescence events, it is necessary to define collision efficiency. This efficiency will be a function of the contact time between bubbles and the time required for bubbles to coalesce. An expression for the coalescence efficiency (η) is given by (Coulaloglou and Tavlarides, 1977), as follows:

$$\eta = \exp(-\tau / T) \qquad 3.22$$

Here, τ, is the film drainage time while T is the contact time for the two bubbles in a turbulent system. Coalescence times have been successfully modelled in stagnant fluids by examining the time required for the liquid film between bubbles to thin from an initial thickness to a critical value where rupture occurs as illustrated in section 3.3 in the literature review. The coalescence and drainage of drops are in dynamic equilibrium in turbulent flow under steady state. As two drops are brought together in dispersion, a thin liquid film forms between them and drains. During drainage, turbulent fluctuations could separate the drops again. Assuming that the eddies in the inertial sub range are responsible for the motion of drops, (Levich, 1962) in his book estimated the average contact time, T, between drops in turbulent flow as:

$$T = \left(d^2/\varepsilon\right)^{1/3} \qquad 3.23$$

Thomas (1981) estimated the film drainage time as:

$$\tau = \frac{3}{32\pi}\mu\rho\varepsilon^{2/3}d^{8/3}\left(d/\sigma h\right)^2 \qquad 3.24$$

Where, *h*, is the film thickness. Assuming h = 0.1μm, the energy of dissipation, ε = $1.95\text{x}10^{-3}\text{m}^2\text{s}^{-3}$ and considering the physical properties of the system, then the values of T and τ are calculated for minimum drop size d_{min} =33.7 μ m to be $8.4\text{x}10^{-3}$s and

1.62 x 10^{-13}s respectively. Therefore, from the values obtained in the current work, the criteria for coalescence is satisfied since τ < T.

With equations (3.22), (3.23) and (3.24), we obtain an expression for coalescence efficiency for mobile interfaces in a pure system as follows:

$$\eta = \exp(-0.094\mu_c \rho_c \sigma^{-2} h^{-2} \varepsilon d^{14/3}) \qquad 3.25$$

Evaluating equation 3.25 gives, η = 0.9103 (approx. 0.91). It indicates that coalescence may be prevented by increasing turbulence intensity of the total system. That is if the kinetic energy of the oscillations induced in the coalescing droplet pair due to turbulence pressure fluctuations is higher than the energy of adhesion between the drops.

3.6.4 Video analysis

The results of video recordings and images obtained have not been analysed properly in comparison with the Focused Beam Reflectance Measurements (FBRM) of drop sizes and drop size distributions. However, some characteristic images of selected typical experimental runs obtained by the high speed camera technique for dispersed phase oil fractions of 20%, 30%, 40%, 50%, 60% and 70%, with impeller speeds of 800 rpm, 900 rpm, 1200 rpm, are shown in Figure 3.35 to 3.40.

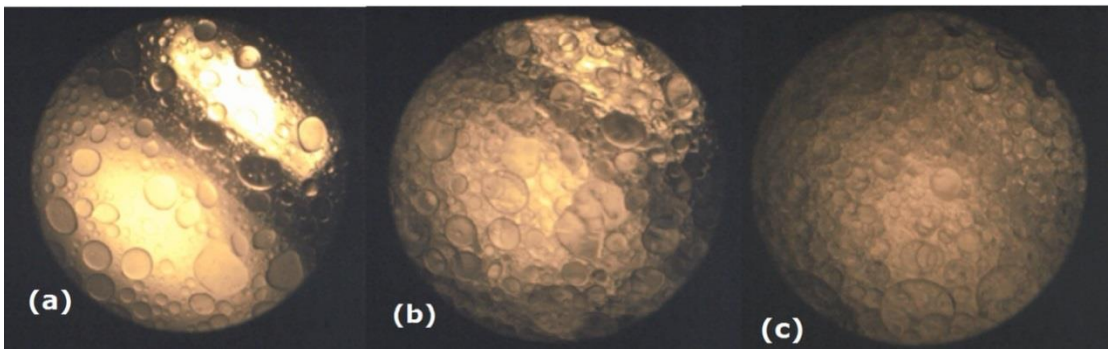

Figure 3-35 High speed camera images of 30% oil fraction (a) 800 rpm (b) 900 rpm (c) 1200 rpm.

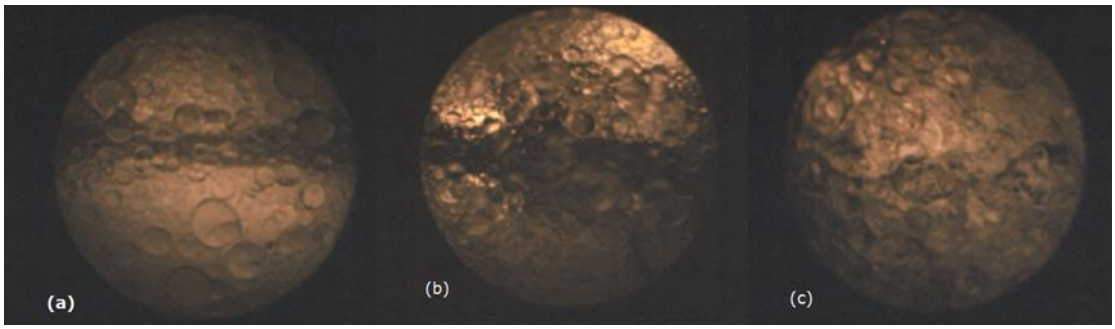

Figure 3-36 High speed camera images of 40% oil fraction (a) 350 rpm (b) 400 rpm (c) 1200 rpm.

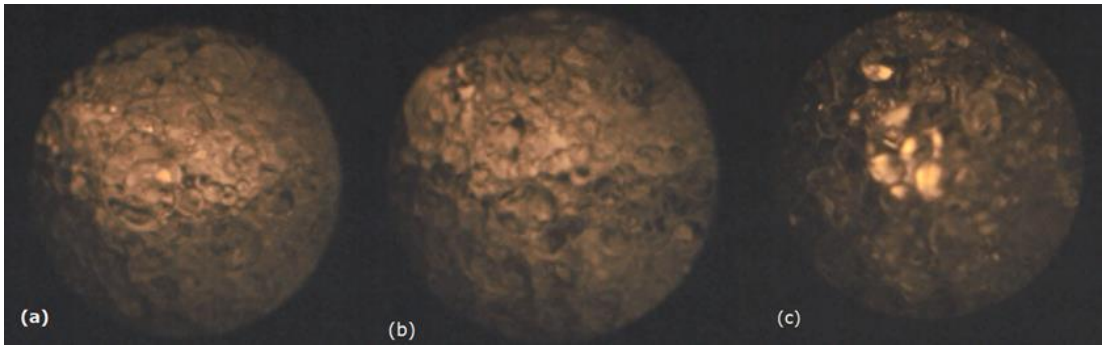

Figure 3-37 High speed camera images of 50% oil fraction (a) 800 rpm (b) 900 rpm (c) 1200 rpm.

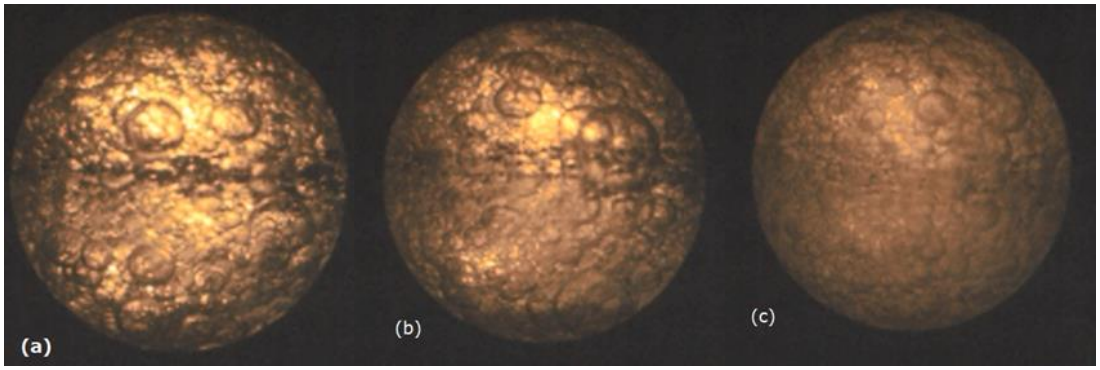

Figure 3-38 High speed camera images of 70% oil fraction (a) 800 rpm (b) 900 rpm (c) 1200 rpm.

It was observed that the droplet sizes formed at higher impeller speed are smaller than those of lesser speed, which is expected. Drop coalescence was seen to take place immediately after the stirrer was turned off as shown in Figure 3.40 (a). Fast moving silicone oil droplets having kinetic energy collides with each other and coalesce together, after which they rise to the bulk of liquid at the interface as shown in Figure 3.40 (b).

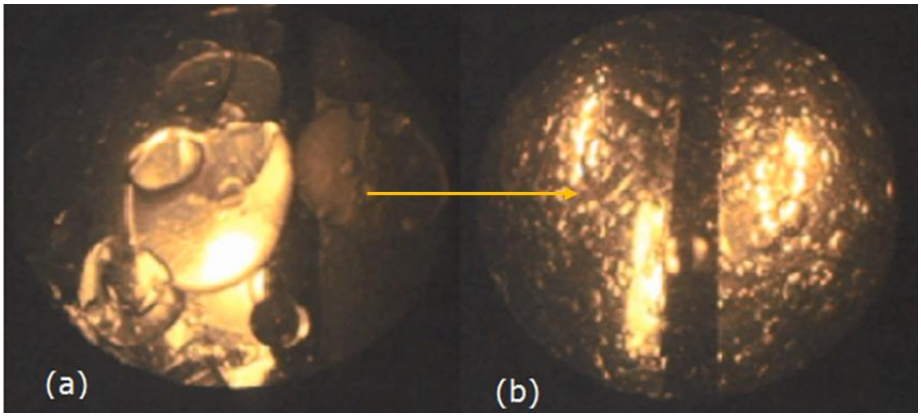

Figure 3-39 Photographs of drop break up from (a) to (b).

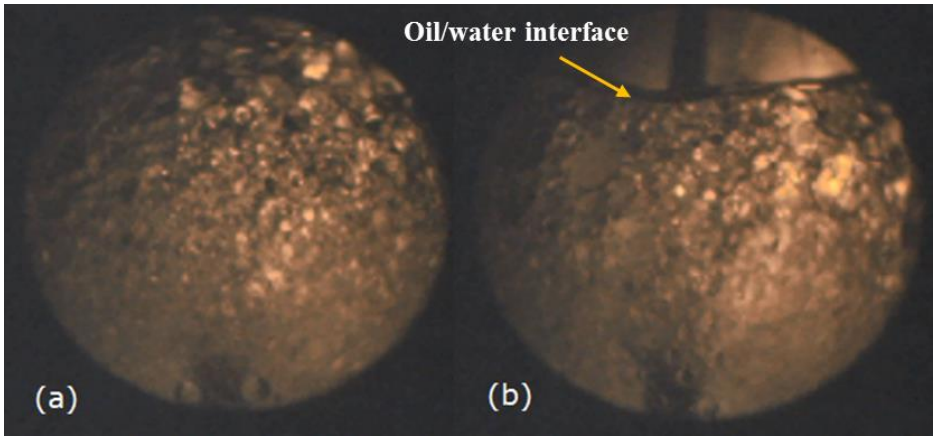

Figure 3-40 Photographs images of (a) drop coalescence (b) drop coalescence at the liquid –liquid silicone oil/water interface.

3.7 Summary

Focused Beam Reflectance Measurement (FBRM), was used to obtain drop sizes and drop size distributions in silicone oil-in- water dispersions for dispersed phase oil volume fractions from 20% to 80%. From the results obtained, both Rosin-Rammler and log normal distribution was found to fit satisfactorily with the experimental data. However, the Log-normal distribution fits better and also found to be in large agreement with the actual drop diameters of the experimental data, when both distributions were compared.

From the results obtained using the Sauter mean diameter analysis, it was found that an increase in impeller speed results in the evolution of smaller droplet sizes and the distribution shifting towards smaller drops. This signifies drop breaking up process taking place. There was also some significant effect by increasing the dispersed phase volume fraction leading to an overall decrease in Sauter mean diameter (SMD), as observed in the current work. The results also indicates an increase in drop size as coalescence process progresses with time, thereby resulting to an increase in volume of both oil and water.

Chapter 4 EXPERIMENTAL RIG AND INSTRUMENTATION

This chapter focuses on the description of the liquid – liquid facility used to carry out the experimental campaign. An investigation of previous research work in liquid – liquid systems reveals the possibilities of the use of sudden pipe expansion as phase separators for liquid-liquid two phase flows. This geometry is designed to give a greater understanding of the hydrodynamics of coalescence process in the two phase liquid – liquid flow system, by obtaining drop size distribution information. In addition, flow parameter steady state data, on flow patterns, pressure gradients, liquids flowrates and liquids holdup, are also collected.

In order to achieve the above geometry of horizontal pipeline with sudden expansion, a liquid-liquid flow facility was designed, built and commissioned for the experimental investigation.

4.1 Description of liquid-liquid horizontal flow sudden expansion rig facility

The experimental rig was designed to run two phase mixtures of oil and water both horizontally and with some inclinations. Provision is also made for three phase flow studies of air/oil/water in the future.

The rig is made up of a test section, separator tank, liquid storage tanks, and a control system. Figure 4.1 shows a schematic diagram of the liquid-liquid facility. The liquids supply tank farm is located outside of the L3 main laboratory building due to space and environmental safety reasons. Details of all equipment for the liquids supply including pump requirements and specifications are described in the following sections.

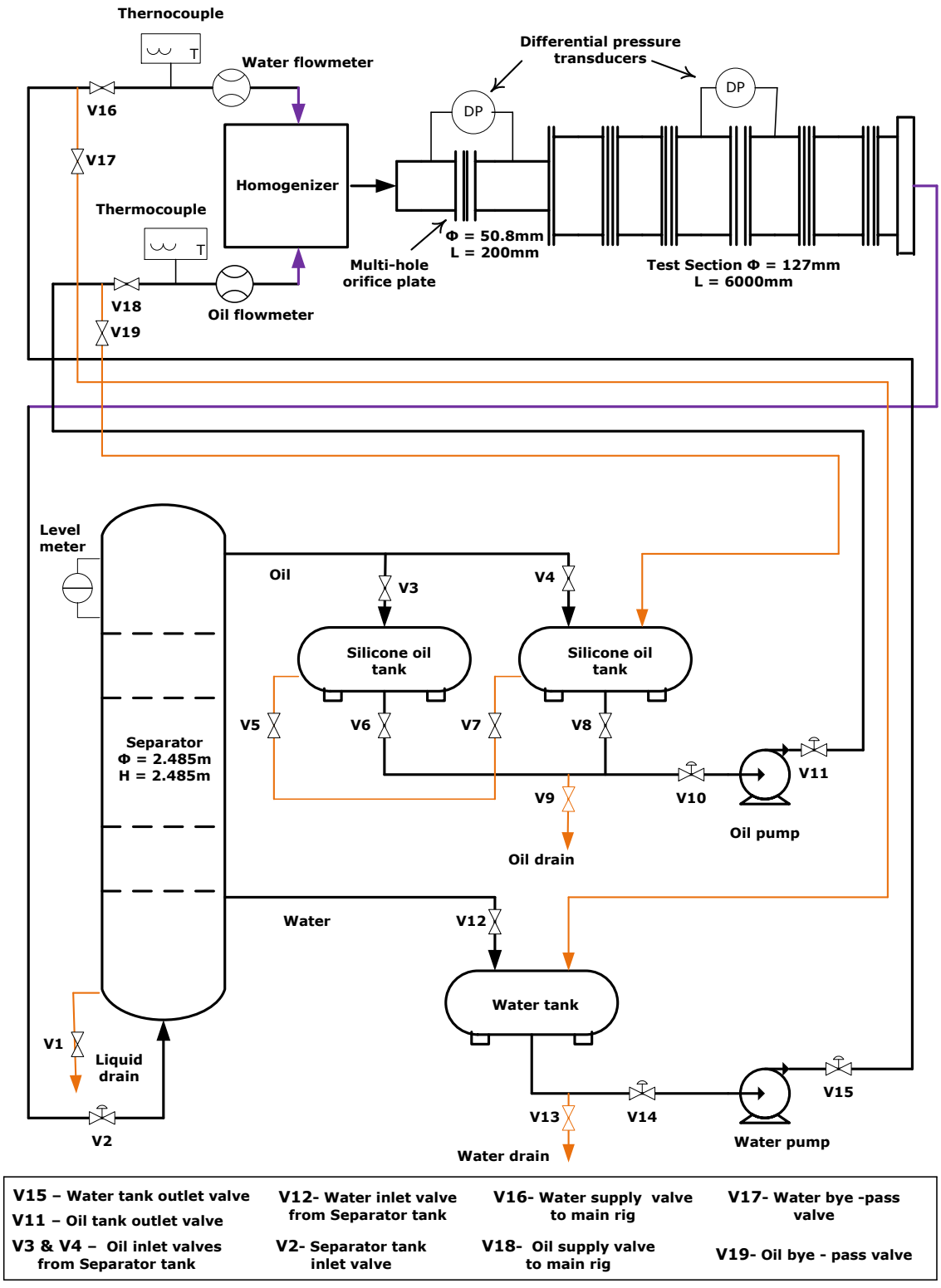

Figure 4-1 Schematic diagram of liquid-liquid flow sudden pipe expansion rig facility

4.1.1 Separator and fluids storage tanks

For an effective supply of fluids and the smooth running of the Liquid – Liquid flow facility a tank and separator system with auxiliary equipment is connected with external pipe work outside the L3 Laboratory building. A brief description of the tank farm includes the following:

a. Two stainless steel cylindrical tanks of which, one of them is for storage of water and the other for silicone oil. The water and silicone tanks have equal dimensions of diameters and lengths of ϕ 1.828 m x 1.854 m respectively. They both have equal capacities of 4.87 m^3 and were positioned horizontally in the tank farm, outside the Laboratory building. A total quantity of 7,600 litres of silicone oil and 9,423 litres of water are required to carry out the experiment successfully.

Figure 4-2 Liquid Storage Tanks and Separator vessel

b. A cylindrical stainless steel vessel for separation purposes of the two phase mixture of silicone oil and water placed in a vertical position. The separator vessel has dimensions of ϕ2.438 m x 2.438 m height, containing ϕ0.15 x 10 mm x 1 m long ‘’Knitmesh’’ coalescer cartridges, manufactured by Knitmesh

Ltd. These cartridges are filled with very fine fibre glass wool that acts as a coalescing medium for the tiny droplets of dispersed phase. About 30 pieces of these Knitmesh coalescers are arranged inside the separator tank and is sitting on a solid cylindrical block of ϕ2.238 x 0.6 m high. The oil flow outlet to the two (2) oil storage tanks is about 2m from the bottom of the separator vessel. It has a total capacity of 11.38 m^3.

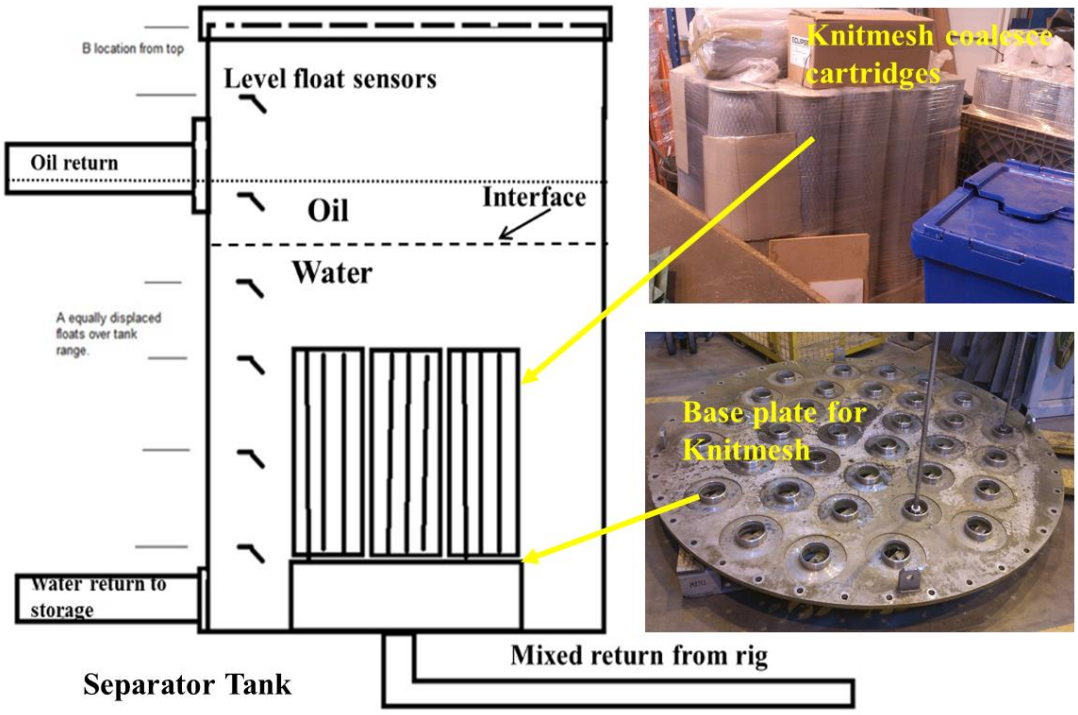

Figure 4-3 Internal arrangement of Separator tank

c. Two centrifugal pumps: An E-Line Dresser centrifugal pump, pressure pump division, , RPM: 2900, , for the Silicone Oil, with capacity 120m^3h^{-1} and total head 25.54 m and 2900 rpm. An Ingersoll–Dresser centrifugal pump, for the water, with capacity 36m^{-3}h and total head 42 m of water and 2900 rpm, manufactured by Worthington Simpson ltd.

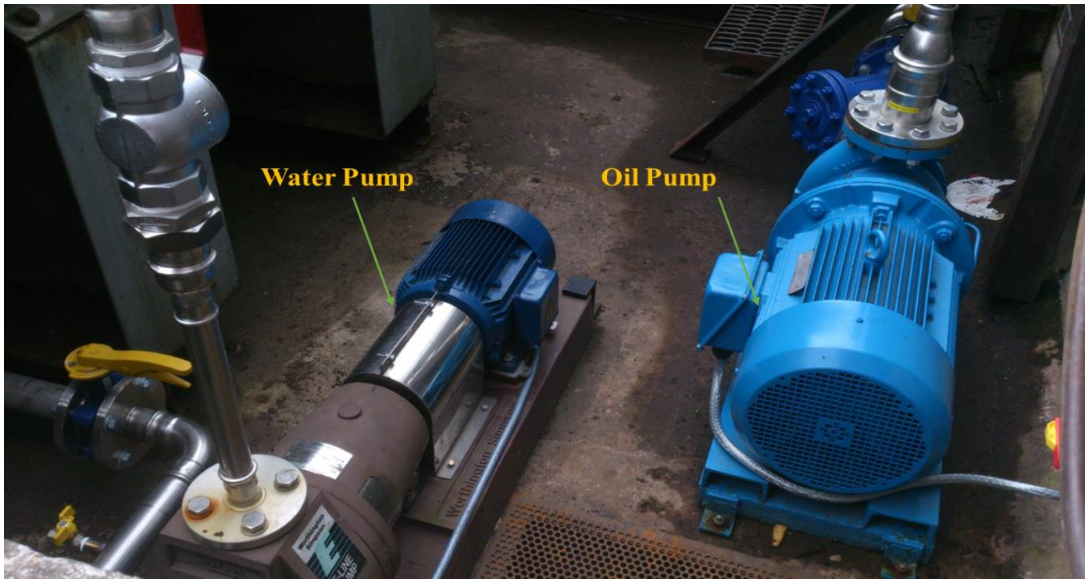

Figure 4-4 Two Centrifugal pumps for water and silicone oil

4.1.2 Control systems

A control system was designed and incorporated into the LabVIEW programme in order to monitor the liquid levels in the Separator tank, the two (2) oil storage tanks and water tanks respectively, located at the tank farm outside the L3 laboratory main building. Pressure transducers were calibrated and installed at the bottom part of each tank (see Figure 4.5). The pressure output signals in (bar), were then converted into voltage and current, which is fed into the routine LabVIEW programme to display the level of each tank. Figure 10 and 11, in Appendix F shows a diagram of the LabVIEW.

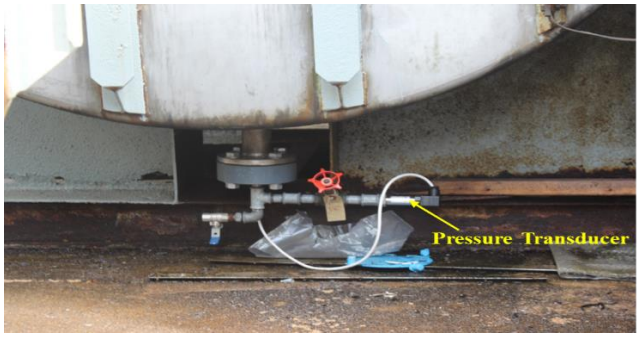

Figure 4-5 Pressure transducers installed at bottom of water storage tank for level sensing

Other major components of the control system include the two pump switches, oil and water flowmeters, two differential pressure cells adjustable butterfly valves, which are manually controlled by opening and closing to desired setting. Figure 4.6 shows a section of control valve system for the introduction of liquids into the test section. Before commencing any experiment, the system is allowed to run for at least 10mins residence time to stabilize fluid flow circulation and remove air trapped within the pipes.

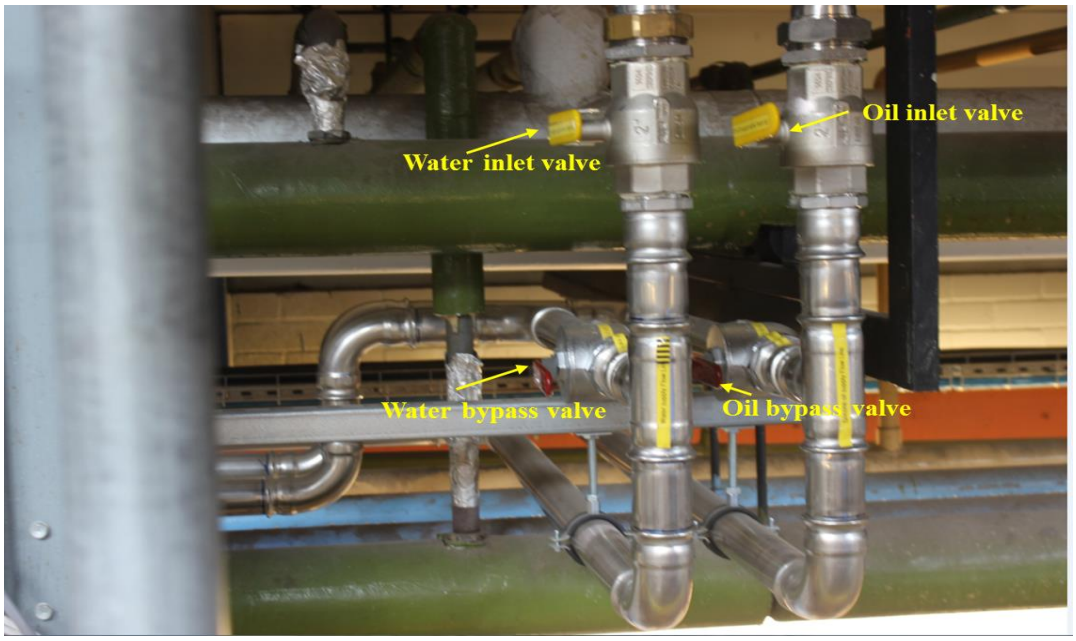

Figure 4-6 Control valves for fluids inlet

The oil and water inlets are connected to a specially designed static homogenizer with flexible hose, where the fluids are pre-mixed before the mixture flows into the test section. There is also another flexible hose connected at the end part of the test section for return of the mixture back to the horizontal gravity separator tank outside the building. The liquid levels in the tanks are checked regularly before and during the experiment to ensure the pumps are not run dry or the tanks overflowing. A detailed process risk assessment and operational procedure is given in Appendix G.

4.1.3 Fluids requirements

A total volume of 5.5 cubic meters of Silicone oil (5 cp) was used in the liquid-liquid Oil-Water horizontal sudden expansion rig in L3 Laboratory. 2,710 litres is required in the silicone oil storage supply tank and 2,790litres for the separator tank and in the rig pipeline test section. The total volume of water required is 4,870 litres in the storage tank. Appendix D gives details of flow rate calculations, pressure drop estimations along the pipeline, total head loss, actual power input and fluids requirement.

4.1.4 Test section

The test section consists of a sudden pipe expansion from an internal diameter of ϕ 50.8 mm x 2000 mm long to ϕ127 mm x 6000 mm long, at the outlet to be used for drop size and flow pattern measurement, see Figure 4.7. At the inlet of the test sections a specially designed static mixer is used to combine the phases and passed through a sudden expansion into the test section. A provision is made at a distance of 500mm from the sudden expansion for the introduction of a multi orifice plate. However, the orifice plate was not used in the current experiment because the homogenizer was sufficient to give the required mixing of the liquid phases. The entire test section was fabricated from transparent acrylic pipe to enable flow visualization and imaging.

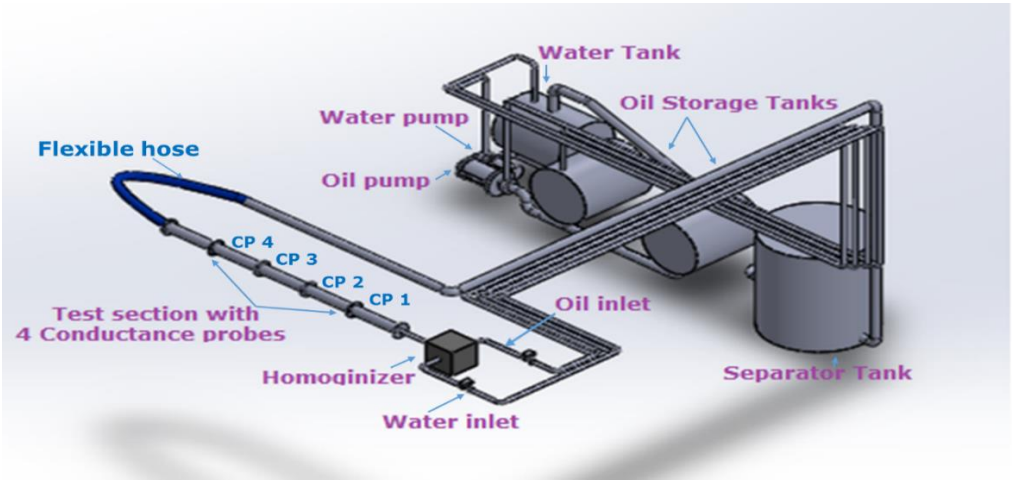

Figure 4-7 Large scale liquid-liquid rig facility model (Pipe diameter ϕ 127 mm)

Figure 4-8 Liquid – liquid horizontal flow pipeline sudden expansion rig in L3 Main Laboratory,

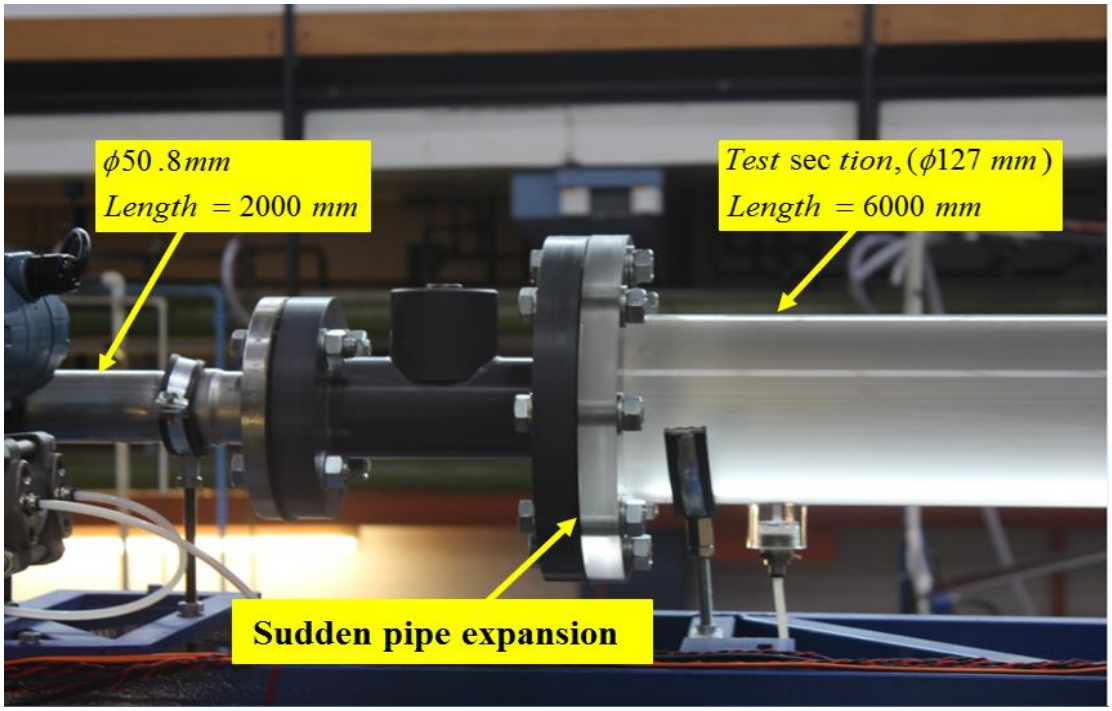

Figure 4-9 Cross- section of sudden pipe expansion

Two flow meters are to be used for flow rate measurements of the Silicone oil and water. An electromagnetic flow meter for water and Truflo paddle wheel flow meter for silicone oil, which can been seen both installed on the respective pipe flow lines in Figure 4.10

Figure 4-10 Photograph of both flow meters in place for flowrate measurements

Both water and silicone oil phases are introduced onto the static mixer block. This arrangement is chosen to ensure that any dispersion created was caused by the hydrodynamics of the flow rather than any mixing effects.

Figure 4-11 Specially fabricated homogenizer made of Perspex block with inner mixing chamber, connected with two pipes for oil and water dispersions.

4.1.5 Fluids properties

The fluids, Silicone oil and Water used for the large scale liquid-liquid rig are the same with that of the baffled stirred tank experiment in Chapter 3. Table 4.1 bellow presents a summary of the physical properties of the two fluids used.

Table 4-1 Physical properties of fluids (Silicone oil and Water) @ 21^0C

Fluid	***Tap Water***	***Silicone oil, 5cSt***
Density (kg/m3)	$\rho_w = 998$	$\rho_o = 916$
Viscosity μ (kg/m.s or	$\mu_w = 0.0010$	$\mu_o = 0.0052$
Refractive index	-	1.52045
Permittivity (α)	710×10^{-12}	23×10^{-12}
Relative permittivity	79	2.7

4.2 Experimental design

The evolution of droplet sizes distribution through a sudden pipe expansion is affected by the rig configuration and operational conditions. The factors related to rig configuration includes: pipe orientation, the expansion ratio (ratio of downstream to upstream pipe cross-sectional area) and the length of both upstream and downstream sections. For the purpose of stratification, an investigation of drop size downstream of the pipe expansion is to be made. El-Hamouz et al. (1995), did some work on drop size distribution measurement of oil-water dispersion using a Par-Tec M300 laser back-scatter instrument. (Yang, 2003, Hasan, 2006, Yusoff, 2012) has also done similar drop size measurements with different pipe diameters and orientations. The drop sizes expected to be seen at the expansion are those created in the mixing chambers from the homogenizer.

4.2.1 Determination of inlet parameters

Two crucial factors have been identified for the operational conditions, which are input oil fraction and mixture velocity. Therefore, experiments were designed to distribute the dispersed regimes in the inlet of test section and expected stratified flow

with mixing at the interface after expansion. In order to validate, build confidence and consolidate on work previously done by (Yusoff, 2012) and to enable comparison with other published research work on the subject area; all the downstream experiments are designed to distribute in the stratified (ST) and stratified with mixed (ST & MI) regimes. Therefore flow patterns are expected to be classified according to (Trallero et al., 1997). The flow patterns starts from upstream superficial mixture velocity (Usmu) and ends at a corresponding downstream superficial mixture velocity (Usmd) in the expansion test section.

The superficial velocity of a phase is its volumetric flow rate per unit of cross-sectional area of the pipe. For oil-water flow in pipe with cross-section area A, if Q_o and Q_w are the input volumetric flowrates of oil and water respectively, then the input parameters can be defined as follows:

$$Q_{mix} = Q_o + Q_w \tag{4.1}$$

$$U_{mix} = U_{so} + U_{sw} \tag{4.2}$$

$$U_{ws} = \frac{Q_w}{A} = \frac{A_w U_w}{A} \tag{4.3}$$

$$U_{os} = \frac{Q_o}{A} = \frac{A_o U_o}{A} \tag{4.4}$$

Where, U_{mix} is mixture velocity. The input water volumetric fraction or **water cut, W_c** and input oil fraction, O_c is given by

$$W_c = \frac{Q_w}{Q_m} = \frac{Q_w}{Q_w + Q_o} \tag{4.5}$$

$$O_c = \frac{Q_o}{Q_m} = \frac{Q_o}{Q_m + Q_o} \tag{4.6}$$

The fraction of cross-sectional area occupied by the water and that occupied by oil are called average water in-situ volume fraction, ε_w and average oil in-situ volume fraction, ε_o. This in-situ parameters are defined as follows:

$$\varepsilon_w = \frac{A_w}{A} \qquad \varepsilon_o = \frac{A_o}{A} \qquad 4.7$$

$$U_w = \frac{Q_w}{A_w} \qquad U_o = \frac{Q_o}{A_o} \qquad 4.8$$

From equations 4.1 to 4.8, the following relationship can be established:

$$U_w = \frac{U_{ws}}{\varepsilon_w} \qquad U_o = \frac{U_{os}}{\varepsilon_o} \qquad 4.9$$

The input volume fractions are different from the average in-situ volume fractions and therefore the resultant average in-situ velocities of the two phases may also be different. The slip velocity or slip ratio can therefore be defined as:

$$S = U_R = \frac{U_o}{U_w} \qquad 4.10$$

4.2.2 Test matrix

The experiments for oil-water flow were conducted on the simultaneous flow of the two liquids by keeping the total mixture superficial liquid velocity constant (i.e. oil superficial velocity + water superficial velocity = constant) (Equation 4.2). Invariably, the mixture flowrate is kept constant (Equation 4.1). Whenever the input **water cut,** W_c changes, the total mixture's liquid superficial velocity or the mixture flowrate will be adjusted to keep it fixed in the system. The input water cut W_c were changed in steps from 20%, 30%, 40%, 50%, 60%, 70%, 80%. Different values of mixture superficial liquid velocities (U_{mix}), of 0.20, 0.25, 0.30, 0.35, 0.50, 1.00, 1.50, 2.00, 2.50, 3.00, 3.50 ms^{-1} were tested. At each flow rate the water cut varied from 20 - 80%.

Measurements of average water and oil fractions (in-situ fractions) for each test point of oil-water two-phase flows experiment were determined by using conductance probes. The measurement were made at four (4) axial distances downstream the expansion of 10D, 20D, 30D and 40D, where D is the internal diameter of the pipe (127 mm) and a test section of 6m long. Experiments were carried out in different orientation, (i.e. horizontal and inclined angles), of the rig with the same conditions

mentioned above. The summary of the experimental conditions is given in Table 4.2. The experiments are designed to encounter as many flow patterns as possible together with interfacial shapes and wave's evolution within the flow development from dispersed to stratified flow through the sudden pipe expansion. Figure 4.12 is a flow pattern map showing the flow patterns encountered and experimental limits within the rig in the current work.

Table 4-2 Experimental conditions

a. Mixture velocity upstream, U_{mix} (m/s)

Mixture velocity, Umu (m/s)	Water cut	Oil Flowmeter (m3/hr)	Water Flowmeter (m3/hr)	Angle of rig orientation
0.2	0.2	1.2	0.3	+4°, +2°, 0°, -2°, -4°
	0.3	1.05	0.45	
	0.4	0.9	0.6	
	0.5	0.75	0.75	
	0.6	0.6	0.9	
	0.7	0.45	1.05	
	0.8	0.3	1.2	
0.25	0.2	1.44	0.36	
	0.3	1.26	0.54	
	0.4	1.08	0.72	
	0.5	0.9	0.9	
	0.6	0.72	1.08	
	0.7	0.54	1.26	
	0.8	0.36	1.44	
0.3	0.2	1.76	0.44	
	0.3	1.54	0.66	
	0.4	1.32	0.88	
	0.5	1.1	1.1	
	0.6	0.88	1.32	
	0.7	0.66	1.54	
	0.8	0.44	1.76	
0.35	0.2	2.08	0.52	
	0.3	1.82	0.78	
	0.4	1.56	1.04	
	0.5	1.3	1.3	
	0.6	1.04	1.56	
	0.7	0.78	1.82	
	0.8	0.52	2.08	

Table 4.2 Experimental conditions (cont'd)

b. Mixture velocity middle, U_{mm} (m/s)

Mixture velocity, Umm (m/s)	Water cut	Oil Flowmeter (m3/hr)	Water Flowmeter (m3/hr)	Angle of rig orientation
0.5	0.2	2.96	0.74	+4°, +2°, 0°, -2°, -4°
	0.3	2.59	1.11	
	0.4	2.22	1.48	
	0.5	1.85	1.85	
	0.6	1.48	2.22	
	0.7	1.11	2.59	
	0.8	0.74	2.96	
1	0.2	5.84	1.46	
	0.3	5.11	2.19	
	0.4	4.38	2.92	
	0.5	3.65	3.65	
	0.6	2.92	4.38	
	0.7	2.19	5.11	
	0.8	1.46	5.84	
1.5	0.2	8.8	2.2	
	0.3	7.7	3.3	
	0.4	6.6	4.4	
	0.5	5.5	5.5	
	0.6	4.4	6.6	
	0.7	3.3	7.7	
	0.8	2.2	8.8	

c. Mixture velocity Downstream, U_{md} (m/s)

Mixture velocity, Umd (m/s)	Water cut	Oil Flowmeter (m3/hr)	Water Flowmeter (m3/hr)	Angle of rig orientation
2	0.2	11.68	2.92	+4°, +2°, 0°, -2°, -4°
	0.3	10.22	4.38	
	0.4	8.76	5.84	
	0.5	7.3	7.3	
	0.6	5.84	8.76	
	0.7	4.38	10.22	
	0.8	2.92	11.68	
2.5	0.2	14.64	3.66	
	0.3	12.81	5.49	
	0.4	10.98	7.32	
	0.5	9.15	9.15	
	0.6	7.32	10.98	
	0.7	5.49	12.81	
	0.8	3.66	14.64	
3	0.2	17.52	4.38	
	0.3	15.33	6.57	
	0.4	13.14	8.76	
	0.5	10.95	10.95	
	0.6	8.76	13.14	
	0.7	6.57	15.33	
	0.8	4.38	17.52	
3.5	0.2	20.48	5.12	
	0.3	17.92	7.68	
	0.4	15.36	10.24	
	0.5	12.8	12.8	
	0.6	10.24	15.36	
	0.7	7.68	17.92	
	0.8	5.12	20.48	

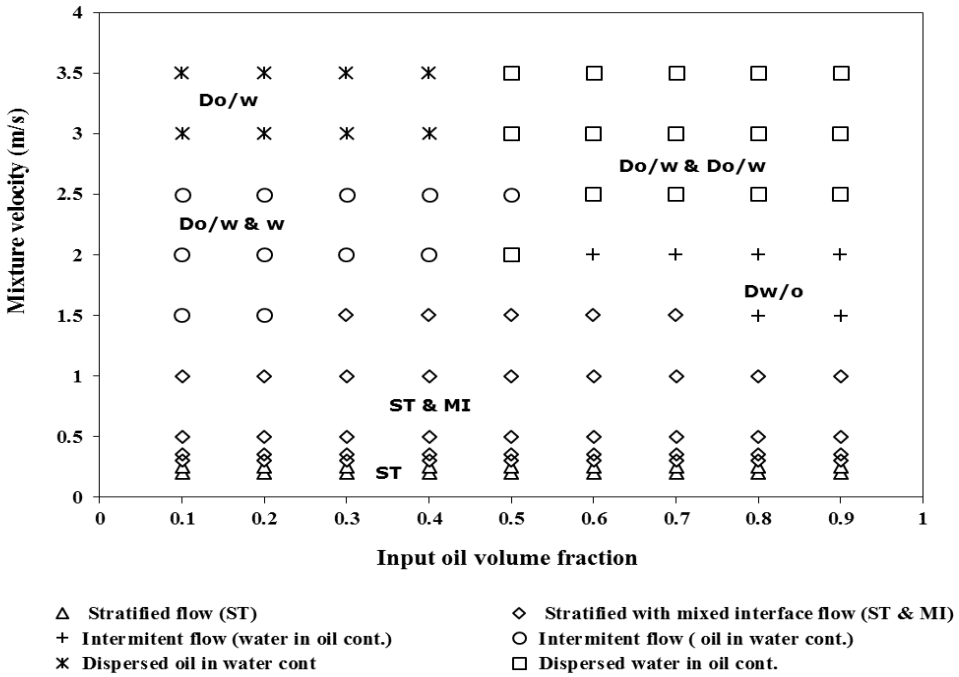

Figure 4-12 Experimental flow pattern map of current work. $D = 127mm$, $\mu_o/\mu_w = 5.2$, $\rho_o/\rho_w = 0.918$

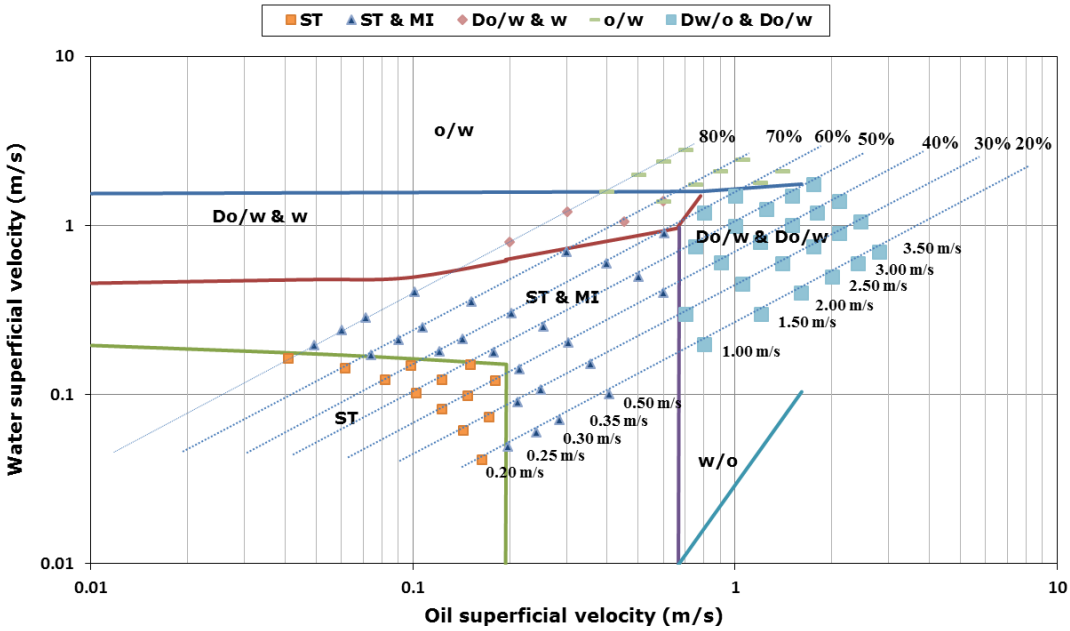

Figure 4-13 Possible operational limits and flow patterns to be encountered within the rig in current study, plotted in the flow pattern map of Trallero et al. (1997).

The flow conditions are also plotted on the flow pattern map of (Trallero et al., 1997) in Figure 4.13. For the same experimental conditions, drop size measurements and video recordings were made simultaneously at each position with the FBRM M500P Laser and Phantom high speed camera respectively. Data collection procedures for the various instruments are further explained in section 4.3.

4.3 Instrumentation

4.3.1 Lasentec FBRM M500P Laser and drop size measurement

Measurements of drop size were made downstream of the sudden expansion horizontal test section. Specific removable measurement test section for the instrumentation were designed and fabricated from clear acrylic resin or PVC. The total length of the test section is 6000mm.

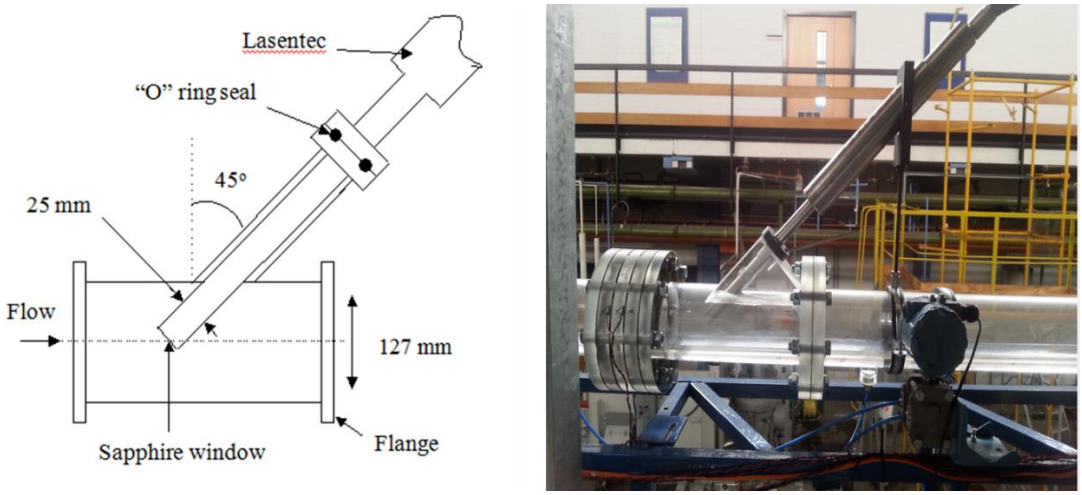

Figure 4-14 Photograph of the removable measurement section with position for FBRM M500P laser instrumentation.

The instruments for the measurement are organized and inserted in a way that there was no interference. Adjustable openings are made at interval distances of 10D, 20D, 30D and 40D for the installation of Conductance probe, Lasentec FBRM M500P Laser and High speed camera for data collection. The test section is mounted horizontally on steel frames across three vertically positioned rigs, inside L3 main Laboratory. This

arrangement justifies the removable measurement section design. Parameters such as drop size are measured using the Lasentec FBRM M500P laser. The probe is mounted at 45^0 to the pipe against the flow direction as shown in Figure 4.14. This arrangement minimizes eddies, droplet breakage at measurement point and allow the probe to scan and detect particles streaming past the sapphire window. Flow disturbance were only noticed after measurements are made.

The FBRM M500P laser positions, at a particular measurement point were also adjustable. This allows drop size measurements to be taken at the top, oil/water interface and bottom layers of the pipe (see Figure 4.15). A continuous measurement was logged by a computer and allowed the propriety software to produce chord length distributions as shown in Figure 4.16. The data collected from the computer are transferred into excel file format for further statistical processing and analysis.

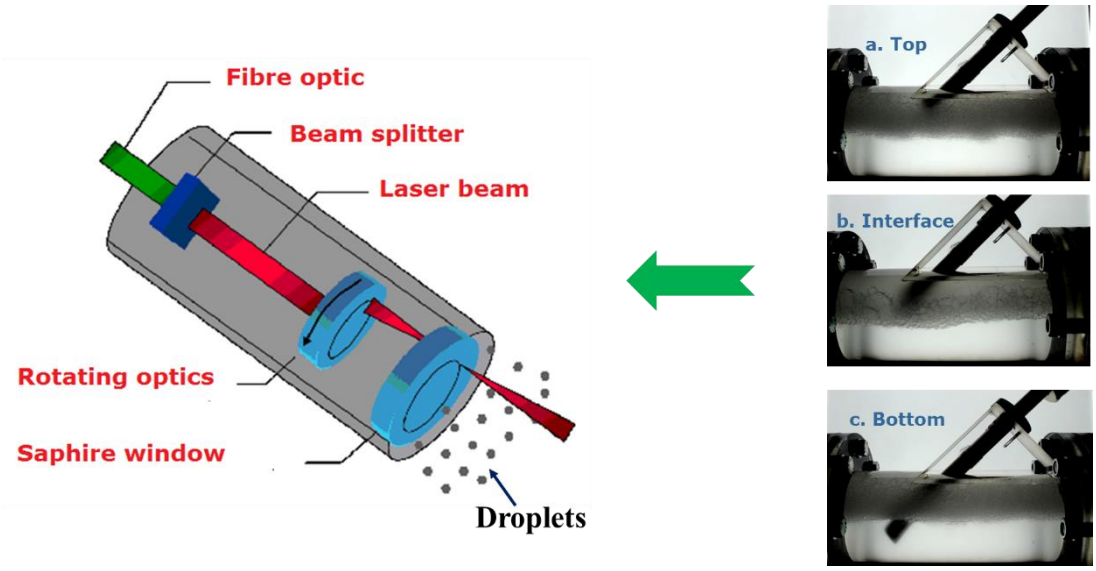

Figure 4-15 FBRM M500P laser measurements at top, interface and bottom of pipe

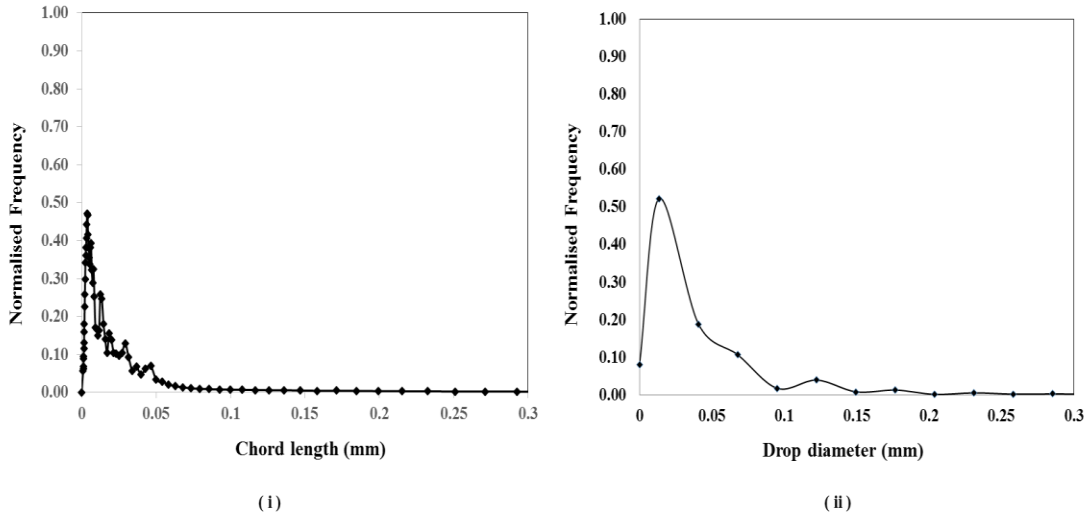

Figure 4-16 FBRM M500P laser measurements (i) Chord length distribution, (CLD) (ii) Drop diameter distribution (DDD)

4.3.2 Differential pressure transducers

Two differential pressure cells (DP cell) with liquid purging system was used. The pressure drop upstream at the inlet section before the expansion and downstream at the test section was measured by the two electronic pressure transducers which are calibrated to convert the current generated in (m A) directly into pressure drop in (bar). Figure 4.17 shows a photograph of the differential pressure transducers for the rig. They are both same model, ROSEMOUNT 1151 Smart series with a range of 0 to 1bar for the inlet and 0 to 0.375bar for the test sections respectively. Figure 4.18 shows the calibration curves for the two DP Cells, which were determined using standard pressure gauge.

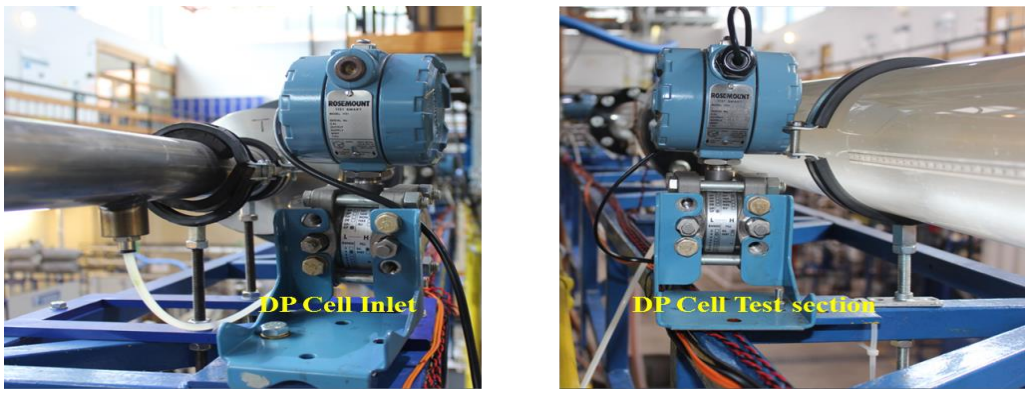

Figure 4-17 Photograph of Differential pressure transducers installed on the rig.

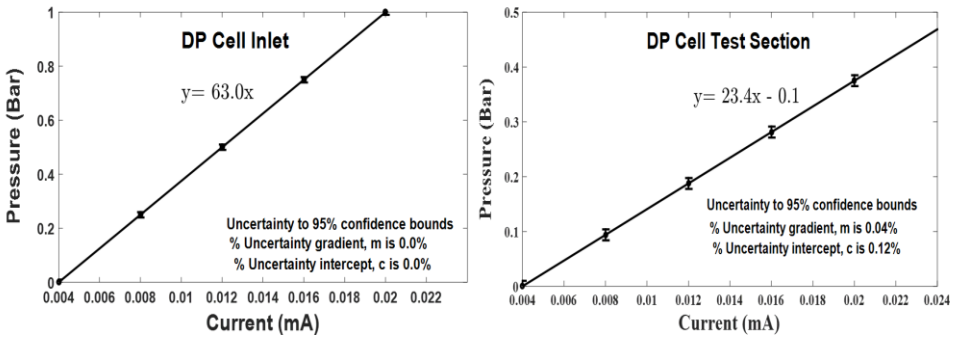

Figure 4-18 Calibration results of the differential pressure cells.

4.3.3 Flowrate meters

The water flowrate is measured by an electromagnetic flowmeter (EMF). Measurement is based on Faraday's law of induction, according to which a voltage is induced in an electrically conductive body, which passes through a magnetic field.

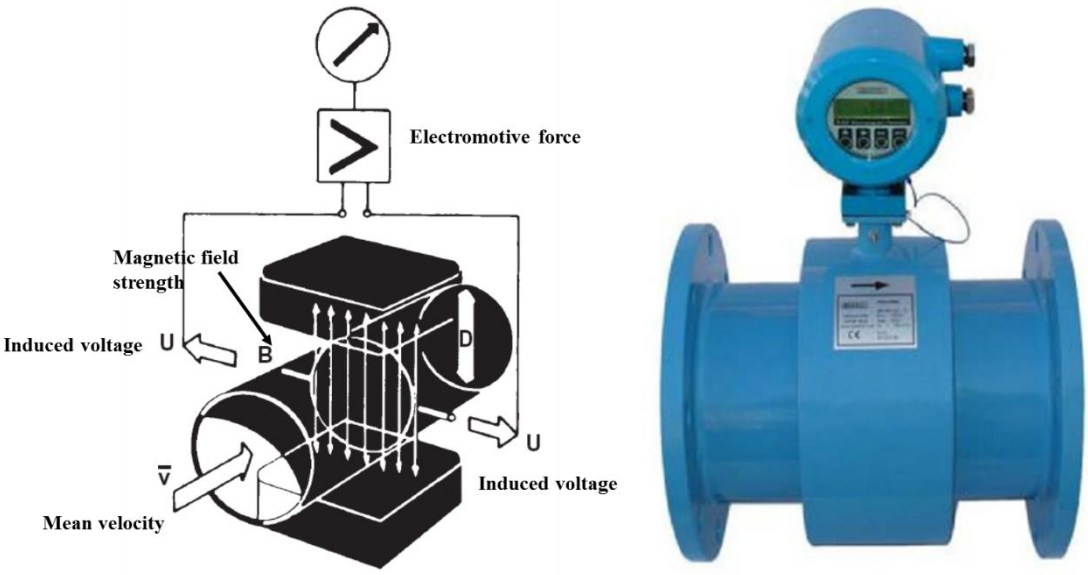

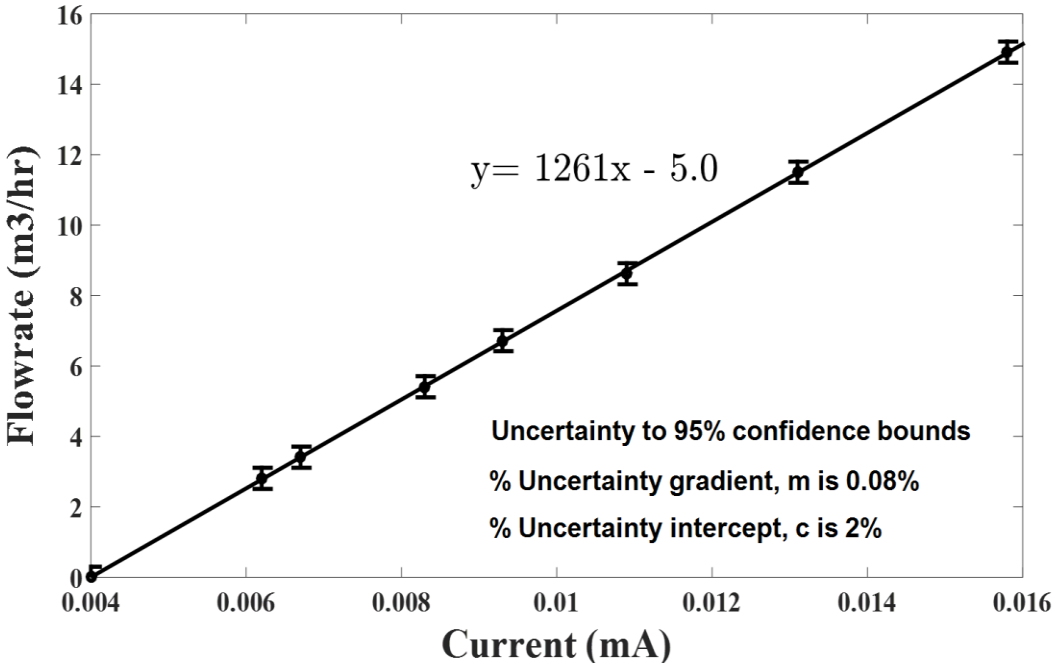

Figure 4-19 Electromagnetic flowmeter (M920)

The following expression is applicable to the voltage:

$$U = K \times B \times v \times D \qquad 4.11$$

Where, K is an instrument constant and D is the pipe diameter. Thus the induced voltage is proportional to the mean flow velocity, when the field strength is constant. Inside the electromagnetic flowmeter, the fluid passes through a magnetic field applied perpendicular to the direction of flow. An electric voltage is induced by the movement of the fluid (which must have a minimum electrical conductivity). This is proportional to the mean flow velocity and thus to the volume of flow. The induced voltage signal is picked up by two electrodes, which are in conductive contact with the fluid and transmitted to a signal converter for a standardized output signal. The flowmeter is manufactured by Maetest, model type M920 with serial number 352411 and has a range between 0 – 88.4 m^3hr^{-1}, max velocity of 12 m/sec) H_2O. The accuracy is +/- 0.25% of reading. It has analogue output current signal of 4 – 20 mA. The flowmeter was calibrated online in the rig and the analogue current signal was converted into flowrate. The resultant straight line equation from the calibration curve (see Figure 4.15) was fed into the LabVIEW programme.

A Paddle wheel flow sensor with local display, model TKM-50-RS-PVC was used to measure the flowrate of oil. The maximum flow velocity range is 0.3 – 10 ms^{-1} (0 – 1500 $lmin^{-1}$), liquid viscosity up to a maximum of 20cps. It has an accuracy of ± 1% of FS and analogue current output signal of 4 – 20 mA. The truflo oil flowmeter has the advantage of adjusting the flow range to desired setting and can also be used for water and other fluids. Paddle wheel flow meters consist of three primary components: the paddle wheel sensor, the pipe fitting and the display/controller. The paddle wheel sensor consists of a freely rotating wheel/impeller with embedded magnets which is perpendicular to the flow and will rotate when inserted in the flowing medium. As the magnets in the blades spin past the sensor, the paddle wheel meter generates a frequency and voltage signal which is proportional to the flow rate. The faster the flow the higher the frequency and the voltage output Flow displays and controllers are used to receive the signal from the paddle wheel meter and convert it into actual flow rate or total flow values. Figure 4.16 shows a photograph of the truflo meter and results of the online calibration curves on the rig. The straight line equation was inputted into the main LabVIEW programme for oil flowrate measurements.

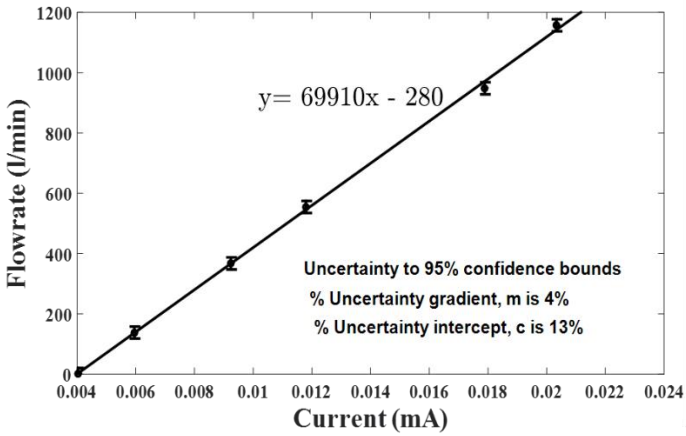

Figure 4-20 Paddle wheel truflo meter (TKM-50-RS-PVC)

4.3.4 Conductance probe

The conductance ring probe technique was chosen to measure liquid holdup fractions because water is an electrical conductor, while oil is essentially resistive or a very poor

conductor of electricity. In this technique, a cross-sectional averaged liquid holdup fraction can be estimated once the relationship between the electrical impedance and the phase distribution has been established. (Andreussi et al., 1988) and(Tsochatzidis et al., 1992) are some of the researchers to have used this method successfully.

Ring-type probes were manufactured in the laboratory. Four (4) acrylic plates and two (2) chromium plated brass with holes on them were stacked alternatively. Careful attention was paid to ensure that the plates were flushed properly on the circumference in the middle holes as part of the flow channel.

4.3.4.1 Design and principles of conductance ring probes

Potential field theory is the basis for flush mounted probes immersed in a two-phase mixture. When electrolytes are subject to alternating current excitation, their electrical behaviour is resistive provided the frequency of the applied signal is high enough. The electrical fields of regions with small dimensions when compared to the wavelength of the electric field can be modelled as time invariant. This problem is described by a Laplace equation and the electric potential with the proper boundary conditions is expressed as follows:

$$\nabla^2 V = 0 \qquad 4.12$$

where V represents electric potential. This expression can be solved analytically or numerically depending on the geometrical configuration of the probe and type of Interface. In the case of ring conductance probe, a mathematical expression can be presented for the conductance between two electrodes and separated by a distance De as follows.

$$Ge = \frac{\gamma A}{De} H_L \qquad 4.13$$

$$Ge^* = \frac{Ge}{\gamma L} \qquad 4.14$$

where Ge is actual conductance in 1/Ω, γ is electrical conductivity in 1/Ωm, and L is the length of electrode in m. (Andreussi et al., 1988) ascertained the applicability of

the correlation for the plate electrodes, which was provided by (Coney, 1973), to ring pair probes:

$$Ge^{*} = \frac{k(m)}{k(1-m)} \qquad 4.15$$

$$k(m) = \int_{0}^{\pi/2} \left(1 - mSin^{2}\theta\right)^{-1/2} d\theta \qquad 4.16$$

Where m,

$$m = \frac{Sinh^{2}\left(\frac{\pi s}{2h}\right)}{Sinh^{2}\left(\frac{\pi(s+De)}{2h}\right)} \qquad 4.17$$

De represents the spacing of the electrodes, s is the width and *k* is the complete elliptic integral of the first kind given by

If in Equation 4.14 the length L is replaced by the wetted length of a liquid layer in stratified configurations for ring electrodes, then the equivalent liquid layer thickness, h_L is given as:

$$h_{L} = \frac{AH_{L}}{P_{w}} \qquad 4.18$$

Where A is the cross sectional area of the pipe, H_L is the fraction occupied by the liquid phase and $P_{w,}$ is the perimeter.

The electronic box for the conductance probes employed is similar to that used by previous researchers, particularly (Fossa, 1998) but slightly modified for better output signal. Figure 4.21 illustrates the old electronic circuit for the probe. Figure 4.22 shows a modification of the rectifier section where the ac signal is rectified before any differencing takes place. Four (4) circuits corresponding to each of the probes were used. Each of the conductance probes occupy a branch of the Wheastone bridge.

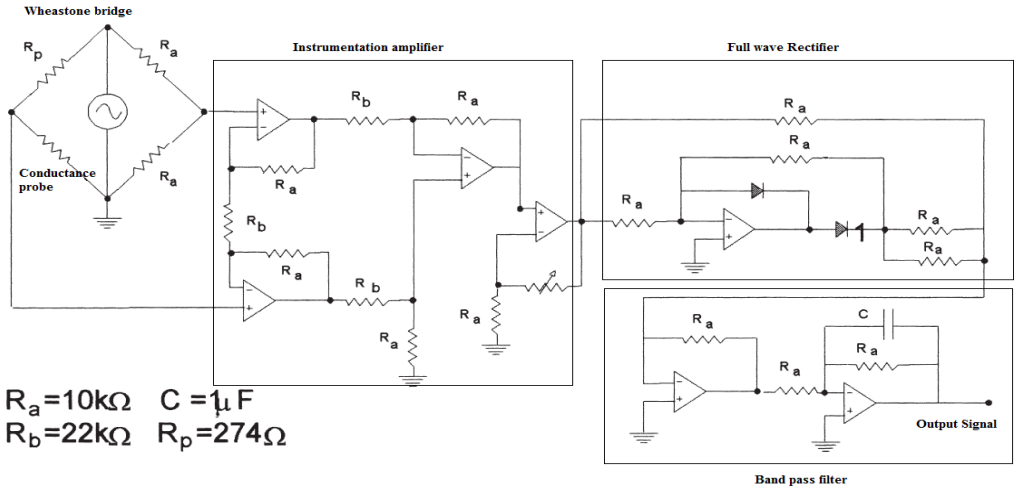

Figure 4-21 Original conductance probe electronics diagram (Fossa, 1998)

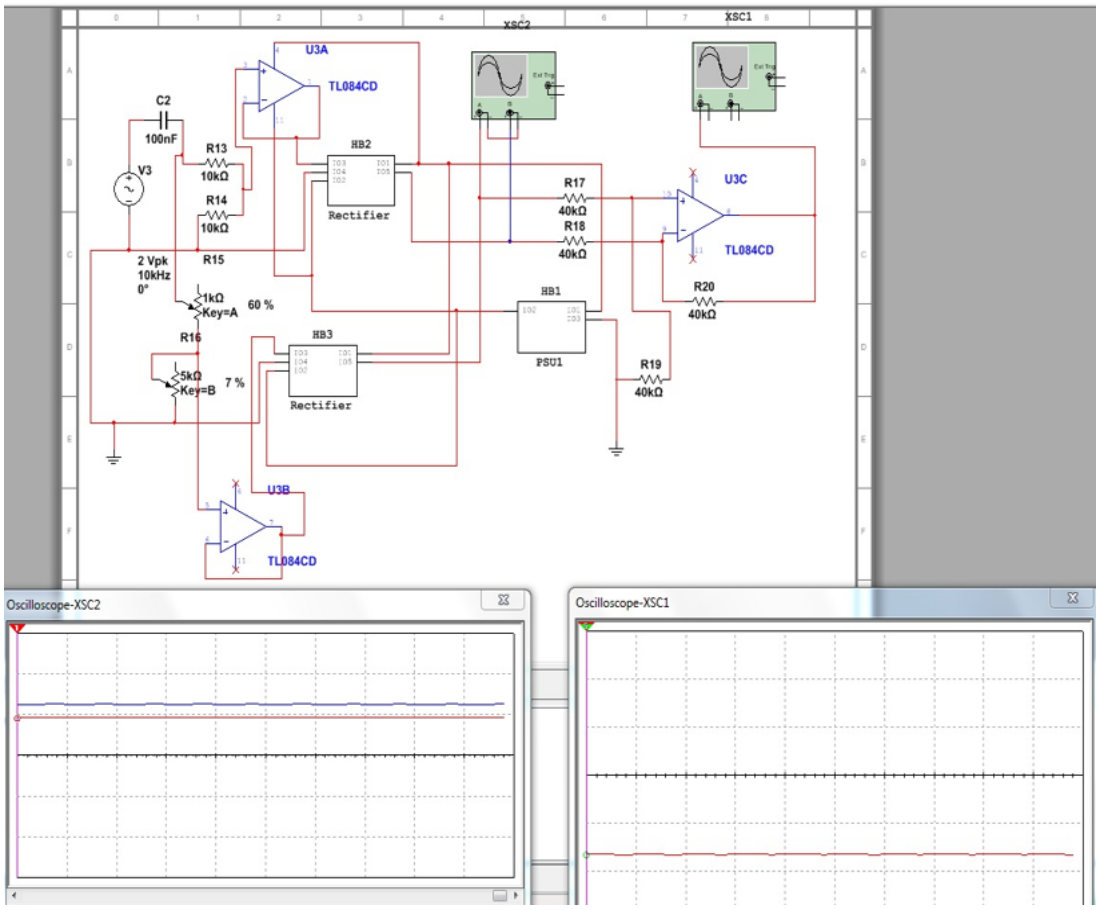

Figure 4-22 Schematic diagram of modified electrical circuit of conductance probes.

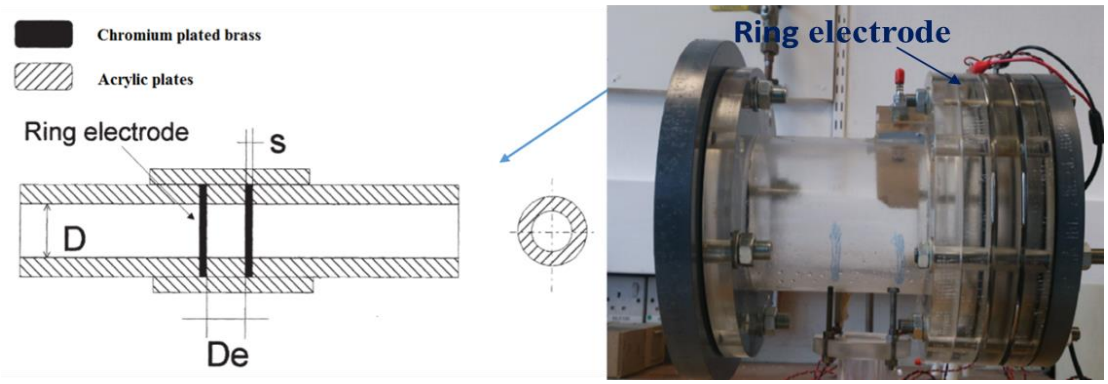

Figure 4-23 Electrode arrangement in the cylindrical test section pipe (ϕ127mm)

The probe assembly is made up of four (4) acrylic plates and two (2) chromium plated brass with same diameter plates (ϕ127mm), as the test section. The probe aspect ratio *De*/D is 0.34 and the width s is 2mm.

The signal passes through an instrumentation amplifier, a full wave rectifier and a band pass filter arrangement installed before it is finally sent to the data acquisition board. The instrumentation amplifier arrangement gives a high dynamic response and a perfect decoupling of the electronic circuit from the measuring bridge. A cut-off frequency 100 Hz was applied to eliminate the high frequency noise generated from power supply. The reference resistance R_{ef} was determined depending on the impedance from the probe as explained in the calibration procedure in section 4.3.4.2.

4.3.4.2 Calibration and validation of conductance probes

The aim of the calibration is to determine a mathematical relationship between accurately known phase fractions (liquid-liquid holdup) and dimensionless conductance to be inputted in the LabVIEW program for data acquisition. The calibration process was done in two stages, namely offline and online. This was necessary for the accurate estimation of liquid holdup of the conductance probes, while been in installed online in the test section.

Before running the offline experiment, the reference resistance R_{ref}, as shown in Figure 4.24 was determined depending on the impedance from the variable resistor probe, R_x. The conductance probe response depends on the cross sectional phase distribution, liquid fraction, liquid conductivity and physical properties. A precision variable resistor, Rx ranging from 1 KHz to 5 KHz was employed between the probe electrodes in the Wheatstone. The probe assembly has a total volume of 1160 litres. Instantaneous liquid fractions were artificially created over the conductance probe by introducing 100% water initially and the corresponding voltage and frequency noted. This process was done continuously until the calibration section was filled with 100% oil and no water.

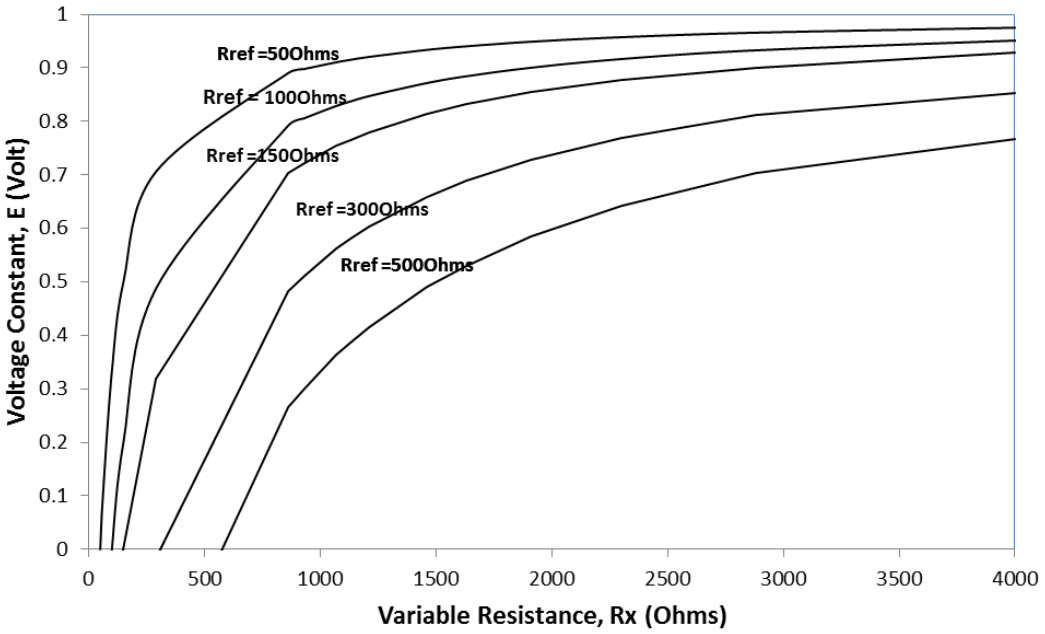

Figure 4-24 Relationship between voltage constant E, and variable resistance R_x and reference resistance R_{ref}

From the graph in Figure 4.24, it shows that for typical responses for liquid-liquid, silicone – oil/water mixture in a 127 mm diameter tube, an R_{ref} of 50 Ohms and R_x above 100 Ohms gives good precision and a wide range of values of the output Voltages. R_{ref} needs to be set higher in smaller diameter pipes since the impedance becomes higher when full of water. The variable known resistance is replaced by a range of various liquid fractions of silicone oil/water in the calibration test section and the voltage output, Vout, is measured. The dimensionless conductance, Ge* is

determined from the voltage response, Vout (as detailed in Appendix E) and correlated with the corresponding liquid fractions. A third order polynomial fit of the form:

$$OVF = a(Ge^*)^3 + b(Ge^*)^2 + c(Ge^*) + d \qquad 4.19$$

is applied to obtain a unique calibration curve for each probe (Figure 4.25).

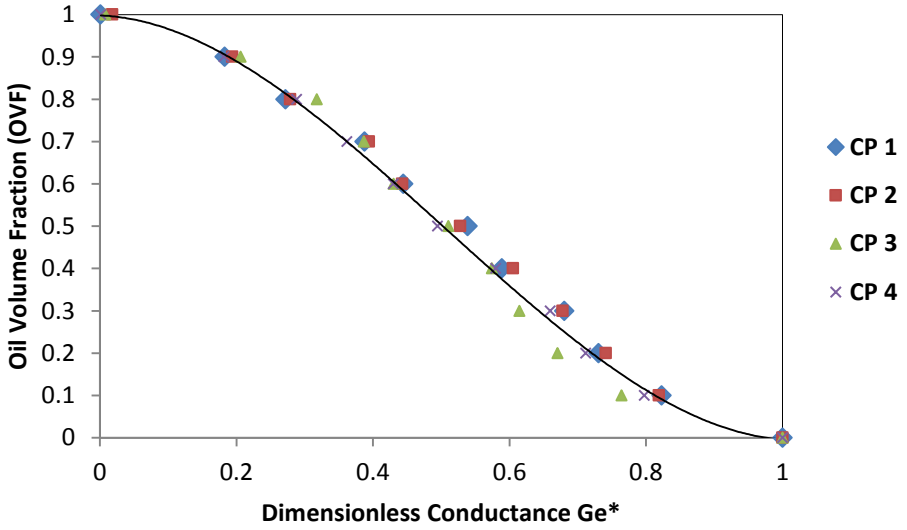

Figure 4-25 Calibration curve of oil volume fraction (OVF), vs dimensionless conductance Ge* for individual probes (CP 1, CP2, CP3, CP4 – conductance probe positions)

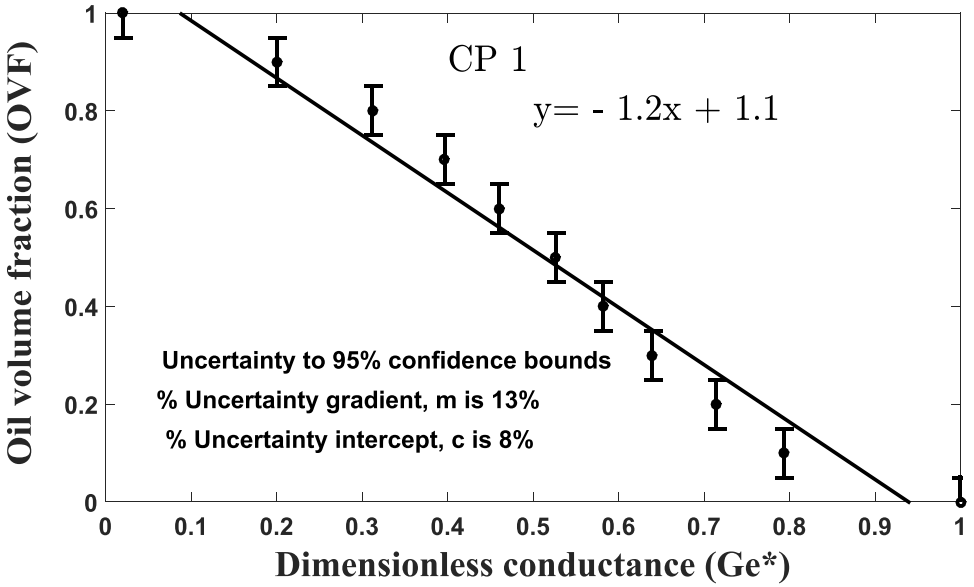

Figure 4-26 Calibration uncertainty for curve, CP 1 of oil volume fraction (OVF), vs dimensionless conductance Ge*

The calibration procedure is discussed further in Appendix E. Each of the conductance ring probes mounted on the 6m long test section of the rig is individually calibrated to obtain a 3rd order polynomial for the respective probe positions. The calibration uncertainties were estimated as shown in Figure 4.26 and the values for each probe was found to be (±13%), (±14%), (±14%) and (±13%) for CP 1, CP 2, CP 3 and CP 4 respectively. The resultant 3rd order polynomial equations are then inputted into the Main LabVIEW programme for data acquisition.

4.3.4.3 Measurement protocol

Measurements from the probes are acquired using a dedicated PC connected with a National Instrument, NI CompactDAQ 8-Slot USB Chassis (NI Cdaq-9178). All the NI module accessories for measuring flow parameters and analogue input are connected to the USB Chassis. These include NI USB-9211 for thermocouples, NI 9203 for differential pressure transducers, oil and water flowmeters, and NI 9205 32-Ch+-200 mV to +-10 V analogue input module for the four(4) various conductance probes. The data acquisition system is shown in Figure 4.27.

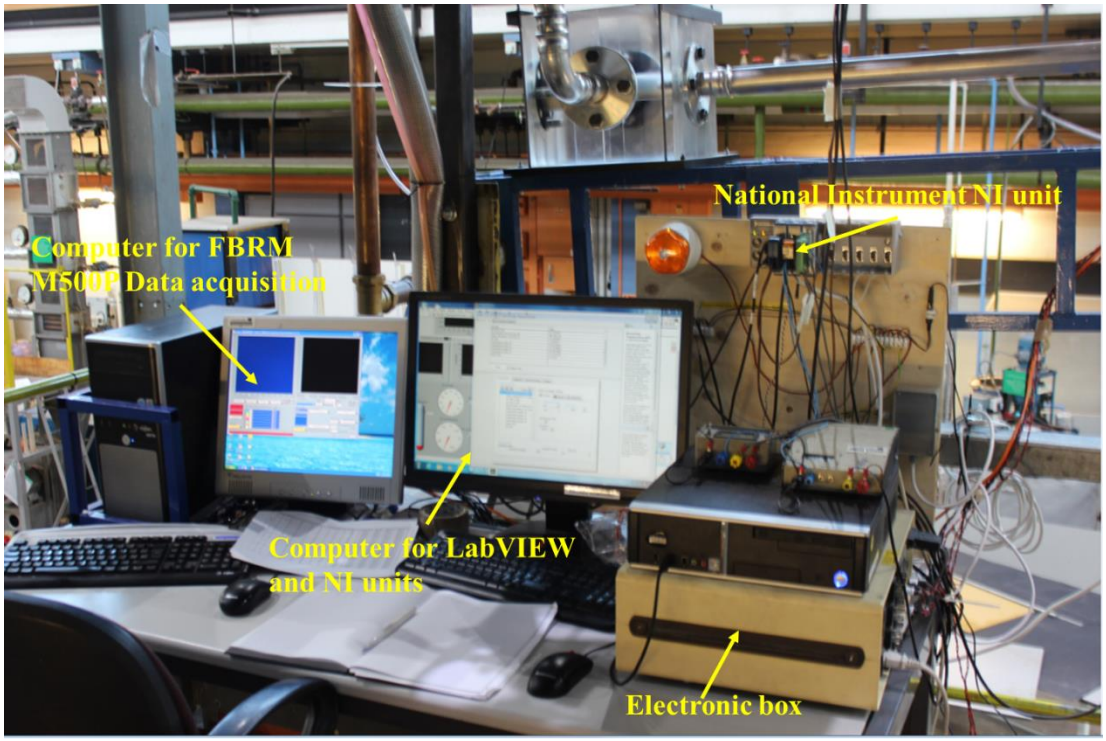

Figure 4-27 Data acquisition system

4.3.4.4 Data acquisition system and normalization with conductance ring probe

A LabVIEW program was written to convert all voltage and current output signals to the respective flow parameters measured. For instance the voltage output signals from the four (4) conductance probes are converted into liquid holdup. Sampling rate of 1 kHz and a frequency of 1 kHz was used with data taken for 2mins. The sub-routines, which is a graphical representation of the calibration equations for the various flow parameters and front panel are shown in Appendix E. All the analogue measurement instruments and equipment for flow parameters including, thermocouples, DP Cell, flowmeters, conductance probes, fluids storage tanks and separator are incorporated in the LabVIEW program. The results therefore contains a display of all the parameters (16 columns) in tdms file format and later converted to xls files for further analysis.

Figure 4.28 shows oil volume fraction time series graphs of the conductance probe measurements at 20%, 50% and 80% water cut, mixture velocity of 0.35 ms^{-1} and horizontal flow for the four (4) different probe positions, i.e. CP 1 (10D), CP 2 (20D), CP 3 (30D), and CP 4 (40D) respectively.

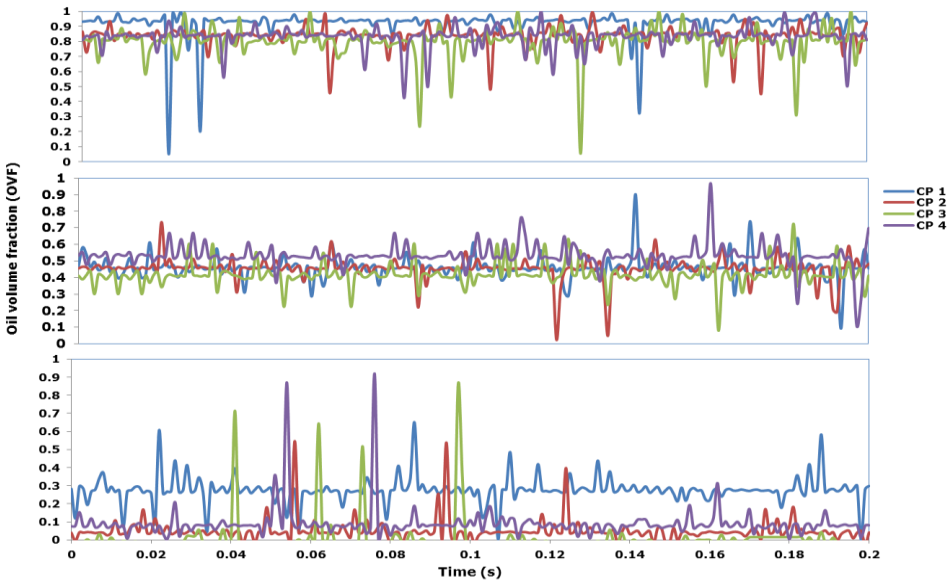

Figure 4-28 An example of conductance probe measurements (oil volume fraction time series plot for water cut 20%, 50% and 80%, mixture velocity 0.35m/s and horizontal flow at the different probe positions)

4.3.4.5 Determination of oil volume fraction (OVF)

Oil volume fractions were determined using the conductance probes measurement technique described in section 4.3.4.4. The oil volume fraction (OVF) is defined as the relative volume occupied by oil in the two-phase flow, which is also called hold-up. The results of the conductance probes are discussed in details in Chapter 6.

4.3.5 Thermocouple

Two 1.5 mm type K thermocouples (Figure 4.29) were fitted to the oil and water flow pipelines immediately after the respective inlet valves of the liquid-liquid flow facility. These thermocouples were used to monitor the temperature during experimental runs. The thermocouple installations can be seen in Figure 4.28.

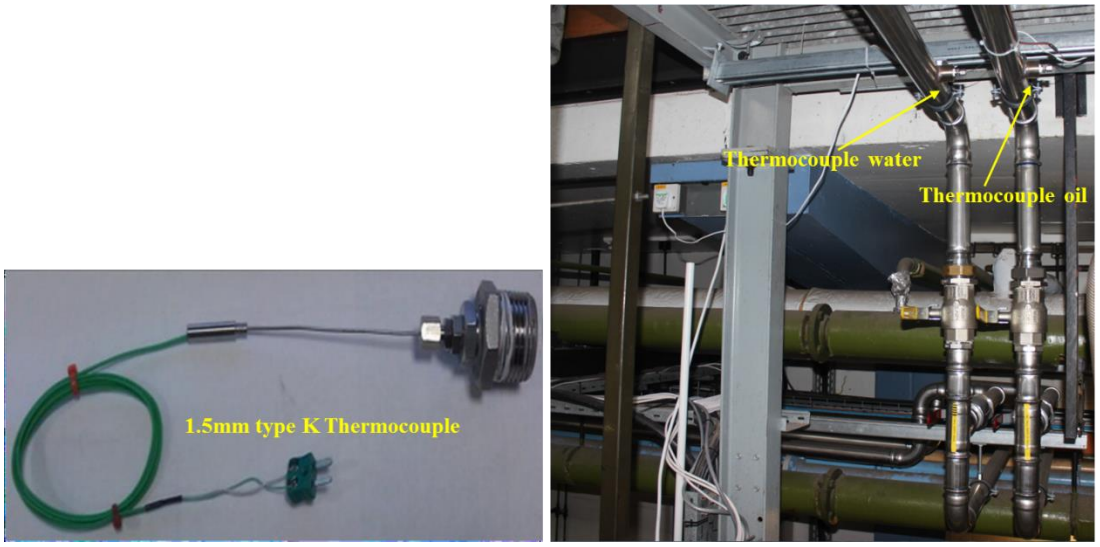

Figure 4-29 Type K thermocouple 1.5mm

4.3.6 Phantom PCC 2.7 High Speed Camera

A Phantom PCC 2.7 high speed camera system produced by Vision Research was used to record flow pattern visualization and interface studies, which is presented in Chapter 6. The camera has a maximum resolution of 1,280 × 800 at which the frame rate is 6,273 fps. Figure 4.30 shows a picture of the experimental setup of the camera in the rig. A 40W Ultra-Slim LED Panel Light - 600 x 600 mm source was used at the background of the pipe test section for illumination purpose.

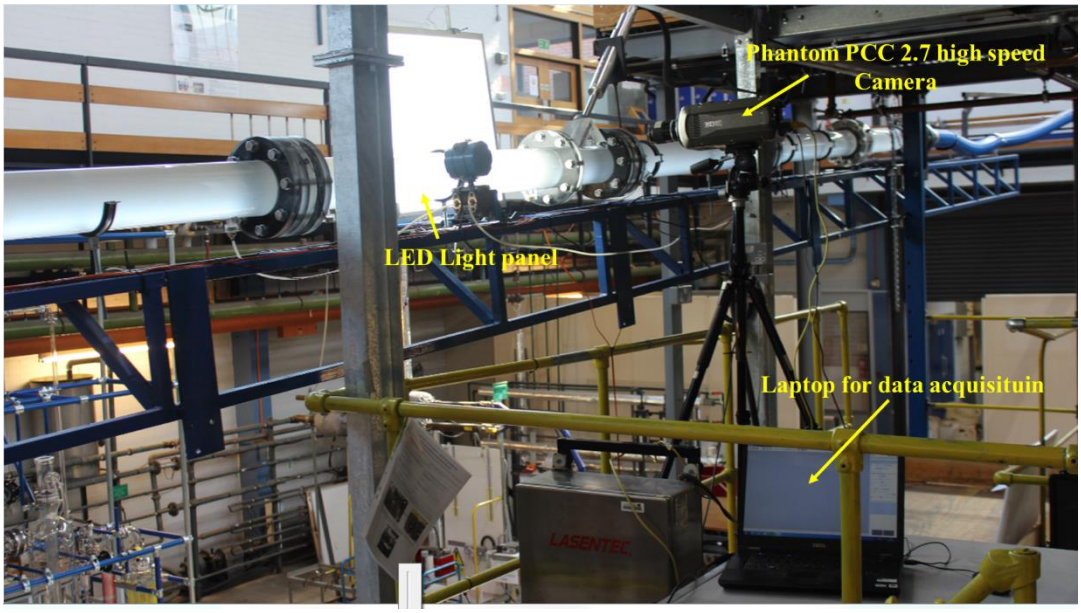

Figure 4-30 Phantom PCC 2.7 Camera setup on the Liquid-liquid rig facility

4.3.6.1 Investigation of oil-water interface

The instantaneous interface level h/D (x,t) is defined as the height of the oil-water interface from the bottom of the pipe. The interface level analysis has been performed by selecting sixty (60) images of maximum temporal spacing to ensure sample independence and by recording height at five (5) points (positions) in each image, as shown pictorially in Figure 4.31 below. Thus, for each flow condition 60 interface height values were generated. In these experiments, 70 pps and 24 pps was selected as the sampling rate and recordings were made for 60s using the Phantom high speed camera. The recorded images were stored in AVI file format for further processing using image j software program. The mean $\mu_{h/D}$ (Equation 4.20) and standard deviation $\sigma_{h/D}$ (Equation 4.21) of the data are determined for each run (i.e. set of conditions).

$$\mu_{h/D} = \frac{1}{n}\sum_{i=1}^{n}\left(\frac{h}{D}\right)_i \qquad 4.20$$

$$\sigma_{h/D} = \sqrt{\frac{1}{n-1}\sum_{i=1}^{n}\left(\left(\frac{h}{D}\right)_i - \mu_{h/D}\right)^2} \qquad 4.21$$

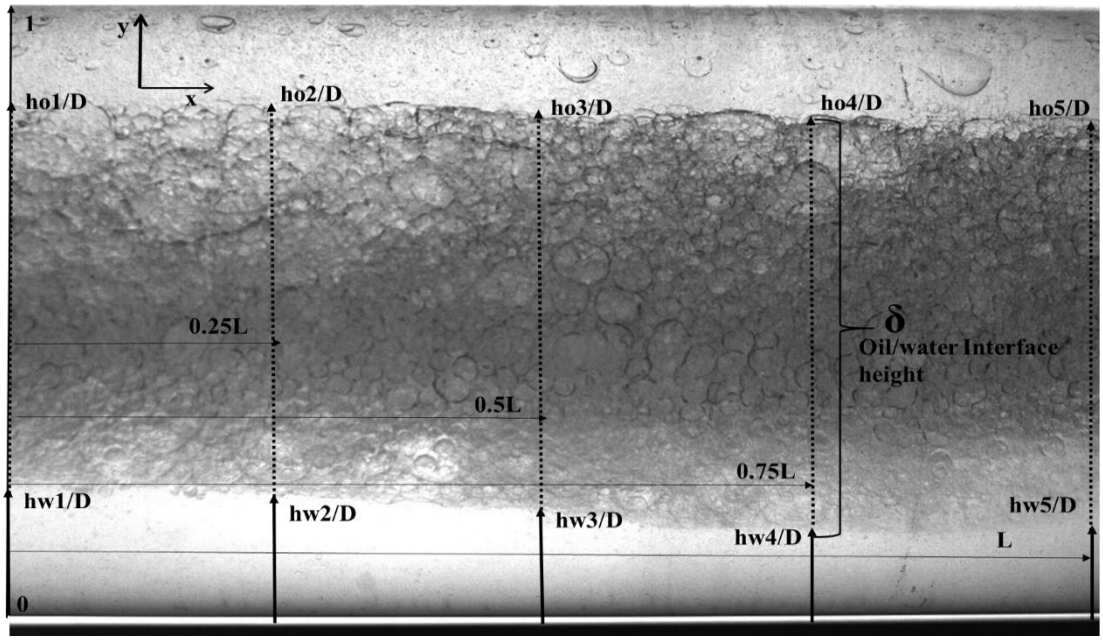

Figure 4-31 Interface height image processing, showing dimensionless oil and water heights

The experimental test conditions starts from a mixture velocity, U_{mix} of 0.30 ms^{-1}, 0.35 ms^{-1}, 0.50 ms^{-1}, 1.00 ms^{-1} and 1.50 ms^{-1} with water cuts of 20%, 50% and 80% for each flowrate run. The mixture velocity is always kept constant, while changing the water cut to the desired percentage. The results are discussed further in Chapter 6.

4.4 Uncertainty of experimental measurements

The errors in the flow rate measurements, differential pressure cells and conductance probes can be obtained from the accuracy of the instruments. The ability of a measuring instrument to give indications of true value of the quantity measured is a characteristic of its uncertainty. Errors are discrepancies or inconsistencies of measurements from the true value. Table 4.3 presents an estimated error in each of the instruments and measurements in the current experimental work. Both the electromagnetic flow meter and Truflo paddle wheel flow meter for water and oil respectively, were calibrated by the suppliers and certificates issued, which are included in Appendix F.

Table 4-3 Total instrumental deviations

Instrument	**Range**	**Specific instrument accuracy**	**Calibration uncertainty**
Electromagnetic flow meter (water flowrate)	0 – 884 m^3hr^{-1}	± 0.25%	± 0.02 m^3hr^{-1}
Truflo paddle wheel flow meter (oil flowrate)	0 – 1500 $litresmin^{-1}$	± 1%	± 0.13 $litresmin^{-1}$
DP Cell inlet	0 – 1 bar	± 0.1%	± 0.0 bar
DP Cell Test section	0 – 1 bar	± 0.1%	± 0.001 bar

All instruments have a specified accuracy, and this accuracy leads to a certain deviation even when the instruments are operated within the calibrated range. The FBRM M500P laser backscatter equipment was re-calibrated and verified using the PVC standard reference measurement procedure as recommended by the Lasentec Company. Details of the procedure have been discussed in section 3.5.1.1 of Chapter 3. The errors in the conductance probe measurements such as in-situ volume fractions and interface height estimation are difficult to measure quantitatively but are discussed qualitatively in Chapter 6.

Chapter 5 DROP SIZE RESULTS AND DISCUSSIONS ON LIQUID-LIQUID FLOW IN PIPES

5.1 Theory and characteristics of drop distribution

As highlighted previously in Chapter 2 and Chapter 3, the phenomenon of liquid – liquid flows occurs widely in oil and gas processing Industries. A major effect in these processes is the formation of liquid dispersions of one phase on the other, as a result of their interactions, together with pressure drop and equipment design. The dispersions can also affect the viscosity of the liquid mixture, thereby requiring more pumping power than for single liquid. This interaction in liquid dispersions is governed mostly by drop coalescence and break-up mechanisms amongst other parameters.

There are a number of other factors affecting the evolution of drops in liquid-liquid flow systems in pipelines. Some of these include the pipe configuration (i.e. pipe expansion or contraction), pipe fittings, pipe diameter and pipe orientations or inclinations. These parameters have direct impact on the momentum transfer of liquid-liquid flow in pipelines. In general, the total pressure gradient components (i.e. acceleration, frictional and gravitational pressure gradients), is affected by the prevailing pipeline configuration and conditions Even though some research have been carried out previously on momentum transport in pipelines, the effect of sudden expansion in a large pipe diameter on drop formation mechanism, in oil-water has not been studied in details.

It is therefore pertinent to investigate and obtain useful information of drop formation mechanism in liquid-liquid dispersions that can be applied in the design and performance of a phase separator if sudden pipe expansion is to be employed.

As explained in section 3.6.2, drops measured using a laser backscatter technique can be characterized by a single number Sauter mean diameter (SMD) or a distribution. The common drop size distributions are namely Rosin-Rammler and Log-normal distributions, which usually takes the form of an equation with two or more adjustable

parameters. The upper limit log-normal distribution was also used by (Simmons and Azzopardi, 2001) and found good agreement with experimental data from pipe flow at dispersions below 43%. Majority of the published work use Rosin-Rammler and Log-normal distribution to correlate particle or droplet size measurements.

The Sauter mean diameter, d_{32}, is a measure of the interfacial area per unit volume, which determines transfer rates of energy, mass and/or chemical reactions in dispersions (Zhou and Kresta, 1998a). Since the Sauter mean diameter (SMD), is generally considered as a better way of drop size representation, it will be applied mostly in the analysis and discussions of results obtained in this current study.

5.1.1 Rosin-Rammler distribution

The Rosin-Rammler distribution is frequently used for representing droplet size distributions in sprays. A detailed description of the distribution can be seen in Chapter 3 under section 3.6.2. Several researchers such as (Karabelas, 1978, Angeli and Hewitt, 2000, Angeli and Hewitt, 2000a, Simmons et al., 2000, Lovick and Angeli, 2004b), have used the Rosin-Rammler distribution for analyzing of their results and found good agreements with experimental data.

5.1.2 Log normal distribution

The log-normal distribution is also used to represent the size of droplets or particles in a dispersion system. The theory involved in this distribution has been discussed previously in Chapter 3. Therefore, attention will be focused mainly on some examples of experimental data plots with the Log-normal distribution.

5.1.3 Sauter mean diameter

The Sauter mean diameter, d_{32}, is commonly used in processes, which depends on the interfacial area and is defined as the ratio of the third moment to the second moment of the drop size distribution.

$$d_{32} = \frac{\sum_{i=1}^{k} n_i d_i^3}{\sum_{i=1}^{k} n_i d_i^2} \qquad 5.1$$

where, d_i is the drop diameter in bin i and n_i is the number of drops with diameter in bin i. The maximum diameter, d_{max} and minimum diameter, d_{min} are generally considered proportional to the Sauter mean diameter, d_{32}.

5.2 Inlet parameters, rig configuration and experimental design

Series of experiments were conducted using the Lasentec Focused Beam Reflectance Measurement (FBRM M500P) Laser equipment to obtain chord length measurements from drops flowing at different locations downstream of the sudden pipe expansion. Experiments were performed for mixture velocities ranging from 0.2ms^{-1} to 3.5 ms^{-1} for input oil fractions from 20%, 30%, 40%, 50%, 60%, 70% and 80% at horizontal and inclinations of -4^0, -2^0, +2^0, +4^0 degrees. The negative and positive angles of inclination from the horizontal refer to downward and upward liquid flow in the pipe, respectively. At these conditions the flow pattern is either stratified, stratified with mixed interface or fully dispersed. However, the analysis of the results is focused mainly on the stratified and stratified with mixed region i.e. at mixture velocities between 0.20 ms^{-1} to 0.35 ms^{-1}.

Drop size distribution measurements were taken downstream of the sudden pipe expansion vertically, by placing the probe position at the central axis and from bottom to top. These probe positions inside the pipe cross-section were labelled Bottom (15.9 mm), Bottom (31.8 mm) Bottom (47.7 mm), Centre (63.5 mm), Top (79.5 mm), Top (95.3 mm), and Top (111.3 mm) as shown in Figure 5.1. The measurement were also made at four (4) axial distances downstream the expansion of 10D, 20D, 30D and 40D, where D is the internal diameter of the pipe (127 mm) and a test section of 6m long.

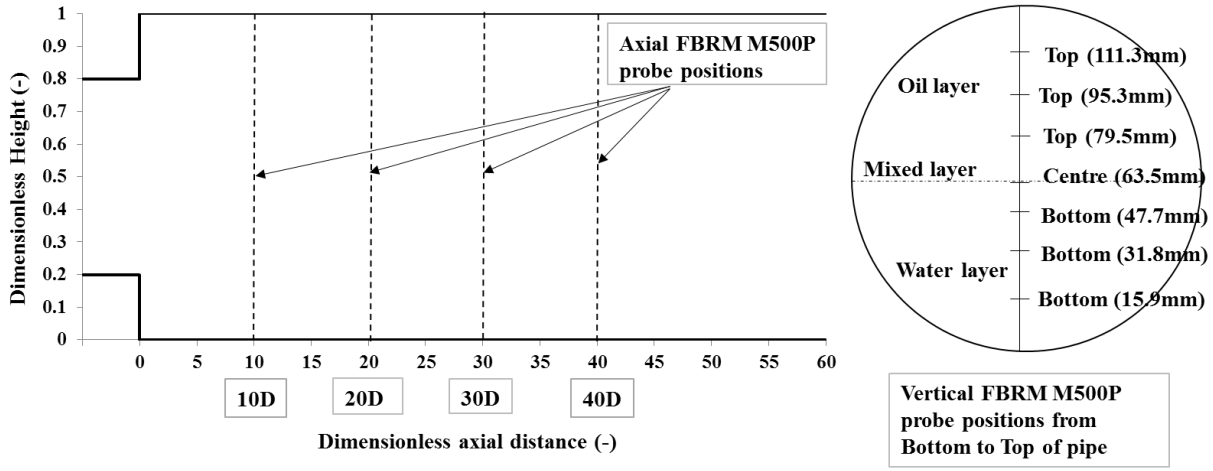

Figure 5-1 Lasentec FBRM M500P laser probe positions, downstream of expansion and vertical height in a pipe cross-section from bottom to top of the pipe

5.2.1 Drop size in horizontal flow

In order to investigate the effect of flow parameters in the flow pattern evolution from dispersed to segregated flow, series of experiments were carried out with the pipe fixed in a horizontal position. Measurements of drop sizes were made axially at the different locations downstream of the expansion and vertically inside the pipe cross-section. This is done to gain better understanding of the factors affecting the flow pattern through sudden pipe expansion and also to know if drop break-up and coalescence models can be applied to describe the data obtained within the region.

Particular attention will be focused on stratification downstream of the dispersion through the expansion. In order to build upon and consolidate on previous phase profile observations by some researchers such as (Yang et al., 2003, Hasan, 2006, Yusoff, 2012), the flow pattern at 40D is fully developed to a stratified flow, i.e. oil layer at the top and water layer at the bottom and drop size measurements were investigated. In the case of downstream mixture velocities of between 0.20 – 0.35 ms^{-1}, the flow patterns develop to the stratified (ST) and stratified with mixed interface (ST& MI). Trallero et al. (1997), in his flow pattern map also predicted the conversion from dispersed flow to stratified regime for similar experimental conditions, as can be seen in Figure 5.2.

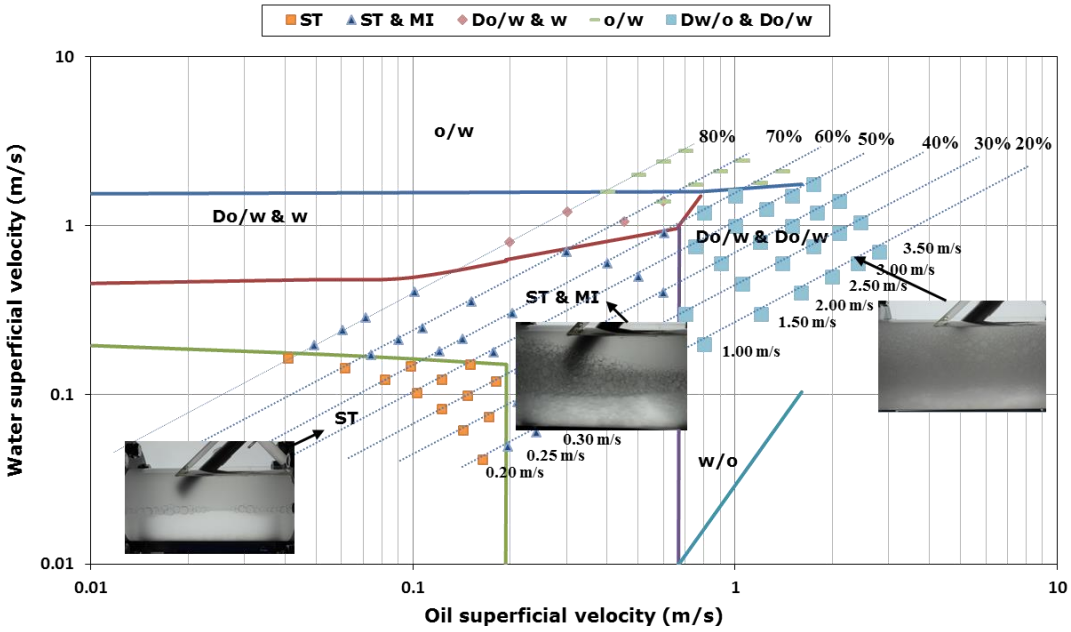

Figure 5-2 Mixture velocities upstream and downstream of flow pattern transition through the sudden expansion plotted on the flow pattern map of Trallero et al. (1997)

The effect of flow parameters such as mixture velocity, input oil fraction and probe position on the phase layer evolution are investigated in the following sections.

5.2.1.1 Effect of input oil volume fraction

Figure 5.3 shows variation of Sauter Mean Diameter (d_{32}), plots for downstream mixture velocity, Usme = 0.20 ms^{-1}, within axial distances (10D, 20D, 30D and 40D), of test section in horizontal pipe orientation, with probe position placed at 15.9 mm from bottom of pipe cross section at different oil volume fraction, OVF. There was clearly and evidently a mixed layer of oil/water flow along the pipe expansion downstream of the singularity. In Figure 5.3 at 80% OVF, oil is considered as the continuous phase and water as the dispersed phase. It can be seen that larger water droplets are formed. This trend is followed by a decreasing SMD drop sizes as the oil volume fraction decreases from 60% OVF to 40% OVF and 20% OVF. In general the water droplets are also seen to be increasing downstream of the expansion in the axial positions. This is due to coalescence of dispersed water drops resulting in bigger drops downstream of the pipe. The smaller drops formed at positions 20D, 30D and 40D for

60% OVF – 20% OVF, suggest a transition of the phases, because the probe was fixed at the 15.9 bottom position of the pipe. From the above it can be inferred therefore that Sauter mean diameters is dependent on high input oil volume fraction at low mixture velocity in an oil continuous flow system.

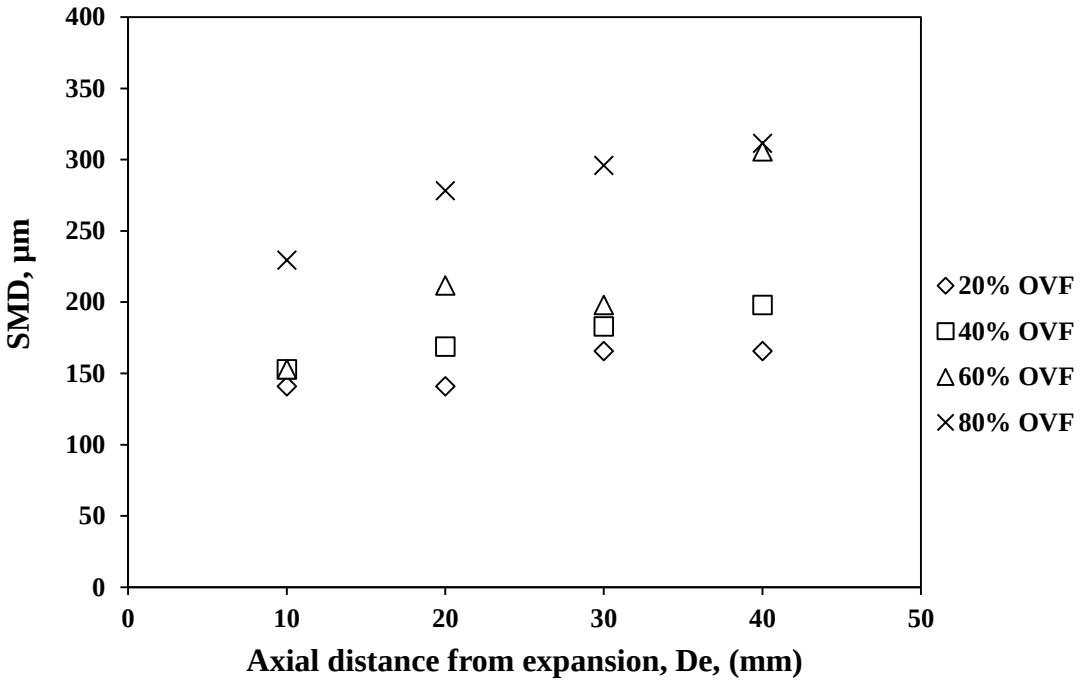

Figure 5-3 Sauter Mean Diameter (d_{32}), for downstream mixture velocity, U_{sme} = 0.20 ms^{-1}, within axial distances of test section in horizontal pipe orientation, probe position 15.9 mm from bottom of pipe at different oil volume fraction, OVF.

The effect of the oil volume fraction on Sauter mean diameter (SMD) for probe position at the Centre of the interface (63.5 mm) for downstream mixture velocity, U_{sme} = 0.20 ms^{-1} at the various axial distances in horizontal pipe is shown in Figure 5.4. Larger droplets can be seen closer to the interface from above and below the mixed layer region of the two phases. This is due to the fact that 40% OVF and 60% OVF are closer to the interface and probe position at the Centre. Considering 40% OVF as oil dispersed phase in water continuous phase, the oil droplets are seen to be coalescing after the inlet position (10D) at downstream positions 20D, 30D and 40D. Similar observation can be noticed for the water dispersed phase in oil continuous phase 60% OVF, were the water droplets are coalescing downstream of the pipe expansion. The interface becomes narrower downstream due to this coalescing

phenomenon of both oil and water droplets. More drops with about 200µm SMD are also formed at the mixed region than the oil and water layers in the pipe. This observations are in agreement with the work of previous researchers such as (Yang et al., 2003, Hasan, 2006, Yusoff, 2012).

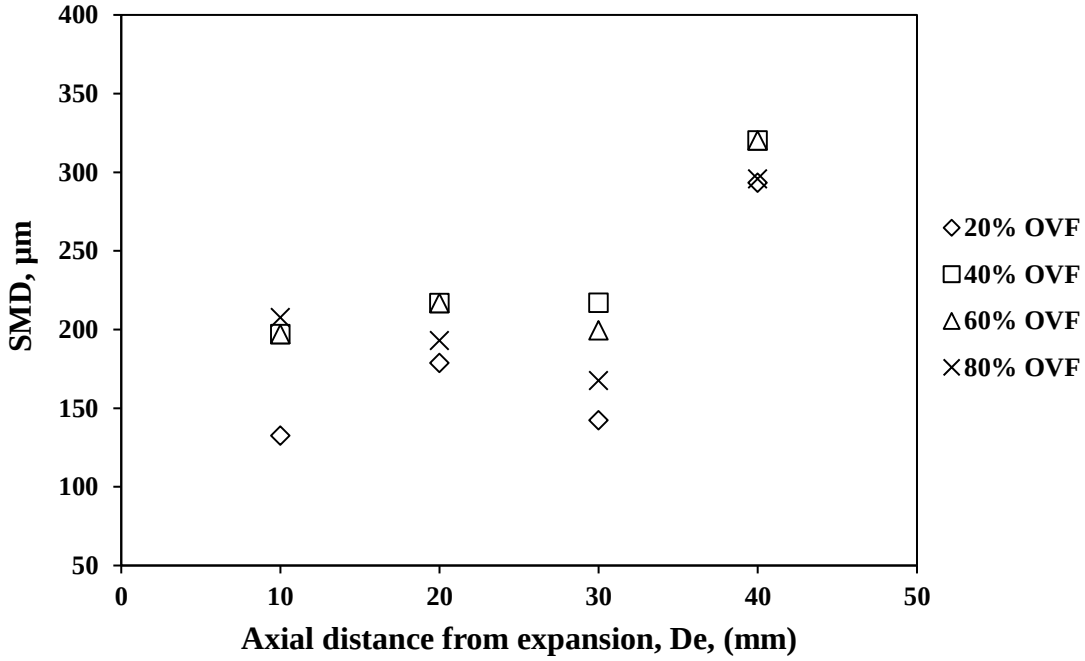

Figure 5-4 Sauter Mean Diameter (d_{32}), for downstream mixture velocity, U_{sme} = 0.20 ms^{-1}, within axial distances of test section in horizontal pipe orientation, probe position interface (63.5 mm) from bottom of pipe at different oil volume fraction, OVF.

Figure 5.5 shows the effect of Sauter mean diameter on oil volume fraction by positioning the probe at the Top (111.3 mm) portion in the pipe for downstream mixture velocity U_{sme} 0.20 ms^{-1}. Larger water drops can be seen as the flow progresses from the inlet to the downstream position along the axial distance of the entire test section for the 80% OVF oil continuous and water dispersed phase system. Similar trend was observed earlier on when the probe was placed at the bottom (15.9 mm) position. However, for this condition, it is clearly seen that for oil volume fractions of 60% OVF, 40% OVF and 20% OVF, the SMD of drop distribution for both water and oil drops are small (150µm). This finding is different from the work of (Yusoff, 2012).

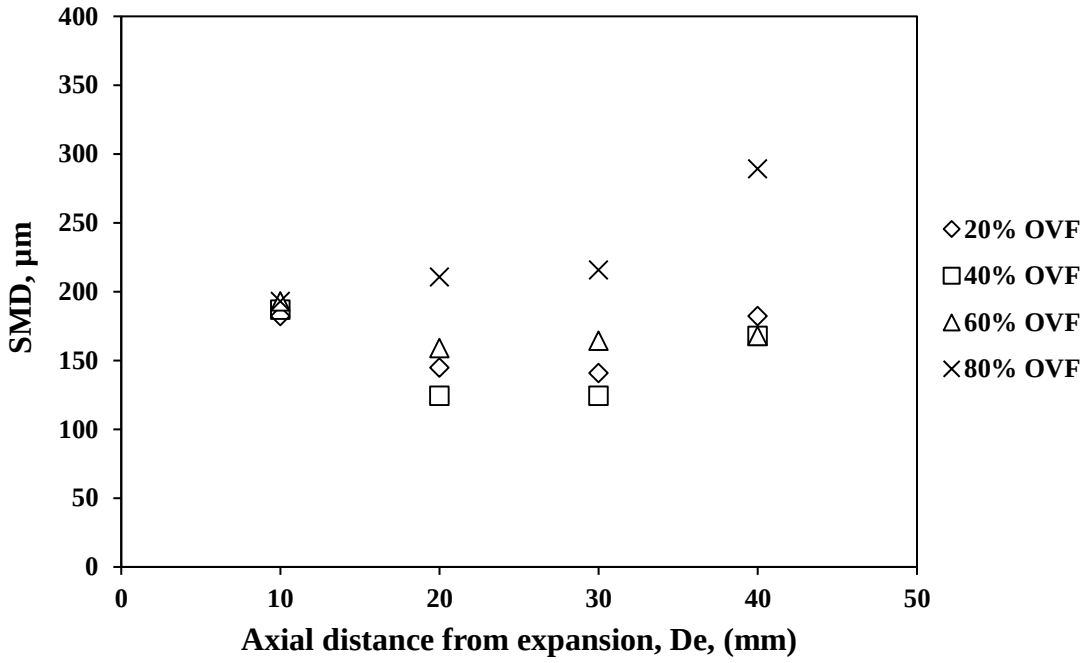

Figure 5-5 Sauter Mean Diameter (d_{32}), for downstream mixture velocity, U_{sme} = 0.20 ms^{-1}, within axial distances of test section in horizontal pipe orientation, probe position Top (111.3 mm) from bottom of pipe at different oil volume fraction, OVF.

In general it can be noticed that coalescence of both water and oil droplets exist. It also indicates that variation of the input oil volume fraction influences the SMD of drop size distribution.

5.2.1.2 Effect of mixture velocity

The influence of downstream mixture velocity on the Sauter mean diameter for different input oil volume fraction OVF, at various axial distances, with the probe positioned at portion of the pipe from bottom to top is demonstrated from Figure 5.6 to Figure 5.13.

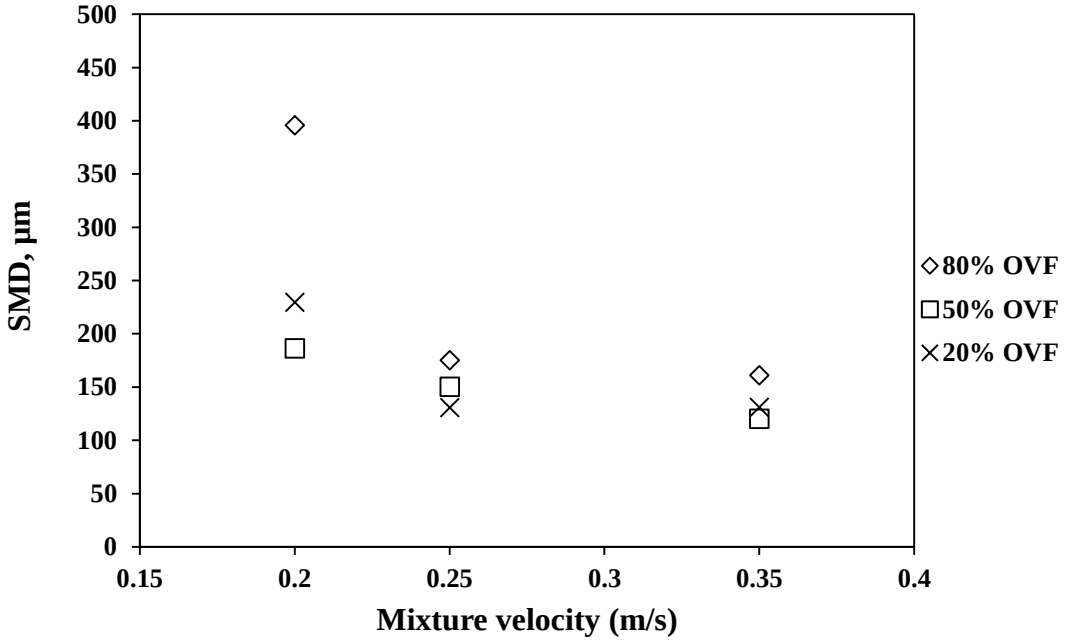

Figure 5-6 Effect of downstream mixture velocity on Sauter Mean Diameter (d_{32}) for flow condition, at 10D axial distance of test section in horizontal pipe orientation, probe position (15.9 mm) from bottom at different input oil volume fraction

The general trends shown in Figures 5.6, 5.7, 5.8 and 5.9 indicates that an increase in downstream velocity results in the formation of smaller droplets regardless of input oil volume fraction and position of the probe downstream of the singularity. By increasing the downstream velocity, the mixed layer hardly decays, reason been that the higher the mixture velocity, the finer the drops produced and also the higher the turbulence intensity which slows the coalescence rate of the droplets in the dispersion.

It is also noticed that lower downstream mixture velocity favors the formation of larger drops. These large drops cannot be dispersed away from the interface due to smaller turbulent diffusive forces. Therefore, it implies that there is a decrease in droplet entrainment of one phase into the other and reduction of dispersed phase fraction as a result of decreasing the velocity (Figures 5.6, 5.7 and 5.8).

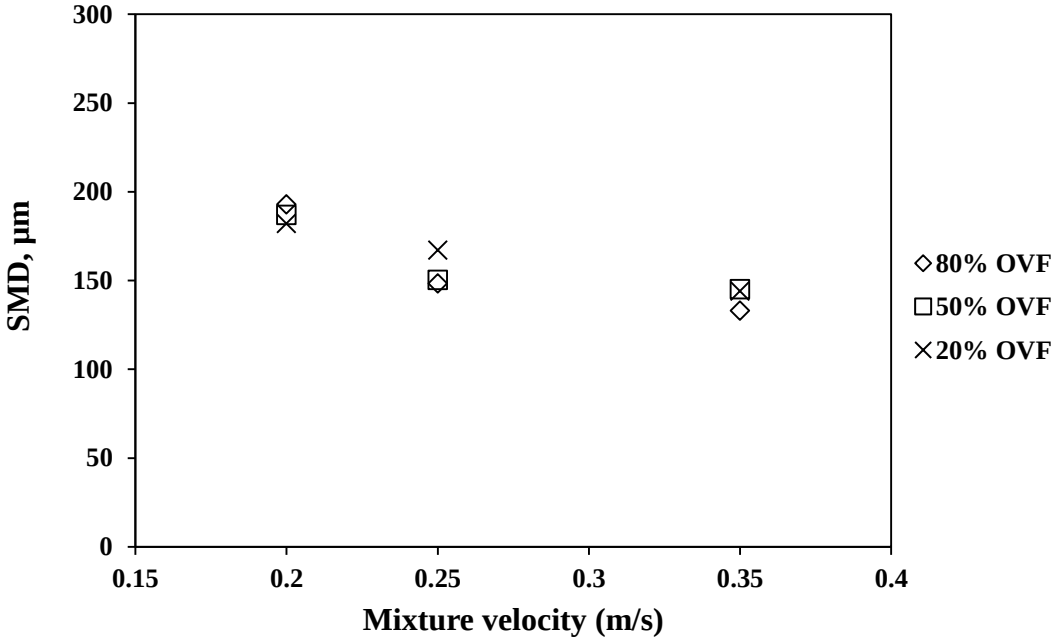

Figure 5-7 Effect of downstream mixture velocity on Sauter Mean Diameter (d_{32}) for flow condition, at 10D axial distance of test section in horizontal pipe orientation, probe position Top (111.3 mm) from bottom at different input oil volume fraction

Considering Figure 5.8, with an input oil volume fraction 80% OVF, which is an oil continuous phase and water dispersed system at low downstream mixture velocity of U_{sme} 0.20 ms^{-1}, the water droplets formed at bottom closed to the inlet part of pipe expansion at 10D are seen to be larger than those formed when the probe position is moved to the top part of the pipe. In both cases, low velocity favours the coalescence mechanism of droplets and also the drifting with accumulation of these droplets to the interface due to gravitational forces. This phenomenon no longer exists as smaller and finer droplets are produced at higher mixture velocity U_{sme} 0.35 ms^{-1}, inhibiting coalescence of droplets and favours dispersion.

Also in Figure 5.8, it can be inferred that there is no clear difference of SMD between the interface and top positions. This indicates a definite gradient in particle size and concentration, resulting in the stratification of the phases.

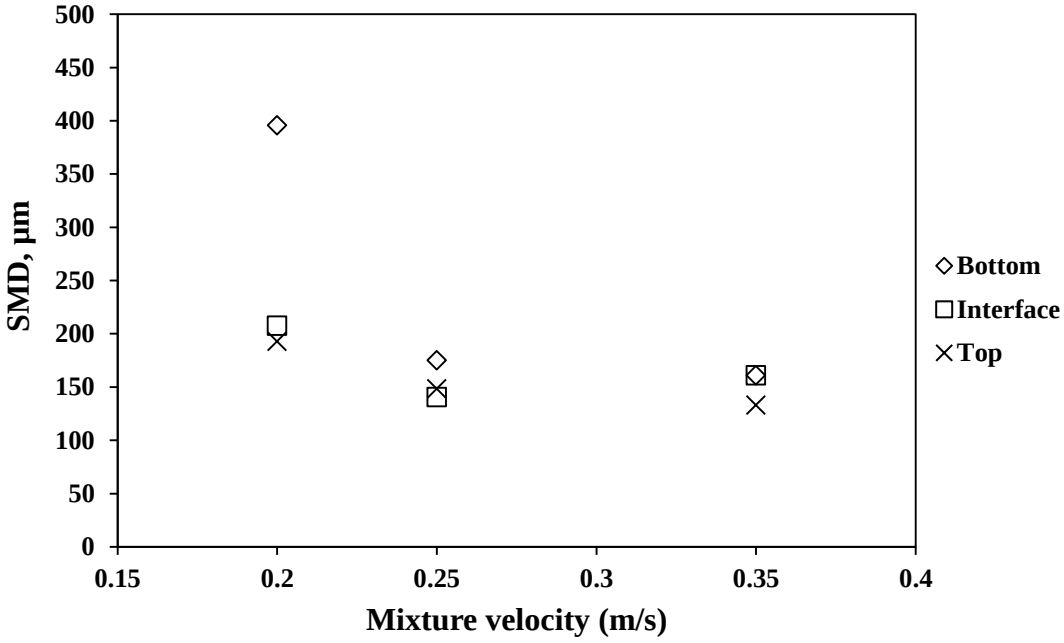

Figure 5-8 Influence of downstream mixture velocity on Sauter Mean Diameter (d_{32}) for flow condition, 80% OVF at 10D axial distance of test section in horizontal pipe orientation, at different probe position

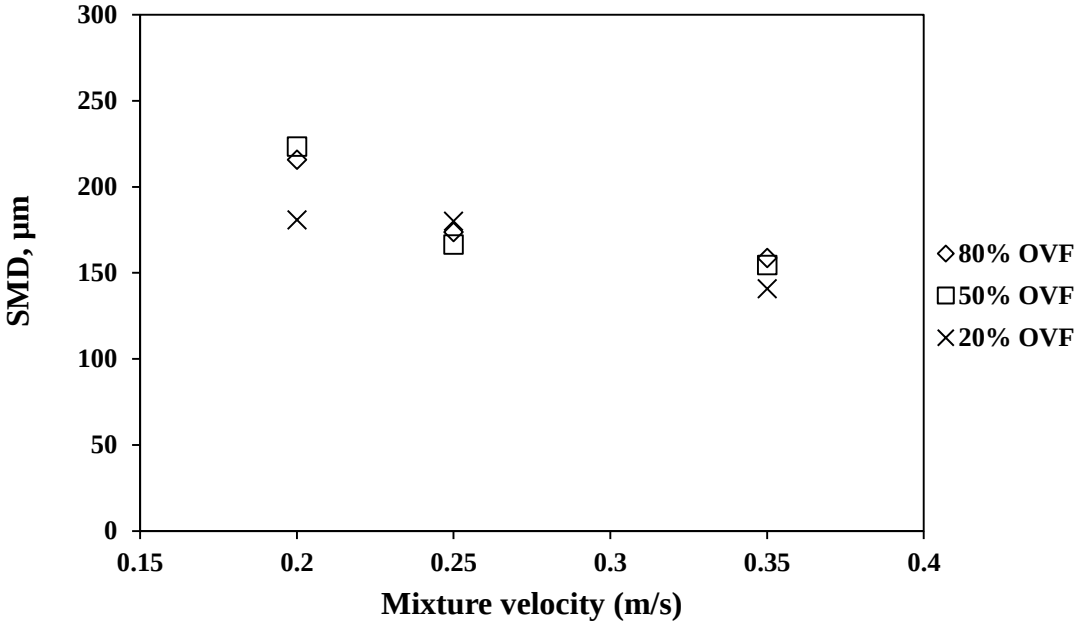

Figure 5-9 Effect of downstream mixture velocity on Sauter Mean Diameter (d_{32}) for flow condition, at 30D axial distance of test section in horizontal pipe orientation, probe position Top (111.3 mm) from bottom at different input oil volume fraction

The influence of different downstream mixture velocity, U_{sme}, on the Sauter mean diameter, d_{32}, of oil droplets for oil volume fraction, 20% OVF at the various axial horizontal orientation test distances, with probe positioned at the top portion is shown in Figure 5.10. The droplets observed are mostly of the same sizes between 150 µm – 200 µm, at the various axial distances from inlet to downstream of expansion for all mixture velocities except position 40D. At higher mixture velocity 0.35 ms^{-1}, the oil droplets are seen to be larger, which clearly shows the simultaneous occurrence of both coalescence and acceleration of droplets taking place in the prevailing system.

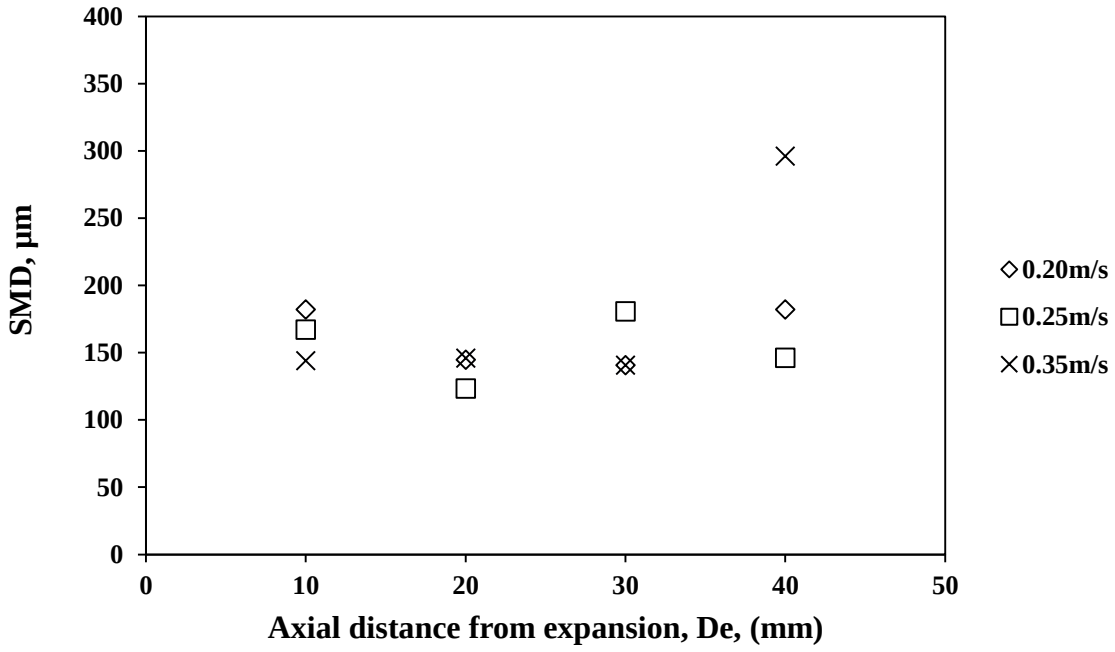

Figure 5-10 Sauter Mean Diameter (d_{32}) for flow condition, 20% OVF, within axial distance of test section in horizontal pipe orientation, probe position Top (111.3 mm) from bottom of pipe at different downstream mixture velocity, U_{sme}.

Figure 5.11 shows a trend different for flow condition, 40% OVF, within axial distance of test section, probe position within axial distance of test section in horizontal pipe orientation, probe position Centre (63.5mm) from bottom of pipe at different downstream mixture velocity, U_{sme} (0.20 ms^{-1}, 0.25 ms^{-1} and 0.35 ms^{-1}). A general increase of Sauter mean diameter, d_{32}, is noticed for all downstream mixture velocities detected by the laser, except slightly bigger droplets at the inlet 10D with lower velocity of 0.20 ms^{-1}. The frequency of collision and coalescence of droplets

appear to dominate the system resulting in the narrowing of the mixed layer downstream of the singularity. This observation is contrary to the earlier findings of both (Sleicher, 1962, Yusoff, 2012), which proposed at high velocities, droplet size decreased. Shinnar (1961), had earlier established that in turbulent flow conditions, simultaneous coalescence and break-up occur. The droplets are exposed to both inertial forces due to velocity fluctuations and to viscous shear forces. Larger droplets are formed in this case and droplets will oscillate about its spherical equilibrium shape concurrently with the surrounding fluid, provided the densities and viscosities of both liquids are constant.

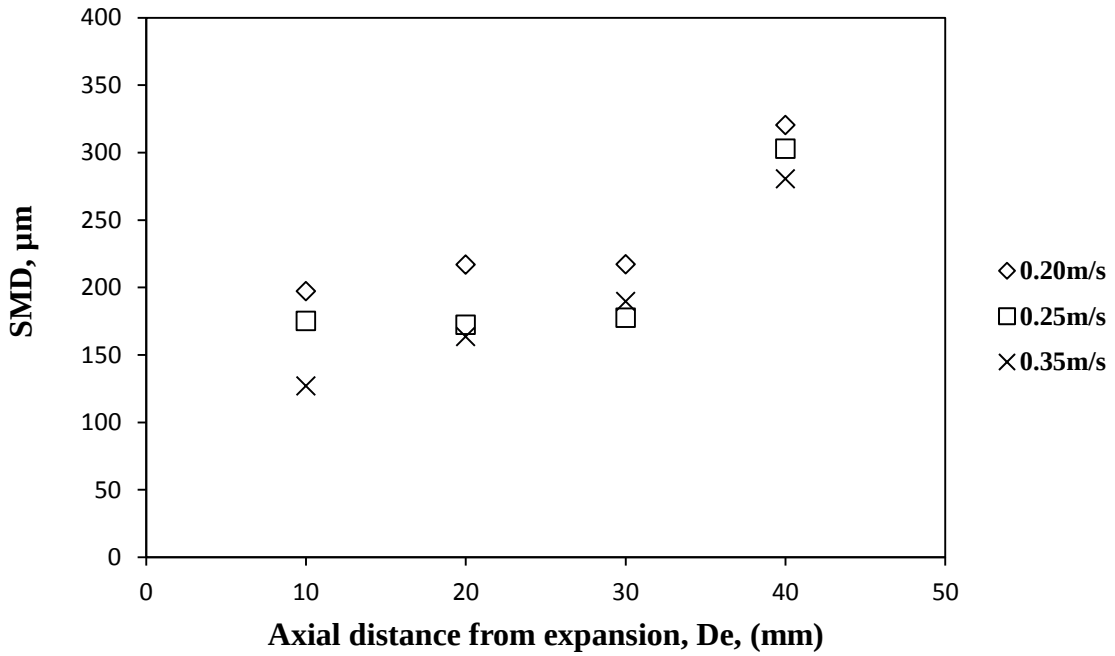

Figure 5-11 Sauter Mean Diameter (d_{32}) for flow condition, 40% OVF, within axial distance of test section in horizontal pipe orientation, probe position Centre (63.5 mm) from bottom of pipe at different downstream mixture velocity, U_{sme}.

Interestingly, a similar trend was noticed when the oil volume fraction is further increased slightly to 60% OVF and 80% OVF as can be seen in Figure 5.12 and Figure 5.13. Droplets formed at low downstream mixture velocity, U_{sme} 0.20 ms^{-1} bigger at all axial position downstream of the expansion. This shows that there was sufficient residence time for droplets to coalesce.

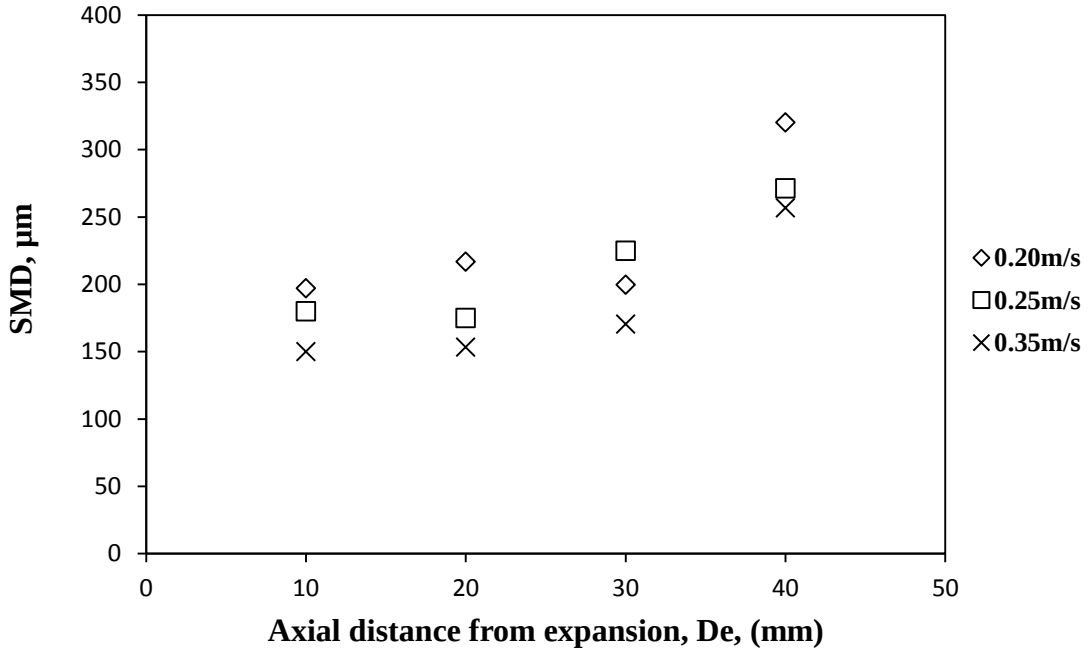

Figure 5-12 Sauter Mean Diameter (d_{32}) for flow condition, 60% OVF, within axial distance of test section in horizontal pipe orientation, probe position Centre (63.5 mm) from bottom of pipe at different downstream mixture velocity, U_{sme}.

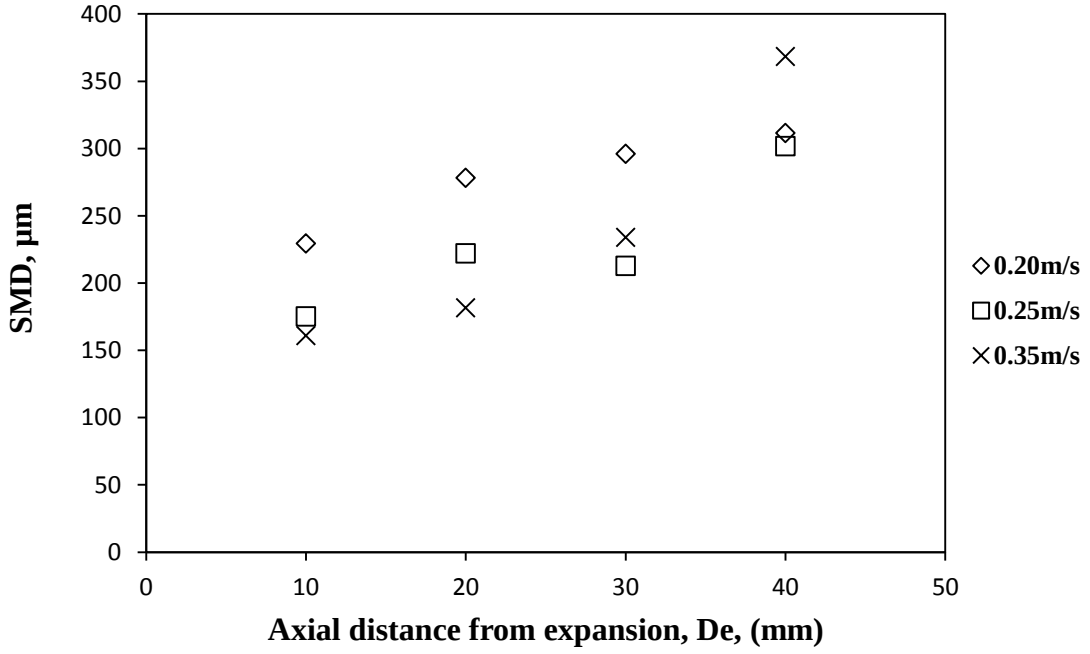

Figure 5-13 Sauter Mean Diameter (d_{32}) for flow condition, 80% OVF, within axial distance of test section in horizontal pipe orientation, probe position Bottom (15.9 mm) from bottom of pipe at different downstream mixture velocity, U_{sme}.

The drop sizes are seen to be bigger and increases at the different axial distances along the horizontal pipe expansion with increasing downstream mixture velocities, as indicated in Figure 5.13. This also shows coalescence of dispersed water droplets at the bottom of oil continuous phase, since the probe was fixed at the bottom (15.9 mm). (Howarth, 1964) in his work on coalescence of drop in turbulent flow had observed an increase in velocity with an increase in coalescence frequency. Bigger water drops were also detected for U_{sme} 0.20 ms^{-1} at 10D downstream of the singularity, similar to the observations made in the findings of (Yusoff, 2012) as shown in Figure 5.13.

5.2.1.3 Effect of probe position

Figure 5.14 shows Sauter Mean Diameter (d32), of oil droplets for mixture velocity, Usme = 0.20m/s, oil volume fraction 20% OVF in horizontal pipe orientation, at different probe positions. It can be seen clearly that coalescence of dispersed droplets progresses from the inlet position 10D and stratifies gradually downstream at 40D from the flow pattern and flow condition, at low downstream mixture velocity, U_{sme} 0.20 ms^{-1}.

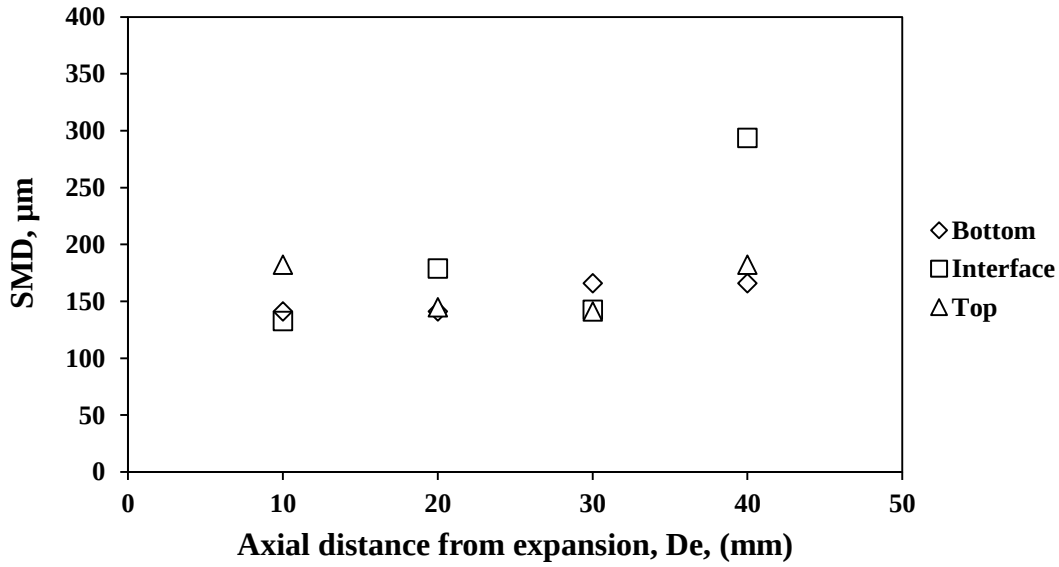

Figure 5-14 Sauter Mean Diameter (d_{32}), of oil droplets for mixture velocity, U_{sme} = 0.20 ms^{-1}, oil volume fraction 20% OVF in horizontal pipe orientation, at different probe positions

Large drops also exist at the mixed region at the 40D axial position downstream of the expansion. There is generally a slight decrease in SMD of droplet size distribution detected by the laser as shown in Figure 5.14 downstream of the singularity.

In contrast, the trend observed in the Figure 5.15 shows an increase in drop size when the oil volume fraction is 50% OVF at low downstream mixture velocity, U_{sme} 0.20 ms^{-1}. However, the flow condition also shows the existence of both bigger and smaller droplets close to the interface at the various axial positions. As the flow progresses, the mixed layer decays by the narrowing of the interface towards the centre thereby enabling the coalescence of more droplets.

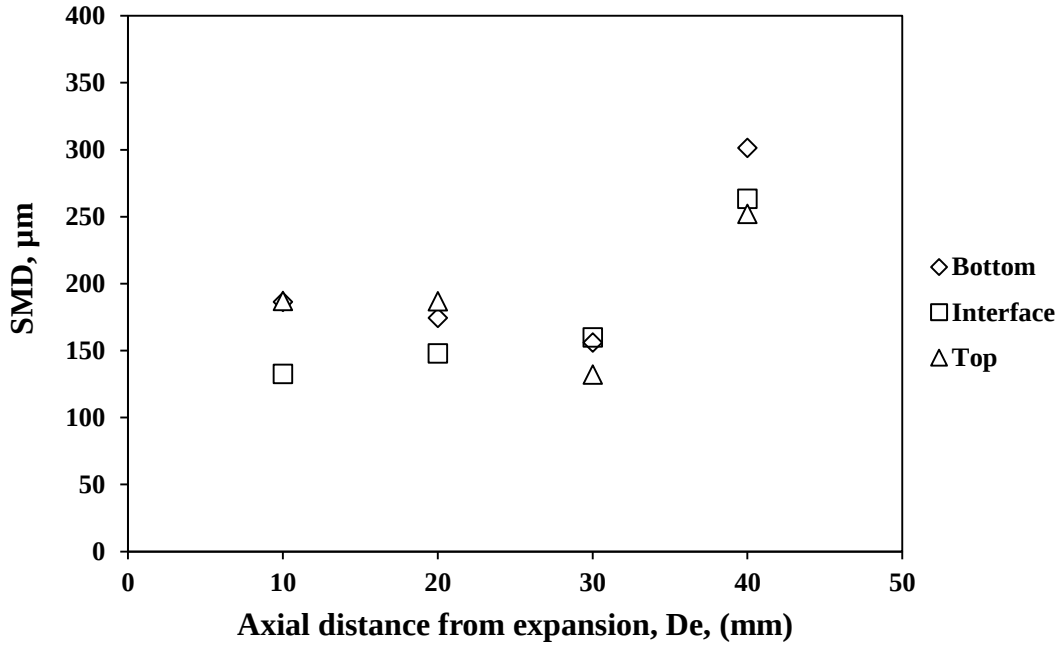

Figure 5-15 Sauter Mean Diameter (d_{32}), of oil and water droplets for mixture velocity, U_{sme} = 0.20 ms^{-1}, oil volume fraction 50% OVF in horizontal pipe orientation, at different probe positions

As noticed before, larger droplets are seen at the bottom of pipe cross-section for flow condition of 80% OVF, where water is considered as the dispersed phase and oil as the continuous phase in Figure 5.16. The drops close to the interface and top are seen to be smaller at the axial distances 10D, 20D and 30D, respectively. This signifies coalescence and settling of the drops towards the Centre, hence larger drops emerge

at the 40D position as shown in Figure 5.16. It is important to note that dispersed phase droplets affect the reflection of the laser beam to a great degree. This is obviously seen when silicone oil is the dispersed phase, in which case the laser light is lower compared to when water is the dispersed phase, because of the differences in refractive index and optical properties. The observations from Figure 5.16 are similar to the findings and work of (Yusoff, 2012).

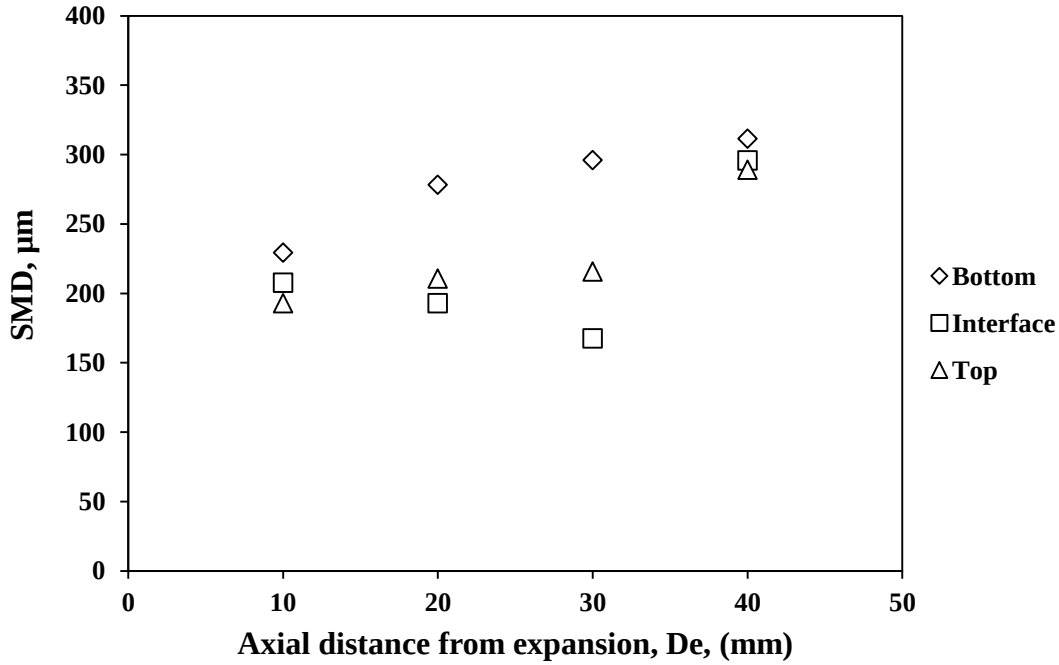

Figure 5-16 Sauter Mean Diameter (d_{32}), of water droplets for mixture velocity, U_{sme} = 0.20 ms^{-1}, oil volume fraction 80% OVF in horizontal pipe orientation, at different probe positions

5.2.1.4 SMD in mixed layer and vertical distance from interface

Figures 5.17, 5.18 and 5.19, shows the dependence of the Sauter mean diameter on 80% OVF oil volume fractions of interface height from pipe bottom. It can be seen from Figure 5.17 that Sauter mean diameter tends to increase above the center of the mixed layer compared to the oil droplets dispersed in water at the bottom of pipe. This indicates coalescence of dispersed water droplets at the top, forming larger drops and drifting towards the center of the mixed interface.

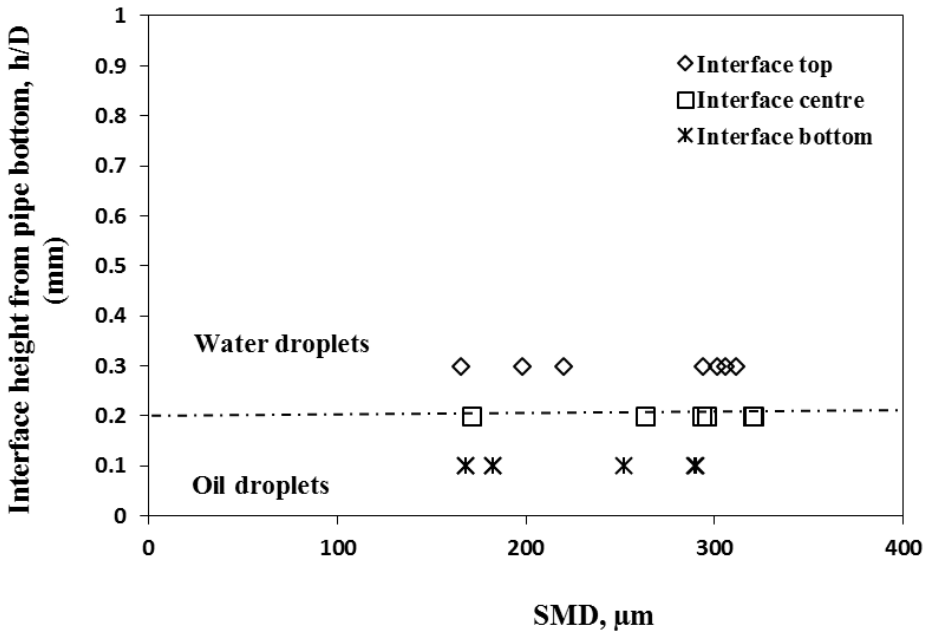

Figure 5-17 Sauter Mean Diameter (d_{32}), as a function of interface height from pipe bottom for mixture velocity, U_{sme} = 0.20 ms^{-1}, and distance from expansion 40D in horizontal pipe orientation, for 80% OVF input oil volume fraction.

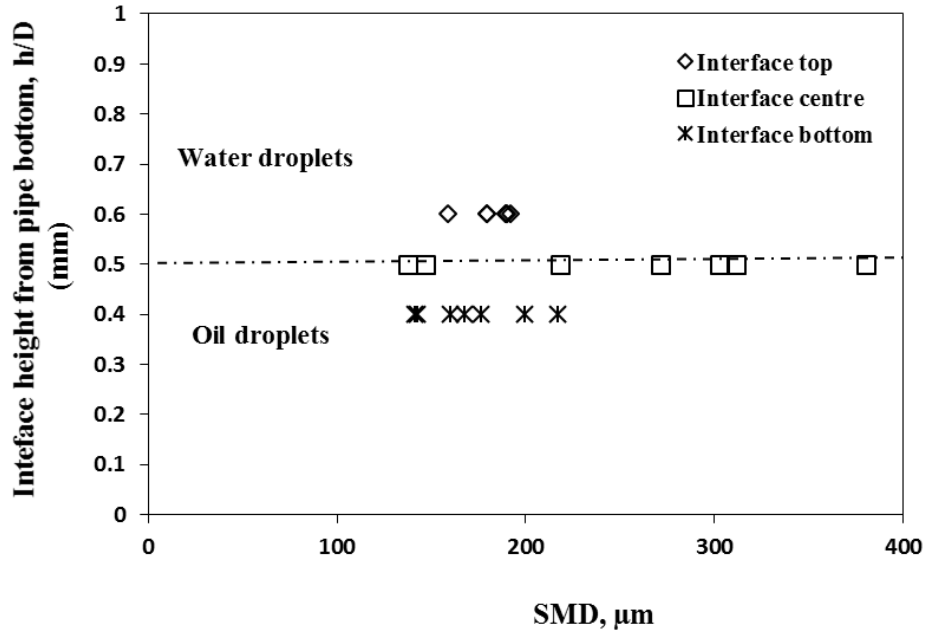

Figure 5-18 Sauter Mean Diameter (d_{32}), as a function of interface height from pipe bottom for mixture velocity, U_{sme} = 0.20 ms^{-1}, and distance from expansion 40D in horizontal pipe orientation for 50% OVF input oil volume fraction

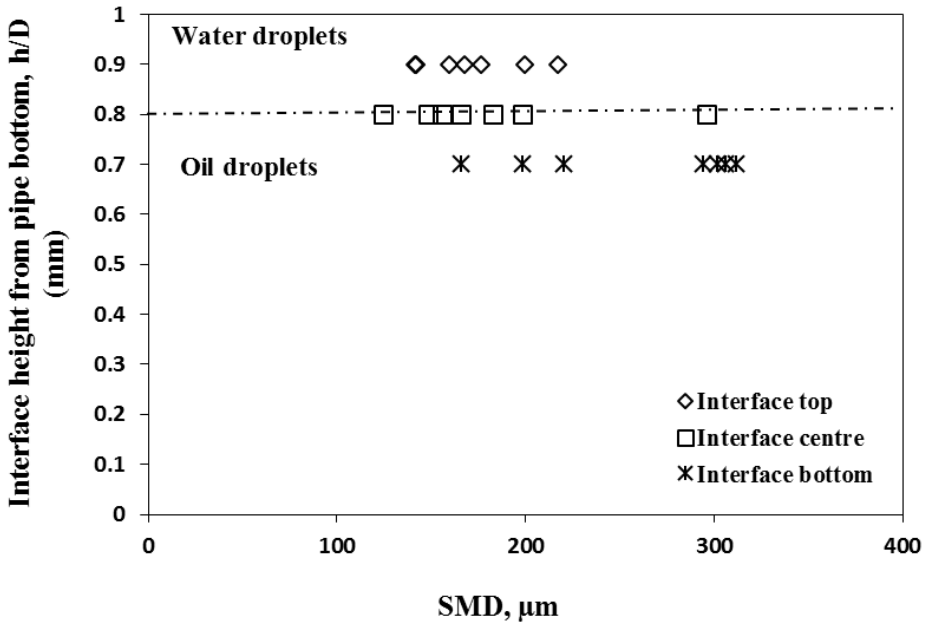

Figure 5-19 Sauter Mean Diameter (d_{32}), as a function of interface height from pipe bottom for mixture velocity, U_{sme} = 0.20 ms^{-1}, and distance from expansion 40D in horizontal pipe orientation for 20% OVF input oil volume fraction

The trend is however different at downstream mixture velocity, U_{sme} 0.20 ms^{-1} and 50% OVF oil volume fraction. Sauter mean diameter (SMD) was found to be smaller close to the mixed layer at the top of the interface than at the center and bottom of the interface. The drops are much larger at the center of the mixed interface. An explanation for this would be that turbulent forces may not be enough to overcome the frictional drag on the drops, which tends to accumulate close to the center of the interface. The resultant oil droplet sizes are also found to be larger below the interface due to coalescence for the water continuous and oil dispersed phase condition, (20% OVF), as shown in Figure 5.19.

The influence of downstream mixture velocity, U_{sme}, on Sauter mean diameter (d_{32}), as a function of the distance from the interface for input oil volume fractions 80% OVF and 50% OVF, distance from expansion 40D in horizontal pipe orientation, is as shown in Figures 5.20 and 5.21. In the mixed flow region where there is an oil-water interface, the distances are either positive (water drops in oil) or negative (oil drops in water).

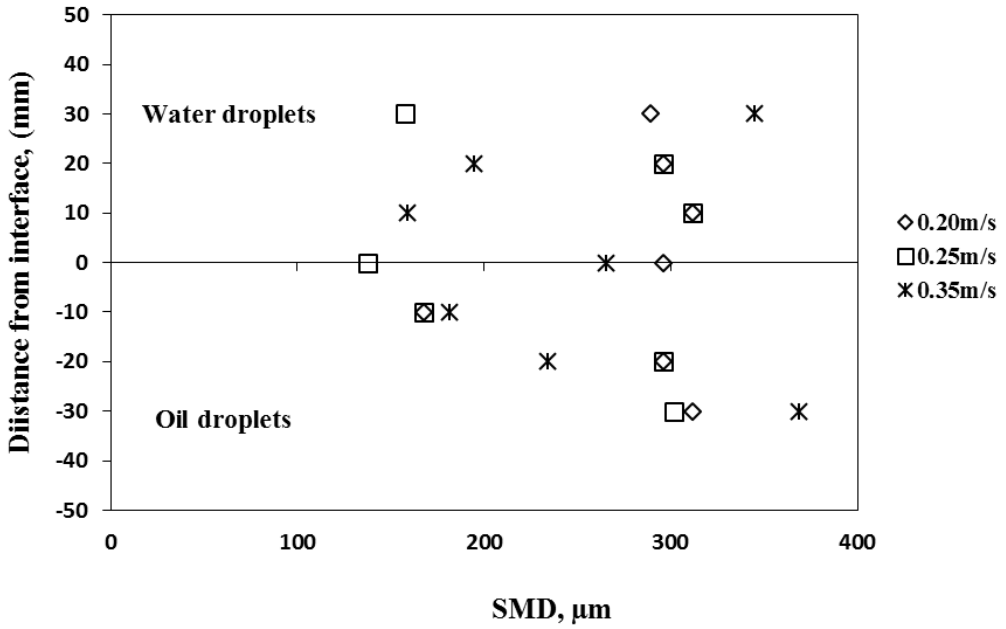

Figure 5-20 Sauter Mean Diameter (d_{32}), as a function of the distance from the interface for input oil volume fraction 80% OVF and distance from expansion 40D in horizontal pipe orientation, at different downstream mixture velocities, U_{sme}.

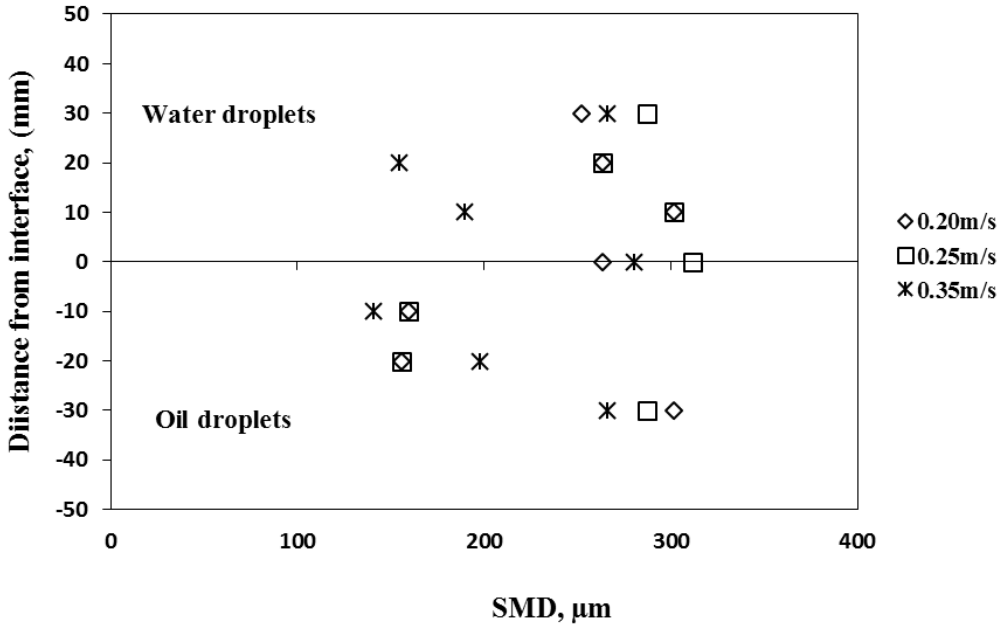

Figure 5-21 Sauter Mean Diameter (d_{32}), as a function of the distance from the interface for input oil volume fraction 50% OVF and distance from expansion 40D in horizontal pipe orientation, at different downstream mixture velocities, $U_{sme.}$

In general, the Sauter mean diameter (SMD) values are larger above and below the mixed layer of the interface for downstream mixture velocity, U_{sme} 0.20m/s than at higher mixture velocity of 0.35 ms^{-1}. The reason for this occurrence have been explained in section 5.2.1.2 above. Also drops at (0.20 ms^{-1} and 0.25 ms^{-1}) are less dispersed in the pipe cross section compared to higher mixture velocity 0.35 ms^{-1}. At the mixed flow region, lower mixture velocities reduces entrainment of phases and turbulent dispersive forces that prevent drops from settling towards the interface. However, these phenomena can also cause reduction in drop size as explained by (Lovick and Angeli, 2004a).

The following can be summarized for SMD of drop diameter distribution in horizontal expansion:

- Input oil volume fraction strongly influenced formation of drop sizes downstream of the expansion as investigation shows larger droplets detected at 40D due to coalescence mechanism of the drops.
- Smaller droplet sizes are formed downstream of the pipe expansion with an increase in downstream mixture velocity.
- Coalescence of dispersed phase droplets progresses from inlet and stratifies gradually downstream of the singularity. In general higher input oil fraction and low mixture velocity (0.20ms^{-1}), favours coalescence producing larger droplets downstream of pipe expansion.

5.2.2 Drop size in upwardly inclined flow

Even though some research work has been done and published previously on drop size distribution measurements in upwardly inclined flow orientation in pipelines, of liquid-liquid oil/water two phase systems, it is evidently not enough to make conclusions or consolidate on the few available data or results. Majority of the earlier research work on vertically and inclined two phase flow systems in pipes, concentrated mostly on other flow parameters rather than in addition also investigating the influence of drop break-up and coalescence mechanism, in understanding the hydrodynamics and stratification of liquid-liquid flow. A summary of some earlier

research work was compiled by (Brauner, 2001), and have been discussed in section 2.2.2 of Chapter 2.

In light of the above, recent research on liquid-liquid oil/water two phase systems in horizontal or inclined pipeline, now focuses on all-inclusive investigation of flow parameters and influence of drop size distribution in the system. Some of the recent work done in this regard include (Karabelas, 1978, Kurban et al., 1995, El-Hamouz and Stewart, 1996, Simmons, 1998, Angeli, 2001, Lovick and Angeli, 2004b), etc. Further attempt has been made by (Yang, 2003, Hasan, 2006, Yusoff, 2012) to investigate the effect of these flow parameters, including measurements of drop sizes through sudden pipe expansion.

Therefore, in other to consolidate in this line of investigation, this section will be focused on presentation of results and discussion of data collected based on measurements of drop size and drop size distribution in upwardly inclined large diameter (ϕ 127 mm) pipe through sudden expansion. The same experimental conditions for the horizontal flow were also applied in the upwardly inclined orientation. The inclination angles are +2 and +4 degrees respectively.

5.2.2.1 Effect of input oil volume fraction on SMD

Figure 5.22, 5.23 and 5.24 shows the influence of Sauter mean diameter (d_{32}), for downstream mixture velocity, U_{sme} = 0.20 ms^{-1}, within axial distances of test section in + 2^0 degrees upward pipe inclination orientation, probe positions 15.9 mm, 63.5mm and 111.3 mm from bottom of pipe at different oil volume fraction, OVF. From Figure 5.22 it can be seen that the Sauter mean diameter (SMD) of drop size distributions for 80% OVF increases downstream of the expansion at the various axial test distances at low downstream mixture velocity, U_{sme} 0.20m/s. Reverse is the case for flow conditions of 60% OVF and 20% OVF, where the Sauter mean diameter (SMD) of the drop sizes decreases gradually throughout the entire test section. Interestingly much smaller oil droplets are formed downstream of the singularity close to the mixed layer at top most part of the interface. Larger oil droplets are also noticed close to the mixed layer at the interface in the oil dispersed and water continuous phase flow condition of 40% OVF.

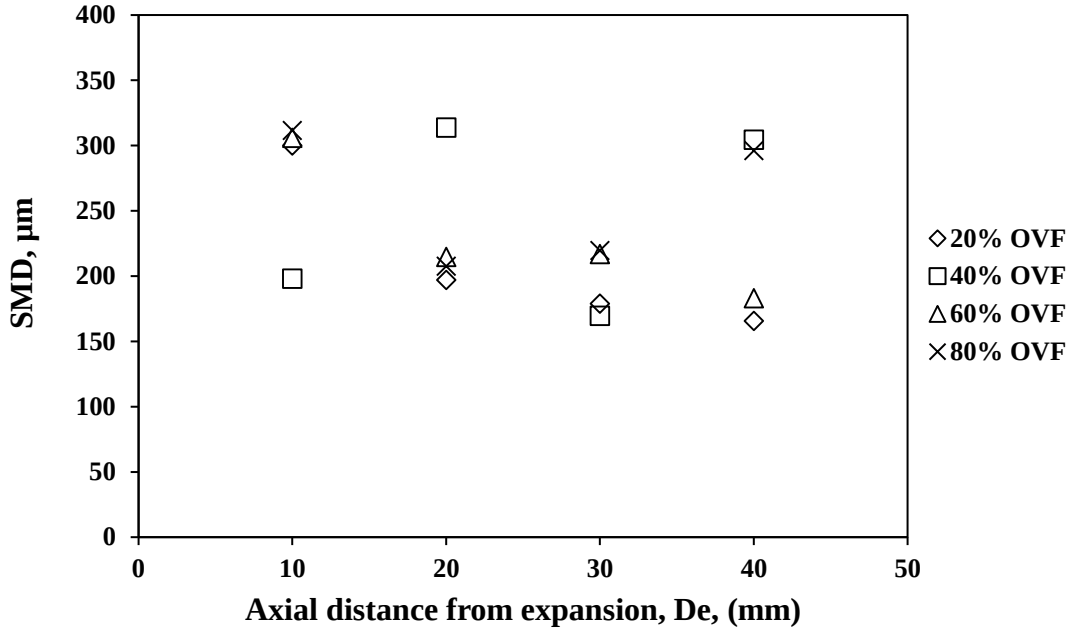

Figure 5-22 Sauter Mean Diameter (d_{32}), for downstream mixture velocity, U_{sme} = 0.20 ms^{-1}, within axial distances of test section in + 2^0 degrees upward pipe inclination orientation, probe position 15.9 mm from bottom of pipe at different oil volume fraction, OVF.

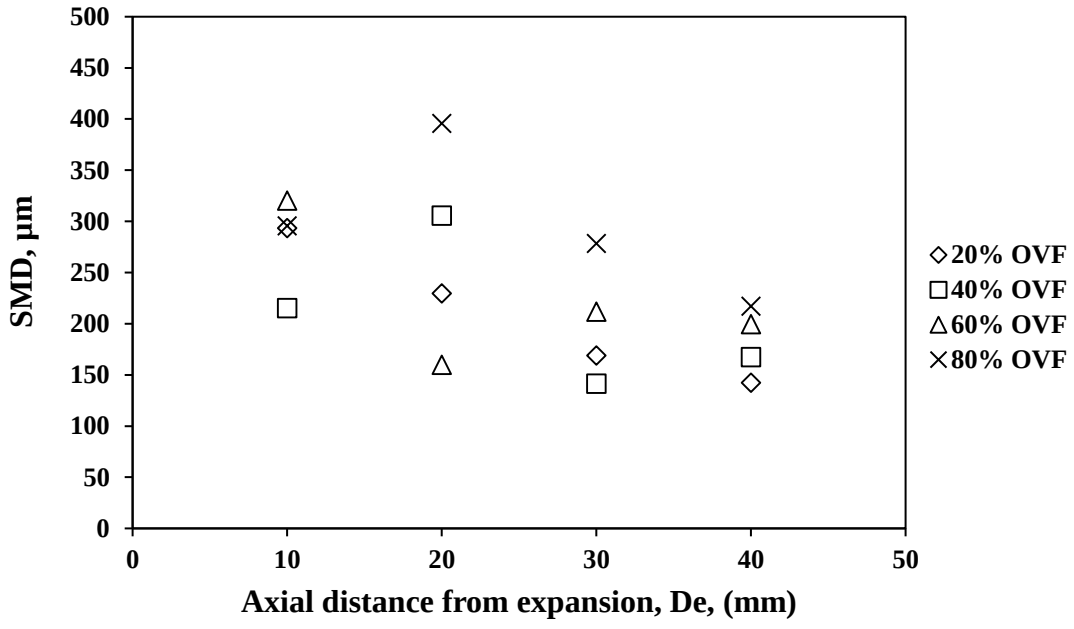

Figure 5-23 Sauter Mean Diameter (d_{32}), for downstream mixture velocity, U_{sme} = 0.20 ms^{-1}, within axial distances of test section in + 2^0 degrees upward pipe inclination orientation, probe position 63.5mm from bottom of pipe at different oil volume fraction, OVF.

The droplets formed are within the range of 165 µm to 313µm throughout the test section, with the largest drops close to the interface at the axial positons of 20D and 40D.

For the flow conditions shown in both Figures 5.23 and 5.24, it can be noticed generally that there is an obvious decrease in the Sauter mean diameter (SMD) throughout the entire axial test distance. This eventually results in the formation of smaller droplets downstream of the expansion, particularly at the 40D position. In the water dispersed and oil continuous flow system, 80% OVF, the water droplets are seen to be larger at the 20D positon and gradually decreases towards the downstream of the expansion as shown in Figure 5.23. Coalescence of droplets seems to have taken place right from the 10D position at the inlet upstream of the singularity. The flow condition presented in Figure 5.24 also indicates the presence of large droplets at the mixed layer interface at position 20D, but dominated by smaller and fine drops downstream of the pipe expansion. As can be seen much smaller droplets are found below the mixed layer of the interface in the 40% OVF system at positions 30D and 40D.

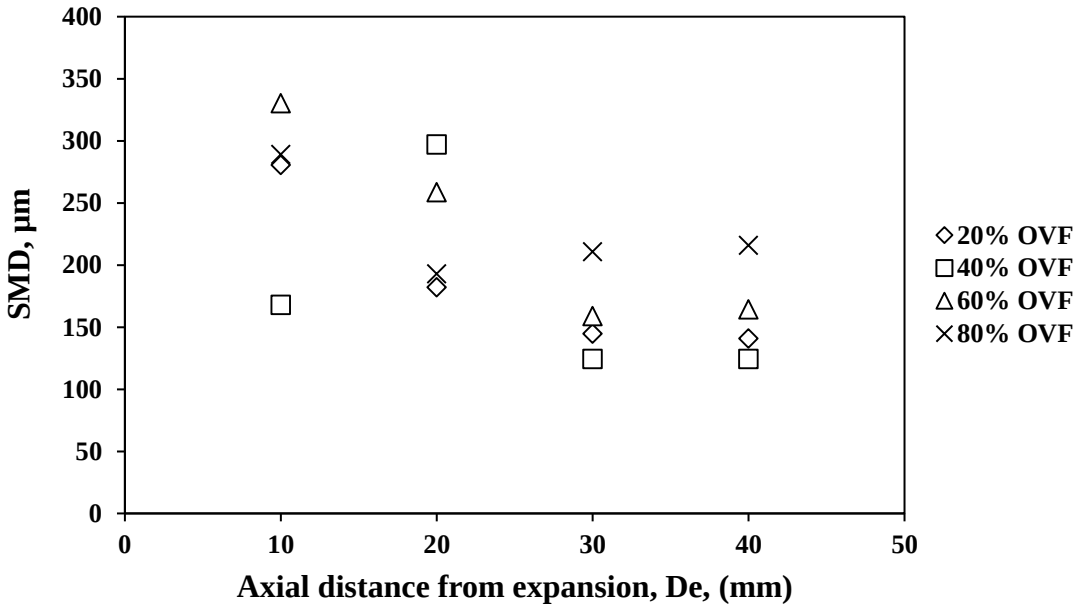

Figure 5-24 Sauter Mean Diameter (d_{32}), for downstream mixture velocity, U_{sme} = 0.20 ms^{-1}, within axial distances of test section in + 2^0 degrees upward pipe inclination orientation, probe position 111.3 mm from bottom of pipe at different oil volume fraction, OVF.

In Figure 5.24 it can be inferred that the larger water droplets detected by the laser in the water dispersed in oil continuous system, 80% OVF at positions 20D, 30D and 40D is as a result of onset of the coalescence of droplets at the 10D position in the inlet. As the flow progresses downstream of the singularity, these droplets merge to together and also with the bulk of the water layer at the bottom of the pipe, enhancing stratification.

5.2.2.2 Effect of mixture velocity

Figure 5.25 gives the Sauter mean diameter (SMD) for flow condition, 80% OVF, within axial distance of test section in + 2^0 degrees upward pipe inclination orientation, probe position, (15.9 mm) from bottom of pipe at different downstream mixture velocity, U_{sme}. There is a significant increase in Sauter mean diameter (SMD) of drop sizes along the various axial test positions for both downstream mixture velocity of 0.20 ms^{-1} and 0.35 ms^{-1} respectively. The droplets observed in the case of 0.25 ms^{-1}, seems to be of the same range, between 100 µm – 160 µm until 30D, where the drop sizes increases due to coalescence.

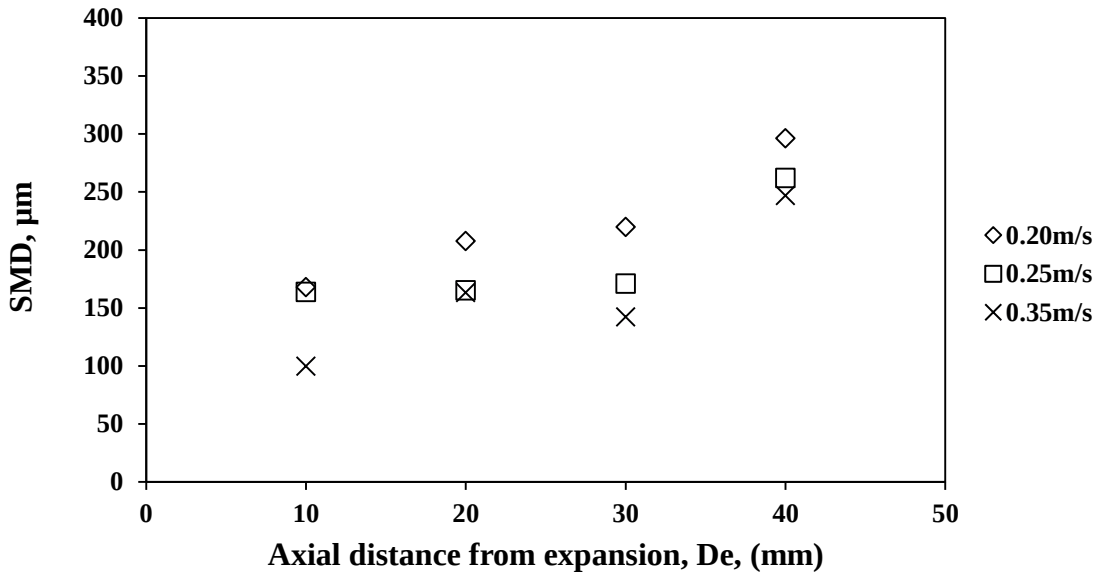

Figure 5-25 Sauter Mean Diameter (d_{32}) for flow condition, 80% OVF, within axial distance of test section in + 2^0 degrees upward pipe inclination orientation, probe position (15.9 mm) from bottom of pipe at different downstream mixture velocity, U_{sme}.

The influence of downstream mixture velocity, U_{sme}, on Sauter mean diameter (SMD) for flow conditions, 60% OVF and 40% OVF, within axial distance of test section in + 2^0 degrees upward pipe inclination orientation, probe position Centre (63.5mm) from bottom of pipe is presented in Figures 5.26 and 5.27. In general, it is noticed that a similar pattern of drop sizes formed is maintained in both cases of flow conditions at the different mixture velocities.

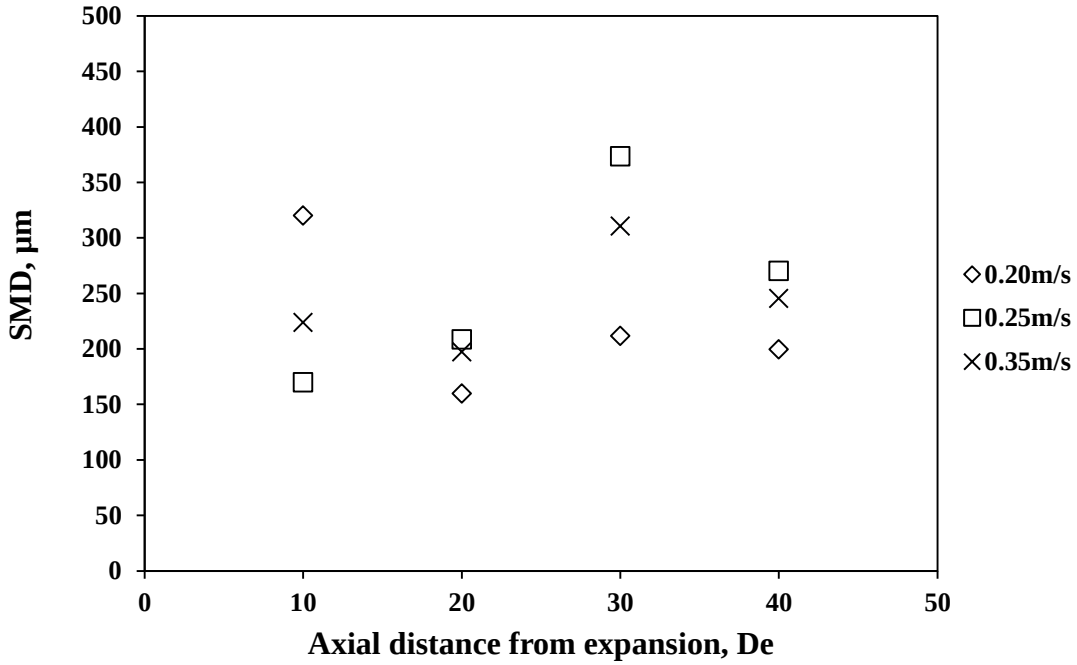

Figure 5-26 Sauter Mean Diameter (d_{32}) for flow condition, 60% OVF, within axial distance of test section in + 2^0 degrees upward pipe inclination orientation, probe position Centre (63.5 mm) from bottom of pipe at different downstream mixture velocity, U_{sme}.

This is expected as the probe is positioned at the mixed layer region at the interface, were the concentration of droplets is dense. The Sauter mean diameter (SMD) of droplets formed around this mixed layer region ranges from 150 µm to 380 µm and it is largest at the 30D and 20D positions in Figure 5.25 and Figure 5.26 respectively.

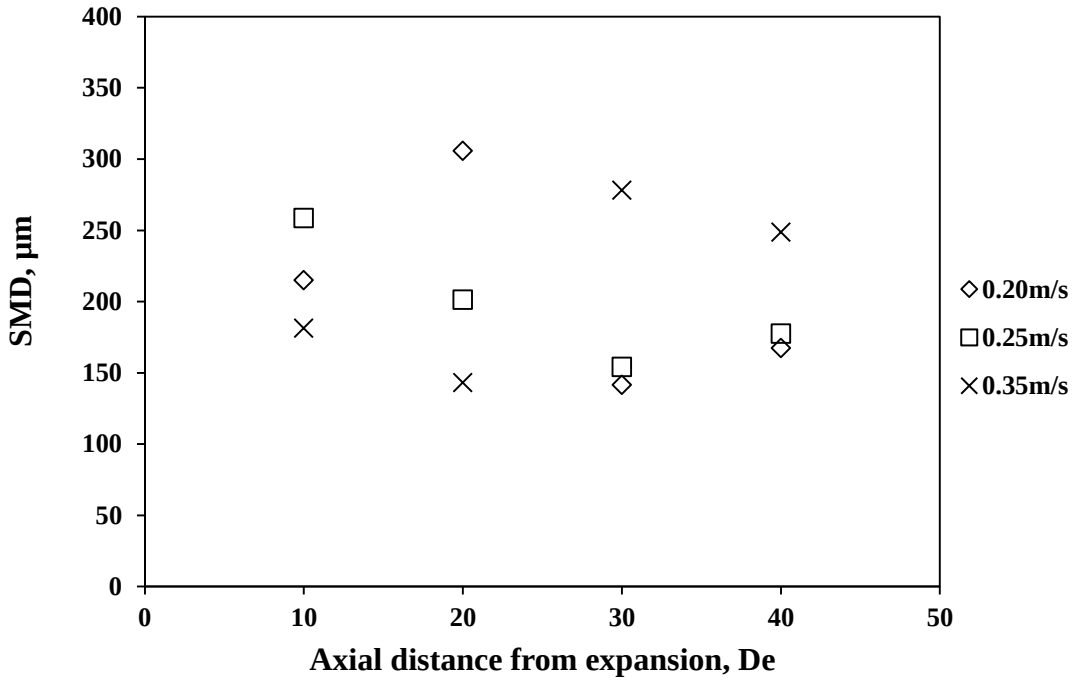

Figure 5-27 Sauter Mean Diameter (d_{32}) for flow condition, 40% OVF, within axial distance of test section in + 2^0 degrees upward pipe inclination orientation, probe position Centre (63.5 mm) from bottom of pipe at different downstream mixture velocity, U_{sme}.

The trend of Sauter mean diameter (SMD) of drops formed in the 20% OVF, oil dispersed in water continuous flow system is a little different as indicated in Figure 5.28. Much larger water droplets, 260µm and 306µm are formed at axial positions 30D and 40D respectively. It is interesting to also note that Sauter mean diameter (SMD) are found to be decreasing as the mixture flows towards the downstream part of the singularity for the 0.20 ms^{-1} and 0.25 ms^{-1} mixture velocities, respectively. This phenomenon was also observed in the work of (Yusoff, 2012) in a smaller pipe (ϕ 68mm) pipe.

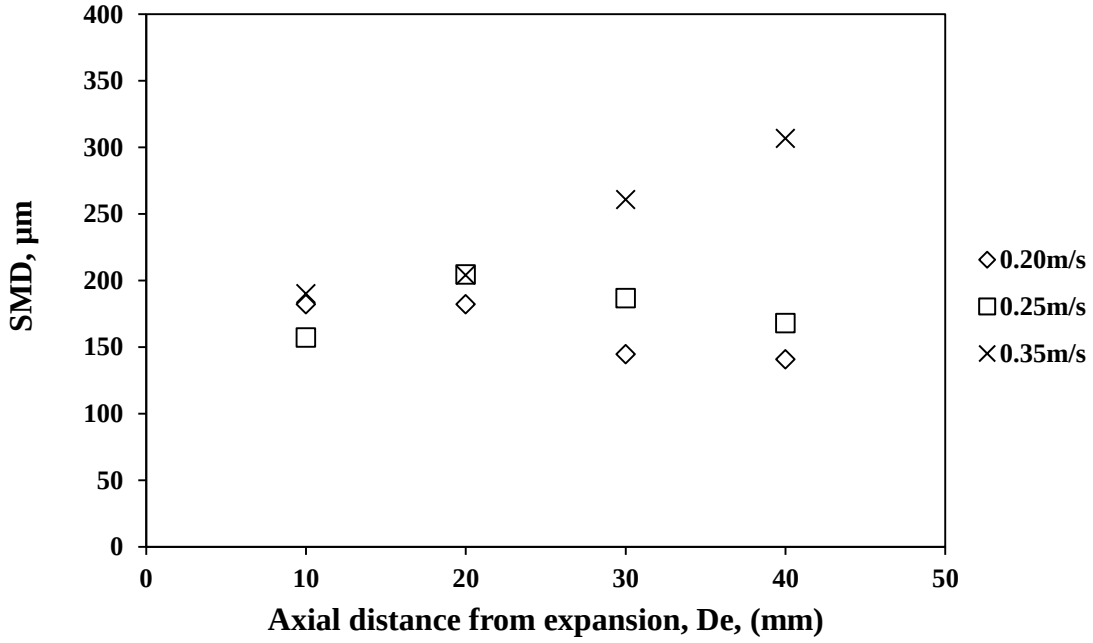

Figure 5-28 Sauter Mean Diameter (d_{32}) for flow condition, 20% OVF, within axial distance of test section in + 2^0 degrees upward pipe inclination orientation, probe position Top (111.3 mm) from bottom of pipe at different downstream mixture velocity, U_{sme}.

Figures 5.29, 5.30 and 5.31 shows the effect of downstream mixture velocity on Sauter Mean Diameter (d_{32}) for flow condition, at 10D axial distance of test section in + 2^0 degrees upward pipe inclination orientation, probe position (15.9 mm) from bottom at different input oil volume fraction.

It is clearly shown that the Sauter mean diameter (SMD) decreases with increasing downstream mixture velocity, resulting in the formation of finer droplets in all flow conditions except for the 80% OVF at the 40D axial positions in Figure 5.29. The production of finer droplets at higher downstream mixture velocity is an indication of the system becoming more dispersed, which impedes settling. This is expected as shear increases with increasing turbulence. The model proposed by (Sleicher, 1962) and the findings of (Yusoff, 2012), are in good agreement with the current results in this case of flow condition (see also section 5.4). As observed earlier in the case of horizontal pipe orientation in section 5.2.1.2, a similar phenomenon exist where at higher downstream mixture velocity, the droplet sizes becomes smaller.

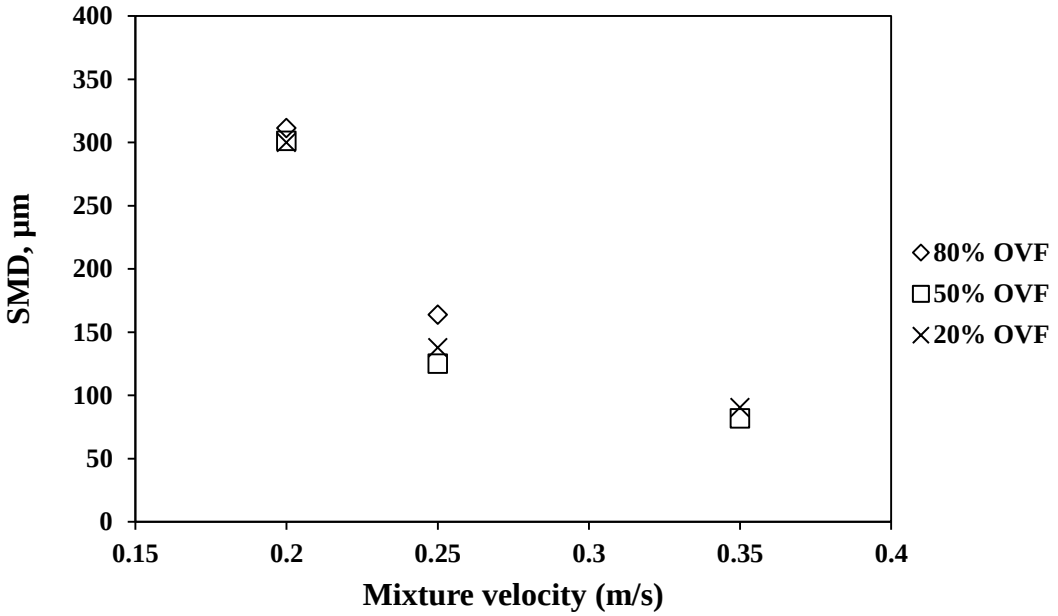

Figure 5-29 Effect of downstream mixture velocity on Sauter Mean Diameter (d_{32}) for flow condition, at 10D axial distance of test section in + 2^0 degrees upward pipe inclination orientation, probe position (15.9 mm) from bottom at different input oil volume fraction.

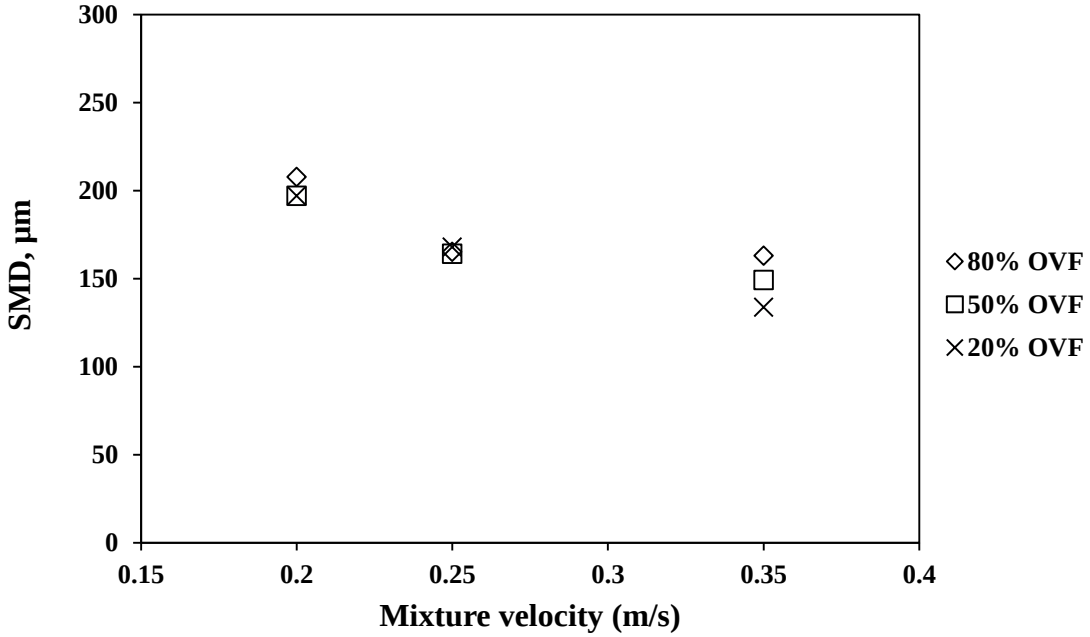

Figure 5-30 Effect of downstream mixture velocity on Sauter Mean Diameter (d_{32}) for flow condition, at 20D axial distance of test section in + 2^0 degrees upward pipe inclination orientation, probe position (15.9 mm) from bottom at different input oil volume fraction.

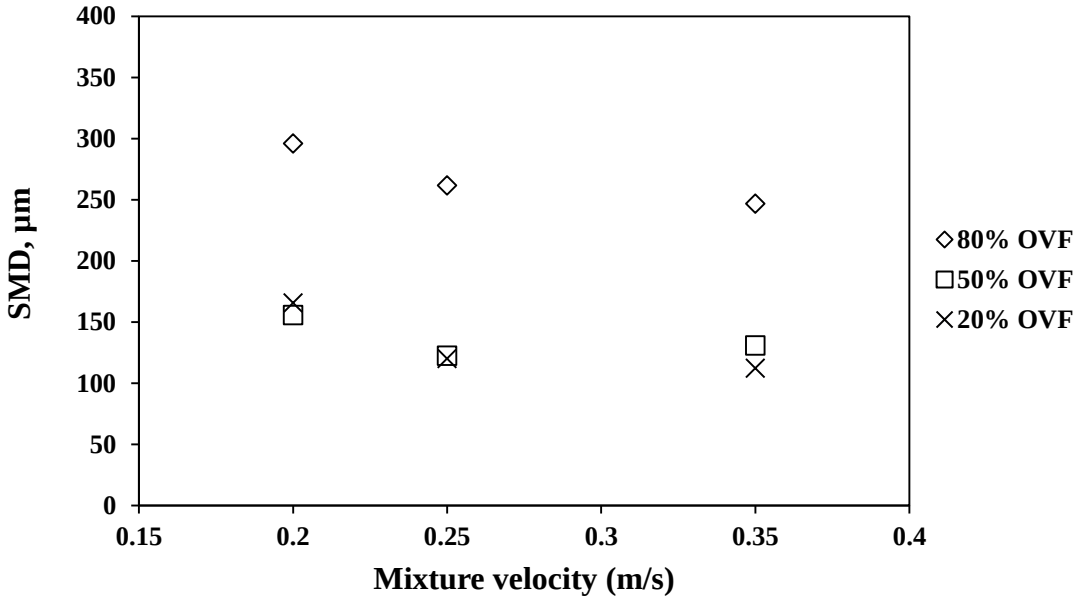

Figure 5-31 Effect of downstream mixture velocity on Sauter Mean Diameter (d_{32}) for flow condition, at 40D axial distance of test section in + 2^0 degrees upward pipe inclination orientation, probe position (15.9 mm) from bottom at different input oil volume fraction.

The larger SMD of water droplets seen in Figure 5.30 at both low mixture velocity 0.20 ms^{-1} and higher velocity 0.35 ms^{-1} is an indication of coalescence of the water droplets in the dispersed water in oil continuous flow condition 80% OVF.

5.2.2.3 SMD in mixed layer and vertical distance from interface

Figure 5.32 and 5.33 illustrates the measurement of Sauter mean diameter (SMD), as a function of interface height from pipe bottom for low mixture velocity, U_{sme} 0.20 ms^{-1} and higher mixture velocity U_{sme} 0.35 ms^{-1} respectively, and distance from expansion 40D in + 2^0 degrees upward pipe inclination, at different input oil volume fractions. As can be seen from Figure 5.32, the water droplets formed are larger at the top of interface than those at center of the mixed layer. This can be explained as a result of initial coalescence of droplets at the inlet upstream test section, and flows along the downstream section of pipe expansion. The equilibrium forces, especially the flow gravitational forces are split into two directions, i.e. acting perpendicularly or parallel to the pipe axis, in upwardly inclined orientation.

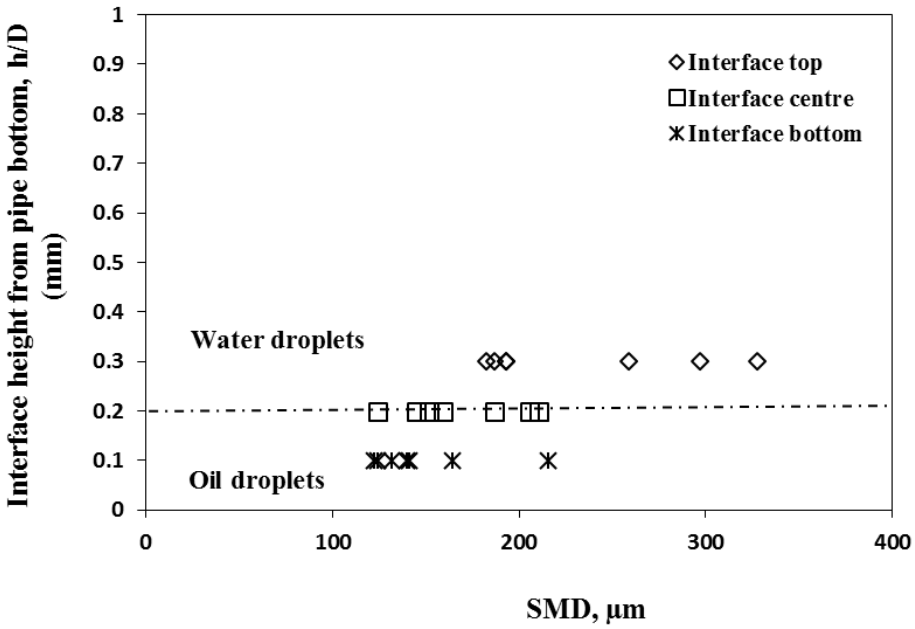

Figure 5-32 Sauter Mean Diameter (d_{32}), as a function of interface height from pipe bottom for mixture velocity, U_{sme} = 0.20 ms^{-1}, and distance from expansion 40D in + 2^0 degrees upward pipe inclination, for 80% OVF input oil volume fraction.

This implies that the normal gravitational force component enhances the setting of droplets towards the bulk layer of the respective fluids, while the parallel component acts against the liquid flow causing the formation of waves. There is also accumulation of oil layer at the top most part with faster flow than the water layer at the bottom due to these opposing forces in action. Figure 5.32 and 5.33 also illustrate the existence of both large and smaller droplets above and below the mixed layer region.

The phenomenon is also similar in the case of Figure 5.33 where measurements of Sauter mean diameter (SMD), are demonstrated as a function of interface height from pipe bottom for mixture velocity, U_{sme} 0.20 ms^{-1}, and distance from expansion 40D in + 2^0 degrees upward pipe inclination, at different input oil volume fractions. Clearly, smaller oil droplets and larger water droplets are formed in the 50% OVF flow condition. This shows that water droplets coalesce faster at the top forming larger ones than the oil droplets at the bottom region.

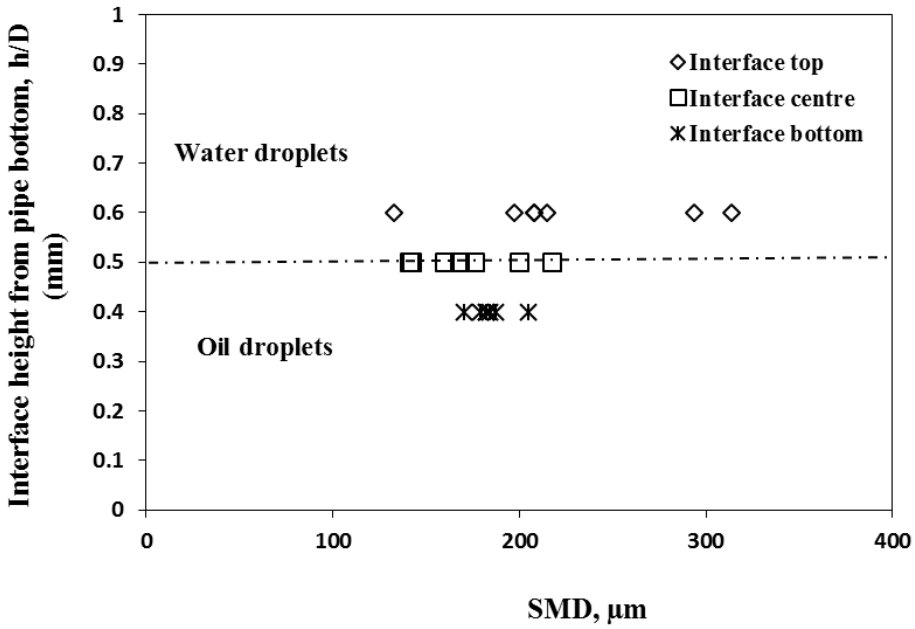

Figure 5-33 Sauter Mean Diameter (d_{32}), as a function of interface height from pipe bottom for mixture velocity, U_{sme} = 0.20 ms^{-1}, and distance from expansion 40D in + 2^0 degrees upward pipe inclination, for 50% OVF input oil volume fraction.

Figure 5.34, 5,35 and 5.36 also gives a demonstration of measurements obtained with Sauter mean diameter (SMD), as a function of the distance from the interface for input oil volume fraction 80% OVF, 50% OVF and 20% OVF respectively, and distance from expansion 40D in + 2^0 degrees upward pipe inclination orientation, at different downstream mixture velocities, U_{sme}.

From the results shown in Figure 5.34, a similar droplet size range is seen in both lower U_{sme} 0.20 ms^{-1}, and higher U_{sme} 0.35 ms^{-1}, downstream mixture velocity flow conditions respectively. When the downstream velocity is increased slightly from U_{sme} 0.20 ms^{-1} to U_{sme} 0.25ms^{-1}, much smaller oil droplets are formed close to the interface than the water droplets at the top in the 80% OVF flow system. This indicates dispersion of the oil droplets due to increase in turbulence forces in the system.

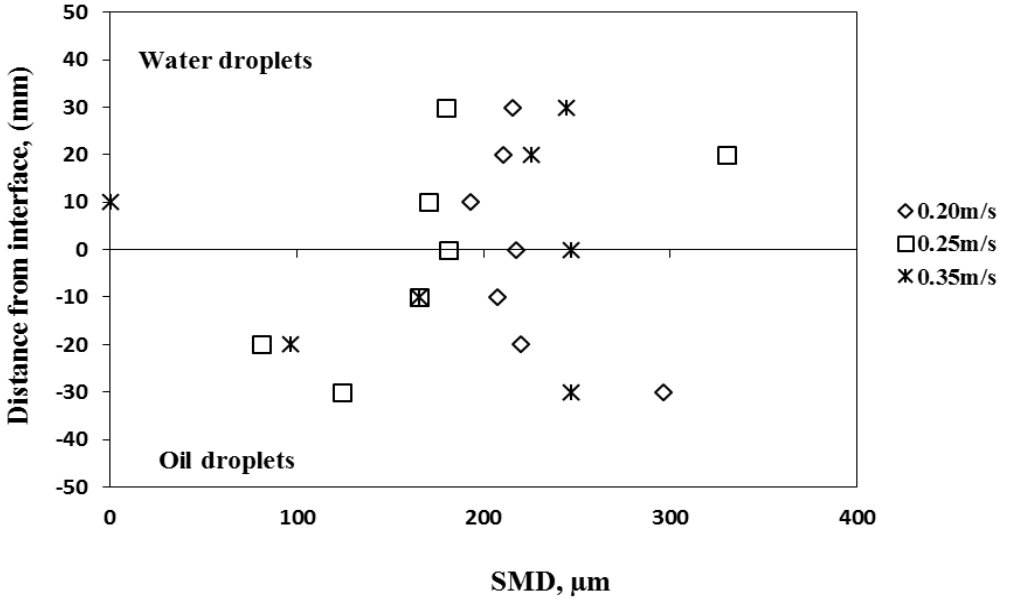

Figure 5-34 Sauter Mean Diameter (d_{32}), as a function of the distance from the interface for input oil volume fraction 80% OVF and distance from expansion 40D in + 2^0 degrees upward pipe inclination orientation, at different downstream mixture velocities, U_{sme}.

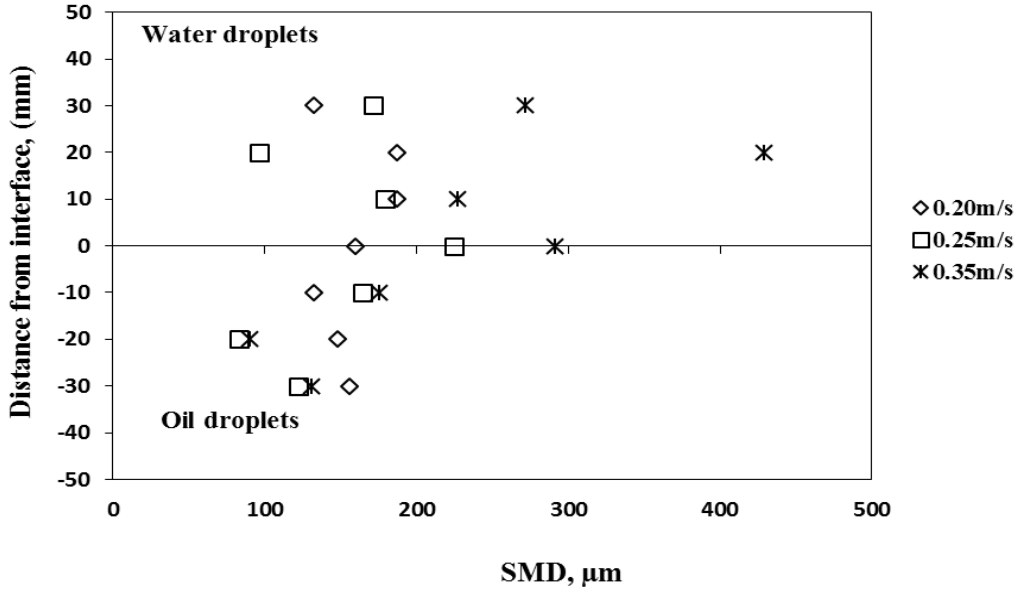

Figure 5-35 Sauter Mean Diameter (d_{32}), as a function of the distance from the interface for input oil volume fraction 50% OVF and distance from expansion 40D in + 2^0 degrees upward pipe inclination orientation, at different downstream mixture velocities, U_{sme}.

The scenario is different as can be seen from Figures 5.35 and 5.36. The water droplets are very large, within the range of between 200 µm – 450 µm at higher mixture velocity U_{sme} 0.35 ms^{-1} in both the 50% OVF and 20% OVF flow conditions. Interestingly, for the oil dispersed in water continuous flow system, 20% OVF, a gradual increase in velocity results in the formation of lager water droplets at the top and smaller oil droplets at the bottom. The frequency of collision and coalescence of droplets at the inlet entrance region appear to dominate the system resulting in the narrowing of the mixed layer downstream of the singularity. (Shinnar, 1961), had earlier established that in turbulent flow conditions, simultaneous coalescence and break-up occur. The droplets are exposed to both inertial forces due to velocity fluctuations, gravitational forces and to viscous shear forces.

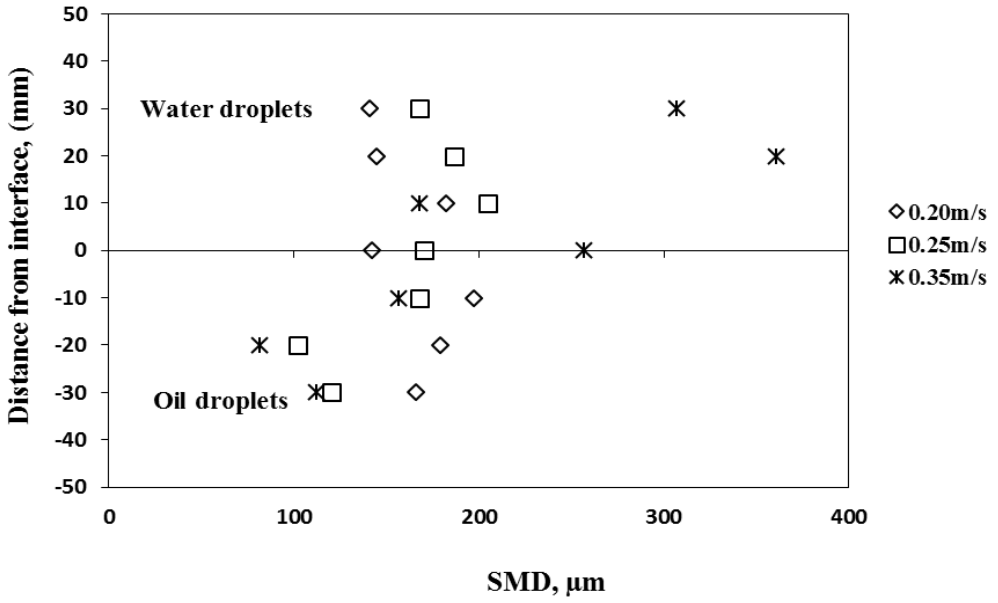

Figure 5-36 Sauter Mean Diameter (d_{32}), as a function of the distance from the interface for input oil volume fraction 20% OVF and distance from expansion 40D in + 2^0 degrees upward pipe inclination orientation, at different downstream mixture velocities, U_{sme}.

Larger droplets are formed in this case neglecting viscous forces, and droplets are found to oscillate about its spherical equilibrium shape concurrently with the surrounding fluid, provided the densities and viscosities of both liquids are constant. It can be concluded therefore that, upward inclined pipe orientation influences the

sizes of droplets formed and invariably the stratification process of two phase oil/water flow system.

5.2.2.4 Effect of probe position

The results of Sauter mean diameter (SMD), of oil droplets for downstream mixture velocity, U_{sme} 0.20 ms^{-1} for oil volume fraction 20% OVF, 50% OVF and 80% OVF in + 2^0 degrees upward pipe inclination orientation, at different probe positions from bottom to top portion of the pipe cross section is represented in Figures 5.37, 5.38 and 5.39.

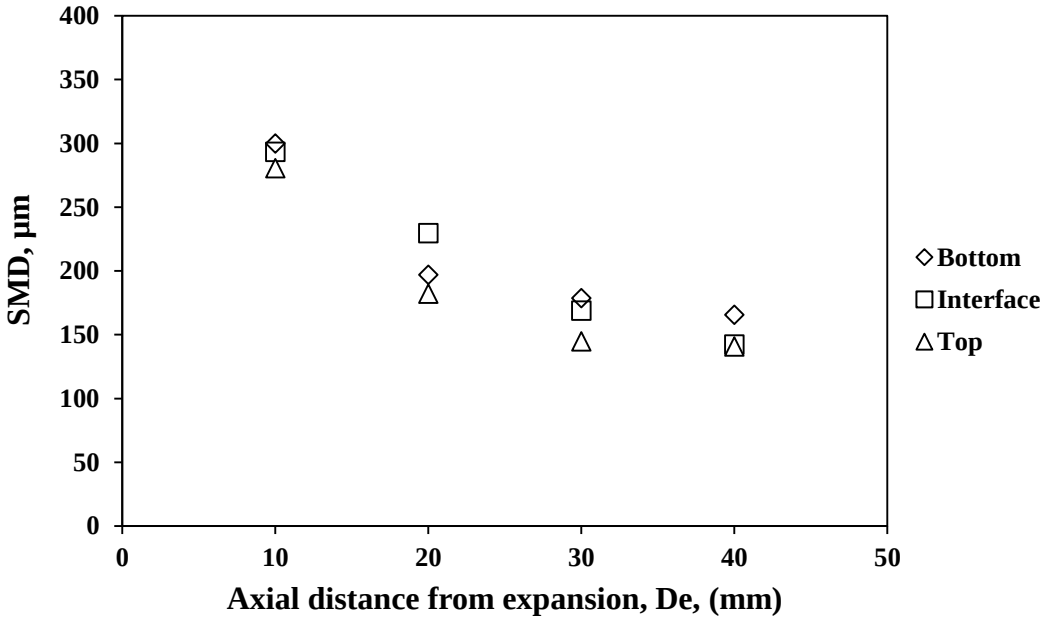

Figure 5-37 Sauter Mean Diameter (d_{32}), of oil droplets for mixture velocity, U_{sme} = 0.20 ms^{-1}, oil volume fraction 20% OVF in + 2^0 degrees upward pipe inclination, at different probe positions

The general trend of Sauter mean diameter (SMD) of droplet sizes indicated in Figure 5.37 with the various axial positions downstream of the expansion shows a significant decrease in the sizes. Quite interestingly, the size of droplet detected by the FBRM M500P laser are found to be within the same range considering the movement of laser from bottom to top position of the pipe cross section. The droplets created at the inlet part (upstream) of the test section, particularly axial position 10D, are larger in all

cases (Figure 5.37 and 5.38), except at the interface in axial position 20D in Figure 5.39. this also show clearly that coalescence of dispersed droplets progresses from the inlet position 10D and stratifies gradually downstream at 40D from the flow pattern mostly for both flow conditions 20% OVF and 50% OVF, at low downstream mixture velocity, U_{sme} 0.20 ms^{-1}. The Figure 5.38 also illustrates the existence of a mixture of both large and smaller droplets detected by the laser around the interface.

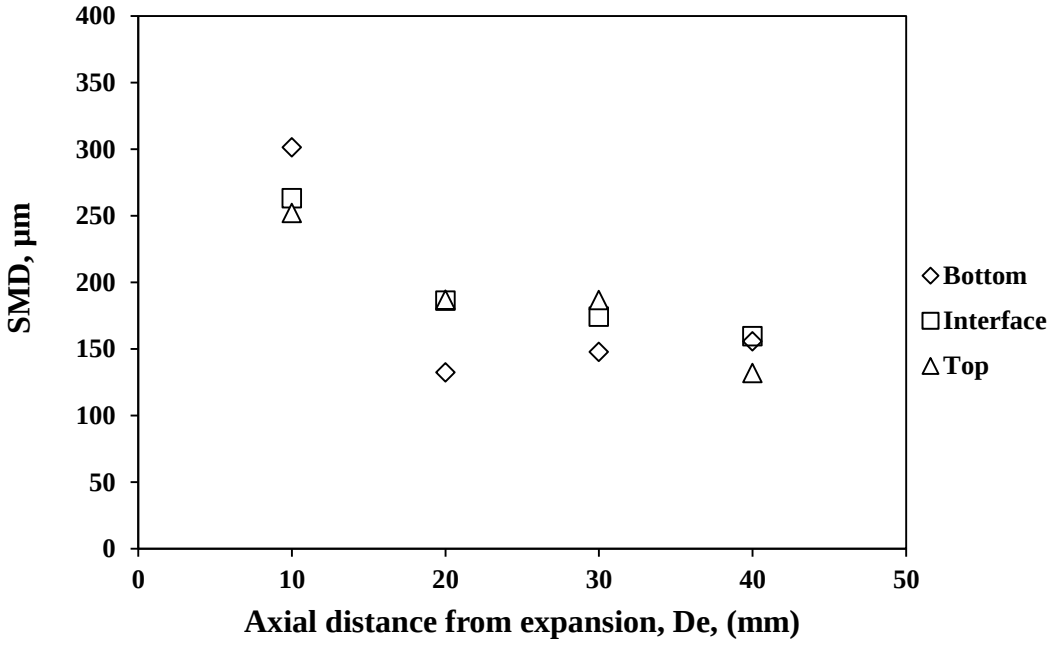

Figure 5-38 Sauter Mean Diameter (d_{32}), of oil and water droplets for mixture velocity, U_{sme} = 0.20 ms^{-1}, oil volume fraction 50% OVF in in + 2^0 degrees upward pipe inclination, at different probe positions

The trend of Sauter mean diameter (SMD) shown in Figure 5.39 is slightly different even though there is clearly, a progressive decrease at the axial distance in the singularity for interface and top positions, detected by the laser. The results obtained at axial position, 20D and 30D in Figure 5.39 shows that larger water droplets are detected at the mixed layer region compared to smaller droplets at bottom and top portion of the pipe, for the prevailing flow condition, 80% OVF. It can also be noticed that at 20D, the SMD has increased at the interface of the pipe cross section. The flow pattern is seen to stratify towards the interface at axial position 40D, as the droplets

travelled further downstream the expansion. This is an indication that at position 10D, coalescence of dispersed water droplets have taken place, hence these large droplets are detected further downstream of the expansion. Large droplets of water seen at the bottom in this location is probably due to earlier coalescence process as explained and drifting of these droplets towards the bulk of water layer by gravitational forces.

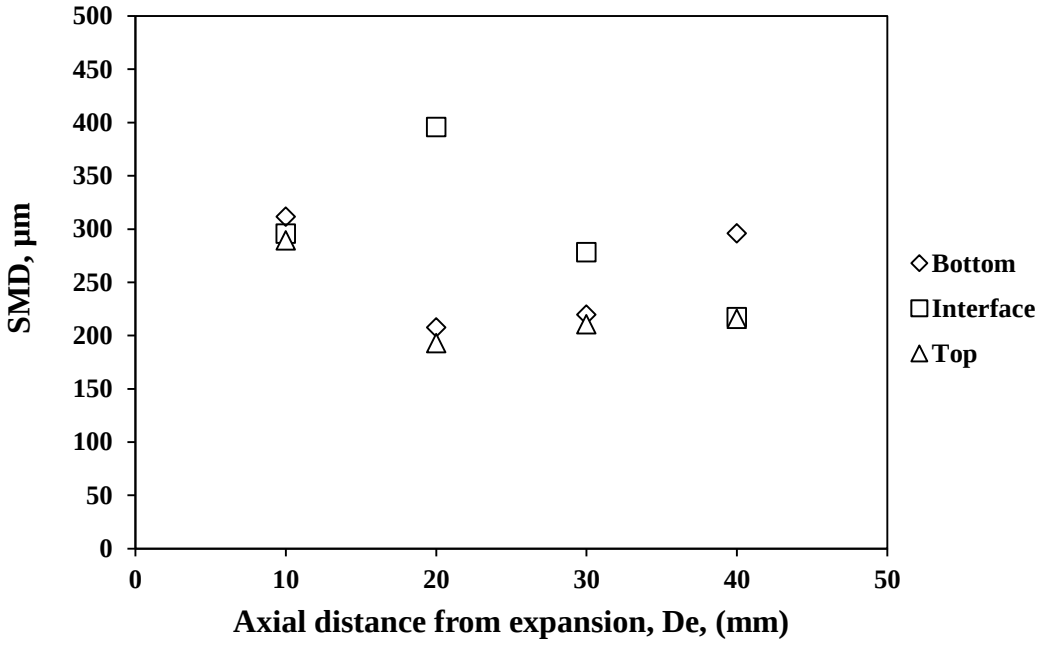

Figure 5-39 Sauter Mean Diameter (d_{32}), of water droplets for mixture velocity, U_{sme} = 0.20 ms^{-1}, oil volume fraction 80% OVF in in + 2^0 degrees upward pipe inclination, at different probe positions

The drops formed are shown to have the same sizes at the inlet position 10D, of SMD 300 µm. At this point there seems to be a homogeneous mixture of the two liquids flowing with same mixture velocity. Further downstream of the expansion, similar drop sizes are maintained for the top and bottom portions in the pipe cross section at the 20D and 30D positions. Also due to increase in frequency of collision and coalescence of droplets at the bottom 15.9 mm, the SMD is seen to increase.

The following summarizes the findings for the SMD in the upward inclination:

- Input oil volume fraction affects the Sauter mean diameter (SMD) of drops throughout the entire axial test distance resulting in the formation of smaller droplets at low mixture velocity (0.20 ms^{-1}).

- Smaller droplet sizes are formed downstream of the pipe expansion with an increase in downstream mixture velocity.

- Sauter mean diameter (SMD) is affected by probe position. Larger droplets were observed above and below the interface region.

- Water droplets coalesce and settle faster than dispersed oil droplet in water continuous phase flow system. The bulk oil layer was also observed to flow faster at the top than the bulk water layer at the bottom in upward pipe inclination orientation.

5.2.3 Drop size in downwardly inclined flow

Sauter mean diameter (SMD) measurements were taken for drop diameter distribution in two-phase oil-water flow in downward inclined pipe flow, which were carried out in the same experimental conditions as in the previous section. Because of limited time frame for the project, the angles of downward inclination flow that was investigated are -2^0 and -4^0 degrees respectively. The influence of downward inclination flow on evolution of drop size distributions is presented in the preceding subsections.

5.2.3.1 Effect of input oil volume fraction

Figures 5.40, 5.41 and 5.42 gives an illustration of the effect of different input oil volume fraction on Sauter Mean Diameter (SMD), for downstream mixture velocity, Usme = 0.20 ms^{-1}, within axial distances of test section in -2^0 degrees downward pipe inclination orientation, for probe positions bottom (15.9 mm), Centre (63.5 mm) and Top (111.3 mm) from bottom of pipe. Interestingly, in all experimental conditions, the droplets sizes are found to fall within the same range between 100µm - 300µm SMD.

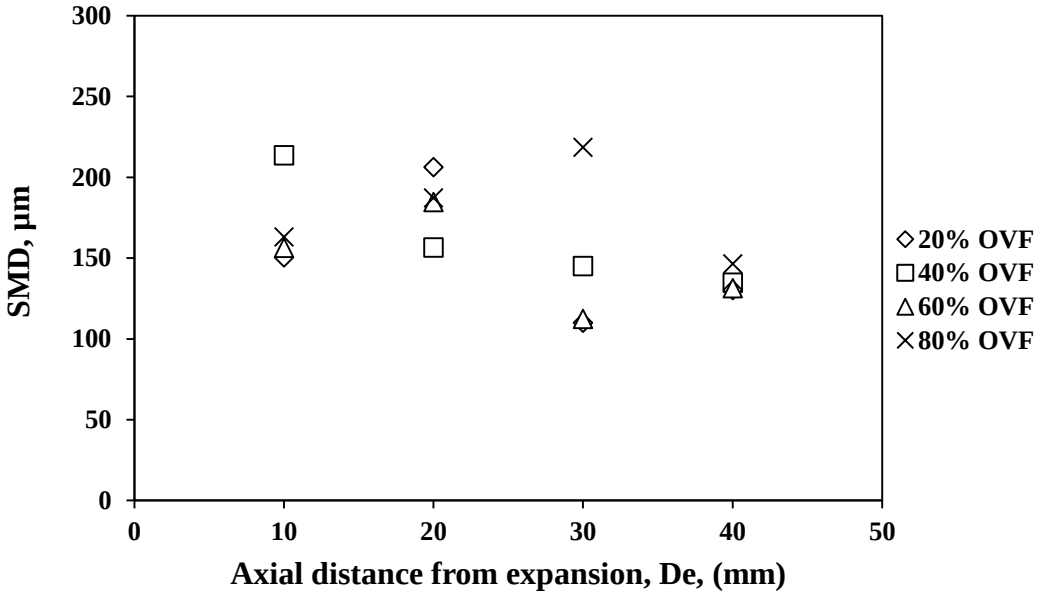

Figure 5-40 Sauter Mean Diameter (d_{32}), for downstream mixture velocity, U_{sme} = 0.20 ms^{-1}, within axial distances of test section in - 2^0 degrees downward pipe inclination orientation, probe position 15.9 mm from bottom of pipe at different oil volume fraction, OVF.

In Figure 5.40, where the probe position is fixed at the bottom portion of the pipe cross section, there is an indication of stratification towards the mixed interface region of the interface at axial position 40D downstream of the expansion. The coalesced oil and water droplets in both the oil dispersed system (20% OVF) and water dispersed system (80% OVF), at the entrance axial position 10D seems to drift towards the interface as the flow progresses downstream of the singularity. However, at position 30D, there is a noticeable increase in water droplets in the 80% OVF flow condition detected by the laser. As explained above, these are coalesced larger water drops at the inlet drifting towards the mixed interface due to the action of buoyance and drag forces.

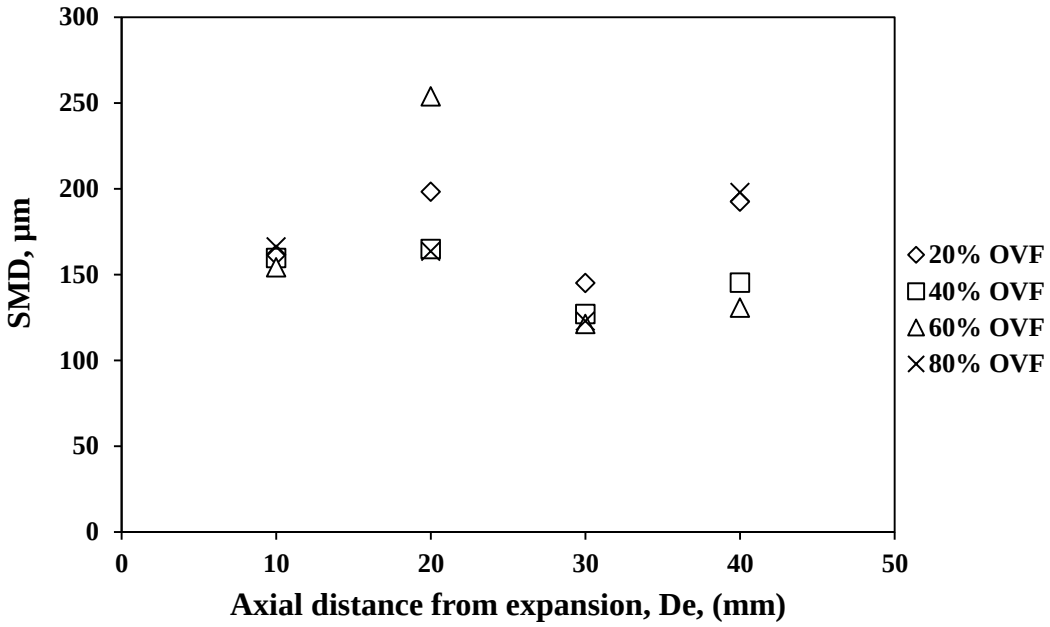

Figure 5-41 Sauter Mean Diameter (d_{32}), for downstream mixture velocity, U_{sme} = 0.20 ms^{-1}, within axial distances of test section in - 2^0 degrees downward pipe inclination orientation, probe position 63.5mm from bottom of pipe at different oil volume fraction, OVF.

Again, in a downward inclined pipe orientation, the gravitational force field is divided normally and parallel along the flow direction. The oil layer at the top was seen to flow faster than the water layer at the bottom part of the pipe. This phenomenon is explained further in sections 6.5, of Chapter 6.

The droplets formed close to the mixed layer in Figure 5.41 at the interface in position 10D are of the same sizes, which is maintained up to position 40D downstream of the expansion except at position 20D. Here, larger water droplets are detected by the laser equipment in the dispersed water and oil continuous flow condition 60% OVF. On the other hand, both the oil and water droplets become larger further down the singularity at position 40D for the 20% OVF and 80% OVF systems respectively, at low downstream mixture velocity U_{sme}, 0.20m/s.

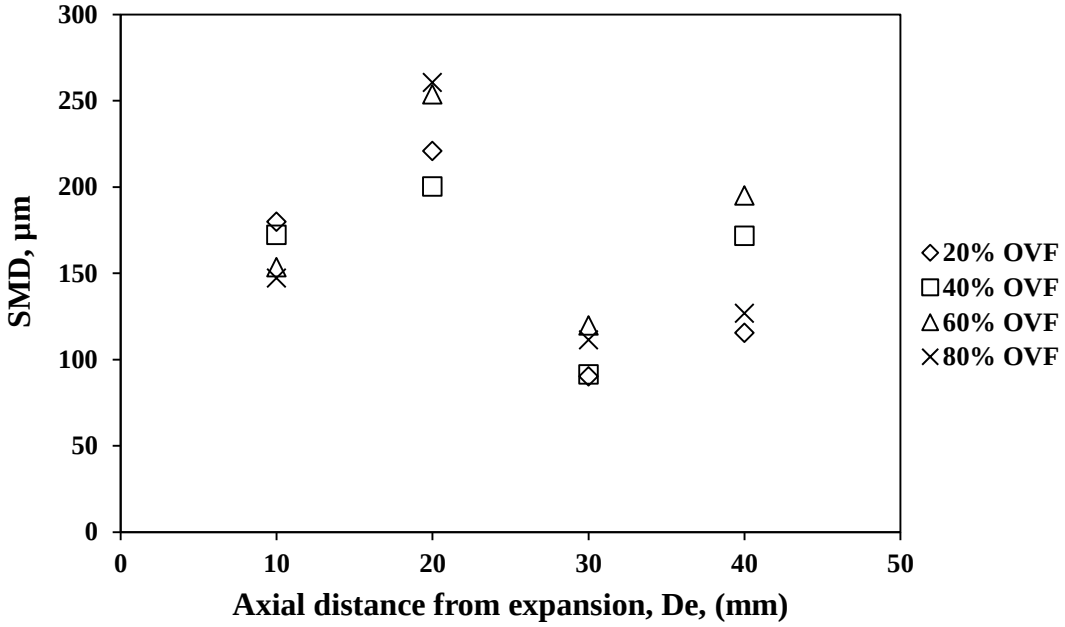

Figure 5-42 Sauter Mean Diameter (d_{32}), for downstream mixture velocity, U_{sme} = 0.20 ms^{-1}, within axial distances of test section in - 2^0 degrees downward pipe inclination orientation, probe position 111.3 mm from bottom of pipe at different oil volume fraction, OVF.

Similar trend of SMD of drop size formation is observed in Figure 5.42. However, clearly in this case, it is noticed that in spite of almost same sizes of droplets formed at the interface, the drops become bigger towards the mixed layer at the interface in position 40D, downstream of the expansion for both 40% OVF and 60% OVF flow condition. This indicates the sifting of the mixed region (interface level), as predicted according to the model of (Taitel and Dukler, 1976), that pipe inclination will affect the interface level between the two phases for the ST regime flow pattern.

5.2.3.2 Effect of mixture velocity

The influence of downstream mixture velocity U_{sme} on Sauter Mean Diameter (SMD) for flow condition, 80% OVF, within axial distance of test section in - 2^0 degrees downward pipe inclination orientation, probe position (15.9 mm) from bottom of pipe is presented as shown in Figure 5.43. In general, there is an increase in SMD of droplet

sizes along the axial position when the downstream velocity is gradually increased from U_{sme} 0.20m/s to 0.35m/s.

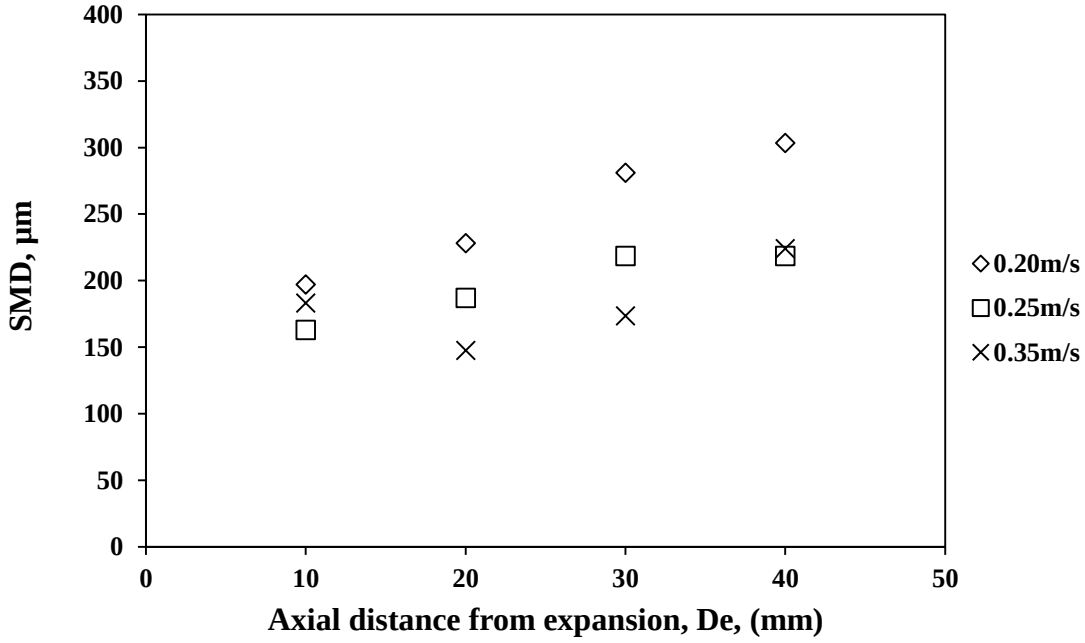

Figure 5-43 Sauter Mean Diameter (d_{32}) for flow condition, 80% OVF, within axial distance of test section in - 2^0 degrees downward pipe inclination orientation, probe position (15.9 mm) from bottom of pipe at different downstream mixture velocity, U_{sme}.

This is a similar occurrence to that of upward pipe inclination as was observed and discussed earlier, were the SMD increases with velocity. It signifies that larger droplets are formed and concentrated at the bottom (15.9 mm) portion of the pipe at 40D. However, it can also be seen that smaller and finer water drop sizes are detected by the FBRM M500P laser for the 80% OVF system at position 30D at high downstream mixture velocity 0.35m/s.

Figure 5.44 shows a demonstration of the Sauter mean drops diameter (SMD) at Centre (63.5mm) of the pipe cross section for – 2^0 degrees downward pipe inclination at 60% OVF input oil volume fraction for various U_{sme}, Clearly, it is found that there is a significant increase in SMD of droplet sizes recorded when the downstream mixture velocity is 0.35 ms^{-1} along the entire test section. This not the case at low velocities of 0.20 ms^{-1} and 0.25ms^{-1}, as no obvious trend is recorded in the various

axial positions. Both big and small droplets exist at the mixed interface region due to coalescence at position 10D. The droplets formed at this position are almost the same with approximately 185µm SMD of drop sizes.

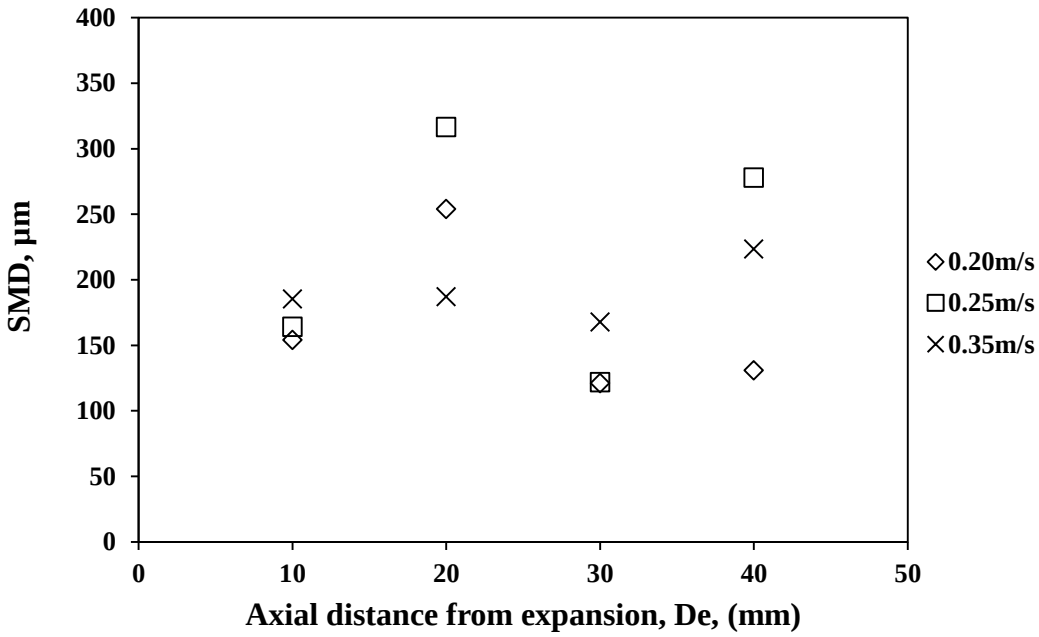

Figure 5-44 Sauter Mean Diameter (d_{32}) for flow condition, 60% OVF, within axial distance of test section in - 2^0 degrees downward pipe inclination orientation, probe position Centre (63.5 mm) from bottom of pipe at different downstream mixture velocity, U_{sme}.

A further movement of the FBRM M500P laser probe below the interface (63.5mm), for flow condition 40% OVF, records a difference in the trend as shown in Figure 5.45. A general downward trend of the Sauter mean diameter (SMD) is observed after initial coalescence at position 10D, resulting in the creation of larger drops at 20D, for all downstream mixture velocities. From this point further downstream of the test section, shows a decrease in Sauter mean diameter (SMD) at all mixture velocities. Interestingly, these droplets accumulate around the interface at position 40D down the expansion, showing the narrowing and stratification of the two phase oil-water flow system.

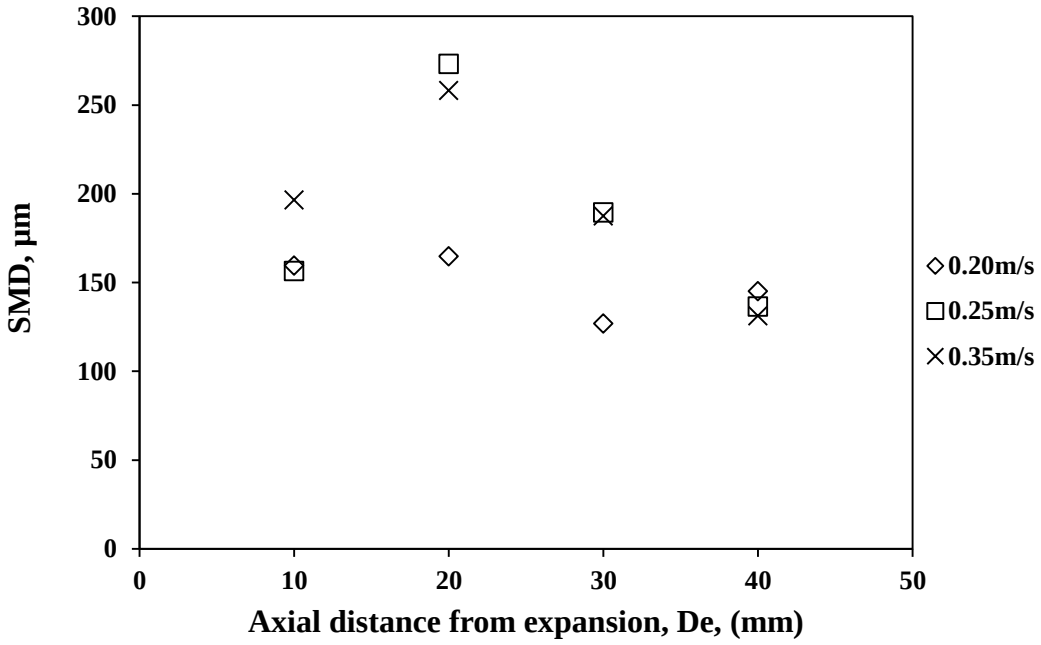

Figure 5-45 Sauter Mean Diameter (d_{32}) for flow condition, 40% OVF, within axial distance of test section in - 2^0 degrees downward pipe inclination orientation, probe position Centre (63.5mm) from bottom of pipe at different downstream mixture velocity, U_{sme}.

When the FBRM M500P laser probe is moved to the top (111.3 mm) portion in the pipe cross section as shown in Figure 5.46, there is no clear pattern of how the droplets are formed along the pipe test section from inlet to the downstream part of the expansion. This shows that there is not much influence of downstream mixture velocity on the Sauter mean diameter (SMD), with respect to the prevailing flow condition of input oil volume fraction 20% OVF. The formation of smaller and finer oil droplets found at axial position 30D can be attributed to increased frequency of collision due to increased turbulence in the pipe as the mixture velocity is changed. However, these droplets are found to be larger at the 40D test position for the various downstream mixture velocities.

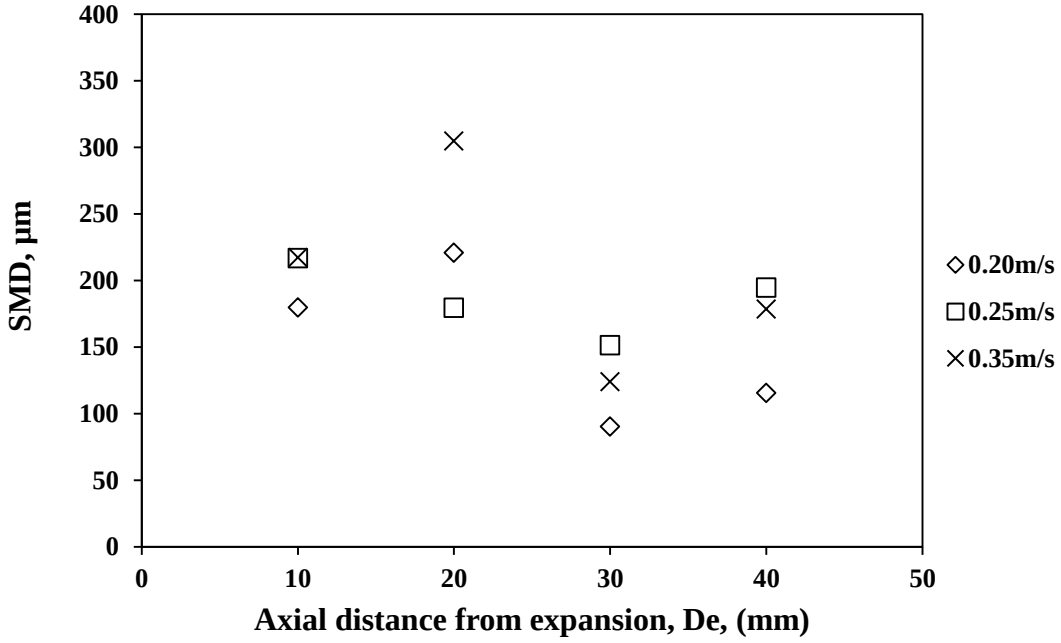

Figure 5-46 Sauter Mean Diameter (d_{32}) for flow condition, 20% OVF, within axial distance of test section in - 2^0 degrees downward pipe inclination orientation, probe position Top (111.3 mm) from bottom of pipe at different downstream mixture velocity, U_{sme}.

Figures 5.47, 5.48 and 5.49 shows the effect of downstream mixture velocity on Sauter mean diameter (d_{32}) for flow condition, at 10D axial distance of test section in – 2^0 degrees downward pipe inclination orientation and probe position (15.9 mm) from bottom at different input oil volume fraction.

It is clearly shown that the Sauter mean diameter (SMD) increases with increasing downstream mixture velocity, resulting in the formation of bigger droplets in all flow conditions for the 20% OVF, 50% OVF and 80% OVF, systems throughout the entire test axial positions as represented in Figure 5.47. This observation is quite different, compared to what was obtained previously, for same experimental condition in both the horizontal and upward inclined pipe orientation, were the Sauter mean diameter (SMD) decreases with increasing mixture velocity.

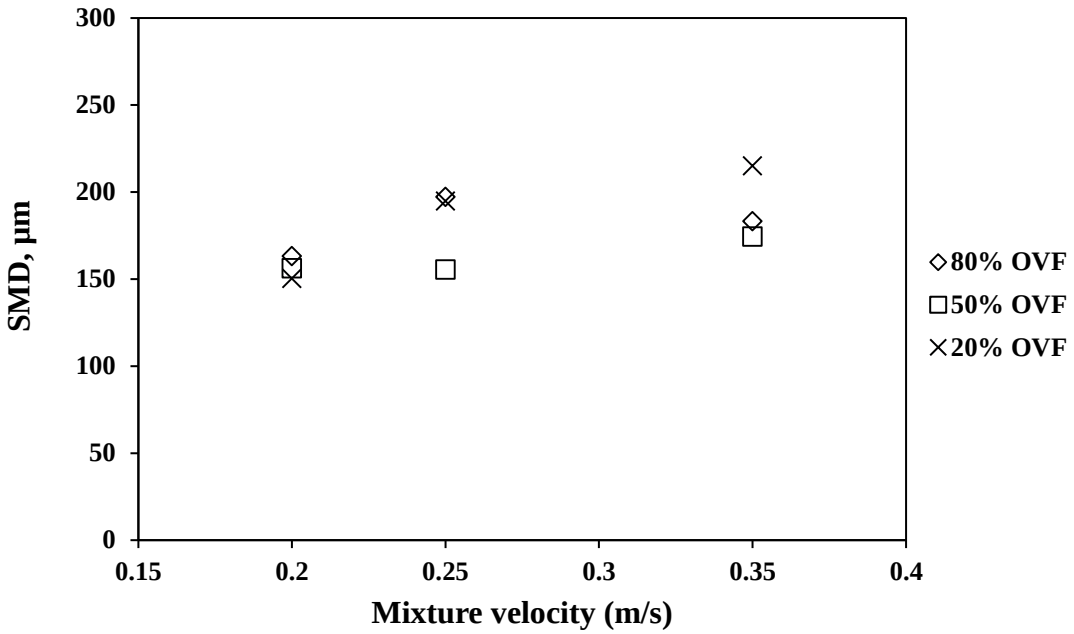

Figure 5-47 Effect of downstream mixture velocity on Sauter Mean Diameter (d_{32}) for flow condition, at 10D axial distance of test section in - 2^0 degrees downward pipe inclination orientation, probe position (15.9 mm) from bottom at different input oil volume fraction.

The influence of downstream mixture velocity on the Sauter mean diameter (SMD) for flow condition, at 20D axial distance of test section in – 2^0 degrees downward pipe inclination orientation, probe position (15.9mm) from bottom at different input oil volume fraction is presented as shown in Figure 5.47. At 20D axial position downstream of the expansion, it is noticed that there is an increase in the size of oil droplets for the 20% OVF system as the downstream mixture velocity is increased. These larger drops could be as a result of initial coalescence of dispersed oil droplets at the inlet upstream, and carried along the flow direction towards the downstream part of the singularity. The flow conditions for both 50% OVF and 80% OVF are seen to increase initially in SMD and slightly decreases as the velocity increases. At higher mixture velocity, U_{sme}, the coalescence of droplets seems to be minimal due to less residence time for drop collision, even though more drops are expected to be created with increase in velocity.

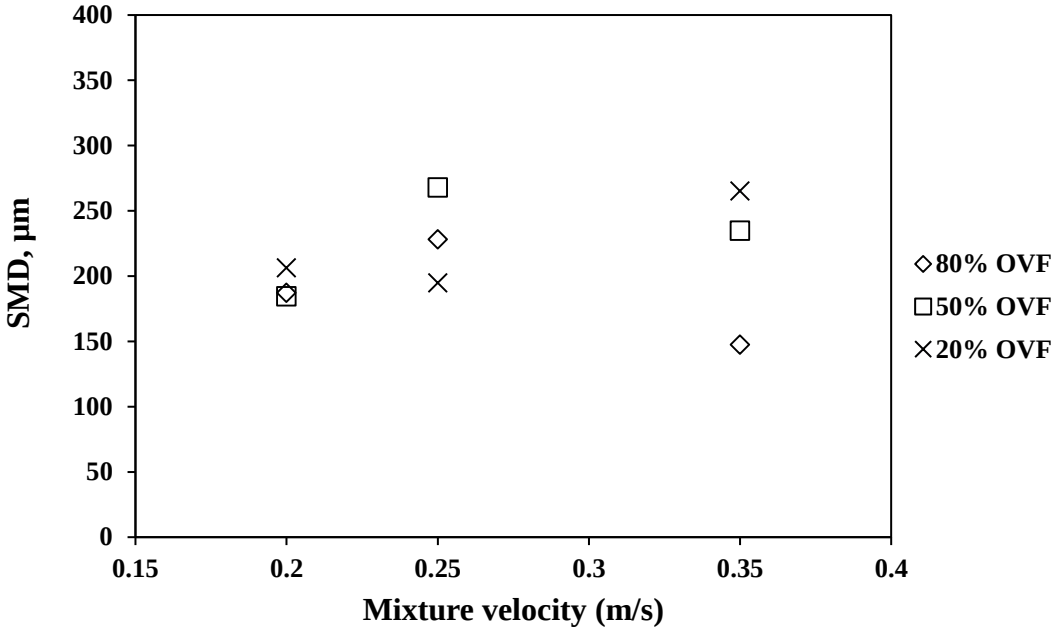

Figure 5-48 Effect of downstream mixture velocity on Sauter Mean Diameter (d_{32}) for flow condition, at 20D axial distance of test section in - 2^0 degrees downward pipe inclination orientation, probe position (15.9 mm) from bottom at different input oil volume fraction.

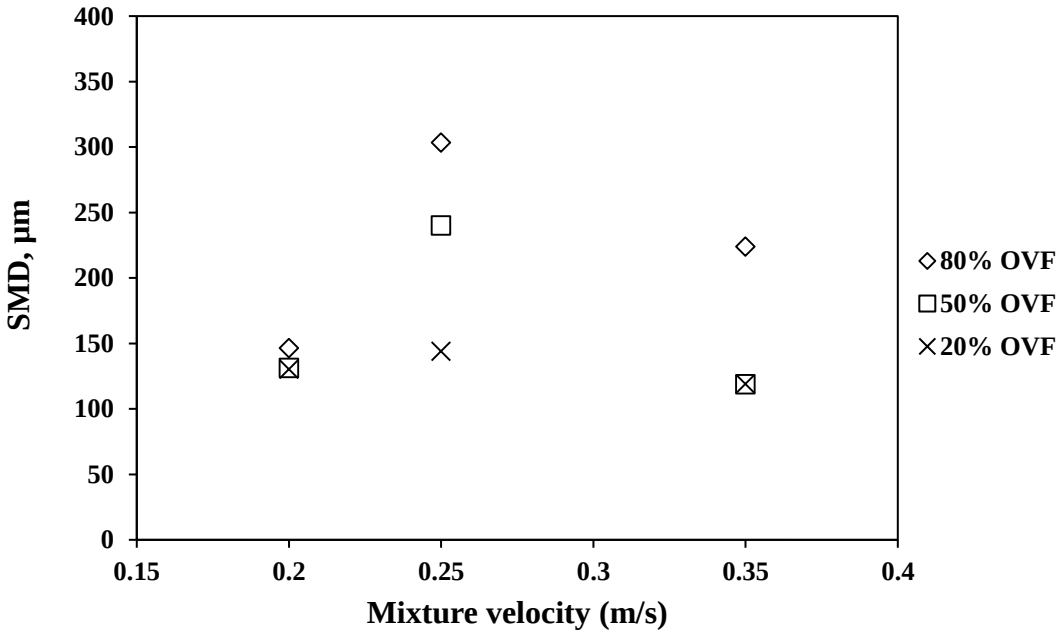

Figure 5-49 Effect of downstream mixture velocity on Sauter Mean Diameter (d_{32}) for flow condition, at 40D axial distance of test section in - 2^0 degrees downward pipe inclination orientation, probe position (15.9 mm) from bottom at different input oil volume fraction.

Interestingly, at position 40D further downstream of the expansion, the phenomenon is clearer as shown in Figure 5.49. Much smaller and finer droplets are created at this position, indicating the coalescence of medium size droplets around the mixed interface region close to the bottom portion of the pipe.

5.2.3.3 SMD in mixed layer and vertical distance from interface

Figure 5.50 and 5.51 illustrates the results obtained from measurement of Sauter mean diameter (SMD), as a function of the distance from the interface for low mixture velocity, Usme 0.20 ms^{-1} and distance from expansion 40D in – 2^0 degrees downward pipe inclination, at 80% OVF and 50% OVF input oil volume fractions, respectively. From Figure 5.50, the droplets formed ranges between 100 µm – 300 µm. It is also noticed that smaller oil and water drops are formed in both the 80% OVF and 50% OVF flow conditions.

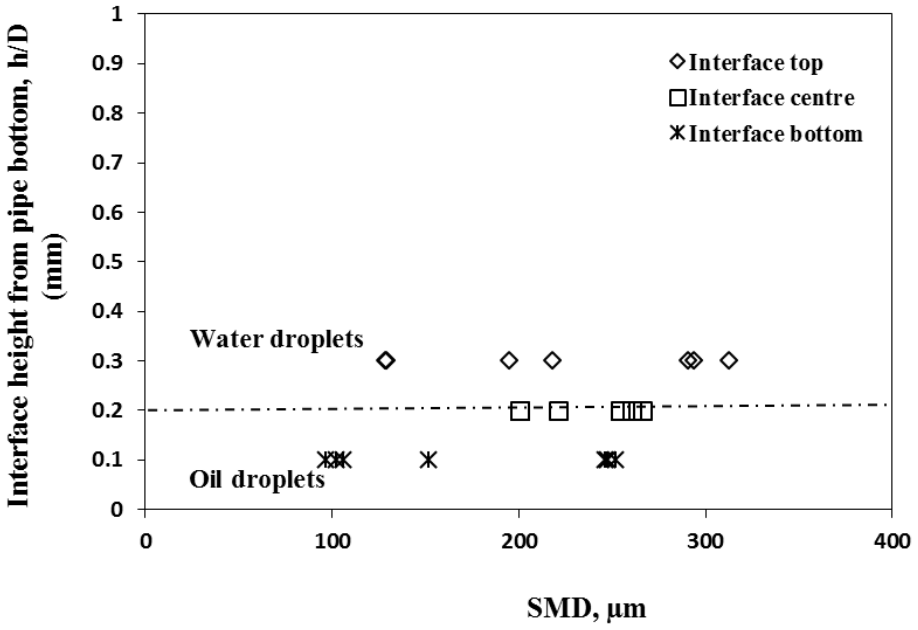

Figure 5-50 Sauter Mean Diameter (d_{32}), as a function of interface height from pipe bottom for mixture velocity, U_{sme} = 0.20 ms^{-1}, and distance from expansion 40D in - 2^0 degrees downward pipe inclination, for 80% OVF input oil volume fraction..

A further increase in downstream mixture velocity causes the generation of both larger oil and water droplets below and above the mixed interface region at the 40D position for the 20% OVF flow condition. This shows that at higher downstream mixture velocity, U_{sme} 0.35 ms^{-1}, both oil and water droplets coalesce faster at the top and bottom forming larger ones and accumulate around the interface as the flow progresses.

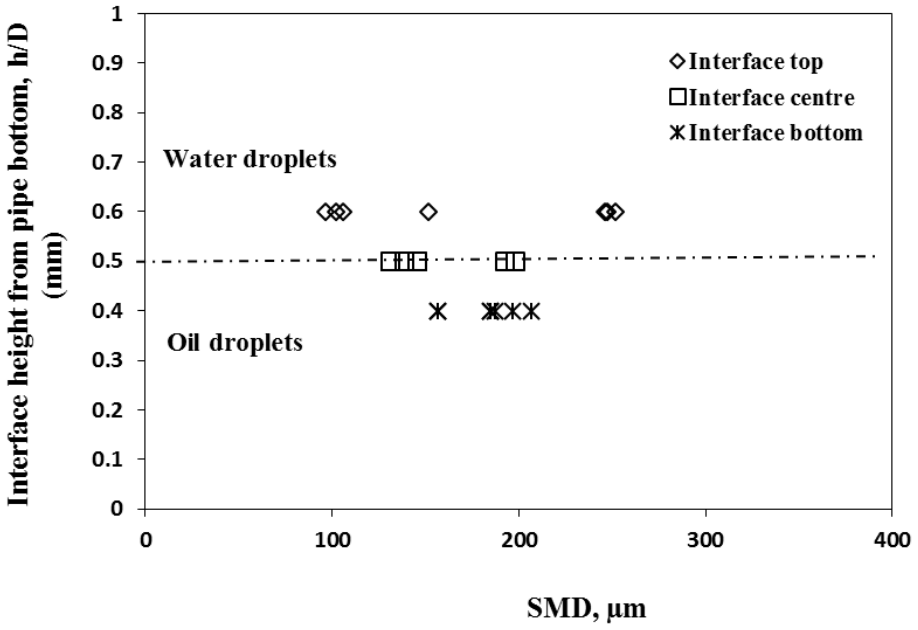

Figure 5-51 Sauter Mean Diameter (d_{32}), as a function of interface height from pipe bottom for mixture velocity, U_{sme} = 0.20 ms^{-1}, and distance from expansion 40D in - 2^0 degrees downward pipe inclination, for 50% OVF input oil volume fraction..

Also very small and finer oil droplets are formed close to the bottom of the pipe cross section, where the interface between oil – water can not readily be identified. However, the values of input oil volumes fractions give an idea of where exactly the interface will be in an ideal condition. This can be seen from the flow pattern maps obtained, which will be given in Chapter 6.

Figure 5.52, 5,53 and 5.54 also gives a demonstration of measurements obtained with Sauter mean diameter (SMD), as a function of the distance from the interface for input oil volume fraction 80% OVF, 50% OVF and 20% OVF respectively, and distance

from expansion 40D in - 2^0 degrees upward pipe inclination orientation, at different downstream mixture velocities, U_{sme}.

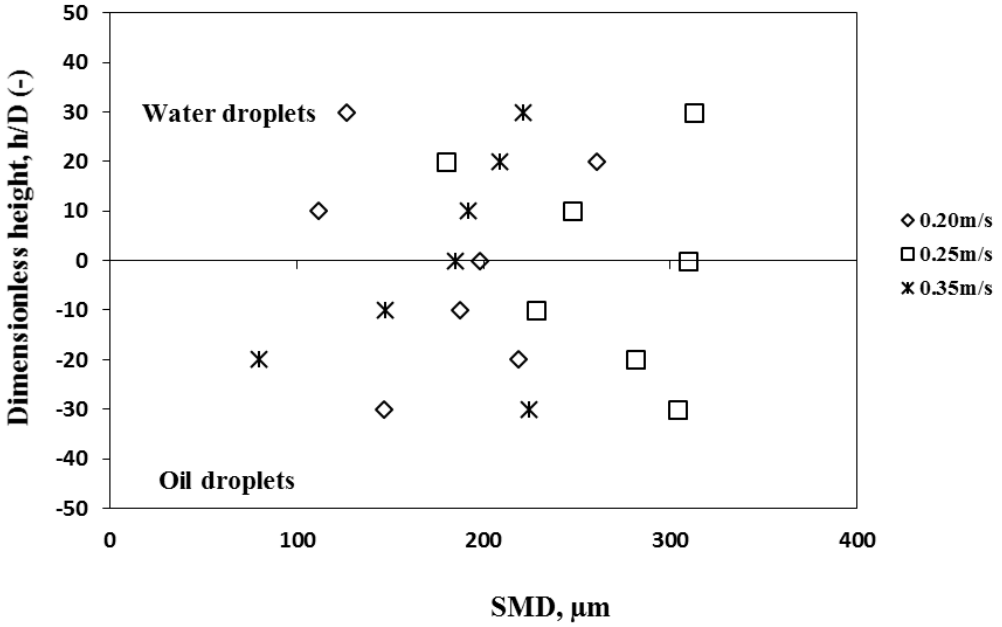

Figure 5-52 Sauter Mean Diameter (d_{32}), as a function of the distance from the interface for input oil volume fraction 80% OVF and distance from expansion 40D in - 2^0 degrees downward pipe inclination orientation, at different downstream mixture velocities, U_{sme}.

From the results shown in Figure 5.52, the droplets formed in general ranges between 90 µm – 300 µm. The results show smaller water and oil droplets throughout the cross section of the pipe at constant input oil volume fraction of 80% OVF, when the velocity is low (0.20 ms^{-1}). However, a slight increase leads to increase in the size of water droplets formed than the oil droplets. The implication is that the dispersed water droplets are coalescing faster at higher velocity. Again the formation of bigger droplets at higher velocity shows that coalescence is favored and dominates the system compared to drop break up mechanism. The small size oil droplets found at a slight velocity increase to 0.35 ms^{-1}, indicates dispersion of the oil droplets due to increase in turbulence forces in the system.

The phenomenon is different as can be seen from Figures 5.53 and 5.54. The majority of oil droplets detected by the laser probe are very small at the bottom of the pipe and also close to the interface region, within the range of between 100µm - 200µm at lower mixture velocity U_{sme} 0.20 ms^{-1} in both the 50% OVF and 20% OVF flow conditions. Interestingly, for the, 50% OVF, a gradual increase in velocity to 0.35m/s results in the formation of both lager oil and water droplets at the top and bottom portion of the interface. These mixtures of droplets are found more concentrated at the interface due to the narrowing of the mixed layer as a result of coalescence.

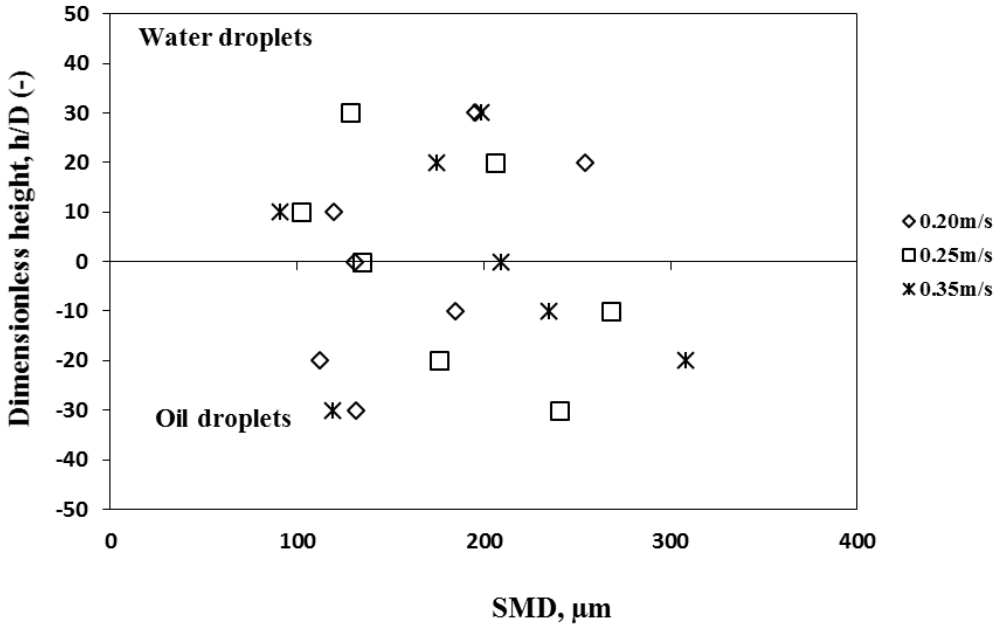

Figure 5-53 Sauter Mean Diameter (d_{32}), as a function of the distance from the interface for input oil volume fraction 50% OVF and distance from expansion 40D in - 2^0 degrees downward pipe inclination orientation, at different downstream mixture velocities, U_{sme}.

The frequency of collision and coalescence of droplets at the inlet entrance region appear to dominate the breakup mechanism in the system resulting in the narrowing of the mixed layer downstream of the singularity. As mentioned earlier, (Shinnar, 1961) had proved that in turbulent flow conditions, simultaneous coalescence and break-up occur. The droplets are exposed to both inertial forces due to velocity fluctuations, gravitational forces and to viscous shear forces.

For the 20% OVF flow condition presented in Figure 5.54, an increase in downstream mixture velocity from 0.20 ms^{-1} to 0.25 ms^{-1} leads to the formation of medium size droplets. Further increase in velocity to 0.35m/s results in an increase in SMD of droplets close to the center of interface, especially of the oil droplets.

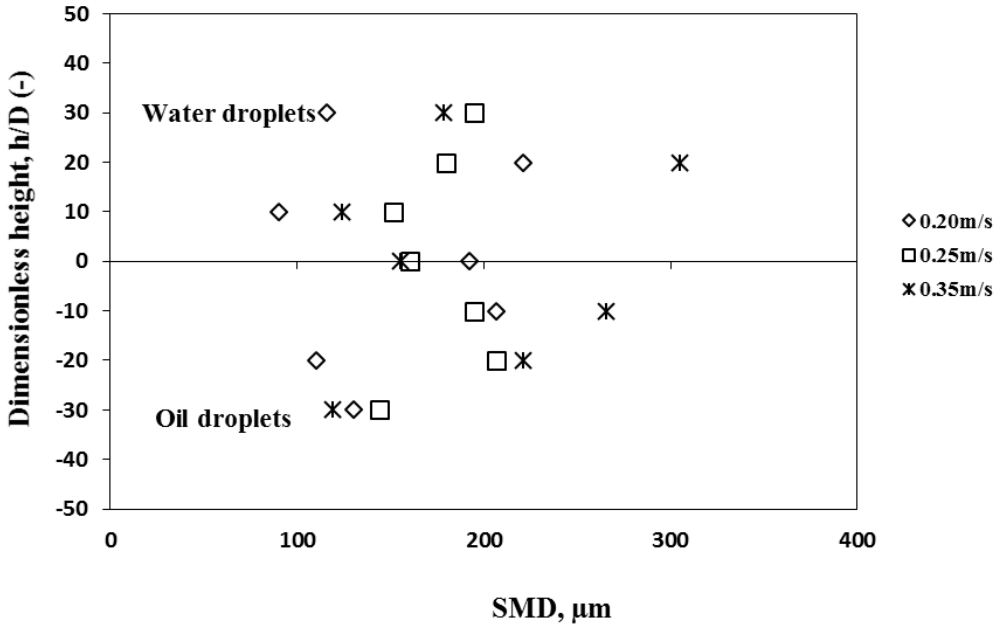

Figure 5-54 Sauter Mean Diameter (d_{32}), as a function of the distance from the interface for input oil volume fraction 20% OVF and distance from expansion 40D in - 2^0 degrees downward pipe inclination orientation, at different downstream mixture velocities, U_{sme}.

Since the system is oil dispersed in water continuous phase, oil droplets coalesce faster at the top portion and drift towards the bulk layer by the action of buoyance forces. Therefore, it is evident that, downward inclined pipe orientation influences the sizes of droplets formed, as well as downstream mixture velocity and invariably the stratification process of two phase oil/water flow system.

5.2.3.4 Effect of probe position

The results obtained for the measurement of Sauter Mean Diameter (SMD), of oil droplets for downstream mixture velocity, U_{sme} 0.20 ms^{-1} for oil volume fractions 20% OVF, 50% OVF and 80% OVF in - 2^0 degrees downward pipe inclination orientation,

at different probe positions from bottom to top portion of the pipe cross section is been presented in Figures 5.55, 5.56 and 5.57 respectively. In general, an overall pattern is seen of Sauter mean diameter (SMD) of droplet sizes with the various axial positions downstream of the expansion at the various positions in the pipe cross section.

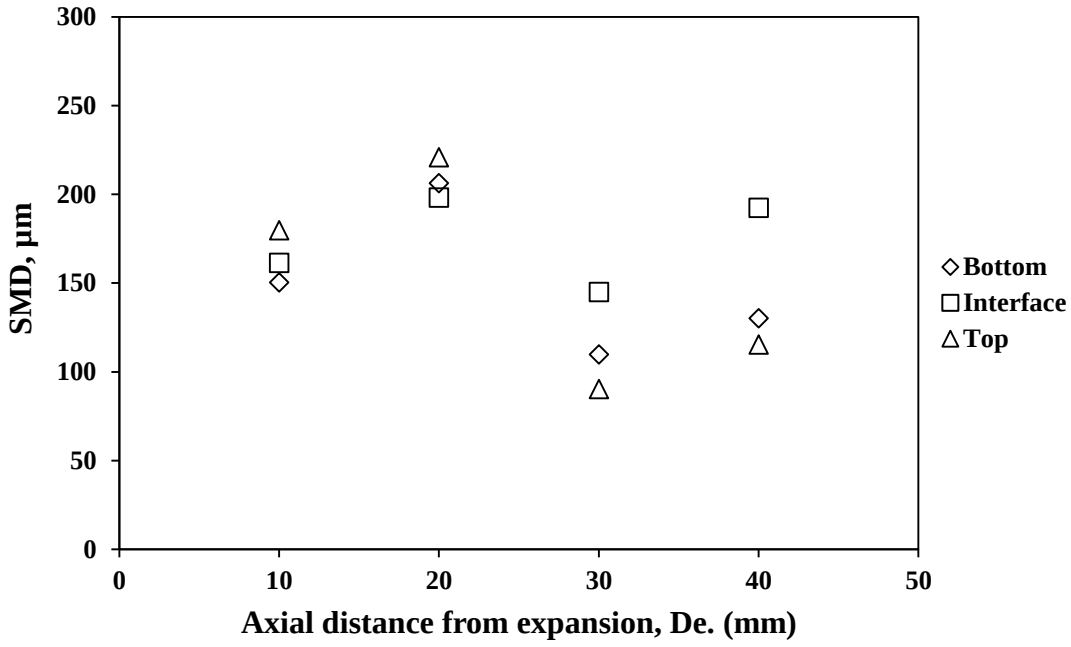

Figure 5-55 Sauter Mean Diameter (d_{32}), of oil droplets for mixture velocity, U_{sme} = 0.20m/s, oil volume fraction 20% OVF in - 2^0 degrees downward pipe inclination, at different probe positions.

Interestingly, in Figure 5.55 it is noticed that majority of droplets detected by the FBRM M500P laser are found to be within the same range, except at axial positions 30D and 40D, while considering the movement of laser from bottom to top position of the pipe cross section. The droplets created just beyond the inlet part at (20D downstream) of the test section, are larger due to coalescence, which has already taken place prior to that point at 10D. These oil droplets are seen to decrease slightly and then increases as the flow progresses towards the downstream of expansion at 40D. The smaller and finer oil drops seen at positions 30D and 40D for both top and bottom of pipe cross section indicates dispersion of droplets yet to coalesce, which are been carried along in the system.

Figure 5.56 also show clearly that coalescence of dispersed droplets progresses from the inlet position 10D and stratifies gradually downstream at 40D from the flow pattern mostly for flow condition 50% OVF at low downstream mixture velocity, U_{sme} 0.20 ms^{-1}. It also illustrates the existence of a mixture of both large droplets at position 20D and smaller droplets detected by the laser around the interface downstream of the singularity.

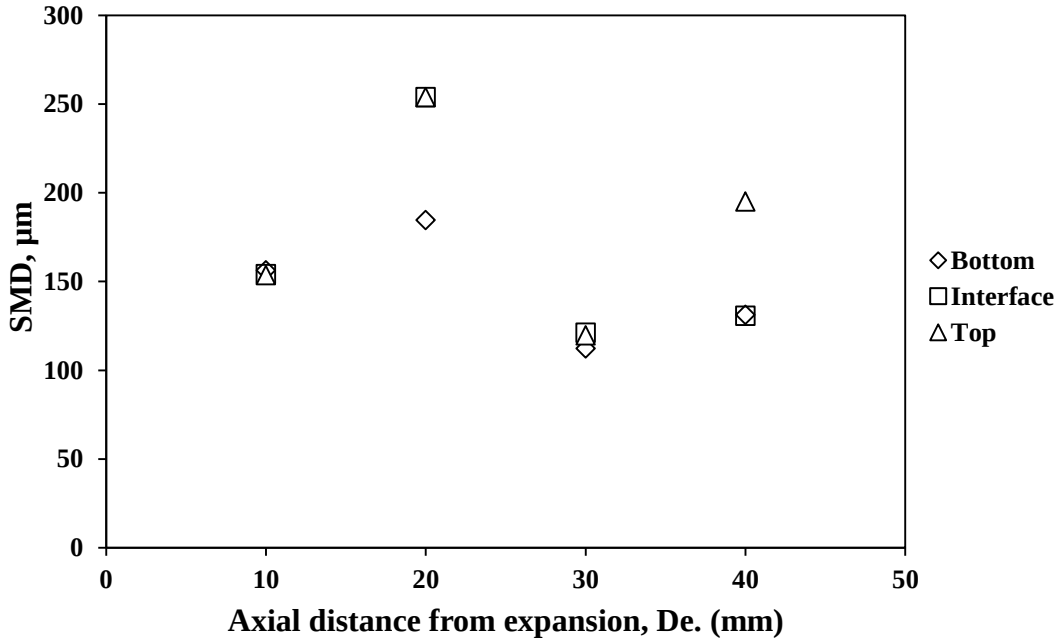

Figure 5-56 Sauter Mean Diameter (d_{32}), of oil and water droplets for mixture velocity, U_{sme} = 0.20m/s, oil volume fraction 50% OVF in - 2^0 degrees downward pipe inclination, at different probe positions

The trend of Sauter mean diameter (SMD) shown in Figure 5.57 for Sauter mean diameter SMD of water droplets for mixture velocity 0.20 ms^{-1} oil volume fraction 80% OVF in – 2^0 degrees downward pipe inclination, at different probe positions. The SMD of water drops are found to be of almost the same sizes at the inlet axial position, 10D. Those water droplets seems to coalesce and become bigger at the 20D and subsequently, position 30D, and slightly decreases downstream at position 40D. Same phenomenon occurs at the top part with initial increase in SMD at 20D and then decreases at position 30D. This implies that enough residence time is given for the dispersed water droplets in the slowly flowing oil continuous phase to coalesce and been carried along in the system.

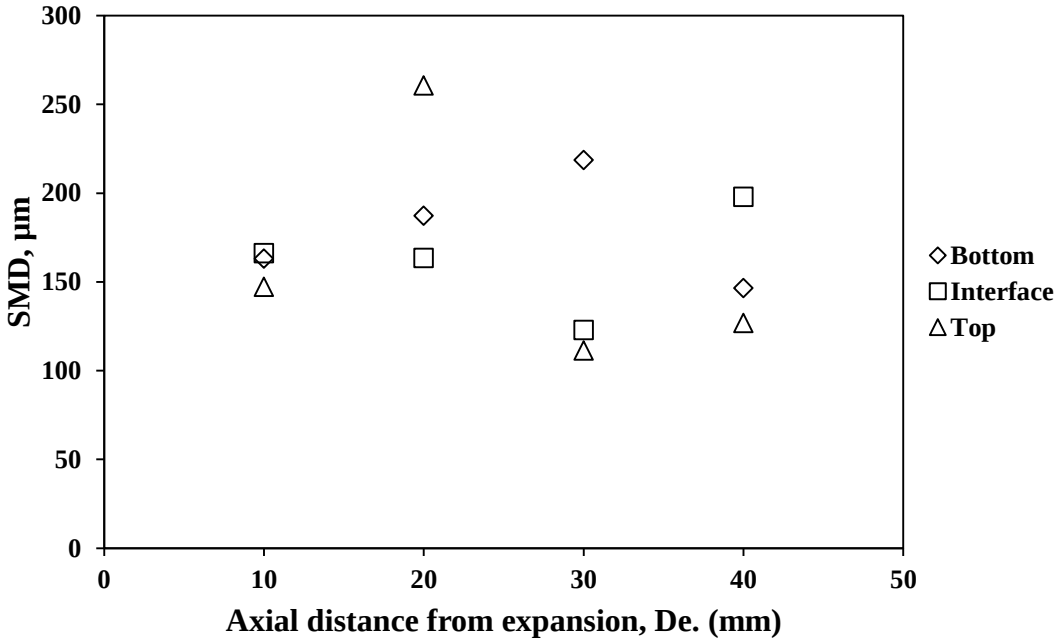

Figure 5-57 Sauter Mean Diameter (d_{32}), of water droplets for mixture velocity, U_{sme} = 0.20 ms^{-1}, oil volume fraction 80% OVF in - 2^0 degrees downward pipe inclination, at different probe positions

It can also be noticed that at 40D, the SMD has increased at the interface of the pipe cross section. The flow pattern is seen to stratify towards the interface at axial position 40D, as the droplets travelled further downstream the expansion. However, smaller water drops are observed both at bottom and top of the pipe cross section at this position. This suggests that at position 40D, coalescence of dispersed water droplets have taken place and drifts towards the interface with larger droplet sizes.

In summary, for SMD in downward orientation, the following conclusions can be made from the investigation:

- Both input oil volume fraction and probe position show minimal effect on the drop sizes formed for downward pipe inclination.

- Sauter mean diameter (SMD) increases with increase in mixture velocity along the entire test section. At higher mixture velocity, both water and oil droplets coalesce faster at the top and bottom pipe

portions respectively and accumulates around the interface downstream of the singularity.

- The larger droplets formed are observed to concentrate mostly at the bottom portion of pipe at position 40D downstream of the expansion.

- Smaller and finer droplets detected at higher mixture velocity (0.35m/s) in position 30D indicate dispersion due to high collision frequency of droplets.

5.3 Comparison between different angles of inclination

This section presents a comparison of the influence of different angles of inclinations (upward, horizontal and downward) on the Sauter mean diameter (SMD) of droplets sizes formed with various downstream mixture velocity, probe positions and axial distance along pipe test section. Complete droplet size measurements were made for inclination angles of Upward ($+2^0$ degree), Downward (-2^0 degree), and Horizontal orientations at all axial test positions (10D, 20D, 30D and 40D). However, it was only possible to take SMD of droplet size measurements at positions 10D and 20D of the expansion for the Upward ($+4^0$ degree), Downward (-4^0 degree), due to limitation of space for the installation of the FBRM M500P laser probe.

Figure 5.58 illustrates the influence of Sauter Mean Diameter (SMD), as a function of the distance from interface for downstream mixture velocity, Usme = 0.20m/s, input oil volume fraction 80% OVF at axial test distance 10D, at different pipe inclination angles. The results show that there is significant effect on the drop sizes formed when the pipe is in the upward ($+2^0$ degree) inclination position. Clearly larger droplets of both water and oil are recorded. On the other hand, drops of sizes within the same (SMD) range, between (100 μm – 300 μm) are found for the flow condition 20% OVF, except that dispersed water droplets at the top portion of interface of both horizontal and downward (-4^0 degree), orientation becomes bigger as shown in Figure 5.59.

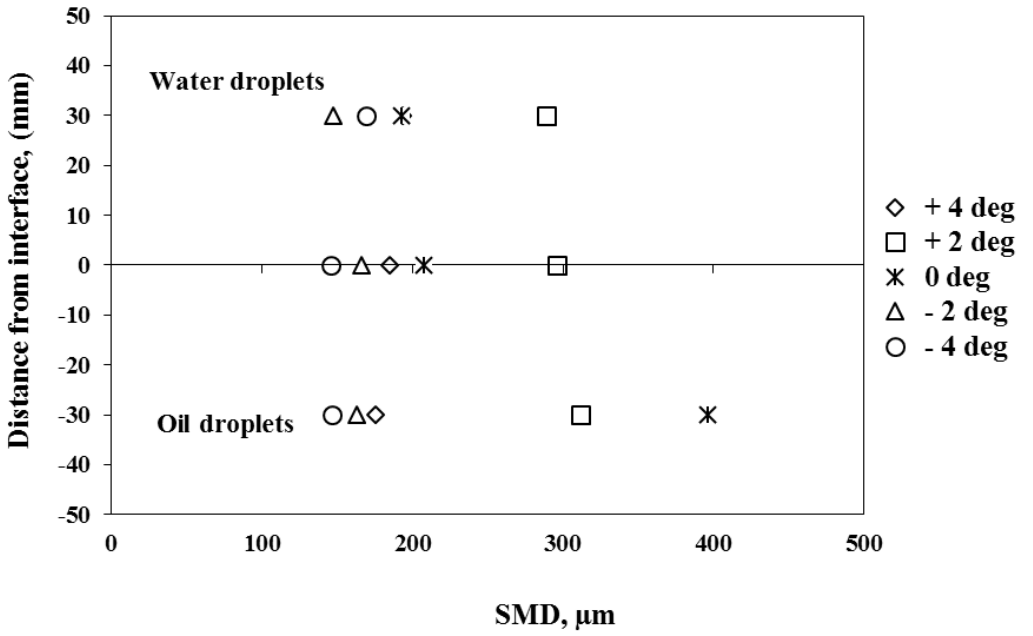

Figure 5-58 Sauter Mean Diameter (d_{32}), as a function of the distance from interface for downstream mixture velocity, U_{sme} = 0.20 ms^{-1}, input oil volume fraction 80% OVF at axial test distance 10D, at different pipe inclination angles.

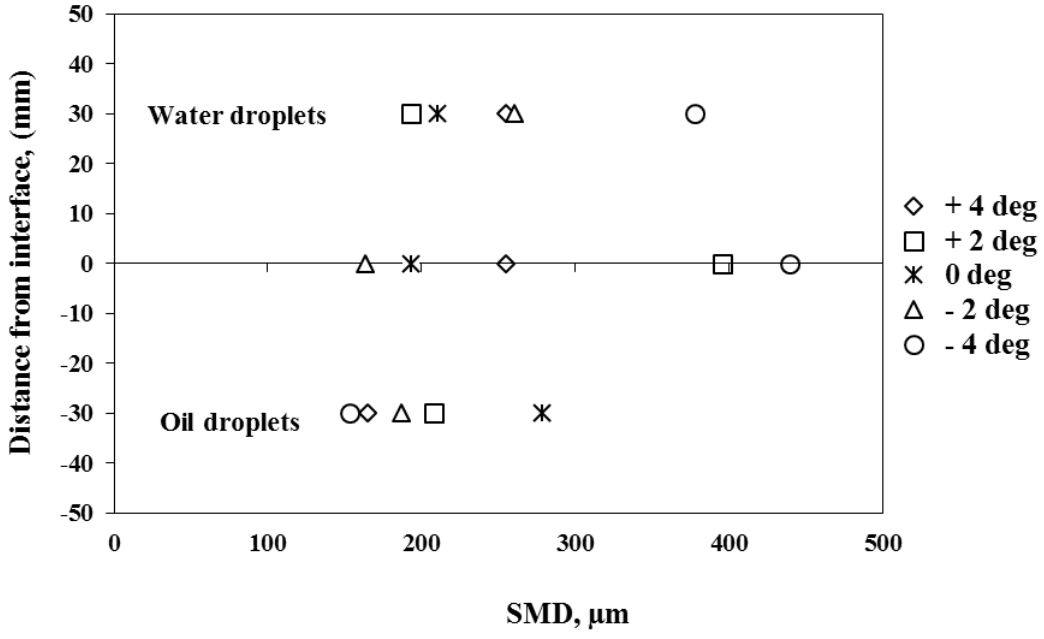

Figure 5-59 Sauter Mean Diameter (d_{32}), as a function of the distance from interface for downstream mixture velocity, U_{sme} = 0.20 ms^{-1}, input oil volume fraction 20% OVF at axial test distance 10D, at different pipe inclination angles.

Further measurement of droplet size was done, at axial position 20D, downstream of the expansion at constant downstream mixture velocity of 0.35 ms^{-1} and input oil volume fractions of 80% OVF and 20% OVF, as shown in Figure 5.60 and 5.61. It can be seen generally from the Figures that smaller drops are formed. The SMD ranges between (100 µm – 250 µm), at the Top, Centre and Bottom portion of mixed interface for all orientations. When the downstream mixture velocity was increased further to 0.35m/s at constant input oil volume fraction 20% OVF as presented in Figure 5.61, the SMD of droplet sizes detected are smaller in all inclination orientations. There is also no significant effect on drop size distribution as the sizes found fall within same range of values (100 µm – 300 µm).

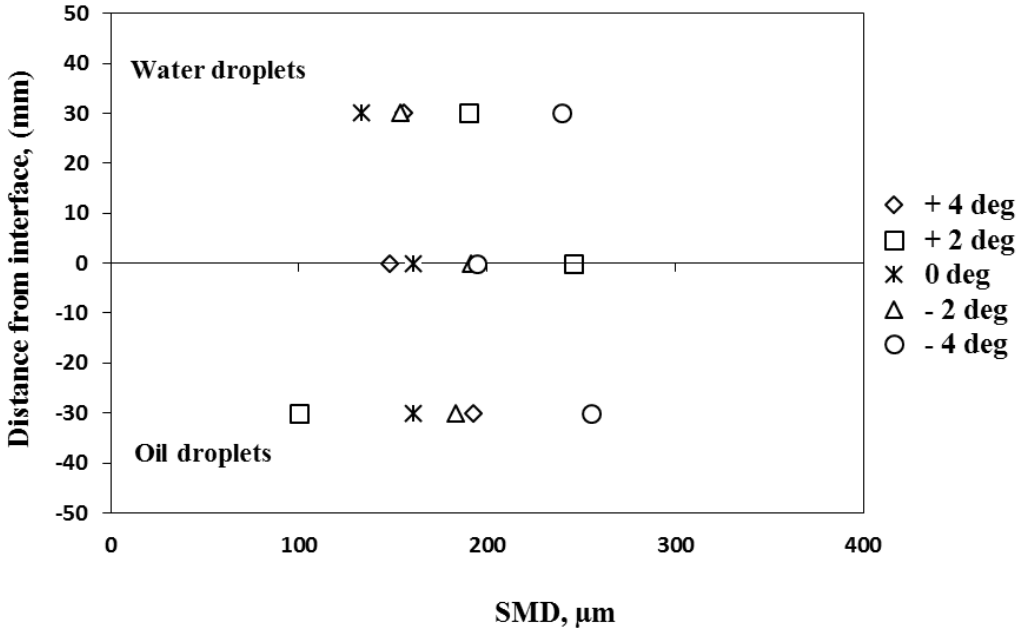

Figure 5-60 Sauter Mean Diameter (d_{32}), as a function of the distance from interface for downstream mixture velocity, U_{sme} = 0.35 ms^{-1}, input oil volume fraction 80% OVF at axial test distance 20D, at different pipe inclination angles.

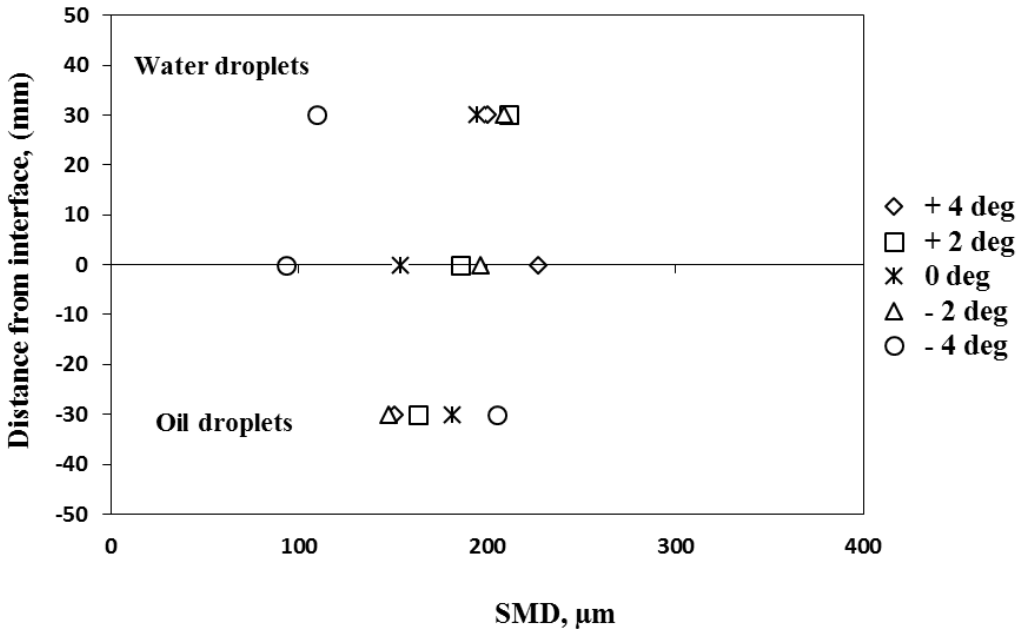

Figure 5-61 Sauter Mean Diameter (d_{32}), as a function of the distance from interface for downstream mixture velocity, U_{sme} = 0.35 ms^{-1}, input oil volume fraction 20% OVF at axial test distance 20D, at different pipe inclination angles.

Further investigation was carried out on the effect of angles of inclination on SMD of both oil and water droplet for 0.20 ms^{-1} and 0.35 ms^{-1} with input oil volume fractions 20% OVF and 80% OVF downstream of the expansion as given in Figures 5.62, 5.63, 5.64, 5.65 and 5.66.

Evidently, form Figure 5.62, the oil droplets formed are smaller at the axial position 10D and becomes larger at 20D, due to coalescence for the upward angles of inclination ($+4^0$ degree) and ($+2^0$ degree). In this condition, the mixed layer is close to the top of the pipe cross section as probe is placed at bottom (15.9 mm), with the oil layer moving faster than the water continuous phase. The slow moving in-situ water continuous phase enables dispersed oil droplets enough residence time to coalesce as explained earlier. There is however, minimal horizontal and downward angles of inclination effect for this particular flow conditions on the SMD as demonstrated in Figure 5.62.

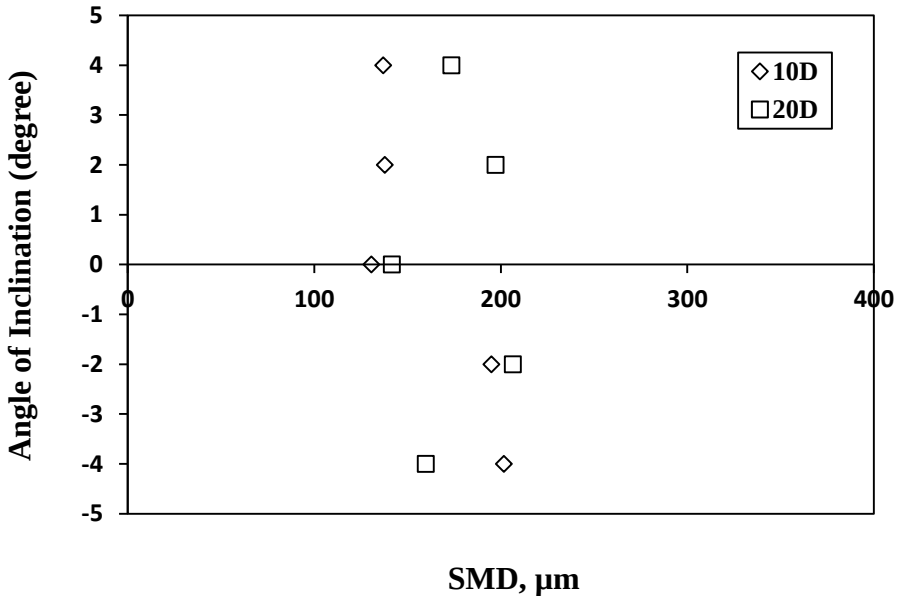

Figure 5-62 Sauter Mean Diameter (d_{32}), of oil droplets for downstream mixture velocity, U_{sme} = 0.20 ms^{-1}, oil volume fraction 20% OVF at bottom (15.9 mm), probe position, within axial test distance at different pipe inclination angles.

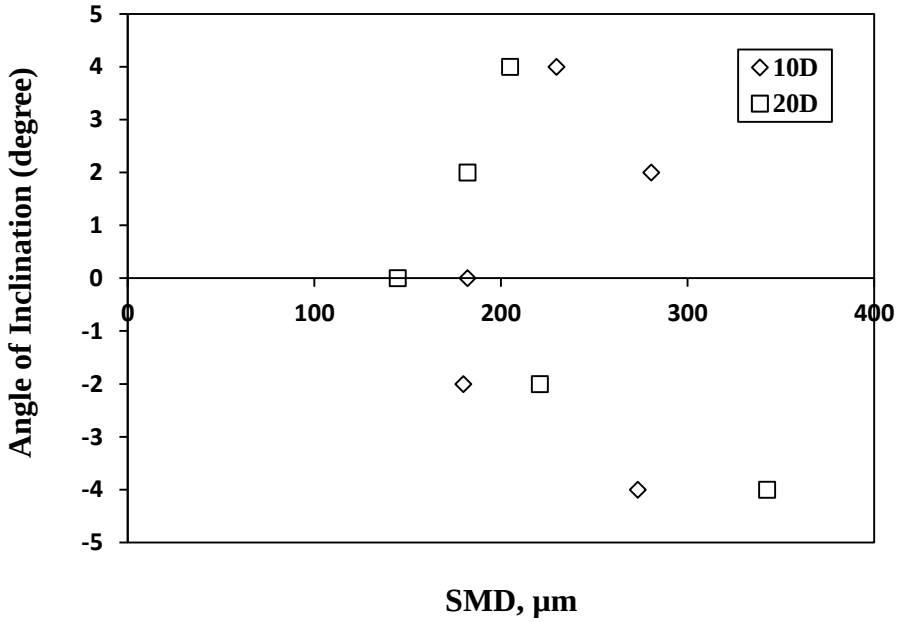

Figure 5-63 Sauter Mean Diameter (d_{32}), of oil droplets for downstream mixture velocity, U_{sme} = 0.20 ms^{-1}, oil volume fraction 20% OVF at Top (111.3 mm), probe position, within axial test distance at different pipe inclination angles.

In Figure 5.63, when the FBRM M500P laser probe was placed at the top portion of the pipe cross section (111.3 mm), the SMD of droplet sizes shows a reverse case of drop size decreasing from 10D to 20D, as measurement is made further downstream of the singularity, for the upward angles of inclination ($+4^0$ degree) and ($+2^0$ degree) and horizontal case. Whereas, SMD of the oil droplets increases for same conditions in the downward angles of inclination (-2^0 degree) and (-4^0 degree).

The effect on SMD of oil droplet size is also conspicuously different with an increase in downstream mixture velocity to 0.35m/s, probe (111.3 mm) and constant flow conditions, as represented in Figure 5.63. Interestingly, there is no clear effect of upward and downward angles of inclination on the SMD, except horizontal angle, with same sizes (150 µm), for this particular flow conditions as demonstrated in Figure 5.63.

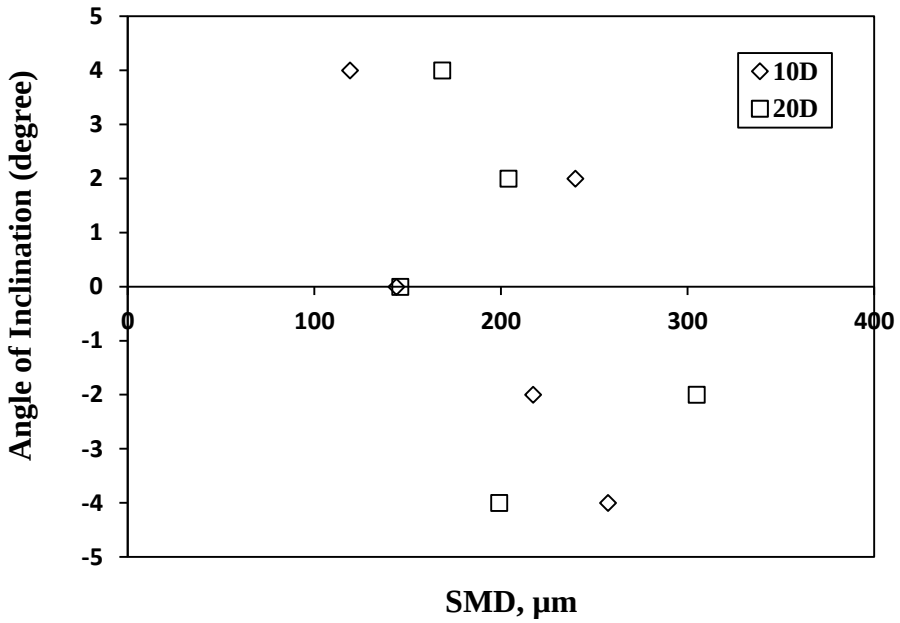

Figure 5-64 Sauter Mean Diameter (d_{32}), of oil droplets for downstream mixture velocity, U_{sme} = 0.35 ms^{-1}, oil volume fraction 20% OVF at bottom (111.3 mm), probe position, within axial test distance at different pipe inclination angles.

A similar observation of this phenomenon was recorded in the works of (Yang et al., 2003, Hasan, 2006, Yusoff, 2012). This implies that the mixed layer would account for the droplet sizes for both the horizontal and downward angles of inclination. The

mixed layer is seen to almost dominate the entire pipe cross section with an increase in downstream velocity, even when the laser probe is positioned at the top portion of the pipe cross section.

The influence of inclination angle on SMD of dispersed water droplets in oil continuous phase flow condition, 80% OVF for downstream mixture velocity 0.20 ms^{-1} and 0.35ms^{-1}, is illustrated in Figures 5.64 and 5.65, respectively.

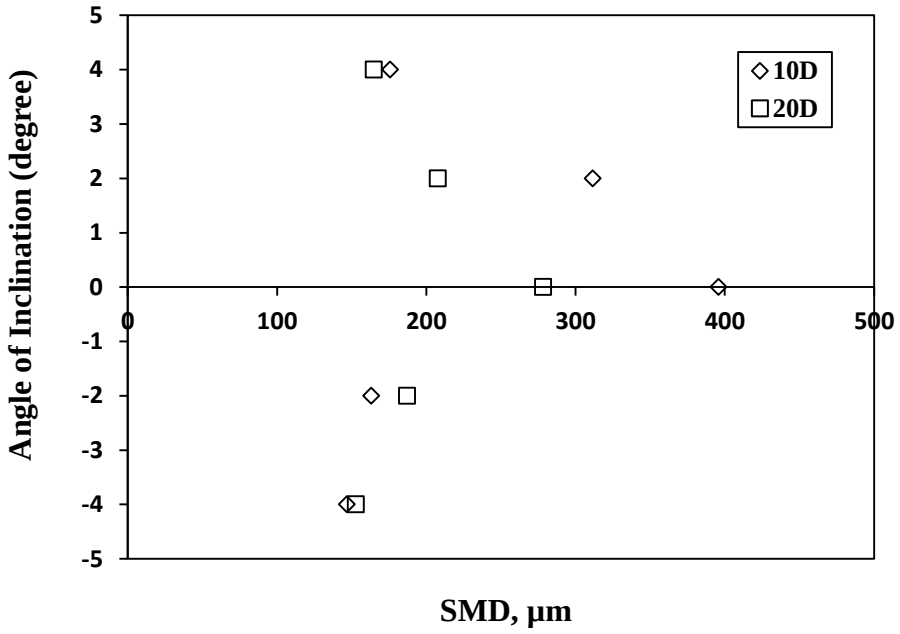

Figure 5-65 Sauter Mean Diameter (d_{32}), of water droplets for downstream mixture velocity, U_{sme} = 0.20 ms^{-1}, oil volume fraction 80% OVF at bottom (15.9 mm), probe position, within axial test distance at different pipe inclination angles.

As can be noticed from Figure 5.65, there is significant effect in the case of upward angles of inclination ($+4^0$ degree) and ($+2^0$ degree) and horizontal orientation on SMD. It shows that the drop sizes became smaller from inlet position 10D to 20D, further downstream of the expansion. This could suggest that the mixed interface region is close to the bottom (15.9 mm), where the laser probe is fixed. Therefore, the probe detects already coalesced and stratifying dispersed water droplets, beyond position 10D.

When the downstream mixture velocity was increased further to 0.35m/s at constant input oil volume fraction 80% OVF as presented in Figure 5.65, the SMD of droplet sizes detected are bigger at 10D than position 20D, for downward angles of inclination (-2^0 degree) and (-4^0 degree) orientations. There is also no significant effect on drop size distribution for the case of upward angles of inclination ($+4^0$ degree), ($+2^0$ degree) and horizontal orientation, as the sizes found fall within same range of values (100 µm – 200 µm).

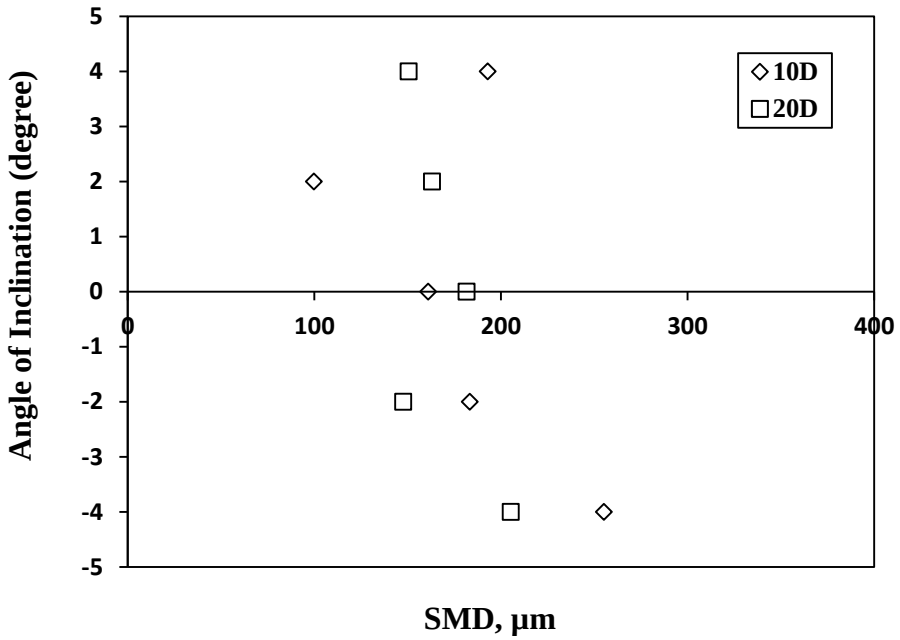

Figure 5-66 Sauter Mean Diameter (d_{32}), of water droplets for downstream mixture velocity, U_{sme} = 0.35m/s, oil volume fraction 80% OVF at bottom (15.9mm), probe position, within axial test distance at different pipe inclination angles.

This occurrence has been explained earlier, in the case of flow condition 20% OVF, (Figure 5.63), where the mixed layer would account for the droplet sizes in both the horizontal and downward angles of inclination. The mixed layer is seen to almost dominate the entire pipe cross section with an increase in downstream velocity, even when the laser probe is positioned at the bottom (15.9 mm) portion of the pipe cross section for the 80% OVF flow condition.

5.4 Comparison with existing models

The current experimental data shows a large amount of agreement when fitted with the Rosin-Rammler distribution function. This can be seen graphically from the distribution plots presented in Figures 5.67 to 5.74. The values of the Rosin-Rammler parameter, ς, ranged from 1.94 – 2.20 as presented in Table 5.1. The Rosin – Rammler function in this work was obtained by using MATLAB, and fitting the experimental cumulative function data to the best distribution parameters. Due to time limitations, the distribution analysis is focused only on Chord length measurements obtained at the Centre (interface) of the pipe cross-section along the sudden expansion. This is regardless of the top and bottom portion of the pipe. Also the values of drop diameter, α as expressed in Equation 3.8, corresponding to $(1\text{-}V_{cum}) = 0.3679$, varied between 75 µm and 763 µm.

The uncertainties of measurements in the FBRM probe are difficult to measure quantitatively due to perturbations as a result of waves in the flow. The uncertainties of measurements were however determined from the slope of the Rosin – Rammler plots at the 95% confidence interval and included in Table 5.1. The uncertainties are as large as ± 14%, which is acceptable as three (3) repeated measurements were taken for each flow rate.

An interesting result emerging from the data of Table 5.1 is that the Rosin – Rammler parameter, ς values are fairly constant and show no significant influence of the flowrate on the shape of the distribution as plotted (Figures 5.75 – 5.77). This is important considering the view point of correlating the entire data points. Similar findings and observations were made by (Karabelas, 1978), in his work on droplet size generated in turbulent pipe flow of dilute liquid/liquid dispersions. The values of Rosin-Rammler parameter in liquid-liquid flow experiments were compared with some published work by (Karabelas, 1978, Angeli and Hewitt, 2000, Lovick and Angeli, 2004b, Hasan, 2006) as presented in Table 5.2. As can be seen, the parameter, ς values are in similar range with that of (Hasan, 2006) and smaller than those of other published work. A number of factors might be responsible for this difference considering the use of low mixture velocity, degree of dispersion created, internal pipe diameter and sudden pipe expansion applied in this experiment.

Table 5-1 Rosin-Rammler parameter values of probe position at Centre (63.5mm) for horizontal pipe orientation

Mixture velocity (m/s)	Water cut (%)	Oil volume fraction(OVF)(%)	10D Interface		20D Interface		30D Interface		40D Interface	
			R-R Parameter, ς	Drop sizes α (μm)	R-R Parameter, ς	Drop sizes α (μm)	R-R Parameter, ς	Drop sizes α (μm)	R-R Parameter, ς	Drop sizes α (μm)
0.20m/s	20	80	1.94 ± 0.14	158	2.13 ± 0.11	207	2.00 ± 0.10	472	2.02 ± 0.01	122
	50	50	2.17 ± 0.06	113	2.20 ± 0.12	268	2.07 ± 0.12	393	2.14 ± 0.12	259
	80	20	2.08 ± 0.08	94	2.09 ± 0.08	79	2.05 ± 0.10	388	2.07 ± 0.08	99
0.25m/s	20	80	2.19 ± 0.10	764	2.20 ± 0.12	441	2.08 ± 0.12	412	2.17 ± 0.09	327
	50	50	2.15 ± 0.11	716	2.13 ± 0.09	75	2.13 ± 0.08	75	2.04 ± 0.10	127
	80	20	2.19 ± 0.11	763	2.05 ± 0.11	467	2.11 ± 0.13	408	2.06 ± 0.11	441
0.30m/s	20	80	2.06 ± 0.12	366	2.06 ± 0.10	198	2.18 ± 0.13	386	2.06 ± 0.10	208
	50	50	2.08 ± 0.12	355	1.97± 0.13	197	2.10 ± 0.11	361	2.01 ± 0.09	516
	80	20	2.20 ± 0.12	428	2.06 ± 0.13	161	2.07 ± 0.12	255	2.04 ± 0.11	417
0.35m/s	20	80	2.04 ± 0.12	416	2.17 ± 0.09	340	2.09 ± 0.11	554	2.08 ± 0.13	238
	50	50	2.14 ± 0.12	406	2.10 ± 0.11	436	2.19 ± 0.10	189	2.05 ± 0.12	317
	80	20	2.07 ± 0.13	375	1.96 ± 0.12	467	2.05 ± 0.09	151	2.10± 0.13	263

Table 5-2 Comparison of Rosin-Rammler parameters in liquid-liquid flow experiments with published work

Researcher	R-RD parameter , ς	Oil volume fraction(OVF)(%)	Mixture velocity (m/s)	Internal diameter of pipe (mm)	Fluids used
Karabelas (1978)	2.30 - 2.90	4.7 - 11.9 (Water injection rate)	1.18 - 3.0	50.4	Kerosene /Water & Trans. oil/water
Angeli & Hewitt (2000)	2.10 - 2.80	3.4 - 9.0	1.10 - 1.70	24	Oil - water
Lovick & Angeli (2004)	2.60 - 4.20	20 - 80	1.50 - 2.50	38	Oil - water
Hassan (2006)	1.20 - 2.20	20 - 70	0.20 - 0.40	100	Kerosene - water
Current expt	1.94 - 2.20	20 - 80	0.20 - 0.35	127	Silicone oil - water

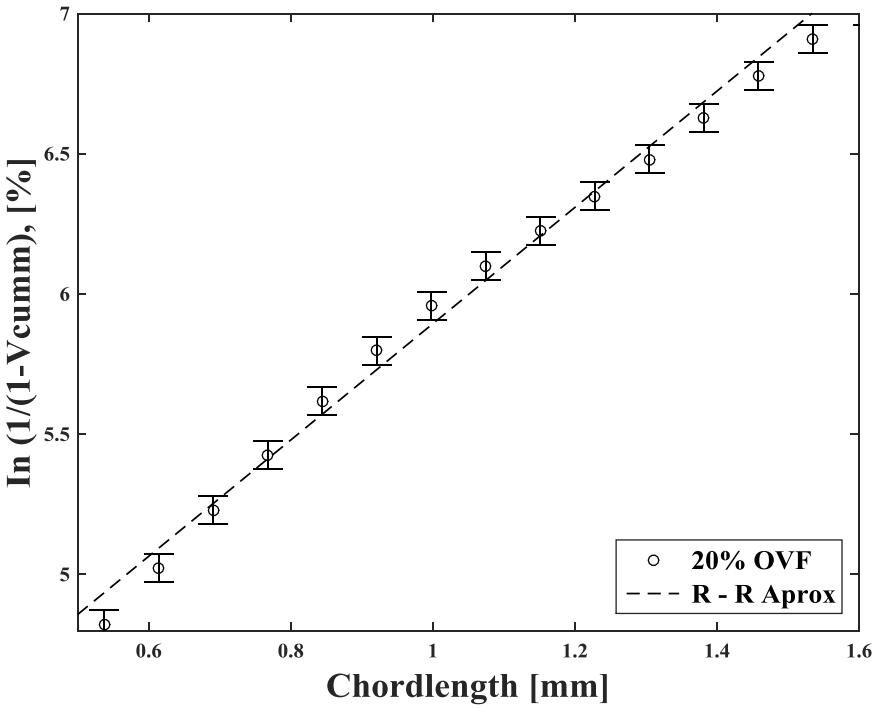

Figure 5-67 Experimental data fitted to the Rosin-Ramler function for downstream mixture velocity, U_{sme} = 0.20 ms^{-1}, oil volume fraction 20% OVF at Centre (63.5 mm) probe position, 40D axial test distance at horizontal pipe orientation.

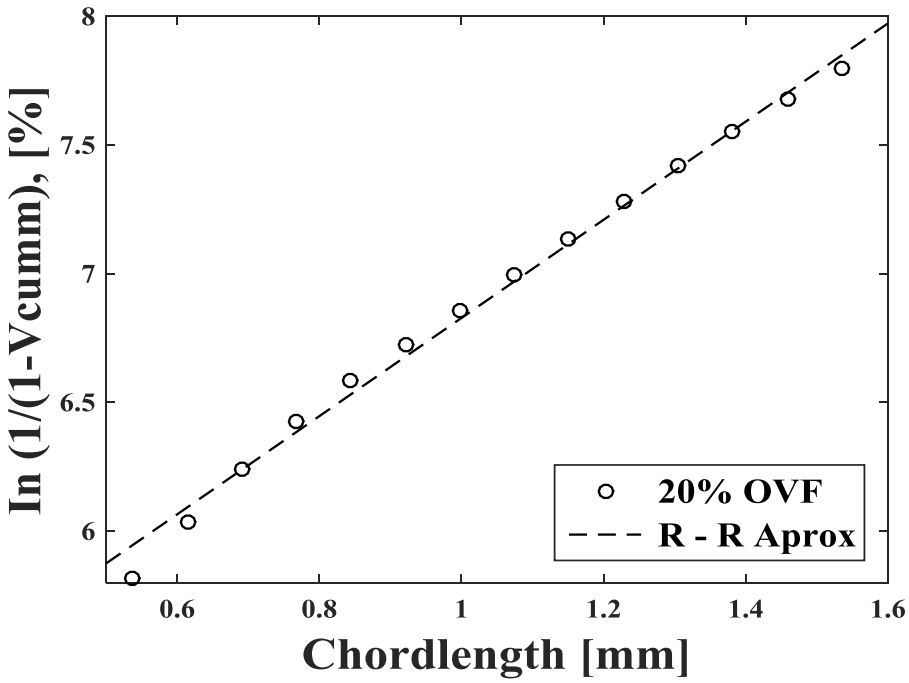

Figure 5-68 Experimental data fitted to the Rosin-Ramler function for downstream mixture velocity, U_{sme} = 0.20 ms^{-1}, oil volume fraction 50% OVF at Centre (63.5 mm) probe position, 40D axial test distance at horizontal pipe orientation.

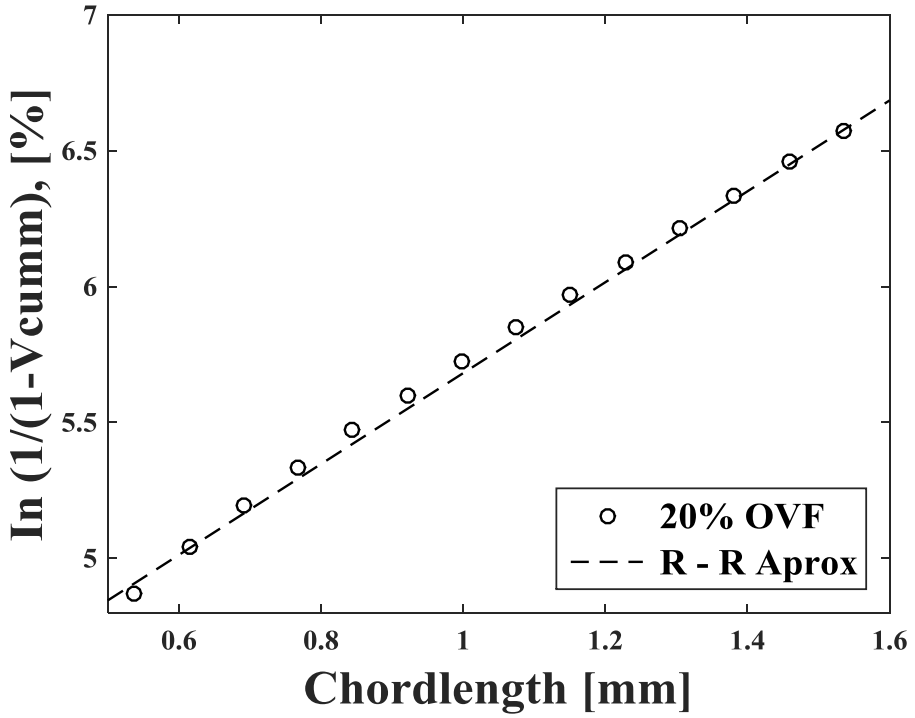

Figure 5-69 Experimental data fitted to the Rosin-Ramler function for downstream mixture velocity, U_{sme} = 0.20 ms^{-1}, oil volume fraction 80% OVF at Centre (63.5 mm) probe position, 40D axial test distance at horizontal pipe orientation.

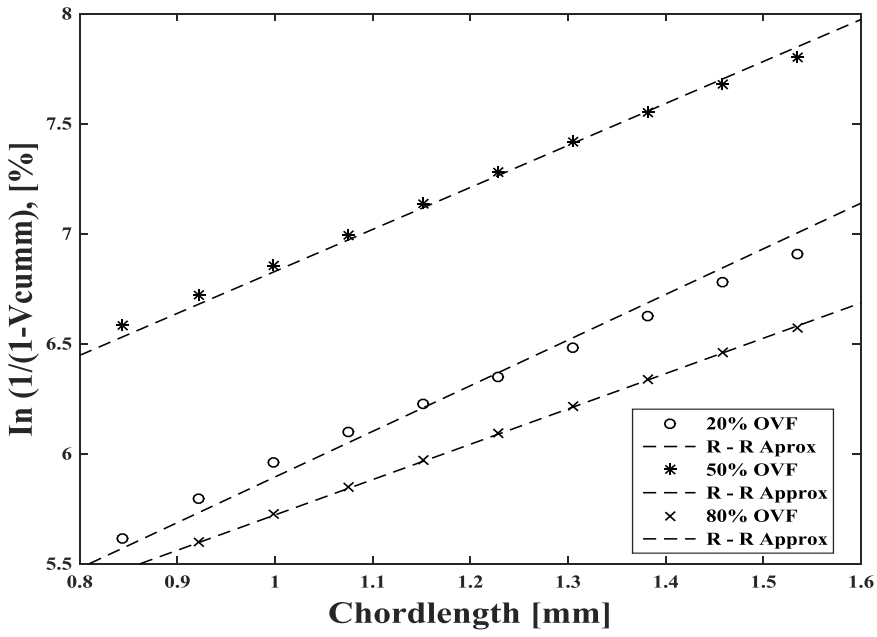

Figure 5-70 Comparison of experimental data fitted to the Rosin-Ramler function for downstream mixture velocity, U_{sme} = 0.20 ms^{-1}, oil volume fractions 20%, 50% and 80% OVF at Centre (63.5 mm) probe position, 40D axial test distance at horizontal pipe orientation.

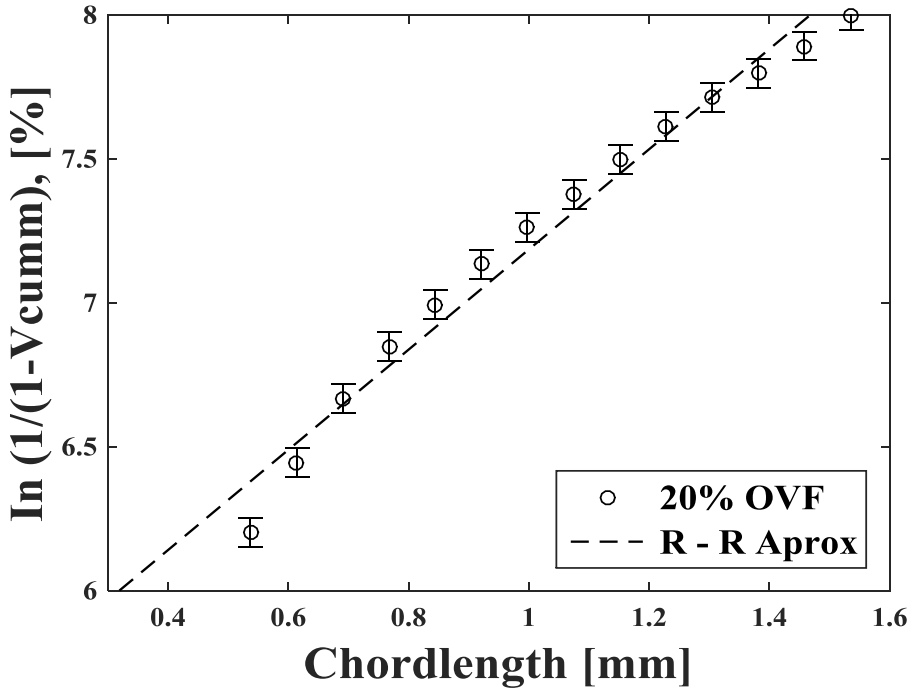

Figure 5-71 Experimental data fitted to the Rosin-Ramler function for downstream mixture velocity, U_{sme} = 0.35 ms^{-1}, oil volume fraction 20% OVF at Centre (63.5 mm) probe position, 10D axial test distance at horizontal pipe orientation.

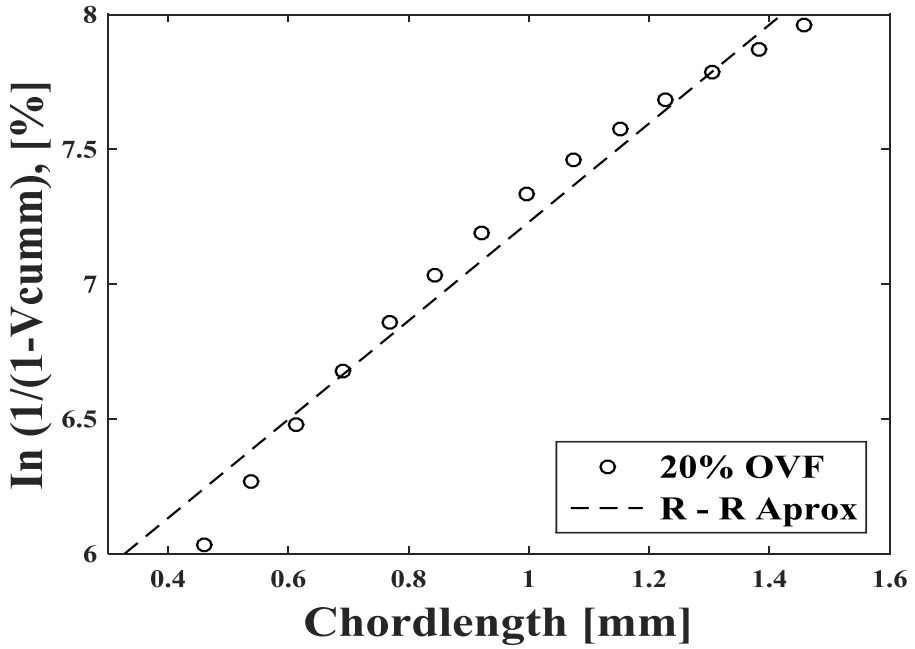

Figure 5-72 Experimental data fitted to the Rosin-Ramler function for downstream mixture velocity, U_{sme} = 0.35 ms^{-1}, oil volume fraction 50% OVF at Centre (63.5 mm) probe position, 10D axial test distance at horizontal pipe orientation.

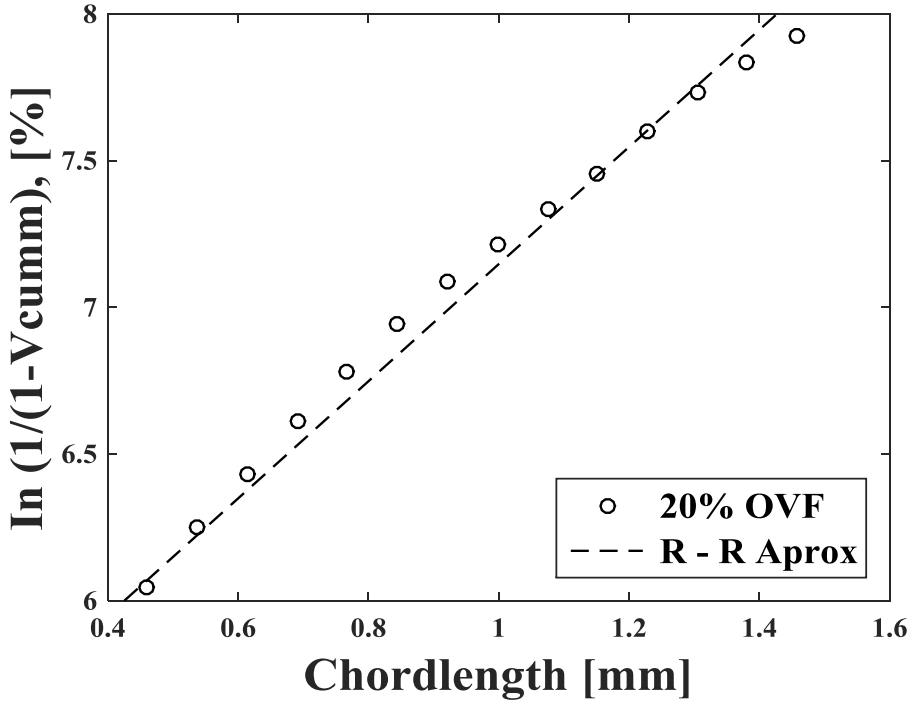

Figure 5-73 Experimental data fitted to the Rosin-Ramler function for downstream mixture velocity, U_{sme} = 0.35 ms^{-1}, oil volume fraction 80% OVF at Centre (63.5 mm) probe position, 10D axial test distance at horizontal pipe orientation.

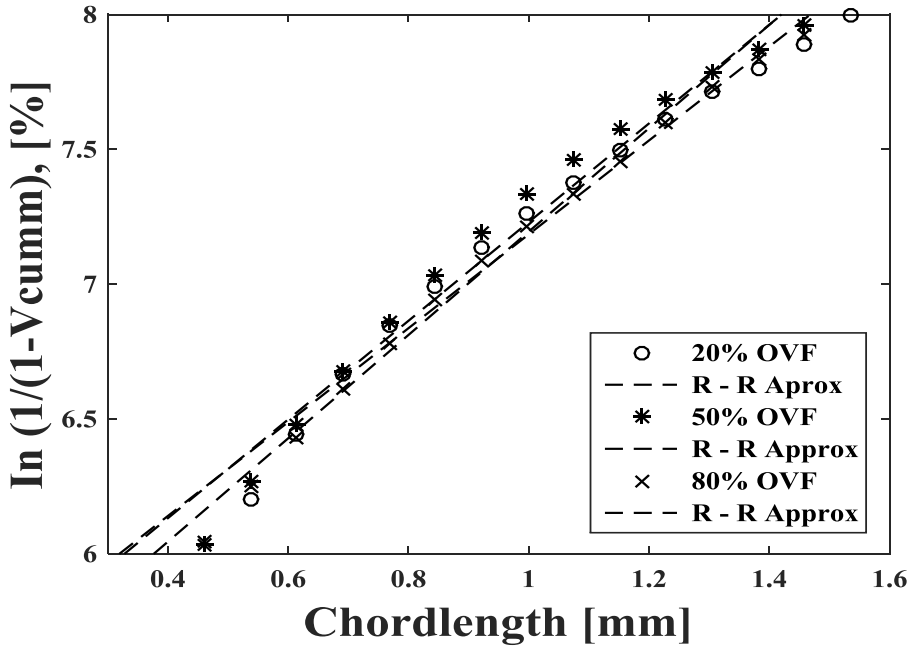

Figure 5-74 Comparison of experimental data fitted to the Rosin-Ramler function for downstream mixture velocity, U_{sme} = 0.35 ms^{-1}, oil volume fractions 20%, 50% and 80% OVF at Centre (63.5 mm) probe position, 10D axial test distance at horizontal pipe orientation

The evolution of Rosin-Rammler parameter for downstream mixture velocities, Usme 0.20 ms^{-1} and 0.35 ms^{-1}, probe position Centre (63.5 mm), within axial test distance and horizontal pipe orientation at different input oil volume fractions are shown in Figures 5.75 and 5.76. In the case of low velocity, 0.20 ms^{-1}, (Figure 5.75), it is noticed that there is a slight increase of ς from position 10D to 20D and then decreases slightly downstream of the pipe expansion for both the water and oil dispersed flow conditions, 80% OVF, 50% OVF and 20% OVF respectively. No distinct trend was observed when the downstream velocity was increased to 0.35m/s as can be seen from Figure 5.76. The results obtained in Table 5.1 also show generally, a strong dependence of the parameter, ς on the drop sizes formed.

A further investigation was done on the evolution of Rosin-Ramler parameter for input oil volume fraction 20% OVF and 80% OVF flow conditions at Centre (63.5 mm) probe position, within axial test distance and horizontal pipe orientation at different downstream mixture velocities as presented in Figures 5.77 and 5.78. A similar trend was observed in both cases of oil dispersed in water continuous (20% OVF) and water dispersed in oil continuous (80% OVF), phases.

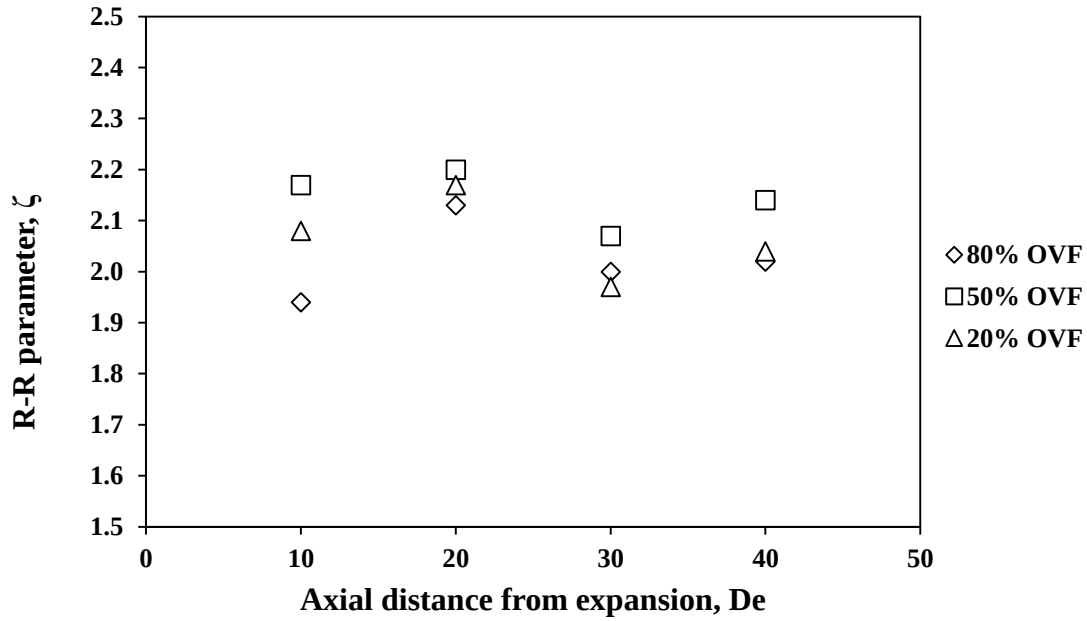

Figure 5-75 Evolution of the Rosin-Ramler parameter for downstream mixture velocity, U_{sme} = 0.20 ms^{-1}, probe position Centre (63.5 mm), within axial test distance and horizontal pipe orientation at different input oil volume fractions.

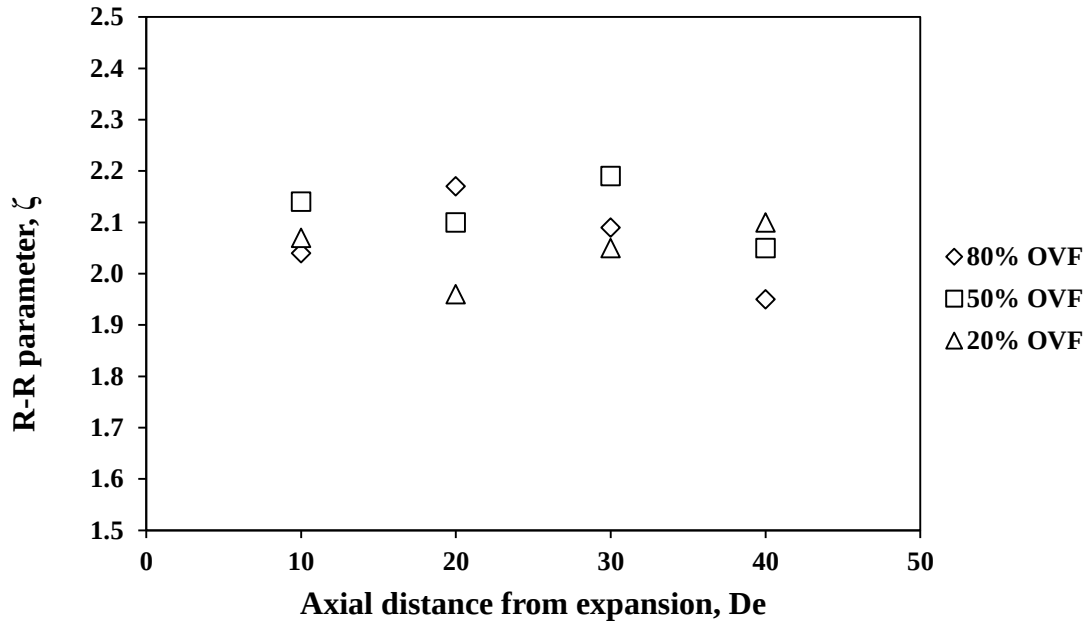

Figure 5-76 Evolution of the Rosin-Ramler parameter for downstream mixture velocity, U_{sme} = 0.35 ms^{-1}, probe position Centre (63.5 mm), within axial test distance and horizontal pipe orientation at different input oil volume fractions

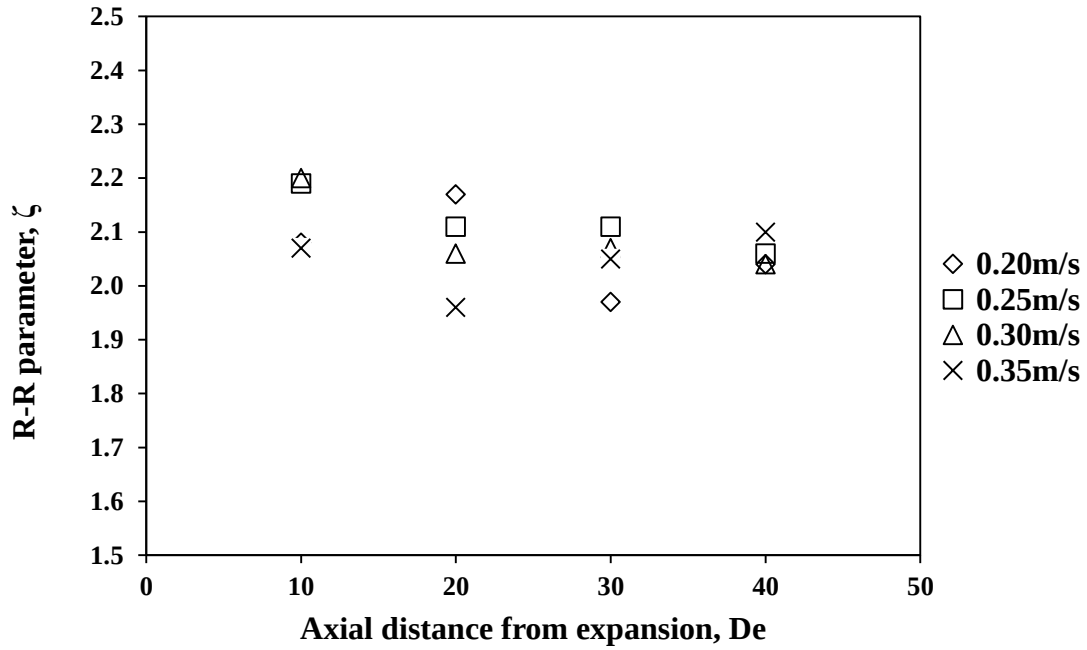

Figure 5-77 Evolution of the Rosin-Ramler parameter for input oil volume fraction 20% OVF at Centre (63.5 mm) probe position, within axial test distance and horizontal pipe orientation at different downstream mixture velocity, U_{sme}

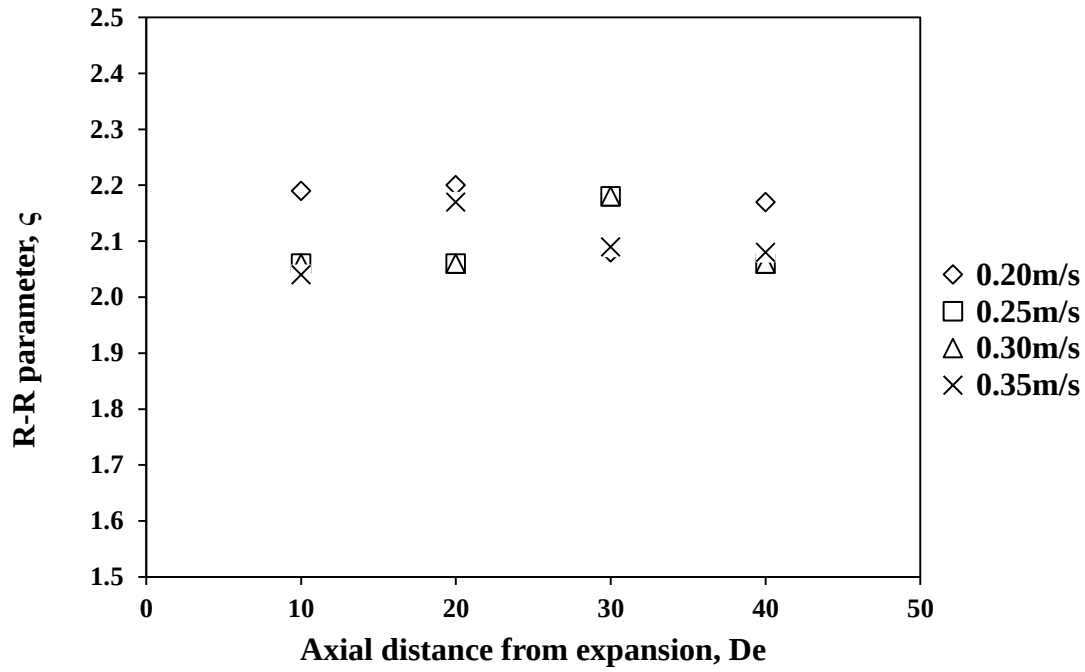

Figure 5-78 Evolution of the Rosin-Ramler parameter for input oil volume fraction 80% OVF at Centre (63.5 mm) probe position, within axial test distance and horizontal pipe orientation at different downstream mixture velocity, U_{sme}

The log-normal distribution function as described in Chapter 3 under section 3.6.2 is applied to the experimental data. The distribution fits were also found to agree largely with the experimental data, especially when the actual drop diameters are used (see Figure 5.79 to 5.81). Results of the values of the distribution parameters, δ and ξ, with δ affecting the distribution height and ξ affecting the distribution width for downstream mixture velocities 0.20 ms^{-1}, 0.25 ms^{-1}, 0.30 ms^{-1} and 0.35m/s are summarized in Table 5.3. The average standard deviation δ, was found to be 0.62 and the mean, $\xi = 1.69$.

Table 5-3 Log – normal distribution parameters values of probe position at Centre (63.5mm) for horizontal pipe orientation

Mixture velocity (m/s)	Water cut (%)	Oil volume fraction (OVF) (%)	Log-normal distribution parameters							
			10D Interface		20D Interface		30D Interface		40D Interface	
			δ	ξ	δ	ξ	δ	ξ	δ	ξ
0.20m/s	20	80	0.61	1.63	0.79	1.51	0.61	1.68	0.73	1.87
	50	50	0.57	1.76	0.53	1.69	0.57	1.67	0.66	1.73
	80	20	0,59	1.62	0.64	1.81	0.58	1.69	0.74	1.96
0.25m/s	20	80	0.61	1.72	0.6	1.69	0.67	1.69	0.56	1.68
	50	50	0.64	1.69	0.75	1.88	0.54	1.75	0.76	1.83
	80	20	0.61	1.72	0.55	1.63	0.61	1.63	0.6	1.69
0.30m/s	20	80	0.61	1.57	0.57	1.68	0.55	1.59	0.73	1.76
	50	50	0.65	1.65	0.68	1.67	0.61	1.73	0.64	1.71
	80	20	0.62	1.66	0.7	1.68	0.68	1.69	0.63	1.7
0.35m/s	20	80	0.62	1.58	0.58	1.73	0.58	1.66	0.75	1.65
	50	50	0.62	1.69	0.59	1.67	0.62	1.75	0.72	1.76
	80	20	0.6	1.69	0.64	1.65	0.58	1.6	0.77	1.76

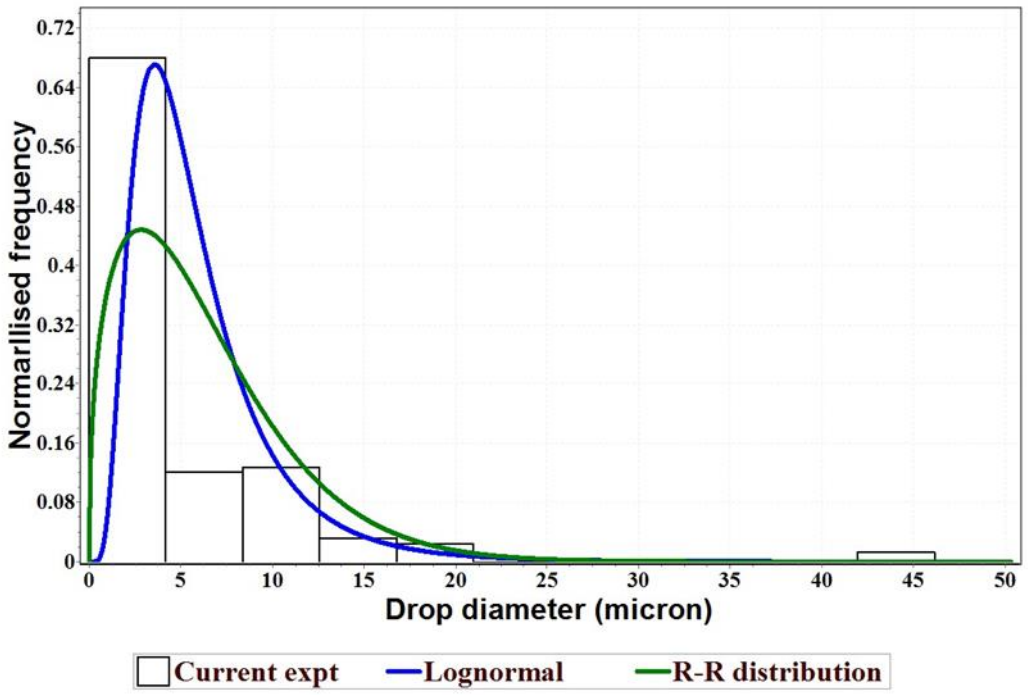

Figure 5-79 Comparison of Log – normal and R-R distribution fits to 0.20 ms^{-1} downstream mixture velocity, 20% OVF input oil volume fraction at Centre (63.5 mm) probe position, 10D axial test distance and horizontal pipe orientation.

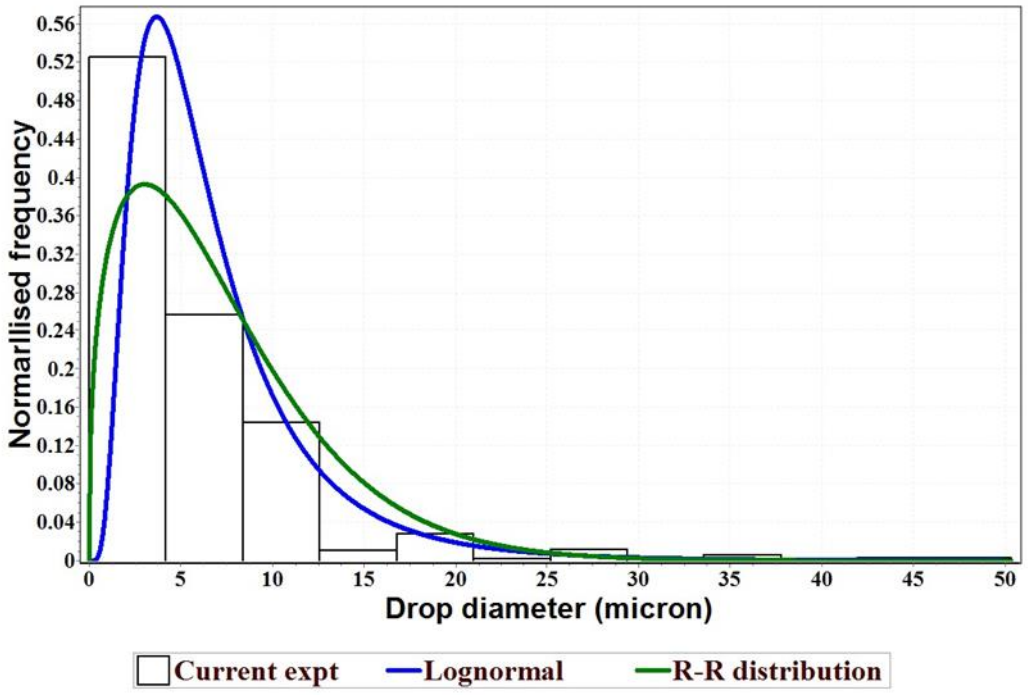

Figure 5-80 Comparison of Log – normal and R-R distribution fits to 0.20 ms^{-1} downstream mixture velocity, 50% OVF input oil volume fraction at Centre (63.5 mm) probe position, 40D axial test distance and horizontal pipe orientation.

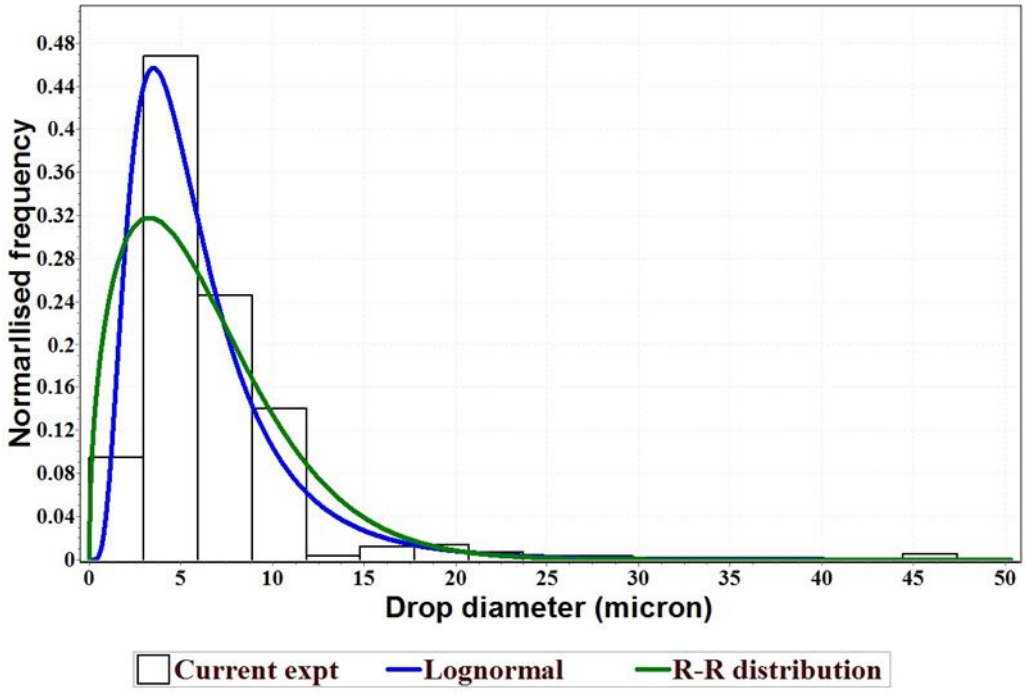

Figure 5-81 Comparison of Log – normal and R-R distribution fits to 0.20 ms^{-1} downstream mixture velocity, 80% OVF input oil volume fraction at Centre (63.5 mm) probe position, 10D axial test distance and horizontal pipe orientation.

In literature, there are several correlations and models published for predicting the maximum drop sizes in dispersed flow systems. The fundamental bases for majority of these models were given by (Hinze, 1955) as discussed in Chapter 2 under section 2.3, (Equations 2.14 and 2.22). In the case of droplets smaller than the length scale of turbulence as proposed by (Kolmogoroff, 1949, Hinze, 1955) for pipe flow, a further modification was given by (Kubie, 1977, Karabelas, 1978), to include velocity fluctuations and differences resulting in Equation 2.23.

$$\left(\frac{d_{\max}\rho_c U_c^2}{\sigma}\right)\left(\frac{f d_{\max}}{4d}\right)^{2/3} = 0.369 \qquad 5.1$$

The results obtained in the current experiment for fully dispersed flow were compared with Equation 5.1 using the Blasius correlation $8\varphi = f = 0.3164\,\mathrm{Re}^{-0.25}$ as frictional factor for $\mathrm{Re} < 10^5$ as shown in Figures 5.80 and 5.81. Sleicher (1962), in his model work had proposed the inclusion of viscosity effect of the various dispersed phases and correlated his data by the following expression in Equation 5.2.

$$(\frac{d_{\max}\rho_c U_c^2}{\sigma})(\frac{\mu_c U_c}{\sigma})^{0.5} = 38\left(1+0.7(\frac{\mu_d U_c}{\sigma})^{0.7}\right) \quad 5.2$$

where U_c, μ_c and μ_d are the continuous phase velocity, the viscosities of the continuous and dispersed phases respectively. This model was also correlated with current experimental results as shown in both Figures 5.81 and 5.82. Other models at high dispersed phase concentrations as suggested by (Brauner and Ullmann, 2002) can also be tested.

$$\left(\frac{d_{\max}}{D}\right) = 2.22 C_H \left(\frac{\rho_c U_c^2 D}{\sigma}\right)^{-0.6} \left(\frac{\rho_m}{\rho_c(1-\varepsilon_d)} f\right)^{-0.4} \left(\frac{\varepsilon_d}{1-\varepsilon_d}\right)^{0.6} \quad 5.3$$

where ε_d is dispersed phase fraction, D is diameter of the pipe, C_H is an adjustable constant, C_H = O(1) and f is the wall friction factor.

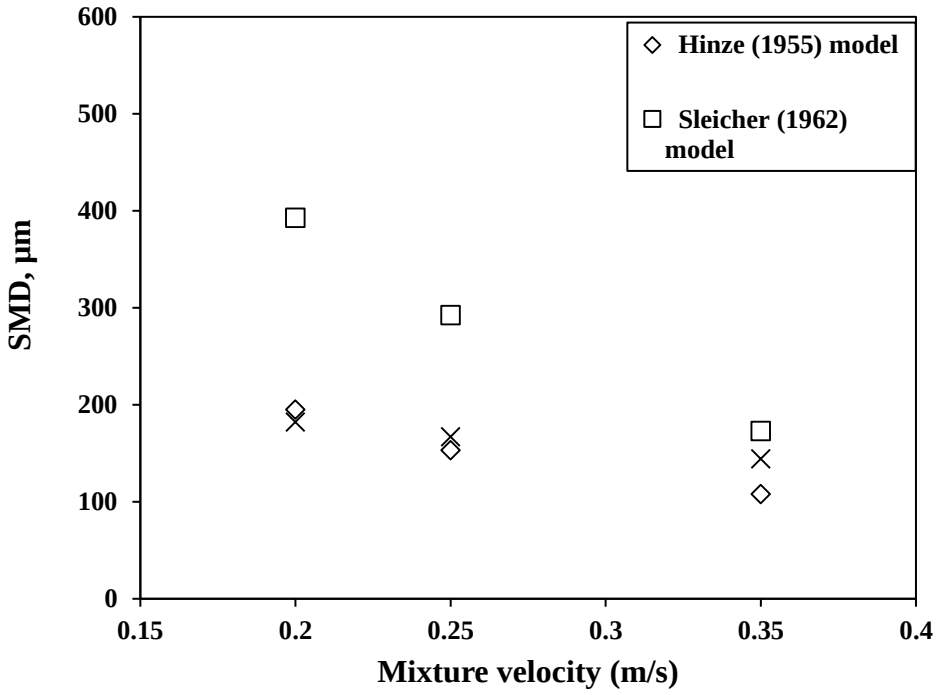

Figure 5-82 Comparison of the experimental Sauter Mean Diameter (d_{32}) for flow condition, 20% OVF at 10D axial distance of test section in horizontal pipe orientation, probe position (111.3 mm) from bottom at downstream velocities of 0.20 m/s, 0.25 ms^{-1} and 0.35 ms^{-1}.

In Figure 5.82, it is clearly seen that the experimental data correlated well with the (Hinze, 1955) model for dilute dispersions in a water continuous and oil dispersed (20% OVF) flow condition. The (Sleicher, 1962) model however, performed better when oil was considered as the continuous phase and water the dispersed phase (80% OVF) as shown in Figure 5.83.

The coalescence phenomenon is more complex since it involves simultaneous processes such as the interaction of droplets together with the drainage and eventual rupture of the intervening liquid film, in which the physical properties of the fluids and the interfaces will play an important part. The coalescence mechanism has been discussed extensively in Chapters 2 and 3. (Shinnar, 1961, Thomas, 1981, Kumar et al., 1993, Tsouris and Tavlarides, 1994, Liu and Li, 1999) etc., are some researchers who have proposed models and correlations for the coalescence process.

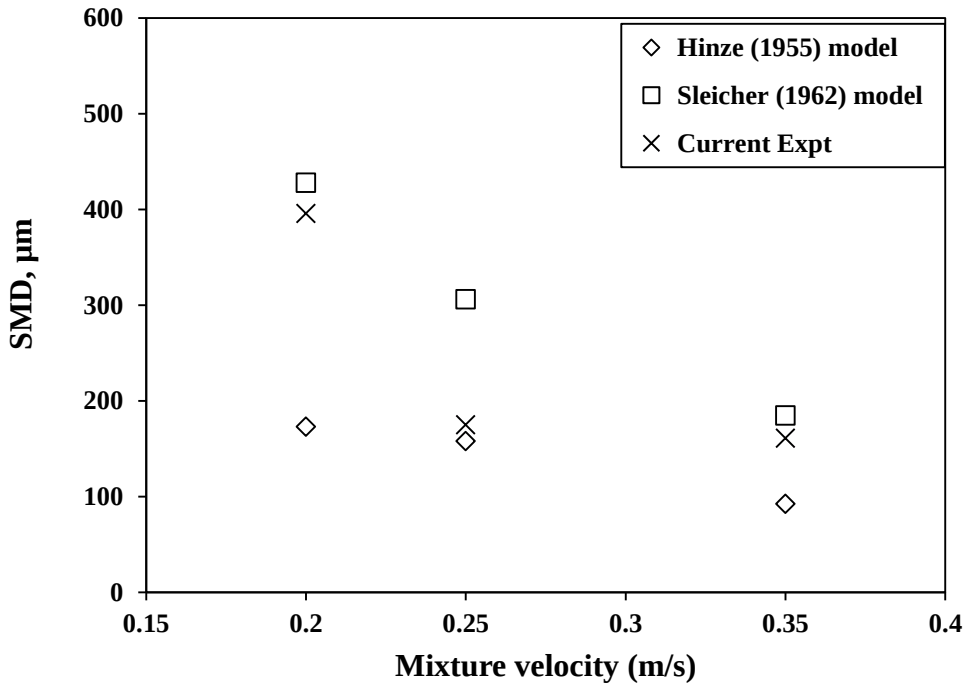

Figure 5-83 Comparison of the experimental Sauter Mean Diameter (d_{32}) for flow condition, 80% OVF at 10D axial distance of test section in horizontal pipe orientation, probe position (15.9 mm) from bottom at downstream velocities of 0.20m/s, 0.25 ms^{-1} and 0.35 ms^{-1}.

However, modelling of coalescence mechanism is quite difficult as the collision frequency of droplets and film drainage depends on many parameters such as fluid properties, vibrations, surfactants and temperature (Valentas and Amundson, 1966). The models proposed by (Shinnar, 1961) and (Thomas, 1981), which was discussed earlier in Chapter 3, gives an understanding of the coalescence process but cannot be applied practically as some parameters such as $A(h_0)$ h_o in Equation 3.19 are unknown and difficult to measure experimentally in a turbulent system. Another limitation is the determination of droplets contact time (T) and film drain time (τ) as given in Equations 3.21 and 3.22 respectively.

5.5 Summary

Drop break-up and coalescence mechanisms have being discussed in details with better understanding of the hydrodynamics in oil-water two phase flow system in both horizontal and inclined angle orientation through a sudden pipe expansion. Focused Beam Reflectance Measurement (FBRM M500P) laser backscatter technique was used to measure chord length distributions of liquid-liquid dispersions at different positions in the pipe cross section downstream of the singularity. Vital information was obtained from the experimental investigation for the influence of mixture velocity, input oil fraction, probe position and pipe orientation (i.e. horizontal, upward and downward pipe inclination), on the drop sizes and distributions formed downstream of the expansion. The following summarizes the findings:

a. For horizontal pipe flow
    - Input oil volume fraction strongly influenced formation of drop sizes downstream of the expansion as investigation shows larger droplets detected at 40D due to coalescence mechanism of the drops.
    - Smaller droplet sizes are formed downstream of the pipe expansion with an increase in downstream mixture velocity.
    - Coalescence of dispersed phase droplets progresses from inlet and stratifies gradually downstream of the singularity. In general higher input oil fraction and low mixture velocity ($0.20ms^{-1}$), favours coalescence producing larger droplets downstream of pipe expansion.

b. Upward inclination orientation pipe flow

- Input oil volume fraction affects the Sauter mean diameter (SMD) of drops throughout the entire axial test distance resulting in the formation of smaller droplets at low mixture velocity (0.20 ms^{-1}).

- Smaller droplet sizes are formed downstream of the pipe expansion with an increase in downstream mixture velocity.

- Sauter mean diameter (SMD) is affected by probe position. Larger droplets were observed above and below the interface region.

- Water droplets coalesce and settle faster than dispersed oil droplet in water continuous phase flow system. The bulk oil layer was also observed to flow faster at the top than the bulk water layer at the bottom in upward pipe inclination orientation.

c. Downward inclination orientation pipe flow

- Both input oil volume fraction and probe position show minimal effect on the drop sizes formed for downward pipe inclination.

- Sauter mean diameter (SMD) increases with increase in mixture velocity along the entire test section. At higher mixture velocity, both water and oil droplets coalesce faster at the top and bottom pipe portions respectively and accumulates around the interface downstream of the singularity.

- The larger droplets formed are observed to concentrate mostly at the bottom portion of pipe at position 40D downstream of the expansion.

- Smaller and finer droplets detected at higher mixture velocity (0.35m/s) in position 30D indicate dispersion due to high collision frequency of droplets.

A comparison between some published models and correlations with current experimental data was carried out. The Rosin – Rammler distribution function was found to fit satisfactorily well with experimental data, especially at the interface mixed region between oil and water. The Rosin-Rammler parameter results also show consistency with previous work on larger pipe diameter but vary with findings from some earlier research work on smaller pipe diameters. The Log-normal distribution fits were also found to be in large agreement with the actual drop diameters of the experimental data. Sauter mean diameter (d_{32}), values of present data also correlated well with (Hinze, 1955) model for water continuous and oil dispersed phase system in horizontal pipeline.

Chapter 6 ESTIMATION OF OIL VOLUME FRACTION DOWSTREAM OF PIPE EXPANSION

6.1 Experimental data analysis

There are several methods of analysis in research programme to understand the flow characteristics of liquid – liquid systems in pipelines. One of such methods is to carry out a time series analysis of the actual signals of the experimental data. These analytical methods will give information about the flow characteristics; however the features observed cannot be easily explained qualitatively. The results obtained from the conductance probes therefore also include investigations using probability density functions (PDF) and power spectral density (PSD) analysis.

Considering the flow pattern map of Trallero et al (1997), all the flow patterns downstream of the pipe expansion are in the stratified and stratified (ST) with mixed interface (ST & MI) flow regimes, when fully developed in the current study. Several factors therefore enhance the phase layer evolution and segregation process, amongst which is the input oil volume fraction (OVF) and the downstream mixture velocity. Data obtained from the ring conductance probes and information from the Phantom camera video recordings will be used to investigate flow development along the pipe expansion and interface shapes of the singularity. A detailed discussion on the effect of flow parameters with axial pipe distance and pipe orientation will be made and also to establish a relationship between captured images and the acquired data.

6.1.1 Probability density function (PDF)

Probability Density Functions (PDFs) can be used to identify flow patterns. The function P(x) dx can be defined following equation, where data x (t) lies on the value between x and x + Δx:

$$P(x)dx = P(x < x(t) \leq x + \Delta x) \qquad 6.1$$

The PDFs can be estimated from a histogram for the case of a discrete signal by dividing the limited data set with the total number of samples. The total area under the PDF is equal to 1, as given in equation 6.2.

$$P(-\infty < x < \infty) = \int_{-\infty}^{\infty} P(x)dx \equiv 1 \qquad 6.2$$

Several parameters characterizes a PDF, which are related to its moments; e.g. Mean, Standard Deviation, Skewness and Kurtosis, which are represented by μ, σ, S, K, respectively. They are defined as follows.

$$\mu = \sum_{i=1}^{N} x_i \qquad 6.3$$

$$\sigma(x) = \sqrt{\frac{1}{N}\sum_{i=1}^{N}(x_i - \mu)^2} \qquad 6.4$$

$$S(x) = \frac{1}{N}\sum_{i=1}^{N}(x_i - \mu)^3 / \sigma^3 \qquad 6.5$$

$$K(x) = \frac{1}{N}\sum_{i=1}^{N}(x_i - \mu)^4 / \sigma^4 - 3 \qquad 6.6$$

6.1.2 Cross correlation and structure velocity

Cross correlation is usually applied to measure the average translational velocity of the flow structure, such as droplets, interfacial waves and/or disturbance waves. When two signals of time series x(t) and y(t) from conductance probes were obtained from a sequence of field and between which the structure was kept, the cross correlation of these signals, r_{xy}, is defined by the equation (6.7), which shows a peak at a certain time delay. This indicates the transit time of the structure between the two probes.

$$r_{xy}(\Delta t) = \frac{\sum_{i=1}^{N}\left[x(t) - \bar{x}\right].\left[y(t+\Delta t - \bar{y})\right]}{\sqrt{\sum_{i=1}^{N}\left[x(t) - \bar{x}\right]^2}.\sqrt{\sum_{i=1}^{N}\left[y(t+\Delta t) - \bar{y}\right]^2}} \qquad 6.7$$

where $\bar{x}$ and $\bar{y}$ are the mean values and Δt is the time delay. The average velocity of the structure between the two probes, U_p, is given as the length divided by the time delay as in equation (6.8).

$$U_p = \frac{L}{\Delta t_{\max}} \tag{6.8}$$

where L is the distance between the probes.

6.1.3 Power Spectrum Density (PSD)

The Power Spectrum Density functions (PSD) is used to obtain dominant frequency information from time series graphs when data is stabilized. This is estimated by using Fourier transform of the Auto Covariance function of void fraction time series. From the time series, the Auto Covariance function at an arbitrary time delay $R_{xx}(k\Delta\tau)$ is defined as:

$$R_{xx}(k\Delta\tau) = \frac{1}{T-\tau}\int_0^{T-\tau}(\varepsilon_l(t)-\bar{\varepsilon}_l)(\varepsilon_l(t+k\Delta\tau)-\bar{\varepsilon}_l)dt \tag{6.9}$$

where T is the sample duration, Δτ is the resolution of time delay, τ is the interrogation time delay and ε_l is the average liquid holdup fraction of the whole time series. The power spectrum density function is then obtained as follows:

$$P_{xx}(f) = \sum_{k=-\infty}^{\infty} R_{xx}(k\Delta\tau)\exp(i2\pi fk\Delta\tau) \tag{6.10}$$

A suitable windowing function can be introduced or applied to suppress the spectrum leakages that mostly exist as the side lobes at the nigh frequency end of the spectrum. The frequency domain, f, lies between 0 to $1/2\Delta\tau$ with increments of $1/(2\Delta\tau N)$. The auto correlation which decays with time is obtained as

$$r_{xx}(k\Delta\tau) = \frac{R_{xx}(k\Delta\tau)}{R_{xx}(0)} \tag{6.11}$$

The dominant frequencies can also be obtained from the power spectral density (PSD) as the value corresponding to highest peak in the spectrum.

6.2 Conductance probe results and discussions

The experimental design for determining oil volume fraction (OVF), in the current work has been given in section 4.2., in Chapter 4. Two flow regimes are clearly identified, which are the segregated (stratified flow), (ST) and stratified with mixed interface (ST& MI). Visual observations and flow pattern images downstream of the expansion obtained with the Phantom camera shows two (2) layers, (i.e. oil top and water bottom layers) for stratified flow (ST) and three (3) distinct layers for stratified with mixed interface flow (ST& MI), i.e. oil top layer, mixed interface layer and water bottom layer. Experiments were conducted with the ring conductance probe in four (4) axial locations downstream of the pipe expansion at 10D, 20D, 30D and 40D for input oil volume fractions 20% to 80% and downstream mixture velocities of 0.20, 0.25, 0.30, 0.35, 0.50, 1.00, 1.50, 2.00, 2.50, 3.00 and 3.50 m/s, in horizontal and inclined (upward and downward), pipe orientations. The results are discussed in details in the sections that follows.

6.2.1 Flow pattern development downstream of pipe expansion

Flow pattern maps are often used to predict the pattern of the liquid-liquid oil-water two phase steady flows, provided both the upstream and downstream flows are fully developed. This dynamic phase evolution from the inlet region to the downstream section of the expansion pipe is caused by a number of factors such as operational conditions, physical properties of the fluids, pipe orientation etc., affecting the phase layers formed. The flow patterns expected downstream of the expansion in the current study are plotted on the flow pattern map of (Trallero et al., 1997) and are in the segregated and stratified with mixed interface regions (Figure 6.2).

This section is therefore dedicated to investigate these factors affecting the evolution of flow patterns in practical such as the pipe length downstream of the expansion,

operational conditions (input oil volume fraction (OVF), water cut, and mixture velocity), at the different pipe orientations.

6.2.1.1 Horizontal pipe expansion

In horizontal flow of two immiscible liquids, the accurate prediction of flow regimes and the characteristics that define them is vital. These flow regime predictions are useful in formulating two-phase phenomenological models and in turn provide accurate quantitative predictions of the flow. Some important flow parameters such as in-situ phase fractions, fluids physical properties (density, viscosity, surface and interfacial tension), and flow geometry (pipe diameter, homogenizing unit), and pressure drop across a multiphase oil production pipeline with thermodynamic operating conditions, are useful in determining whether hydrates will form in the pipelines.

Six (6) distinct flow patterns were identified in the current study and classified into two categories: segregated flow and dispersed flow as presented in Figure 6.1. Stratified flow and stratified flow with some mixing at the interface (ST&MI) are classified as segregated flow patterns. Oil – water intermittent flow and stratified wavy interface flow patterns were also observed with an increase in downstream mixture velocity. Further increase in mixture velocity resulted in Rayleigh Taylor instability 'plume shaped' flow. The dispersed flow was either water dominated or oil dominated. A dispersion of oil in water over a water layer and an emulsion of oil in a water-dominated (Do/w & Dw/o), flow patterns.

The flow patterns observed are in general agreement with majority of the published work on horizontal oil-water two phase flow systems, (Trallero et al., 1997, Soleimani et al., 2000, Lovick and Angeli, 2004b) etc. Arirachakaran et al. (1989) in his experimental work reported the presence of water – annulus annular flow and oil-slugs-in-water, which was not seen in the current campaign. (Arirachakaran et al., 1989) attributed the presence of annular flow to the physical properties of the oil phase, especially the viscosity. His findings was based on the fact that four (4) different oils with different viscosities, (the lowest oil been $\mu_{oil} = 4.7mPa.s$), were used in conducting the experiments. He stated that as the viscosity decreases, the oil

– annulus flow diminishes as a result of the oil not dense and viscous enough to sustain a water core.

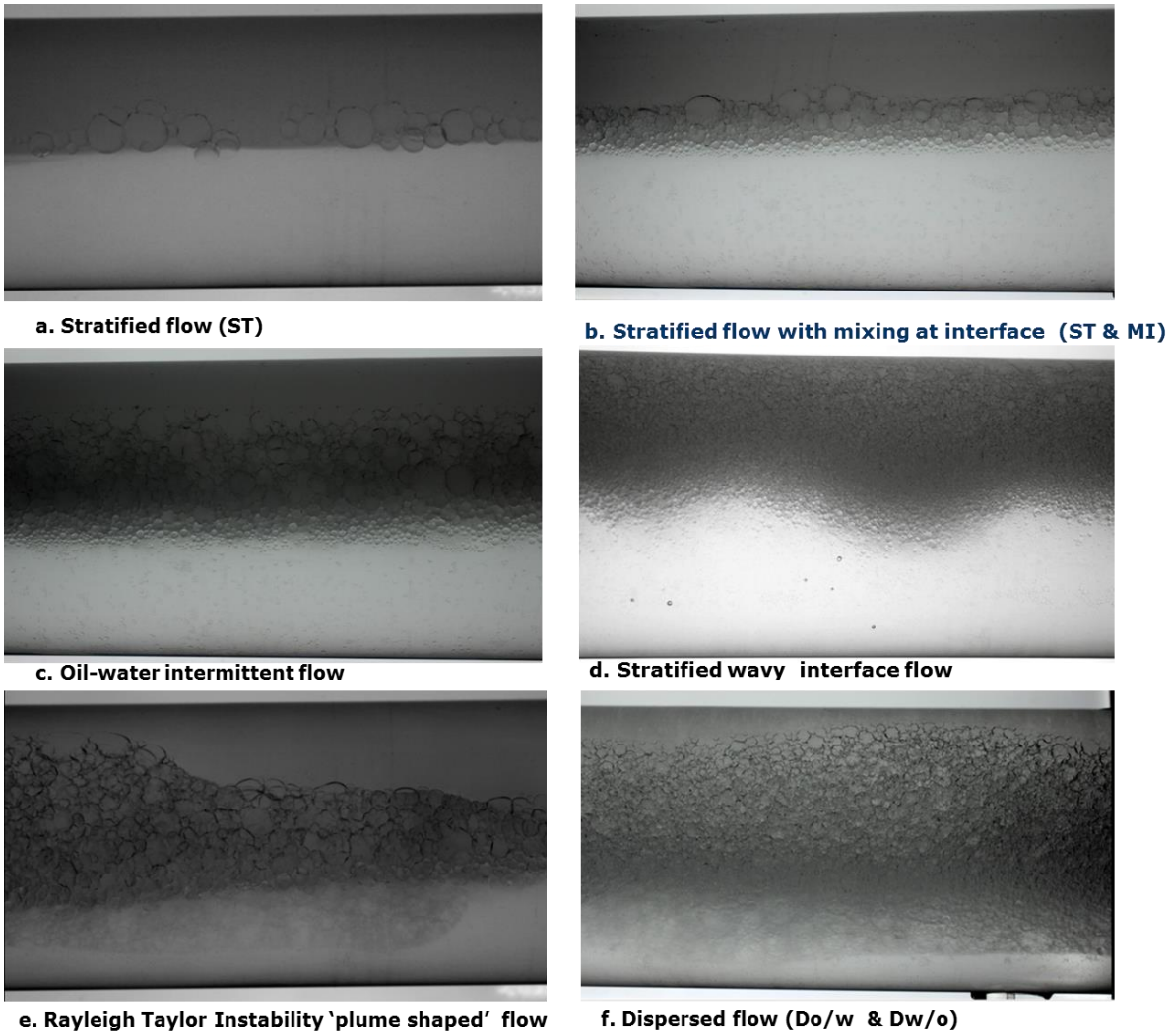

Figure 6-1 Horizontal oil-water flow pattern images observed downstream of the sudden pipe expansion.

A significant and interesting observation of the evolving flow patterns in the current experiment campaign is the appearance of the Raleigh Taylor instability 'plume shaped' flow at downstream mixture velocity between 1.00 – 1.50 m/s (Figure 6.1e). This flow pattern refers to instability of an interface between two fluids of different densities, which occurs when the lighter fluid is pushing the heavier fluid. Raleigh Taylor instability (RTI), develops initial perturbations and progresses from a lower growth phase into a non-linear or exponential growth, eventually developing

‘’plumes’’ flowing upwards (in the gravitational buoyancy sense) and ‘’spikes’’ falling downwards.

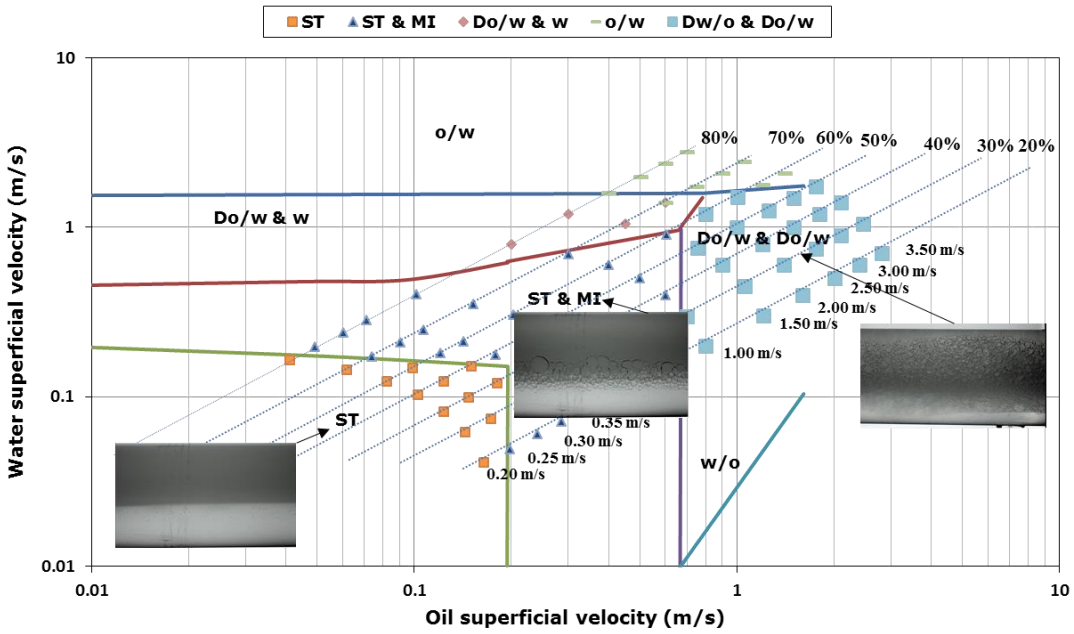

Figure 6-2 Flow patterns encountered within the rig in current study, plotted on the flow pattern map of (Trallero et al., 1997).

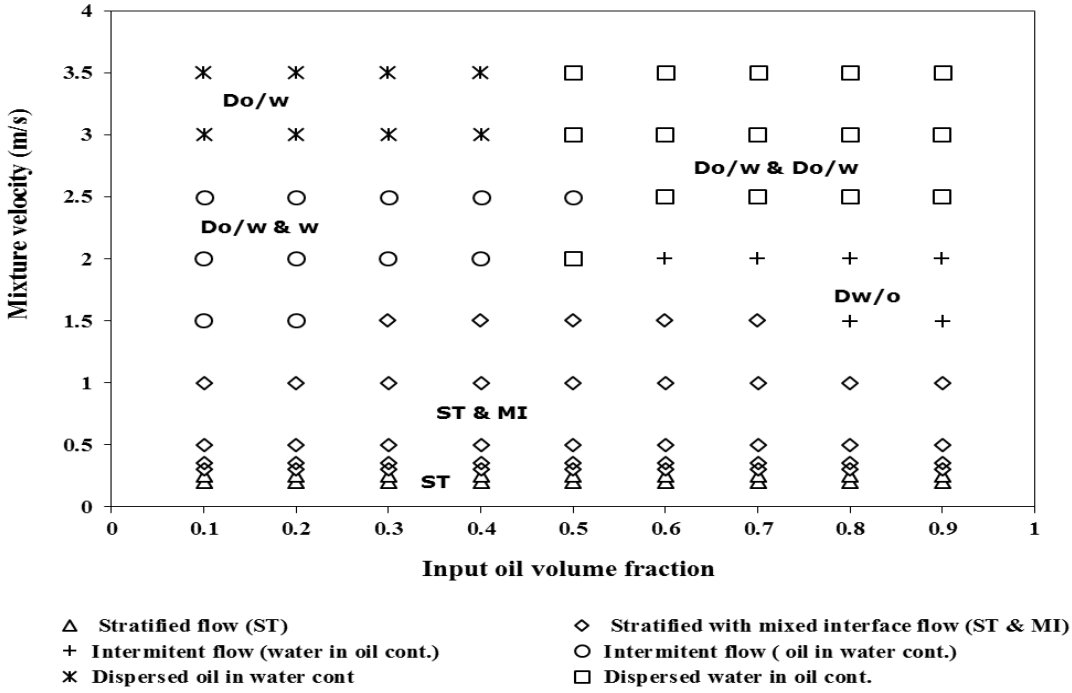

Figure 6-3 Experimental flow pattern map, horizontal for current study.

The difference in fluids densities divided by their sum gives a dimensionless number in fluid dynamics defined as Atwood number, (A). For (A) close to zero, RT Instability flow takes the form of symmetric ‘’fingers’’ of fluids. If A, is close to 1 the much lighter fluid (i.e. oil), ‘below’ the heavier fluid takes the shape of larger bubble-like plumes.

The flow regimes observed from the current study are also plotted on a flow pattern map in terms of mixture velocity against input oil volume fraction as shown in Figure 6.3. It can be seen that at mixture velocities lower than 0.35m/s stratified flow (ST) was observed at all input oil volume fractions (Figure 6.4a-d). A clear interface exists between the two liquid oil - water phases without any entrainment at low mixture velocity, 0.20m/s. The flow is gravity dominated and hence a smooth interface without waves, even though there seems to be a transition to turbulent flow regime. Drops of one phase into the other appears at higher mixture velocities, resulting in the onset of mixed interface flow at 0.35m/s as shown in Figure 6.4d.

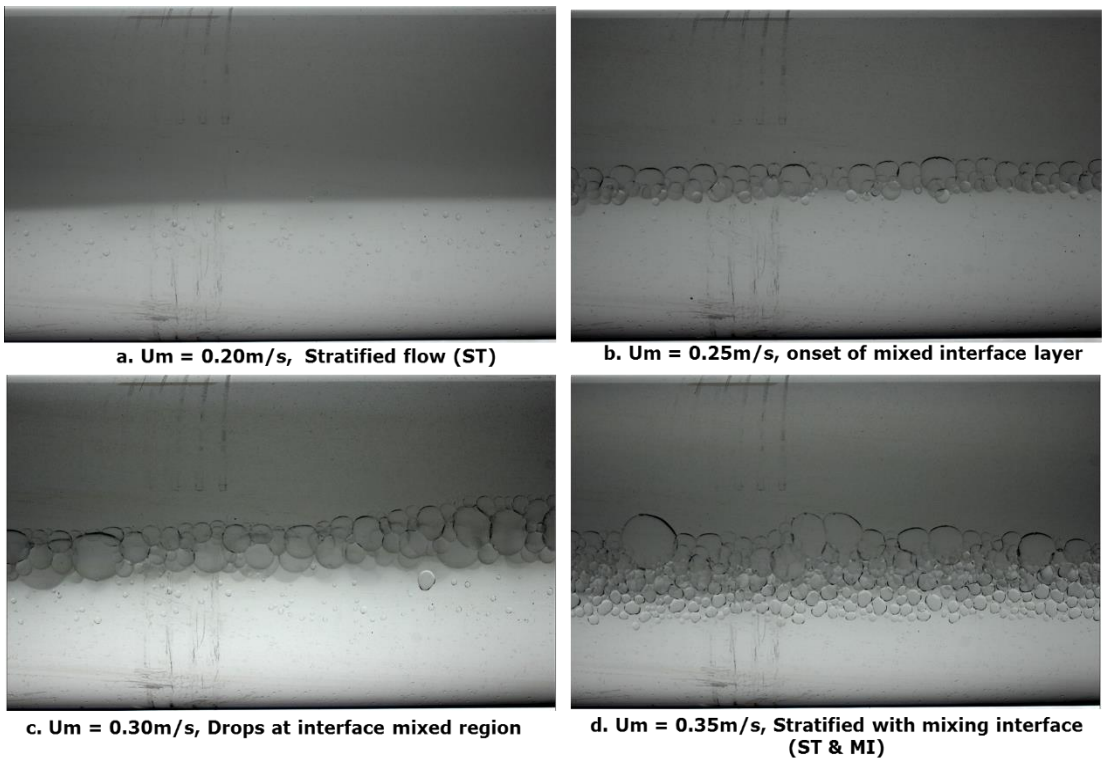

Figure 6-4 Images on the effect of increasing mixture velocity at all input oil volume fraction (20% to 80%), close to inlet axial test distance position 20D.

As the mixture velocity increases further, the range of oil input phase fractions over which three-layer flow is observed diminishes and dispersed flows are seen to cover a broader range of oil input phase fractions. Further increase in the flowrates causes the appearance of interfacial waves (Figure 6.1d). These are capillary waves, mostly modified by the shear stress due to the presence of pipe wall effect. Shorter waves are seen, resulting from the excitation of the frequencies of all wave spectrum from conductance probe data. Both water and oil droplets exist close to the interface, with dynamic and buoyancy forces acting simultaneously on them. The dynamic forces tend to disperse these droplets throughout the pipe, which are opposed by the counteracting gravity settling forces. This phenomenon has been explained in Chapter 5. The generalised Kelvin-Helmholtz instability is often used to predict the onset of these drop formation.

Different flow patterns appears beyond the stratified flow region (ST) and stratified with mixed flow (ST & MI) as mixture velocity is increased more than 1.50m/s as can be seen from the flow pattern map and images in (Figures 6.1f, 6.2, 6.3). There are water in oil (w/o) dispersions and oil in water dispersions (o/w) depending on the conditions under which they are formed. Water or oil can be the dominant phase, depending on which one is the continuous phase, and what the corresponding pressure drop response would be. These dispersions normally occur at a phase inversion point.

Figures 6.5, 6.6 and 6.7, shows the effect of low downstream mixture velocities, (0.20, 0.25, 0.30 and 0.35m/s), on the phase volume fraction along the expansion for input oil volume fractions 80% OVF, 50% OVF, 20% OVF, respectively and horizontal pipe orientation flow of results from the ring conductance probes. The trends show homogeneous flow at the inlet portion (10D) and stratifies downstream of the singularity, especially at 30D, as predicted by each probe. An increase in mixture velocity favours the segregation process for both flow conditions of 80% OVF (water dispersed in oil continuous flow) and 20% OVF (oil dispersed in water continuous flow), which is slightly different from the 50% OVF flow condition.

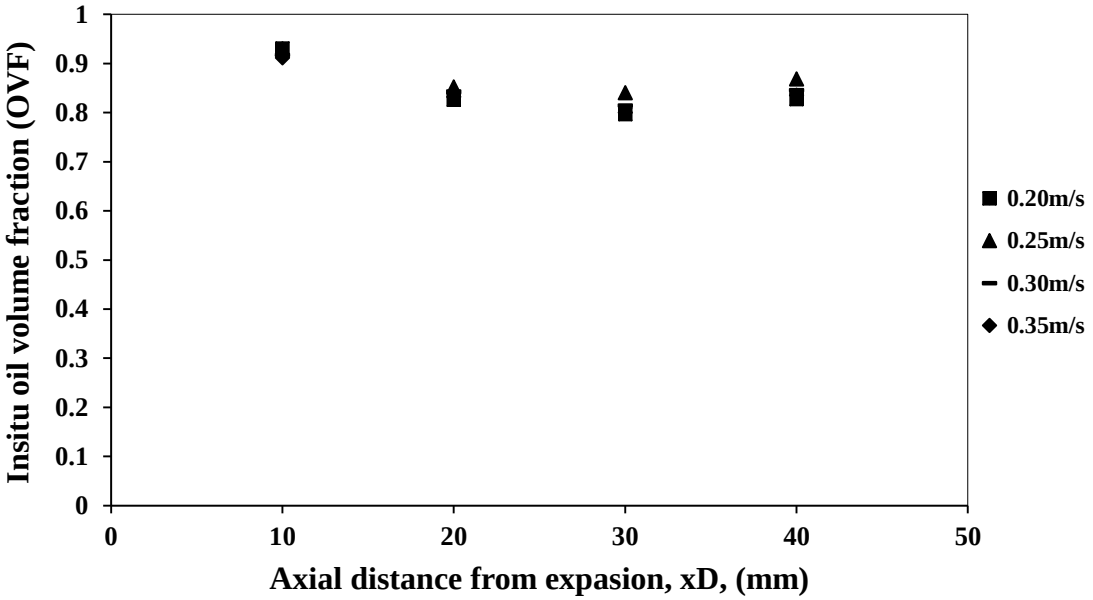

Figure 6-5 In-situ oil volume fractions in a pipe cross section at the various axial distance, input oil volume fraction (80% OVF), and horizontal flow at low downstream mixture velocities.

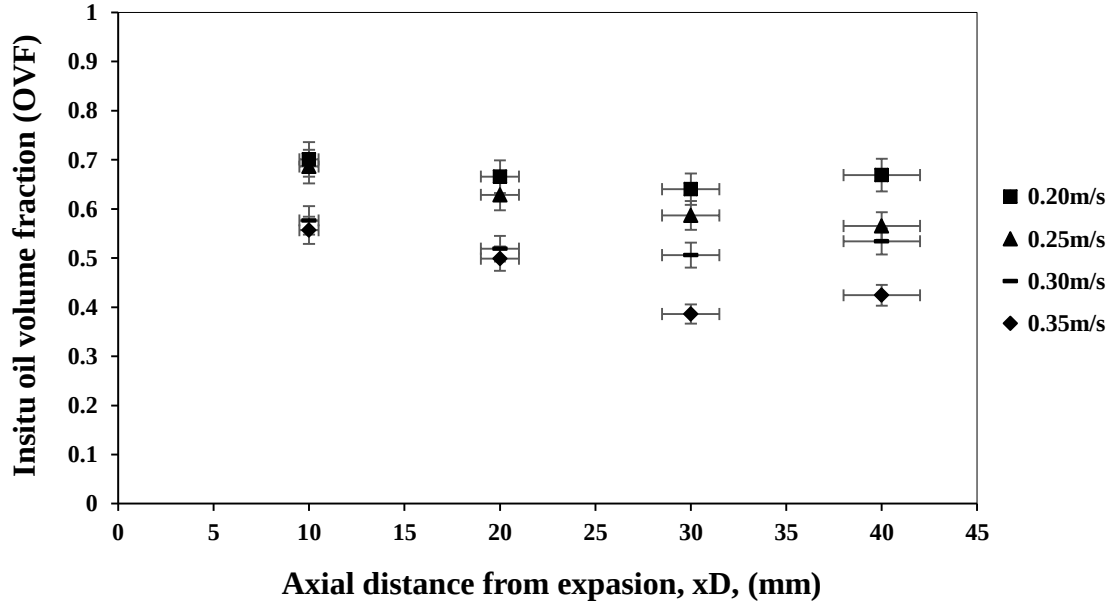

Figure 6-6 In-situ oil volume fractions in a pipe cross section at the various axial distance, input oil volume fraction (50% OVF), and horizontal flow at low downstream mixture velocities.

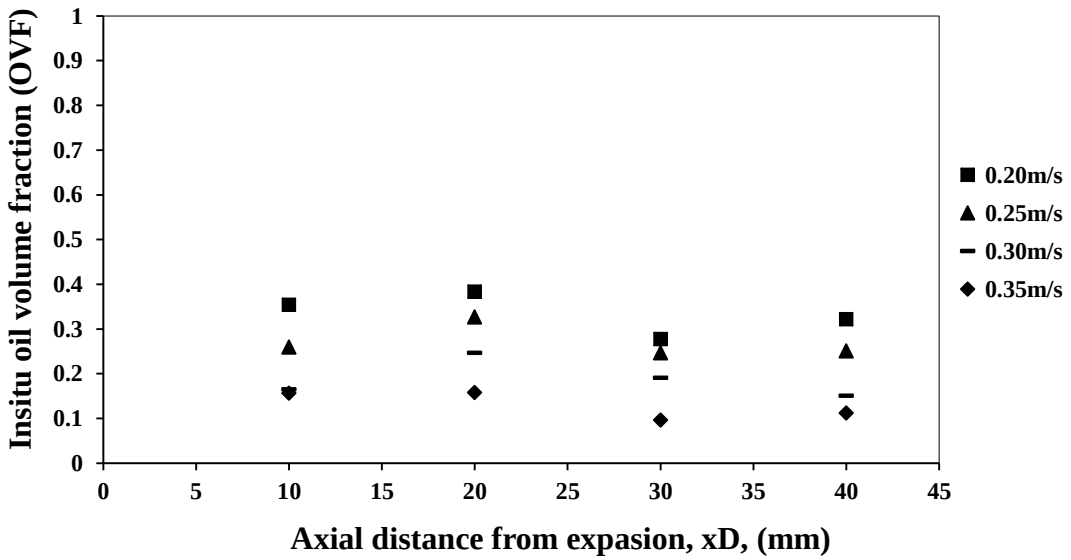

Figure 6-7 In-situ oil volume fractions in a pipe cross section at the various axial distance, input oil volume fraction (20% OVF), and horizontal flow at low downstream mixture velocities.

The effect of higher downstream mixture velocities, (2.00, 2.50, 3.00 and 3.50m/s), on the phase volume fraction along the expansion for input oil volume fractions 80% OVF, 50% OVF, 20% OVF, respectively and horizontal pipe orientation flow of results from the ring conductance probes are presented in Figures 6.8, 6.9 and 6.10 respectively. As shown in Figure 6.8, at high input oil volume fraction, 80% OVF, the dispersed water droplets are not easily detected by the probes as the flow is dominated with oil continuous flow.

For 50% OVF equal input oil volume fraction, an increase in downstream velocity (0.30 and 0.35m/s), favours stratification downstream of the pipe expansion as indicated in Figure 6.9. There exists a constant growth of oil layer close to the interface of pipe cross section as the flow progresses downstream towards the 40D position, where it stabilizes after attaining complete segregation of the oil and water phases. The 20% OVF flow condition seems to have more dispersed oil in water continuous flow at inlet, which gradually diminishes as oil droplets coalesce. The water layer at the bottom of pipe also increases gradually as the flow progresses and eventually stratifies at 30D and 40D, for downstream mixture velocities 0.25 and 0.30m/s.

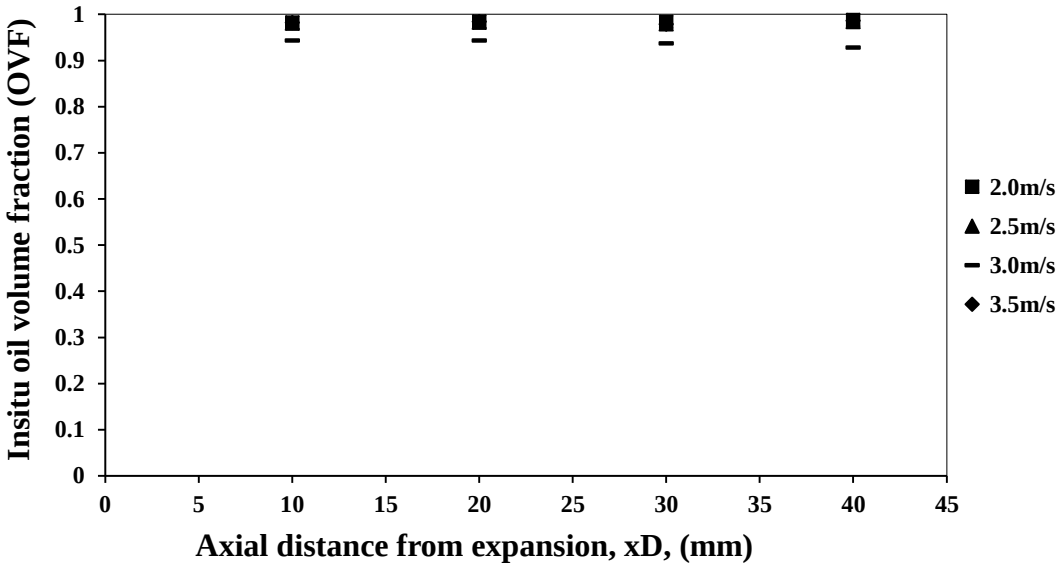

Figure 6-8 In-situ oil volume fractions in a pipe cross section at the various axial distance, input oil volume fraction (80% OVF), and horizontal flow at higher downstream mixture velocities.

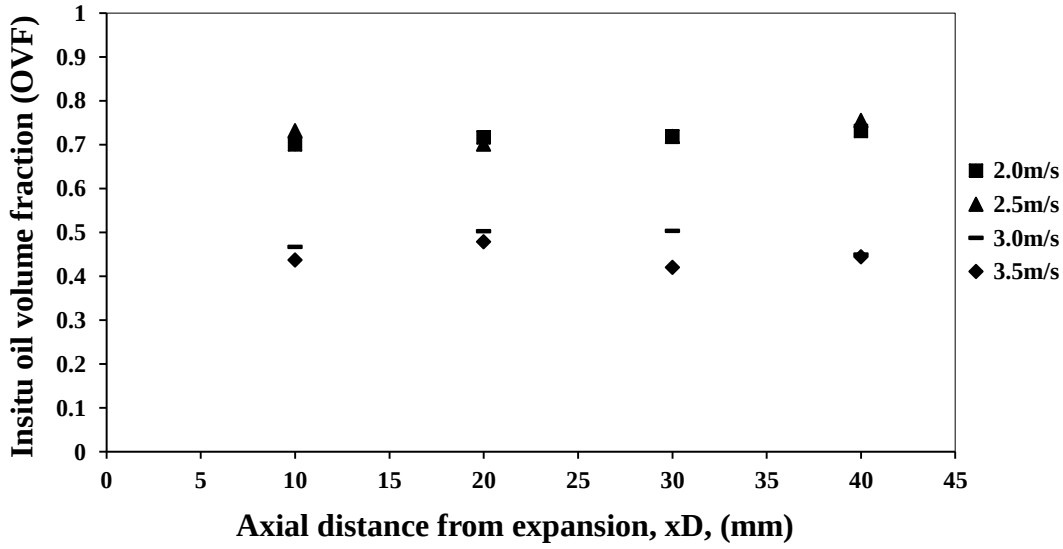

Figure 6-9 In-situ oil volume fractions in a pipe cross section at the various axial distance, input oil volume fraction (50% OVF), and horizontal flow at higher downstream mixture velocities.

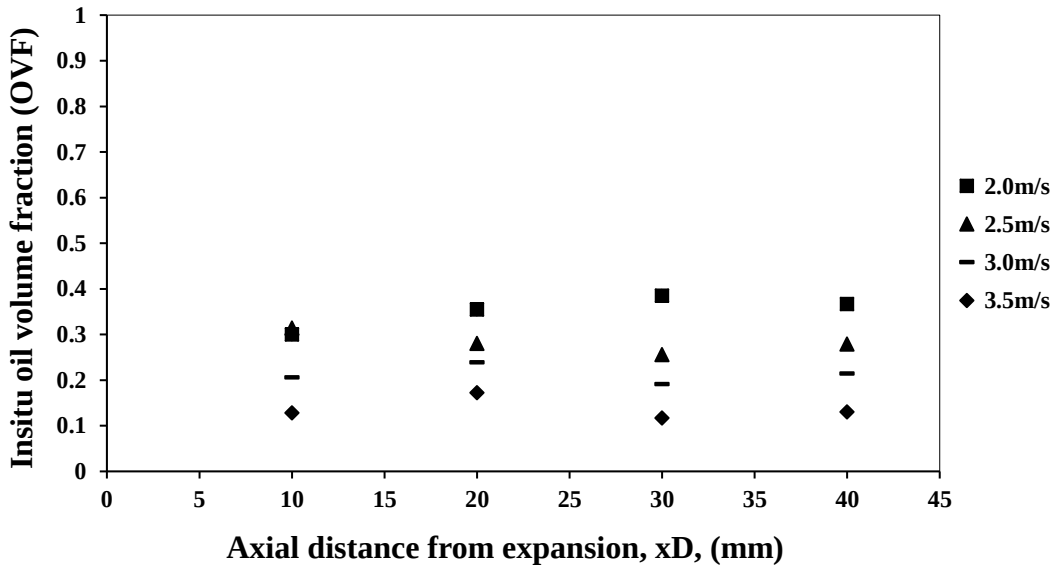

Figure 6-10 In-situ oil volume fractions in a pipe cross section at the various axial distance, input oil volume fraction (20% OVF), and horizontal flow at higher downstream mixture velocities.

Average values of in-situ oil volume fractions are also plotted against the oil and water superficial velocities from results obtained with the conductance probe in horizontal pipe orientation at the different axial positions as presented in Figure 6.11. It is clearly shown generally, from the graphs obtained that as the superficial oil velocities, U_{so}, increases, the average in-situ oil volume fraction increases, when the downstream mixture velocities (U_{mix} 0.30m/s, 1.00m/s and 3.50m/s), are kept constant. However, reverse is the case, when the superficial water velocity, U_{sw}, is increasing, resulting in a decrease in average in-situ oil volume fraction at constant downstream mixture velocities (U_{mix} 0.30m/s, 1.00m/s and 3.50m/s).

Further time series and spectral density analysis of the conductance probe data is done, together with the identification of interface shape evolution in the subsequent sections of this Chapter 6.

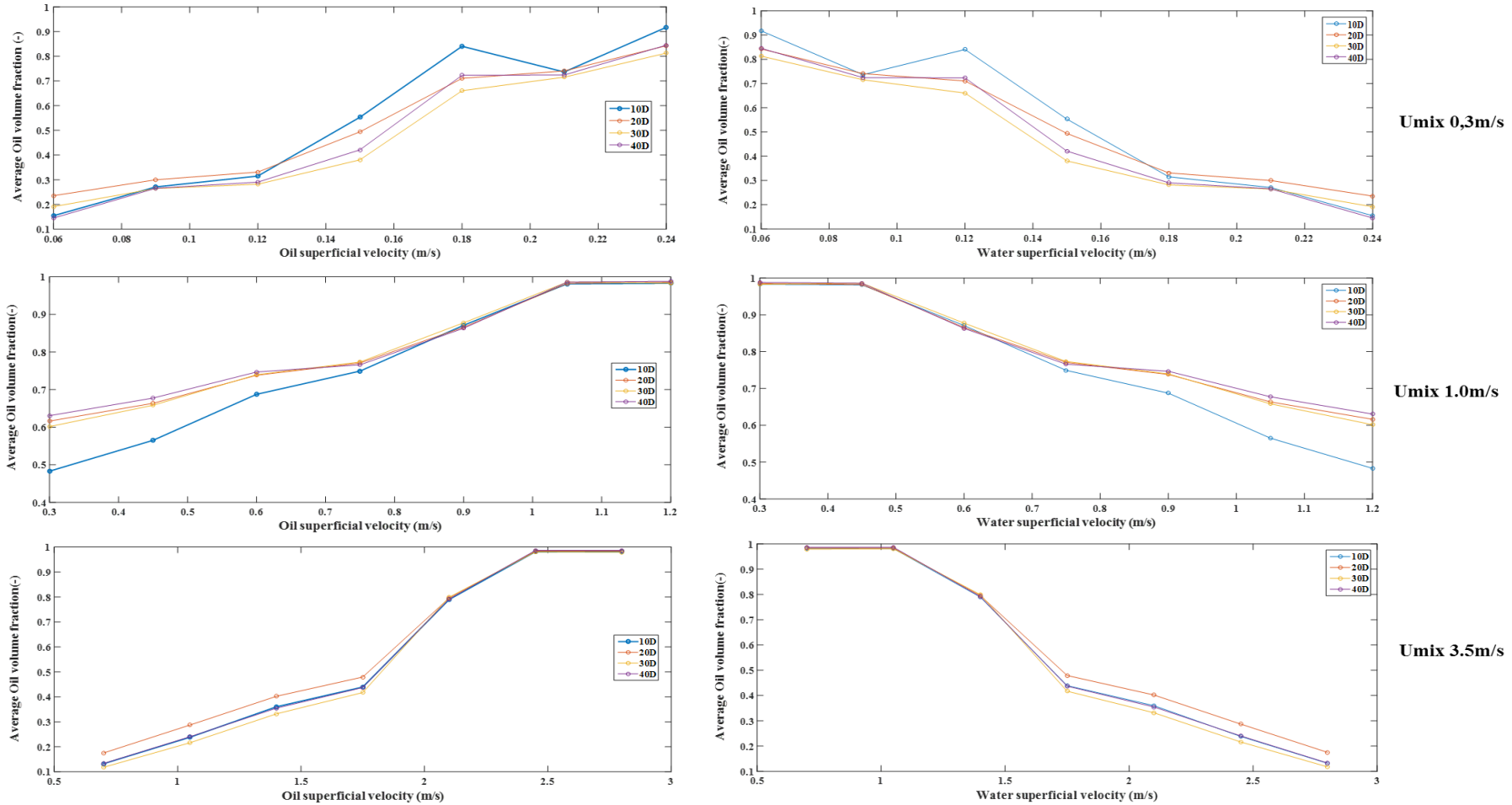

Figure 6-11 Average in-situ oil volume fraction vs superficial oil and water velocities.

The velocity slip ratio between the phases is a typical phenomenon, which occur in liquid–liquid flows in pipes as well as in other multiphase systems. The ratio between the averaged in-situ velocities of the two phases is often given as slip ratio, S, and it can be calculated as:

$$S = \frac{U_{oil}}{U_{water}} = \frac{U_{oil}/U_{water}}{\varepsilon_o/\varepsilon_w} = \frac{A_w U_{so}}{A_o U_{sw}} \qquad 6.1$$

where A_o is the flow area occupied by the oil phase. U_{so} and U_{sw} are superficial velocities for oil and water phases, respectively. The superficial velocities for different phases are defined as follows:

$$U_{ws} = \frac{Q_w}{A} = \frac{A_w U_w}{A} \qquad 6.2$$

$$U_{os} = \frac{Q_o}{A} = \frac{A_o U_o}{A} \qquad 6.3$$

The slip ratio depends on physical properties combined with flow rates, flow pattern and pipe geometry. S > 1 means that the oil phase travels faster than the water phase in the pipe while S < 1 indicates that water is the faster phase.

The velocity ratios S was calculated from the phase distribution data in the expansion pipe cross section and for the cases examined in the current study for horizontal flow are shown in Figure 6.12 and 6.13, plotted against the input oil volume for different mixture velocities. The velocity ratio in most cases is less than unity, or the in-situ oil-water volume ratio is higher than the input one. Majority of the velocity ratio measured, are within the flow regimes were stratified with mixed (ST& MI) interface or three layer exist. In this regime the tube wall is totally covered by oil, which justifies velocity ratios less than unity. In the three Layer regime, where both oil and water are in contact with the tube wall, the preferential wetting of the wall by oil may have resulted to higher tube area covered by the oil, which can explain velocity ratios less than unity. Similar observation was reported by (Angeli and Hewitt, 2000a) in their work on flow structures in horizontal oil-water flow. Also both Figures 6.12 and 6.13 indicates water moving faster than the oil except some few cases in Figure 6.12. Each phases tend to adjust itself to flow at roughly the same mixture velocity as indicated in Figure 6.12 for lower downstream mixture velocities.

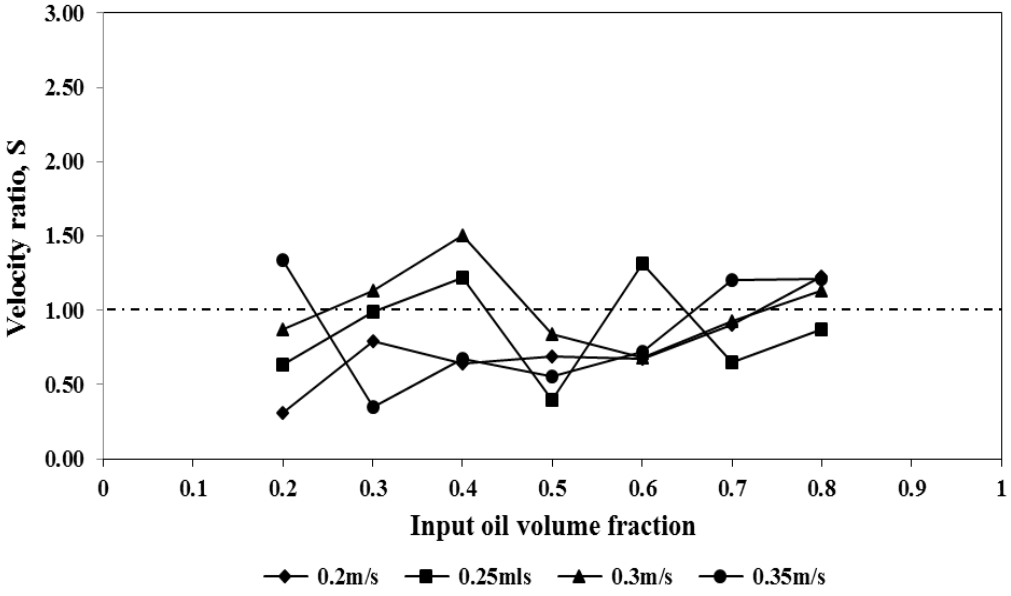

Figure 6-12 Velocity ratio at low mixture velocities and horizontal flow. S > 1 indicates oil flowing faster than water; S < 1 indicates oil flowing slower than water.

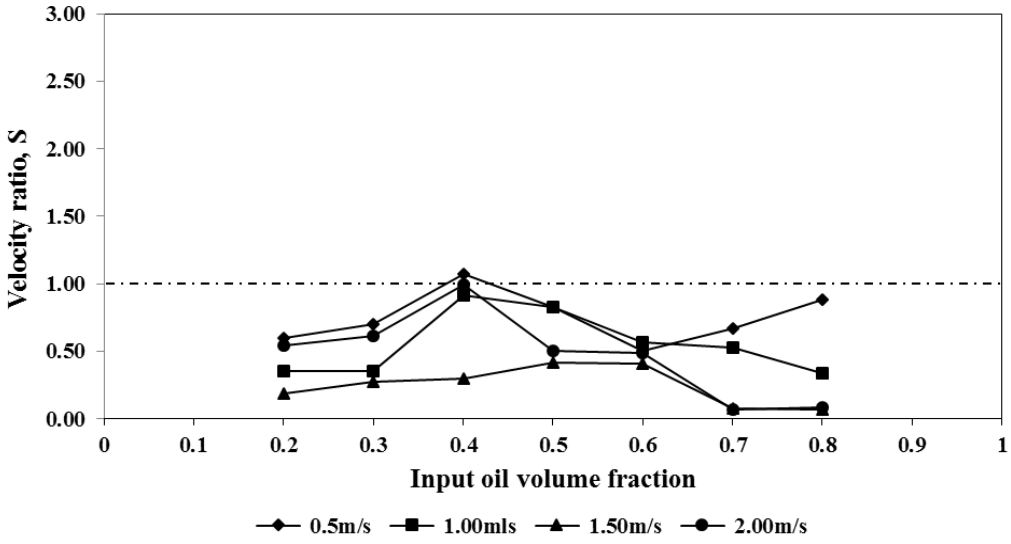

Figure 6-13 Velocity ratio at higher mixture velocities and horizontal flow. S > 1 indicates oil flowing faster than water; S < 1 indicates oil flowing slower than water.

6.2.1.2 Upwardly inclined pipe expansion

In this section, measurements of in-situ oil volume fractions in two phase oil-water flow were made for an upwardly inclined pipe flow, using the same experimental conditions in horizontal flow. The flow patterns observed are presented below.

There is generally no consensus agreement on the flow patterns observed for upward inclined flow due to the different flow conditions applied, especially the prevailing downstream mixture velocity. As discussed in Chapter 2, in the literature review, (Oddie et al., 2003) and (Lum et al., 2004) in their work observed that dispersion of the phases exist even at low mixture velocities as the flow transit from stratified (ST) to stratified with mixed interface flow (ST & MI) regime. For small upwardly inclined angles between $+1^0$ to $+5^0$, (Alkaya, 2000), observed a very smooth interface shape in stratified flow. However, (Kurban, 1997) in their experimental work reported both smooth and wavy interfaces that existed at $+1^0$ angle of pipe inclination.

The flow patterns observed in this large diameter inclined pipe are described in terms of the traditional flow pattern terminology rather than defining new flow patterns. Over the range of flow rates and pipe inclination angles considered here, stratified (ST) and stratified with mixed interface flow (ST& MI), stratified wavy (SW) flow patterns were observed at lower downstream mixture velocities (0.20 ms^{-1} – 0.35 ms^{-1}). The images of all seven (7) of these flow patterns, as they were observed in actual experiments, are shown in Figure 6.14 and 6.15. Similar flow patterns exist when the angle of pipe inclination was increased from $+2^0$ to $+4^0$.

Stratified flow (ST) and stratified with mixing at the interface (ST& MI) were seen at very low mixture velocities. A gradual increase in mixture velocity beyond 0.25 ms^{-1} results in the appearance of waves at the mixed interface. The waves become more irregular and conspicuous at $+4^0$ compared same to that of the horizontal case. A similar phenomenon was reported in the work of (Lum et al., 2006).

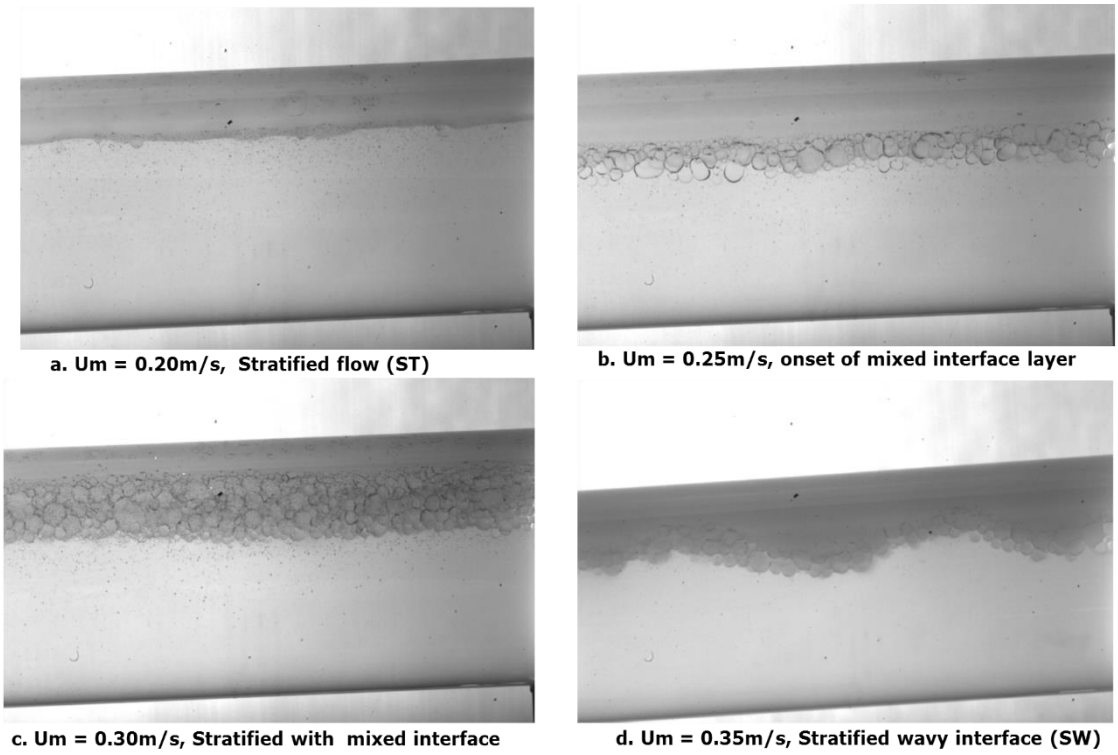

Figure 6-14 Upward inclined oil-water flow pattern images observed at lower mixture velocities (0.20 ms^{-1} – 0.35 ms^{-1}), downstream of the sudden pipe expansion.

As can be seen from Figure 6.15a and 6.15b, the **plug flow** regime begins to emerge at mixture velocities between 0.50m/s - 1.00m/s for various input oil fractions. Initially at mixture velocity of 1.00m/s and 50% OVF, input oil volume fraction, the mixed oil-water interface region increases in width, resulting in the appearance of the Raleigh Taylor instability 'plume shaped' flow (Figure 6.15a). Both oil and water drops occur at the mixed interface and flows along the axial test distance of the singularity. At mixture velocity of 1.00m/s and 80% OVF input oil volume fraction, a time dependent flow pattern occurs, which is characterized by thick plug of oil flowing at the top and intermittent waves in both $+2^0$ and $+4^0$ cases (Figure 6.15b). This is a stable wavy structure resembling a caterpillar, which seemed to occur due to a combined effect of water backflow, detected at the bottom of the pipe, and water recirculation near the interface. Similar ***Caterpillar waves*** were observed and reported in the work of (Rodriguez and Oliemans, 2006) for horizontal flow (see Figure 6.16). The Rayleigh Taylor flow phenomenon was similar to that of the horizontal case but however occurred at higher mixture velocity in the upward inclined flow.

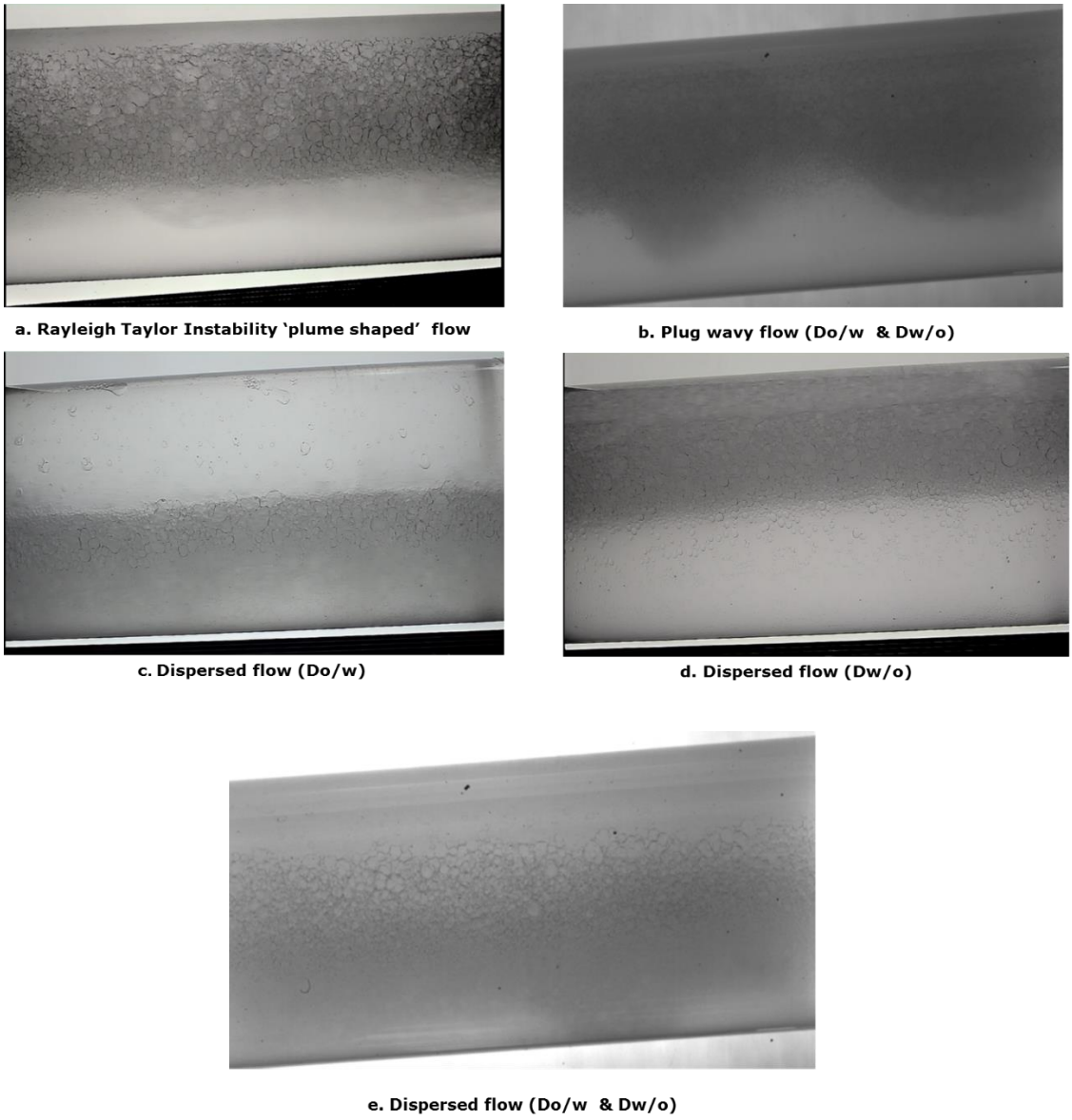

Figure 6-15 Upward inclined oil-water flow pattern images observed at higher mixture velocities (0.50 ms^{-1} – 1.50 ms^{-1}), downstream of the sudden pipe expansion.

Another interesting flow pattern observed was in the fully dispersed flow regime. At 20% OVF input oil volume fraction and mixture velocity between (1.00m/s -1.50m/s), a dispersed oil-in-water (Do/w) flow regime appears and increases as the inclination is increased from $+2^0$ to $+4^0$. It was seen to exist up to 40% OVF input oil volume fraction in both the $+2^0$ and $+4^0$ angle inclinations (Figure 6.15c). This is associated to the higher in situ water content associated with increased upward inclination. It may also be that at increasing inclination, the component of gravity forces perpendicular

to the pipe axis (which is the force that drives drops together and would cause their coalescence to a separate layer), becomes weaker.

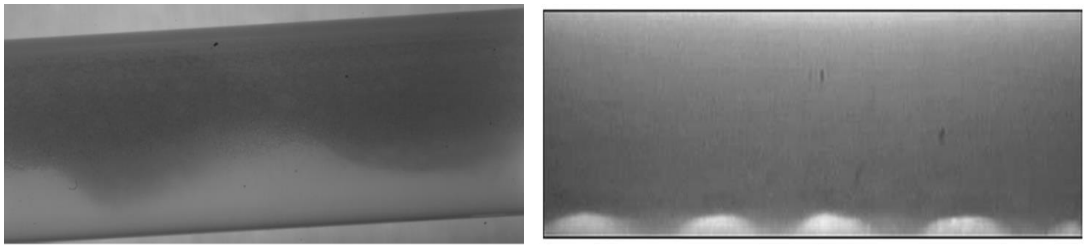

(a) (b)

Figure 6-16 (a) Caterpillar waves observed at mixture velocities (0.50 ms^{-1} – 1.00 ms^{-1}), downstream of the sudden pipe expansion in current work. (b) Similar caterpillar waves observed in the work of (Rodriguez and Oliemans, 2006).

A further increase in the input oil volume fraction beyond 60% OVF up to 80% OVF with mixture velocity between (1.00 ms^{-1} -1.50 ms^{-1}) results in the emergence of a dispersed water-in-oil (Dw/o) flow regime (Figure 6.15d). Although the oil is fully dispersed, the concentration gradient of the oil drops is clearly evident, even at 1.50 ms^{-1} (Figure 6.15e). At 2.00 ms^{-1} – 3.50 ms^{-1}, the video images are not clear and the flow becomes misty with very tiny oil and water droplets, which cannot be identified by the camera.

6.2.1.3 Downwardly inclined pipe expansion

The conventional distinct flow patterns were identified in the current study and classified into two categories: segregated flow and dispersed flow as presented in Figures 6.17 and 6.18, for the downward inclined pipe flow. Stratified flow and stratified flow with some mixing at the interface (ST&MI) are classified as segregated flow patterns and occurred at low mixture velocities (0.20m/s – 0.35m/s) for the various input oil volume fractions. It was observed that for downward pipe inclination (- 4^0 at 0.20m/s), the transition from stratified flow (ST) to stratified with mixing at the interface flow (ST& MI) appeared quickly than the horizontal flow case. At higher downward pipe inclination (- 4^0), the mixing is enhanced resulting in the onset of the mixed interface layer (Figure 6.17b). The oil – water mixed interface width increases

progressively with downstream mixture velocity. Rayleigh Taylor instability 'plume shaped' flow also exists at higher mixture velocity (0.50m/s – 1.00m/s). The dispersed flow was mostly dominated by dispersion of oil in water over a water layer and subsequently a fully dispersed flow (Do/w & Dw/o), flow patterns. Plug flow similar to the caterpillar waves observed in the case of upward flow also appeared at mixture velocity 1.50m/s and 50% OVF downward inclination pipe flow.

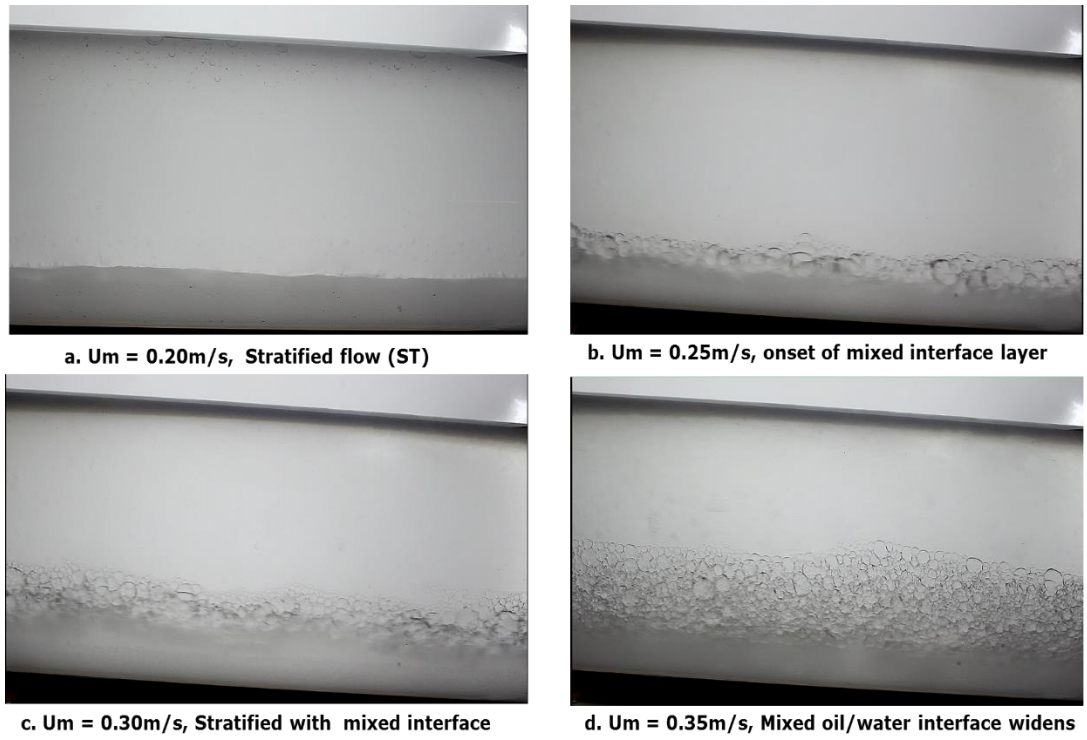

Figure 6-17 Downward inclined oil-water flow pattern images observed at lower mixture velocities (0.20 ms^{-1} – 0.35 ms^{-1}), downstream of the sudden pipe expansion.

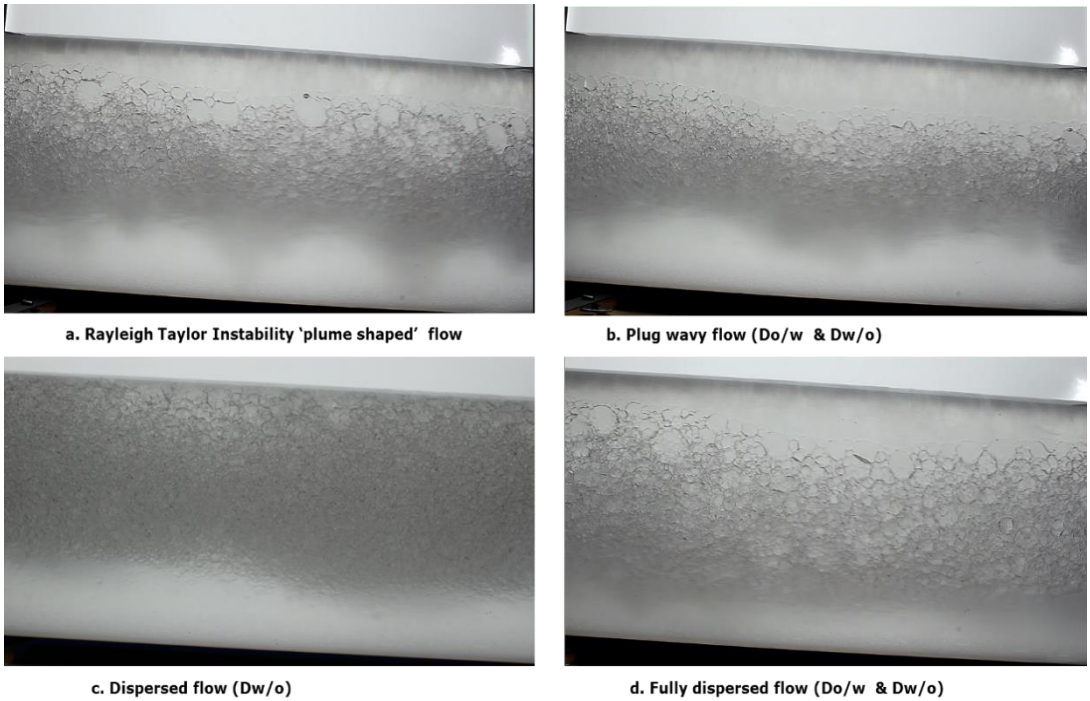

Figure 6-18 Downward inclined oil-water flow pattern images observed at higher mixture velocities (0.50 ms^{-1} – 1,50 ms^{-1}), downstream of the sudden pipe expansion.

6.3 Evolution of interface and the Effect of Inlet parameters and rig configuration on oil volume fraction (OVF) in horizontal flow.

Several proposals have been made in contribution to the design of an effectively simple primary phase separator, to handle two phase immiscible fluids at high velocities. As a foundation, quite reasonable predictions on the evolution and position of liquid-liquid two phase interface have been made using the model of (Taitel and Dukler, 1976), developed for gas-liquid. Based on this foundation, an extensive work has been done and reported for both gas - liquid and liquid - liquid two phase flow in pipes (Valle and Utvik, 1998, Azzopardi and Hills, 2001, Brauner and Ullmann, 2002, Kurban et al., 1995, Simmons, 1998) etc. Thereafter, the effect of pipe orientation (i.e. upward and downward pipe angle inclination) on liquid-liquid flows has been studied by some researchers (Vedapuri et al., 1997, Lum et al., 2006) etc. However, little data and valuable information has been reported in literature about flow pattern evolution through a sudden expansion for liquid-liquid two phase flows, except little latest work by the following researchers (Yang, 2003, Hasan, 2006, Yusoff, 2012).

Therefore, this section is dedicated to experimentally investigate the factors affecting interface layer evolution, downstream of the pipe expansion. This will help provide more data on liquid-liquid two-phase flows through sudden pipe expansion for both horizontal and inclined flows with large diameter (ϕ127mm) pipe.

The evolution of interface layer downstream of the expansion was studied using video recording measurement information gathered, with the Phantom PCC 2.7 High Speed Camera and data obtained from the ring conductance probes. This technique is verified further by the ring conductance probe data analysis in sections 6.2. The data processing technique of the images obtained have been explained briefly in section 4.3.6 of Chapter 4. A careful analysis of these video recordings for the ST and ST& MI regimes is done as shown in Figure 6.19, for all data collected in both horizontal and inclined (upward and downward pipe flow) orientations.

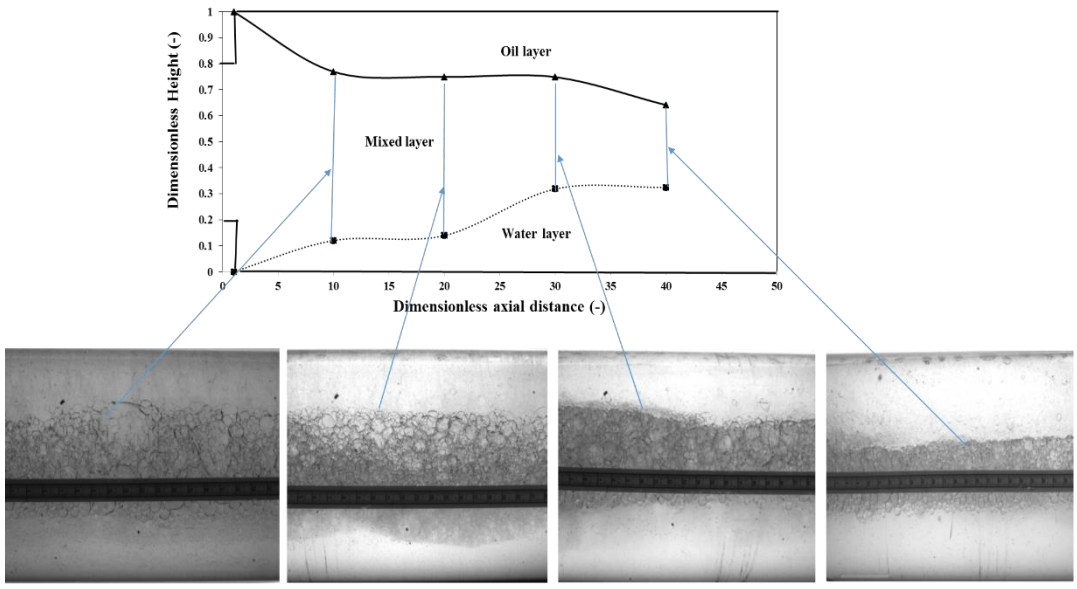

Figure 6-19 Phase layer evolution of interface height downstream of the pipe expansion for flow conditions: 50% OVF, downstream mixture velocity 1.00 ms^{-1} horizontal at different axial test distances.

6.3.1 Effect of input oil fraction

Figure 6.20 shows the influence of the input oil volume fraction on the phase layer evolution downstream of the sudden expansion at a downstream mixture velocity U_m

0.30m/s. For all input oil volume fractions i.e. 20% OVF, 50% OVF and 80% OVF, the flow evolves to a fully developed ST regime within the test distance. The phase layers are quite distinct, with oil clearly flowing at the top of the pipe and water at the bottom of pipe, while a mixed layer flows in between them initially but stratifies at position 40D.

Figure 6.21 shows the effect of the input oil volume fraction on the phase layer evolution downstream of the sudden expansion at a downstream mixture velocity U_m 0.50m/s. It can be seen that the flows were not fully developed to the ST regime as observed previously at lower velocity. In all input oil volume fractions, the oil layer appears at 10D distance and no clear water layer until position 30D except for 80%OVF, which emerged from 10D axial test distance. This indicates that higher input oil volume fraction enhances separation of the heavier phase within the $D_{o/w}$ flow regime, (ST& MI) and lower oil volume fraction helps in the settling down process of the lighter phase. This also suggest a balancing of forces between the turbulent momentum and buoyancy forces that prevails in the separation of the mixtures.

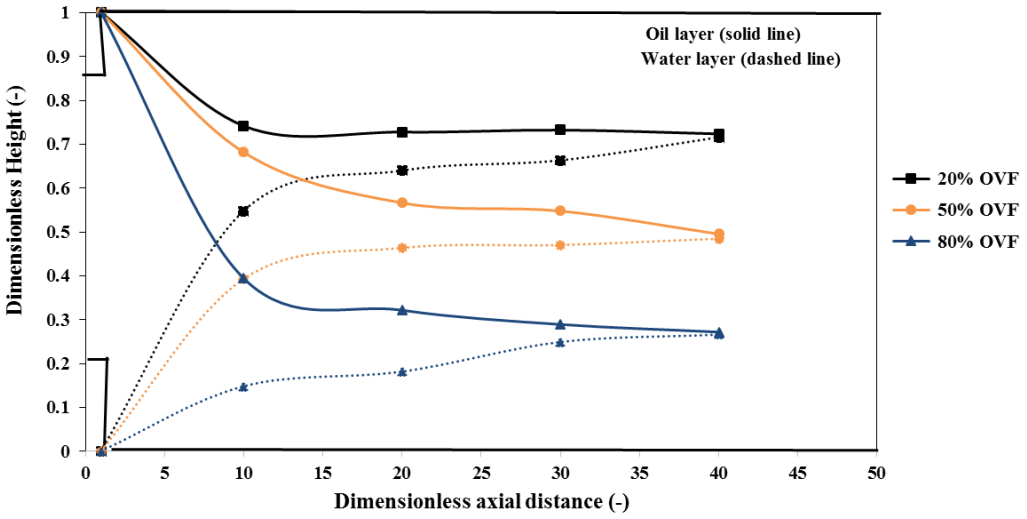

Figure 6-20 Effect of different oil volume fraction (OVF) on phase layer evolution of interface height downstream of the pipe expansion for flow conditions: downstream mixture velocity 0.30 ms^{-1}, horizontal flow at different axial test distances.

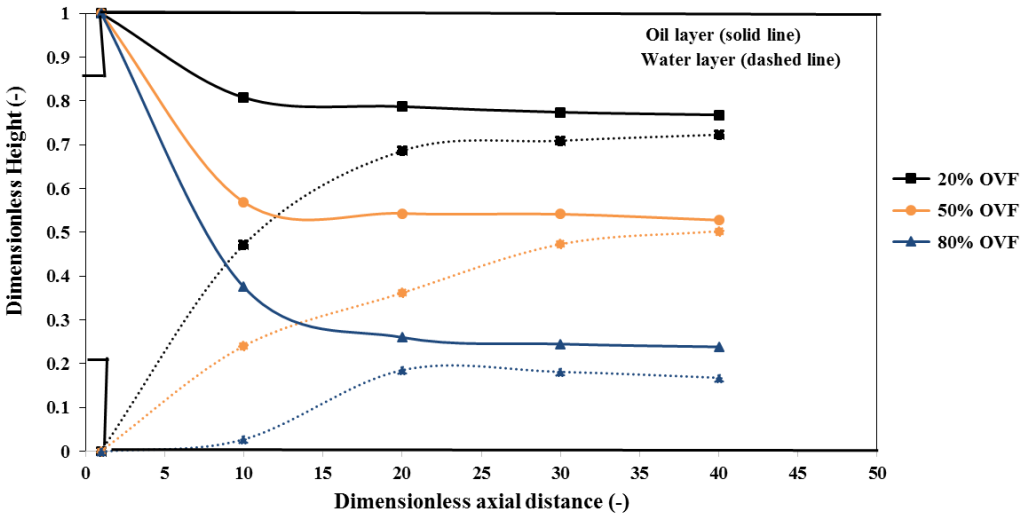

Figure 6-21 Effect of different oil volume fraction (OVF) on phase layer evolution of interface height downstream of the pipe expansion for flow conditions: downstream mixture velocity 0.50 ms^{-1}, horizontal flow at different axial test distances.

More importantly, in all input oil volume fraction at downstream velocity of U_m 0.50m/s, the oil layer occurs at shorter distance and grows thicker as the flow progresses downstream the expansion.

The result is different at a higher downstream velocity of U_m 1.00m/s with the occurrence of three (3) layers with a mixed oil/water interface layer, flowing at the middle of the pipe, as represented in Figure 6.22. However, the three (3) layers were quite visible along the pipe cross section as the flow progresses downstream of the expansion. The interface is wider at the inlet position 10D but gradually becomes narrower towards the 40D position due to coalescence and stratification of oil and water droplets, downstream of the singularity. The oil layer seem to have occurred earlier, in the case of 50% OVF at the 10D position and the flow is seen to be wavy in nature as discussed in section 6.2.1.

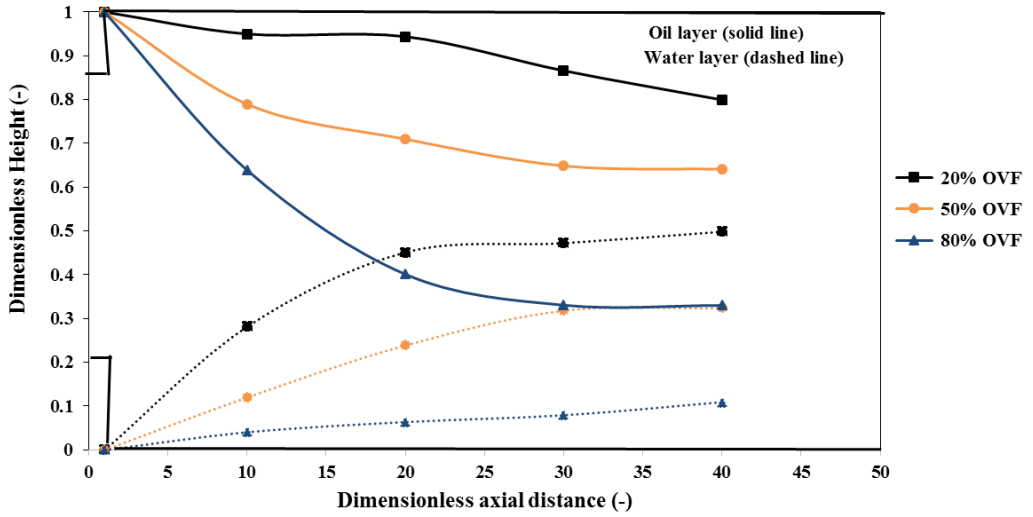

Figure 6-22 Effect of different oil volume fraction (OVF) on phase layer evolution of interface height downstream of the pipe expansion for flow conditions: downstream mixture velocity 1.00 ms^{-1}, horizontal flow at different axial test distances.

6.3.2 Effect of mixture velocity

Figures 6.23, 6.24 and 6.25 show the effect of the downstream velocity on the phase layer evolution in horizontal flows at input oil volume fractions of 80% OVF, 50% OVF and 20% OVF respectively.

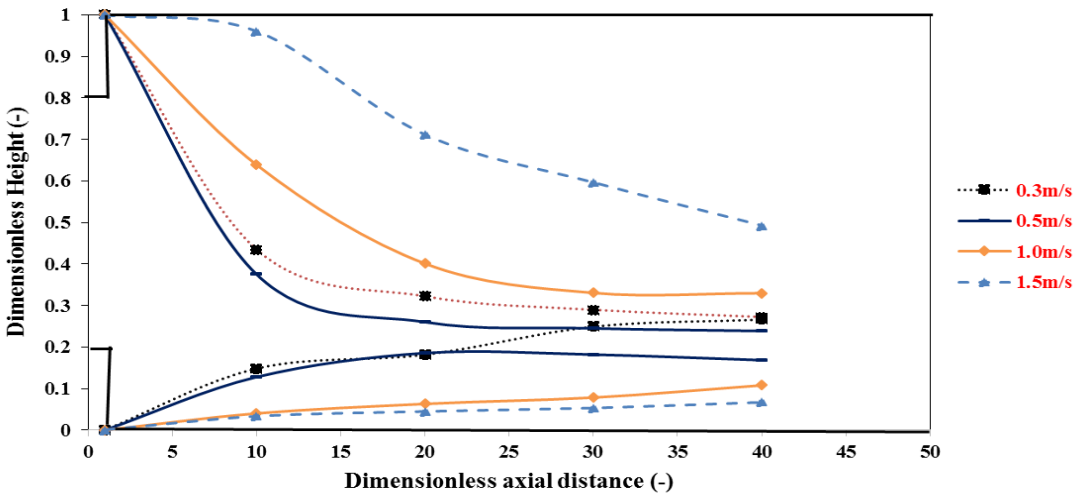

Figure 6-23 Effect of mixture velocity on the phase layer evolution downstream of the singularity with flow conditions, 80% OVF and horizontal flow at different axial test distances.

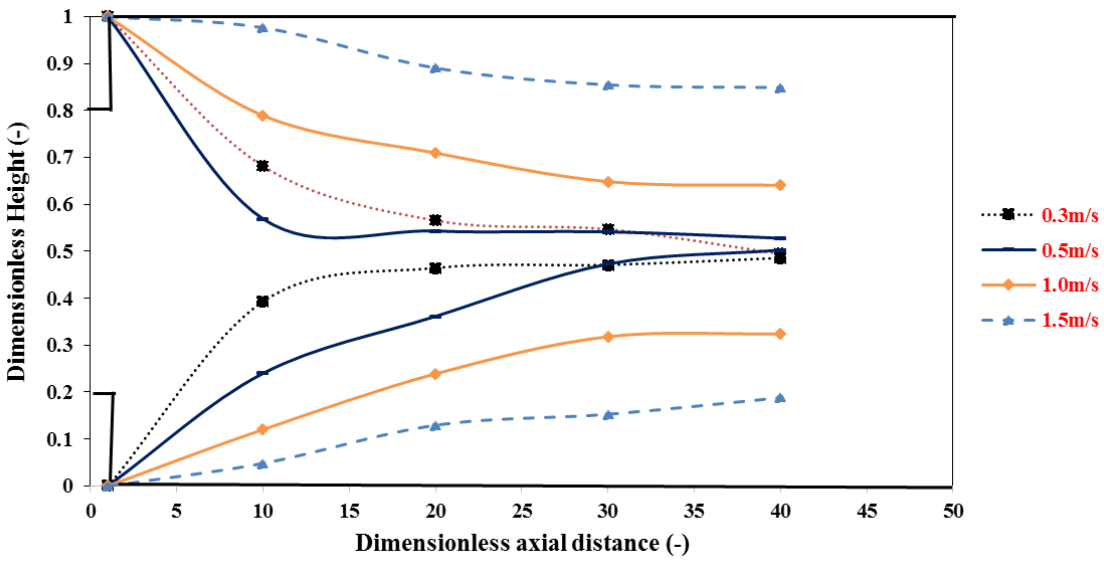

Figure 6-24 Effect of mixture velocity on the phase layer evolution downstream of the singularity with flow conditions, 50% OVF and horizontal flow at different axial test distances.

The flow pattern develops to the ST regime at the 40D position for downstream mixture velocity of 0.30 ms^{-1} for all input volume fractions. An increase in downstream mixture velocity beyond this value affects the mixed interface layer, which hardly decays.

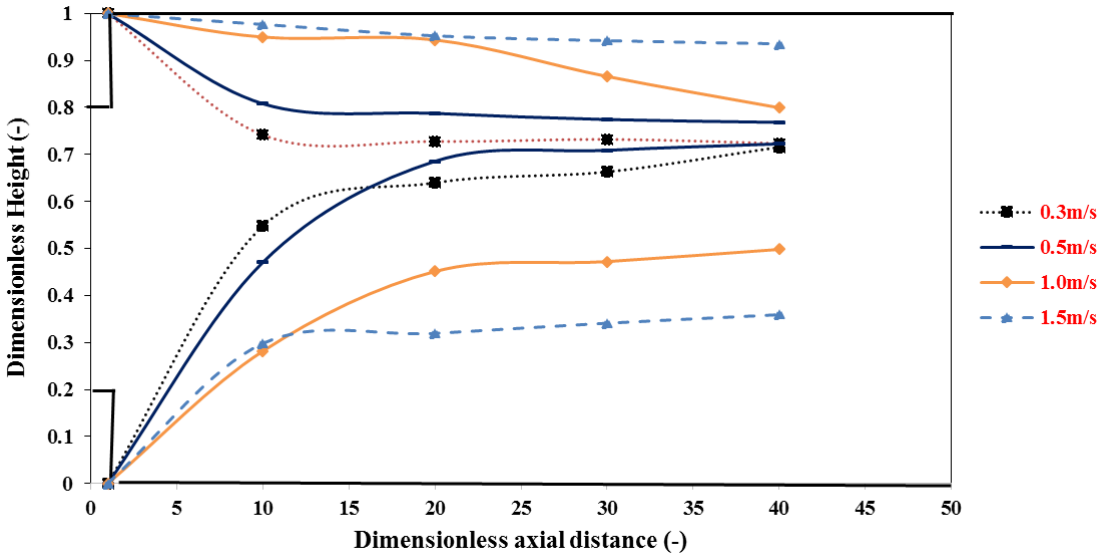

Figure 6-25 Effect of mixture velocity on the phase layer evolution downstream of the singularity with flow conditions, 20% OVF and horizontal flow at different axial test distances.

The oil/water mixed interface region is seen to increase further as the velocity increases to 1.50 ms^{-1} and the flow is gradually becoming fully dispersed, thereby occupying the entire cross section of the pipe within the test distance. This suggests that the higher mixture velocity generates higher turbulence intensity, thereby creating finer and smaller droplets, which inhibits the coalescence mechanism of the resultant dispersion. Similar phenomenon was observed by (Yang et al., 2003). The results are in considerable agreement with the flow pattern map according to (Trallero et al., 1997). For downstream velocity of 0.30ms^{-1}, the targeted flow pattern develops to the ST regime, whereas for higher downstream velocities, the flow evolves to the ST& MI regime. At very short distance, 10D, both oil and water phase layers at top and bottom of pipe develops to a relatively stable state with low mixture velocity, 0.30 ms^{-1}. The three (3) layers were clearly visible at higher mixture velocities between (0.50 ms^{-1} – 1.50 ms^{-1}), beyond which the flow transit to the fully dispersed regime ($D_{o/w}$ & $D_{w/o}$), and occupy the entire pipe. This finding is contrary to earlier observation recorded in the work of (Yang et al., 2003).

6.3.3 Mixed interface height and mixture velocity

Figure 6.26 shows the height of interface mixed region as a function of downstream mixture at different input oil volume fractions on the phase layer evolution along the axial test distance of the pipe expansion. It can be seen generally that there is an increasing trend of the average interface height as the mixture velocity increases at all input oil volume fractions. This increasing trend leads to fully dispersed flow at higher velocities beyond 1.50 ms^{-1}, in which the phase fraction is constant along the vertical axis of the pipe cross section. It can also be inferred from Figure 6.27 that stratified flow was observed at velocities below 0.3 ms^{-1}, beyond which there is a transition to mixed and subsequently dispersed flows.

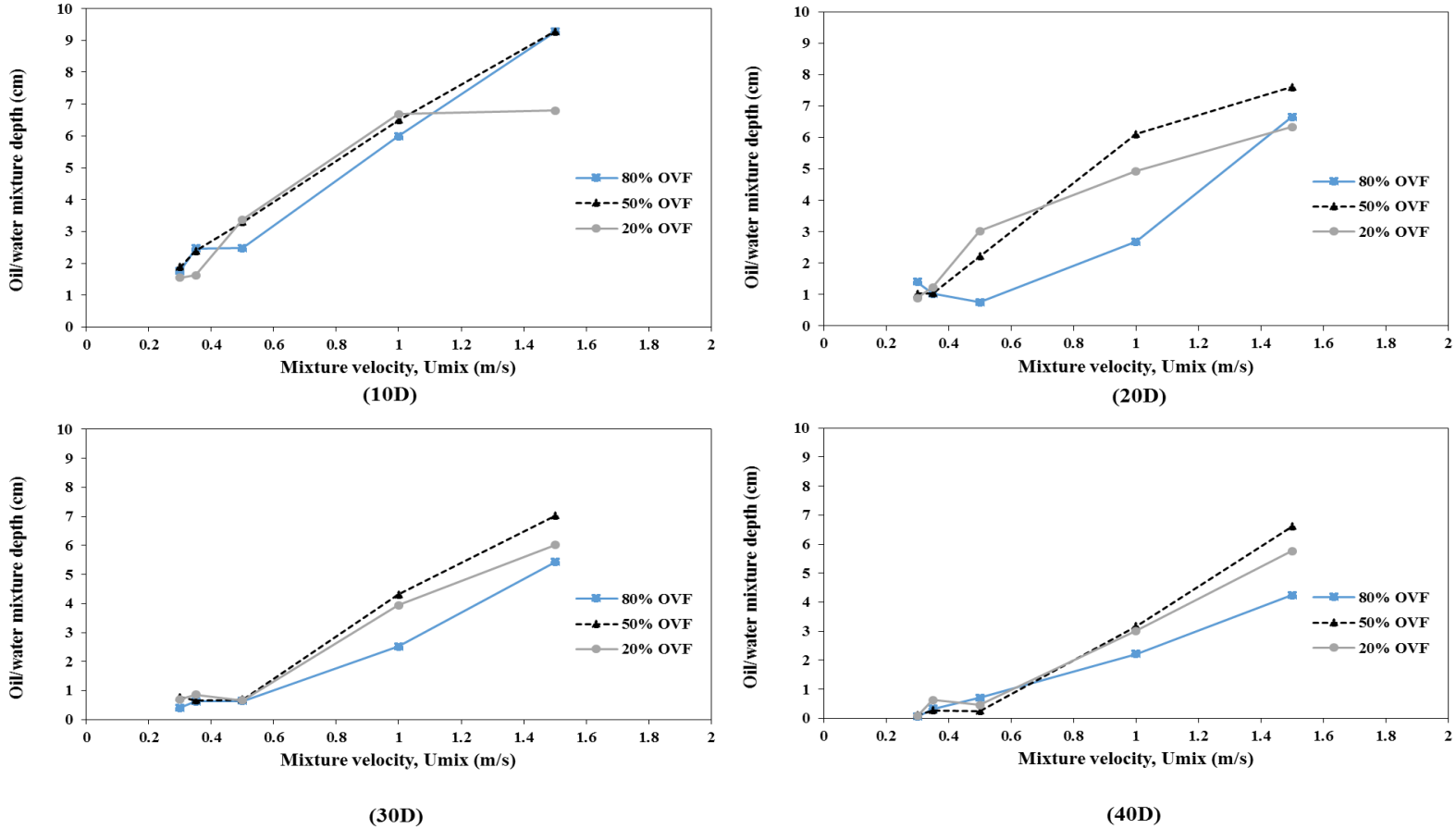

Figure 6-26 Oil/water mixed interface region vs mixture velocity on the phase layer evolution downstream of the singularity with flow conditions, 20% OVF, 50% OVF, 80% OVF and horizontal flow at different axial test distances.

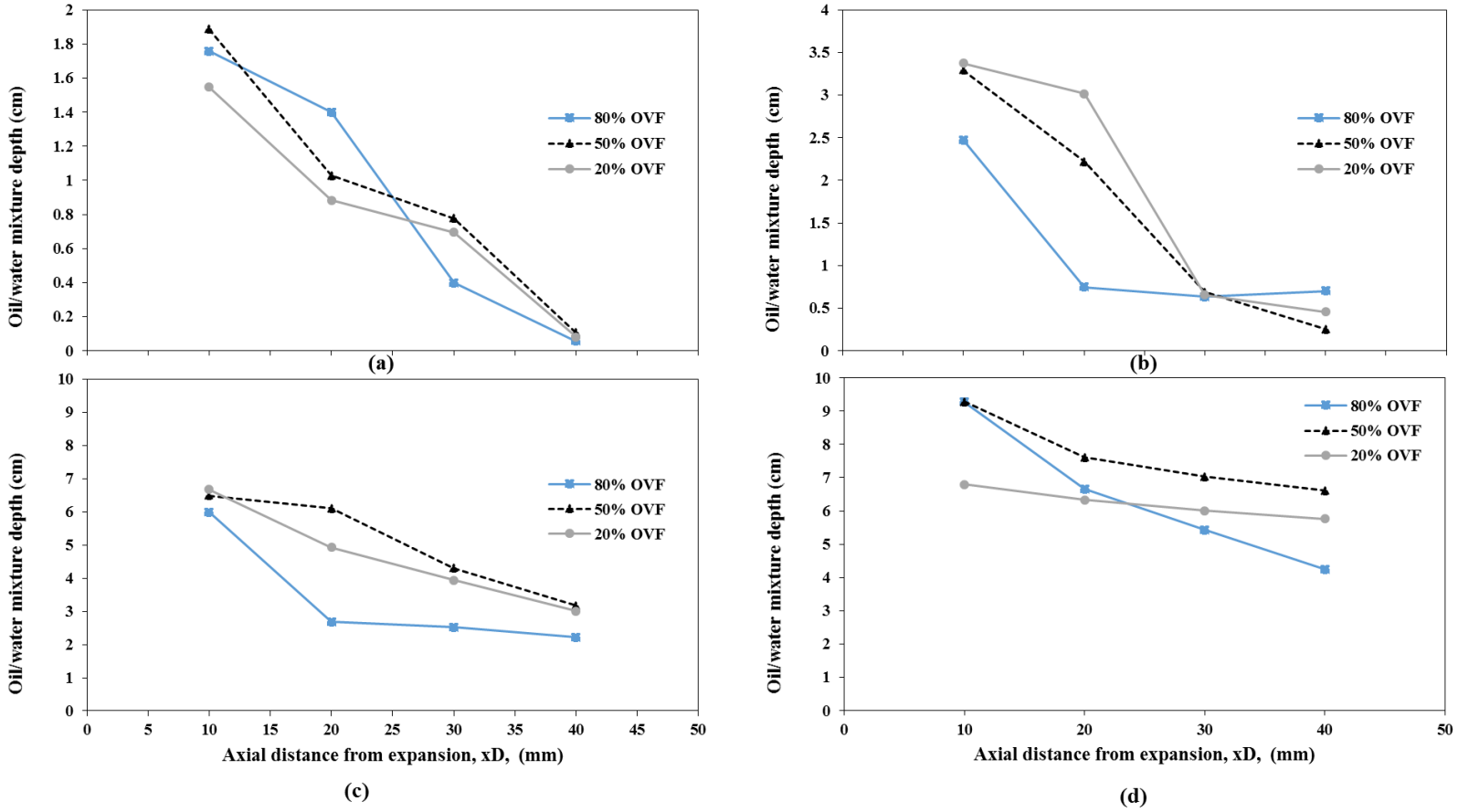

Figure 6-27 Oil/water mixed interface region vs axial distance along pipe expansion at various mixture velocities (a) 0.30m/s (b) 0.50m/s (c) 1.00m/s (d) 1.50m/s; horizontal pipe flow orientation.

6.3.4 Evolution of mixed interface height

The evolution of the average interface height from the homogeneous upstream inlet part of the expansion to the downstream of the singularity, at the different axial distances along pipe for various mixture velocities (a) 0.30 ms^{-1} (b) 0.50 ms^{-1} (c) 1.00 ms^{-1} (d) 1.50 ms^{-1}, is as shown in Figure 6.26. It was found that the interface height typically decreased along the pipe test section indicating stratification, downstream of the expansion for all input oil volume fractions. The stepper slop observed in Figure 6.26 (a) for mixture velocity 0.30 ms^{-1}, suggest a much faster segregation process of the oil from the water compared to that at higher velocity (1.50 ms^{-1}).

From the above results and discussion, the following conclusions can be made for the flow evolution through the horizontal pipe expansion:

- Fully developed stratified flow (ST) can be obtained at mixture velocities below 0.30 ms^{-1} at different input oil volume fractions within the 6m long pipe test section.
- There was evidence of stratification of the mixed interface as its height, narrows downstream of the expansion due to coalescence of droplets and the effect of other flow parameters such as liquids flowrate, input oil volume fraction (OVF) etc,

6.4 Evolution of interface and Effect of Inlet parameters and rig configuration on oil volume fraction (OVF) in upwardly inclined flow

(Taitel and Dukler, 1976) in there modelling work has predicted that pipe inclination will influence the interface level between the two phases for stratified flow regime. They reported in their findings that a slight upward angle pipe inclination results in the lighter phase flowing much faster at the top of pipe than the heavier phase layer at the bottom. Similar observations were also made in the research work of (Vedapuri et al., 1997, Yang et al., 2003, Lum et al., 2004). The phase layer evolution process is however influenced by several other factors which are investigated further in this section. The same experimental conditions used for the horizontal flow is been

employed also for the upward inclination. The results are analyzed and discussed as presented in the subsections.

6.4.1 Effect of input oil fraction

Figure 6.28 shows the effect of oil volume fraction on phase layer evolution on interface height downstream of the pipe expansion for low downstream mixture velocity 0.30 ms^{-1}, upward inclination angle pipe ($+2^0$) flow at different axial test distances. It can be seen visibly that the oil and water layers are clearly distinct from each other with a mixed interface layer, flowing at the middle section within the test distance. The homogeneous oil-water interface layer at position 10D inlet section, gradually narrows downstream of the singularity due to coalescence and settling forces as explained previously. The present result is in agreement with the (Taitel and Dukler, 1976) model prediction as the interface level decreases with increasing oil volume fraction i.e the interface level increases as the water cut increases when the pipe is upward inclined for stratified flow patterns (Figure 6.28).

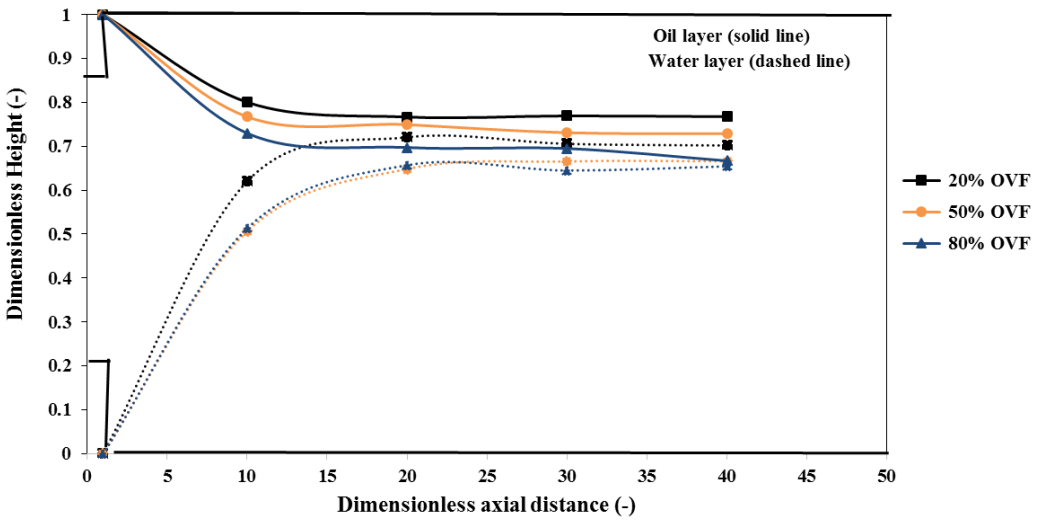

Figure 6-28 Effect of oil volume fraction (OVF) on phase layer evolution of interface height downstream of the pipe expansion for flow conditions: downstream mixture velocity 0.30 ms^{-1}, upward inclination angle pipe ($+2^0$) flow at different axial test distances

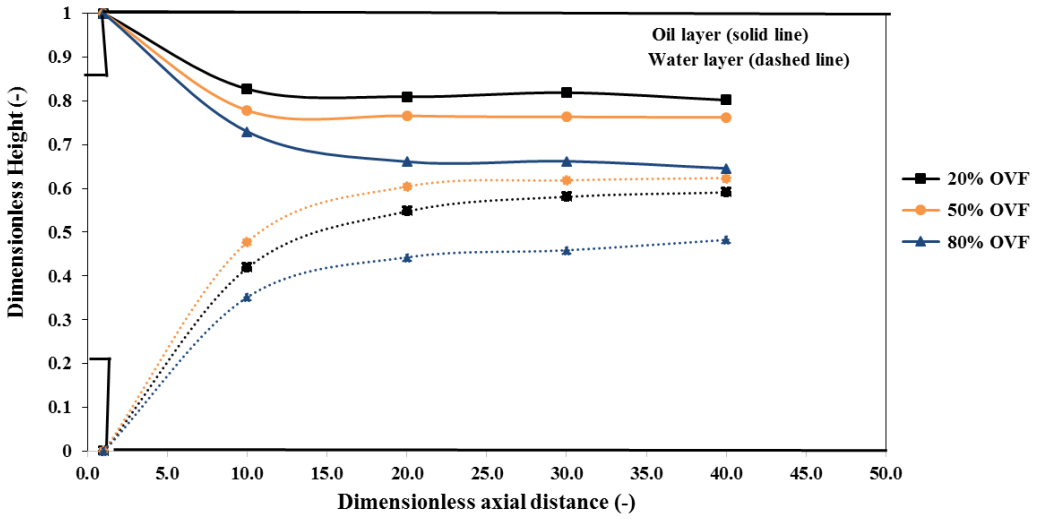

Figure 6-29 Effect of oil volume fraction (OVF) on phase layer evolution of interface height downstream of the pipe expansion for flow conditions: downstream mixture velocity 0.50 ms^{-1}, upward inclination angle pipe ($+2^0$) flow at different axial test distances

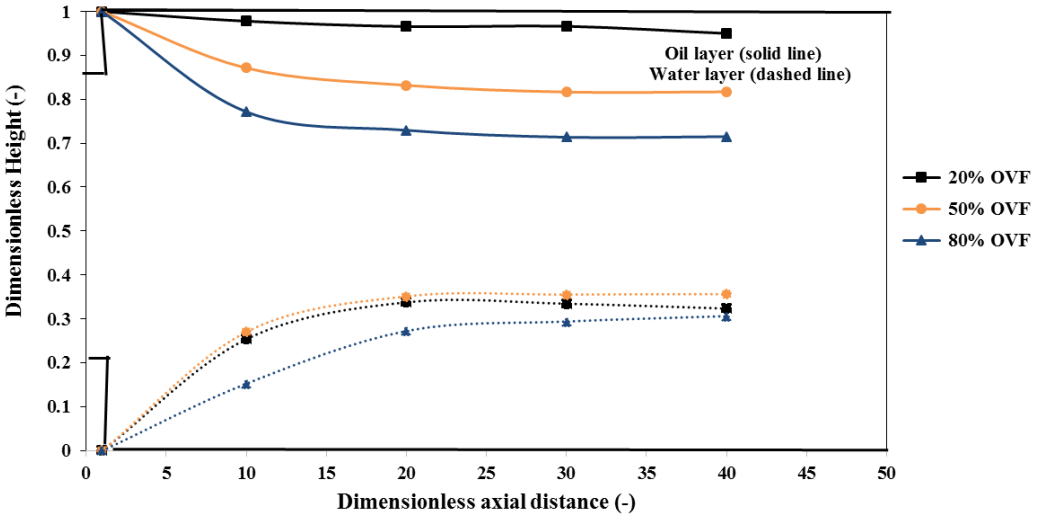

Figure 6-30 Effect of oil volume fraction (OVF) on phase layer evolution of interface height downstream of the pipe expansion for flow conditions: downstream mixture velocity 1.00 ms^{-1}, upward inclination angle pipe ($+2^0$) flow at different axial test distances

At position 40D the flow is fully stratified for 80% OVF but still mixed in the case of 20% OVF and 50% OVF respectively. This observation is quite different compared

to the horizontal flow were there was complete segregation of both oil and water layers downstream of the expansion in the stratified (ST) flow regime.

For higher downstream mixture velocities shown in Figure 6.29 and 6.30 for 0.50m/s and 1.00m/s respectively, there exist a clear interface layer of oil and water flowing at the pipe top and bottom with a mixed layer in between them. The mixed layer is seen to grow thicker and widened as the velocity increases for all oil volume fractions. Both oil and water layers become thinner as the velocity increases. This phenomenon was also reported in the work of (Yusoff, 2012) using the Wire Mesh Sensor (CapWMS) technique.

The phase inversion occurs at input oil volume fraction around 50% OVF and mixture velocities above 0.30m/s. By increasing the oil volume fraction at the phase inversion point, the continuous phase transits from water to oil and vis versa from oil to water for the dispersed phase. The water drops are broken down, as well as exchange between the continuous and dispersed phase within the mixed layer occurs during the flow evolution for flow condition 80% OVF in the dispersed water in oil continuous ($D_{w/o}$) regime. Large waves also emerged at the 80% OVF flow condition for 1.00m/s at the interface between the water and mixed layer due to kinetic interaction of drops in dispersion and phase inversion process (see Figure 6.29). This plug wavy flow observation can be confirmed from the flow pattern images previously discussed in section 6.2.1.2 and Figure 6.15b.

6.4.2 Effect of mixture velocity

Figures 6.31, 6.32 and 6.33 shows the influence of the downstream velocity on the phase layer evolution for flow conditions 80% OVF, 50% OVF and 20% OVF respectively and upward angle pipe inclination along the test distance. Again, it can be seen that both oil and water layers clearly occurred for the upward pipe angle inclination flow orientation with mixed layer flowing between them. At 80% OVF, the flow is however, fully stratified at position 40D downstream of the expansion as presented in Figure 6.31 for low mixture velocity of 0.30m/s. The thickness of these oil and water layers become thinner while the mixed interface region increases in size and spreads wider with increase in mixture velocity. Large waves are also noticed at

the interface between the oil and water layers at higher velocity (1.00m/s) for both 80% OVF and 50% OVF. The amplitude of the waves are independent of the angle of inclination and is within 0.1D – 0.15D pipe diameter range.

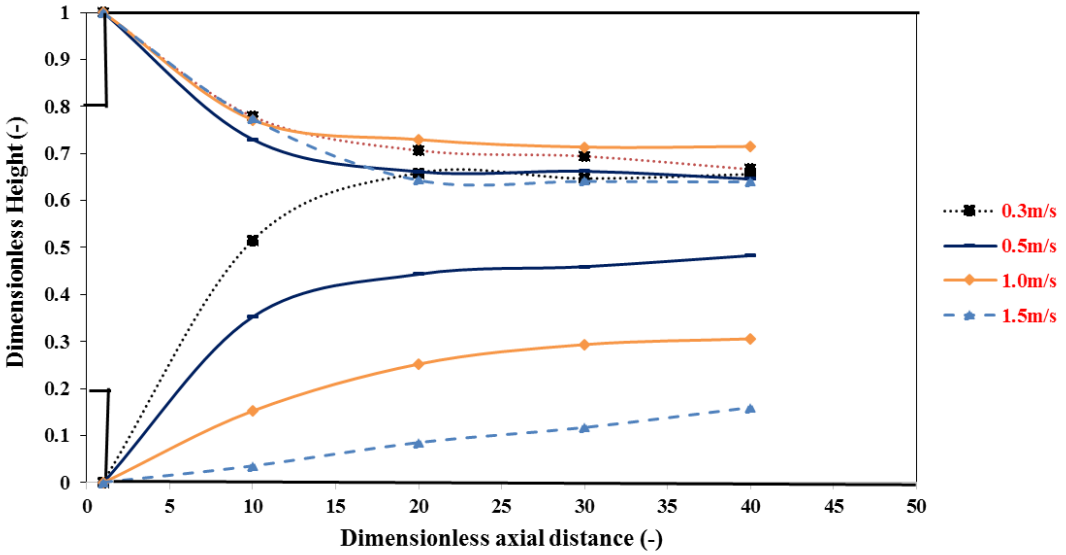

Figure 6-31 Effect of mixture velocity on the phase layer evolution downstream of the singularity with flow conditions, 80% OVF and upward inclined pipe ($+2^0$) flow at different axial test distances.

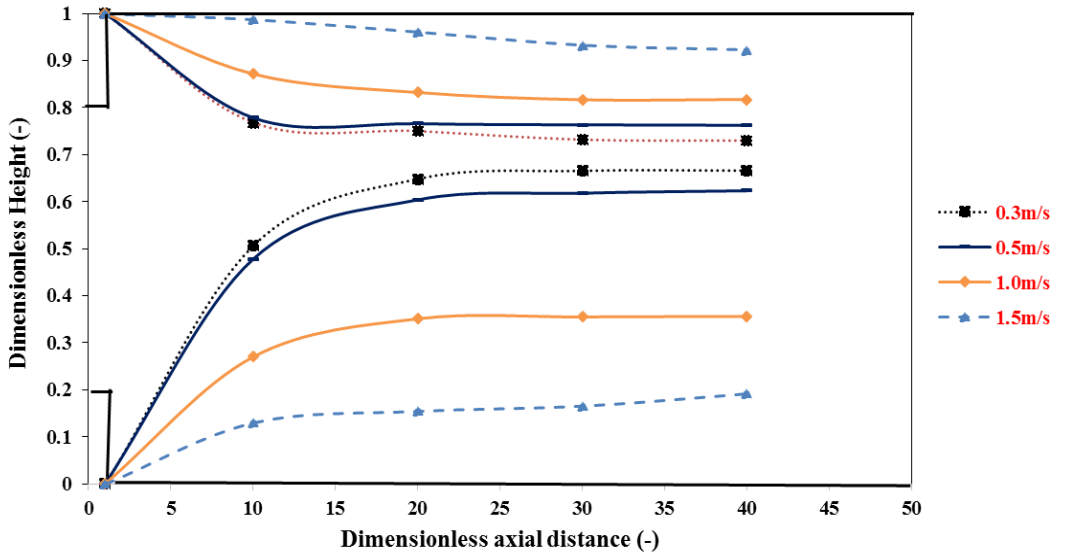

Figure 6-32 Effect of mixture velocity on the phase layer evolution downstream of the singularity with flow conditions, 50% OVF and upward inclined pipe ($+2^0$) flow at different axial test distances.

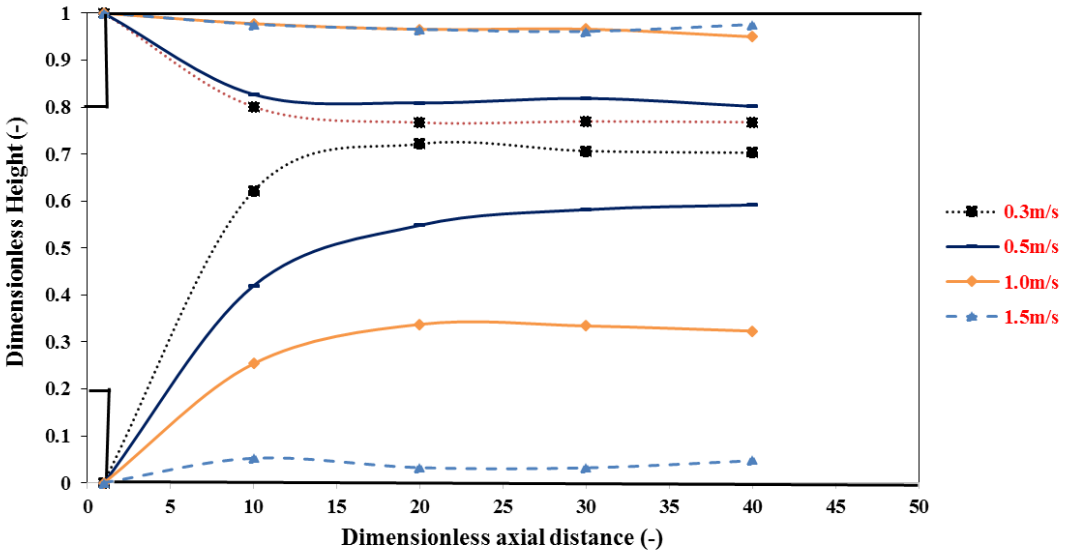

Figure 6-33 Effect of mixture velocity on the phase layer evolution downstream of the singularity with flow conditions, 20% OVF and upward inclined pipe ($+2^0$) flow at different axial test distances.

6.4.3 Mixed interface height and mixture velocity

Figure 6.34 shows the height of interface mixed region as a function of downstream mixture at different input oil volume fractions on the phase layer evolution along the axial test distance of the pipe expansion for upward angle pipe inclination. The trends generally indicates an increase in the average interface height as the mixture velocity increases at all input oil volume fractions, similar to what was observed in the horizontal case. This increasing trend leads to fully dispersed flow at higher velocities beyond 1.50 ms^{-1}, in which the phase fraction is constant and spreads along the vertical axis of the pipe cross section. It can also be inferred from Figure 6.34 that stratified flow was observed at velocity 0.3m/s and 80% OVF, beyond which there is a transition to mixed and subsequently dispersed flows.

6.4.4 Evolution of mixed interface height

The evolution of the mixed interface height for upwardly inclined pipe orientation, from the homogeneous upstream inlet part of the expansion to the downstream of the singularity, at the different axial distances along pipe for various mixture velocities (a) 0.30 ms^{-1} (b) 0.50 ms^{-1} (c) 1.00 ms^{-1} (d) 1.50 ms^{-1}, is as shown in Figure 6.35. The

trend of interface height was found to decrease along the pipe test section indicating stratification, downstream of the expansion for all input oil volume fractions

From the above results and discussion, the following points can be summarized for the flow evolution through the upwardly inclined pipe expansion:

- Fully developed stratified flow (ST) can be obtained at mixture velocity, 0.30m/s and water dispersed in oil continuous flow (80 %OVF) within the 6m long pipe test section. Also large waves emerges at the interface between the oil and water layers at higher mixture velocity (1.00 ms^{-1}) for both 80% OVF and 50% OVF, with amplitudes independent of pipe angle inclination.
- The lighter oil layer at the top flows much faster than the heavier water layer at bottom of pipe. Therefore, the slowly moving water layer settles down easily with increasing thickness compared to lighter oil layer evolving towards the mixed region. There was also evidence of stratification of the mixed interface as its height, narrows downstream of the expansion due to coalescence of droplets and the effect of other flow parameters such as liquids flowrate, input oil volume fraction (OVF) etc,

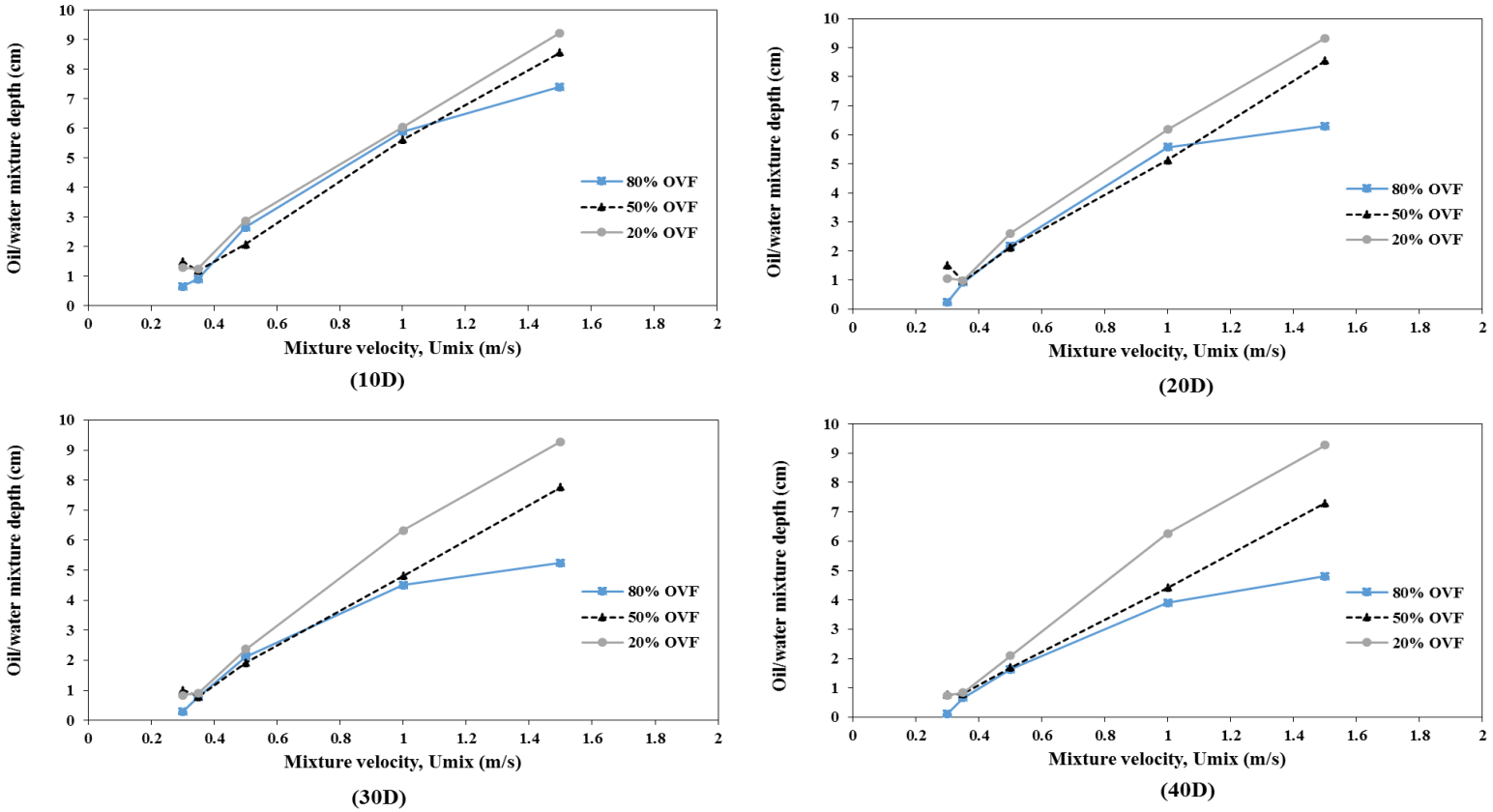

Figure 6-34 Oil/water mixed interface region vs mixture velocity on the phase layer evolution downstream of the singularity with flow conditions, 20% OVF, 50% OVF, 80% OVF and Upward flow at different axial test distances

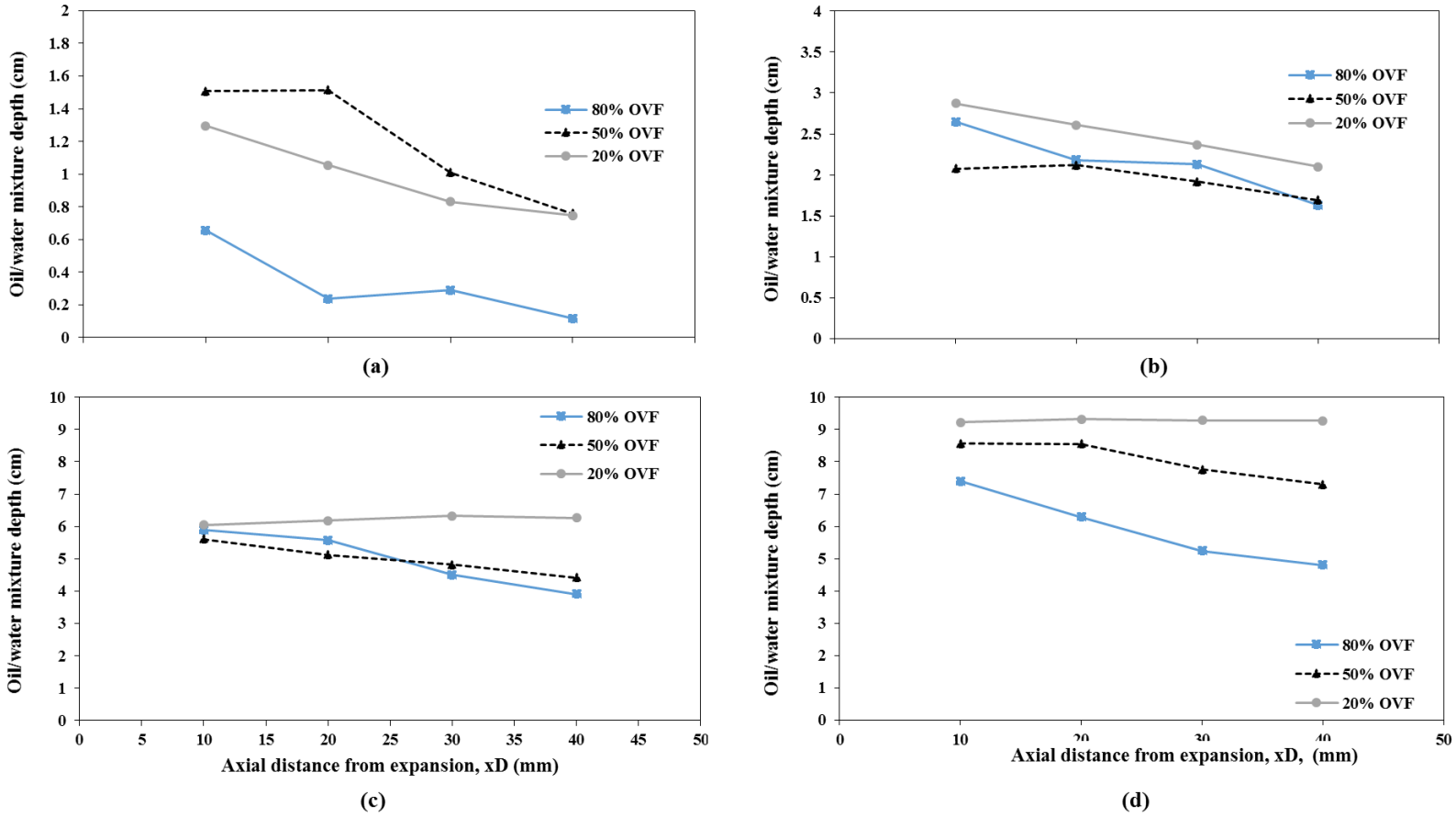

Figure 6-35. Oil/water mixed interface region vs axial distance along pipe expansion at various mixture velocities (a) 0.30 ms^{-1} (b) 0.50 ms^{-1} (c) 1.00 ms^{-1} (d) 1.50 ms^{-1}; Upward pipe flow orientation.

6.5 Evolution of interface and Effect of Inlet parameters and rig configuration on oil volume fraction (OVF) in downwardly inclined flow

Majority of the research work and data obtained on flow pattern studies in liquid-liquid two phase is focused mainly in horizontal and vertical pipeline. There is little data and published work on flow pattern studies in downwardly inclined pipeline. It has been predicted also that a slight downward pipe inclination affects the interface level as well as phase layer evolution in pipes. This section is dedicated to investigate the factors affecting phase layer evolution in downward pipe inclination with same experimental conditions used previously for both horizontal and upward inclined flow.

6.5.1 Effect of input oil fraction

The influence of input oil volume fraction on the phase evolution downstream of the expansion at downstream mixture velocities of 0.3m/s, 0.50m/s and 1.00m/s for downward inclination within test distance is presented in Figures 6.36, 6.37 and 6.38 respectively.

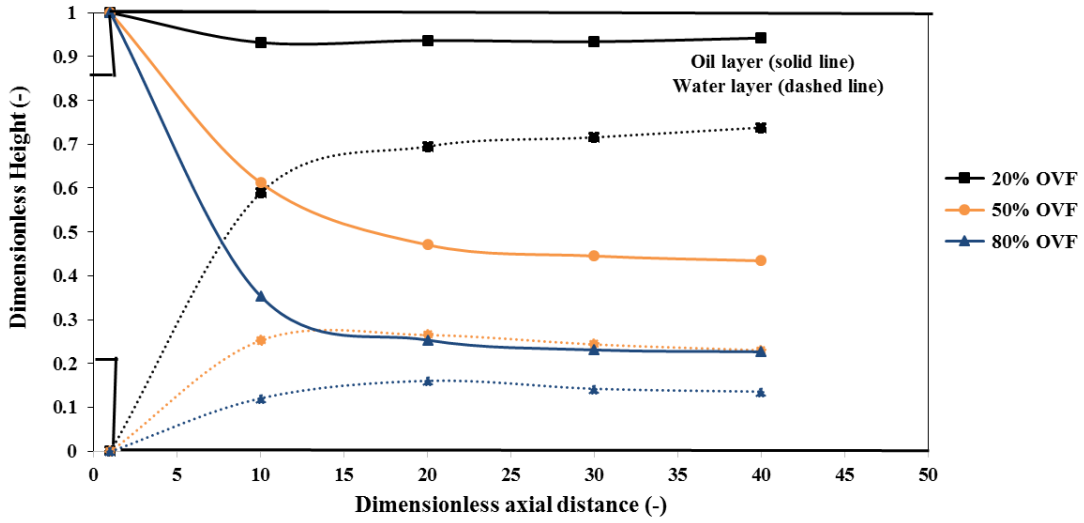

Figure 6-36 Effect of oil volume fraction (OVF) on phase layer evolution of interface height downstream of the pipe expansion for flow conditions: downstream mixture velocity 0.30m/s, downward inclination angle pipe (-2^0) flow at different axial test distances

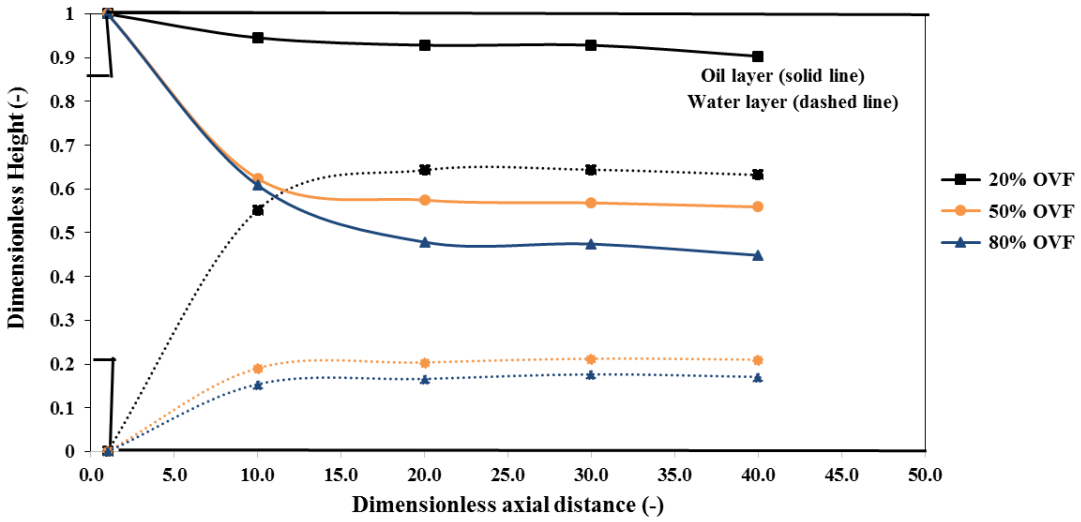

Figure 6-37 Effect of oil volume fraction (OVF) on phase layer evolution of interface height downstream of the pipe expansion for flow conditions: downstream mixture velocity 0.50m/s, downward inclination angle pipe (-2^0) flow at different axial test distance

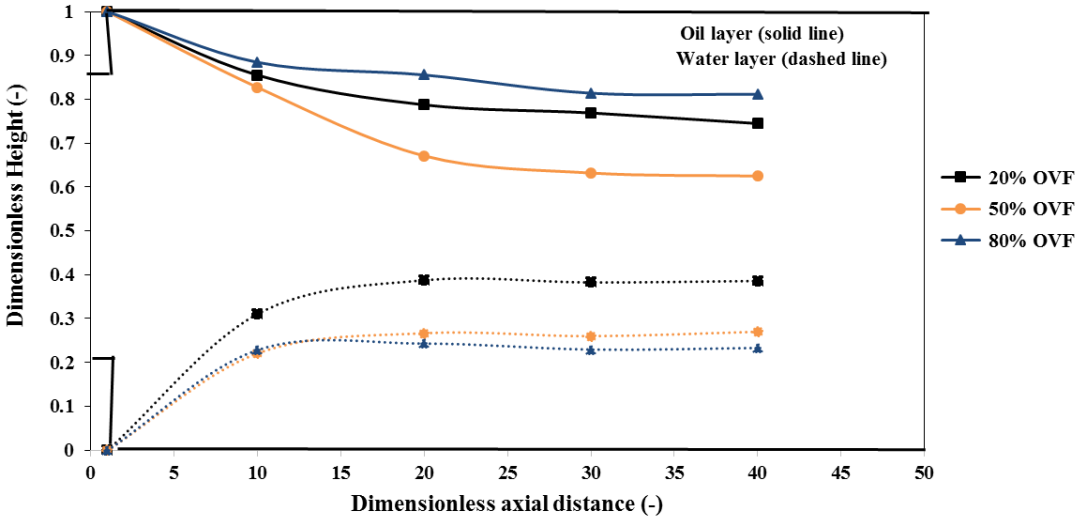

Figure 6-38 Effect of oil volume fraction (OVF) on phase layer evolution of interface height downstream of the pipe expansion for flow conditions: downstream mixture velocity 1.00m/s, downward inclination angle pipe (-2^0) flow at different axial test distance

Generally, clear oil and water layers exist with mixed layer flowing between them along the pipe test section. Both the oil and water layers grow thinner while the mixed layer becomes thicker and wider, with decreasing oil volume fraction for lower mixture velocity 0.30m/s. Stratification was not achieved within test distance for all

flow conditions in the downward inclination pipe orientation. However, there is no significant effect on phase layer evolution at higher mixture velocities, 0.50m/s and 1.00m/s. It is interesting that the oil layer is thicker for higher oil volume fraction at low velocity 0.30m/s as expected, which is in agreement with model predictions of (Taitel and Dukler, 1976) as against the findings of (Yang et al., 2003).

6.5.2 Effect of mixture velocity

Figures 6.39, 6.40 and 6.41 shows the effect of the downstream velocity on the phase layer evolution for flow conditions 80% OVF, 50% OVF and 20% OVF respectively and downward angle pipe inclination along the test distance. Clear oil and water layers with mixed interface flowing between them is seen at lower mixture velocity, with the mixed region gradually increasing in thickness and both oil and water layers at top and bottom of pipe disappearing with increasing mixture velocity. A recirculation flow of the clear oil layer at the pipe top was noticed towards the end of the singularity of the test distance for 50% OVF and 80% OVF flow conditions at increasing mixture velocity.

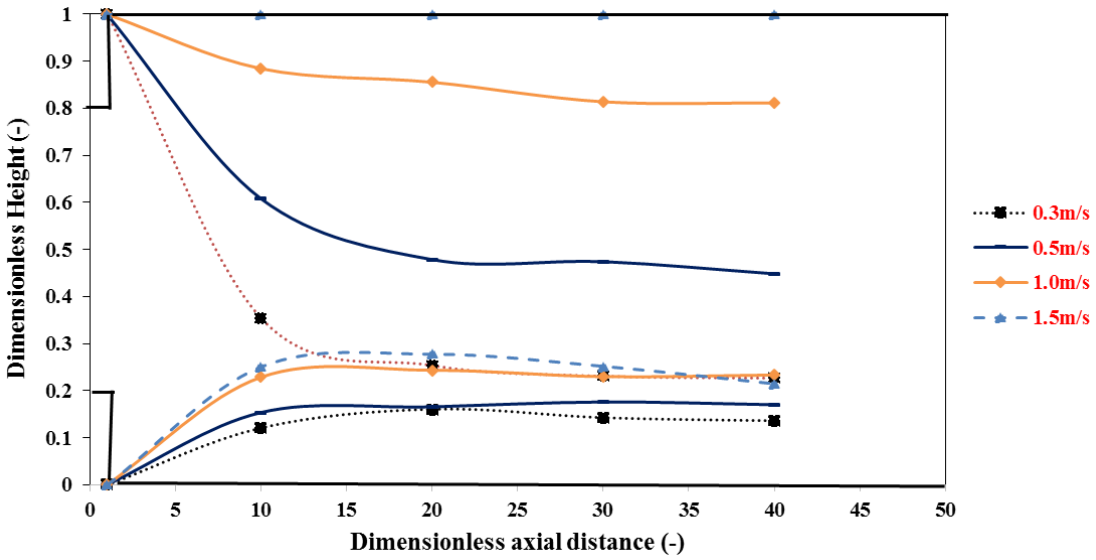

Figure 6-39 Effect of mixture velocity on the phase layer evolution downstream of the singularity with flow conditions, 80% OVF and downward inclined pipe (-2^0) flow at different axial test distances.

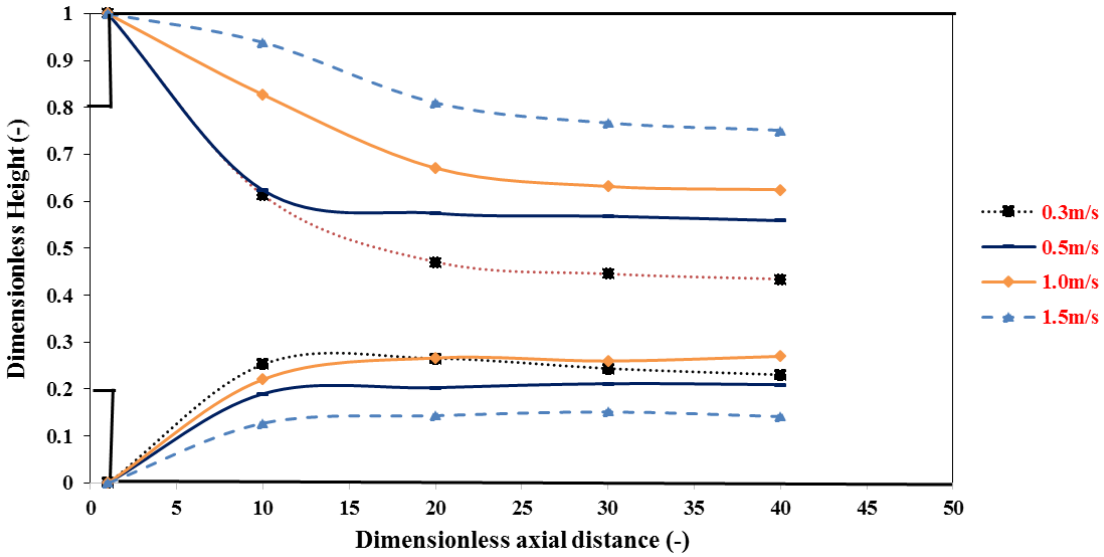

Figure 6-40 Effect of mixture velocity on the phase layer evolution downstream of the singularity with flow conditions, 50% OVF and downward inclined pipe (-2^0) flow at different axial test distances.

This phenomenon also contributes to the thinning effect of the lighter oil layer at the end of test section caused by buoyancy forces and neck design connecting the test section and flow exiting hose, downstream of the expansion. The heavier water layer was also observed to flow faster at bottom than the oil layer at the top of the pipe.

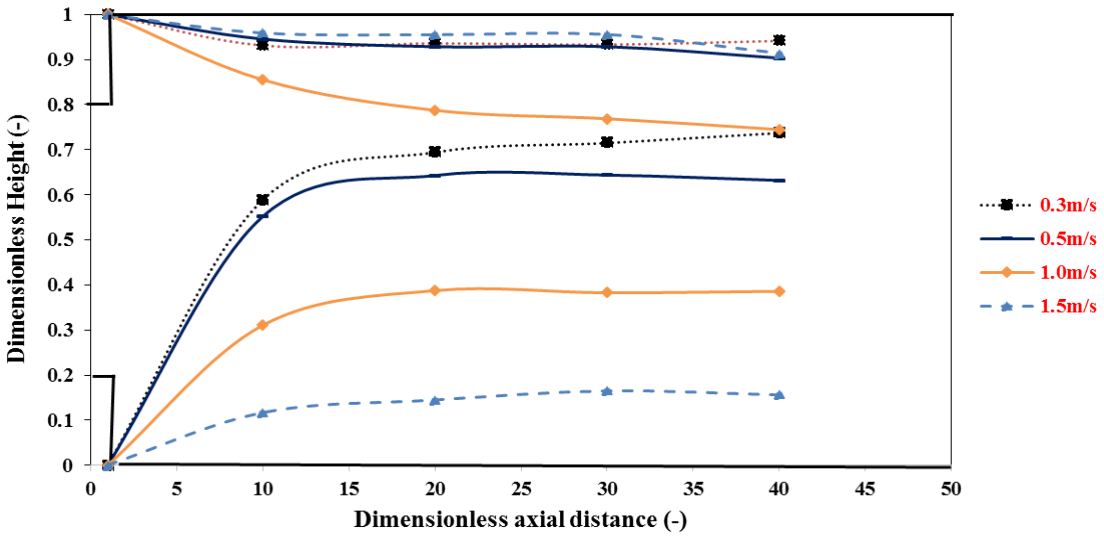

Figure 6-41 Effect of mixture velocity on the phase layer evolution downstream of the singularity with flow conditions, 20% OVF and downward inclined pipe (-2^0) flow at different axial test distances.

6.5.3 Mixed interface height and mixture velocity

Figure 6.42 shows the height of interface mixed region as a function of downstream mixture at different input oil volume fractions on the phase layer evolution along the axial test distance of the pipe expansion for downward angle pipe inclination. The trends generally indicates an increase in the average interface height as the mixture velocity increases at all input oil volume fractions, similar to what was observed in the horizontal and upward inclination cases. A fully dispersed flow occurs earlier for downward flows at higher velocities beyond 1.00m/s, in which the phase fraction is constant and expands along the vertical axis of the pipe cross section. Stratified flow was only observed at very low velocity 0.20 m/s (see Figure 6.18a), beyond which there is a transition to mixed and subsequently dispersed flows.

6.5.4 Evolution of mixed interface height

The evolution of the mixed interface height from the homogeneous downstream inlet part of the expansion to the downstream of the expansion, at the different axial distances along pipe for various mixture velocities (a) 0.30m/s (b) 0.50m/s (c) 1.00m/s (d) 1.50m/s, is as presented in Figure 6.43. Same generally decreasing trend of the interface height along the pipe test section, was noticed downstream of the expansion for all input oil volume fractions.

The following findings can be summarized for the phase layer evolution in the downward inclination pipe flow:

- Fully developed stratified flow (ST) only existed at very low velocity (0.20ms) at different input oil volume fractions within the 6m long pipe test section. Beyond this velocity the flow transit from the usual three (3) layers to fully dispersed regime.
- The heavier water layer at pipe bottom was found to move faster than the lighter oil layer at top of pipe. Lower mixture velocity enhances the thickness of the evolution of oil layer at pipe top.

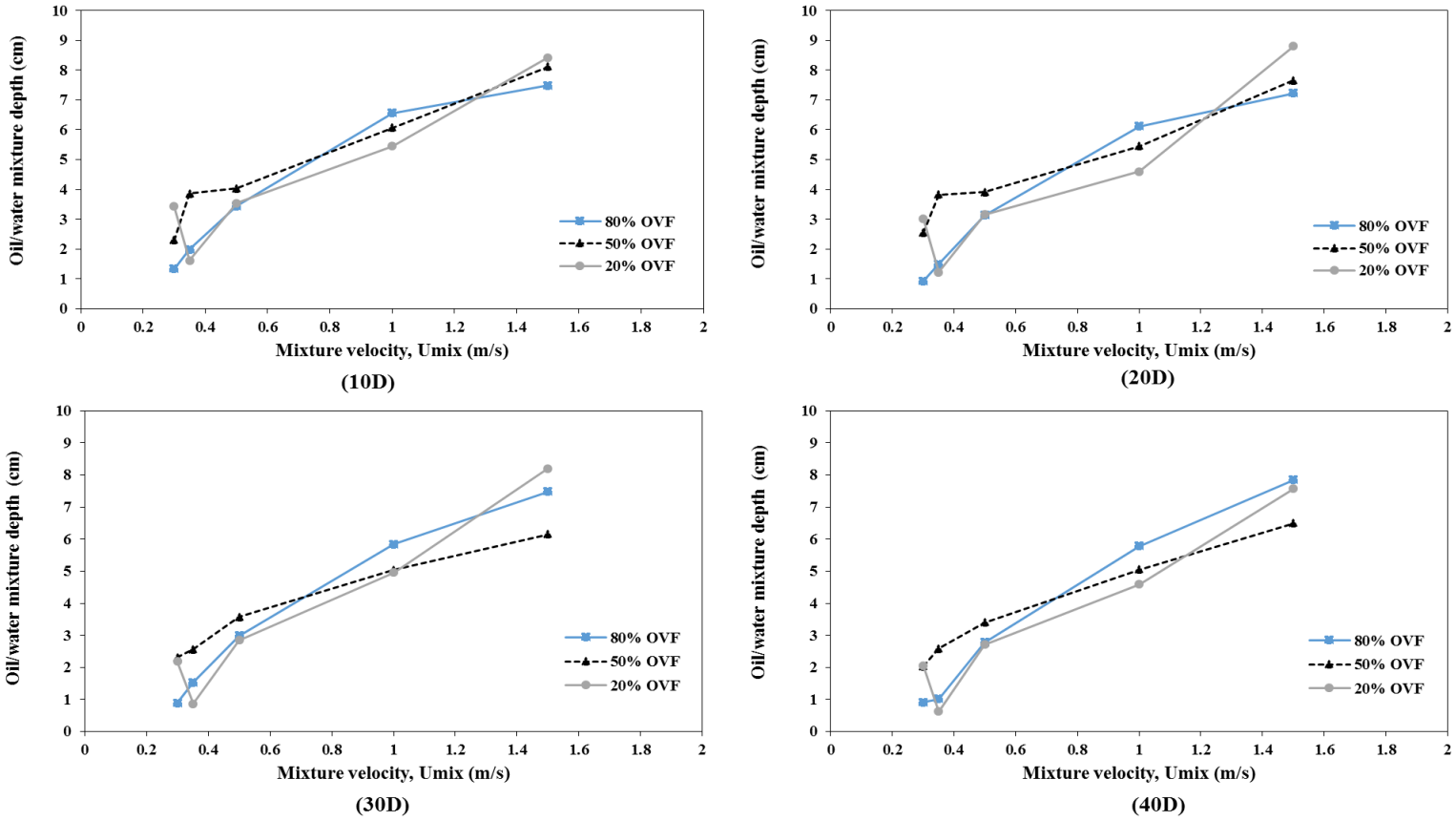

Figure 6-42 Oil/water mixed interface region vs mixture velocity on the phase layer evolution downstream of the singularity with flow conditions, 20% OVF, 50% OVF, 80% OVF and Downward flow at different axial test distances

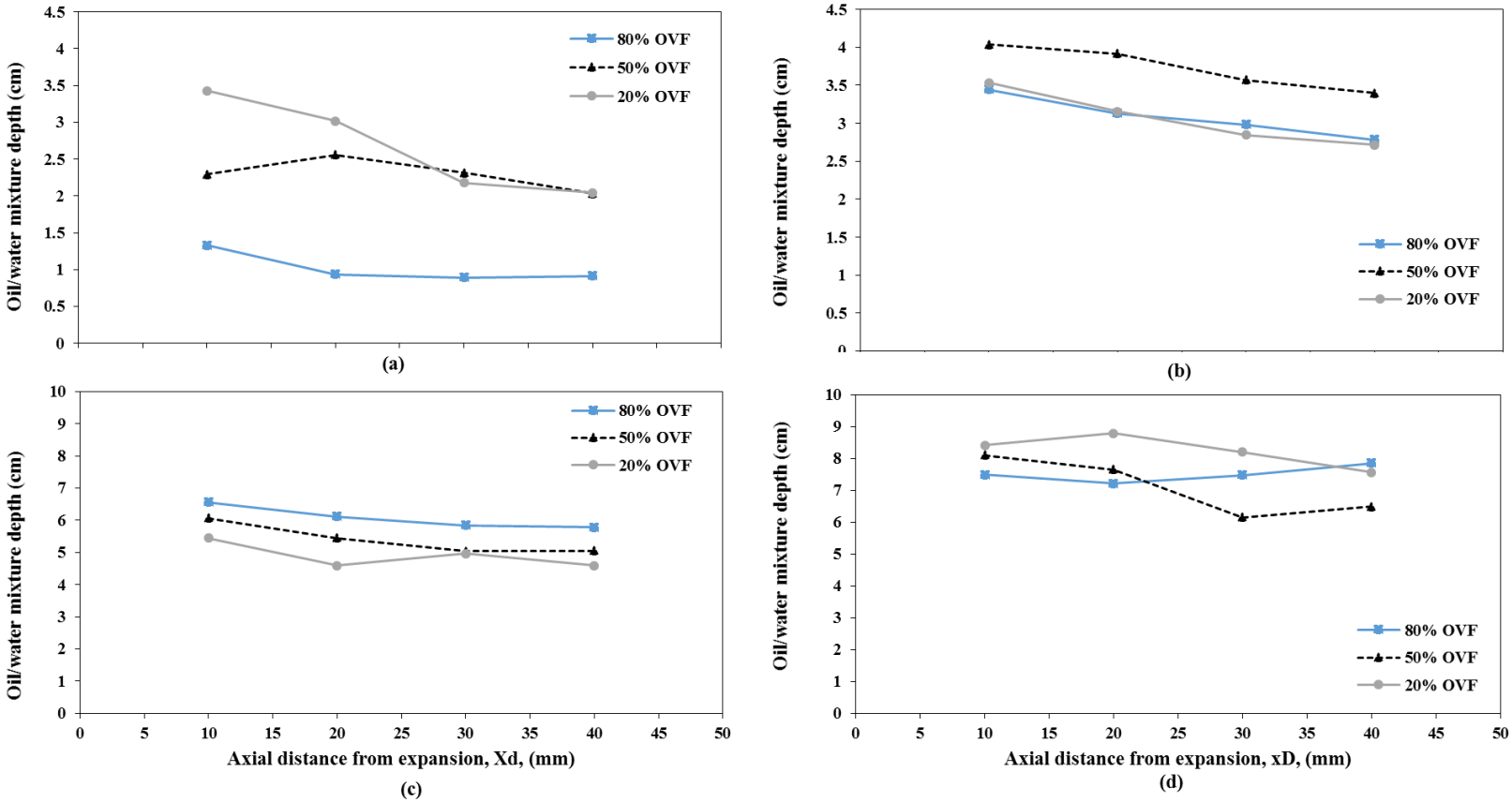

Figure 6-43 Oil/water mixed interface region vs axial distance along pipe expansion at various mixture velocities (a) 0.30m/s (b) 0.50m/s (c) 1.00m/s (d) 1.50m/s; Downward pipe flow orientation.

6.5.5 Comparison between different angles of inclination

Figure 6.44 shows the effect of different angle of pipe inclination on the phase layer evolution at a downstream velocity of 0.30m/s and 20% OVF. It can be seen that fully stratified flow only occurred for the horizontal flow downstream at position 40D. For other angles of inclination, the three (3) layers exist i.e oil and water layers at top and bottom of pipe with mixed interface between them. Both oil and water layers increases thickness downstream as the fro progresses but maintains ST& MI regime up to end of the expansion (40D).

There is no significant difference when the downstream velocity is increased further to 0.50m/s except that the flow pattern has transited to the ST& MI regime and continues to the end of the expansion end at fully developed flow as presented in Figure 6.43. Waves also emerge at the mixed interface region for the horizontal flow condition.

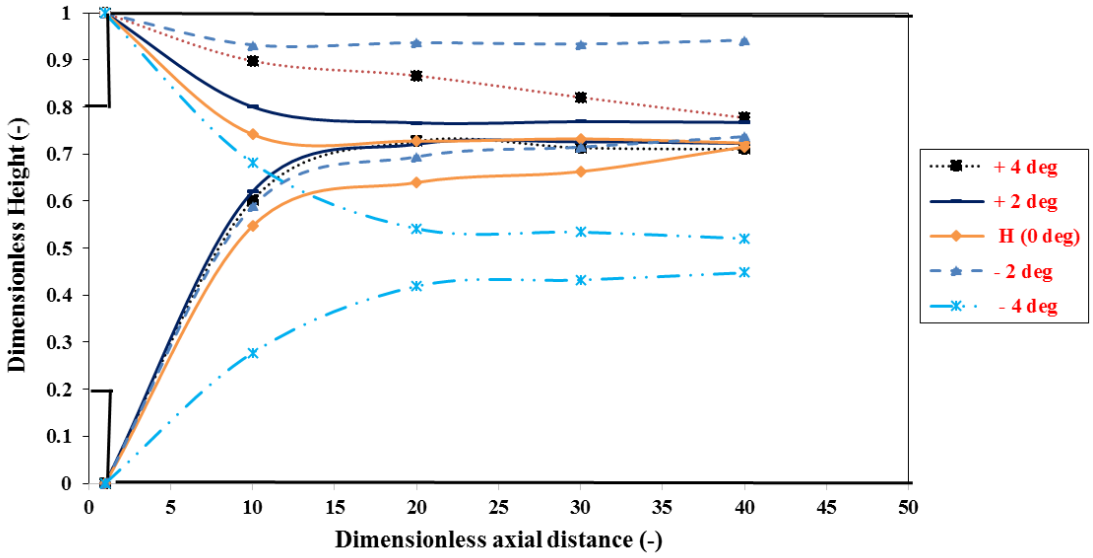

Figure 6-44 Effect of the angles of pipe inclination on the phase layer evolution downstream of the singularity with flow conditions, 20% OVF and downstream mixture velocity 0.30m/s within axial test distance.

A careful observation of the trends from Figures 6.45 – 6.47 reveals that for downward flows, the heavier water layer flows faster than the oil layer at the top of the pipe and reverse is the case for upward flow, were the oil flows faster at the top and the water flows slower at the pipe bottom. An explanation for this phenomenon is that the fast moving lighter layer tends to become homogeneous due to turbulence created in the flow. The lighter oil layer evolves quite slowly compared to the heavier water layer at bottom of pipe and increases faster in thickness as it evolves much quicker. This was confirmed from the video recordings and images obtained with the Phantom high speed camera.

The thickness of the mixed interface region for the horizontal orientation in all the Figures is seen to be thinner and becomes fully stratified flow conditions at the tail end of the expansion for fully developed flow. Both upward and downward flow inclinations tend to increase and expand the mixed interface region. Therefore, it can be recommended that the horizontal pipe flow orientation is more suitable for dispersed flows to be converted to segregated flow in a sudden pipe expansion phase separation system.

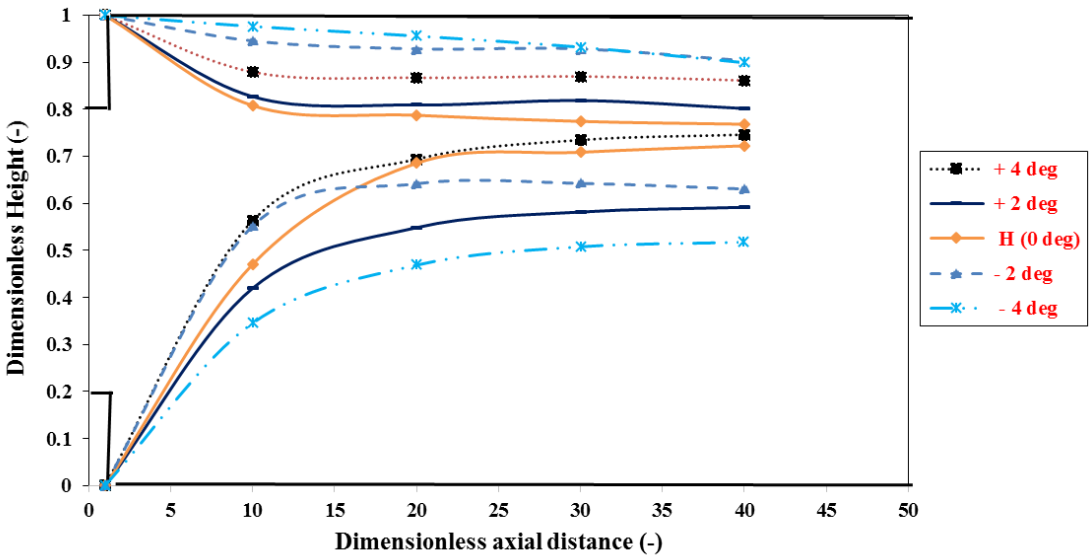

Figure 6-45 Effect of the angles of pipe inclination on the phase layer evolution downstream of the singularity with flow conditions, 20% OVF and downstream mixture velocity 0.50m/s within axial test distance.

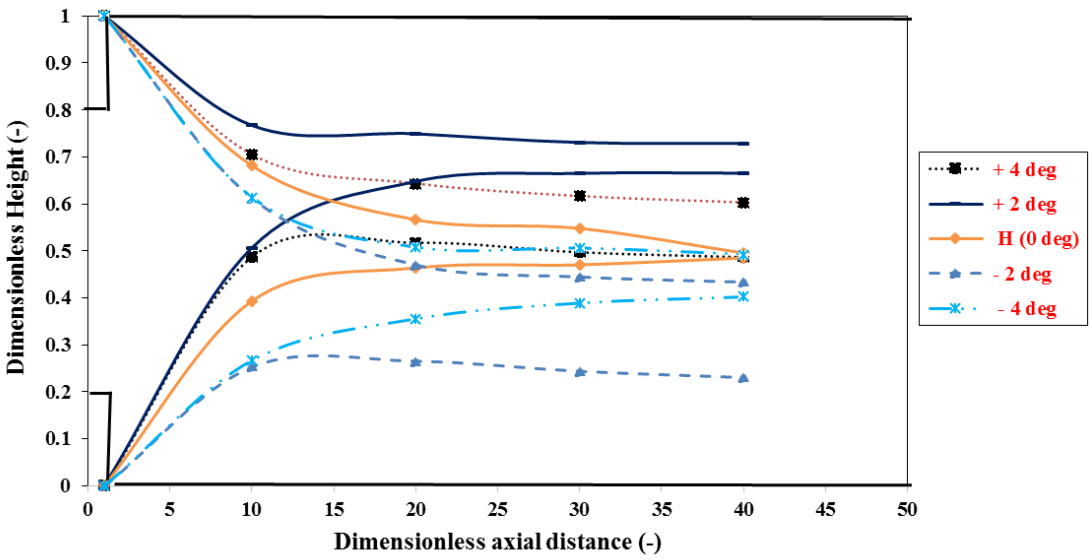

Figure 6-46 Effect of the angles of pipe inclination on the phase layer evolution downstream of the singularity with flow conditions, 50% OVF and downstream mixture velocity 0.30m/s within axial test distance.

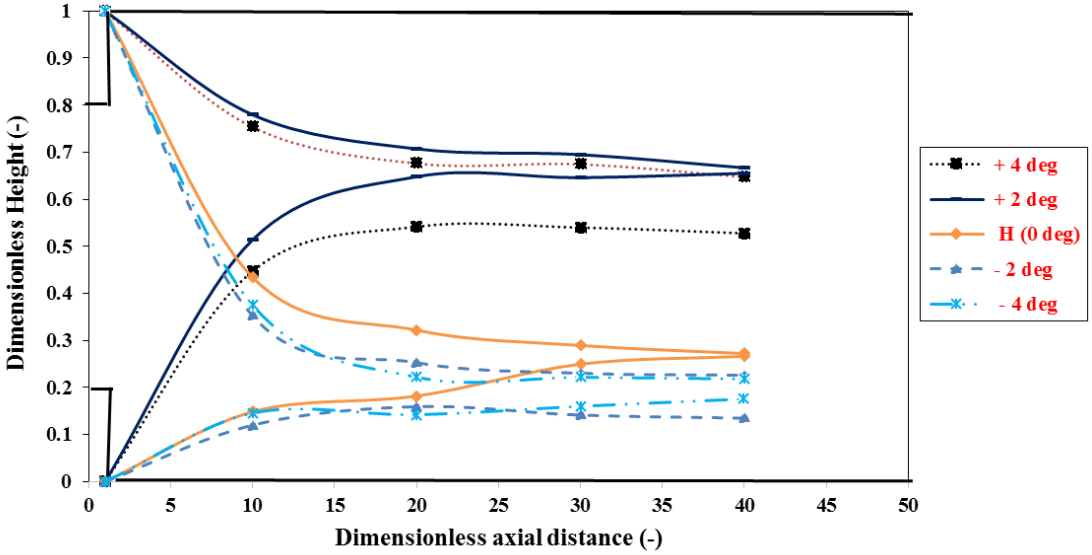

Figure 6-47 Effect of the angles of pipe inclination on the phase layer evolution downstream of the singularity with flow conditions, 80% OVF and downstream mixture velocity 0.30m/s within axial test distance.

6.5.6 Characteristics of oil-water two-phase structure in 127mm pipe

Time series of cross sectional average liquid hold up or in-situ oil volume fraction at several axial locations and pressure gradient were simultaneously measured on the 127mm diameter sudden pipe expansion test facility. From these, the details of the physical structure and flow patterns have been identified in a series of experiments as discussed earlier in section 6.1. The results from the four (4) conductance ring probes are further analyzed and presented for fully developed flows downstream of the singularity.

6.5.6.1 Time series and Probability Density Function (PDF)

Figure 6.48, 6.49 and 6.50 shows time series graphs of in-situ oil volume fractions 80% OVF, 50% OVF and 20% OVF respectively of stratified to dispersed transition and typical PDFs at fully developed flow downstream of expansion position, 40D. The conductance probe readings, changes for fixed mixture velocities (0.20m/s, 0.50m/s and 2.00m/s) at various input oil volume fractions. For the lowest mixture velocity 0.20m/s, at the various oil volume fractions OVF and stratified flow (ST), the flow is composed of continuous layers of oil (at the top) and water layer (at bottom) with sparse pack of droplets of both kinds flowing in between them. The phantom high speed camera images are in agreement (section 6.2.1) with these results obtained from the conductance probes (see also Figures 6.5 – 6.10). There is also less perturbation at the interface as indicated from the time series graphs.

At higher mixture velocity U_{sme} 0.50 ms^{-1}, both water and oil drops entrainment at the mixed interface region is enhanced and formed. Three (3) layers finally emerges i.e clear oil layer at pipe top, a mixed interface layer and water layer at the pipe bottom. From the PDF in flow condition 50% OVF, the peak of the graph is more or less flattened. This indicates that the conductance probes are affected by the presence of oil and water droplets formed at the interface region, resulting to a shift in readings. As explained earlier in this Chapter 6 in section 6.2.1.1 and Figure 6.1d, stratified wavy flow (plug wavy flow) is obtained, at mixture velocities between (U_{sme} 1.00 ms^{-1} – 1.50 ms^{-1}).

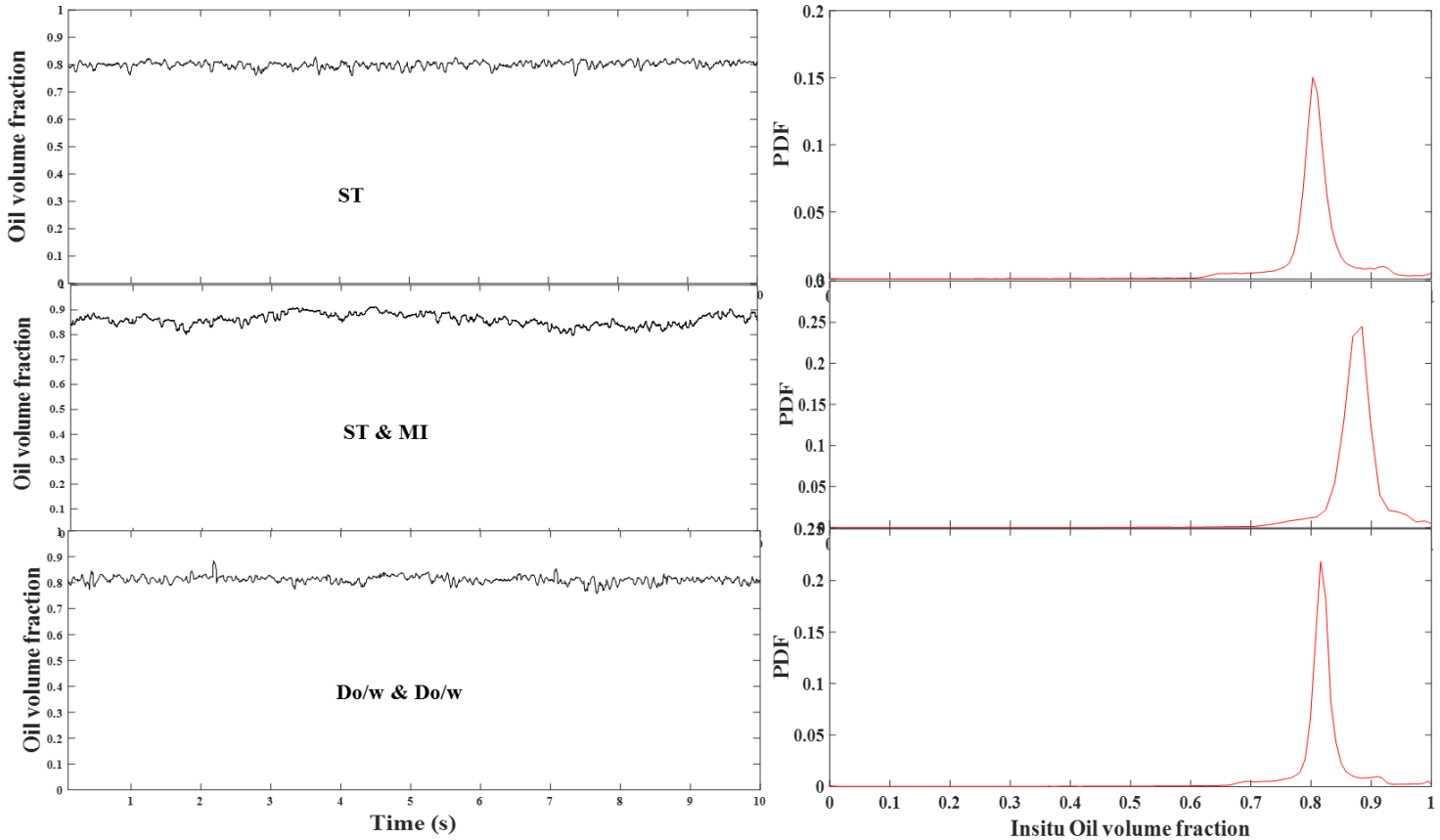

Figure 6-48 Time series of in-situ oil volume fraction 80% OVF in the 127 mm pipe, (a) stratified (ST), (U_{sme} 0.20 ms^{-1}), (b) stratified with mixed interface (ST & MI), (U_{sme} 0.50 ms^{-1}), (c) dispersed flow ($D_{o/w}$ & $D_{w/o}$), (U_{sme} 2.00 ms^{-1}), transition and typical PDFs at fully developed flow downstream of expansion (40D)

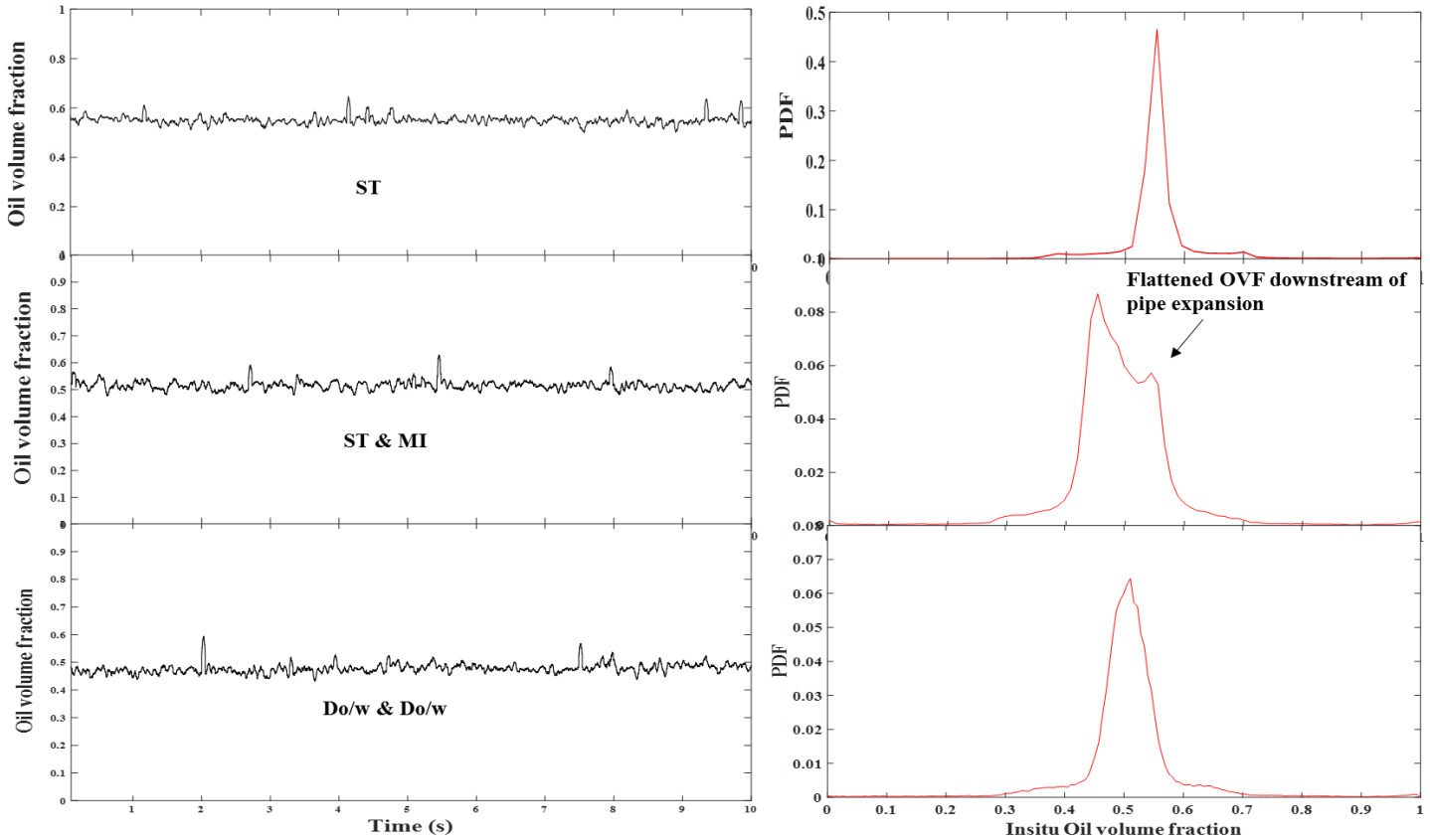

Figure 6-49 Time series of in-situ oil volume fraction 50% OVF in the 127 mm pipe, (a) stratified (ST), (U_{sme} 0.20 ms^{-1}), (b) stratified with mixed interface (ST & MI), (U_{sme} 0.50 ms^{-1}), (c) dispersed flow ($D_{o/w}$ & $D_{w/o}$), (U_{sme} 2.00 ms^{-1}), transition and typical PDFs at fully developed flow downstream of expansion (40D)

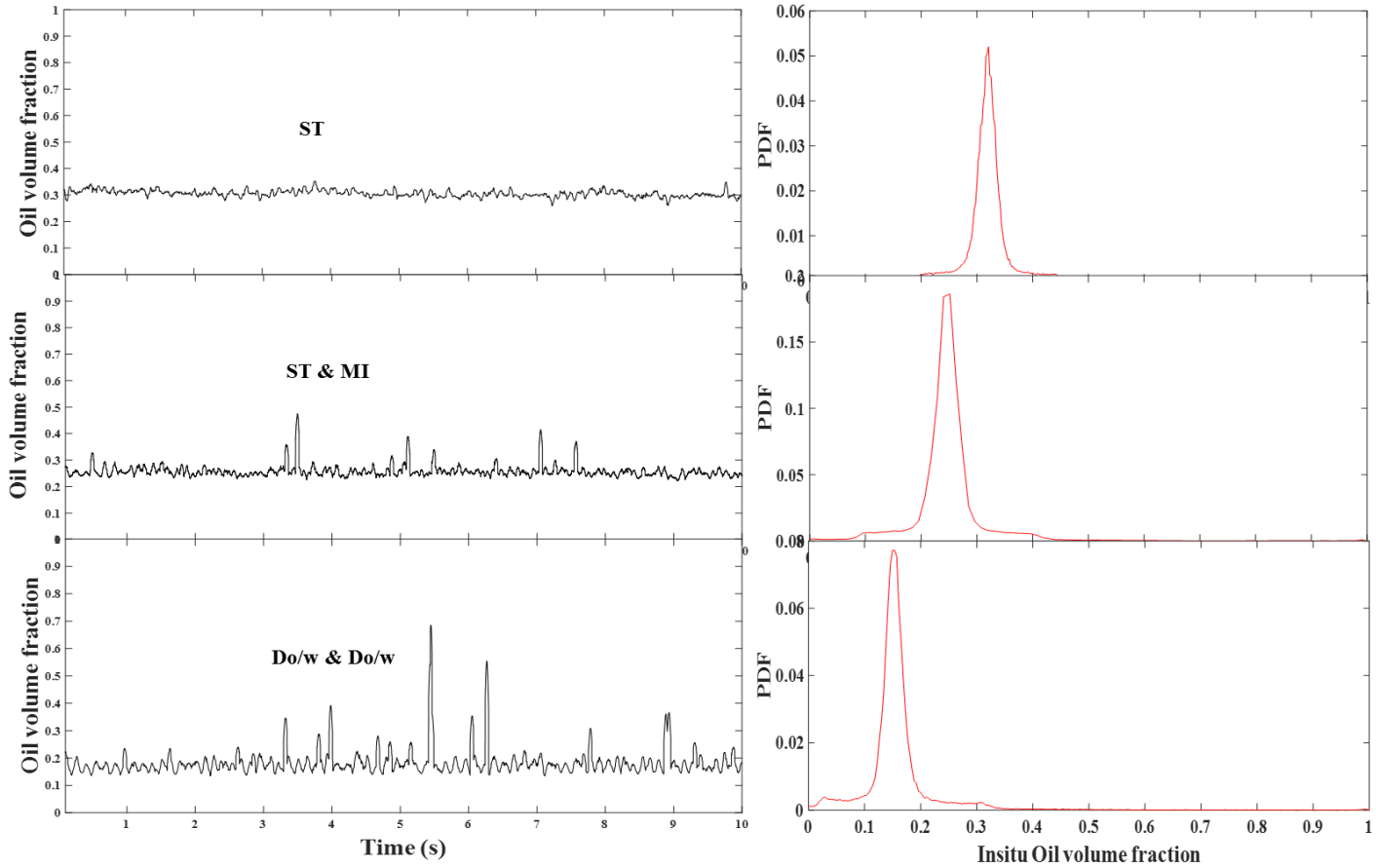

Figure 6-50 Time series of in-situ oil volume fraction 20% OVF in the 127 mm pipe, (a) stratified (ST), (U_{sme} 0.20 ms^{-1}), (b) stratified with mixed interface (ST & MI), (U_{sme} 0.50 ms^{-1}), (c) dispersed flow ($D_{o/w}$ & $D_{w/o}$), (U_{sme} 2.00 ms^{-1}), transition and typical PDFs at fully developed flow downstream of expansion (40D)

As the mixture velocity is increased further to Usme 2.00 ms^{-1}, the result becomes more chaotic and perturbation increases at the mixed interface region. The flow becomes fully dispersed at this stage resulting to water in oil (w/o) dispersions and oil in water dispersions (o/w) depending on the conditions under which they are formed. This indicates that the flow becomes oscillatory and wavy than was obtained at low mixture velocities.

The dominant frequencies were estimated by counting the periodic peaks of the time series graph, (Figure 6.50) and dividing it with time. Therefore, from Figure 6.50, the dominant frequencies are 1.5 Hz and 2.5 Hz for the stratified with mixed, (ST & MI) and dispersed ($D_{o/w}$ & $D_{w/o}$), flow regimes respectively.

Water or oil can be the dominant phase, depending on which one is the continuous phase, and what the corresponding pressure drop response would be. These dispersions normally occur at a phase inversion point.

The conductance probe signals collected at 1000Hz over 2 mins, after de-trending, exhibited the features of randomness and normality, which followed a Gaussian distribution as can be seen from Figures 6.48, 6.49 and 6.50. However, the data is not entirely stationary as the mean and variance are different in some cases.

6.6 Summary

Data obtained from the four (4) ring conductance probes and information from the Phantom (PCC 2.7) high speed camera video recordings were used to investigate flow development along the pipe expansion and interface shapes of the singularity. A detailed analyses and discussion on the effect of flow parameters with axial pipe distance and pipe orientation (horizontal, upward and downward angle inclination), were made and also establishing a relationship between captured images and the acquired dataset. The results from the investigations described in this Chapter 6 show that the performance of the ring conductance probes and video recordings from the camera for measuring the concentration of oil-water two-phase flows is reliable, with

correct calibration procedure, connected to a Labview program in an automated National Instrument (NI) centrally controlled unit.

A comparison of the results obtained was made with previous research work (Yang, 2003, Hasan, 2006, Yusoff, 2012) etc. and also plotted on the flow pattern map of (Trallero et al., 1997). The results obtained satisfactorily agree well with their findings and therefore can be used to substantiate the flow patterns predicted in the Trallero map. However, additional flow patterns were observed such as Raleigh Taylor plume shaped flow in the horizontal flow and plug wavy flow (Caterpillar like waves) in both upward and downward inclination, which have not been reported.

Fully developed stratified flow (ST) can be obtained at mixture velocities below 0.30m/s at different input oil volume fractions within the 6m long pipe for both horizontal and upward inclined pipe flow conditions. The lighter oil layer at top of pipe was found to move faster than the bottom water layer for the upward pipe inclination, whereas the reverse case occurred for the downward pipe flow condition. Also there was evidence of stratification of the mixed interface layer downstream of the expansion in the various pipe orientations.

Chapter 7 CONCLUSION AND RECOMMENDATIONS

A simple and compact sudden pipe expansion can be considered for phase separation, which is safer and more economical compared to the conventional separators commonly used. A systematic experimental campaign was therefore carried out on liquid-liquid oil-water two-phase flow separation facility with a sudden pipe expansion. This Chapter presents a summary o

f the research work done and the findings from the investigations in the subsections that follows.

7.1 Findings and Contributions to knowledge

The present research work included the design and construction of a large scale versatile liquid-liquid oil-water sudden expansion rig facility, which was completed and commissioned for use, capable of handling 5,000litres of silicone oil with viscosity of 5cp.

A comprehensive experimental dataset was obtained in the current study to provide predictions of flow parameters such as oil-water flow patterns and their transitions, two-phase pressure gradient, liquid temperatures, liquid flow rate and holdups (oil and water volume fractions) in oil/water two phase systems, useful in solving complex liquid-liquid flow problems This will help in contribution towards effective design and performance of phase separators in liquid-liquid systems.

7.2 Comments on experimental programme

A preliminary study was conducted initially on a bench top scale to have an understanding of the hydrodynamics of liquid-liquid oil-water system, which is reported in Chapter 3 of this Thesis. The rest experimental campaign was carried out

on the 6m long sudden expansion test section of the large scale oil-water liquid-liquid flow facility. The fluids employed were silicone oil (5cp, 916kg/m^3 density) and tap water (998kg/m^3 density). The experimental conditions include, water cuts from 20% to 80%, mixture velocities of 0.20m/s, 0.25m/s, 0.30m/s, 0.35m/s, 0.50m/s, 1.00m/s, 1.50m/s, 2.00m/s, 2.50m/s, 3.00m/s, 3.50m/s, at different angles of pipe inclination ($+4^0$, $+2^0$, horizontal, -2^0, -4^0). Instrumentation use include, FBRM M500P laser developed by Lasentec for drop size measurements, Phantom PCC 2.7 high speed camera, Ring conductance probes, Truflo meter for oil flowrate, Electromagnetic flow meter for water flowrate and two (2) Differential pressure (Dp cells for pressure drop measurements. All the analogue measurement instruments and equipment for flow parameters including, thermocouples, DP Cell, flowmeters, conductance probes, fluids storage tanks and separator are incorporated in the LabVIEW program and automated using a National .Instrument (NI) Chasis unit measurement protocol.

7.3 Drop size distribution

For the preliminary investigation, a Focused Beam Reflectance Measurement (FBRM) technique was used to obtain drop sizes and drop size distributions in silicone oil-in- water dispersions. From the results obtained, both Rosin-Rammler and log normal distribution was found to fit satisfactorily with the experimental data. However, the Log-normal distribution fits better and also found to be in large agreement with the actual drop diameters of the experimental data, when both distributions were compared.

Results from Sauter mean diameter (SMD) analysis reveals that an increase in impeller speed results in the evolution of smaller droplet sizes and the distribution shifting towards smaller drops. This signifies drop breaking up process taking place. There was also some significant effect by increasing the dispersed phase volume fraction leading to an overall decrease in Sauter mean diameter (SMD). The results also indicates an increase in drop size as coalescence process progresses with time, thereby resulting to an increase in volume of both oil and water.

In the large scale rig, results presented for drop size distribution are unique as measurements were made at different vertical and axial locations in a sudden pipe expansion test cross section. The following summaries the findings on drop size distributions for the large scale sudden expansion rig facility:

A. For horizontal pipe flow

- Input oil volume fraction strongly influenced formation of drop sizes downstream of the expansion as investigation shows larger droplets detected at 40D due to coalescence mechanism of the drops.
- Smaller droplet sizes are formed downstream of the pipe expansion with an increase in downstream mixture velocity.
- Coalescence of dispersed phase droplets progresses from inlet and stratifies gradually downstream of the singularity. In general higher input oil fraction and low mixture velocity (0.20m/s), favours coalescence producing larger droplets downstream of pipe expansion.

- The results were in good agreement when fitted with some existing models such as Rosin-Rammler and Log-normal and with the (Hinze, 1955) model.

B. Upward inclination orientation pipe flow

- Input oil volume fraction affects the Sauter mean diameter (SMD) of drops throughout the entire axial test distance resulting in the formation of smaller droplets at low mixture velocity (0.20m/s).

- Smaller droplet sizes are formed downstream of the pipe expansion with an increase in downstream mixture velocity.

- Sauter mean diameter (SMD) is affected by probe position. Larger droplets were observed above and below the interface region.

- Water droplets coalesce and settle faster than dispersed oil droplet in water continuous phase flow system. The bulk oil layer was also

observed to flow faster at the top than the bulk water layer at the bottom in upward pipe inclination orientation.

D. Downward inclination orientation pipe flow

- Both input oil volume fraction and probe position show minimal effect on the drop sizes formed for downward pipe inclination.

- Sauter mean diameter (SMD) increases with increase in mixture velocity along the entire test section. At higher mixture velocity, both water and oil droplets coalesce faster at the top and bottom pipe portions respectively and accumulates around the interface downstream of the singularity.

- The larger droplets formed are observed to concentrate mostly at the bottom portion of pipe at position 40D downstream of the expansion.

- Smaller and finer droplets detected at higher mixture velocity (0.35m/s) in position 30D indicate dispersion due to high collision frequency of droplets.

A comparison between some published models and correlations with current experimental data was carried out. The Rosin – Rammler distribution function and log-normal distribution was found to fit satisfactorily well with experimental data, especially at the interface mixed region between oil and water. The Rosin-Rammler parameter results also show consistency with previous work on larger pipe diameter but vary with findings from some earlier research work on smaller pipe diameters. Sauter mean diameter (d_{32}), values of present data also correlated well with (Hinze, 1955) model for water continuous and oil dispersed phase system in horizontal pipeline.

7.4 Flow patterns and flow pattern maps

The results obtained satisfactorily agree well with the existing conventional flow patterns and flow pattern maps. The flow patterns identified includes, stratified flow (ST), stratified with mixed interface (ST& MI), oil-water intermittent flow, stratified

wavy flow and dispersed flow in all pipe orientations. Additional flow patterns were also observed such as Raleigh Taylor plume shaped flow in the horizontal flow and plug wavy flow (Caterpillar like waves) in both upward and downward inclination, which have not been reported.

7.5 Stratification of dispersion in large diameter pipe

The sudden expansion facility is designed for liquid-liquid oil water two-phase system to evolve and develop from dispersed to stratified phase flow downstream of the singularity. There was evidence of stratification for fully developed ST regime at short distance from inlet (10D) at mixture velocities below 0.30m/s in both horizontal and upward inclinations. The lighter oil layer at top of pipe was found to move faster than the bottom water layer for the upward pipe inclination, whereas the reverse case occurred for the downward pipe flow condition. Interfacial waves were also found with amplitudes of about 0.1D – 0.15D pipe diameter in all pipe orientations. There was no significant effect of these waves with pipe inclinations. The best orientation was that of the horizontal flow position for dispersed flows to separate quickly as both the upward and downward inclined pipe flow conditions tend to hamper the evolution process by increasing the mixed layer region.

7.6 Oil volume fraction

Instantaneous online in-situ oil volume fraction measurements were obtained with ring conductance probes without any flow obstructions or intrusion. The results obtained strongly demonstrate the influence of liquid-liquid flow parameters (mixture velocity, input oil volume fraction etc) and rig configuration. Two (2) layers consisting of oil at pipe top and water at pipe bottom predominates in the stratified flow condition for low mixture velocity below 0.30 ms^{-1}. Beyond this velocity ranging from 0.35 ms^{-1} – 1.50 ms^{-1}, three (3) layers exist i.e. oil and water layers at top and bottom of pipe respectively with mixed interface layer flowing between them. The flow transits to fully dispersed flow from 2.00 ms^{-1} and beyond.

Velocity ratio behavior was explained with the help of phase distribution in a pipe cross section. The slip ratio S, slightly increased with increasing oil volume fraction for lower mixture velocities (0.20 ms^{-1} – 0.35 ms^{-1}) and become closer to 1. $S > 1$ means that the oil phase travels faster than the water phase in the pipe. Each phases tend to adjust itself to flow at roughly the same mixture velocity for lower downstream mixture velocities.

At higher mixture velocities (0.5 ms^{-1} – 2.0 ms^{-1}), the slip ratio in general is less than unity ($S < 1$ indicates that water is the faster phase). Majority of the velocity ratio measured, are within the flow regimes were stratified with mixed (ST& MI) interface or three layer exist. In this regime the tube wall is totally covered by oil, which justifies velocity ratios less than unity. In the three Layer regime, where both oil and water are in contact with the tube wall, the preferential wetting of the wall by oil may have resulted to higher tube area covered by the oil, which can explain velocity ratios less than unity.

7.7 Recommendations for future work

In the current work, the ring conductance probe technique was employed to obtain useful information on liquid-liquid oil – water two phase system. This technique in combination with the use of the backscatter Lasentec FBRM M500P laser for drop size measurements and Phantom PCC 2.7 high speed camera for imaging, provided quality and quantitative dataset, useful for solving complex liquid-liquid system problems.

However, additional measurement techniques such as the use of Wire Mesh Sensor and Particle Image Velocimetry (PIV) are recommended for further experiments to be done. This will expand the data bank on large diameter pipes (ϕ127mm) and also help to validate and consolidate upon the already existing information. An advantage of a combination of WMS with conductance probe would be to investigate the mixed interface region in details to study the behaviour of the waves and droplet sizes formed, simultaneously at every point on the rig facility. It will also enable comparison of dataset with other measurement techniques. A governing

phenomenological model can be derived from a combination of this information, which can be used universally to solve complex liquid – liquid two-phase systems.

The homogenizer design can be modified as well as the application of orifice plates is recommended to improve upon the dispersed inlet condition of the rig.

Due to the versatility of the rig facility, three (3) phase flows i.e gas – oil – water flow, experiments can be conveniently carried out for different pipe angle orientation in the future.

REFERENCE

Ai-Wahaibi, T. & Angeli, P. 2008. Droplet size and velocity in dual continuous horizontal oil-water flows. *Chemical Engineering Research & Design,* 86**,** 83-93.

Al-Wahaibi, T. & Angeli, P. 2011. Experimental study on interfacial waves in stratified horizontal oil-water flow. *International Journal of Multiphase Flow,* 37**,** 930-940.

Alamu, M. B. & Azzopardi, B. J. 2011. Simultaneous Investigation of Entrained Liquid Fraction, Liquid Film Thickness and Pressure Drop in Vertical Annular Flow. *Journal of Energy Resources Technology-Transactions of the Asme,* 133.

Alkaya, B. 2000. Oil-water flow patterns and pressure gradients in slightly inclined pipes. M. S. Thesis. *The University of Tulsa, USA.* .

Andrea, J. M., Hauser, E. A. & Tucker, W. R., . 1938. Equation for determining 1/H versus S values in computer calculations of Interfacial Tension by the Pendant Drop Method *J. Phys. Chem. 42, 1001,* 42, pp 1001.

Andreussi, P., Didonfrancesco, A. & Messia, M. 1988. An Impedance Method for the Measurement of Liquid Hold-up in 2-Phase Flow. *International Journal of Multiphase Flow,* 14**,** 777-785.

Andritsos, N. 1992. Statistical-Analysis of Waves in Horizontal Stratified Gas-Liquid Flow. *International Journal of Multiphase Flow,* 18**,** 465-473.

Angeli, P. 2001. Droplet size in two-phase liquid dispersed pipeline flows. *Chemical Engineering & Technology,* 24**,** 431-434.

Angeli, P. & Hewitt, G. F. 1998. Pressure gradient in horizontal liquid-liquid flows. *International Journal of Multiphase Flow,* 24**,** 1183-1203.

Angeli, P. & Hewitt, G. F. 2000. Drop size distributions in horizontal oil-water dispersed flows. *Chemical Engineering Science,* 55**,** 3133-3143.

Angeli, P. & Hewitt, G. F. 2000a. Flow structure in horizontal oil-water flow. *International Journal of Multiphase Flow,* 26**,** 1117-1140.

Arirachakaran, S., Oglesby, K. D., Malinowsky, M. S., Shoham, O., Brill, J. P. & 1989. An Analysis of Oil/Water Flow Phenomena in Horizontal Pipes,. *SPE Paper 18836, SPE Production Operations Symposium, Oklahoma, March 13-14, 1989***,** pp. 155-167.

Asali, J. C., Hanratty, T. J. & Andreussi, P. 1985. Interfacial Drag and Film Height for Vertical Annular-Flow. *Aiche Journal,* 31**,** 895-902.

Azzopardi, B. J. 1986. Disturbance Wave Frequencies, Velocities and Spacing in Vertical Annular 2-Phase Flow. *Nuclear Engineering and Design,* 92**,** 121-133.

Azzopardi, B. J. 1997. Drops in annular two-phase flow. *International Journal of Multiphase Flow,* 23**,** 1-53.

Azzopardi, B. J. & Hills, J. 2001. Modelling and Experimentation in Two Phase Flow, CISM Courses and Lectures No. 450, Published in; Bertola, V (2003),. *International Centre for Mechanical Sciences, ,* ISBN 3-211-20757-0, Springer-Verlag Wien, New York.

Bannwart, A. C., Rodriguez, O. M. H., De Carvalho, C. H. M., Wang, I. S. & Vara, R. M. O. 2004. Flow patterns in heavy crude oil-water flow. *Journal of Energy Resources Technology-Transactions of the Asme,* 126**,** 184-189.

Barral, A. H. 2014. Stratified wavy oil-water flows. *Ph.D. Thesis, Chemical Engineering, University College London*

Barral, A. H. & Angeli, P. 2014. Spectral density analysis of the interface in stratified oil-water flows. *International Journal of Multiphase Flow,* 65**,** 117-126.

Beck, M. S., Green, R. G. & Thorn, R. 1987. Nonintrusive Measurement of Solids Mass-Flow in Pneumatic Conveying. *Journal of Physics E-Scientific Instruments,* 20**,** 835-840.

Bell, J. M., Chin, Y. D., Kvaerner, A. & Hanrahan, S. 2005. State of the art of ultra deepwater production technologies *2005 Offshore Technology Conference (2nd - 5th May 2005), Houston, Texas, USA, (OTC 17615)*.

Belt, R., Djoric, B., Kalali, S., Duret, E. & Larrey, D. 2011. Comparison of commercial multiphase flow simulators with experimental and field databases. *First presented at BHR Group's Multiphase Production Technology Conference in Cannes, Process Department, Total EP, france, Stavanger Research Centre, Total EP, Norway*.

Beyer, M., Szalinski, L. & Schleicher, E. 2012. Wire-Mesh Sensor Data Processing Software, . *Institute of Fluid Dynamics Helmholtz-Zentrum Dresden-Rossendorf, 01314 Dresden, Germany,* WMS-Software User Manual, Version 01.02**.,** 1 - 28.

Blaney, S. 2008. "Gamma Radiation Methods for Clamp-on Multiphase Flow Metering", PhD thesis, Cranfield University, UK.

Blaney, S. & Yeung, H. 2008. Investigation of the exploitation of a fast-sampling single gamma densitometer and pattern recognition to resolve the superficial phase velocities and liquid phase water cut of vertically upward multiphase flows. *Flow Measurement and Instrumentation,* 19**,** 57-66.

Bolton, G. T., Korchinsky, W. J. & Waterfall, R. C. 1999. Imaging immiscible liquid-liquid systems by capacitance tomography. *Chemical Engineering Research & Design,* 77**,** 699-708.

Brauner, N. 2000. The onset of drops atomization and the prediction of annular flow boundaries in two-phase pipe flow. *Internal Report-5101, Faculty of Engineering, Tel-Aviv, Israel.*

Brauner, N. 2001. Modelling and Contorl of Two - Phase Phenomena: Liquid - Liquid Two - phase flow systems. *School of Engineering, Tel Aviv University, Israel, Tel Aviv 69978 Israel*.

Brauner, N. & Maron, D. M. 1989. 2 Phase Liquid Liquid Stratified Flow. *Physicochemical Hydrodynamics,* 11**,** 487-506.

Brauner, N., Maron, D. M. & Rovinsky, J. 1998. A two-fluid model for stratified flows with curved interfaces. *International Journal of Multiphase Flow,* 24**,** 975-1004.

Brauner, N. & Moalem Maron, D. 1992. Flow pattern transitions in two-phase liquid-liquid flow in horizontal tubes. *International Journal of Multiphase Flow,* 18**,** 123-140.

Brauner, N. & Ullmann, A. 2002. Modeling of phase inversion phenomenon in two-phase pipe flows. *International Journal of Multiphase Flow,* 28**,** 1177-1204.

Bs En 60825-1 2014. "Safety of Laser products part 1: Equipment classification, requirements and user guide". *British Standard Institution and European Standard Institution.* .

Charles, M. E., Govier, G. W. & Hodgson, G. W. 1961. The Horizontal Pipeline Flow of Equal Density Oil-Water Mixtures, . *The Canadian Journal of Chemical Engineering.*

Chesters, A. K. 1991. The Modeling of Coalescence Processes in Fluid Liquid Dispersions - a Review of Current Understanding. *Chemical Engineering Research & Design,* 69**,** 259-270.

Chisholm, D. & Laird, D. K. 1958. "Two-phase flow in rough tubes", . *Transaction ASME,* , Vol 80**,,** pp. 276-286.

Clark, N. N. & Turton, R. 1988. Chord Length Distributions Related to Bubble-Size Distributions in Multiphase Flows. *International Journal of Multiphase Flow,* 14**,** 413-424.

Clayton, C., Sommerfeld, M. & Tsuji, Y. 1998. Multiphase Flows with Droplets and Particles. pp43-50.

Cohen, R. D. 1991. Shattering of a Liquid-Drop Due to Impact. *Proceedings of the Royal Society of London Series a-Mathematical Physical and Engineering Sciences,* 435**,** 483-503.

Coney, M. W. E. 1973. Theory and Application of Conductance Probes for Measurement of Liquid Film Thickness in 2-Phase Flow. *Journal of Physics E-Scientific Instruments,* 6**,** 903-910.

Coulaloglou, C. A. & Tavlarides, L. L. 1977. Description of Interaction Processes in Agitated Liquid-Liquid Dispersions. *Chemical Engineering Science,* 32**,** 1289-1297.

Da Silva, M. J., Schleicher, E. & Hampel, U. 2007. Capacitance wire-mesh sensor for fast measurement of phase fraction distributions. *Measurement Science & Technology,* 18**,** 2245-2251.

Delhaye, J. M. 1981. Singular pressure drops. In; Two Phase Flow and Heat transfer in the power and process industries. A. E. Bergles (ED), Hemisphere Pub. Corp.

Devia, F. & Fossa, M. 2003. Design and optimisation of impedance probes for void fraction measurements. *Flow Measurement and Instrumentation,* 14**,** 139-149.

Dikken, B. J. 1990. Pressure-Drop in Horizontal Wells and Its Effect on Production Performance. *Journal of Petroleum Technology,* 42**,** 1426-1433.

Dong, F., Liu, X. P., Deng, X., Xu, L. J. & Xu, L. A. 2001. Identification of two-phase flow regimes in horizontal, inclined and vertical pipes. *Measurement Science & Technology,* 12**,** 1069-1075.

Dyakowski, T. 1996. Process tomography applied to multi-phase flow measurement. *Measurement Science & Technology,* 7**,** 343-353.

El-Hamouz, A. M. & Stewart, A. C. 1996. On-line drop size distribution measurement of oil-water dispersion using a Par-Tec M300 laser back-scatter instrument. *SPE International, 36672***,** pp1-14.

El-Hamouz, A. M., Stewart, A. C. & Davies, G. A. 1995. A Study of Kerosene-Water Dispersions in Shear Flow Through Pipes and Fittings, Two-Phase Flow Modelling and Experimentation. pp987-997.

Elseth, G. 2001. An Experimental Study of Oil–Wate rFlow in Horizontal Pipes. *Ph.D. Thesis,The Norwegian University of Science and Technology*

Elseth, G., Kvandal, H. K. & Melaaen, M. C. 2001. Measurement of velocity and phase fraction in stratified oil/water flow. *International Symposium on Multi-Phase Flow and Transport Phenomena***,** 341-348.

Fairuzov, Y. V., Arenas-Medina, P., Verdejo-Fierro, J. & Gonzalez-Islas, R. 2000. Flow pattern transitions in horizontal pipelines carrying oil-water mixtures: Full-scale experiments. *Journal of Energy Resources Technology-Transactions of the Asme,* 122**,** 169-176.

Flores, J. G., Chen, X. T., Sarica, C. & Brill, J. P. 1997. Characteristics of oil-water flow pattern in vertical and deviated wells. *SPE Annual Technical Conference and Exhibition San Antonio Texas***,** 38810.

Fossa, M. 1998. Design and performance of a conductance probe for measuring the liquid fraction in two-phase gas-liquid flows. *Flow Measurement and Instrumentation,* 9**,** 103-109.

Greaves, D., Boxall, J., Mulligan, J., Montesi, A., Creek, J., Dendy Sloan, E. & Koh, C. A. 2008. Measuring the particle size of a known distribution using the focused beam reflectance measurement technique. *Chemical Engineering Science,* 63**,** 5410-5419.

Guet, S., Rodriguez, O. M. H., Oliemans, R. V. A. & Brauner, N. 2006. An inverse dispersed multiphase flow model for liquid production rate determination. *International Journal of Multiphase Flow,* 32**,** 553-567.

Hadziabdic, M. & Oliemans, R. 2007. Parametric study of a model for determining the liquid flow-rates from the pressure drop and water hold-up in oil-water flows. *International Journal of Multiphase Flow,* 33**,** 1365-1394.

Hasan, N. M. 2006. Stratifying liquid-liquid flows. *Ph.D. Thesis, University of Nottingham, United Kingdom.*

Helmholtz - Zentrum & Dresden-Rossndorf. 2012. Wire Mesh Sensors, . *HZDR.*

Hinze, J. O. 1955. Fundamentals of the Hydrodynamic Mechanism of Splitting in Dispersion Processes. *Aiche Journal,* 1**,** 289-295.

Hobbel, E. F., Davies, R., Rennie, F. W., Allen, T., Butler, L. E., Waters, E. R., Smith, J. T. & Sylvester, R. W. 1991. Modern Methods of Online Size Analysis for Particulate Process Streams. *Particle & Particle Systems Characterization,* 8**,** 29-34.

Howarth, W. J. 1964. Coalescence of Drops in a Turbulent Flow Field. *Chemical Engineering Science,* 19**,** 33-38.

Hwang, J., C.-Y. & Pal, R. 1997. Flow of two-phase oil/water mixtures through sudden expansions and contractions. *Chemical Engineering Journal,* l 68 pp157-163.

Jayawardena, S. S., Alkaya, B., Redus, C. L. & Brill, J. P. 2000. A new model for dispersed multi-layer oil-water flow. *2nd North American Conference on Multiphase Technology***,** 77-89.

Jurman, L. A., Bruno, K. & Mccready, M. J. 1989. Periodic and Solitary Waves on Thin, Horizontal, Gas-Sheared Liquid-Films. *International Journal of Multiphase Flow,* 15**,** 371-384.

Kadri, U., Mudde, R. F., Oliemans, R. V. A., Bonizzi, M. & Andreussi, P. 2009. Prediction of the transition from stratified to slug flow or roll-waves in gas-liquid horizontal pipes. *International Journal of Multiphase Flow,* 35**,** 1001-1010.

Karabelas, A. J. 1978. Drople Size Spectra Generated in Turbulent Pipe Flow of Dilute Liquid-Liquid Dispersions. *AICHhE Journal,* 24**,** 170 - 180.

Kolmogoroff, A. N. 1949. The breakup of droplets in a turbulent stream. *Doklady Akad. Nauk SSSR (NS),,* 66, No. 5**,** pp 825 - 828.

Kubie, J., And Gardner, G. C., 1977. Drop Sizes and Drop Dispersion in Straight Horizontal Tubes and Helical Coils. *Chem. Eng. Sci.,,* 32**,** 195 202.

Kumar, S., Ganvir, V., Satyanand, C., Kumar, R. & Gandhi, K. S. 1998. Alternative mechanisms of drop breakup in stirred vessels. *Chemical Engineering Science,* 53**,** 3269-3280.

Kumar, S., Kumar, R. & Gandhi, K. S. 1993. A New Model for Coalescence Efficiency of Drops in Stirred Dispersions. *Chemical Engineering Science,* 48**,** 2025-2038.

Kumara, W. a. S., Halvorsen, B. M. & Melaaen, M. C. 2010. Single-beam gamma densitometry measurements of oil-water flow in horizontal and slightly inclined pipes. *International Journal of Multiphase Flow,* 36**,** 467-480.

Kurban, A. P. A. 1997. Stratfied liquid-liquid flow. *PhD Thesis, Imperial College, University of London, UK.*

Kurban, A. P. A., Angeli, P. A., Mendestatsis, M. A. & Hewitt, G. F. 1995. Stratified and dispersed oil-water flows in horizontal pipes. *Multiphase 95, 7th International Conference***,** 277-291.

Langston, P. A. 2002. Comparison of least-squares method and Bayes' theorem for deconvolution of mixture composition. *Chemical Engineering Science,* 57**,** 2371-2379.

Langston, P. A., Burbidge, A. S., Jones, T. F. & Simmons, M. J. H. 2001. Particle and droplet size analysis from chord measurements using Bayes' theorem. *Powder Technology,* 116**,** 33-42.

Langston, P. A. & Jones, T. F. 2001. Non-spherical 2-dimensional particle size analysis from chord measurements using Bayes' theorem. *Particle & Particle Systems Characterization,* 18**,** 12-21.

Lasentec 2007. Lasentec M-Series hardware manual", Mettler-Toledo, Rev 1.

Levich, V. G. 1962. Physicochemical Hydrodynamics. Enlewood Cliffs, N J: Prentice - Hall. *Book.*

Li, M. & Wilkinson, D. 2005. Determination of non-spherical particle size distribution from chord length measurements. Part 1: Theoretical analysis. *Chemical Engineering Science,* 60**,** 3251-3265.

Liu, S. P. & Li, D. M. 1999. Drop coalescence in turbulent dispersions. *Chemical Engineering Science,* 54**,** 5667-5675.

Liu, W. & Clark, N. N. 1995. Relationships between Distributions of Chord Lengths and Distributions of Bubble Sizes Including Their Statistical Parameters. *International Journal of Multiphase Flow,* 21**,** 1073-1089.

Liu, W. D., Clark, N. N. & Karamavruc, A. I. 1998. Relationship between bubble size distributions and chord-length distribution in heterogeneously bubbling systems. *Chemical Engineering Science,* 53**,** 1267-1276.

Lockhart, R. W. & Martinelli, R. C. 1949. Proposed Correlation of Data for Isothermal 2-Phase, 2-Component Flow in Pipes. *Chemical Engineering Progress,* 45**,** 39-48.

Lovick, J. & Angeli, P. 2004a. Droplet size and velocity profiles in liquid-liquid horizontal flows. *Chemical Engineering Science,* 59**,** 3105-3115.

Lovick, J. & Angeli, P. 2004b. Experimental studies on the dual continuous flow pattern in oil-water flows. *International Journal of Multiphase Flow,* 30**,** 139-157.

Lovick, J., Bristow, R. & Angeli, P. 2001. Pressure drop and hold-up in liquid-liquid flows. *International Symposium on Multi-Phase Flow and Transport Phenomena***,** 548-555.

Lovick, J., Mouza, A. A., Paras, S. V., Lye, G. J. & Angeli, P. 2005. Drop size distribution in highly concentrated liquid-liquid dispersions using a light back scattering method. *Journal of Chemical Technology and Biotechnology,* 80**,** 545-552.

Lum, J. Y., Lovick, J. & Angeli, P. 2004. Low inclination oil-water flows. *Canadian Journal of Chemical Engineering,* 82**,** 303-315.

Lum, J. Y. L., Al-Wahaibi, T. & Angeli, P. 2006. Upward and downward inclination oil-water flows. *International Journal of Multiphase Flow,* 32**,** 413-435.

Maaß, S., Wollny, S., Voigt, A. & Kraume, M. 2011. Experimental comparison of measurement techniques for drop size distributions in liquid/liquid dispersions. *Experiments in Fluids,* 50**,** 259-269.

Morgan, R. G. 2012. Studies of liquid - liquid two phase flows using Laser - Based method. *PhD Thesis*.

Morgan, R. G., Christos N. Markides, Ivan Zadrazil & Hewitt, G. F. 2013. Characteristics of horizontal liquid–liquid flows in a circular pipe using simultaneous high-speed laser-induced fluorescence and particle velocimetry. *International Journal of Multiphase Flow,* 49(2013)**,** 99 - 118.

Nädler, M. & Mewes, D. 1997. Flow induced emulsification in the flow of two immiscible liquids in horizontal pipes. *International Journal of Multiphase Flow,* 23**,** 55-68.

Ng, T. S., Lawrence, C. J. & Hewitt, G. F. 2001. Interface shapes for two-phase laminar stratified flow in a circular pipe. *International Journal of Multiphase Flow,* 27**,** 1301-1311.

Oddie, G., Shi, H., Durlofsky, L. J., Aziz, K., Pfeffer, B. & Holmes, J. A. 2003. Experimental study of two and three phase flows in large diameter inclined pipes. *International Journal of Multiphase Flow,* 29**,** 527-558.

Oglesby, K. D. 1979. An Experimental Study on the Effects of Oil Viscosity Mixture Velocity and Water Fraction on Horizontal Oil-Water Flow, M.Sc Thesis, University of Tulsa.

Pacek, A. W., Moore, I. P. T., Nienow, A. W. & Calabrese, R. V. 1994. Video Technique for Measuring Dynamics of Liquid-Liquid Dispersion during Phase Inversion. *Aiche Journal,* 40**,** 1940-1949.

Pal, R. 1993. Pipeline flow of unstable and surfactant-stabilized emulsions. *AIChE J.* , 39**,** 1754–1764.

Petalas, N. & Aziz, K. 2000. A mechanistic model for multiphase flow in pipe. *J. Can. Pet. Technol,* 39**,** 43–55.

Raj, T. S., Chakrabarti, D. P. & Das, G. 2005. Liquid-liquid stratified flow through horizontal conduits. *Chemical Engineering & Technology,* 28**,** 899-907.

Reinecke, N., Petritsch, G., Boddem, M. & Mewes, D. 1998. Tomographic imaging of the phase distribution in two-phase slug flow. *International Journal of Multiphase Flow,* 24**,** 617-634.

Rodriguez, O. M. H. & Baldani, L. S. 2012. Prediction of pressure gradient and holdup in wavy stratified liquid–liquid inclined pipe flow. *Journal of Petroleum Science and Engineering,* 96–97**,** 140-151.

Rodriguez, O. M. H. & Bannwart, A. C. 2006. Experimental study on interfacial waves in vertical core flow. *Journal of Petroleum Science and Engineering,* 54**,** 140-148.

Rodriguez, O. M. H. & Oliemans, R. V. A. 2006. Experimental study on oil-water flow in horizontal and slightly inclined pipes. *International Journal of Multiphase Flow,* 32**,** 323-343.

Ruf, A., Worlitschek, J. & Mazzotti, M. 2000. Modeling and experimental analysis of PSD measurements through FBRM. *Particle & Particle Systems Characterization,* 17**,** 167-179.

Russell, T. W. F., Hodgson, G. W. & Govier, G. W. 1959. Horizontal Pipeline Flow of Mixtures of Oil and Water,. *The Canadian Journal of Chemical Engineering*.

Scott, G. M. 1985. A study of two-phase Liquid - Liquid flow at variable inclinayions, M. Sc Thesis. University of Texas, U S.

Shi, H., Cai, J. & Jepson, W. P. 2001. Oil-water two-phase flows in large-diameter pipelines. *Journal of Energy Resources Technology-Transactions of the Asme,* 123**,** 270-276.

Shinnar, R. 1961. On the Behaviour of Liquid Dispersions in Mixing Vessels. *Journal of Fluid Mechanics,* 10**,** 259-&.

Simmons, M. J. H. 1998. Liquid - Liquid flows and separation. *Thesis Submitted to the Univesity of Nottingham for PhD*.

Simmons, M. J. H. & Azzopardi, B. J. 2001. Drop size distributions in dispersed liquid-liquid pipe flow. *International Journal of Multiphase Flow,* 27**,** 843-859.

Simmons, M. J. H. & Hanratty, T. J. 2001. Droplet size measurements in horizontal annular gas-liquid flow. *International Journal of Multiphase Flow,* 27**,** 861-883.

Simmons, M. J. H., Langston, P. A. & Burbidge, A. S. 1999. Particle and droplet size analysis from chord distributions. *Powder Technology,* 102**,** 75-83.

Simmons, M. J. H., Zaidi, S. H. & Azzopardi, B. J. 1997. Investigation of liquid/liquid flows using laser based optical systems. *Optical Technology in Fluid, Thermal, and Combustion Flow Iii,* 3172**,** 453-461.

Simmons, M. J. H., Zaidi, S. H. & Azzopardi, B. J. 2000. Comparison of laser-based drop-size measurement techniques and their application to dispersed liquid-liquid pipe flow. *Optical Engineering,* 39**,** 505-509.

Sleicher, C. A. 1962. Maximum Stable Drop Size in Turbulent Flow. *AIChE Journal,* 8**,** 471 - 477.

Soleimani, A., Lawrence, C. J. & Hewitt, G. F. 1997. Effect of Mixers on Flow Pattern and Pressure Drop in Horizontal Oil-Water Pipe Flow. *International Symposium on Liquid-Liquid Two-Phase Flow and Transport Phenomena, ICHMT, Antalya Turkey,*.

Soleimani, A., Lawrence, C. J. & Hewitt, G. F. 2000. Spatial distribution of oil and water in horizontal pipe flow. *Spe Journal,* 5**,** 394-401.

Sprow, F. B. 1967. Drop Size Distributions in Strongly Coalescing Agitated Liquid-Liquid Systems. *Aiche Journal,* 13**,** 995-&.

Taitel, Y. & Dukler, A. E. 1976. Model for Predicting Flow Regime Transitions in Horizontal and near Horizontal Gas-Liquid Flow. *Aiche Journal,* 22**,** 47-55.

Thomas, R. M. 1981. Bubble Coalescence in Turbulent Flows. *Int. J. Multiphase Flow* 7**,** 709 - 717.

Trallero, J. L. 1995. Oil - Water flow patterns in horizontal pipes. *PhD Thesis, The University of Tulsa*.

Trallero, J. L., Sarica, C. & Brill, J. P. 1997. A study of oil/water flow patterns in horizontal pipes. *SPE Production & Facilities,* 12**,** 165-172.

Tsochatzidis, N. A., Karapantsios, T. D., Kostoglou, M. V. & Karabelas, A. J. 1992. A Conductance Probe for Measuring Liquid Fraction in Pipes and Packed-Beds. *International Journal of Multiphase Flow,* 18**,** 653-667.

Tsouris, C. & Tavlarides, L. L. 1994. Breakage and Coalescence Models for Drops in Turbulent Dispersions. *Aiche Journal,* 40**,** 395-406.

Ullmann, A. & Brauner, N. 2006. Closure relations for two-fluid models for two-phase stratified smooth and stratified wavy flows. *International Journal of Multiphase Flow,* 32**,** 82-105.

Valentas, K. J. & Amundson, N. R. 1966. Breakage and Coalescence in Dispersed Phase Systems. *Industrial & Engineering Chemistry Fundamentals,* 5**,** 533-+.

Valle, A. & Utvik, O. H. 1998. Pressure drop, flow pattern and slip for two phase crude oil/water flow: Experiments and model predictions. *International Symposium on Liquid-Liquid Two Phase Flow and Transport Phenomena***,** 63-74.

Van Der Meulen, G. P. 2008. Horizontal two - phase liquid - liquid flow through a sudden contraction. *Masters Degree Thesis (M Sc),* Department of Petroleum and Environmental Process Engineering, School of Chemical and Envoronmental Engineering.

Vedapuri, D., Bessette, D. & Jepson, W. P. 1997. A segregated flow model to predict water layer thickness in oil-water flows in horizontal and slightly inclined pipelines. *8th International Conference on Multiphase '97 - How Deep? How Far? How Soon?***,** 75-105.

Victor, V., Lusheng, Z., Karolina, L. & Panagiota, A. 2016. Evolution of unstable liquid-liquid dispersions in horizontal pipes. *BHR Group, Experts in Fluid Engineering*.

Vigneaux, P., Chenais, P. & Hulin, J. P. 1988. Liquid-Liquid Flows in an Inclined Pipe. *Aiche Journal,* 34**,** 781-789.

Wang, Z. L., Gabriel, K. S. & Manz, D. L. 2004. The influences of wave height on the interfacial friction in annular gas-liquid flow under normal and microgravity conditions. *International Journal of Multiphase Flow,* 30**,** 1193-1211.

Wilkens, R. J. 1997. Prediction of the flow regime transitions in high pressure, large diameter inclined multiphase pipelines. . *Ph.D. Dissertation, Ohio University, OH*.

Worlitschek, J., Hocker, T. & Mazzotti, M. 2005. Restoration of PSD from chord length distribution data using the method of projections onto convex sets. *Particle & Particle Systems Characterization,* 22**,** 81-98.

Wynn, E. J. W. 2003. Relationship between particle-size and chord-length distributions in focused beam reflectance measurement: stability of direct inversion and weighting. *Powder Technology,* 133**,** 125-133.

Xu, W. F., Xu, L. J., Cao, Z., Chen, J. J., Liu, X. B. & Hu, J. H. 2012. Normalized least-square method for water hold-up measurement in stratified oil-water flow. *Flow Measurement and Instrumentation,* 27**,** 71-80.

Yang, L. 2003. Liquid - Liquid two - phase flow at T - Junctions and through Expansions, PhD, Thesis,. The University of Nottingham, UK.

Yang, L., Azzopardi, B. J., Baker, G., Belghazi, A. & Giddings, D. 2003. The approach to stratification of a dispersed Liquid - Liquid flow at a Sudden Expansion, 41st European Two - phase Flow Group Meeting, Tronheim, Norway, 12-13 May.

Yang, L., Azzopardi, B. J. & Belghazi, A. 2001. Application of T - Junctions as a partial separator for Liquid - Liquid flows. *Proceedings 5th Int. Conf. on Experimental Heat Transfer, Fluid Mechanics and Thermodynamics, Thessaloniki*.

Yusoff, N., H. 2012. Stratifying of Liquid - Liquid Two Phase Flows Through Sudden Expansion. *Thesis Submitted to the Univesity of Nottingham, UK for PhD.*

Zhai, L. S., Jin, N. D., Zong, Y. B., Wang, Z. Y. & Gu, M. 2012. The development of a conductance method for measuring liquid holdup in horizontal oil-water two-phase flows. *Measurement Science & Technology,* 23.

Zhou, G. W. & Kresta, S. M. 1998a. Correlation of mean drop size and minimum drop size with the turbulence energy dissipation and the flow in an agitated tank. *Chemical Engineering Science,* 53**,** 2063-2079.

Zhou, G. W. & Kresta, S. M. 1998b. Evolution of drop size distribution in liquid-liquid dispersions for various impellers. *Chemical Engineering Science,* 53**,** 2099-2113.

APPENDIX A

Table 2.1 Summary of Experimental Systems of Liquid – Liquid Horizontal Flow as presented by (Brauner, 2001), with velocity ranges

Author	***D (cm)*** ***Pipe material***	***Velocity range*** U_{ws} U_{os} ***(m/s)***	***Viscosity*** μ_o / μ_w ***(cP)***	***Density*** ρ_o / ρ_w (kg/m^3)	***σ*** ***(dyne/cm)***	***Additional Measurements***	***Observed flow patterns***
(Russell et al., 1959)	2.03 Cellulose Acetate-Butyrate	0.04 - 1.08	20.13	0.840		dP/dl, ε_w	SM, Do/w, Bo
(Charles et al., 1961)	2.64 Cellulose Acetate-Butyrate		6.29 16.8 65	1 1 1	44 45 30	dP/dl, ε_w	Do/w, ANw, SLo, Bo
(Guzhov et al., 1973)	3.94 Steel	Um = 0.20-.1.70	21.8	0.898	44.8	dP/dl	SM, Dw/o, Do/w&w, Dw/o & o/w
(Malinowsky, 1975)	3.84 Steel		3.33	0.850	22.3	dP/dl	SM, Dw/o, Do/w, Dw/o & o/w
(Laflin and Oglesby, 1976)	3.84 Steel	0.17 - 1.16 0.17 - 1.16	4.12	0.830		dP/dl	ST; ST & MI; Do/w&w; o/w; Dw/o & Do/w; w/o
(Oglesby, 1979)	4.10 Steel	0.07 - 2.71 0.03 - 3.19	32 61 167	0.859 0.863 0.870	30.1 29.4 35.4	dP/dl	Do/w, Dw/o Dw/o & o/w

Table 2.1 Continued

(Cox, 1985)	5.08 Acrylic	0.05 - 0.64 0.05 - 0.64	1.54	0.756		ε_w	S, Do/w, Do/w &w
(Scott, 1985)	5.08 Acrylic	0.05 - 0.64 0.05 - 0.64	1.54	0.756		ε_w	S, Do/w, Do/w & w
(Stapelberg and Mewes, 1990)	2.38, 5.90 Acrylic glass	0.06 - 1.20 0.04 - 0.65	30	0.852	50	dP/dl	
(Fujii et al., 1994)	2.5 Acrylic		61.5	0.980	29	dP/dl, ε_w	Bo, Bw, SLo, SLw, ANo
(Valle and Kvandal, 1995)	3.75 Glass	0.20 - 1.20 0.25 - 1.15	2.55	0.79	37.3	dP/dl, ε_w (Conductivity & sampling probes)	S, SM, Do/w&w, Dw/o & o/w
(Trallero, 1995)	5.08 Acrylic	Um = 0.2 - 1.6	29.7	0.852	36	dP/dl, ε_w	S, SM, Do/w & w, Do/w, Dw/o Dw/o & o/w Do/w & w
(Nädler and Mewes, 1997)	5.9 Perspex		18-35	0.848		dP/dl Phase continuity (Conductivity sampling probes	S, SM, Do/w & w, Do/w, Dw/o Dw/o & o/w, Do/w & w Dw/o & w,

Table 7.1 Continued

(Vedapuri et al., 1997)	10.12 Plexi – glass		2			ε_w Isokinekic probe	SM Dw/o & o/w
(Bereta et al., 1997)	0.3 Borosilicate glass		9.9 51.3 71.2	0.87 0.89 0.87	37.4, 36, 31.5	dP/dl	Do/w, SLo, Bo, ANw
(Kurban et al., 1995)	2.43, 2.4, St Steel Acrylic		1.6	0.803	17	dp/dl, ε_w (Conductivity & Impedance probe)	S, SM, Dw/o
(Andreini et al., 1997)	0.3, 0.6 Borosilicate, Glass, Steel, Copper, PVC		562 920 1307	0.886 0.880 0.893		dP/dl	Do/w, SLo, PLo ANw
(Valle and Utvik., 1997)	7.62 Steel		1	0.74 1		dp/dl (Conductivity probes)	S, Do/w, Dw/o
(Hapanowicz et al., 1997)	1.2 1.6 2.2,Glass		40 40	1.2 0.915			S, Do/w, Dw/o, Do/w & w Dw/o & o/w Dw/o & o, DANo, PL, Foam

Table 2.1 Continued

(Angeli and Hewitt, 1998)	2.43, 2.4, Stainless Steel Acrylic		1.6	0.803	17	ε_w, (Conductivity & Impedance probe)	S, Do/w& w, Do/w,Dw/o, Dw/o & o, Dw/o & o/w
(Soleimani et al., 2000)	2.43, 2.4 Stainless Steel		1.6	0.803		dP/dl, Phase distribution High Frequency Impedance probe & Gamma Densiometer	SM, Dw/o & o/w,
(Angeli and Hewitt, 2000)	2.43, 2.4 Stainless Steel Acrylic		1.6	0.803	17	ε_w, (Conductivity & Impedance probe)	S, Do/w&w, Do/w, Dw/o, Dw/o & o, Dw/o & o/w
(Fairuzov et al., 2000)	36.35 Steel		5.07	0.853		Volume fraction (Multi-Point Sampling Probe)	S, Do/w & w
(Lovick et al., 2001)	3.8 Stainless Steel		5.25	0.828	44.7	dP/dl, (Conductivity probe)	S, SM, Do/w & Dw/o
(Simmons and Azzopardi, 2001)	6.3 PVC		1.125	0.684	10	Drop size, Velocity & distribution (PAR Tec 300C, Malvern 2600)	SM, Dw/o & w, Dw/o
(Angeli, 2001)	3.8 Sainless Steel		5.25	0.828	44.7	dP/dl, Phase distribution (Impedance & conductivity probe)	SW, Do/w, Dw/o & o/w, Dw/o

Table 2.2 Summary of some recent experimental work on Liquid – Liquid Horizontal Flow

(Yang, 2003)	9.98 uPVC	Um = 0.2 – 2.0	2.1	0.7976	24	Chord length, phase volume fractions (FBRM M500P), High speed camera	ST, ST & IM, Do/w & w, Do/w, Dw/o,Dw/o & o/w, Do/w & w
(Van der Meulen, 2008)	2.6 uPVC	Um = 0.11 – 2.43	2.1	0.796	24	Chord length, phase volume fractions (Optical probe technique), High speed camera (Kodak EKtaPro EM Motion Analyser.	ST, SW, Do/w & w, Do/w, Dw/o,Dw/o & o/w, Do/w & w
(Yusoff, 2012)	6.8 uPVC	Um = 0.20 – 3.50	5.2	0.903 Silicone oil	44.7	Chord length, phase volume fractions (FBRM M500P), Wire Mesh Sensor (CapWMS)	ST, ST & IM, Do/w & w, Do/w, Dw/o Dw/o & o/w Do/w & w
(Morgan, 2012)	9.98 Stainless steel	Um = 0.07 – 1.46	2.1	Exxsol D80 (0.792 - 0.806), Eosin Y (1.204 – 1.216)	17.30	Drop size, Phase volume fractions, Planar laser induced florescence (PLIF) and Particle induced velocimetry (PIV) ,High speed camera	ST, Mixed flow, Two layer, Dispersed over/under continuous flows
(Barral, 2014)	3.8 Acrylic	Um = 0.50 – 2.50	5.5	Exxsol D140 (0.830)	39.6	Velocity profiles, turbulent properties (PIV Technique), Conductance probe	ST, Dual continuous, Intermidiate flow

APPENDIX B

Table 3.1 Experimental conditions for liquid-liquid flow in stirred baffled vessel

		FBRM Probe test height of stirred tank = 25mm			
	Impeller Speed, N(rpm)	Volume fraction of dispersed phase (Silicone oil) (Dispersed phase holdup) (%)	FBRM Scan Duration (S)	Chord Length (D)	PAM2
RUN 1					
a	800	20%			
b	900	20%			
c	1000	20%			
d	1100	20%			
e	1200	20%			
RUN 2					
a	800	30%			
b	900	30%			
c	1000	30%			
d	1100	30%			
e	1200	30%			
RUN 3					
a	800	40%			
b	900	40%			
c	1000	40%			
d	1100	40%			
e	1200	40%			
RUN 4					
a	800	50%			
b	900	50%			
c	1000	50%			
d	1100	50%			
e	1200	50%			
RUN 5					
a	800	60%			
b	900	60%			
c	1000	60%			
d	1100	60%			
e	1200	60%			
RUN 6					
a	800	70%			
b	900	70%			
c	1000	70%			
d	1100	70%			
e	1200	70%			
RUN 7					
a	800	80%			
b	900	80%			
c	1000	80%			
d	1100	80%			
e	1200	80%			

Table 3.1 Experimental conditions for liquid-liquid flow in stirred baffled (cont'd)

		FBRM Probe test height of stirred tank = 45mm			
	Impeller Speed, N(rpm)	**Volume fraction of dispersed phase (Silicone oil) (Dispersed phase holdup) (%)**	**FBRM Scan Duration (S**	**Chord Length (D)**	**PAM2**
RUN 8					
a	800	20%			
b	900	20%			
c	1000	20%			
d	1100	20%			
e	1200	20%			
RUN 9					
a	800	30%			
b	900	30%			
c	1000	30%			
d	1100	30%			
e	1200	30%			
RUN 10					
a	800	40%			
b	900	40%			
c	1000	40%			
d	1100	40%			
e	1200	40%			
RUN 11					
a	800	50%			
b	900	50%			
c	1000	50%			
d	1100	50%			
e	1200	50%			
RUN 12					
a	800	60%			
b	900	60%			
c	1000	60%			
d	1100	60%			
e	1200	60%			
RUN 13					
a	800	70%			
b	900	70%			
c	1000	70%			
d	1100	70%			
e	1200	70%			
RUN 14					
a	800	80%			
b	900	80%			
c	1000	80%			
d	1100	80%			
e	1200	80%			

Table 3.1 Experimental conditions for liquid-liquid flow in stirred baffled (cont'd)

		FBRM Probe test height of stirred tank = 105mm			
	Impeller Speed, N(rpm)	Volume fraction of dispersed phase (Silicone oil) (Dispersed phase holdup) (%)	FBRM Scan Duration (S)	Chord Length (D)	PAM2
RUN 15					
a	800	20%			
b	900	20%			
c	1000	20%			
d	1100	20%			
e	1200	20%			
RUN 16					
a	800	30%			
b	900	30%			
c	1000	30%			
d	1100	30%			
e	1200	30%			
RUN 17					
a	800	40%			
b	900	40%			
c	1000	40%			
d	1100	40%			
e	1200	40%			
RUN 18					
a	800	50%			
b	900	50%			
c	1000	50%			
d	1100	50%			
e	1200	50%			
RUN 19					
a	800	60%			
b	900	60%			
c	1000	60%			
d	1100	60%			
e	1200	60%			
RUN 20					
a	800	70%			
b	900	70%			
c	1000	70%			
d	1100	70%			
e	1200	70%			
RUN 21					
a	800	80%			
b	900	80%			
c	1000	80%			
d	1100	80%			
e	1200	80%			

APPENDIX C

MATLAB Code: Modified (Probability Apportioning Method (PAM)

```
% particle diameter bins, length units as per user
dl = 0;
dh = 272; %50; largest diameter
nd = 100; % no. dia bins
ndw= 10000; % no. chord bins for analysis
p = zeros(1,nd);
pn = zeros(1,nd);
diam = zeros(1,nd);
ph = zeros(ndw,nd);
dw = zeros(1,ndw);
pht = zeros(1,nd);
prhit= zeros(1,nd);
fq = zeros(1,nd);
data = xlsread('Run1.xlsx'); % read excel file
[m,ncut] = size(data); % ncut = number of chord bins measured
chordl = data(1,:); % chord sizes measured
pchordl = data(3,:); % probabilities
pchordt = sum(pchordl);
disp(pchordt) % check equal unity
dband = (dh-dl)/nd;
for i = 1:nd
   diam(i) = (i-0.5)*dband; %  changed 2014-01-28
   pn(i) = 0;
   fq(i) = 1/nd; % initialise frequency
end


dwidth=dh/ndw; % width of analysis chord bins
```

```
for j = 1:ndw
   dw(j) = (j-0.5)*dwidth; % analysis chord bin sizes
end
for i = 1:nd
   d = diam(i);
   pht(i) = 0;
for j = 1:ndw
   d1 = dw(j) - 0.5*dwidth;
   d2 = d1 + dwidth;
   if (d2 <= d)
      ph(j,i) = (sqrt(d*d - d1*d1) - sqrt(d*d - d2*d2))/d;
   else
      ph(j,i) = 0; % probability hit chord j given particle i
   end
      pht(i) = pht(i) + ph(j,i); % check should sum to unity
 end
end
disp(pht) % check output
disp(diam)
iter = 0;
n_iter=10; % no. iterations between output
igo = input('Start iteration type 1: ');
while (igo == 1) % could use a for loop if many iterations required
for iter=1:n_iter
   prhitt = 0;                              % step 2
for i = 1:nd
prhit(i) = fq(i)*diam(i);
prhitt = prhitt + prhit(i);
end
for i = 1:nd
   prhit(i) = prhit (i)/prhitt;
```

```
    pn(i) = 0;
end
                                        % step 3
for k = 1:ncut
    cl = chordl(k);
    j = round(cl/dwidth + 0.5); % identify analysis chord bin
    pt = 0;
    for i = 1:nd
        p(i) = ph(j,i)*prhit(i);
        pt = pt + p(i);
    end
                                        % step 4
    if (pt ~= 0)
        for i = 1:nd
            p(i) = p (i)/pt;
            pn(i) = pn(i) + p(i)*pchordl(k);
        end
    end
end
                                        % step 5
fqtot = 0;
for i = 1:nd
    prhit(i) = pn(i);
    fq(i) = prhit (i)/diam(i);
    fqtot = fqtot + fq(i);
end
for i = 1:nd
    fq(i) = fq (i)/fqtot;
end
end
                                        % step 6
```

```
   disp(fq)
% hold on
% plot (diam,fq,'b')
% xlabel ('Diameter')
% ylabel ('Fq')
% plot (diam,pht,'r')
% xlabel ('Diameter')
% ylabel ('pht')
% hold off
igo = input('Continue?: ');
end
disp (diam')
disp (fq')
disp (pht')
Adiam=diam';
Afq=fq';
Apht=pht';
xlswrite('filename1.xlsx',Adiam,'A1:A90'); % why only 90?
xlswrite('filename1.xlsx',Afq,'B1:B90');
xlswrite('filename1.xlsx',Apht,'C1:C90');
```

APPENDIX D

Theory of Lasentec FBRM M500P

The Lasentec Focused Beam Reflectance Measurement (FBRM M500P) instrument is categorized as a class 1 laser, which makes it quite safe to use. The probe is made of stainless steel casing of dimensions 24.8 mm diameter and 318mm length. There is an optical fibre system arrangement inside the probe casing that receives laser beams generated form the Electronic Field Unit (EFU). It operates by scanning a high-intensity laser beam over the droplets and measuring the time duration backscattered pulse of light. The laser beam emitted from the solid state diode has a maximum power of 0.6 mW and 708 nm wavelength. With the optical fibre system arrangement, the light intensity is focused on a small beam spot, 2 x 0.8 μm at the sapphire window and focal point exceeding 2 x 10^{10} Wm^{-2}. The edge of droplets flowing past the focal point normally at minimum speed of 2m/s is intersected as the beam scans across the sapphire window. Once this happens, backscattering of the light occurs, which continues until it gets to the opposite edge of the droplets/particles. This light energy is then collected and transmitted back through the probe to the Electric Field Unit (EFU) as a laser source separated by a splitter and converted into electrical signal by a photodetector.

The resultant scan duration and frequency of signals are indications of particle chord length and counts respectively. Therefore, the measured chord length is defined as a straight line between the two edges or points of a particle as stated in the operational manual (Lasentec, 2007).

The output signal from the EFU is isolated by a unique circuit discrimination arrangement and fed into a dedicated computer for data processing and analysis. The FBRM Control Interface (CI) software version 6.7.0 enables the acquired chord length data to be discretized into series of user-defined intervals or channels. The CI is composed of three modules namely: Data Acquisition Control Interface (Acquisition module), Data Review Module and Trend Compare Module. The Acquisition module performs the functions of measurement configuration setup, displays chord length distributions and statistic trends in real time and saves un-processed chord length data for later review.

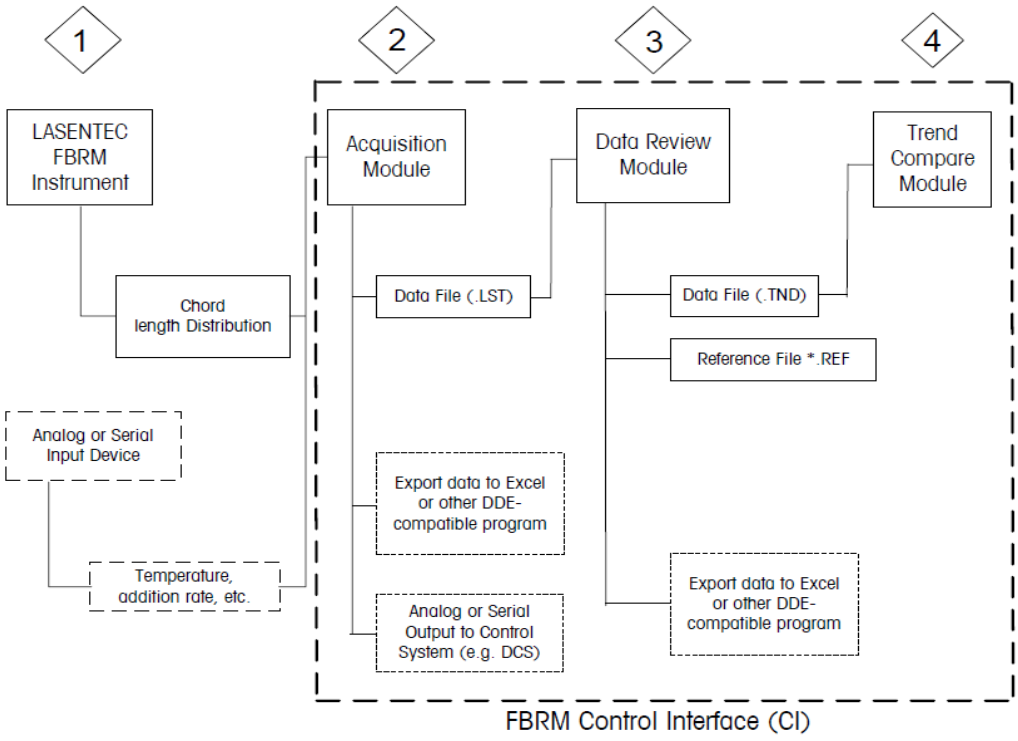

Figure 3.9 How information is transferred between modules Lasentec 2007

The resultant scan duration and frequency of signals are indications of particle chord length and counts respectively. Therefore, the measured chord length is defined as a straight line between the two edges or points of a particle as stated in the operational manual (Lasentec, 2007).

The output signal from the EFU is isolated by a unique circuit discrimination arrangement and fed into a dedicated computer for data processing and analysis. The FBRM Control Interface (CI) software version 6.7.0 enables the acquired chord length data to be discretized into series of user-defined intervals or channels. The CI is composed of three modules namely: Data Acquisition Control Interface (Acquisition module), Data Review Module and Trend Compare Module. The Acquisition module performs the functions of measurement configuration setup, displays chord length distributions and statistic trends in real time and saves un-processed chord length data for later review.

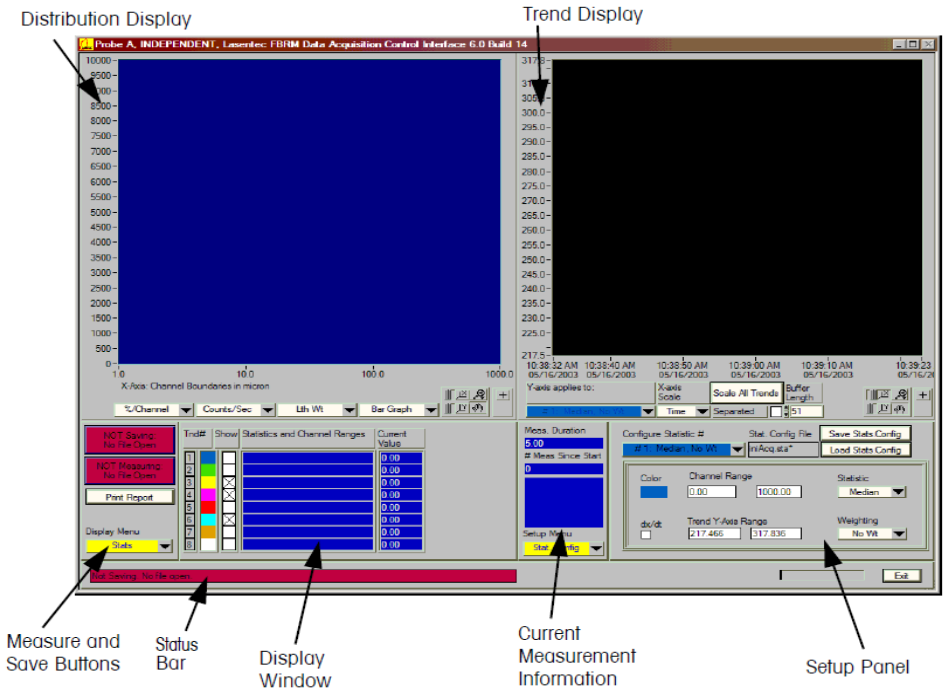

Figure 3.9 Acquisition module main display interface

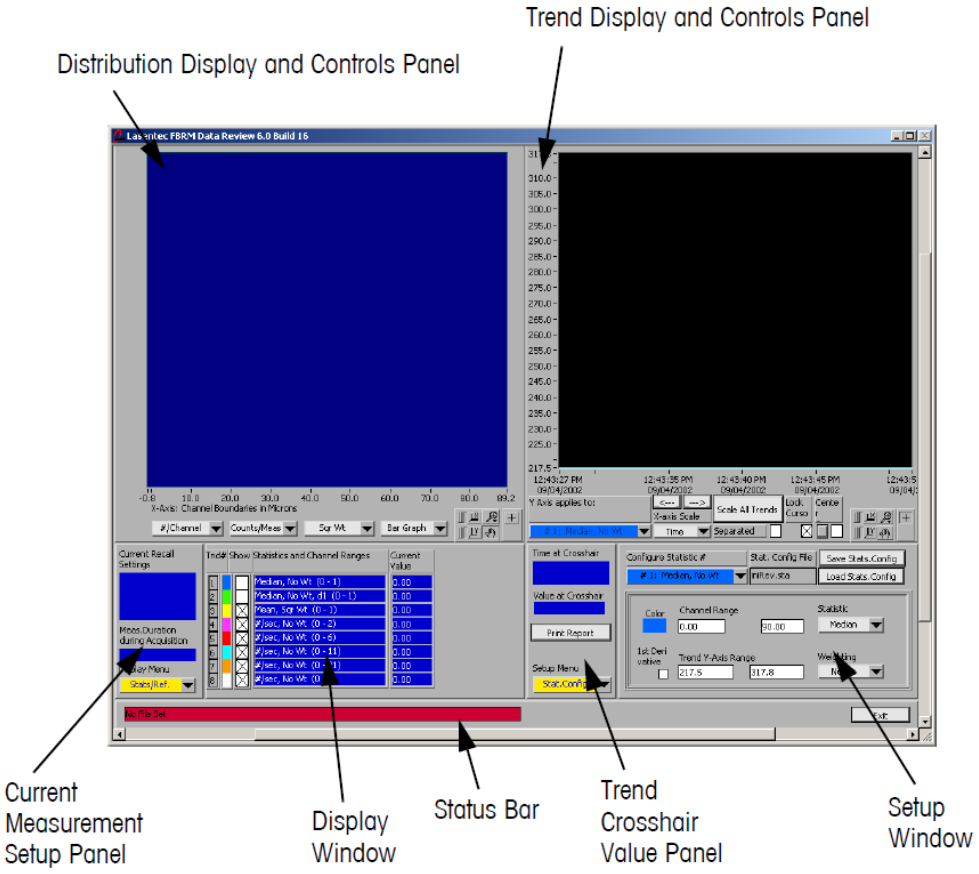

Figure 3.10 Data review module main display

Chord length data were collected using 100 linear-channels over the range of 1 to 1,000 microns. Measurement duration of 10s was used, with an average of 10 consecutive

measurements for each distribution made. This setting was robust enough to ensure sufficient sample numbers for all experimental conditions under investigation. The counts axis, which is the y-axis, represents the number of counts per second. Therefore, typically up to 1,000 microns chord lengths are measured per second, which results in a chord length distribution. Data can then be exported from the FBRM viewer interface as excel file in form of number counts, percentage counts, cumulative counts or cumulative percentage counts, preferable by user. Safety regulations and standard guidelines for the use of laser equipment as recommended by (BS EN 60825-1, 2014), were strictly adhered to at all times throughout the period of experimental work.

APPENDIX E

ESTIMATION OF FLUID FLOW PARAMETERS AND PRESSURE DROP CALCULATIONS

PRESSURE DROP CALCULATIONS

For safety reasons in order to avoid the risk of environmental pollution, flammability, etc and to minimise cost, and considering the flow pattern information that could be obtained, the test fluids, Silicone oil and Water were chosen for the present experimental work. Table 3.1., bellow presents a summary of the physical properties of the two fluids used.

	Tap Water	***Silicone oil, 5cSt***
Density ρ	ρ_w = 998	ρ_o = 916
Viscosity μ (kg/m.s or Pa	μ_w = 0.0010	μ_o = 0.0052
Refractive index	-	1.52045
Permittivity (α)	710 x 10^{-12}	23 x 10^{-12}
Relative permittivity	79	2.7

Table 3.1 Physical properties of fluids (Silicone oil and Water) @ 25°C

Other parameters: Superficial oil velocity, U_{os},= 0.62m/s, Superficial water velocity, U_{ws},= 0.62m/s,

Pipes Area: 5'' inches (ϕ0.127m) – diameter, $A_4 = \frac{\pi D^2}{4} = \frac{\pi 0.127^2}{4} = 12.7x10^{-3} m^2$

2'' inches (ϕ0.0508m) – diameter, $A_2 = \frac{\pi D^2}{4} = \frac{\pi 0.0508^2}{4} = 2.03x10^{-3} m^2$

Total pressure drop (ΔP_T) is as follows:

$$\Delta P_T = \rho_w g H_{upward} + \frac{1}{2}\rho_w U_{ws}^{\ 2}\left\{ f\frac{L}{D} + K_n \right\}$$
$$+\frac{1}{2}\rho_m J_m^{\ 2}\left\{ K_{mixer} + f\frac{L_{5m}}{D} + f\frac{L_{6m}}{D} + K_{n2ph} + f\frac{L_{down}}{D} \right\} \quad \text{..... (3.1)}$$

$$\Delta P_T = \Delta P_i + \Delta P_{ii} + \Delta P_{iii} \quad \text{..... (3.2)}$$

A. For ΔP_i

$$\Delta P_i = 998x9.8x3.43 = 33546.77 N/m^2$$

B. For ΔP_{ii}

Flow rates through 2'' inches pipe and total length of pip, L = 22.79m

$$Q_o = U_{os} A_2 = 16.44x2.03x10^{-3} = 33.36x10^{-3} m^3/s$$

$$Q_w = U_{ws} A_2 = 4.92x2.03x10^{-3} = 10x10^{-3} m^3/s$$

U_{os} = 16.44m/s (Silicone oil pump) and U_{ws} = 4.92m/s (Water pump)

$$8\varphi = f = 0..3164\,\mathrm{Re}^{-0.25}$$ for $\mathrm{Re} < 10^5$ (Blasius correlation)

N/B: The friction factor can also be found from the Moody chart. Chemical Engineers Hand book.

$$\mathrm{Re}_w = \frac{\rho_w D_2 U_{ws}}{\mu_o} = \frac{998x0.0508x4.92}{0.001} = 249436.13$$

$$\mathrm{Re}_o = \frac{\rho_o D_2 U_{ws}}{\mu_o} = \frac{916x0.0508x16.5}{0.0052} = 147652.16$$

$\varphi = f = 0..3164(249436.13)^{-0.25} = 0.014$; K_n --- 5 (90^0 elbows) = 0.6 x 5 = 3 (from table)

$\varphi = f = 0.3164(147652.16)^{-0.25} = 0.016$; K_n --- 5 (90^0 elbows) = 0.6 x 5 = 3 (from table)

$$\Delta P_{iiw} = \frac{1}{2} x998x4.92^2 \left\{ \frac{0.014x22.79}{0.0508} + 3 \right\} = 112101.62 N/m^2$$

$$\Delta P_{iio} = \frac{1}{2} x916x16.5^2 \left\{ \frac{0.016x22.79}{0.0508} + 3 \right\} = 1276973.27 N/m^2$$

C. For ΔP_{iii}

$$J_m = \frac{Q_o + Q_w}{A_2} = \frac{33.36x10^{-3} + 10x10^{-3}}{2.03x10^{-3}} = 21.36 m/s$$

$$\rho_m = \rho_o \frac{U_{os}}{J_m} + \rho_w \frac{U_{ws}}{J_m} = \frac{916x16.5}{21.36} + \frac{998x4.92}{21.36} = 937.5Kg/m^3$$

$$\mu_m = \mu_o \frac{U_{os}}{J_m} + \mu_w \frac{U_{ws}}{J_m} = \frac{0.0052x16.5}{21.36} + \frac{0.001x4.92}{21.36} = 4.25x10^{-3}\,Pa.s$$

$$Q_m = Q_o + Q_w = 43.36x10^{-3} m^3/s$$

$K_n \approx 20$ for Static mixer & Multi-holes orifice plate

$$\mathrm{Re}_m = \frac{\rho_m D_2 J_m}{\mu_m} = \frac{937.5x0.0508x21.36}{4.25x10^{-3}} = 23935.76 = 23936$$

$$f = 0..3164(23936)^{-0.25} = 0.03 \qquad \text{for Re} < 10^5$$

Length L = 0.5m,

$$f_{m5}\frac{L}{D} = 0.03\frac{0.5}{0.0508} = 0.29$$

Length L = 6m,

$$Q_o = U_{os}A_4 = 16.5x12.7x10^{-3} = 0.21m^3/s$$

$$Q_w = U_{ws}A_4 = 4.92x12.7x10^{-3} = 0.06m^3/s$$

$$Q_m = 0.27m^3/s$$

$$J_m = \frac{Q_o + Q_w}{A_4} = \frac{0.27}{12.7x10^{-3}} = 21.3m/s$$

$$\mathrm{Re}_m = \frac{\rho_m D_4 J_m}{\mu_m} = \frac{937.5x12.7x10^{-3}x21.3}{4.26x10^{-3}} = 59531.25$$

$$f = 0..3164(59531.25)^{-0.25} = 0.02$$

$$f_{m6}\frac{L}{D} = 0.02\frac{6}{0.127} = 0.96$$

K_{n2ph} --- 5 (90^0 elbows) = 0.6 x 5 = 3 (from table)

Total pipe length downstream (2 phase), L = 37.79m,

$$f_m \frac{L}{D} = 0.02\frac{37.79}{0.127} = 5.95$$

$$\Delta P_{iii} = \frac{1}{2}\rho_m J_m{}^2 \left\{ K_{mixer} + f\frac{L_{5m}}{D} + f\frac{L_{6m}}{D} + K_{n2ph} + f_m\frac{L_{down}}{D} \right\}$$

$$\Delta P_{iii} = \frac{1}{2} 937.5x21.3^2 \{20 + 0.29 + 0.96 + 3 + 5.95\} == 6422800.244 N/m^2$$

$$\Delta P_T = \Delta P_i + \Delta P_{ii} + \Delta P_{iii}$$

$$\Delta P_{Twater} = 33546.77 + 112101.62 + 6422800.244 = 6568448.634 N/m^2 = 66 bar$$

$$\Delta P_{Tsiliconeoil} = 33546.77 + 1276973.27 + 6422800.244 = 7733320.284 N/m^2 = 77 bar$$

(100,000N/m^2 = 1bar)

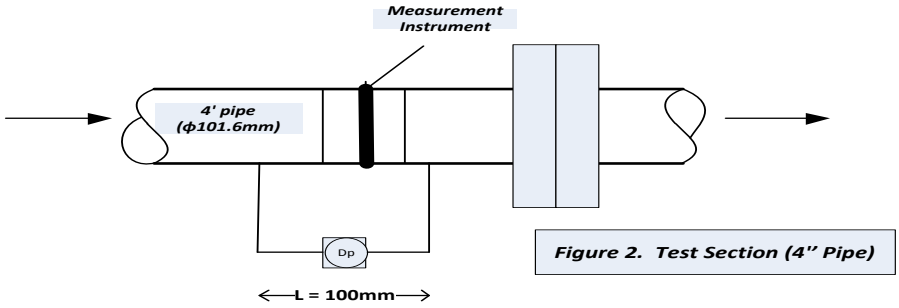

Figure 2. Test Section (4" Pipe)

Pressure drop along 5'' pipe Test Section (Transducers measurements):

$$\Delta P_{TestSection} = \frac{1}{2} \rho_m J_m^{\ 2} \left\{ f \frac{L_{6m}}{D} \right\}$$

$$\Delta P_{TestSection} = \frac{1}{2} 937.5x21.3^2 \{0.96\} == N/m^2 = 204160.5 N/m^2 = 2 bar$$

$$\Delta P_{MeasurementSection} = \left(\frac{\Delta P_{TestSection}}{L_{6m}} \right).l = \left(\frac{204160.5}{6} \right) x0.1 = 3402.68 N/m^2 = 0.034 bar$$

Total Head loss (H_p):

$$H_{p\,oil} = \frac{\Delta P_T}{\rho_m g} = \frac{7733320.284}{937.5x9.8} = 842 m$$

$$H_{p\,water} = \frac{\Delta P_T}{\rho_m g} = \frac{6568448.234}{937.5x9.8} = 715 m$$

Actual Power input:

$$P_{Oil} = \frac{Q_w \rho g H_p}{\eta} = \frac{Q_w \Delta P}{\eta} = \frac{10x10^{-3} x7733320.284}{0.8} = 96667 W \approx 97 KW$$

$$P_{water} = \frac{Q_o \rho g H_p}{\eta} = \frac{Q_o \Delta P}{\eta} = \frac{33.34x10^{-3} x6568448.234}{0.8} = 273740.08 W \approx 273 KW$$

Flow rate measurement R_Q

$$R_Q = 0.27x10^3 x60 = 16200 litres/\min$$

VOLUME OF FLUIDS CALCULATIONS IN STORAGE TANKS

a. Volume of Silicone Oil in tank about (1m)

Diameter of Separator**, ϕ = 1.83m, Length L = 1.854m**

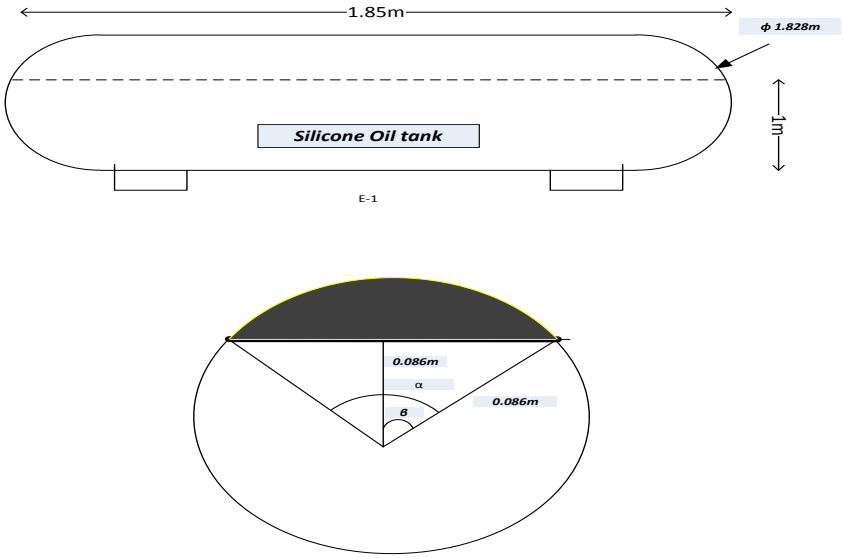

Figure 3. Calculation of silicone oil volume in tank

Volume of oil = Overall volume – Volume of segment.

$$Cos\beta = \frac{0.086}{0.914} = 0.094 \quad : \beta = 84^0 : \alpha = 2\beta = 169^0$$

$$Segment = \frac{r^2}{2}\left\{\frac{\pi 169}{180} - Sin169\right\} \quad \text{or} \quad Segment = \frac{0.914^2}{2}\left\{\frac{\pi 169}{180} - Sin169\right\}$$

$= 1.16m^2$

Area of tank, $A_T = \pi r^2 = \pi x 0.914^2 = 2.62m^2$

Area occupied by oil = 2.62 – 1.16 = $1.46m^2$

Volume occupied by oil in tank = $1.46m^2$ x 1.854m = $2.71m^3$ = **2,710litres**

N/B: This volume is for each silicone storage tanks.

Total Capacity of Silicone oil tank

$$C_{oil} = \pi r^2 L = \pi x 0.914^2 x 1.854 = 4.87m^3 = 4{,}870litres$$

Capacity of Water tank

Diameter of Water tank**, ϕ = 1.83m, Length L =1.854m**

$$C_{water} = \pi r^2 L = \pi x 0.914^2 x 1.854 = 4.87m^3 = 4{,}870litres$$

b. Total volume of Silicone oil in Separator Vessel of about (0.5m)

Diameter of Separator**, ϕ = 2.438m, Length L = 2.438m**

$$V_o = \pi r^2 L = \pi x 1.219^2 x 0.5 = 2.33414 m^3 = 2.334 litres$$

c. Total volume of Water in Separator Vessel of about (1.46m)

$$V_w = \pi r^2 (L-1) = \pi x 1.219^2 x 1.46 = 6.816 m^3 = 6{,}816 litres$$

Total volume of Liquids in separator vessel

$$C_s = \pi r^2 L = \pi x 1.219^2 x 1.96 = 9.15 m^3 = 9{,}15 litres$$

d. Total volume of liquid in pipeline, including test section (4'' pipe & 2'' pipe)

Lengths: L_2 =57.98, L_5 = 626.19m

$$V_T = A_2 L_2 + A_5 L_5$$

$$V_T = 2.03x10^{-3} x57.98 + 12.7x10^{-3} x26.19 = 0.450 m^3 = 450 litres$$

$$V_T = 0.450 m^3 = 450 litres$$

N/B: The total volume of oil required for the experiment is a combination of all the cumulative oil volumes in the pipeline section, separator vessel, storage tank and allowance for exigencies, which is approximately, 5,000litres.

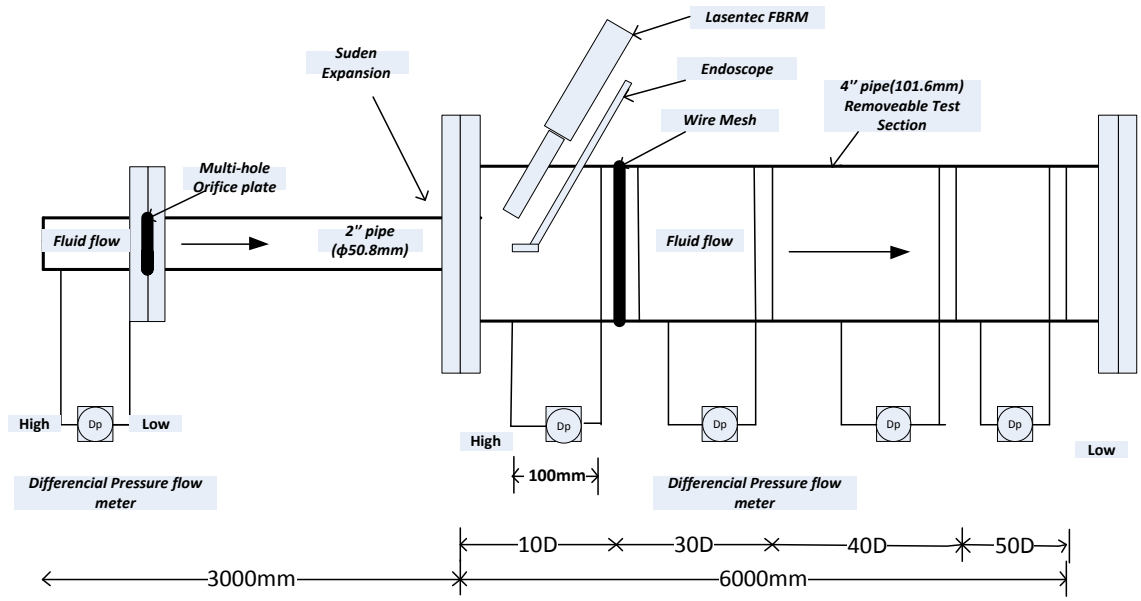

Figure 4. Schematic diagram of the Removeable Test Section

APPENDIX F

CALIBRTION PROCEDURE OF CONDUCTANCE PROBE

The aim of the calibration is to determine a mathematical relationship between accurately known phase fractions (liquid-liquid holdup) and dimensionless conductance to be inputted in the LabVIEW program for data acquisition.

Offline calibration of conductance ring probe

Before running the experiments a calibration of the phase fractions against liquid conductance was necessary. In order to be accurate in the estimation of liquid hold up (oil volume fraction), an offline calibration of the conductance probes was carried out. The probe assembly has a total volume of 1160litres. 100% water was introduced initially into this volume and the corresponding voltage acquired with sampling frequencies noted. The water was then reduced to 90% and mixed with 10% oil and voltage measurements were recorded afterwards. This process was done continuously until the calibration section was filled with 100% oil and no water. A detailed step by step experimental procedure is highlighted in the section that follows. The calibration set up is as shown in the photograph bellow.

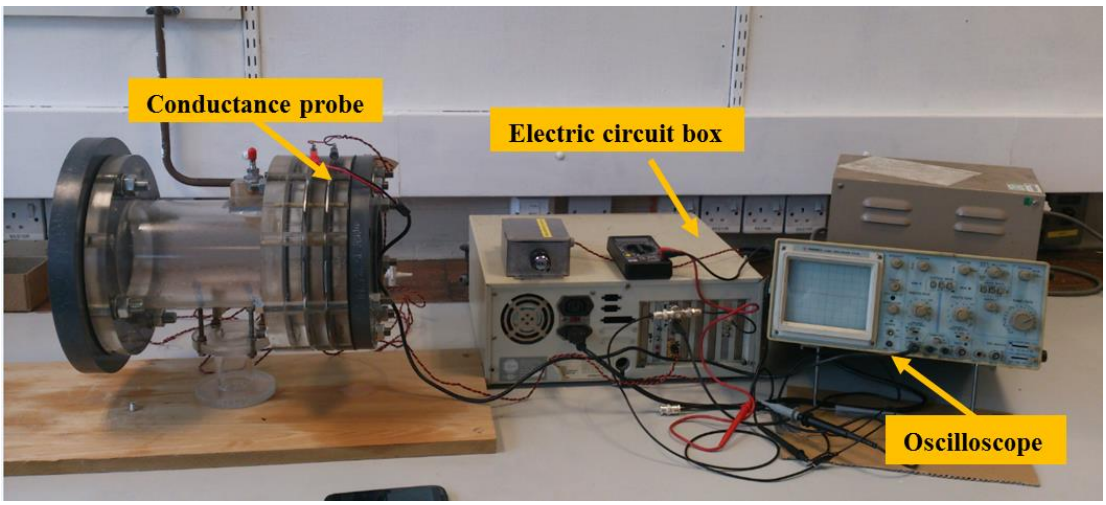

Figure 1. Offline conductance ring probe calibration set up.

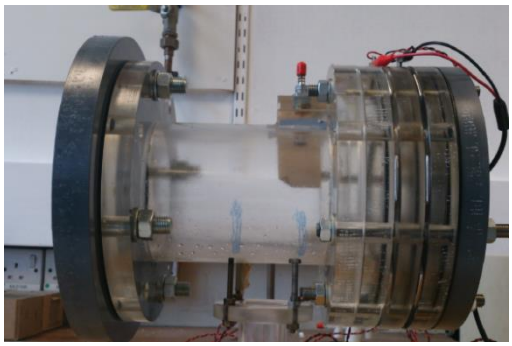


Figure 2 Conductance ring probe assembly, Variable resistance box and voltmeter

Step 1

The reference resistance (R_{ref}) as shown in Figure 5, was determined depending on the impedance from the variable resistor probe, R_X. The probe response depends on

- Cross-sectional phase distribution and fraction of liquid.
- Liquids conductivity Fossa (1998).
- Physical properties and condition of the liquids.

A precision variable resistor, R_x ranging from 1KHz to 5KHz was employed between the probe electrodes.

The first set of experiment is to choose a reference resistance, R_{ref} in the Wheatstone bridge to increase the precision of the liquid holdup fraction measurements by expanding the range of the voltage output, V_{out}. In other to achieve this, a variable known resistance, Rx is put in place of the two-phase flow mixture and a relationship between the voltage constant, E and probe resistance, Rx for various reference resistance, R_{ref} is established. The values of Rx are found to be higher than R_{ref}.

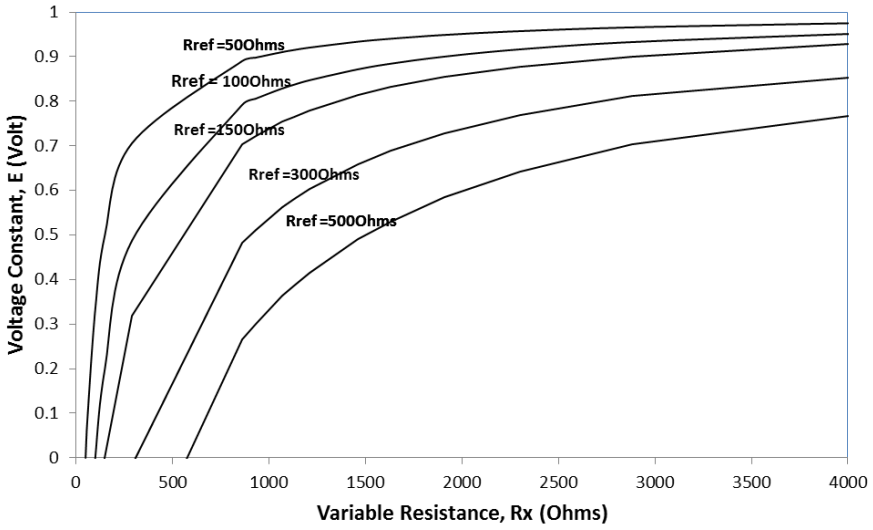

Figure 4. Relationship between Voltage constant E, Variable resistance R_x and Reference resistance R_{ref}

From the graph in Figure 4, it shows that for typical responses for liquid-liquid, silicone – oil/water mixture in a 127mm diameter tube, an R_{ref} of 50 Ohms and Rx above 100 Ohms gives good precision and a wide range of values of the output Voltages. R_{ref} needs to be set higher in smaller diameter pipes since the impedance becomes higher when full of water.

Step 2

The second set of experiment is to measure the output voltage V_{out} of the variable resistance, R_x and establish a linear relationship between E and V_{out}. By applying Ohms law to the Whetstone Bridge circuit arrangement in Figure 5, the output voltage, V_{out} can be deduced as follows:

$$V = IxR \tag{1}$$

Where V is voltage, I is current and R is total resistance. It therefore follows that,

$$V_{out} = V_{24} = V_{12} - V_{14} = \frac{V_{in}}{R_{ef} + R_x} R_x - \frac{V_{in}}{R_a + R_a} R_a \tag{2}$$

$$V_{out} = \frac{V_x}{2}\left(\frac{Rx/R_{ref} - 1}{Rx/R_{ref} + 1}\right) \tag{3}$$

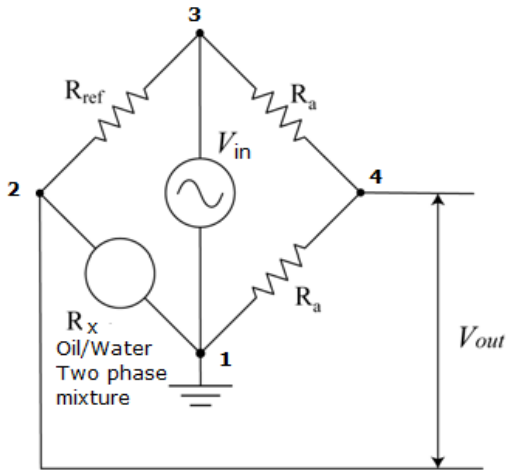

Figure 5. Schematic diagram of Whetstone Bridge in electronic box

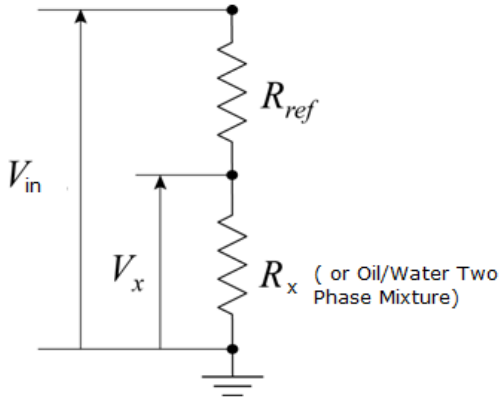

Figure 6 Schematic diagram of the left half of the Whetstone Bridge circuit in electronic box.

The term in the bracket represents potential impedance, E. The actual voltage signal does not fit this equation (3) due to this potential impedance within the electrical circuit.Therefore, the calibration of the output voltage with known impedance was necessary and carried out to correct this anomaly. A graphical plot of this relationship gives a straight line graph and the values of the constants a_1 and a_2 are determined from equation 4.

$$E = a_1 V_{out} + a_2 \qquad (4)$$

In order to estimate a_1 and a_2, a range of values of V_{out} and E were determined using a variable resistor R_x in place of the two-phase liquid – liquid oil/water mixture in the Wheatstone bridge circuit. V_{out} and V_x are measured directly on application of alternating current to the system and the magnitude of R_x, which is used to calculate the impedance, E (from equation 3) is found directly.

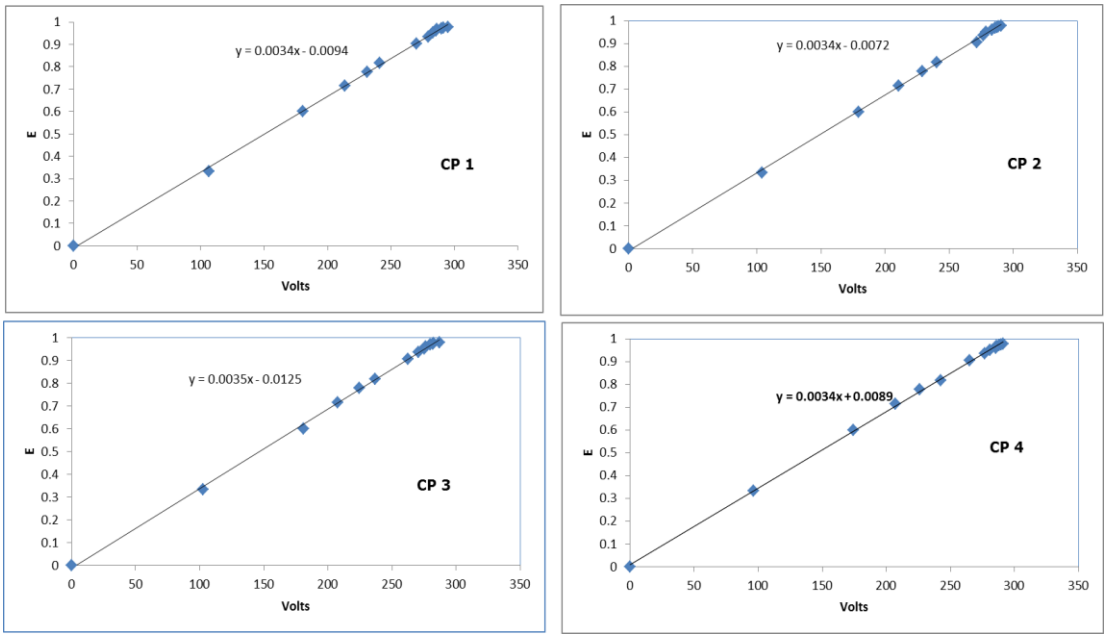

Figure 7. Graph of E vs V_{out} to determine constants a_1 and a_2.

Step 3

The variable known resistance is replaced by a range of various liquid fractions of silicone oil/water in the calibration test section and the voltage output, V_{outE}, is measured. Since E is a ratio of the resistances in the Wheatstone bridge and with the constants a_1 and a_2 known, then the real values of R_{x2} from the two phase mixtures are determined from equation 5.

$$R_{x2} = R_{ref}\left[\frac{(E+1)}{(1-E)}\right] \qquad (5$$

A dimensionless conductance, Ge*, is defined as

$$Ge^* = \frac{R_{waterfull}}{R_{x2}} = \frac{R_{ref}\left[\frac{1+E_{full}}{1-E_{full}}\right]}{R_{ref}\left[\frac{1+E_{probe}}{1-E_{probe}}\right]} \qquad (6)$$

where $R_{waterfull}$ is the impedance when the whole cross-sectional area is filled with water and R_{x2} is the liquid volume fractions. Ge* versus liquid holdup or oil volume fraction

(OVF), is plotted and a 3rd order polynomial fit is applied to the data to obtain the constants a, b, c, d.

$$OVF = a(Ge^*)^3 + b(Ge^*)^2 + c(Ge^*) + d \quad (7)$$

Table 1 Offline calibration results of Conductance Probe (CP 1), with silicone oil and water

Volume oil	Volume water	Water fraction	oil volume fraction	dc Volt	Ge*
0	1160	1	0	124.36	1
116	1044	0.9	0.1	147.16	0.822721
232	928	0.8	0.2	160.05	0.73042
348	812	0.7	0.3	167.36	0.680381
464	696	0.6	0.4	181.34	0.588993
580	580	0.5	0.5	189.43	0.538536
696	464	0.4	0.6	205.26	0.444561
812	348	0.3	0.7	215.35	0.387726
928	232	0.2	0.8	237.25	0.271832
1044	116	0.1	0.9	255.46	0.182534
1160	0	0	1	296.67	0.00087

Online calibration of conductance ring probe

Each of the conductance ring probes mounted on the 6m long test section of the rig is individually calibrated. With all the four (4) probes connected to the electronic circuit box, step 3 was carried out to obtain a 3rd order polynomial for the respective probe positions. Table 2 summaries the calibration results of all the parameters in equation (4) and (7). The resultant 3rd order polynomial equations are then inputted into the Main LabVIEW programme for data question.

Table 2 Calibration results of all Conductance Probes on the 127mm pipe and 6m long test section (CP *x*: Probe numbers correspond to each locations from upstream to downstream)

S/N	CP 1	CP 2	CP 3	CP 4
a_1	0.0034	0.0034	0.0035	0.0034
a_2	-0.0094	-0.0072	-0.025	0.0089
a	1.5665	1.5928	2.8093	1.8282
b	-2.4975	-2.5475	-4.2398	-2.7681
c	-0.071	-0.0503	0.4373	-0.0622
d	0.9935	0.9968	0.99	0.9981

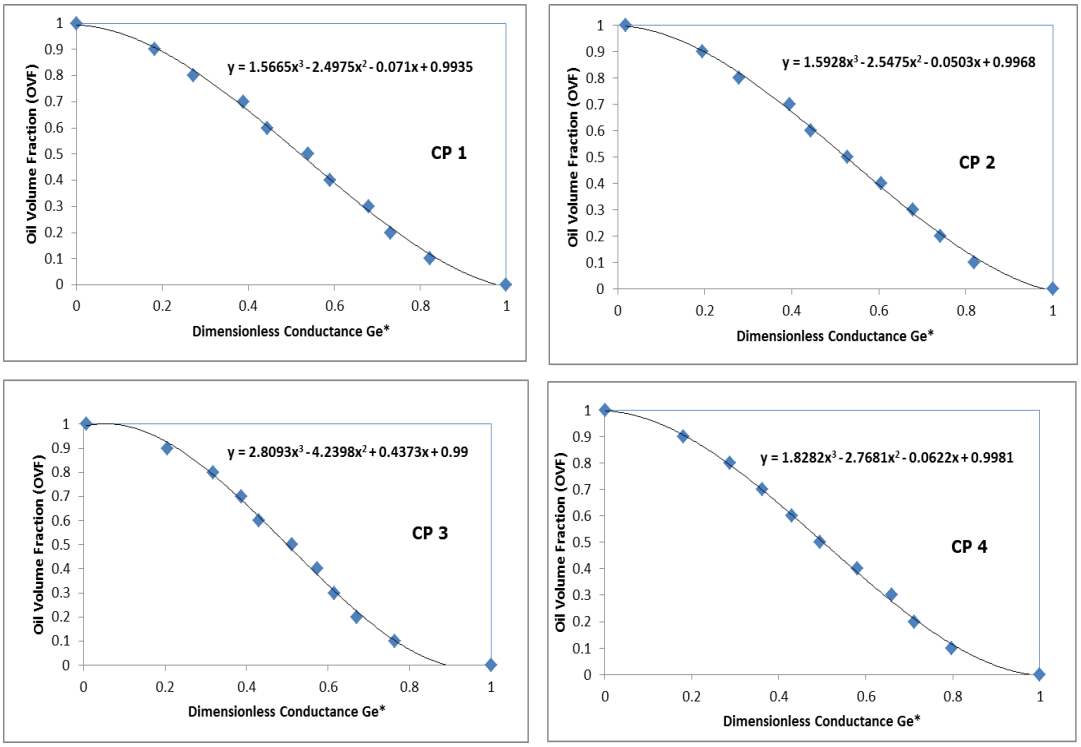

Figure 8. Calibration curve of oil volume fraction (OVF), liquid hold up VS dimensionless conductance Ge* for individual probes

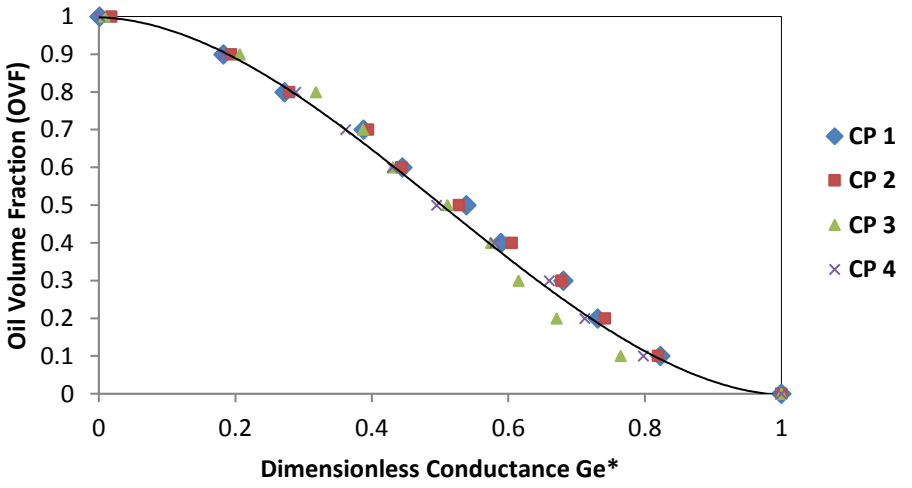

Figure 9. Repeated Calibration experimental curves of oil volume fraction (OVF), liquid hold up VS dimensionless conductance Ge*

Main Program PhD liquid liquid.vi
H:\Corrected Experiment Program 2015 new\Labview Komo PhD Main Program liquid liquid Folder\Main Program PhD liquid liquid.vi
Last modified on 17/12/2015 at 11:12
Printed on 12/08/2016 at 20:32

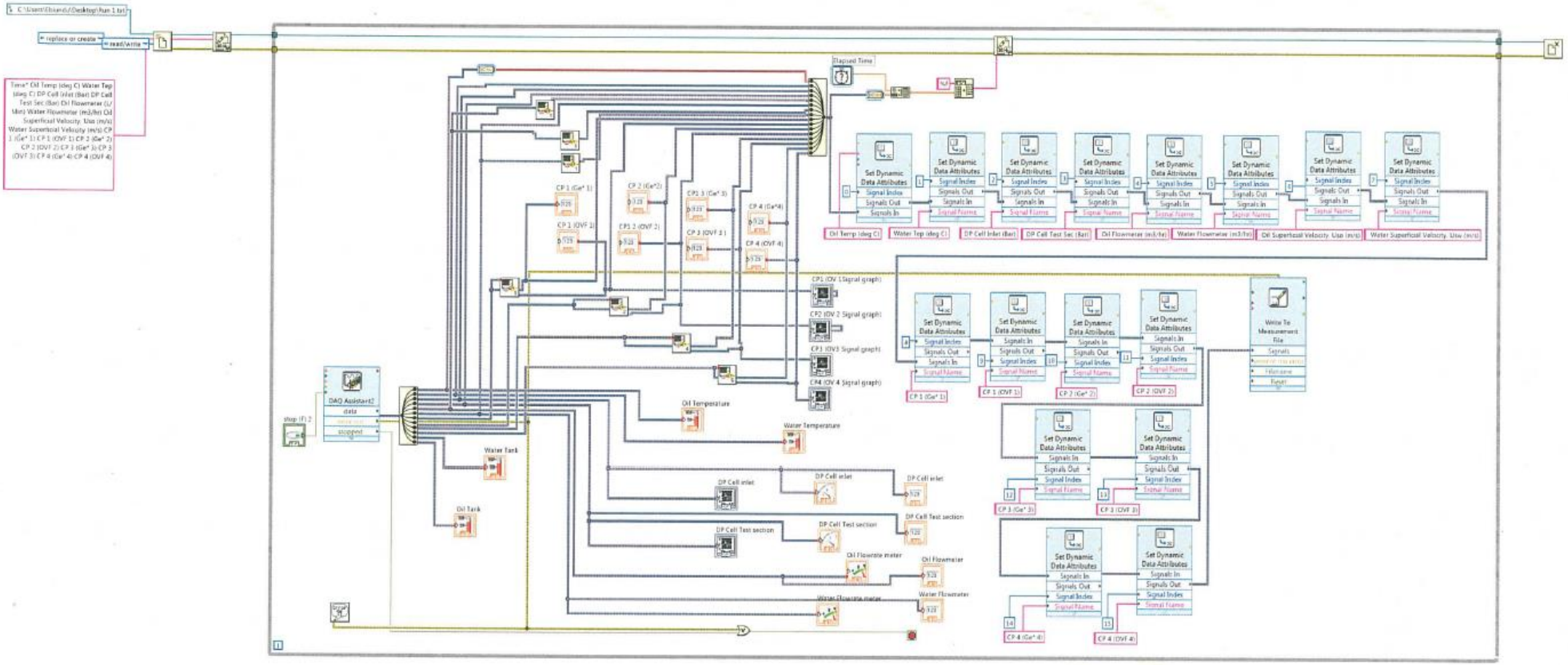

Figure 10 Labview program block diagram

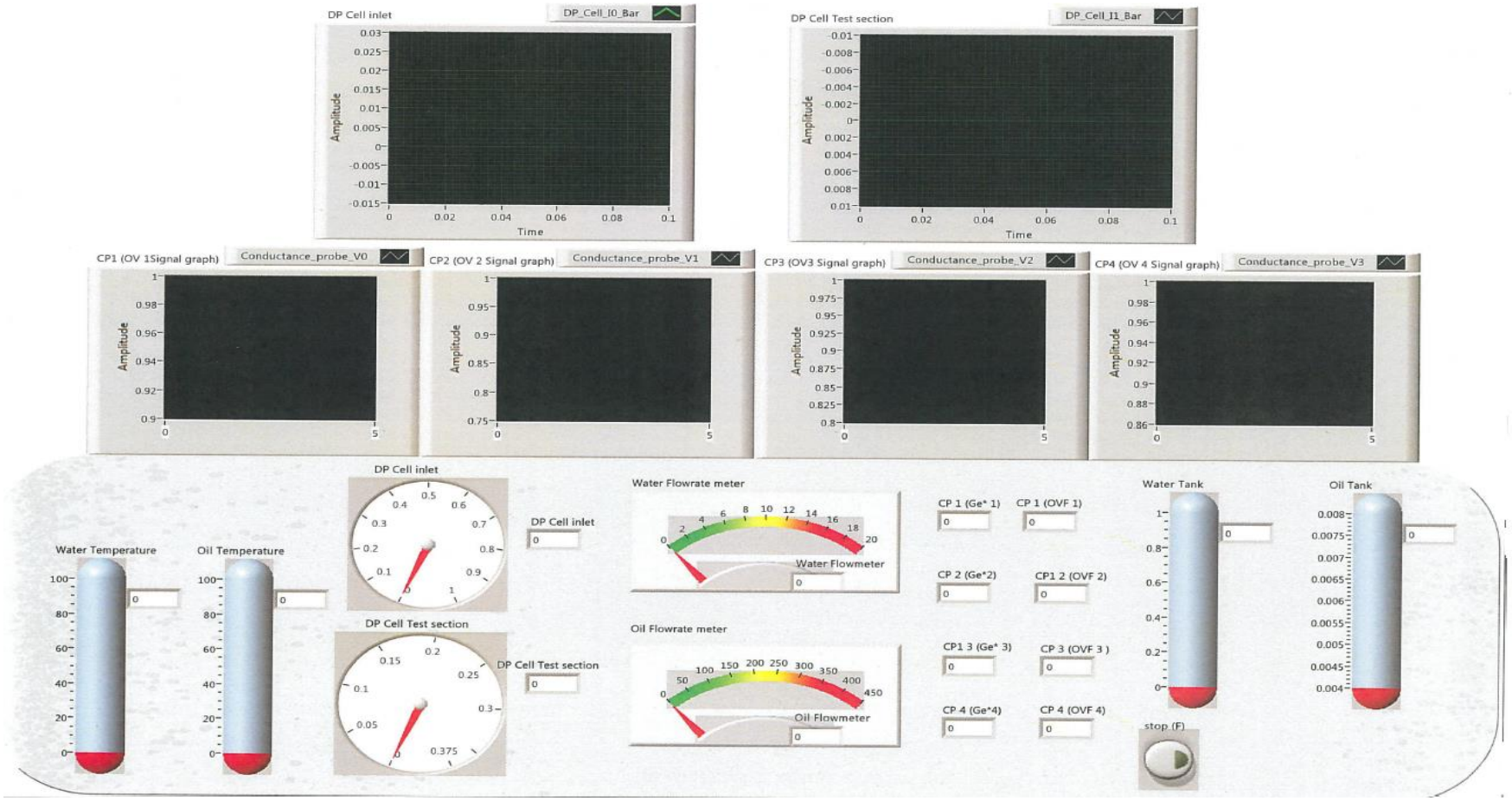

Figure 11 Labview front pane

APPENDIX G

Flow meter calibration certificates

a. M920 Electromagnetic flowmeter (Water flowrate)

MEATEST, spol. s r.o.
Železná 3, 619 00 Brno, Czech Republic
Tel: +420 543 250 886, 887
Fax: +420 - 543 250 890
E-mail: meatest@meatest.cz www.meatest.cz

Instruments for measurement and calibration

MEATEST

Calibration certificate No: 257141

Customer:	Techniquip
Manufacturer:	Meatest
Type:	M920
Serial number:	352411
DN (diameter):	50 mm
Range [m^3/h]:	20

Test conditions:

Test was done by a comparison with the standard flowmeters using volumetric method and flying start.

Standard flowmeters:	YOKOGAWA AXF 015G DN15, YOKOGAWA AXF 015G DN80
Meter position:	horizontal
Test medium:	clean water
Water temperature in test:	21°C ± 1°C
Uncertainty of test:	0.3%
Output setting during test:	10000 Hz/Qmax

Measured values:

Range in %	Deviation [%]
50	0.00
25	0.23
10	0.15

Date: 21.10.2014

MEATEST, spol. s r.o.
K. Ambrožová

MEATEST spol. s r.o.

b. TKM Truflo meter (Oil flowrate)

Riverside, Canal Road, Sowerby Bridge,
West Yorkshire HX6 2AY, England
Tel.: 01422 829920 Fax.: 01422 829921 Web: www.flowquip.co.uk

flowquip
flowmetering systems

Flowmeter Calibration Certificate

Certificate No. 9598

Customer	: Techniquip Ltd	**Date:**	: 04/08/2015
Meter	: TKM Truflo	**Job Ref.**	: 150804B
Size	: 50mm	**P.O. Nr.**	: T/13413/NU
Serial No	: 1444	**Cal. Fluid**	: Water
Flow Range	: 114 - 1140 L/min	**Fluid Temp.**	: 17.0 to 18.2 degC
K-Factor	: 9.3 (LITRES)	**Calibration Ref.**	: FQM001

Final 3 Flowrate points + 3 Repeats

Run Nr.	Flow Rate Lts/min	Meter under test Lts	Reference meter Lts	Deviation	Flow % Error
1a	1140 – 20mA	2034	2015.250	18.75	0.93
1b	1140.0	2038	2023.500	14.50	0.72
1c	1140.0	2027	2035.100	-8.10	-0.40
2a	570 – 12mA	1022	1022.450	-0.45	-0.04
2b	570.0	1012	1013.800	-1.80	-0.18
2c	570.0	1010	1012.950	-2.95	-0.29
3a	114.0	471	502.350	-31.35	-6.24
3b	114.0	482	517.350	-35.35	-6.83
3c	114.0	463	501.900	-38.90	-7.75

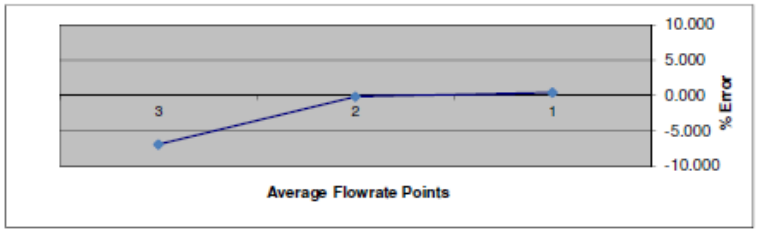

Calibration Traceable to UKAS Standards

Sales Director **Calibration Engineer**

Registered No. 1623009 ENGLAND & WALES

UNIVERSITY OF NOTTINGHAM - FACULTY OF ENGINEERING

Process and Risk Assessment Record

APPENDIX H

Any Change to Processes, Location or Circumstances, Requires a Review of the Current Process and Risk

Section 1: General Information

Assessment Number: *(Leave blank)* CEE – 2015-172	Location / Building and Room Number: *(where to process etc. will be carried out)* L3 Main Lab
Title of Process/Activity/Project/Experiment and/or Rig Name/Number: Liquid-Liquid horizontal flow sudden expansion rig	
Assessor Name: *(Person completing assessment record)* Ebiundu Komonibo Status: PhD Research student Signature: Date:	Academic/Line Manager/Other Supervisor Name: Dr Buddhi Hewakandamby /Prof Barry Azzopardi Status: Supervisor Signature: Date:
Laboratory Supervisor Name: Philip Bennett Signature: Date:	Area Safety Officer Name: Signature: Date:

Emergency Shut-Off Procedure: *(Include annotated digital photographs on a separate page)*

1. Turn off the water and oil pumps by pressing on the red stop buttons mounted on the panel near the workstation. The switches are shown in the photographs:

Date of Printing: 26 November 2017

2. Drain and empty liquid in test section after all experimental runs for each day by opening any of the differential pressure tap points to let air into the test section as shown in photograph.

3. Turn off Lasentec FBRM and also turn off main electrical supply if it is safe to do so.

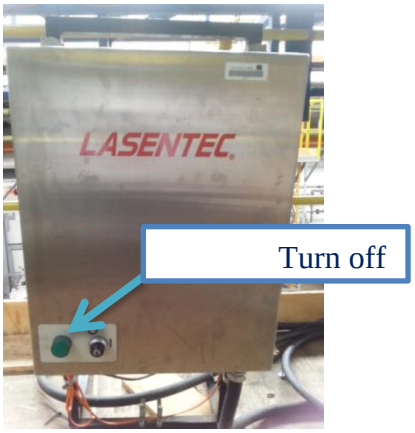

4. Check to ensure there are no leakages
5. Immediately notify the laboratory technicians in case of any major spillage.

IN CASE OF EMERGENCY CONTACT DETAILS:

Name: Ebiundu Komonibo Contact

email:enxek6@nottingham.ac.uk Mobile:

UNIVERSITY OF NOTTINGHAM - FACULTY OF ENGINEERING

Process and Risk Assessment Record

Physical conditions of rig/activity: Temperature (details): 5^0C to 40^0C Pressure (details): Relative humidity 50% (temp 40^0C) and 80% (31^0C), atmospheric pressure Electrical equipment Electricity in the presence of liquid Possible slippage hazard Laser class 1 Working at height	**Chemicals involved:** (*List any chemicals used in the process)* Scott's Tap water Silicone Oil (5cSt)
Environmental considerations: Non-toxic to environment but oil is special waste and must not enter drains- but generally will be recycled	**Special precautions for chemicals and experimental work:** Avoid spillage of chemicals Wear personal protective equipment, laboratory coat, safety glasses, safety footwear and disposable nitrile gloves while handling chemicals Avoid contact of chemicals with eyes, skin and body. Details of first aid measures and precautions attached Check glassware for cracks before use, handle with care Visual PAT check on electrical equipment before use Electrical equipment should be shielded/separated from possible liquid spillage Clear any spillage immediately Safety screen should be in place. Laser registered and assessed by Laser Protection Officer as class 1 and therefore requires no special protection.
Equipment details*:* *(identify tools and equipment to be used)* Electrical equipment Lasentec FBRM M500P Laser (Class 1)	**Details of any biological effects:** Risk of legionella. Change water regularly

Date of Printing: 26 November 2017

PC and Electronic box Conductance probes and Wire Mesh Sensor (WMS)	Cannot use biocides as it affects the experiment. The water tank is only sterilized initially with about 100ml of clear water algaecide to prevent future algae growth (See attached msds on application instructions)
Other notes: Operator must be authorised and trained to use this equipment. Display experiment in progress sign. First aid by exit door Fire extinguisher by exit door Spill kit- bag of clay granules in case of spillage Also see process assessment CEE-2013-161 and CEE-2013-162	

Section 2: Risk Assessment:

Section 3: Risk Assessment Check List

Section 4: Process Description, Operating Instructions, Method Statement, etc

LIQUID–LIQUID FLOW HORIZONTAL PIPELINE SUDDEN EXPANSION RIG

Objective: To determine the process of coalescence of droplets in liquid – liquid dispersions in Horizontal pipeline under turbulence in oil – water two phase system by measurements of minimum droplet sizes and drop size distribution and imaging techniques. Also to obtain flow parameters such as flowrates, flow patterns, liquid holdup, differential pressure drop, temperature etc of the system.

RIG OPERATING PROCEDURE

INITIAL PREPARATIONS:

1. Before installation of the Lasentec FBRM probe, an offline calibration and validation experiment is carried out using the PVC reference procedure. A PVC reference procedure is a means of verifying proper calibration of Lasentec FBRM instrumentation (See appendix A).

2. Make sure the different parts of the apparatus are properly connected and in good working condition and in the correct position. This includes the positioning of the Lasentec FBRM M500P probe at 45^{o} angle to the horizontal flow along the pipe test section and the four conductance ring probes.

3. Offline calibration of the conductance probes is also done before installation at the different positions (See appendix B). Ensure there are no leakages through the flanges on the horizontal pipe sections.

RIG START UP:

1. Check silicone oil and water tank levels to be sure there is sufficient liquid, about ¾ full in each of the three (3), tanks.

2. Ensure that the outlet valves (V11 and V15), on both pipelines from the silicone oil and water pumps are fully open. Always make sure the two oil tank inlet valves (V3 and V4) with water tank inlet valve V12 are fully open.

3. Ensure that the separator inlet valve, V2 (i.e. liquid mixture return from rig), is fully open.

4. Make sure that the Oil and Water bypass valves (V17 and V19), are fully open before starting the pumps.

5. The oil and water supply valves (V18 and V16) to the main rig, for both liquids remain closed before start.

6. Switch on the water and silicone oil pumps on the panel close to the pumps outside, in the tank farm area and also on the rig platform panel.

7. Close slightly bypass valves (V19 and V17), for both silicone oil and water to allow silicone oil and water flows respectively.

8. Adjust flows to desired input flowrate values by manipulating both the main valves for silicone oil V18 and water V16 into the rig and the bypass valves (V19 and V17), respectively. The desired flowrates can be checked on the display on both flowmeters.

9. Start taking measurements from all instruments after fixing desired flow of both liquids.

N/B: It is very important to monitor the tank levels of both silicone oil and water regularly, every 15mins to 30mins, depending on the flowrates being used during continuous operations of the rig. This action will avoid damaging the pumps by running them dry. A balance should be maintained between the water and silicone oil flowrates used and the liquid level in the discharge separator tank to allow enough water flow from the discharge separator to the water tank. Ensure the water tank level does not fall below ¼ during continuous operation. This can be achieved by regularly checking the oil and water tank levels on the front panel of the LabVIEW program.

RIG SHUT DOWN:

1. At the end of each run, the main rig valves (V18 and V16) for both silicone oil and water are closed temporarily, while leaving both bypass valves (V19 and V17), fully open. This will enable balancing of the liquid levels in the respective tanks for 5mins.

2. At the end of every session, close both main valves supplying silicone oil and water into the rig with bypass valves fully open.

3. Open the water valve V16 and allow water running for few minutes to flush the system and close it thereafter.

4. Switch off both silicone oil and water pumps from the panel on rig platform and outside in the tank farm.

ALGAE GROWTH PREVENTION IN WATER TANK AND RIG TEST SECTION

1. Check to ensure PH level of water is within range 7.2 – 7.6 always before adding clear water algaecide product.
2. Gradually pour about 100ml of the solution into the water tank initially and inject about 10ml into the test section through the pressure tapings provided on the rig. Allow water to run through the entire rig for about 5mins to ensure proper circulation. (see Clear water algaecide MSDS). **NOTE:** Do not add algaecide afterwards as it will affect the experiment.
3. This procedure can only be done occasionally to prevent any future algae growth if the rig is not in full use. It is advisable to ensure that the rig is run regularly, at least once a week, while in full operation.

Section 5: Photograph

Liquid – Liquid Horizontal Flow Pipeline Sudden Expansion Rig in L3 Main Laboratory, Process and Manufacturing Engineering, Faculty of Engineering, Nottingham.

Section 6: Flow diagrams: *(for the process – include labelling of items such as switches, valves, pressure gauges and other important items)*

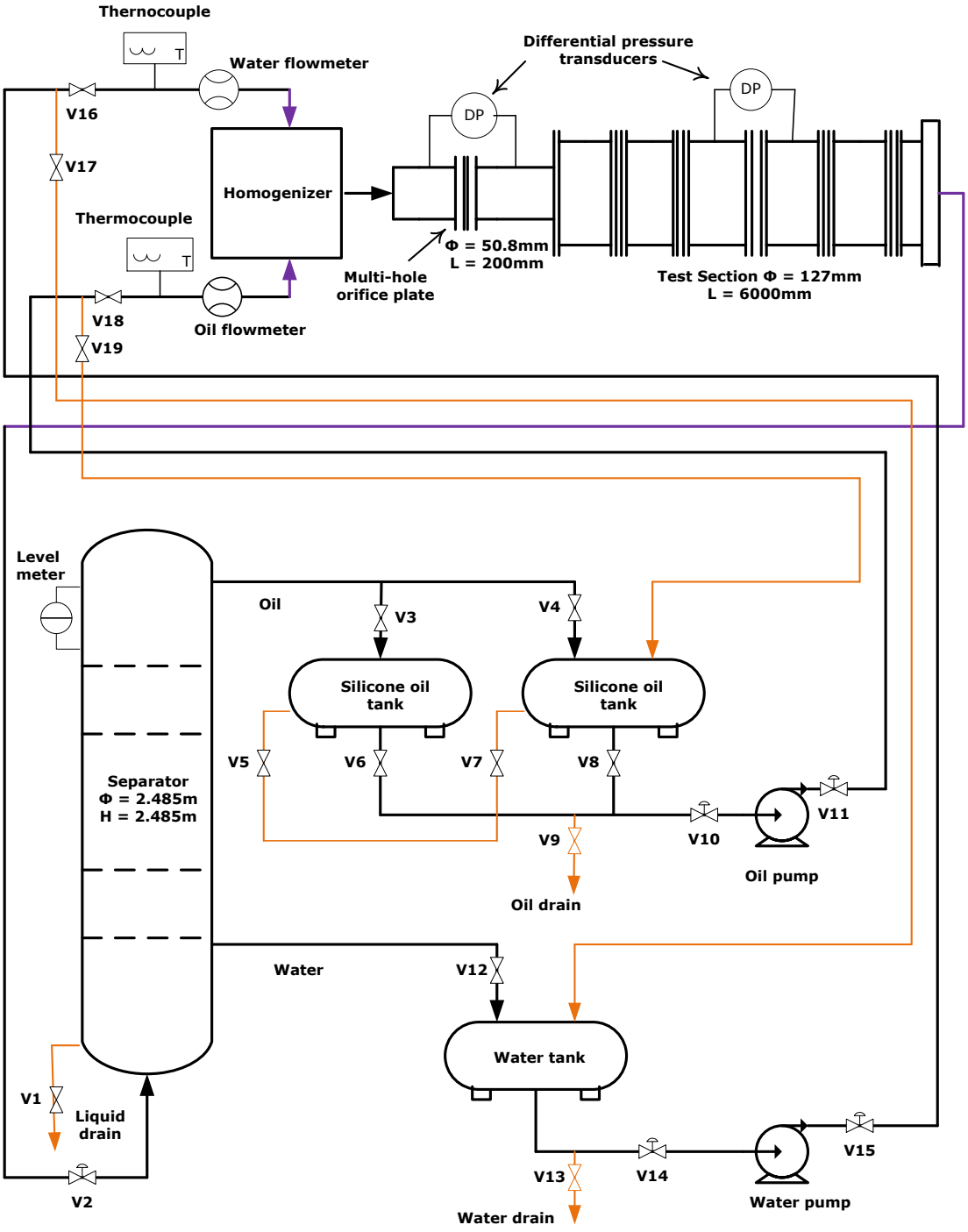

V15 – Water tank outlet valve	**V12- Water inlet valve from Separator tank**	**V16- Water supply valve to main rig**	**V17- Water bye -pass valve**
V11 – Oil tank outlet valve			
V3 & V4 – Oil inlet valves from Separator tank	**V2- Separator tank inlet valve**	**V18- Oil supply valve to main rig**	**V19- Oil bye - pass valve**

Section 7: Supplier's Literature (other than Material Safety Data Sheets)

(For example: Manuals, certificates, Calibration/conversion charts, Relevant graphs, etc.): As attached

Section 8. Control Of Substances Hazardous to Health (COSHH)

Name of chemical	Clear Water Algaecides (2,3-Dichloro – 1,4-naphthoquinone)
Synonyms	
CAS No	117-80-6
Name of assessor	Ebiundu Komonibo
Date	5th October 2015
Storage Room: L3 Main Lab	**Cabinet/category:** Acute toxicity, oral (category 4), Eye irritation (category 2), Skin irritation (category 2), Acute aquatic toxicity(category 1), Chronic aquatic toxicity (category 1). **Other:** L3 Main Lab (Store in cool and dry condition). Keep container tightly closed in a dry and well ventilated place
Hazard class and category	Classification according to EU Directives 67/548/EEC or 1999/45/EC Harmful if swallowed. Irritating to eyes and skin. Very toxic to aquatic organisms may cause long-term adverse effects in the aquatic environment.
Pictograms	
Signal word and hazard statements	Warning
Precautionary statements	Avoid breathing vapours/aerosols. Avoid release to the environment. If in eyes, rinse with for several minutes.

Precautions for safe handling	Normal measures for preventive fire protection. Avoid contact with eyes, skin and direct inhalation of chemical Keep container upright and seal carefully and store in a ventilated area.
Spillage	Slippery when spilt. Avoid accidents, clean up immediately. Clean spillages with water. For small spills soak up with inert absorbent material, sweep up and remove to a suitable, clearly marked container for SPECIAL WASTE disposal.
Disposal	Dispose of chemical substance in accordance with departmental waste procedure

Name of chemical	Clear Water Algaecides (2,3-Dichloro – 1,4-naphthoquinone)	
Synonyms		
CAS No	117-80-6	
Name of assessor	Ebiundu Komonibo	
Date	5th October 2015	
Storage	**Room:** L3 Main Lab	**Cabinet/category:** Acute toxicity, oral (category 4), Eye irritation (category 2), Skin irritation (category 2), Acute aquatic toxicity(category 1), Chronic aquatic

		toxicity (category 1),
		Other: L3 Main Lab (Store in cool and dry condition). Keep container tightly closed in a dry and well ventilated place
Hazard class and category		Classification according to EU Directives 67/548/EEC or 1999/45/EC Harmful if swallowed. Irritating to eyes and skin. Very toxic to aquatic organisms may cause long-term adverse effects in the aquatic environment.
Pictograms		
Signal word and hazard statements		Warning
Precautionary statements		Avoid breathing vapours/aerosols. Avoid release to the environment. If in eyes, rinse with for several minutes.
Precautions for safe handling		Normal measures for preventive fire protection Avoid contact with eyes, skin and direct inhalation of chemical Keep container upright and seal carefully and store in a ventilated area

Spillage	Slippery when spilt. Avoid accidents, clean up immediately Clean spillages with water. For small spills soak up with inert absorbent material, sweep up and remove to a suitable, clearly marked container for SPECIAL WASTE disposal.
Disposal	Dispose of chemical substance in accordance with departmental waste procedure

NOTE: The Clear Water Algaecide is a small mixture container composed of (2,3-Dichloro – 1,4-naphthoquinone), which is contained in 1litre plastic bottles as supplied by the company. (See attached msds).

Emergency Procedures

SPILLAGE/ACCIDENTAL RELEASE MEASURES:

(MSDS section 6)

FIRE-FIGHTING MEASURES:

(MSDS section 5)

FIRST AID MEASURES: *(MSDS section 4)*

In case of eye contact:

Wash thoroughly with running water.

In case of skin contact:

Immediately consult emergency services

In case of ingestion:

In case of inhalation:

Section 10: Training

Persons trained and authorised to operate the process/activity/project/experiment or equipment.

Name	Trained/Authorised by	Date
Dr Buddhika Hewakandamby	Supervisor	
Ebiundu Komonibo	Researcher and Lasentec (Mr Ian Haley – Mettler Toledo)	
Karl Gregg	Technician in charge	
Philip Bennet	Chief Technician	

Section 11: Declaration

To be signed by all personnel working to this process and risk assessment

I confirm that i have read this process and risk assessment and understand the hazards, risks and control measures associated with the process. I will not make any changes to the processes, location or circumstances, without completing and submitting a revised or new process and risk assessment.

Section 12: Review

This process and risk assessment must be reviewed on a regular basis if there are any changes to the processes, location or circumstances, or if it is deemed to be no longer suitable.